Study of Excited Ξ Baryons in Anti-Proton Proton Collisions with the $\overline{\text{P}}$ANDA Detector

Dissertation
zur
Erlangung des Doktorgrades (Dr. rer. nat.)
der
Mathematisch-Naturwissenschaftlichen Fakultät
der
Rheinischen Friedrich-Wilhelms-Universität Bonn

von
Jennifer Ingrid Pütz geb. Stoll
aus
Eschweiler

Bonn 2019

Angefertigt mit Genehmigung der Mathematisch-Naturwissenschaftlichen Fakultät der Rheinischen Friedrich-Wilhelms-Universität Bonn

1. Gutachter:	Priv. Doz. Dr. Albrecht Gillitzer
2. Gutachterin:	Prof. Dr. Ulrike Thoma

Tag der Promotion:	29.01.2020
Erscheinungsjahr:	2020

Abstract

Understanding the excitation pattern of baryons is indispensable for the understanding of non-perturbative QCD. Up to now only the nucleon excitation spectrum has been subject to systematic experimental studies, in contrast very little is known on excited states of double or triple strange baryons. A better knowledge of the baryon spectrum in the double and triple strange sector is however important to scrutinize the models developed using data on N^* and Δ states. In studies of antiproton-proton collisions, the $\overline{\mathrm{P}}$ANDA experiment is well-suited for a comprehensive baryon spectroscopy program in the multi-strange and charm sector.
For final states containing a $\Xi^- \, \overline{\Xi}^+$ pair, cross sections of the order of μb are expected, corresponding to production rates of $\sim 10^6/\mathrm{d}$ at a luminosity $L = 10^{31}\,\mathrm{cm}^{-2}\,\mathrm{s}^{-1}$. The present thesis focuses on excited Ξ states and investigates the possibility to reconstruct the reaction $\bar{\mathrm{p}}\mathrm{p} \rightarrow \overline{\Xi}^+ \, \Xi^*$ and its charged conjugate channel with the $\overline{\mathrm{P}}$ANDA detector. Furthermore, first steps towards a partial wave analysis of the $\overline{\Xi}^+ \, \Lambda \, \mathrm{K}^-$ and $\Xi^- \, \bar{\Lambda} \, \mathrm{K}^+$ final states are presented.

Zusammenfassung

Um die nicht-perturbative QCD zu verstehen ist ein weitreichendes Verständnis des Anregungsmusters der Baryonen notwendig. Bisher war nur das Nukleon-Anregungsspektrum Gegenstand systematischer experimenteller Untersuchungen, während nur wenig über die Anregungszustände von Baryonen, die aus mehr als einem Strange-Quark bestehen, bekannt ist. Ein besseres Verständnis des Baryon-Spektrums im Doppel- und Dreifach-Strange-Sektor is jedoch wichtig, um die Modelle, die anhand der Daten zu N^*- und Δ-Zuständen entwickelt wurden, zu überprüfen. In Studien zu Antiproton-Proton-Kollisionen eignet sich das $\overline{\mathrm{P}}$ANDA Experiment für ein umfassendes Baryon-Spektroskopie-Programm im Multi-Strange- und Charm-Sektor.
Für Endzustände, die ein $\overline{\Xi}^+ \, \Xi^-$ Paar enthalten, werden Wirkungsquerschnitte in der Größenordnung μb erwartet. Dies entspricht bei einer Luminosität von $L = 10^{31}\,\mathrm{cm}^{-2}\,\mathrm{s}^{-1}$ einer Produktionsrate von etwa $10^6/\mathrm{d}$. Die vorliegende Arbeit konzentriert sich auf angeregte Ξ Zustände und untersucht die Rekonstruktionsmöglichkeit der Reaktion $\bar{\mathrm{p}}\mathrm{p} \rightarrow \overline{\Xi}^+ \, \Xi^*$ und dessen ladungskonjugierten Kanal mit dem $\overline{\mathrm{P}}$ANDA Detektor. Des Weiteren werden die ersten Schritte im Hinblick auf eine Partialwellenanalyse des $\overline{\Xi}^+ \, \Lambda \, \mathrm{K}^-$ und des $\Xi^- \, \bar{\Lambda} \, \mathrm{K}^+$ Endzustandes präsentiert.

Contents

CHAPTER 1

Introduction

Already in ancient Greece, the first attempts were made to describe the processes in nature in a systematic way. Thus, the Greek philosopher Democritus postulated an indivisible object, called atom, which all matter in nature is composed of. Until the beginning of the 20th century, it was believed that the atom was the fundamental building block of matter. In the 1910s, by performing α particle scattering experiments, Rutherford showed that atoms have an internal structure.
Since this discovery above a century ago, the knowledge about the constituents of matter increased. Today, it is known that the fundamental particles of matter are composed of quarks and leptons. These fundamental particles, along with their fundamental interactions, are listed in the Standard Model of Particle Physics (SM). The SM was formulated and further developed in the second half of the 20th century by the effort of experimental and theoretical physicists. Even though the predictions of the SM are accurate, some phenomena can not be explained. One example is the mechanism how hadrons acquire their mass which is not given by the mass of their valence quarks. Therefore, comprehensive measurements of the particle properties are needed. These measurements can then be used to formulate and validate new models to deepen our understanding of the strong interaction.

The modern way to describe fundamental interactions is via quantum field theory. The quantum field theory describing the strong interaction is Quantum Chromodynamics (QCD), which is well probed at high energies. But in the low-energy regime many aspects are still not understood.
At low energies, the strong coupling constant has large values and therefore, perturbative QCD is no longer applicable. Up to now, there is no concept of using a first-principle theory such as QCD in the non-perturbative regime. Consequently, theoretical models have to be used which need experimental data to constrain the parameters used by the model. Instead of quarks and gluons, in the low-energy regime, the degrees of freedom are hadrons interacting via exchanging hadrons. Since hadrons are composed particles, they have internal degrees of freedom and thus an excitation spectrum. Therefore, two main types of studies are on the experimental side: reaction dynamics and spectroscopy. Studies on reaction dynamics focus on investigation of hadron production and hadron-hadron interactions, which will give insight into the dynamics of quarks and gluons. In studies on hadron spectroscopy the structure of hadrons is investigated. Both studies will provide data and hence the parameters for the models to describe the underlying physics. In this work the focus is on spectroscopy, in particular hyperon spectroscopy.
The spectra and properties of most hyperons are still not understood. A good opportunity to get access to these properties and spectra are $\bar{\mathrm{p}}\mathrm{p}$ induced reactions resulting in a baryon-antibaryon intermediate state. Here, it is possible to directly populate the intermediate states where one or both of these particles can be in an excited state. This intermediate state will in general give rise to final states with respect to the strong

interaction which consists of baryon-antibaryon pair plus one or more mesons. The particles produced in this state may further decay weakly or electromagnetically. The resonant baryon or antibaryon states are visible in the (anti-)baryon-meson combined system. If the resonances are sufficiently narrow, it is possible to access their mass and width directly. In addition, a Partial Wave Analysis (PWA) will give a possibility to access observables, which can not be determined directly, such as spin and parity quantum numbers.

The call for comprehensive measurements leads to a dramatic increase in experimental requirements. This, in turn, leads to the need of large-scale experiments, which partly reach the limit of what is technically feasible. The future Antiproton Annihilation at Darmstadt ($\overline{\mathrm{P}}$ANDA) experiment which will be located at the FAIR facility, currently under construction, is one of these large-scale experiments. $\overline{\mathrm{P}}$ANDA will be a multi-purpose detector to study antiproton-proton induced reactions at beam energies up to 15 GeV/c, corresponding to a center-of-mass energy of 5.5 GeV. Since experimental data on the excited $\bar{\Xi}\Xi$ states are poor, one of the main research topics at $\overline{\mathrm{P}}$ANDA is the study of hadrons with strange and also charm quark content.

The production of extra strange mesons is not needed for balancing the strangeness in the production of (multi-)strange baryons when using the $\bar{\mathrm{p}}\mathrm{p}$ entrance channel. Due to the expected cross section in the order of μb for final states containing a $\overline{\Xi}^{+}\ \Xi^{-}$ pair, it will be possible to collect high statistics data at $\overline{\mathrm{P}}$ANDA. Furthermore, it is possible to estimate the production cross section of $\overline{\Xi}^{+}\ \Xi^{*}$ by using the available $\bar{\mathrm{p}}\mathrm{p} \rightarrow \bar{Y}Y$, $\bar{Y}Y^{*}$ and $\bar{Y}^{*}Y^{*}$ data on single strange hyperons and comparing their ground state and excited state production cross sections.

This thesis presents a feasibility study for the reconstruction of the reaction $\bar{\mathrm{p}}\mathrm{p} \rightarrow \overline{\Xi}^{+}\ \Lambda\ \mathrm{K}^{-}$ as well as its charge conjugate channel at $\overline{\mathrm{P}}$ANDA. The study includes also Ξ^{-} and $\overline{\Xi}^{+}$ resonances, i.e. the $\Xi\,(1690)^{-}$ ($\overline{\Xi}\,(1690)^{+}$) and $\Xi\,(1820)^{-}$ ($\overline{\Xi}\,(1820)^{+}$) states. Furthermore, first steps towards a PWA of the three-body final state $\overline{\Xi}^{+}\ \Lambda\ \mathrm{K}^{-}$ are shown.

Chapter 2 gives an overview on the Standard Model of Particle Physics (SM) and an introduction to the strong interaction.

In Chapter 3, the FAIR facility with its planned scientific program and accelerator facility is introduced.

After that, the $\overline{\mathrm{P}}$ANDA experiment is introduced in Chapter 4. In the first part of the chapter, an overview on the physics program at $\overline{\mathrm{P}}$ANDA is given. Subsequently, the detector concept will be explained, before a short introduction to the PandaRoot simulation and analysis is given.

The main topic of this thesis, the study of excited Ξ baryons, is presented in Chapter 5. Here, investigations on a feasible reconstruction of the process $\bar{\mathrm{p}}\mathrm{p} \rightarrow \overline{\Xi}^{+}\ \Xi^{*}$ within $\overline{\mathrm{P}}$ANDA are shown. Beside the simulation and reconstruction of the event topology, the resolution and the efficiency for the reconstruction is obtained and a study of background is performed.

In Chapter 6, the first steps towards a PWA for the $\overline{\Xi}^{+}\ \Lambda\ \mathrm{K}^{-}$ final states as well as for the charge conjugate final state are presented. The chapter includes also a concise introduction to the formalisms and methods of a PWA.

Chapter 7 concludes the result of this thesis.

CHAPTER 2

Physics Background

2.1 Standard Model of Particle Physics

The SM is the theoretical description of the fundamental forces including three of the four known forces: the electromagnetic, the weak and the strong force. In addition, it classifies all known elementary particles. The formulation of the SM was finalized in the 1970s. Since its completion, it has been tested by various experiments which finally confirmed the three remaining particles: the top quark in 1995, the tau neutrino in 2000 and the Higgs boson in 2012.
The elementary particles included in the SM can be divided into two groups based on their spin. Particles with half-integer spin are called fermions, while particles with integer spin are called bosons. 12 fermions as well as their antiparticles are included in the SM. The fermions can be grouped into three families of quarks and leptons, but only the members of the first family are the buildings blocks of stable matter. The bosons are the mediators of the three fundamental interactions. Table 2.1 and Table 2.2 summarize

Table 2.1: Fermion properties for the three generations of quarks and leptons. Data from [1].

	1st Generation	2nd Generation	3rd Generation
	Quarks		
Symbol	u	c	t
Charge[e]	+2/3	+2/3	+2/3
Mass[GeV/c^2]	$2.3 \cdot 10^{-3}$	1.275	173.21
Symbol	d	s	b
Charge[e]	−1/3	−1/3	−1/3
Mass[GeV/c^2]	$4.8 \cdot 10^{-3}$	$95 \cdot 10^{-3}$	4.18
	Leptons		
Symbol	e	μ	τ
Charge[e]	−1	−1	−1
Mass [MeV/c^2]	0.511	105.66	1776.82
Symbol	ν_e	ν_μ	ν_τ
Charge[e]	0	0	0
Mass[MeV/c^2]	$< 2 \cdot 10^{-6}$	< 0.19	< 18.2

Table 2.2: Overview on the boson properties listed in the SM. Data from [1].

Boson	Mass	Charge	Associated interaction
γ	$< 1 \cdot 10^{-18}$ eV	0	electromagnetic
gluon	0	0	strong
$W^{\pm}$	80.39 GeV/c^2	± 1	weak
Z	91.19 GeV/c^2	0	
H	125.7 GeV/c^2	0	higgs

the properties of fermions and bosons, respectively.
The mathematical description of the SM is provided by a renormalizable Quantum Field Theory (QFT). It applies the successful basic concept for the description of the Quantum Electrodynamics (QED)[2] to the description of the other fundamental forces. These theories require a Lagrangian which is invariant under local transformation. This type of field theory is called *gauge theory* and its invariant transformation is called *symmetry*. The SM is defined by the local SU (3) × SU (2) × U (1) symmetry. The gauge group SU (2)×U (1) is the basis of the electroweak interactions combining the description of the electromagnetic and the weak interactions [3]. A massless particle, the photon, and the $W^{\pm}$, Z bosons are included in this theory. The mass of the bosons prevents the theory from being renormalizable. However, the introduction of spontaneous symmetry breaking included with the Higgs mechanism [4] restores the renormalizability. The SU (3) is the symmetry group of the QCD describing the strong interaction. Because the physics simulations used for this thesis concentrate on strongly interaction particles, the following section will focus on the strong interaction.

Although the SM makes accurate predictions, some phenomena can not be explained by the model. For example, the baryon asymmetry which is the imbalance between the baryonic matter, like protons and the anti-baryonic matter (e.g. antiprotons) in the universe is not described. Furthermore, there is no room left in the SM for dark matter particles. Neutrino oscillations and the non-zero masses of neutrinos are also not included in the SM.

2.2 Strong Interaction

The mediator particle of the strong interaction is the gluon which both couples to the color charge and carries a color charge. Quarks and gluons are the only elementary particles carrying color charge. As already mentioned in Section 2.1, the theory describing the strong interaction is the QCD which is based on the same principles as QED. Many researchers contributed to QCD, which led to two Nobel Prizes in this research field. Murray Gell-Mann received the Nobel Prize in 1969 [5] for the contribution to the classification of particles and their interactions. The second prize was given to Gross, Politzer and Wilczek in 2004 [2] for the discovery of asymptotic freedom in strong interactions.
The strength of the strong interaction is given by the coupling constant α_s. According to [6], α_s can be expressed in terms of the squared four-momentum transfer Q^2:

$$\alpha_s\left(Q^2\right) = \frac{\alpha_s\left(\mu^2\right)}{1 + \frac{\alpha_s(\mu^2)}{12\pi}\left(33 - 2n_f\right)\log\left(Q^2/\mu^2\right)} \tag{2.1}$$

where n_f is the number of flavors in the given energy region μ. Equation (2.1) implies a decreasing α_s with increasing momentum transfer. The property of small α_s values for high Q^2 is called *asymptotic freedom*. Several experimental determinations of α_s have been performed. The current status is shown in Figure 2.1. To make the obtained results from the different experiments comparable, a common reference value at the Z boson mass $m_z = 91.2\,\mathrm{GeV/c^2}$ is used [1]:

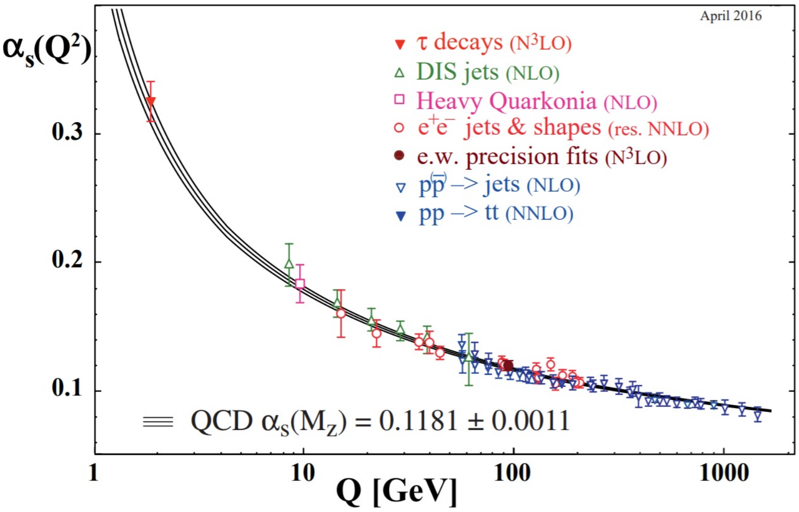

Figure 2.1: Measurements of the coupling constant α_s as a function of the energy from different experiments. The used degree of QCD perturbative theory for the extraction of α_s are NLO (next-to-leading order), NNLO (next-to-next-to-leading order), res. NNLO (NNLO matched with resumed next-to-leading logs), and N^{3}LO (next-to-NNLO), and are indicated in brackets, respectively. Image from [1].

$$\alpha_s\left(m_z\right) = 0.1181 \pm 0.0011 \tag{2.2}$$

With decreasing Q^2 the coupling constant α_s increases such that below a certain Q^2 value perturbative QCD is not applicable anymore. This critical energy scale characterizing this transition is denoted by Λ_{QCD}. The square of Λ_{QCD} is given by [6]

$$\Lambda^2_{\mathrm{QCD}} = \mu^2 \exp\left[\frac{-12\pi}{\left(33 - 2n_f\right)\alpha_s\left(\mu^2\right)}\right]. \tag{2.3}$$

Therefore, Equation (2.1) can be written as

$$\alpha_s\left(Q^2\right) = \frac{12\pi}{\left(33 - 2n_f\right)\log\left(Q^2/\Lambda_{\mathrm{QCD}}\right)}. \tag{2.4}$$

At high energies where α_s is small, QCD can be described by using perturbation theory techniques, also called perturbative QCD. The perturbation theory is used if a problem cannot be solved exactly, but by adding "small" correcting terms to the mathematical description. An approximation to the solution is reached by an expansion in terms proportional to α_s^n. Depending on the computational power, the expansion is cut. In principle, this technique allows to achieve any precision. Below energies of about 1 GeV perturbative QCD cannot be applied anymore. Therefore, other mathematical approaches are needed to describe the theory of the strong interaction. Actually, two approaches are well established.

One of them is the Lattice Quantum Chromodynamics (LQCD) [7] which solve the non-perturbative QCD by using numerical simulations. These simulations require a huge amount of computational power [1]. During the last decades, LQCD made big progress and impressing results have been achieved for hadron spectroscopy. The second approach utilizes the confinement for low energies. This effective field theory was proposed by Weinberg[8] and is called *chiral perturbation theory*.
The discussion above implies that it is possible to divide the strong interaction into two areas: the high-energy regime where the interaction is described by the perturbative theory and the low-energy regime. While QCD is well tested for high energies, there are many aspects in the low-energy regime that are not yet understood. For example: What are the effective degrees of freedom in the baryon excitation spectrum?[9]
In this section, the strong interaction for the two different energy regimes are discussed, beginning with the well-known high energy regime, followed by the low-energy regime.

2.2.1 At High Energies

The region well above 1 GeV is the regime of perturbative QCD. A large number of experimental probes were invented to reach the energies where the perturbation theory is applicable. One of the most prominent techniques to investigate the structure of the nucleon is to scatter a beam of electrons off it[6]. The first experiments using high-energy electrons were performed in 1968 at the Stanford Linear Accelerator Center (SLAC)[10]. The determined results of these *deep inelastic scattering* (DIS) experiments reminiscent of the results from Rutherford's experiments [11]: most of the incoming electrons pass through, while a small number is scattered back implying that the proton charge is concentrated in point-like constituents called partons. In 1961, Gell-Mann introduced the Eightfold Way [12] to describe the symmetries of baryons and mesons. This description was the basis for the development of the quark model. The introduction of QCD connected both, DIS and the quark model. In case of the proton, the constituents could be identified as three quarks. But, the Pauli principle forbids the existence of two identical fermions in the same quantum state, like it is the case, e.g. for Δ^{++} with quark content (uuu). Since its spin angular momentum is $J^P = 3/2$ [1], all quark spins have to be aligned, meaning that the spin quantum numbers are the same for all three u quarks. Since in addition with three u quarks, all quarks have the same flavor, the Δ^{++} would have to consist of three fermions being in an identical quantum state. The introduction of the color charge as a quark quantum number solved this conflict with the Pauli principle. There are different types of color charge: red, green, blue and their anti-colors antired, antigreen, and antiblue. The types of color charge add up to a total color charge of zero and thus form a colorless or "white" object.

As shown in Section 2.1, there are six quarks, u,d,s,c,b, and t, as well as their antiquarks. The light quarks, u,d, and s, are represented in the SU(3) symmetry group and form a triplet with spin 1/2 and baryon number 1/3. This triplet consists of an isospin doublet (u and d), with electromagnetic charge 2/3 for the u quark, $-1/3$ for the d quark and strangeness $S = 0$, and a singlet (s) with electromagnetic charge $-1/3$ and strangeness $S = -1$. By convention, the sign of the flavor quantum number (S,C,B) is the same as the sign of the charge of the respective quark. Table 2.3 summarizes the quantum numbers for the three light quarks. At high Q^2, the mass splitting between the s and the u and d quarks are negligible, as one can e.g. see in pp collisions atLarge Hadron Collider (LHC) since the created $s\bar{s}$ pairs are almost as abundant as $u\bar{u}/d\bar{d}$ pairs. The representations of quarks and antiquarks in SU(3) due to the sign change of B, S and I_3 are not identical, resulting in the two multiplets shown in Figure 2.2. The multiplets are in the Y-I_3 plane, where $Y = B + S_q$ denotes the hypercharge, an additive quantum number which is related to the electromagnetic charge $Q = I_3 + \frac{Y}{2}$ with quark isospin I_3. Assuming a perfect symmetry, the particles within an SU(3) multiplet would have the same mass in addition to the same spin-parity. In other words, they would be degenerate. But this degeneracy is removed by the breaking of flavor symmetry caused by the fact that the quark masses are not equal. However, this does not explain, why there are particles, like for example ρ and π, having the same quark content and are both in the ground state, but do not have the same mass [11]. The difference in the mass of these particles is assigned to a spin-spin interaction which is the QCD analog to the hyperfine splitting in the hydrogen ground state.

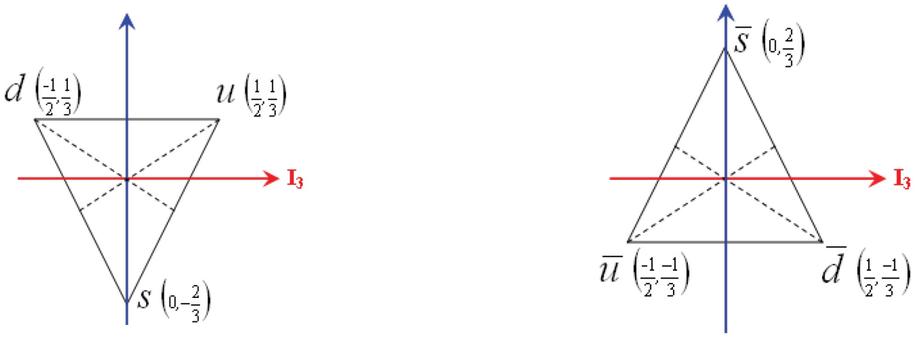

(a) Quark multiplet.

(b) Antiquark multiplet.

Figure 2.2: The SU(3) multiplets for quarks and antiquarks. Hypercharge and Strangeness are connected by $Y = B + S$. Adapted from [13].

2.2.2 At Low Energies

As already mentioned, below energies of 1 GeV the perturbative QCD cannot be applied anymore. Certain regions in the non-perturbative regime are not well investigated, e.g. the (multi-)strangeness sector. The energy scale for strangeness production, which is limited by the mass of the strange quark $m_s = 95\,\text{MeV}$, is close to Λ_{QCD}. Therefore, the production of strange hyperons will probe QCD in the non-perturbative regime.

In general, the bound states based on the strong interaction are called hadrons. According to their quark content, hadrons can be divided into two groups. The first group consists of a quark-antiquark pair, called mesons, and the second group is formed by three quarks or antiquarks, called baryon or antibaryon, respectively. Since in this thesis the focus is on strange baryons, a more detailed overview only on bound states of the light quarks u,d, and s are given. Baryons with heavy quark c, and b content, can be formed analogue to the strange baryons by a replacement of the strange quark. Since the lifetime of the t quark is short, it is likely that no bound state hadron containing a t quark exists [1].
The relevant quantum numbers for hadrons with light quark content are the total electromagnetic charge Q, the total angular momentum J, and the parity P. The total angular momentum J is the sum of the spin S and the orbital angular momentum L. Particles with strange quark content also have strangeness. To differentiate between the strangeness and the spin of a particle, the strangeness is denoted by S_q in the

Table 2.3: Quantum numbers of the u,d, and s quarks.

	S	B	S_q	Q	Y	I_3
u	1/2	1/3	0	2/3	1/3	1/2
d	1/2	1/3	0	−1/3	1/3	−1/2
s	1/2	1/3	-1	−1/3	−2/3	0

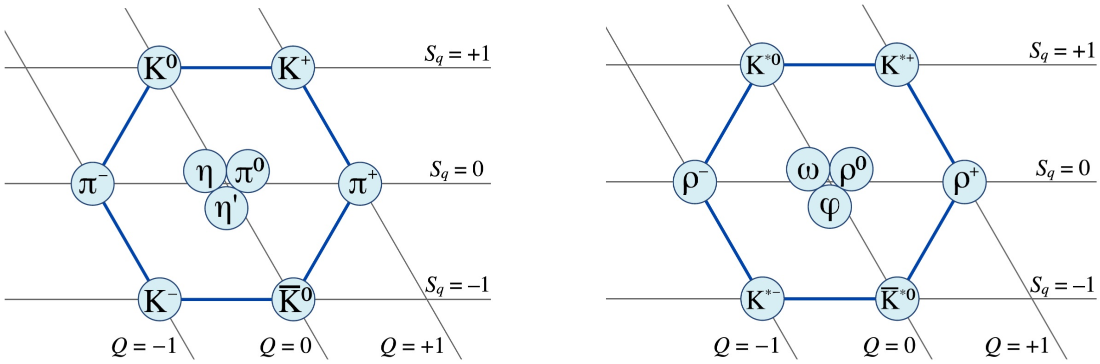

(a) Meson nonet for $J = 0$.

(b) Meson nonet for $J = 1$.

Figure 2.3: Ground state mesons with light quark content, ordered by the isospin z component I_3 along the x axis and strangeness S_q along the y axis. Adapted from [14–16].

following.

It is also possible to form more complex combinations. These combinations are investigated in experimental and theoretical researches, and described in Section 4.1.

For mesons, the quark spins can be antiparallel, forming a $S = 0$ state, or parallel forming a $S = 1$ state. Focusing only on the ground states, $L = 0$, for mesons, this leads to two possible total angular momenta: $J = 0$ and $J = 1$. In case of $J = 0$ quark-antiquark pairs within the u,d, and s flavor sector are arranged in a pseudoscalar nonet, while the $J = 1$ configuration gives a vector nonet. Both isospin nonets are shown in Figure 2.3, respectively.

Baryons consisting of u, d, and s quarks are also grouped into multiplets based on SU(3) flavor symmetry. The wave function of baryons is composed of several parts: a spatial part, describing the orbital degree of freedom in configuration space, a spin part, a flavor part describing the configuration in flavor space, and a color term.

$$\psi = \psi\,(\text{space})\ \phi\,(\text{spin})\ \xi\,(\text{flavor})\ \chi\,(\text{color}) \tag{2.5}$$

The total wave function has to be antisymmetric with respect to the permutation of any two quarks. In the ground state, the spatial wave function has to be symmetric since for $L = 0$, there is no angular dependence [11]. However, the spin state is either antisymmetric for $J = 1/2$ or symmetric for $J = 3/2$, while the color wave function is always antisymmetric. An antisymmetric color wave function implies that the rest of the total wave function in Equation (2.5) is symmetric. For the flavor, there are 27 possibilities which can be reorganized into symmetric, antisymmetric, and mixed symmetry combinations. This requires that the light quark baryons belong to the multiplets shown on the right side of

$$3 \otimes 3 \otimes 3 = 10 \oplus 8 \oplus 8 \oplus 1 \tag{2.6}$$

According to Equation (2.6), they are forming an SU(3) flavor octet ($J = 1/2$) and an SU(3) flavor decuplet ($J = 3/2$) as shown in Figure 2.4.

Up to now, all baryons included in the ground state multiplets are known, while the information on the excited states are poor or even missing. The comparison of the experimentally confirmed excited states in the non-strange sector and the predictions from theoretical models, shown in Figure 2.5, indicates several discrepancies. There are two main problems [1]:

- the N(1440)$1/2^+$ and the Δ(1600)$3/2^+$ appear lower than the negative parity states (N(1535)$1/2^-$ and Δ(1700)$3/2^-$) and lower than predicted by the theoretical models

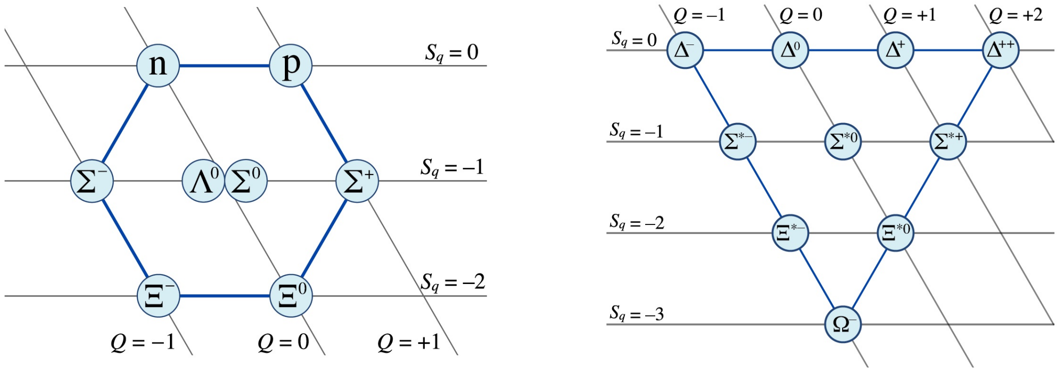

(a) Baryon octet for $J = 1/2$.

(b) Baryon decuplet for $J = 3/2$.

Figure 2.4: Ground state baryon octet and decuplet, ordered by the isospin z component I_3 along the x axis and strangeness S_q along the y axis. Adapted from [14, 17, 18].

- the energies of negative parity Δ states in the $N = 3$ band ($\Delta(1900)1/2^-$, $\Delta(1940)3/2^-$, and $\Delta(1930)5/2^-$) are too low.

In addition, more states are predicted than observed. This phenomenon is also called "missing resonances" problem [20].

Baryons containing at least one strange or heavier quark are called *hyperons*. Like all baryons, hyperons are fermions with half-integer spin. In general, the ground states decay weakly to lighter baryons, since the strong and the electromagnetic interaction conserve strangeness. Therefore, the life time of Λ, $\Sigma^{\pm}$, Ξ^0, Ξ^- and Ω^- hyperons is in the order of 10^{-10} s which corresponds to a decay length of $\mathcal{O}$(cm). This leads to an unambiguous signature of hyperons in the detector.

The hyperon-antihyperon pair production in $\bar{p}p$ collisions will provide important insight into strange and charm production. Since $\bar{p}p$ consists of light quarks, processes where the light quarks are replaced by heavier quarks are necessary.

Adding a c quark to the light quarks will extend the SU(3) flavor symmetry to SU(4). An illustration of the SU(4) multiplets is shown in Figure 2.6. Their bottom levels show an SU(3) octet and a SU(3) decuplet, respectively. Figure 2.7 shows the actual spectrum of the lowest states for the Λ, Σ, Ξ and Ω hyperons compared to the predictions from theoretical models. The figure shows indications that the predictions from theory and the experimental data do not always agree. Nevertheless, for the lower states of the hyperons experimental data is available, while data for higher states is poor or non-existent [1]. In many cases the quantum numbers are missing. Since the focus of this thesis is on Ξ resonances, the Ξ states will be discussed in detail.

The Ξ is the lowest state of double-strange baryons with quark content (uss) in case of Ξ^0 and (dss) in case of Ξ^-. Both, the Ξ^0 and the Ξ^-, decay weakly by converting a strange quark into u or d quark. In both cases, a Λ baryon is predominantly produced which decays again weakly. The corresponding branching ratio for Ξ^0 is BR($\Xi^0 \rightarrow \Lambda + \pi^0$)= 99.5 % and for Ξ^- is BR($\Xi^- \rightarrow \Lambda + \pi^-$)= 99.887 %[1]. Due to this decay sequence, the Ξ baryon has two well-separated decay vertices which gives the name *cascade baryon*. Figure 2.8 sketches a typical process for $\bar{p}p \rightarrow \overline{\Xi}^+ \Xi^-$.

Ξ states are experimentally not well investigated. The experimental status for Ξ resonances is shown in Table 2.4. Mostly, the available information is from bubble chamber experiments with small number of events. Only one experiment at the European Organization for Nuclear Research (CERN) has observed

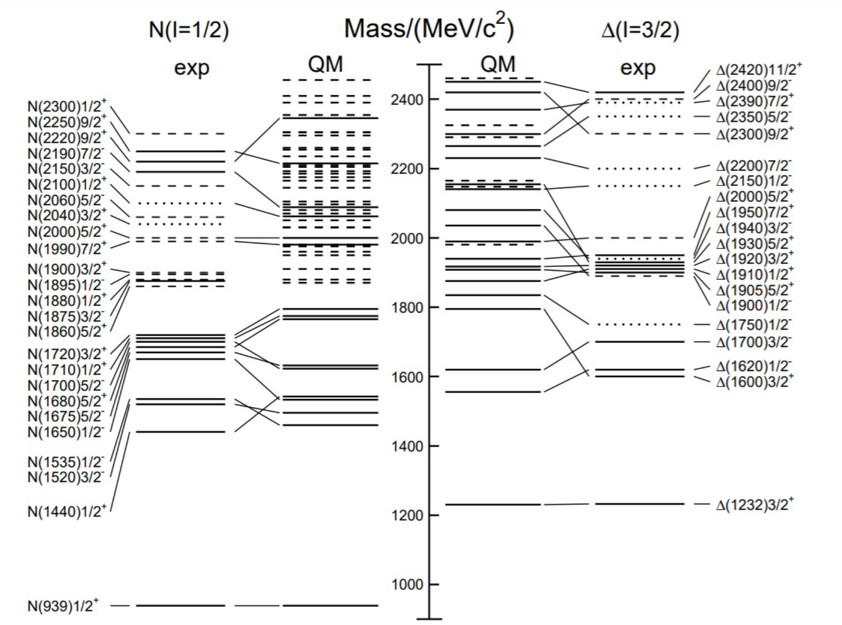

Figure 2.5: The nucleon excitation spectrum. The comparison between the excited states identified in experiments and the predicted states from quark model calculation is shown. On the left hand side the isospin $1/2$ N-states and on the right hand side the isospin $3/2$ Δ states are shown. The experimental results are shown in the column "exp" where full lines indicate three- and four-star, dashed lines two-star, and dotted lines one-star resonances. The predictions of the Quark Model [19] are listed in the column labeled as "QM" where full lines denote tentative assignments to observed states, and dashed lines non-observed counterparts. Image from [1].

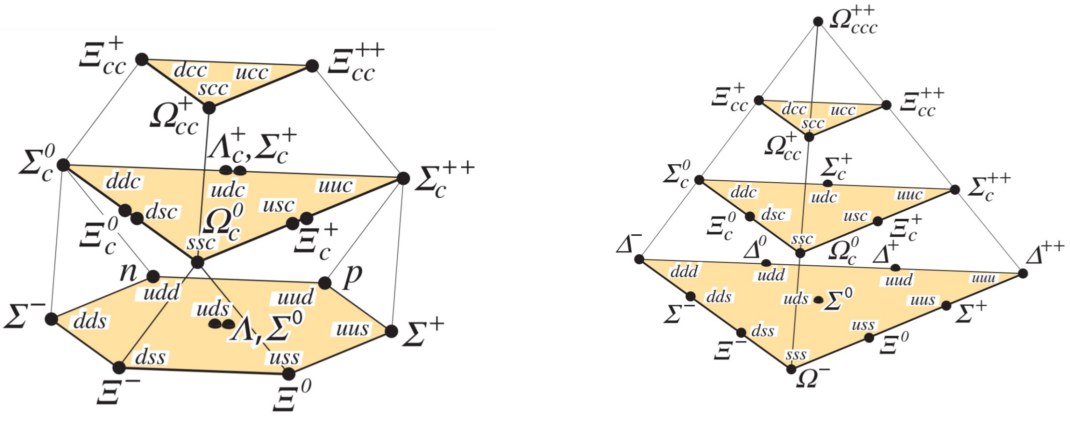

(a) (b)

Figure 2.6: SU(4) multiplets for baryons consisting of u, d, s, and c quarks. Subfigure (a) shows the 20-plet with an SU(3) octet and Subfigure (b) shows the 20-plet with an SU(3) decuplet. Images from [1].

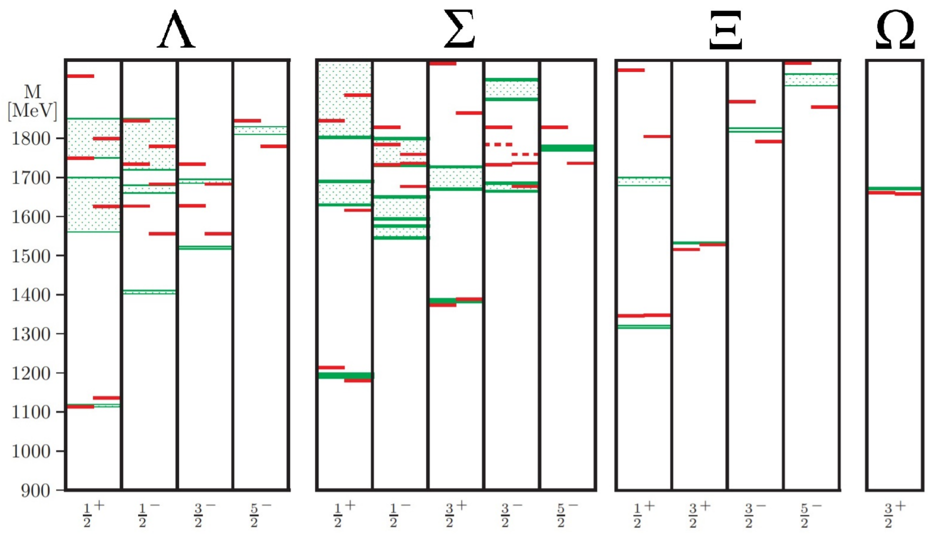

Figure 2.7: Hyperon Spectrum for the lowest states of Λ, Σ, Ξ and Ω. The measured results and their uncertainties are shown as green areas and the theoretical prediction is shown as red line. Two different theory models are used: one gluon exchange (left) and Goldstone boson exchange (right). The dashed red lines in the Σ spectrum are predicted eigenstates for $J^P = 3/2^-$ without experimental equivalent. Image from [21].

three events for the reaction $\bar{p}p \rightarrow \bar{\Xi}^{+}\,\Xi^{-}$ with a cross section of $\sigma = (2 \pm 1)\,\mu$b [23].
For the theoretical description of the Ξ production and for the estimation of the production cross section, different approaches are used. The approaches differ by the model used for the double strangeness production mechanism. The first and most naive approach is the double gluon process used by [24]. As shown in Figure 2.9(a) a simultaneous annihilation of two uū-pairs is assumed. Both uū-pairs are emitting a gluon which produces a ss̄-pair. The annihilation of a quasi-bound state of two quarks, also called diquark, inside the hadron is used by [25]. An illustration of the diquark annihilation is shown in

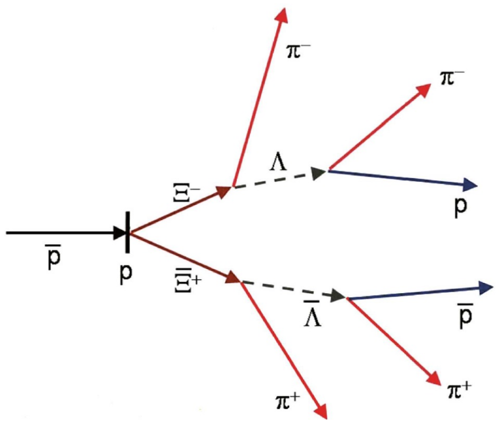

Figure 2.8: Sketch of a typical process for $\bar{p}p \rightarrow \bar{\Xi}^{+}\,\Xi^{-}$ with the predominant decays according to [1]. The solid lines indicate charged particles, while the dashed lines indicate neutral particles. Image from [22].

Table 2.4: Experimental status of Ξ Resonances. The status is given as poor(*), fair(**), likely(***) and well explored(****). Data from [1].

Particle	J^P	Status
$\Xi(1318)$	$1/2^+$	****
$\Xi(1530)$	$3/2^+$	****
$\Xi(1620)$		*
$\Xi(1690)$		***
$\Xi(1820)$	$3/2^-$	***
$\Xi(1950)$		***
$\Xi(2030)$		***
$\Xi(2120)$		*
$\Xi(2250)$		**
$\Xi(2370)$		**
$\Xi(2500)$		*

Figure 2.9(b). For the third approach a simplified picture of exchanging mesons can be used. The hadron exchange mechanism is justified with the low energy regime. The calculations are done by using either a pseudoscalar meson exchange, i.e. a K, or a vector meson exchange, e.g. K^*, to describe the conversion of a proton into an intermediate baryon with one strange quark constituent. This intermediate baryon is then converted by a second meson exchange into a Ξ baryon, see also Figure 2.9(c).

Up to now, there are no predictions on the production cross section for the excited Ξ states in $\bar{p}p$ processes. Comparing the measurements [26] and the theoretical predictions [24] for other excited baryons shows, for example, that the measured cross section for $\bar{p}p \rightarrow \bar{\Sigma}\Sigma^*$ of $\sigma_{\text{exp}} = (9 \pm 2)\ \mu\text{b}$ is in the same order of magnitude as the cross section of the corresponding ground state $\sigma_{\text{exp}} = (8 \pm 4)\ \mu\text{b}$. Therefore, the cross section for $\bar{p}p \rightarrow \overline{\Xi}^+\ \Xi^*$ is estimated to be in the order of $\sigma = 1\ \mu\text{b}$.

As mentioned before, more complex combinations of antiquark and quarks are possible, for example baryons containing more than three quarks or antiquarks, also called exotic baryons. Their existence, as

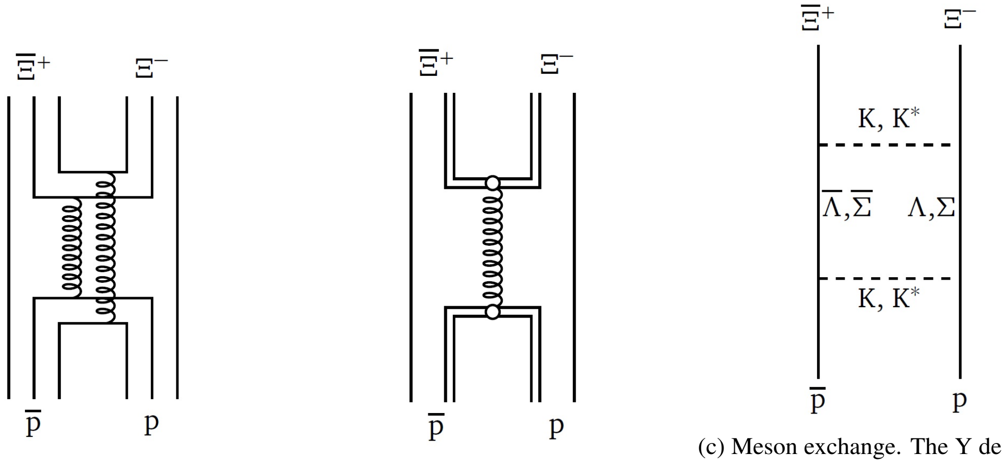

(a) Double gluon exchange.

(b) Diquark annihilation.

(c) Meson exchange. The Y denotes a Λ or a Σ baryon.

Figure 2.9: Exchange models used for the calculation of hyperon production in $\bar{p}p$ processes. Images from [27], adapted from [28].

well as the existence of exotic mesons, was proposed by Gell-Mann [29]. The most prominent candidate for an exotic baryon is the *pentaquark* ($qqqq\bar{q}$) consisting of four quarks and one antiquark. The name pentaquark was used for the first time by Lipkin [30]. In 2015, the LHCb collaboration, observed two resonances in the proton J/ψ two-body system which could reflect the existence of the hidden charm pentaquark states $P_c\,(4380)^+$ and $P_c\,(4450)^+$ [31]. Recently, LHCb announced the discovery of two new pentaquark states, $P_c\,(4312)^+$ and $P_c\,(4457)^+$, and confirmed the discovered pentaquark state $P_c\,(4450)^+$ [32]. Up to now, there is no knowledge of the binding mechanism for pentaquarks. Possible mechanisms could be: tightly bound quarks [33], a diquark-diquark-antiquark model [34], a diquark-triquark model [35], a coupled channel model [36], a weakly bound baryon-meson molecule [37], and dynamical generation [38]. It is proposed to study the search for pentaquarks for example in proton-nuclear collisions [39] and in electron-proton collisions [40].

CHAPTER 3

Overview of FAIR

The Facility for Antiproton and Ion Research (FAIR) is an international accelerator facility in Europe for the research with antiprotons and ions. FAIR is located in Darmstadt, Germany, and is still under construction. Four experiments form together the pillars of the scientific program at FAIR. The topics of those experiments spread from atomic and plasma physics to baryonic matter, nuclear structure and astrophysics, and antiproton induced hadron physics to investigate fundamental questions about the evolution of the universe and the structure of matter. $\overline{\text{P}}$ANDA will be one of those experiments.
This chapter introduces the experiments hosted at FAIR. Furthermore, an overview of the accelerator layout is given. More information can be found on the official web page of FAIR [41] and in the FAIR baseline technical report [42].

3.1 Physics Program of FAIR

3.1.1 APPA

One of the research pillars is Atomic, Plasma Physics and Applications (APPA). It combines a wide research field by hosting four different experiments which share the installations and experiment techniques.

BIOMAT FAIR provides heavy ions with energies up to 10 AGeV [43]. These ions will be used by the Biology and Material Science (BIOMAT) collaboration which plan to build the BIOMAT irradiation facility for biophysical experiments and experiments for ion-induced changes in solids.
The facility will be located in the High-Energy Cave and will be shared with SPARC which is described later in this section.

FLAIR For the study of fundamental symmetries, the gravitation of antimatter, atomic collisions and antiprotons as hadronic probes, antiproton energies in the lower energy region are needed. Those antiprotons will be provided by the Facility for Low-Energy Antiproton and Heavy Ion Research (FLAIR) [44] which will consist of a complex of two storage rings, the magnetic Low Energy Storage Ring (LSR) and the electrostatic Ultra-low Energy Storage Ring (USR). In the first phase of FAIR, not all storage rings will be ready. The so-called Modularized Start Version (MSV)[45] will not include the Recuperated Experimental Storage Ring (RESR), New Experimental Storage Ring (NESR) and SIS300. Therefore, other options for the low-energy antiproton program at FAIR were investigated. In 2012, it was decided that an additional storage ring, the CRYRING, is transferred from Manne Siegbahn Laboratory (MSL)

Stockholm to Helmholtzzentrum für Schwerionenforschung (GSI) and set up behind the Experimental Storage Ring (ESR) [46].

SPARC The experiments which are part of Stored Particles Atomic Research Collaboration (SPARC) are focusing on two major research topics. One of the main topics is the exploration of fundamental interactions between electrons and heavy nuclei up to bare uranium [47]. The second focus is laid on the study of collision dynamics in strong electromagnetic fields.

HED@FAIR High Energy Density Science at FAIR (HED@FAIR) will host several experiments located within the APPA cave exploiting the unique properties of intensive heavy-ion pulses to heat matter. The main focus is laid on investigations of the properties of different materials in the phase diagram [42]. An intense heavy ion beam deposits energies above $10\,\mathrm{kJg^{-1}}$ which heats up a target quickly and uniformly.

3.1.2 CBM

Compressed Baryonic Matter (CBM) uses nucleon-nucleon collisions between 10 and 45 AGeV to explore the QCD phase diagram for high baryon densities [48]. The research includes studies on the equation of state of nuclear matter at neutron star densities [49] as well as the search for the phase transition of QCD and the chiral symmetry restoration [48].
The CBM detector is designed for the measurement of [49]:

- rare multi-strange baryons
- charmed particles, mainly $J/\Psi \rightarrow e^+ + e^-$, D and Λ_c
- vector mesons which decay into leptons

To achieve the required precision, reaction rates up to 10 MHz will be used [48].

3.1.3 NuSTAR

The Nuclear Structure, Astrophysics and Reactions (NuSTAR) collaboration incorporates several experiments [50]: DESPEC/HISPEC, ELISe, EXL, ILIMA, LaSpec, MATS, R3B and SuperFRS.
NuSTAR focus on direct studies of the nuclei involved in processes which are relevant for the energy production and the element synthesis in a stellar environment [51]. In addition, the study of nuclear reactions will provide information on the dynamics of nuclear few- and many-body states. For example, one of the basic properties of an exotic nucleus which could be determined whether or not it is bound with respect to proton and neutron emission [51]. Another part of the experimental program is the test of predictions from modern nuclear models by extracting the nuclear ground state properties and information from the spectroscopy of excited states. Therefore, the NuSTAR collaboration contains not only experimental, but also theoretical programs. For all studies the experiments use beams of radioactive species separated and identified in the Super-FRS.

3.1.4 $\overline{\text{P}}$ANDA

$\overline{\text{P}}$ANDA is one of the key experiments at FAIR. Its goal is to investigate the structure and dynamics of hadrons. The experiment is used to perform basic physics research on topics around strong and weak forces, exotic states of matter and the structure of hadrons. The $\overline{\text{P}}$ANDA detector consists of different

sub-detectors which will perform a precise trajectory reconstruction, energy and momentum measurement and an efficient identification of charged particles [9].
A more detailed description of the detector and the physics program of $\overline{\text{P}}$ANDA is given in Chapter 4.

3.2 Accelerator Facility

The FAIR facility consists of a system of storage rings and experimental stations. The construction area is connected to the already existing part of the GSI consisting of the linear accelerator, Universal Linear Accelerator (UNILAC), a heavy-ion synchrotron (SIS18) and the ESR. These accelerators will be used as first accelerator stages. The FAIR complex which is still under construction, will consist of the superconducting double-synchrotron SIS100/SIS300, the Collector Ring (CR), the RESR, the NESR, an antiproton target and the HESR. The key component of FAIR will be the SIS100/SIS300 accelerator with a circumference of 1,100 meters. Figure 3.1 illustrates the planned layout of the FAIR complex.

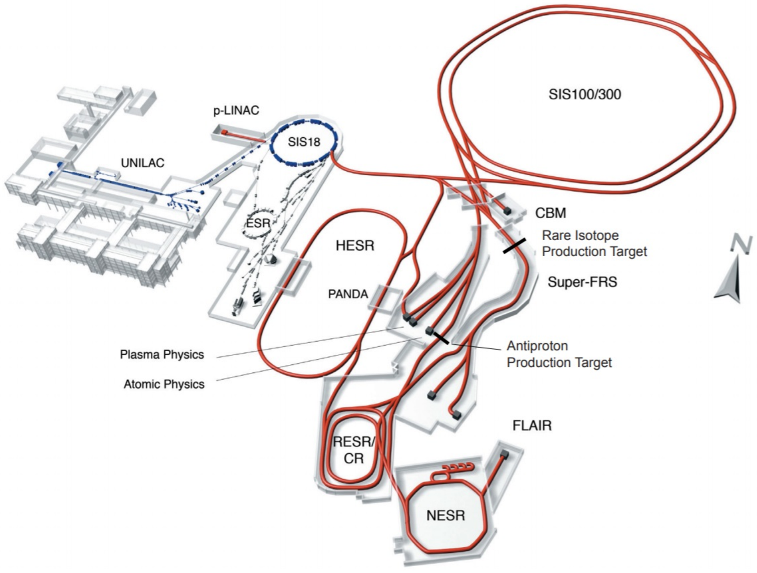

Figure 3.1: Illustration of the FAIR and GSI facility. The picture is taken from [42].

This section gives an overview of the different planned storage rings and accelerators. If not otherwise specified, the information has been taken from [52].

SIS100/SIS300

With its circumference of about 1,100 meters the superconducting double-synchrotron SIS100/SIS300 is the core accelerator of the new planned FAIR complex and is currently under construction. The already existing SIS18 and UNILAC will be used as injectors to accelerate ions with high intensity.
SIS100 is meant to produce U^{28+} with energies up to 2.7 GeV/u which can be compressed to bunches of about 60 ns. For further acceleration, it will be possible to directly extract or inject these particle bunches in the SIS300. In addition, the SIS100 will accelerate protons up to 29 GeV. Those protons will subsequently interact with the antiproton target. Since for the production of antiprotons a high-intensity proton beam is needed, the construction of a Proton Linear Accelerator (p-LINAC) is planned which will then be used as an injector for the SIS18.

Two modes of operation are planned for the SIS300. It will be possible to provide a slow extraction and maximum energy provided by the SIS100. The second option is the acceleration of a heavy-ion beam, e.g. U^{92+} with energies up to 34 GeV/u, also called high-energy mode.

Additional Storage Rings

In addition to the SIS100/SIS300, several storage rings complete the accelerator complex of FAIR. The CR is used for the stochastic cooling of radioactive beams and antiproton beams up to 3 GeV. Antiprotons, previously cooled in the CR, are accumulated in the RESR. Short-lived nuclei are rapidly decelerated in the CR. The NESR is equipped with stochastic and electron cooling to cool and decelerate stable and radioactive ions as well as antiprotons for low-energy and trap experiments. For antiprotons with momenta between 1.5 GeV/c and 15 GeV/c the High Energy Storage Ring (HESR) is planned. The storage ring will be equipped with an electron cooler for beam momenta up to 8 GeV/c and stochastic cooling over the full beam momentum range up to 15 GeV/c. Since the $\overline{\text{P}}$ANDA experiment is located at the HESR, a more detailed description follows, separately.

Parallel Operation of FAIR

The parallel operation of the research fields is an important consideration for FAIR. The operation scheme of the facility aims for these synergies, implying that FAIR operates as a dedicated facility for the different experimental programs. During the MSV of FAIR, the facility will be able to serve two experiments at the same time [53]. With the full setup, it will be possible to serve up to four different scientific programs in parallel. Figure 3.2 shows the operation scheme for the full FAIR setup. A proton (orange), which is accelerated in SIS100, produces antiprotons in the antiproton target-station. These antiprotons (orange dashed) are then collected, accumulated and cooled in the CR and RESR – as far as the RESR is available – before they are transferred to the HESR or NESR for experiments. During the time in which the SIS100 is not needed for protons, a radioactive ion beam (blue) can be accelerated and is slowly extracted to the

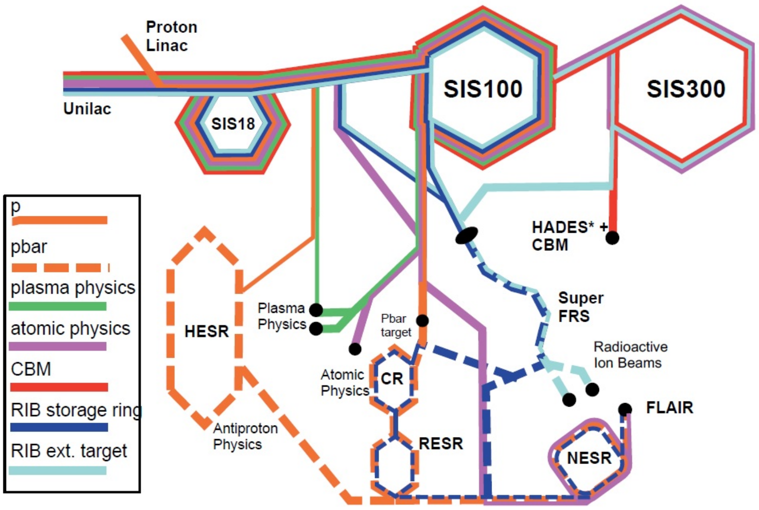

Figure 3.2: Scheme for parallel operation with the full setup of FAIR. Image from [52]

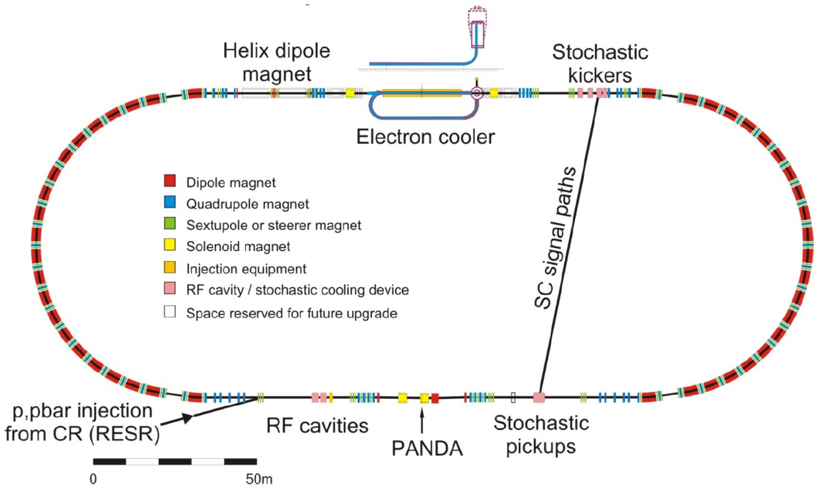

Figure 3.3: Illustration of the HESR. Image from [54].

Super-FRS where radioactive secondary beams (cyan dashed) for fixed target experiments are produced. Instead of antiprotons, the radioactive beam could be sent to the CR/RESR (blue dashed).

Every 10 – 100 s, a high energy heavy-ion beam (red) is accelerated in the SIS100/SIS300 before it is slowly extracted for nuclear collision experiments. For plasma physics experiments, every few minutes, intense beam pulses (green) are provided. During the time in which no antiprotons are produced, atomic physics experiments (violet) can be served by the SIS100.

HESR

The HESR is an essential part of the physics program of FAIR and is optimized for high energy antiprotons. The main research areas planned at the HESR are investigations on charmonium, hadronic structure and quark-gluon dynamics.

The design of the storage ring is based on the shape of a racetrack with a circumference of 574 m[52]. The two straight sections have a length of 132 m each. One straight section is dedicated for hosting the electron cooling system and the kicker of the stochastic cooling, while the stochastic pick-up and the $\overline{\text{P}}$ANDA experiment are part of the second straight section. The design includes 48 dipole magnets to achieve a maximum rigidity of $50\text{T} \cdot \text{m}$.

As already mentioned, two cooling techniques are used to ensure the high beam quality and the luminosity. The idea of electron cooling is to shrink the six-dimensional phase space (spatial volume times volume in momentum space) of a charged particle beam while the number of particles stays the same. The method of electron cooling was invented by Gersh Budker at the Institut of Nuclear Physics (INP) in Novosibirsk, in 1966 [55]. In this method a beam of quasi-monoenergetic electrons is merged with the beam to be cooled. The average velocity of the electrons is made equal to the average velocity of the particles inside the beam. If the velocity distribution of the electrons is plotted in the scale of both the longitudinal and transverse velocity distribution of the beam, the one for the electrons can be described by a delta-function. Using a thermodynamical picture, the hadron or ion beams are hot and the electron beam cold. Due to the Coulomb scattering of the ions in the gas-like environment of the electrons, momentum is exchanged until a thermodynamical equilibrium is reached. This thermodynamical equilibrium is reached if the mean velocity of the electrons and ions are equal. Therefore, the described interactions cause a reduction of the energy spread for the ions and the occupied six-dimensional phase space shrinks. Due to the lighter

mass of the electrons, the magnetic rigidity for the electrons is lower than for the ions at same velocity by a factor m_e/M, where M is the mass of the particle to be cooled. Therefore, the electron beam can be easily separated and bent away from the antiproton beam by a dipole magnet.
Stochastic cooling is used to control the spread of the particle in position and momentum phase space. This method was invented by Simon van der Meer at CERN in 1972 [56] and was mainly used to collect and cool antiprotons. A so-called pick-up system measures the momentum of the particles in the beam and corrects the momentum with a so-called kicker by sending an electrical signal across the storage ring. For each coordinate, longitudinal and transverse, independent pick-up and kicker systems are used.
Two operation modes are foreseen for the HESR[57]:

1. High resolution mode: provides luminosities up to $2 \cdot 10^{31}\,\mathrm{cm}^{-2}\,\mathrm{s}^{-1}$ and a momentum spread of $\Delta p/p = 4 \cdot 10^{-5}$
2. High luminosity mode: peak luminosity of $2 \cdot 10^{32}\,\mathrm{cm}^{2}\,\mathrm{s}^{-1}$ and a momentum resolution of $\Delta p/p = 10^{-4}$

Since the RESR in not available at the beginning of the stepwise realization of FAIR, the operation of HESR in the high luminosity mode is not supported and a modification of the injection and accumulation for the antiprotons is needed [53]. In the MSV the antiprotons are collected and cooled in the CR. An antiproton packet of $\sim 10^8$ antiprotons is then injected in HESR for accumulation. The accumulation inside the HESR causes another loss factor for the injected antiprotons, since the antiprotons cannot be used for experiments during the accumulation. Accumulation, acceleration and measurements are alternating about every 30 minutes [53]. In the later stage, the accumulation of the antiprotons is done in the RESR, as soon as it is available. This allows the injection of up to 10^{11} antiprotons in HESR.

CHAPTER 4

The $\overline{\text{P}}$ANDA Experiment

The $\overline{\text{P}}$ANDA experiment will be part of FAIR and is currently under construction. It is planned that $\overline{\text{P}}$ANDA is the internal detector at HESR. The wide physics program aims to deepen the knowledge of the strong interactions and of the hadron structure where the focus is set to the study of fundamental questions of hadron and nuclear physics. With measurements of the charmonium, D meson and baryon spectrum as well as of exotic states, e.g. hybrids and glueballs, $\overline{\text{P}}$ANDA will significantly contribute answering these open questions. In addition, new perspectives for studies of the forces between hyperons and nucleons will be opened. Furthermore, investigations on the structure of the nucleon are planned to determine the electromagnetic form factors of the proton in the time-like region.

This chapter starts with an overview of the $\overline{\text{P}}$ANDA physics program. Furthermore, the $\overline{\text{P}}$ANDA detector as well as all sub-detectors will be described. Finally, a short introduction to the simulation and analysis framework of $\overline{\text{P}}$ANDA is given.

4.1 Physics Program at $\overline{\text{P}}$ANDA

The $\overline{\text{P}}$ANDA experiment is one of the major projects of FAIR. Since the $\overline{\text{P}}$ANDA detector is located at the HESR, studies of interactions between the antiproton beam and fixed target protons and nuclei are performed. The antiprotons will have momenta in the range of 1.5 GeV/c and 15 GeV/c, corresponding to energies between $\sqrt{s} = 2.25\,\text{GeV}$ and $\sqrt{s} = 5.47\,\text{GeV}$. The scientific program aims to answer the fundamental questions of QCD, mostly in the non-perturbative regime. The planned measurements will profit from the high cross section of antiproton induced reactions. Complementary to e^+e^- induced reactions, $\bar{\text{p}}\text{p}$ collisions allow all non-exotic quantum number combinations for directly formed states. In addition, states with exotic quantum numbers will be observable in production reactions. The precision which can be achieved in direct formation of resonant states is very high and is only limited by the small energy spread of the cooled antiproton beam. This high precision allows measuring the widths of very narrow states.
In the following, an overview on the scientific program with its different physics cases is given. Further information can be found in [58].

Charmonium

Charmonium consists of a $c\bar{c}$ pair with properties in close analogy to positronium. The potential describing the interaction inside the positronium is a Coulomb potential and additional terms for spin-orbit, spin-spin

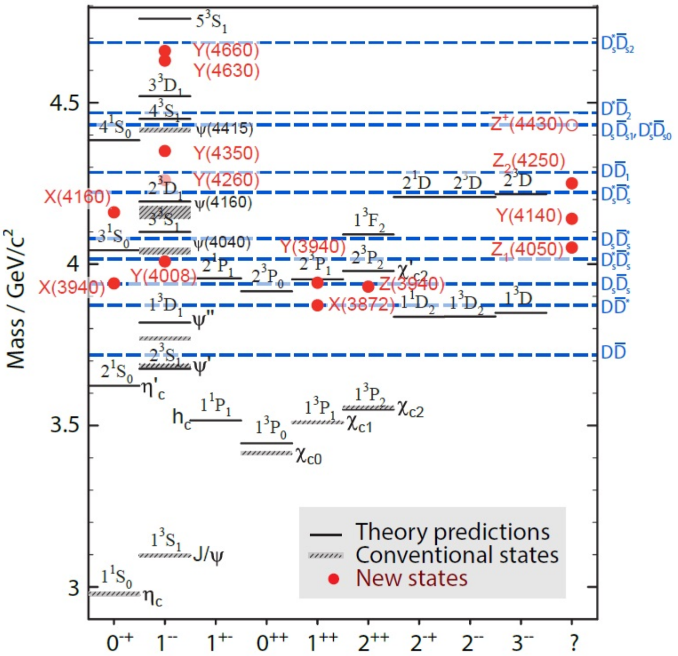

Figure 4.1: Illustration of the charmonium spectrum. The solid lines are the predicted and the shaded lines are the observed conventional charmonium states. The blue dashed lines represents different thresholds. Image from [14], adapted from [59].

and QED effects while the potential describing the charmonium interaction can be expressed as the sum of a Coulomb-like potential and a linear part. Figure 4.1 shows the charmonium spectrum. All states below the $D\bar{D}$ threshold of 3.7 GeV/c^2, also called the open-charm threshold, are experimentally established. Measurements with high accuracy have been achieved for the triplet states but not for the singlet states. A significant number of unpredicted states were found above the open-charm threshold. These states are called X, Y, Z states and in most cases it is still not clear which type of states they are. Y states are neutral states with $J^{PC} = 1^{--}$, while Z states are charged states which thus cannot be $c\bar{c}$ states. Due to the predominant decay via charmonium states, the discovered states were associated with charmonium [59]. Also a few of the states are identified as conventional states, others states, the so-called exotic states, are considered as possible indicators of physics beyond the conventional quark model. Possible theoretical descriptions for these exotic states are [60]:

- Molecular states: Description of two mesons which are loosely bound by two mechanism: quark/color exchange for interaction at short distances and pion exchange at large distances. The pion exchange is expected to be the dominant mechanism.
- Tetraquarks: Tightly bound four-quark states with properties different from those of molecular states. They have a diquark-diantiquark structure grouped in color-triplet scalar and vector clusters in which interactions are dominated by spin-spin interactions.
- Hybrids: Charmonium states with excited gluonic degree of freedom.

Up to now, the best resolution ($\delta p/p = 10^{-4}$) and luminosity ($2 \cdot 10^{31}\,\text{cm}^{-2}\,\text{s}^{-1}$) has been achieved in the E760 [61] and E835 [62] experiment at Fermilab. The $\overline{\text{P}}$ANDA detector design is optimized for charmonium physics and exploits the full mass region above and below the open-charm threshold. The momentum resolution in the high resolution mode will be $4 \cdot 10^{-5}$. In addition, the luminosity of $\overline{\text{P}}$ANDA in the high luminosity mode will be ten times higher than the achieved luminosity at Fermilab. At full luminosity, it will be possible to collect a high number of $c\bar{c}$ states per day. Thus, e.g. above 6.4 GeV/c 100 D meson pairs are predicted to be produced per second around $\psi(4040)$ [63] which corresponds to $\sim$ 8.6 million D meson pairs per day.

Exotic Excitations of Mesons and Baryons

In the previous paragraph, exotic states are already mentioned. This paragraph will give an overview on these exotic states. Recently, the $\overline{\text{P}}$ANDA Collaboration published the results of a Monte Carlo (MC) study for energy scan measurements, where the charmonium-like $X(3872)$ state is chosen as specific example [64]. The $X(3872)$ state was discovered by the Belle Collaboration in 2003 [65] and is a prominent candidate for an exotic state because it does not fit in to the quark model due to its quantum numbers. The study has shown that measurements of the natural width and line shape of $X(3872)$ with $\overline{\text{P}}$ANDA is feasible.

Multiquarks Exotic states can be divided into two categories: manifestly and crypto-exotic states. A Crypto-exotic state has a mass and a width which does not fit in meson or baryon spectra and, therefore, implies an overpopulation of the spectra [66]. Another nature of a crypto-exotic state is that the production or decay properties of the candidate are incompatible with those of conventional mesons or baryons. In case of a manifestly exotic state, the quantum numbers (spin-parity, charge, flavor) exclude the $q\bar{q}$ and qqq states, since these quantum numbers are not allowed for conventional mesons and baryons. Hence, a state with more than three valence quarks or a quark-antiquark pair is required. QCD gives no specific limitation on the quark composition of hadrons. Both conventional hadrons and exotic states however have to be color neutral. The existence of hadrons consisting of four, five, and six quarks and antiquarks is possible. These hadrons are called multiquarks. Hadrons with $qq\bar{q}\bar{q}$ content are called tetraquarks and, as already mentioned in the previous paragraph, are tightly bound states with a diquark-antidiquark structure. A bound state composed of two mesons was first suggested by [67] for the mesons a(980) and f(980). This idea was also applied to the X(3872) by [68], observed by Belle [65]. More recently, another tetraquark candidate, the $Z_c(3900)$ has been observed independently by Belle [69] and BESIII [70].
Molecular states, where a light π meson maintains the binding, are also possible. Here, either two mesons, a meson and a baryon, or two baryons could couple. In case of a coupled meson and baryon, the quark content is $(qqqq\bar{q})$, also called pentaquark, which is already described in Section 2.2.1. The coupling of two baryons is called dibaryon and consists of six quarks. In 2014, a potential dibaryon candidate was found by the WASA-at-COSY Collaboration [71].
Several measurements try to access multiquarks states, but statistics are not high enough for a clear answer. At $\overline{\text{P}}$ANDA, it will be possible to collect more precise data to improve the picture of multiquarks, particularly in the meson sector.

Hybrids $q\bar{q}$ states which are excited by one or more constituent gluons are called hybrids. The additional degrees of freedom, e.g. vibrations, contribute to the quantum numbers of the meson state and can cause quantum numbers which are not possible for conventional mesons. Charmonium hybrids are expected to have a mass in the region of 3 GeV/c^2 and 5 GeV/c^2. Theoretical calculations come mainly from the bag model [72], the flux tube model [73], constituent gluon model [74] and LQCD [75],[76]. In $\overline{\text{P}}$ANDA it is planned to exploit charmonium hybrids at high antiproton energies of 15 GeV to cover the exotic and the non-exotic states. In a second step, measurements will be done by scanning the antiproton energy in small steps in the region where potential candidates for hybrids in the production measurements are observed.

Glueballs Glueballs have only constituent gluons but not constituent quarks within the model description. Theoretical calculations predict 15 glueball states [77] for the mass region of HESR. Some of these states are expected to have exotic quantum numbers. If glueballs have non-exotic quantum numbers, they will mix with ordinary mesons. In this case, it is not a priori clear how pure the glueballs are. Glueballs with exotic quantum numbers, the so-called oddballs, do not mix with conventional mesons and are predicted to be narrow and easy to identify [78]. Since the spin structure of an oddball is different, the comparison of oddballs with non-exotic glueballs could give a deep insight into the unknown glueball structure.

Glueball states can either be formed directly in antiproton-proton annihilations or can be produced together with another particle. So far, two experiments at the Low Energy Antiproton Ring (LEAR) found hints on the existence of glueballs. The Jetset collaboration found an indication for a tensor state but statistics were not sufficient for clear conclusions[79]. The best candidate for a pseudo-scalar glueball was found by the Obelix collaboration [80]. This interpretation has however not been widely accepted because LQCD calculations predict higher masses [81].

Within the $\overline{\text{P}}$ANDA experiment, it will be possible to perform similar studies with statistics which are two orders of magnitude higher than in previous experiments [58].

Heavy-Light-Systems

The D meson consists of charm quark as heavy quark and a light quark. Therefore, it may be called the hydrogen of the QCD. To understand the strong interaction, D mesons are interesting because there is the heavy quark as a static color source. Within the heavy quark limit, heavy-light systems are degenerated with respect to the spin degree of freedom of the heavy quark [82]. The experimentally observed D meson spectrum is consistent with the theoretical predictions while the situation, e.g. for D meson with strange content, also called D_s is different. For example, the $D_s(2317)$ was discovered by [83] and is at least 150 MeV below the expectations of the quark-model. Only an upper limit of 3.8 MeV/c^2 is achieved for the width of the D_s [84]. Figure 4.2 shows that the new observed D_s states do not match the quark-model predictions for heavy-light mesons.

Due to the small momentum spread in the HESR, at $\overline{\text{P}}$ANDA it will be possible to measure the D_s width in a threshold scan with high energy resolution in the order of 100 keV [87, 88]. Because of the small cross sections, this energy scan will primarily be important after the RESR has been added to FAIR.

Strange and Charmed Baryons

Understanding the excitation spectrum of baryons is one of the main goals of non-perturbative QCD. So far, experiments are mainly focused on the nucleon sector, but the agreement with the quark model is small. The energies of low-lying states are not matching the predictions, whereas higher states are not observed in experiments [1]. This absence of higher states is called ‘missing resonances’ [89]. Different explanations are discussed:

- a quark-diquark structure would reduce the internal degrees of freedom which reduces the number of states or
- a lack of experimental sensitivity. So far studies have focused on pionic decay modes of the resonances as well as on $\text{N}^* \rightarrow \text{N}\eta$, $\text{K}\Lambda$, $\text{K}\Sigma$.

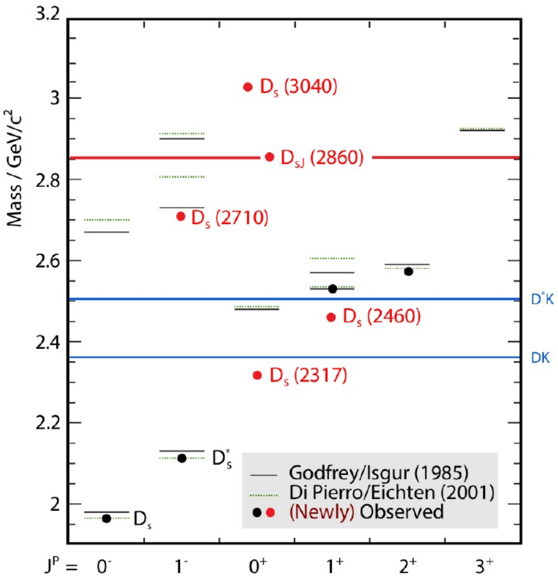

Figure 4.2: The comparison between the predicted charmed-strange spectrum by Godfrey and Isgur [85](solid lines) and Di Pierro and Eichten [86](dotted lines). The experimentally observed states are shown as black and red dots. The red dots are denoting the most recent observations. On the horizontal axis the J^P of the states are shown while the vertical axis shows the mass of the states expressed in GeV/c^2. The blue solid lines indicate the thresholds for the decays into D^*K and DK pairs. Image from [14], adapted from [59].

Strange Baryons To answer the question whether the excited spectra of baryons with light quark content (u,d and s quarks) follow SU(3) symmetry, the knowledge of the spectrum of all strange baryon species, i.e. Λ, Σ, Ξ and Ω, is necessary. If strangeness is added as additional degree of freedom, the quality of experimental data gets poor. This is already true for Λ and Σ, also some new states were observed [90][91]. Ξ and Ω baryon excited states have been seen as bumps in inclusive experiments, mostly from bubble chamber experiments. The only assignment was achieved on $\Xi\,(1530)^0$, while there are no assignments for Ω baryons. Only three excited states were seen: one three-star and two two-star resonances. Some theoretical studies were done by [92] and [93] on the Ξ and Ω spectrum. But more experimental data are needed to confirm these calculations.
The $\overline{\mathrm{P}}$ANDA detector is well suited for a comprehensive baryon spectroscopy program, since a large fraction of the inelastic cross section in $\bar{p}p$ collisions is associated with channels resulting in baryon and antibaryon pairs. At high antiproton momenta the ratio final states with a baryon-antibaryon pair to purely mesonic final states exceeds unity. In $\bar{p}p$ collisions the production of extra K or D mesons is not needed to balance strangeness and charm.
Strange, multi-strange and charm baryons can be characterized by their displaced vertices or the displaced vertices of their daughter particles. Due to the good capability of the $\overline{\mathrm{P}}$ANDA tracking detectors (see Section 4.2), it is possible to identify the characteristic displaced vertices. The yield for Ξ^* and $\overline{\Xi}^*$ will be sufficient enough for collecting data samples with high statistics. For the ground state Ξ production, i.e. $\bar{p}p \rightarrow \overline{\Xi}^+\ \Xi^-$, the cross section has been measured to $2\,\mu$b [23]. This cross section leads, with a luminosity of $\mathcal{L} = 1 \cdot 10^{32}\,\mathrm{cm}^{-2}\,\mathrm{s}^{-1}$, to a production rate of 720,000 $\overline{\Xi}^+\ \Xi^-$ pairs per hour. In the case of the Ω baryon, the cross section, for example for the reaction $\bar{p}p \rightarrow \Omega\bar{\Omega}$, is predicted to be in the order of $\sigma = 2\,\mathrm{nb}$. With a luminosity of $\mathcal{L} = 1 \cdot 10^{32}\,\mathrm{cm}^{-2}\,\mathrm{s}^{-1}$ it would be possible to produce 700 $\Omega\bar{\Omega}$ pairs per

hour.

Nucleon Structure

In $\overline{\text{P}}$ANDA also studies including perturbative aspects of QCD will be done. These studies will give the opportunity to study the class of hard exclusive processes which will give insight into the intermediate region. This region marks the transition towards the perturbative QCD effects.

Generalized Parton Distribution Recently, a theoretical framework of Generalized Parton Distributions (GPDs) [94] to treat hard exclusive processes in lepton scattering experiments has been developed. Under suitable conditions, the factorization of long and short distance contributions to the reaction mechanism is possible. The corresponding processes can be described by the QCD handbag diagram, dividing the process into a hard perturbative QCD process and a soft part which is parametrized by GPDs. Due to a small cross section, the measurement of the process is challenging. At $\overline{\text{P}}$ANDA it is envisaged to study the reaction $\bar{\text{p}}\text{p} \rightarrow \gamma\gamma$. The high luminosity and the 4π electromagnetic calorimeter of $\overline{\text{P}}$ANDA should give the possibility to separate this process from the hadronic background. In addition, a test of Transition Distribution Amplitude (TDA) models by measuring the reaction $\bar{\text{p}}\text{p} \rightarrow J/\Psi\pi^0$ is foreseen, since nucleon-to-pion TDAs were introduced as generalization of GPDs [95].

Electromagnetic Form Factors of the Proton in the time-like Region Electromagnetic form factors provide information on the electromagnetic charge distributions inside hadrons. Therefore, they are good probes to investigate the nucleon structure. In general, particles with spin $1/2$ have two form factors, the electric (G_E) and the magnetic (G_M) form factor. The form factors are experimentally extracted from the cross section of the elastic scattering process $e^- + p \rightarrow e^- + p$ (space-like, $q^2 < 0$) and its crossed annihilation process $\bar{\text{p}}\text{p} \rightarrow e^+e^-$ (time-like, $q^2 > 0$). In e^-N elastic scattering the interaction of the electron with the nucleon can be described by the exchange of one photon with space-like four momentum transfer.

Several experiments, like BaBar [96], LEAR [97] and BESIII [98] performed measurements with $\bar{\text{p}}\text{p}$ and e^+e^- collisions, but the results are not consistent or have large uncertainties. The $\overline{\text{P}}$ANDA detector will give the possibility to determine the electromagnetic form factors in the time-like region with high accuracy. Due to the high luminosity and the good particle identification, with $\overline{\text{P}}$ANDA it will be possible to perform precise measurements of the form factors up to $q^2 = 14\,(\text{GeV})^2$. In a feasibility study of the proton electromagnetic form factors in the time-like region it was shown, that a background suppression in the order of 10^8 can be achieved [99].

Hypernuclei

Hypernuclei are systems in which the nucleons are replaced by hyperons. This leads to the introduction of strangeness as new quantum number into the nucleus. So far, single and double Λ hypernuclei have been discovered [100]. With a $\bar{\text{p}}$ beam an efficient production of hypernuclei is possible. Since a single hyperon is not restricted by the Pauli principle, a Λ hyperon can populate deeply bound hypernuclear states. These states are directly accessible in experiments. The presence of a hyperon inside the nuclear medium could give rise to new nuclear structures. Furthermore, the comparison of hypernuclei with conventional nuclei may give new insights in the key questions like the question for the origin of the nuclear spin-orbit forces [101]. Due to the possibility of a precise multi-strange hypernucleus spectroscopy at $\overline{\text{P}}$ANDA, it will be possible to explore the hyperon-hyperon interaction. Therefore, a two-step production mechanism, illustrated in Figure 4.3, is applied using a bound Ξ hypernuclear state as gateway to form double Λ

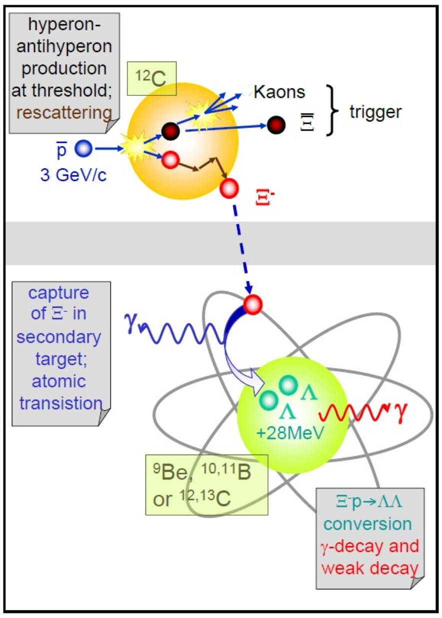

Figure 4.3: Production mechanism for double Λ hypernuclei by using an antiproton beam. In the initial reaction a Ξ is produced which is re-scattered in the primary target and subsequently stopped in the external secondary target. After the Ξ is captured in the nucleus, it is transformed into two Λ. Image from [58].

hypernuclei [102]. It is planned to use the reactions $\bar{p} + p \rightarrow \Xi^- \, \overline{\Xi}^+$ and $\bar{p} + n \rightarrow \Xi^- \, \overline{\Xi}^0$ to produce a low energy Ξ baryon which is re-scattered in the primary target nucleus. The Ξ will be stopped in the external secondary target and forms a Ξ hypernucleus. Via the reaction $\Xi^- \, p \rightarrow \Lambda \, \Lambda$, the Ξ hypernucleus will be converted into a double Λ hypernucleus. This procedure requires a modular and highly flexible modified setup of the central $\overline{\text{P}}$ANDA detector as well as dedicated runs for hypernuclei studies.

4.2 The $\overline{\text{P}}$ANDA Detector

The physics program described in Section 4.1 defines several requirements for the different detector parts. In general, a modular and flexible design, the ability to detect charged and neutral particles, high resolution in a wide range of energies, good particle identification and a full angular coverage are required. The $\overline{\text{P}}$ANDA detector (Fig. 4.4) with a length of around 13 m is composed of two main parts: the Target Spectrometer which surrounds the interaction point in a shell-like arrangement and the Forward Spectrometer which consists of a sequence of different detectors along the beam line. The acceptance of the Forward Spectrometer is up to 10° in the horizontal plane and up to 5° in the vertical plane.
In the following, the sub-detectors are shortly described. However, this section will provide only an overview of the detector parts. Therefore, references for each component of the $\overline{\text{P}}$ANDA detector will be given.

Target

The planned measurements within $\overline{\text{P}}$ANDA define the requirements for the target. Since multiple-scattering must be avoid, the target has to be a very thin and localized chunk of matter in ultra-high

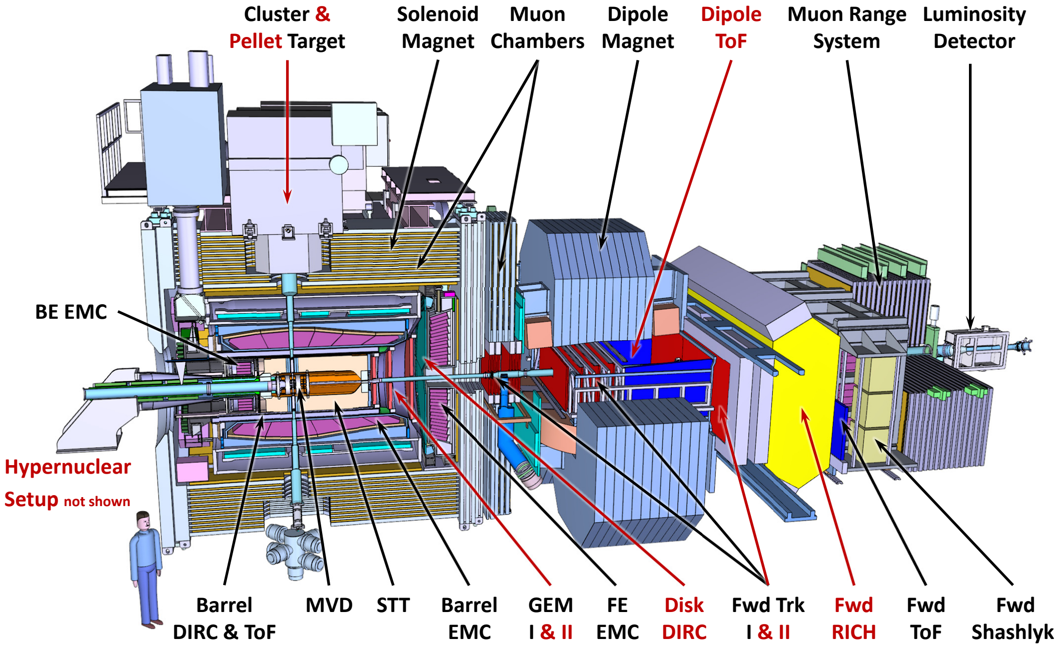

Figure 4.4: Illustration of the planned $\overline{\text{P}}$ANDA detector with its total length of about 13 m. The red labeled sub-detectors will not be part of the start configuration of $\overline{\text{P}}$ANDA and will be added in a later phase. Image from [103].

vacuum. This can be realized by nano- and microsized condensed matter particles, like clusters, droplets or pellets, passing the antiproton beam in the transverse direction. Most measurements of the physics program require a pure proton target with very high purity. Any pollution would result in disturbing background. The best suitable target consists of gaseous or solid state hydrogen or deuterium. For the planned studies of $\bar{\text{p}}\text{p}$ annihilation in nuclear matter, heavier target material like N_2 and the noble gasses Ne, Ar, Kr, and Xe would be desirable. To avoid large beam heating effects a target density below $\rho = 10^{16}\,\frac{\text{nucleons}}{\text{cm}^2}$ is necessary. According to the maximum luminosity of $\mathcal{L} = 2 \cdot 10^{32}\,\text{cm}^{-2}\,\text{s}^{-1}$, the antiproton production rate of $\dot{N} < 2 \cdot 10^7\,\bar{\text{p}}/\text{s}$, the number of antiprotons in the beam $N_{\text{beam}} = 10^{11}$ and the beam revolution frequency $f_{\text{beam}} = 413\,\text{kHz}$ the target beam density is expected to be $\rho = 4.5 \cdot 10^{15}\,\frac{\text{atoms}}{\text{cm}^2}$. A large fraction of the listed requirements can be served by installing a cluster-jet or a pellet target. It is foreseen to provide both target types in $\overline{\text{P}}$ANDA while the cluster-jet target will be part of the start configuration.

In the following an overview on both target types will be given. If not otherwise stated, for further information the reader can consult [104].

Cluster-Jet Target

Clusters are commonly produced by the expansion of pre-cooled gases. Due to the Joule-Thomson effect of real gases, the gas cools down during its passage through a nozzle and forms a super-sonic beam. Since the cluster has a relatively high mass, the angular smearing of the particle trajectories which is caused by scattering is negligible. The cluster size is influenced by the experimental conditions but is typically on the nanometer scale with $10^3 - 10^5 \, \frac{\text{atoms}}{\text{cluster}}$. At $\overline{\text{P}}$ANDA it is planned to use the so-called Münster-Type cluster-jet target operating in the regime where hydrogen is already fluid before entering the nozzle. This leads to higher densities of the target beam. The achieved target density for the prototype cluster-jet target is $2 \cdot 10^{15} \, \frac{\text{atoms}}{\text{cm}^2}$ [104].

Pellet Target

The use of pellet targets has two main advantages: the very high effective target thickness and the possibility to know the position of the pellets at the time of interaction. But the characteristics of pellets could also cause large variations in thickness. The central part of the pellet production is the triple-point chamber. Inside the chamber, a cryogenic liquid is injected into a gas (same or different kind) close to the triple-point. Subsequently, a periodic excitation is imposed by a piezoelectric transducer. When the perturbation amplitude is equal to the jet radius, the gas disintegrates into drops. By this method, a regular drop flow is provided [105]. These drops pass through a thin tube and cool down due to surface evaporation which then leads to a regular flux of frozen pellets.

Two operation modes of the pellet target are possible: the pellet tracking mode and the pellet high luminosity mode. The tracking system for the pellet tracking mode is based on optical detection methods. A high accuracy in pellet tracking at $\overline{\text{P}}$ANDA is required to perform e.g. measurements on charmonium and hyperon decays. In the high luminosity mode, the target thickness is higher than in the tracking mode but a smooth time structure.

First work on a pellet target suitable for $\overline{\text{P}}$ANDA was done by the The Svedberg Laboratory (TSL) in Uppsala, the Institut für Technische Physik (ITEP), the Moscow Power Engineering Institute (MPEI) and the Forschungszentrum Jülich (FZJ). The WASA pellet target provides hydrogen or deuterium pellets with a size of $25 - 30\,\mu$m and a thickness of 10^{15} atoms/ cm^2. But the variations in thickness are large and further investigations are needed.

Pellets of other elements than hydrogen or deuterium are also possible but there are technical challenges. The pellet size must be half or less to reach a similar thickness as for hydrogen or deuterium which again is a problem for pellet tracking.

Magnets

In both spectrometers of $\overline{\text{P}}$ANDA the momentum and the energy loss of charged particles will be measured. Here, it is exploited that charged particles in a magnetic field follow a curved trajectory. In a homogenous solenoid field, the radius of the projection to a plane perpendicular to the field direction is directly proportional to the particle momentum. Therefore, two types of magnets are planned for the $\overline{\text{P}}$ANDA detector: A superconducting solenoid magnet for the Target Spectrometer and a dipole magnet for the Forward Spectrometer. In this section an overview of the properties and requirements on the two magnet types are given, while further information can be found in [106].

The solenoid magnet will have a magnetic length of 2.5 m and underlies manifold requirements. The main requirement is to deliver a 2 T field parallel to the beam line and which is uniform over the whole tracking detector region. There are several requirements for the field homogeneity and the stray field: The field magnitude must not vary by more than 2 % over the whole tracking region and the radial component of the magnetic field must remain low. For the regular maintenance of the detector parts, the solenoid has to be removable with the restriction that the HESR can continue. Therefore, a movable rail-guided carriage is planned which moves the solenoid and the inner detector parts more than 10 m away from the beam line. This procedure must not take longer than one week in total.

For the Forward Spectrometer a dipole magnet with 2T · m bending power is foreseen to extend the solenoid in the forward region. The dipole magnet is foreseen to be part of the accelerator lattice of HESR. The dipole magnet will have a length of 2.5 m along the beam line which is optimized to balance the requirements for the magnet and the detector. In total the height and the width of the dipole magnet is 3.9 m and 5.3 m, respectively. The major challenge is the achievement of 2T · m field integral over a short longitudinal distance. Since the area of the forward detectors increases quadratically with the distance to the interaction point, it is necessary to minimize the dimensions of the dipole in this direction. The design foresees a race-track shape of the coils which will lead to a good magnetic rigidity.

Tracking Detectors

In this section the $\overline{\text{P}}$ANDA tracking detectors will be introduced. Further information is given in [107] for the Micro Vertex Detector (MVD), in [108] for the Straw Tube Tracker (STT) and in [109] for the Forward Tracker (FT).

Micro Vertex Detector

The Micro Vertex Detector (MVD) is the innermost part of the central tracking system inside the Target Spectrometer and will use silicon detectors as sensitive elements. Two different detector technologies, hybrid pixel detectors and double-sided micro-strip detectors, will be used. This imposes specific requirements for the sensor production and characterization as well as for front-end electronics and hybridization. The MVD will deliver 3D hit information close to the interaction point. In addition, it will be possible to provide information on the time of the track which is an important input for the event reconstruction. Fast particle detection can be used as time reference for the outer detector systems while the track information in the solenoid field will give access to the particle momentum and the event topology. The major task of the MVD is the identification of open charm and strangeness. Therefore, a good resolution of secondary decays of short-lived particles in displaced vertices is required. Another task is the measurement of the energy loss for slow protons, kaons and pions which will provide additional information for the global particle identification.

The physics goals and the experimental conditions in which the detector will operate impose the following basic requirements:

- The detection of the first track point very close to the decay point is mandatory for displaced vertices.
- Since the full $\overline{\text{P}}$ANDA detector will cover nearly the full solid angle, the MVD is required to cover the region from $\Theta = 3\,^\circ$ to $150\,^\circ$.
- In the forward region, a good spatial resolution of at least $100\,\mu$m in z and $\sim 10\,\mu$m in the x and y direction is needed.
- To avoid multiple-scattering of low-energy particles inside the silicon layers, a minimization of the material budget is mandatory. The total material budget for the MVD and the STT in terms of radiation length is foreseen to be $\frac{X}{X_0} = 10\,\%$.

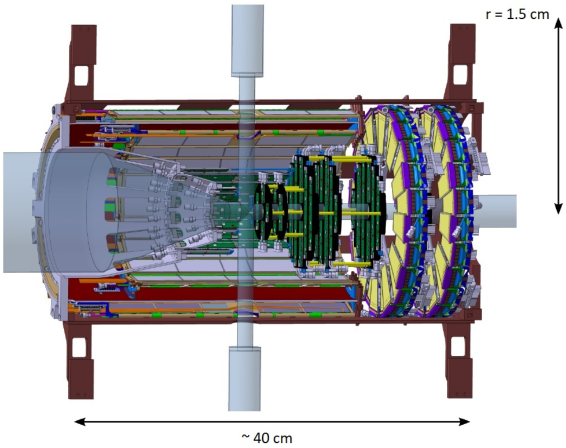

Figure 4.5: CAD drawing of the MVD including support structure. Image adapted from [111].

- Due to the small distance to the interaction point, a high radiation hardness is required. Assuming an overall lifetime for $\overline{\text{P}}$ANDA of ten years and a duty cycle of 50%, the requested radiation tolerance in terms of 1 MeV neutron equivalent is $10^{14} n_{\text{eq}}\,\text{cm}^{-2}$ [110].
- The time resolution should be in the order of 10 ns which requires a fast and flexible read-out system.
- Additional input on global particle identification for low-energy particles.

Figure 4.5 shows the CAD drawing of the MVD design which is optimized to match the above mentioned requirements. The MVD will consist of two parts, a barrel and a disc part, and will have a maximum radius of 15 cm and the active volume ranges from −17 cm to 23 cm in z direction with respect to the interaction point. The barrel part consists of 4 layers, where the two innermost layers are equipped with silicon hybrid pixel detectors and the two outer with double-sided silicon micro-strip detectors (Fig. 4.6). Polar angles from 40 ° up to 150 ° (Fig. 4.7) will be covered with the barrel part. Six discs are planned for the forward part of the MVD consisting of silicon hybrid pixel detectors. As outer radial component of the last two layers, double-sided silicon micro-strip detectors are used. The forward part will cover the

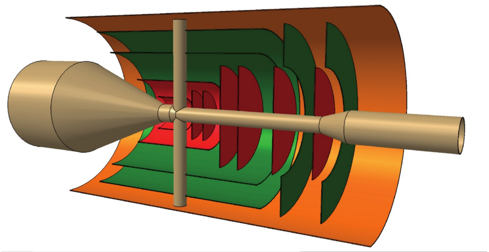

Figure 4.6: Basic layout of the MVD. The silicon hybrid pixed sensors are shown in red and the double-sided silicon micro-strip detectors are indicated in green. Image from [107].

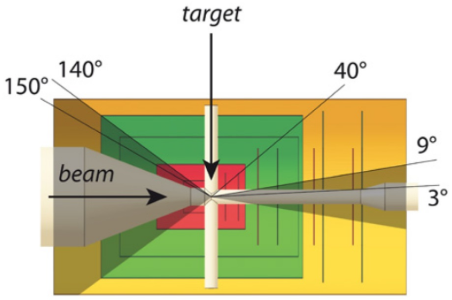

Figure 4.7: Illustration of the polar angle coverage for the MVD. The polar angle range from 3 ° up to 150 ° are covered. The gray shaded part indicates the not covered region. Image from [112].

polar angle region between 3 ° and 40 °. In addition to the forward discs, two extra discs are envisaged in forward direction which will be used for the reconstruction of hyperons. The conceptual design of these discs is similar to the MVD discs.

Straw Tube Tracker

The Straw Tube Tracker (STT) is the main tracking detector for charged particles in the $\overline{\text{P}}$ANDA target sprectrometer and consists of 4224 single straw tubes arranged in a cylindrical volume around the interaction point enclosing also the MVD. Along the beam line the STT is followed by the Gaseous Electron Multipliers (GEM) planes which are described in the next paragraph. The straw tubes are gas-filled cylindrical tubes with a conductive cathode as inner layer and an anode wire along the cylinder axis. Ions and electrons, produced along the trajectory of a charged particle in the gas volume, are separated by the electric field between the inner layer and the wire. Usually, the wire has a positive voltage of a few keV and achieves an amplification of the primary charged signal of $10^4 - 10^5$.
The main task of the STT is the precise spatial reconstruction of the helical trajectory of charged particles with a momentum range between 100 MeV/c and 6 GeV/c. By reconstructing the trajectory of charged particles in the solenoid magnetic field, the particle momentum is measured. In addition, a measurement of the specific energy-loss for particle identification will be done to separate protons, kaons and pions in the momentum region below 1 GeV/c. The value of the specific energy loss is derived from the number of ionization electrons per track length. It is also possible to measure the drift-time for the earliest arriving electrons which allows the calculation of a minimum distance for the particle track from the wire. The use of straws has some advantages. Straws have

- a robust electrostatic configuration,
- a robust mechanical stability, if they are arranged in closely packed multi-layers,
- a high detection efficiency (about 99.5 %),
- minimal dead zones (order of mm) at the tube ends and
- a small radiation length of $X/X_0 \sim 0.05\,\%$ per tube, if straws with $\sim 30\,\mu$m film tubes are used.

The straw tubes used for the $\overline{\text{P}}$ANDA STT have a length of 1400 mm, an inner diameter of 10 mm, a wall thickness of $27\,\mu$m and consist of two $12\,\mu$m thin aluminized Mylar film layers. A gold-plated tungsten-rhenium wire with a diameter of $20\,\mu$m is used as the anode. According to studies on suitable gas mixtures, a mixture of Ar + 10 % CO_2 is chosen.
The pressurized straw tubes are glued together to form closely-packed (gap is less than $20\,\mu$m) planar multi-layer modules. These modules are then arranged in a hexagonal layout. Each hexagonal sector consists of eight straw layers parallel to the beam line, four stereo double layers with tubes skewed by ±2.9 °, another four parallel layers followed by additional seven parallel layers with decreasing number of straws per layer. Figure 4.9 shows an illustration of the straw tube arrangement. In the border region of the skewed layers some shorter straw tubes are used. To keep the MVD and the target accessible, the STT is divided into two semi-cylinders with a gap of 42 mm. A semi-cylinder is formed by three hexagonal sections. The full STT has an inner radius of 150 mm, an outer radius of 420 mm and a total length of 1650 mm positioned between −550 mm and 1100 mm with respect to the interaction point. This leads to a material budget of $X/X_0 = 1.23\,\%$. The STT will cover the particle detection in a polar angle between 10 ° − 140 ° while the azimuthal coverage is only limited by the gap for the target pipe at $\phi = \pm 90\,°$. In simulation studies an isochrone resolution better than $150\,\mu$m and a momentum resolution of $\sigma_p/p \sim 1 - 2\,\%$ for charged particles is achieved. The determined energy resolution is better than 8 %.

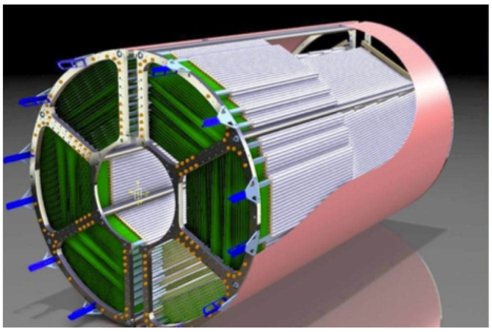

Figure 4.8: 3D drawing view the STT including the mechanical frame. The STT has a total length of 1650 mm and an outer radius of 420 mm. Image from [108].

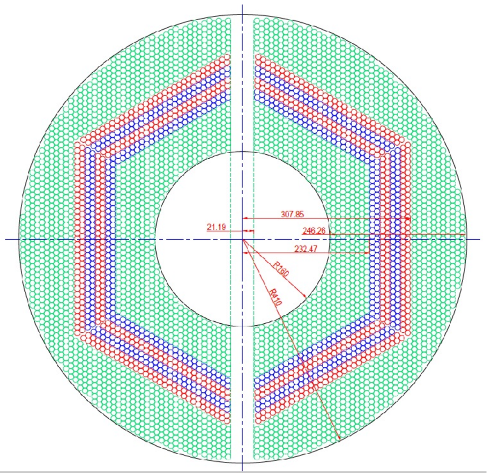

Figure 4.9: Layout of the straw tubes in the STT in xy-view. The parallel straw layers are marked in green and the red and blue marked layers are skewed by −2.9 ° and 2.9 °, respectively. Image from [108].

Gas Electron Multiplier

The Gaseous Electron Multipliers (GEM) detector is part of the tracking detector in the Target Spectrometer and covers the forward region of polar angles between 5 ° and 22 °. Therefore, the GEM follows directly the STT. It is planned that the GEM detector consists of 3 planar stations placed between 80 cm and 189 cm downstream with respect to the interaction point. Each station will be made of two planes with two projections per plane and will be equipped with gaseous micro pattern detectors based on Gaseous Electron Multipliers foils as amplification stage. The foil consists of $50\,\mu$m kapton with a $5\,\mu$m copper layer on both sides and is pierced with a high number of holes, typically in the order of 100holes/ mm^2 [113]. The GEM foil is inserted between a drift and a charge collection electron. By applying a potential of typically a few keV/cm, field lines around the holes are created. Electrons which are produced by incoming particles will be accelerated along the field lines and produce an avalanche multiplication of the primary charge which is collected at the readout anode. For the GEM detector at $\overline{\text{P}}$ANDA the spatial resolution is expected to be better than $100\,\mu$m [114].

Forward Tracker

Since $\overline{\text{P}}$ANDA is a fixed target experiment, a coverage of the 4π solid angle and a high momentum resolution for charged particles is necessary. As already mentioned, the Forward Spectrometer will cover the region below ±10 ° in the horizontal and ±5 ° in the vertical plane.

The Forward Tracker (FT) will be the tracking system for charged particles in the Forward Spectrometer. One of its tasks is the measurement of low momentum pions, e.g from Λ decays [109]. The FT consists of three pairs of tracking stations. Figure 4.10 shows a CAD drawing of the FT including also a section of the dipole magnet. It is foreseen to place the first pair upstream of the dipole magnet, the second pair inside the magnetic gap and the third pair downstream of the dipole magnet. A tracking station consists of four double-layers which consists of two straw tube modules. The two first pairs of tracking stations upstream of the dipole contain straws which are skewed by ±5 °, respectively. This arrangement allows three-dimensional track reconstruction at each station which is useful for the reconstruction of multi-track events. In general, the modules consist of 32 straw tube detectors placed in two staggered layers which

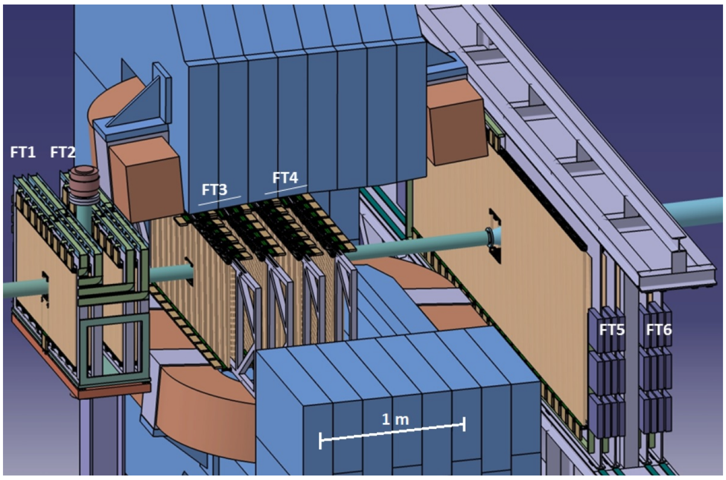

Figure 4.10: CAD drawing of the FT including a section of the dipole magnet and support structures. Image from [109].

are glued together. The tracking stations on both sides of the dipole magnet will have narrower modules close to the beam pipe containing only 24 straw tubes.

Since multiple-scattering as well as photon conversions has to be minimized, the material budget has to be lower than 5 $\%X_0$. Therefore, it is foreseen to use the same straw tube detectors as for the STT. To assure a high invariant mass resolution, the momentum resolution of the FT is required to be at least comparable with the momentum resolution of 1.5 % for the Target Spectrometer. Simulation studies of selected benchmark channels and of background reactions have been performed to estimate the momentum and the position resolution of the FT. The expected resolution is better than 1 % for the momentum and in the order of 100 μm for the position. In addition, the FT will provide information about track parameters in the forward RICH and the forward ToF wall which are located downstream of the dipole magnet. Since the total counting rate is expected to be in the order of $5 \cdot 10^7$ tracks/s, it is necessary that the FT is resistant against aging effects. According to the high counting rates, a fast front-end and digitization electronics is required.

Detectors for Particle Identification

Beside the tracking of charged particles, the particle identification (PID) is important for the event reconstruction. Therefore, the conceptional design of the $\overline{\text{P}}$ANDA detector includes also sub-detectors for the PID, i.e. Cherenkov detectors, namely the Detection of Internal Cherenkov Light (DIRC) and the Ring Imaging Cherenkov (RICH) detector, the Barrel Time of Flight detector, the Forward Time of Flight (FToF) detector and the Muon Detector System (MDS). In this section an introduction to the different detectors for PID is given.

DIRC and RICH

Cherenkov detectors collect photons which are produced by a charged particle traveling through a dielectric medium. If the particle velocity v is larger than the speed of light in the medium with refractive index n, $v > \mathrm{c}/n$, the photons are emitted on a cone with half opening angle given by $\cos\Theta_\mathrm{C} = 1/\beta n$. By combining the evaluated information on the emission angle and the measured momentum information from the tracking detectors, the mass of the particle can be determined with a certain resolution. At

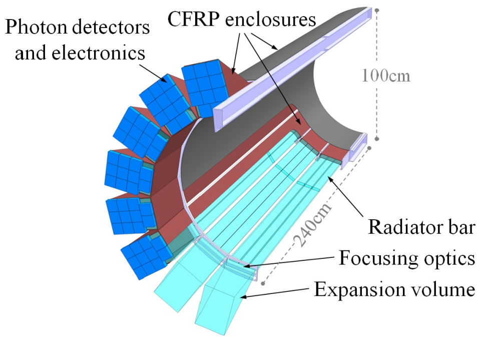

Figure 4.11: Schematic drawing of the barrel DIRC detector. Here, only one half of the detector is shown. Image from [115].

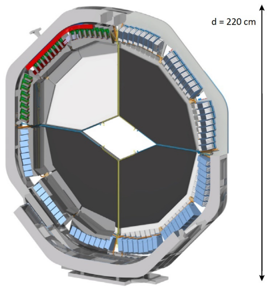

Figure 4.12: Partial cut-away of the Disc DIRC. The support structure are partially included in this picture. Image adapted from [116].

$\overline{\mathrm{P}}$ANDA, two DIRC systems, using the same detection principle, are foreseen for the Target Spectrometer [115]. Furthermore, a RICH detector will be located in the Forward Spectrometer.

DIRC detectors are based on the detection of internally reflected Cherenkov light. The barrel DIRC is located in the Target Spectrometer and placed at a radial distance of 47.6 cm extending 2.4 m along the beam line [115]. Figure 4.11 shows a schematic picture of the barrel DIRC. The detector consists of 16 optically isolated sectors. Each sector is composed of three 17 mm thick fused silica bars with a refractive index $n = 1.473$. At the forward end surface of each bar, a flat mirror is attached to reflect photons towards the read-out system at the upstream. An array of 11 life-time enhanced MCP-PMTs, having a position and time resolution of 2 mm and 100 ps, respectively, measures the location and the arrival time of the photons. The barrel DIRC covers the polar angle range between 22 ° and 140 ° and separates pions and kaons for momenta up to 4.2 GeV/c.
The second Cherenkov detector in the Target Spectrometer is the disc DIRC (Fig. 4.12). It consists of 2 cm thick active areas made of fused silica arranged in a dodecagon [117]. The disc DIRC with a radius of 110 cm is placed upstream of the forward endcap calorimeter and covers polar angles from 10 ° to 22 °.
The Cherenkov detector in the Forward Spectrometer is the RICH detector. It covers polar angles up to 5 ° in the vertical plane and up to 10 ° in the horizontal plane. The main goal of the RICH detector is the identification of hadrons with high momenta. The Cherenkov light, produced in a double-layer radiator made of aerogel and gas, is focused by a mirror to an array of PMTs placed outside the detector acceptance. With the RICH it is possible to separate pions and kaon up to 2.8 GeV/c and kaons and protons up to 4.7 GeV/c.

Barrel Time of Flight Detector

The Barrel Time of Flight detector surrounds the interaction point at a distance of about 50 cm and will cover the polar angle region between 22 ° and 140 °. One of the main goals is the identification of low momentum particles at large polar angles and to deliver a reference time t_0 for the event [118]. A CAD drawing of the Barrel ToF including also a magnified drawing of a pair scintillator tiles is shown in Figure 4.13. Since the Barrel ToF shares its mechanical support with the Barrel DIRC, the segmentation structure also consists of 16-sections which are acting independently from each other. The 20 mm thick and 87 mm long segments, also called super-modules, are composed of 120 scintillating tiles, each, arranged in two columns of 60 scintillators. Four SiPMs combined in a single unit are used to readout each ends. Since the scintillator tiles are made of materials with fast response, a time resolution of

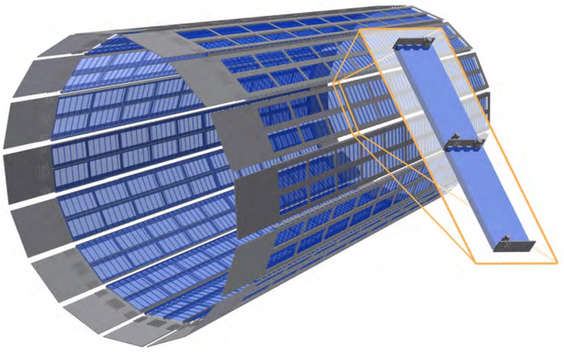

Figure 4.13: CAD drawing of the Barrel Time of Flight (ToF) with a magnified drawing of a pair of scintillator tiles. The scintillator tiles are indicated in blue and the PCBs in gray. The Barrel ToF as a total length of 2460 mm and an external radius of 538 mm. Image from [118].

$\sigma_t < 60$ ps for a single tile is obtained, which is better than the original design goal of 100 ps.

Forward Time of Flight Detector

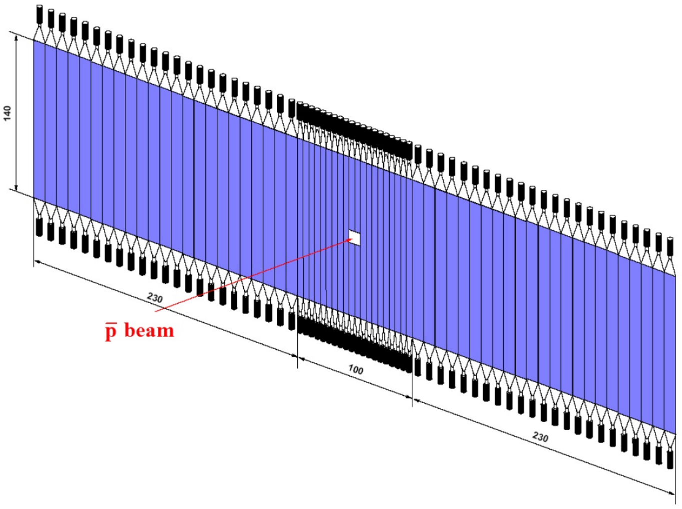

Figure 4.14: CAD drawing of the FToF scintillation wall. Image from [119].

The Forward Time of Flight (FToF) is dedicated for the hadron identification in the Forward Spectrometer [119]. While the RICH will provide an effective hadron separation in the momentum region between 2 GeV/c and 4 GeV/c, the FToF will provide the PID information at particle momenta below 4 GeV/c. Beside the PID, the detection of event time stamps in one or more scintillation blocks is one of its main tasks. The measured information will give the possibility to reconstruct the event start time for relativistic particles. Therefore, the time resolution has to be better than 100 ps.
As its name already indicates, the FToF will be part of the Forward Spectrometer and is located 7.5 m downstream of the interaction point. A general view of the FToF detector is shown in Figure 4.14. The FToF is composed of 20 scintillator slabs with a width of 5 cm in the central part and of 23 slabs with a width of 10 cm in the outer region on either side. Arranged in a scintillation wall, the total sensitive area

has a width of 5.6 m, a height of 1.4 m and a thickness of 2.5 cm. The read-out is done with 1” PMTs in the central part and with 2” PMTs in the outer region. All PMTs are positioned vertically so that their axes are parallel to the y-axis of the $\overline{\text{P}}$ANDA detector.
The achieved online time resolution is 200 – 250 ps while a time resolution of 90 – 80 ps can be obtained in an offline analysis.

Muon Detector System

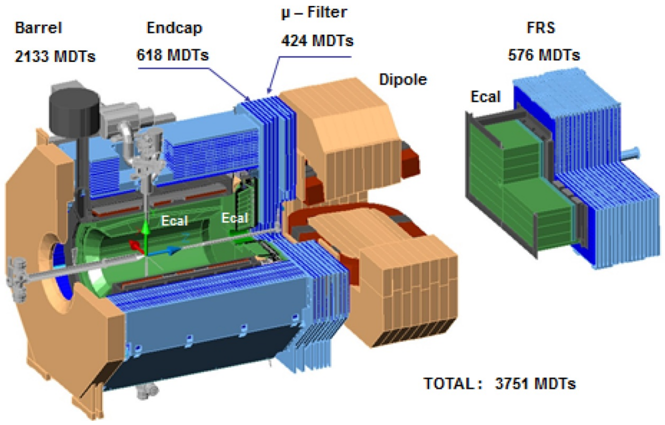

Figure 4.15: Illustration of the MDS components (blue parts) with the number of MDTs for each subsystem. Image from [120].

A good muon identification is needed in $\overline{\text{P}}$ANDA to measure muons with a momentum up to 10 GeV/c. The muon identification in the $\overline{\text{P}}$ANDA spectrometer can be done with different detector systems: the muon filter, the calorimeter, the scintillator detectors and the Cherenkov detectors, while the muon filter will be the main one for muon identification [120]. By correlating the signals from all listed systems, a desirable level of signal purity will be provided. The main task of the MDS will be the muon identification by using pattern recognition and matching the track segments to the tracks of the detectors inside the magnets.
The MDS, which is illustrated in Figure 4.15, consists of a barrel part and a End-Cap in the Target Spectrometer and a range system in the Forward Spectrometer. For the barrel part of the MDS, 13 sensitive layers with a thickness of 3 cm, alternating with 3 cm thick iron absorber layers, are planned. A sensitive layer consists of MDTs and strip boards which are attached to each other. Due to mechanical reasons, the first and the last iron absorber layer are 6 cm thick.
The End-Cap is composed of six sensitive layers with five iron absorber layers in between. For a better muon detection, the iron absorber in the End-Cap has to be thicker than in the barrel part. Therefore, a thickness of 6 cm is chosen. In addition to the End-Cap part, a muon filter is planned. The mechanical structure of the filter is chosen according to the structure of the End-Cap, but different in the number of layers. Five sensitive layers enclosing four iron absorber layers are planned which will be located in the gap between the solenoid and the dipole magnet. In total about 4000 MDTs are included in the full MDS.

Electromagnetic Calorimeter

Within the comprehensive $\overline{\text{P}}$ANDA physics program, many channels have photons or electron-positron pairs in the final state [121]. The main task of the Electromagnetic Calorimeter (EMC) is the efficient

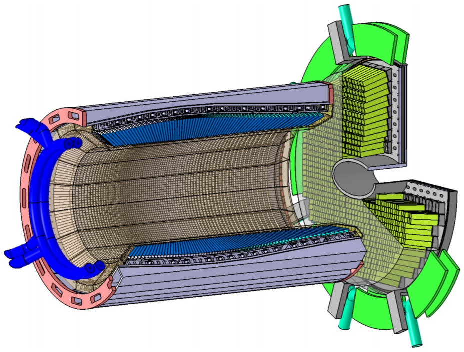

Figure 4.16: CAD drawing of the EMC barrel (length: 2.5 m, inner radius: 0.57 m) and the forward endcap (diameter: 2 m). Image from [121].

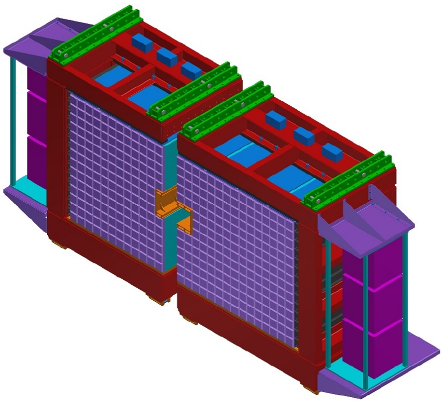

Figure 4.17: Sketch of the FSC as seen from the front side. The dimensions of the detector are 3.6 m in width and 2.2 m in height. Image from [122].

reconstruction of electrons, positrons and photons while suppressing the background efficiently. Beside the measurement of the deposited energy, the EMC will also provide time information to make a distinction between different events which are close to each other in time. Due to the high count rates and the compact design of the Target Spectrometer, a fast scintillator material with a short radiation length for the construction of the EMC is required. Lead tungstate ($PbWO_4$), an inorganic scintillator, optimized for large scale production, provides a sufficient energy and time resolution for the detection of photons, electrons and hadrons. In order to achieve an energy resolution better than 2 % at 1 GeV, the crystals of the $\overline{\text{P}}$ANDA EMC (Fig. 4.16) are 20 cm long which corresponds to a radiation length of 22 X_0. The tapered crystals have a front size of $2.1 \times 2.1\,\text{cm}^2$ and will be mounted with an inner radius of 57 cm. Therefore, more than 15,000 $PbWO_4$ crystals will be mounted to the barrel EMC which will be operated with a temperature of $-25\,°C$ to increase the light yield by a factor 4 compared to the operation at +25 °. The EMC has to cover an energy range between 10 MeV and 15 GeV while covering nearly the full polar angle region. Therefore, the EMC in the Target Spectrometer is composed of a barrel part and two endcaps, the forward and the backward endcap. The polar angle region between 5 ° and 22 ° is covered by the forward endcap. Particles with angles between 22 ° and 140 ° will be measured in he barrel part. The backward region with respect to the beam direction corresponds to polar angles between 140 ° and 150 ° and will be covered by the backward endcap. This leads to a coverage of about 99 % of the full solid angle. Beside the angular coverage, the different EMC parts also cover different energy regions. Table 4.1 summarizes the energy and the angular coverage for all three parts of the EMC in the Target Spectrometer.

In the Forward Spectrometer, a shashlyk-type calorimeter is foreseen, which is positioned about 7 m downstream from the interaction point. Figure 4.17 shows a sketch of the Forward Spectrometer electromagnetic Calorimeter (FSC). Since the FSC will be located between the FToF and the MDS, the

Table 4.1: Energy range and covered polar angle region of the different EMC parts.

	energy range	polar angle range
backward endcap	10 MeV – 0.7 GeV	5 – 22 °
barrel EMC	10 MeV – 7.3 GeV	22 – 140 °
forward endcap	10 MeV – 14.6 GeV	140 – 150 °

total depth is limited by the length of the Forward Spectrometer [122]. Therefore, the depth of the FSC in terms of radiation length is $20\,X_0$. The calorimeter will consist of 378 modules with four cells of $55 \times 55\,\text{mm}^2$ each, covering a total active area of $3\,\text{m} \times 1.5\,\text{m}$. The FSC at $\overline{\text{P}}$ANDA is meant to detect photons and electrons within a energy region of $10\,\text{MeV} - 15\,\text{GeV}$and covers a polar angle region up to $5\,°$. The expected energy resolution is $\sigma_\text{E}/\text{E} \approx (2-3)\,\%/\sqrt{\text{E}/\text{GeV}}$.

Luminosity Detector

A large fraction of the spectroscopy studies is focused on the formation processes of hadrons. By varying the beam energy, for example, it is possible to observe the production of a resonant state. A precise measurement of the beam energy and the luminosity allows to unfold the physical shape of the resonance [123]. Since the measurement has to be normalized with the time integrated luminosity for each beam energy, an accurate measurement of the luminosity is necessary. The LMD at $\overline{\text{P}}$ANDA measures elastically forward scattered antiprotons at small momentum transfers, while the distance to the interaction has to be large enough, so that the interacting particles are not masked by non-interacting beam particles. Therefore, it is foreseen to mount the LMD 10.5 m downstream of the interaction point. The LMD will allow measuring elastically scattered particles in the angular region between 3 mrad and 8 mrad. A CAD drawing of the planned LMD is shown in Figure 4.18. It will consist of four detector planes with a radius of 15 cm and is equipped with 400 actively cooled High Voltage Monolythic Active Pixel Sensors (HV-MAPS) lowered inside a vacuum box. The HV-MAPS are produced as individual squares with a size of $2 \times 2\,\text{cm}^2$. To cover a 2π acceptance around the beam pipe, the sensors are overlapping.

To determine the t-dependence of the cross section, particle tracks reconstructed in the LMD will be back-propagated to the interaction point. Subsequently, a fit of the expected cross section to the angular distribution will lead to a value for the time integrated luminosity. The expected precision for the absolute time-integrated luminosity will be better than 5 % and for the relative time-integrated luminosity better than 1 %[123].

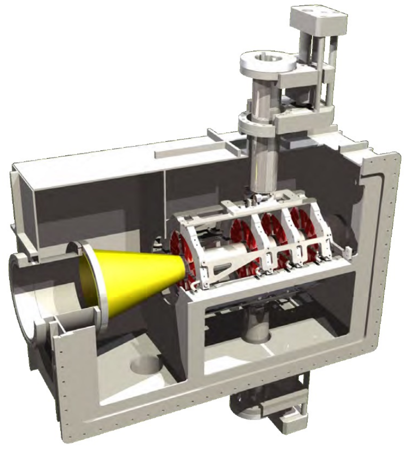

Figure 4.18: CAD drawing of the Luminosity Detector (LMD). The detector planes have a radius of 15 cm. Modified image from [123].

4.3 Software Framework

The software framework used for the $\overline{\mathrm{P}}$ANDA experiment is called PandaRoot and is based on ROOT [124] and the Virtual Monte Carlo (VMC) packages [125]. The implementation of the simulation code for the $\overline{\mathrm{P}}$ANDA detector and the reconstruction code is done within the FairRoot software framework [126] which was developed by the GSI-IT with the aim to have a common computing structure for all future FAIR experiments [127]. FairRoot itself is also based on the ROOT package and provides dynamic data structures. VMC handles the detector simulation and therefore allows the usage of the transport models Geant3 and GEANT4 with the same detector code. Within PandaRoot several event generators, i.e. EvtGen,DPM, UrQMD, Pyhtia and Fluka, are used for the production of physics and background events. These events are then sent to the transport model by VMC. The geometry of the detector can be described by using ASCII files or ROOT objects. An additional application allows converting CAD drawings into ROOT geometries.
After the simulation of the events and the propagation through the detector, the detector response is simulated by digitizers.

Tracking

In order to form charged particle tracks, hits in the tracking detectors are combined. Therefore, a reconstruction code is used which merges the information from the different tracking detectors.
The tracking for the target detector assumes a constant magnetic field and helix trajectories for charged tracks. To achieve a high momentum resolution in the reconstruction the magnetic field inhomogeneities, energy loss as well as the different data structure and the error calculation for the different detectors have to be taken into account. Therefore, the Kalman Filter GENFIT [128] and GEANE [129] as track follower are used. The tracking algorithms for the forward tracker are still under development.
Actually, within the realistic tracking algorithms the particle origin is assumed to be equal to the interaction point. This leads to the fact, that the track reconstruction of secondary particles does not work properly. Furthermore, this poses a problem for the studies of hyperons, i.e. Ξ and Λ baryons. Due to their relatively long lifetime, hyperons decay with displaced vertices, which are not reconstructable with the current realistic tracking algorithm. Therefore, for current hyperon studies, only the usage of ideal tracking algorithms is possible. The ideal tracking algorithms group the hit points along a particle track based on the generated particle information. However, this leads to the reconstruction of particle tracks with only one hit point in one of the tracking detectors.

Particle Identification

The information on the reconstructed particle tracks coming from the tracking detectors are correlated to the information of the PID detectors in order to form charged candidates. If the tracks are not correlated to clusters inside the electromagnetic calorimeter, neutral candidates are formed. Since the PID detectors have different concepts, for the development of the PID methods, two approaches are followed: the implementation of standard algorithms based on Bayesian approaches for a fast particle identification and a multivariate analysis technique which is under implementation. The first approach can be used, if the signals can be easily separated while the second approach is used for high level identification to extract small signals from large data sets. For each PID detector, the approaches assign a particle probability value to each candidate. The probability values can be merged to a global probability value according to the specific analysis.

Analysis

To perform a high-level analysis, a modified version of the Rho package [130] has been implemented in PandaRoot. This package provides the possibility to select particle candidates according to defined PID selection criteria and kinematic constraints. The selected particles can be combined and different kinematic and vertex fitting algorithms can be applied.

CHAPTER 5

Simulation and Reconstruction of Excited Cascade States

5.1 The Reaction Channel $\bar{p}p \to \overline{\Xi}^{+} \Lambda K^{-}$

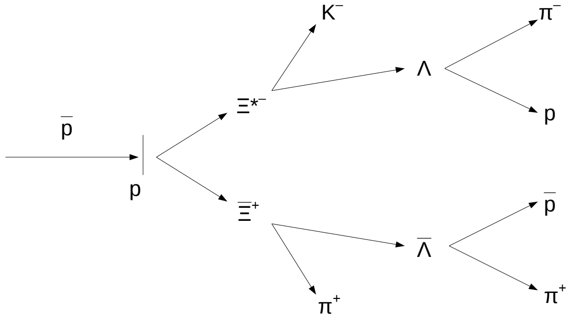

Figure 5.1: Illustration of the reaction chain

The quark model presented in Section 2.1 predicts a significant number of light baryons which have not been observed, yet. Furthermore, there is no theoretical model which can explain the measured baryon spectrum. To find and validate models allowing a general correct description of all baryon spectra in the light quark sector input is needed.

Up to now only the nucleon excitation spectrum has been subject to systematic studies while much less information is available on excited states of double or even triple strange baryons. The experimental data on Ξ resonances are coming almost entirely from bubble chamber experiments. This lack of information to a large extent is caused by the complicated topology of the reactions producing Ξ resonances [1]. A second reason is their small production cross section when using proton or electron beams. Since 1988 "nothing of significance on Ξ resonances was added" [1] to the Particle Data Group (PDG) editions. The experimental status indicates that only a few Ξ resonances states are well established by independent observations in different experiments. Further investigations are needed to determine the properties like spin and parity quantum numbers of those states the existence of which is considered to be very likely. Table 5.1 lists the predicted Ξ resonances according to [1]. In addition, in a recent publication, the Belle

Table 5.1: Status of the Ξ Resonances. The evidence for the existence is indicated by the stars: from poor (*) to certain(****). Modified table from [1]

Particle	J^P	Overall status	Seen in Λ K
Ξ(1318)	1/2+	****	
Ξ(1530)	3/2+	****	
Ξ(1620)		*	
Ξ(1690)		***	***
Ξ(1820)	3/2−	***	***
Ξ(1950)		***	**
Ξ(2030)		***	**
Ξ(2120)		*	*
Ξ(2250)		**	
Ξ(2370)		**	
Ξ(2500)		*	*

collaboration has shown the existence of the $\Xi\,(1620)^0$ resonance [131]. Furthermore, evidence for the existence of the $\Xi\,(1690)^0$ was found.
An ideal entrance channel for baryon spectroscopy in the multi-strange sector is provided by antiproton-proton collisions. A large fraction of the p̄p cross section is associated to final states with a baryon-antibaryon pair together with additional mesons, giving access to excited states both in the baryon and antibaryon sector. For final states containing a $\overline{\Xi}^+$ Ξ^- pair cross sections up to the order of μb are expected. This feasibility study is focused on excited Ξ states decaying into Λ K^- and $\bar{\Lambda}$ K^+ in the charge conjugate case at an antiproton momentum of 4.6 GeV/c. Beside the continuum case the two (***)-resonances Ξ(1690) and Ξ(1820) are included in this study. The chosen beam momentum corresponds to a center-of-mass energy about 100 MeV above the $\overline{\Xi}^+$ $\Xi\,(1820)^-$ production threshold. For the reconstruction of reactions of the type $\bar{p}p \rightarrow \overline{\Xi}^+ \Lambda K^-$ and $\bar{p}p \rightarrow \Xi^- \bar{\Lambda} K^+$ the development of two analysis algorithms is done. Both algorithms should be able to reconstruct the events according to the decay tree shown in Figure 5.1. The generation and the reconstruction of the events are carried out with the PandaRoot framework [127]. Next to the reactions $\bar{p}p \rightarrow \overline{\Xi}^+ \Xi^*$ and $\bar{p}p \rightarrow \overline{\Xi}^* \Xi^-$, called signal channels, another data sample containing p̄p reactions to present the inelastic hadronic cross section is analyzed. Those events are called background events in the following.

5.2 Event Generation

In this study, the events to be analyzed were generated with the event generator EvtGen [132]. The chosen momentum of the antiproton beam is $p_{\bar{p}} = 4.6$ GeV/c. This value corresponds to a center-of-mass energy of $\sqrt{s} = 3.25$ GeV and is about 320 MeV above the production threshold of $\overline{\Xi}^+$ Λ K^- or Ξ^- $\bar{\Lambda}$ K^+ in the charge conjugate (c.c.) channel. Within the kinematically allowed region given by the chosen beam momentum, the population of the resonant states $\Xi\,(1690)^-$ and $\Xi\,(1820)^-$ as well as $\overline{\Xi}\,(1690)^+$ and $\overline{\Xi}\,(1820)^+$ is possible. Table 5.2 shows the values for the mass and the width of the resonances according to [1]. Table 5.3 shows the cross section ratio between the resonant and non-resonant final state. This ratio is an assumption based on measured total production cross sections of both excited states and ground states of single strange hyperons (see [26]).

Table 5.2: Mass and width of the resonances implemented for the event generation.

State	Mass [MeV/c^2]	Γ [MeV/c^2]
$\Xi(1690)^-$	1690	30
$\Xi(1820)^-$	1823	24

Table 5.3: Decay modes and chosen ratios implemented for the event generation.

Fraction	Channel	Channel (c.c.)
0.4	$\overline{\Xi}^+\ \Xi(1820)^-$	$\Xi^-\ \overline{\Xi}(1820)^+$
0.4	$\overline{\Xi}^+\ \Xi(1690)^-$	$\Xi^-\ \overline{\Xi}(1690)^+$
0.2	$\overline{\Xi}^+\ \Lambda\ K^-$	$\Xi^-\ \bar{\Lambda}\ K^+$

In absence of experimental data and theoretical predictions for the reaction $\bar{p}p \rightarrow \overline{\Xi}^+\ \Xi^*$ the Phase Space (PHSP) model, generating an isotropic angular distribution, is chosen for each decay mode. This simplification does not affect the selection strategy presented in this study, but ensures that baryon and anti-baryon, respectively, are underlying the same detector acceptance. In addition, the decay of each resonance is assumed to be isotropic.

The production cross-section for $\bar{p}p \rightarrow \overline{\Xi}^+\ \Xi^*$ is unknown. However, for the production of $\Xi^-\ \overline{\Xi}^+$ in $\bar{p}p$ collisions a cross section $\sigma \simeq 2\,\mu$b has been measured at $p = 3$ GeV/c [23]. A comparison of the ground state and the excited single strange hyperon production shows similar cross sections for both species [26]. Therefore, in this work the cross section σ for $\bar{p}p \rightarrow \overline{\Xi}^+\ \Xi^*$ is assumed to be $1\,\mu$b.

Within EvtGen, the curved trajectories of Ξ^- and $\overline{\Xi}^+$ in the magnetic field of the solenoid as well as their interaction with the detector volume are not taken into account. For this reason the propagation and the decay of Ξ^- and $\overline{\Xi}^+$ are managed by GEANT4. The branching ratio of both cascades into $\Lambda\,\pi$ is 99.98% [1]. Different from Ξ^- and $\overline{\Xi}^+$, Λ and $\bar{\Lambda}$ have various decay modes. In this study, the focus is on $\Lambda \rightarrow p + \pi^-$ and $\bar{\Lambda} \rightarrow \bar{p} + \pi^+$ with a branching ratio of BR($\Lambda \rightarrow p + \pi^-$)= 0.634 each. To avoid the production of unwanted decay modes for Λ and $\bar{\Lambda}$, the branching ratio is set to 100% in GEANT4, respectively. Therefore, the final result is scaled by the correct branching ratios.

5.3 Event Analysis

This Section presents two different analysis strategies. The first strategy shows the reconstruction of the composite state particles (Ξ^-, $\overline{\Xi}^+$, Λ and $\bar{\Lambda}$) using the conventional fitting procedures, i.e. vertex fitting and kinematic fitting with mass constraints and 4-momentum constraints. During this analysis it has been shown, see Section 5.3.1, that the fit methods do not work properly. Since the cause for this has not yet been found, a second strategy using a DecayTreeFitter [133] is shown. The DecayTreeFitter fits the full decay tree recursively. In this analysis the DecayTreeFitter uses vertex fits as well as kinematic fits with mass constraints for the composite state particles and 4-momentum constraints.

The input of the analysis algorithms are the final state particles, namely p, $\bar{p}$, π^-, π^+, K^- and K^+, after tracking and PID. Beginning with these particles, the reconstruction is carried out according to the decay tree shown in Figure 5.1 to achieve the reconstruction of the full event up to the $\bar{p}p$ system.

Track filtering

As already mentioned in Section 4.3, the tracking algorithms in PandaRoot assume the particles to come from the interaction point. Since the lifetimes of Ξ^- ($c\tau = 4.91\,\mathrm{cm}$[1]) and Λ ($c\tau = 7.89\,\mathrm{cm}$[1]) are relatively long, the implemented tracking algorithms are not able to reconstruct the final state particles of this reaction. Therefore, an ideal pattern recognition algorithm is used. This algorithm groups the hit points caused by the particle inside the detector based on their Monte Carlo (MC) information. A consequence of this is that even particles with only one hit in any of the detector parts will be reconstructed. Since this is not the case in the real experiment, a track filtering is necessary to reject those reconstructed tracks. Therefore, for the analysis only those final state particles are kept which leave at least 4 hits in one of the inner tracking detectors, either MVD, STT or GEM. The selection criterion is motivated by the trajectory of the particle in a homogenous magnetic field. Particles propagating through a magnetic field follow a helix trajectory. Assuming that the particle is moving along the z-axis, the projection of the trajectory onto the x-y-plane is a circle. To define a circle, three hits inside the detector part are needed. A fourth hit will then confirm the track hypothesis.

5.3.1 Sequential Fit Procedure

A data sample of 10 million events has been generated for the analysis with conventional fitting. The sample contains 5 million events each for $\bar{\mathrm{p}}\mathrm{p} \rightarrow \overline{\Xi}^+ \, \Lambda \, \mathrm{K}^-$ and $\bar{\mathrm{p}}\mathrm{p} \rightarrow \Xi^- \, \bar{\Lambda} \, \mathrm{K}^+$.

5.3.1.1 Final State Particle Reconstruction

As mentioned before, the analysis of the sample starts with the selection of the final state particles. After the track filtering, the candidates for π^-, π^+, p, $\bar{\mathrm{p}}$, K^- and K^+ are filled into the corresponding candidate lists according to the PID probability. As a starting point a simplified PID algorithm is chosen which uses the information on the particle species given in the generated data. This algorithm sets the probability of particle for the true species to 1, and to 0 for all others.
Since the decay tree includes 6 final state particles for $\bar{\mathrm{p}}\mathrm{p} \rightarrow \overline{\Xi}^+ \, \Lambda \, \mathrm{K}^-$ as well as 6 final state particles in the charge conjugate channel, only a selection of evaluated histograms are shown in this section. For the completeness of the analysis, the remaining histograms are listed in Appendices A.1.1 and A.2.1.

Reconstruction efficiencies The reconstruction efficiency is defined as the ration of MC matched reconstructed candidates and the number of generated candidates. This means, that only those reconstructed particles which have a corresponding partner in the MC-truth list are taken into account. MC matching also includes the check of a correct event genealogy up to the initial $\bar{\mathrm{p}}\mathrm{p}$ system.

Table 5.4 shows the reconstruction efficiencies for the final state particles. The statistical error on the efficiency for all particle types is $\sigma_\epsilon \simeq 0.1\%$. For the charge conjugate channel the reconstruction efficiencies are significantly higher. The reason is still unknown and further investigations are needed.

Momentum and Angular Distributions For each final state particle two dimensional histograms of transverse momentum versus longitudinal momentum, as well as absolute momentum versus polar angle are generated. As an example, Figures 5.2 – 5.5 show the transverse momentum versus the longitudinal momentum distribution for the π^- emitted in the Λ decay. The transverse momentum distribution of the π^- is expected to be up to 0.25 GeV/c with a peak between 0.04 GeV/c and 0.15 GeV/c. The range of the longitudinal momentum is $0\,\mathrm{GeV/c} \leq p_z \leq 0.8\,\mathrm{GeV/c}$ with a peak between 0.05 GeV/c and 0.35 GeV/c. The generated distributions can be used as reference plots to deduce the quality of the reconstruction.

Due to the kinematics of the decays, the generated distributions are expected to have sharp boundaries with no event being outside. Nevertheless, for all final state particles the distributions contain a significant number of events outside the kinematically allowed region. One reason is the interaction of the generated particles inside the detector material or with the beam pipe during their propagation. Those interactions can lead to additional recoil particles so that Λ, $\bar{\Lambda}$, $\overline{\Xi}^{+}$ and Ξ^{-} could have more than two daughter particles. Therefore, some generated events will not fulfill the genealogy shown in Figure 5.1. Requesting that Λ and $\overline{\Xi}^{+}$ as well as $\bar{\Lambda}$ and Ξ^{-} have only two daughters, reduces the number of events outside the kinematically allowed region significantly as shown in Figure 5.3.

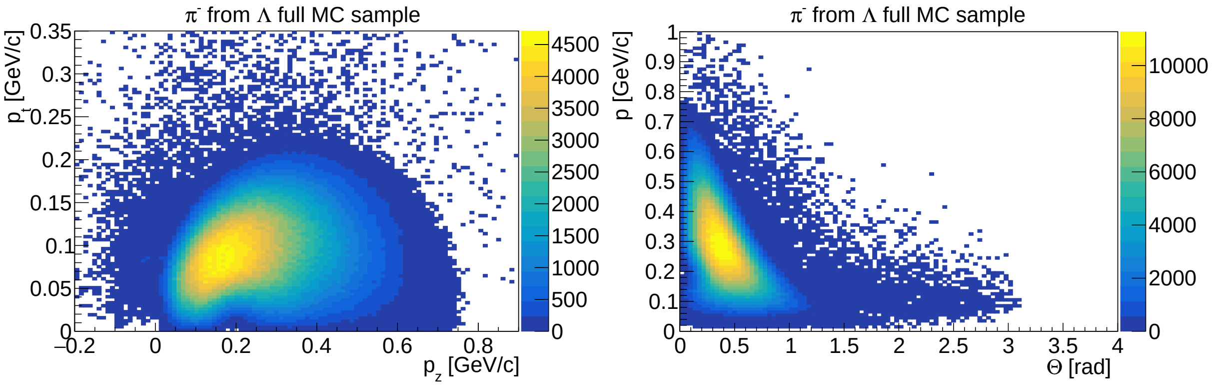

(a) (b)

Figure 5.2: Transverse versus longitudinal momentum (a) and momentum versus polar angle Θ (b) for the generated π^{-} from Λ decay.

Momentum Resolution For all final state particles the momentum resolution is evaluated. The momentum resolution is defined as

$$\frac{p^{\text{reco}} - p^{\text{MC}}}{p^{\text{MC}}} \tag{5.1}$$

the difference between the reconstructed and the generated (MC) momentum normalized to the MC momentum. This measurement requires that the reconstructed candidate has a MC truth partner. By performing a double Gaussian fit the resolution of the resulting distribution is determined and the width of the inner Gauss fit is used to specify the resolution. Table 5.4 shows the determined fit values for all

Table 5.4: Reconstruction efficiencies and momentum resolution for all final state particles.

Particle type	$\epsilon[\%]$	$dp/p[\%]$
π^{-} (Λ)	63.9	1.61
π^{+} ($\bar{\Lambda}$)	61.1	1.64
π^{+} ($\overline{\Xi}^{+}$)	65.9	1.49
K^{-} (Resonance)	76.3	1.65
K^{-} (Continuum)	76.5	1.65
p	79.7	1.63
$\bar{p}$	74.0	1.59

(a) $\bar{p}p \rightarrow \overline{\Xi}^{+}\,\Lambda\,K^{-}$

Particle type	$\epsilon[\%]$	$dp/p[\%]$
π^{-} (Λ)	67.5	1.65
π^{+} ($\bar{\Lambda}$)	69.9	1.61
π^{-} (Ξ^{-})	72.6	1.48
K^{+} (Resonance)	86.7	1.65
K^{+} (Continuum)	86.9	1.65
p	85.8	1.61
$\bar{p}$	83.4	1.61

(b) $\bar{p}p \rightarrow \Xi^{-}\,\bar{\Lambda}\,K^{+}$

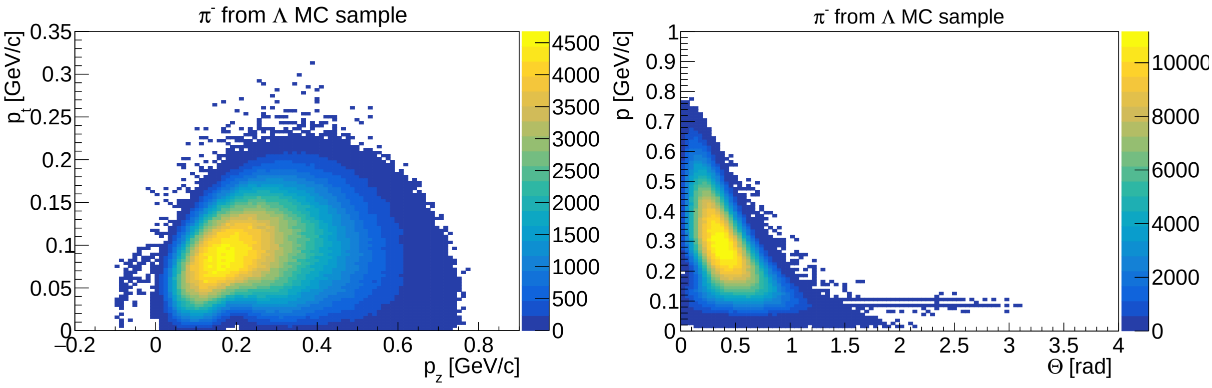

(a) (b)

Figure 5.3: Transverse versus longitudinal momentum (a) and momentum versus polar angle Θ (b) for the generated π^- from Λ decay requesting that Λ and Ξ^- have only two daughter particles.

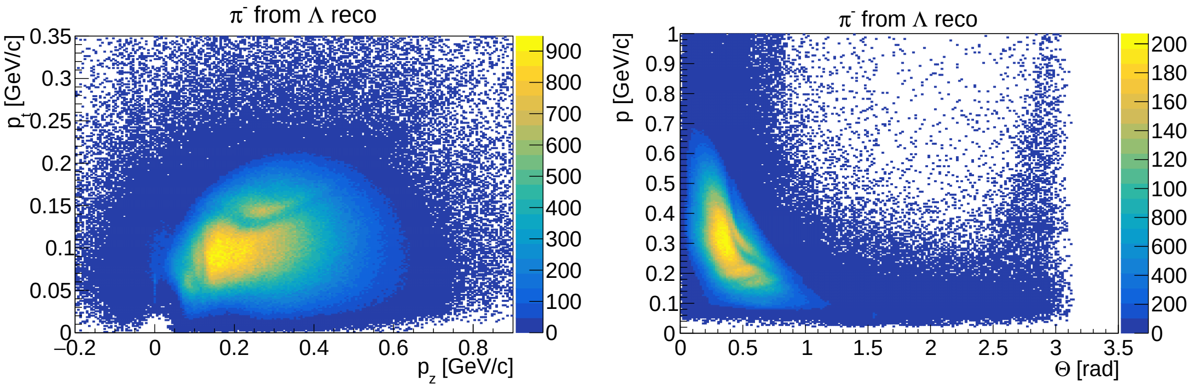

(a) (b)

Figure 5.4: Transverse versus longitudinal momentum (a) and momentum versus polar angle Θ (b) for the reconstructed π^- from Λ decay.

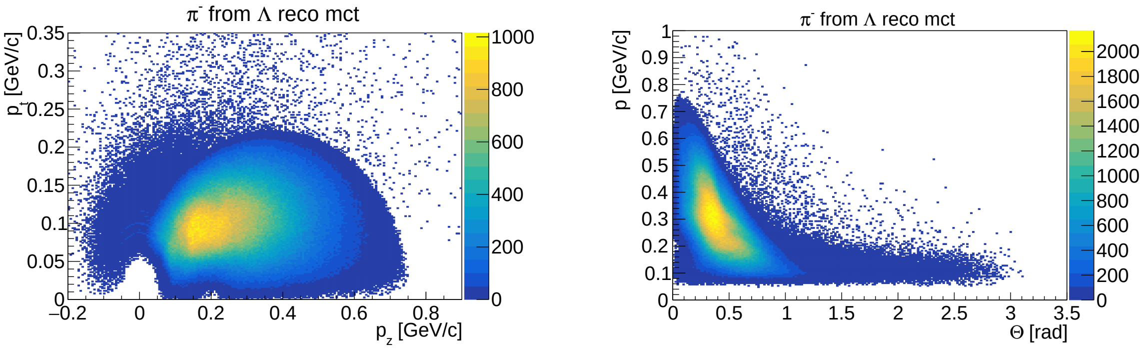

(a) (b)

Figure 5.5: Transverse versus longitudinal momentum (a) and momentum versus polar angle Θ (b) for the MC partners of the reconstructed π^- from Λ decay.

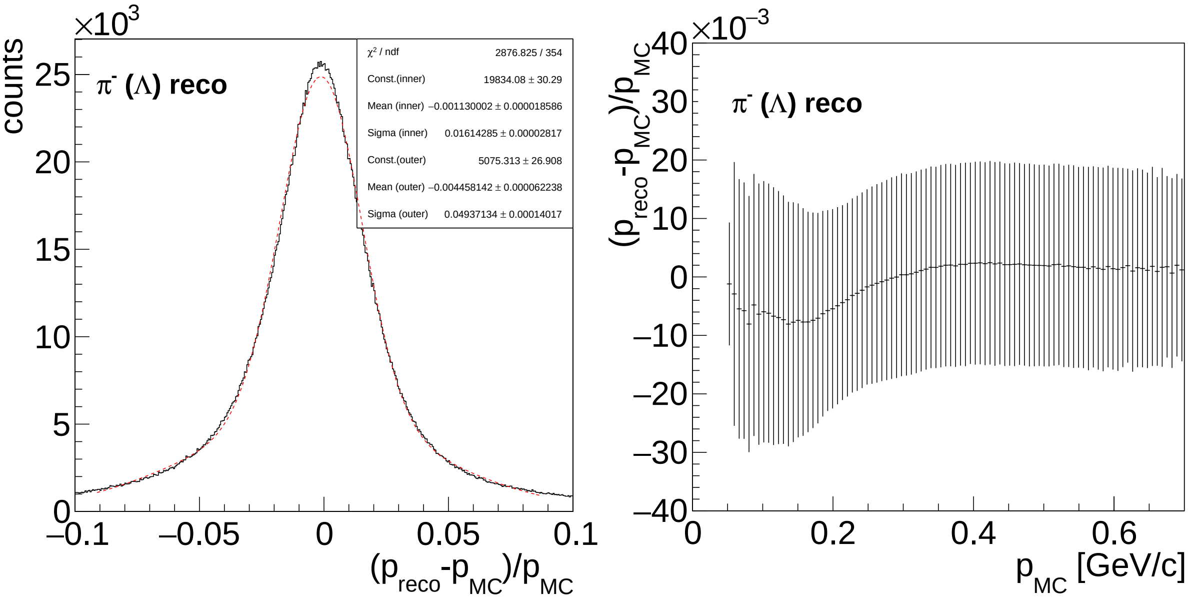

(a) (b)

Figure 5.6: Momentum resolution dp/p (a) and momentum resolution versus total generated momentum (b) of π^- from Λ decay.

final state particles. The best momentum resolution is measured to $dp/p = 1.49\%$ for the π^- from Ξ^- and $dp/p = 1.49\%$ for π^+ from $\overline{\Xi}^+$. The contribution of the systematic error has been estimated to be 0.09% by varying the fit parameters. Figure 5.6 shows the momentum resolution of the π^- candidates.
The momentum resolution depends on the total momentum of the particle. For systematic studies the relative momentum is plotted against the total generated momentum. Here a profile plot is used where each entry represents the mean value of the relative momentum deviation combined with its Root Mean Square (RMS) in the respective bin of the total momentum. For all pions the profile plots show that up to a generated total momentum of 0.3 GeV/c the mean value of the reconstructed total momentum is smaller than the generated value. Figure 5.6(b) shows the profile plot for π^- from Λ decay. Between 0.3 GeV/c to 0.6 GeV/c the mean deviation of reconstructed and generated momentum is centered close to zero. Above a total generated momentum of 0.6 GeV/c the mean deviation of reconstructed and generated total momentum is again going to negative values. For the kaons, regardless of whether they are produced promptly or as a daughter of one of the resonances, the profile plots show a dip in the relative deviation down to -0.02 around a generated total momentum of 0.4 GeV/c. A similar behavior as for the pions is seen for the protons and anti-protons. Up to 1 GeV/c the profile plots show that the reconstructed total momentum is smaller than the generated one. Between 1 GeV/c and 2.8 GeV/c the relative deviation of the reconstructed and the generated total momentum spreads around zero.

The distinct drop towards lower momenta could be related to the treatment of particle propagation through matter in the Kalman Filter of the GENFIT [134] software package which is used for track reconstruction and depending on the particle species. Since on the track reconstruction stage no information on the particle identity is available, a hypothesis has to be set. By default, the pion hypothesis is assumed. For a given momentum within this kinematic region, the higher the particle mass, the higher the energy deposited in the material. This leads to an imprecise Kalman Filter estimation for heavier particles like protons. The same behavior was also observed in previous studies [27, 135].

5.3.1.2 Reconstruction of Λ and $\bar{\Lambda}$

This paragraph describes the reconstruction of Λ and $\bar{\Lambda}$. The shown figures correspond to the reconstructed Λ from $\bar{p}p \rightarrow \Xi^- \bar{\Lambda} K^+$, while the figures for $\bar{\Lambda}$ are shown in Appendix A.1.2 and those for the charge conjugate channel in Appendices A.2.2 and A.2.3.

The first step of Λ and $\bar{\Lambda}$ reconstruction is the combination of π^- and proton for Λ and π^+ and $\bar{p}$ for $\bar{\Lambda}$. Since the number of possible combinations is expected to be large, a mass window cut of $\pm 0.15\ \mathrm{GeV/c^2}$ symmetrically around the nominal Λ mass $M_\Lambda = 1.116\,\mathrm{GeV/c^2}$ is used to reduce the number of wrongly combined candidates with a mass far from the nominal Λ mass. The lower limit of the mass distribution is defined by the sum mass of p and π^-. After the mass window cut, the mass distribution (see also Figure 5.9) shows a plateau for the mass region between $1.13\,\mathrm{GeV/c^2}$ and $1.16\,\mathrm{GeV/c^2}$. This plateau is caused by combinatorial background. The source of this background is mainly the combination of secondary particles with high momenta.

Candidate Selection The selection of the candidates which are passed to the next reconstruction stage is divided in two steps. The first part is the performance of a vertex fit with the PndKinVtxFitter, implemented in the PandaRoot framework, on the candidates passing the mass window cut. The vertex fit assures that both daughter particles, π^- and p or π^+ and $\bar{p}$ for $\bar{\Lambda}$, originate from the same production point. Therefore, the fitting procedure corrects the momentum vectors of both particles to fulfill this condition. The quality of the vertex fit is represented by the χ^2 distribution. Since the number of degrees of freedom for the vertex fit is one, the χ^2 distribution is expected to have a prominent peak around 1. The expected χ^2 value for a well fitted candidate should be close to 1. Therefore, a bad fit corresponds to a fit probability close to zero and we expect the probability distribution to be flat for values larger than 0.01.

The selection criterion used in this analysis is chosen according to the fit probability. Only those candidates pass the vertex fit if their fit probability is better than or equal to 0.01. The χ^2 and the vertex fit probability distribution for Λ is shown in Figure 5.7. While the χ^2 distribution fulfill the expectations, the probability distribution displays a rising behavior for values close to 1. The reason for this behavior is not fully understood, yet. However, this behavior has also been observed in previous studies [27, 135].

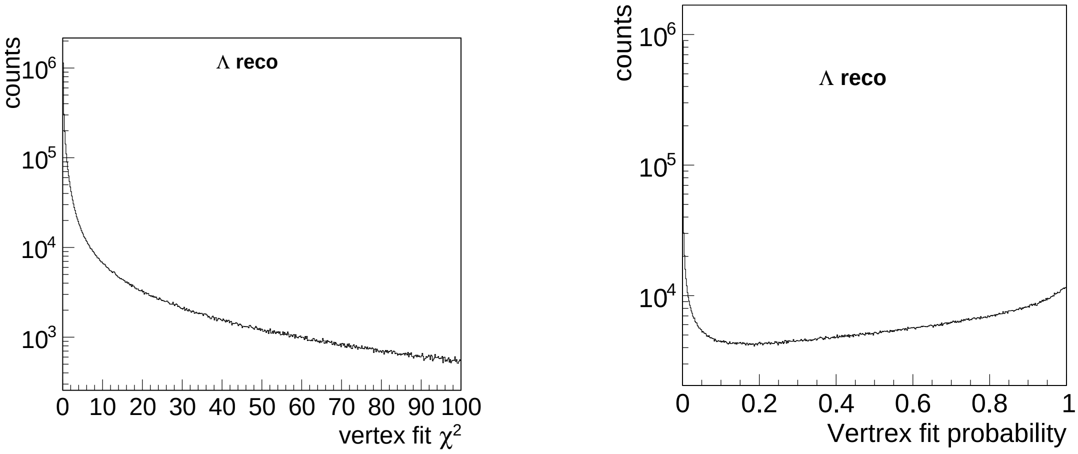

(a)

(b)

Figure 5.7: χ^2 (a) and probability (b) distributions for the vertex fit.

The second step in the candidate selection is the usage of a kinematic fit with a mass constraint to match the Λ and $\bar{\Lambda}$ mass. In this analysis the PndKinFitter implemented in PandaRoot is used for all kinematic fits. The kinematic fit is applied to the vertex fitted candidate. Since the fit forces the 4-momentum vector of the daughter particles to match the invariant mass of the Λ, the usage of the corrected vertex fitted candidates could have counter-productive effects on the quality of the candidate. Therefore, the performed fit is only used to apply a quality cut. The vertex fitted candidate having a fit probability of at least 1% in the kinematic fit with mass constraint is passed to the next reconstruction stage. Here again the rising behavior of the fit probability (Fig.5.8) is observable.

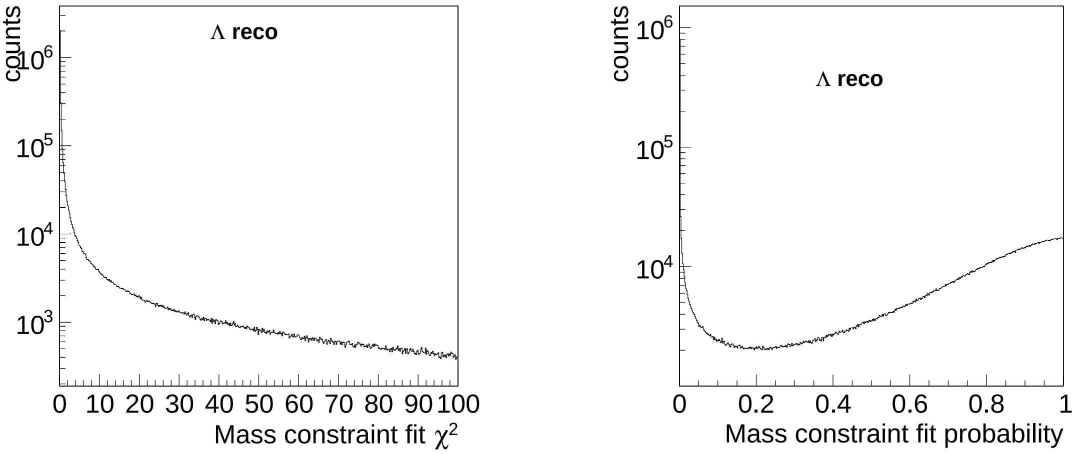

(a)

(b)

Figure 5.8: χ^2 (a) and fit probability (b) distribution for the kinematic fit with mass constraint condition.

According to the decay tree only one candidate is expected to survive the applied cuts. Nevertheless, the huge amount of combinatorial background leads in most cases to more than one candidate in the selection. If there is more than one candidate surviving the applied cuts, the candidate with the smallest χ^2-value in the kinematic fit is selected. This candidate is called best candidate in the following description of the analysis.

The π^+ as well as the π^- as daughter of the best candidate are removed from the π^+ (π^-) list passed to the reconstruction of the $\overline{\Xi}^+$ and Ξ^- to reduce the combinatorial background on that stage.

After all cuts applied to the candidates, the reconstruction efficiency for Λ and $\bar{\Lambda}$ are 49.5% and 45.4%, respectively. The purity of the best candidates for Λ is 95% and for $\bar{\Lambda}$ 83.4%. In the charge conjugate channel a reconstruction efficiency of 51.6% for Λ and 53.7% for $\bar{\Lambda}$ is achieved with a purity of 82.5% for Λ and 96.8% for $\bar{\Lambda}$. Since the π^+ mesons appear twice in the signal – same for π^- in the charge conjugate channel – the purity for the best $\bar{\Lambda}$ (Λ) candidates is expected to be lower than the purity for the best Λ ($\bar{\Lambda}$) candidates.

Mass Resolution Applying the different cuts for the candidate selection has a significant impact on the mass distribution of the candidates. The mass distribution for Λ at each stage of selection is shown in Figure 5.9. As mentioned before, the Λ mass distribution after the mass window cut (blue line) shows a plateau which is caused by the wrongly combined daughter particles. This plateau is substantially reduced in the mass distribution of the vertex fitted candidates (red line). After the cut on the mass constraint fit probability the combinatorial background is suppressed. Since performing a Gaussian fit to the $\bar{\Lambda}$ mass does not work, the peak position of the mass distribution is taken as reconstructed Λ and $\bar{\Lambda}$ mass for the vertex fitted candidates after the mass constraint cut (black line in fig 5.9). In addition, the Full Width

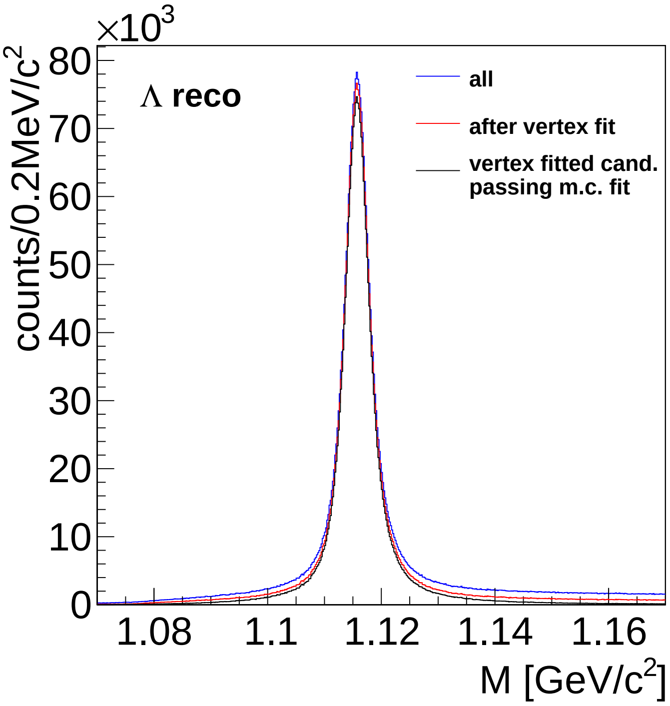

Figure 5.9: Mass distribution for Λ after the different steps of reconstruction. In blue after the mass window cut, in red after the vertex fit and the mass distribution of the vertex fitted candidates passing the mass constraint fit is shown in black.

at Half Maximum (FWHM) of the mass distribution is calculated. Table 5.6 is listing the evaluated fit values for Λ and $\bar{\Lambda}$, respectively. The systematic error of the mean values are estimated to be in the order of the bin width. The determined mass values for Λ and $\bar{\Lambda}$ are consistent with the input value M_Λ = 1.115683 GeV/c² [1]. The mass resolution is evaluated by performing a double Gaussian fit to deviation of the reconstructed and the generated mass for the Λ (fig 5.10) and $\bar{\Lambda}$ candidates, where the inner σ value is taken as measurement for the mass resolution. With the double Gaussian fit a mass resolution of σ_M = (2.33 ± 0.003(stat.) ± 0.1(sys.)) MeV/c² for Λ and σ_M = (2.37 ± 0.003(stat.) ± 0.1(sys.)) MeV/c² for $\bar{\Lambda}$. In the charge conjugate channel the mass resolution is σ_M = (2.22 ± 0.003(stat.) ± 0.1(sys.)) MeV/c² for $\bar{\Lambda}$ and σ_M = (2.18 ± 0.003(stat.) ± 0.1(sys.)) MeV/c² for Λ. The systematic error on the fit values is estimated by varying the fit parameters.

Table 5.6: Reconstructed mass for the vertex fitted Λ and $\bar{\Lambda}$ candidates after the mass constraint fit.

	Mass [MeV/c²]	FWHM [MeV/c²]
Λ	1115.7 ± 0.2	4.8
$\bar{\Lambda}$	1115.8 ± 0.2	4.8

(a) $\bar{p}p \to \bar{\Xi}^+ \Lambda K^-$

	Mass [MeV/c²]	FWHM [MeV/c²]
Λ	1115.9 ± 0.2	4.8
$\bar{\Lambda}$	1115.7 ± 0.2	4.8

(b) $\bar{p}p \to \Xi^- \bar{\Lambda} K^+$

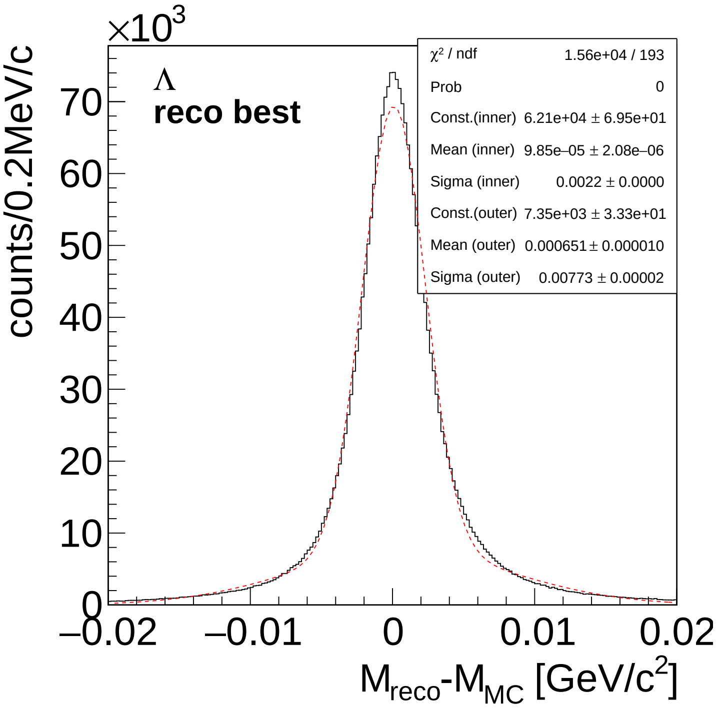

Figure 5.10: Deviation of reconstructed and generated Λ mass.

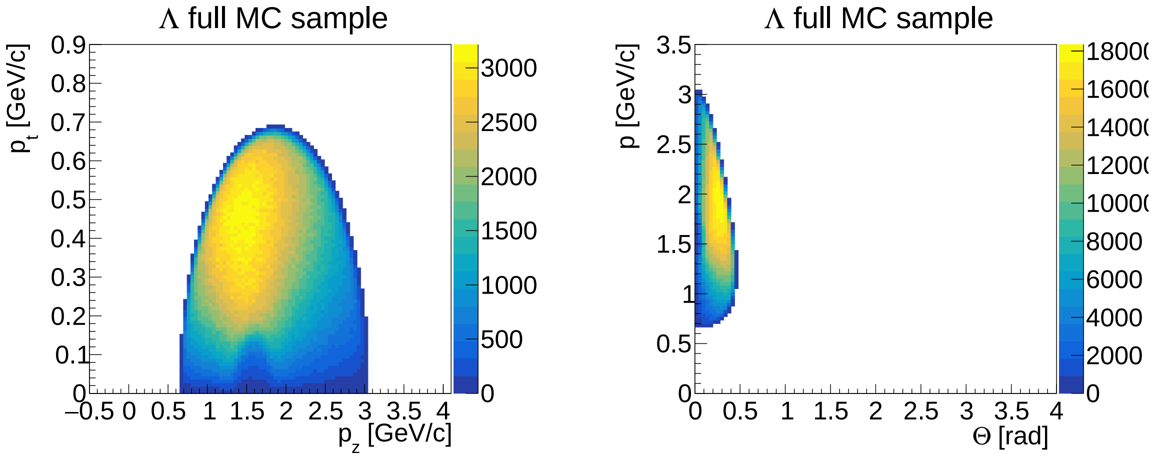

(a)

(b)

Figure 5.11: Transverse versus longitudinal momentum (a) and total momentum versus Θ angle (b) for generated Λ.

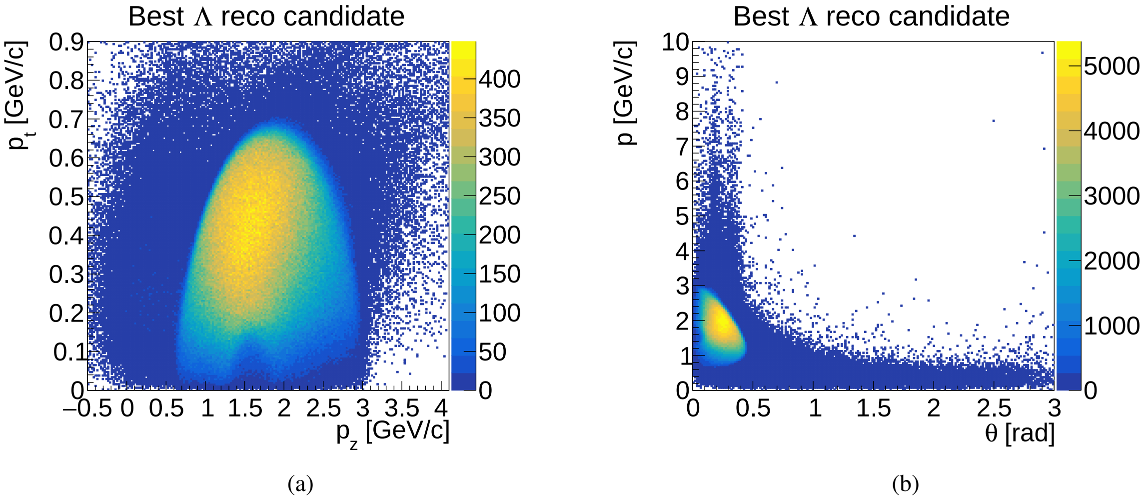

(a)

(b)

Figure 5.12: Transverse versus longitudinal momentum (a) and total momentum versus Θ angle (b) for the reconstructed best Λ candidates.

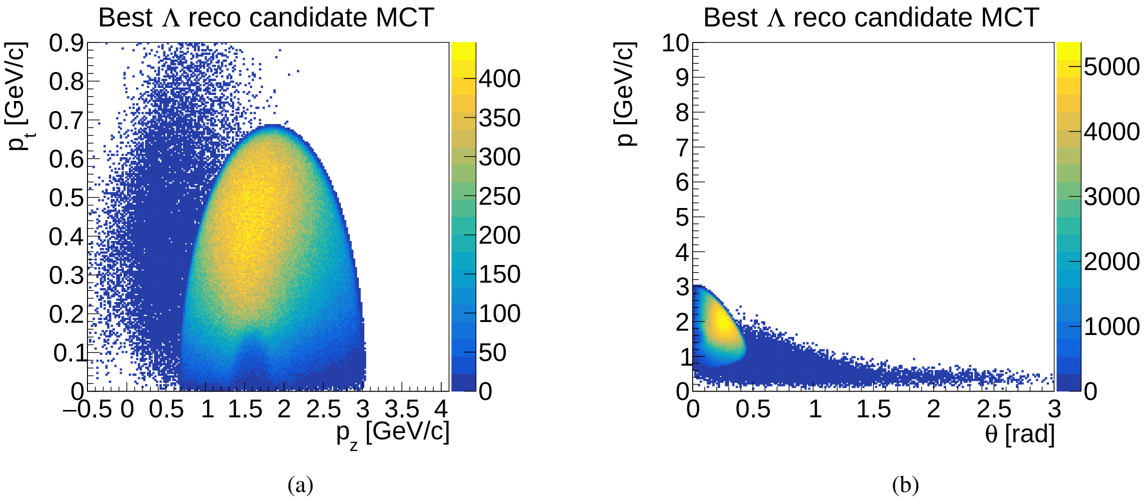

(a)

(b)

Figure 5.13: Transverse versus longitudinal momentum (a) and total momentum versus Θ angle (b) for the MC truth partners of the reconstructed best Λ candidate.

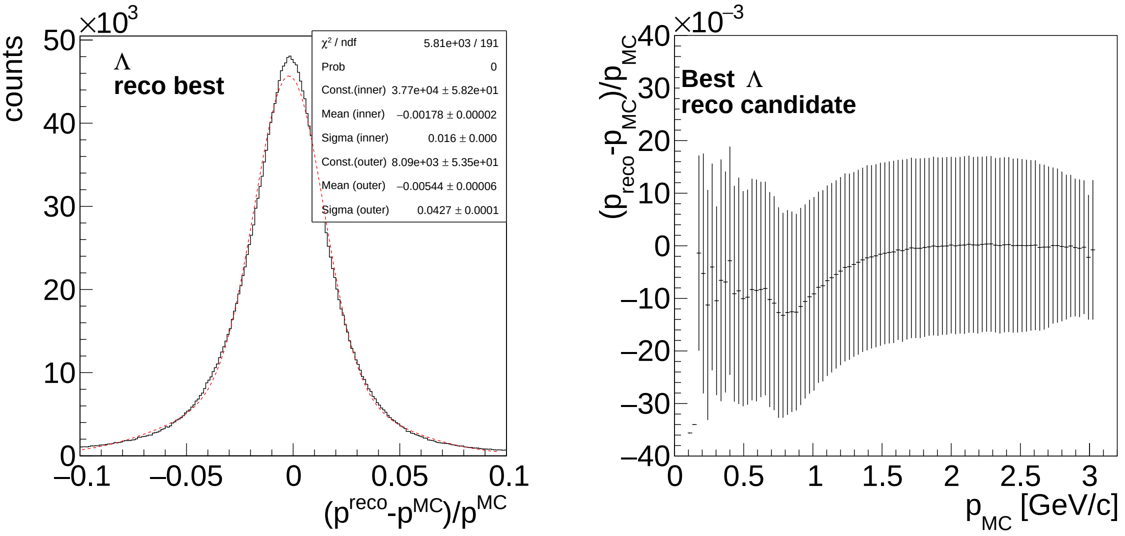

(a)

(b)

Figure 5.14: Momentum resolution (a) and relative deviation of the reconstructed and generated total momentum (b) for Λ.

Momentum Distributions and Momentum Resolution The transverse momentum versus the longitudinal momentum as well as the total particle momentum versus θ for the generated (full MC sample), the cleaned MC sample, the best candidates and the MC truth partner of the best candidates are shown in Figures 5.11 – 5.13. For the Λ the transverse momentum is expected to be up to 0.7 GeV/c. The longitudinal momentum is expected to be in the range between 0.5 GeV/c and 3.2 GeV/c. The angular distribution of the Λ is expected to be between 0 rad and 0.5 rad. Figure 5.12 shows that the reconstructed best candidates populate mainly the kinematically allowed region. The population of the space outside the kinematic boundaries is caused by the wrong combination of the daughter particles, as one can see in the distribution for the MC truth partners (Figure 5.13) of the best candidates.

The relative deviation of the reconstructed and the generated momentum (Fig. 5.14(a)) is fitted with a double Gaussian fit. As a measure for the momentum resolution the σ value of the inner Gauss fit is taken. The evaluated momentum resolution for Λ is $dp/p = 1.60\,\%$ and for $\bar{\Lambda}$ $dp/p = 1.57\,\%$ and $dp/p = 1.59\,\%$ for $\bar{\Lambda}$ and $dp/p = 1.58\,\%$ for Λ in the charge conjugate channel. The error of the fit value is dominated by the systematic error which is estimated by the variation of the fit parameters.

The dependence of the relative deviation of reconstructed and generated momentum on the total generated momentum is shown in Figure 5.14(b). Up to 1.5 GeV/c the reconstructed total momentum is smaller than the generated total momentum. Between 1.5 GeV/c and 3 GeV/c the relative deviation is spreading around a central value of zero.

Vertex Resolution For the evaluation of the vertex resolution the deviation of the reconstructed decay vertex position and the true decay vertex position is plotted for each spatial coordinate. Figure 5.15 shows all three distributions for Λ. Since the distributions are not Gaussian shaped, the width of the peak is evaluated using the FWHM. The obtained results for the vertex resolution in each spatial direction are shown in Table 5.8. To evaluate the error on the FWHM a systematic study on the deviations for different numbers of bins is done.

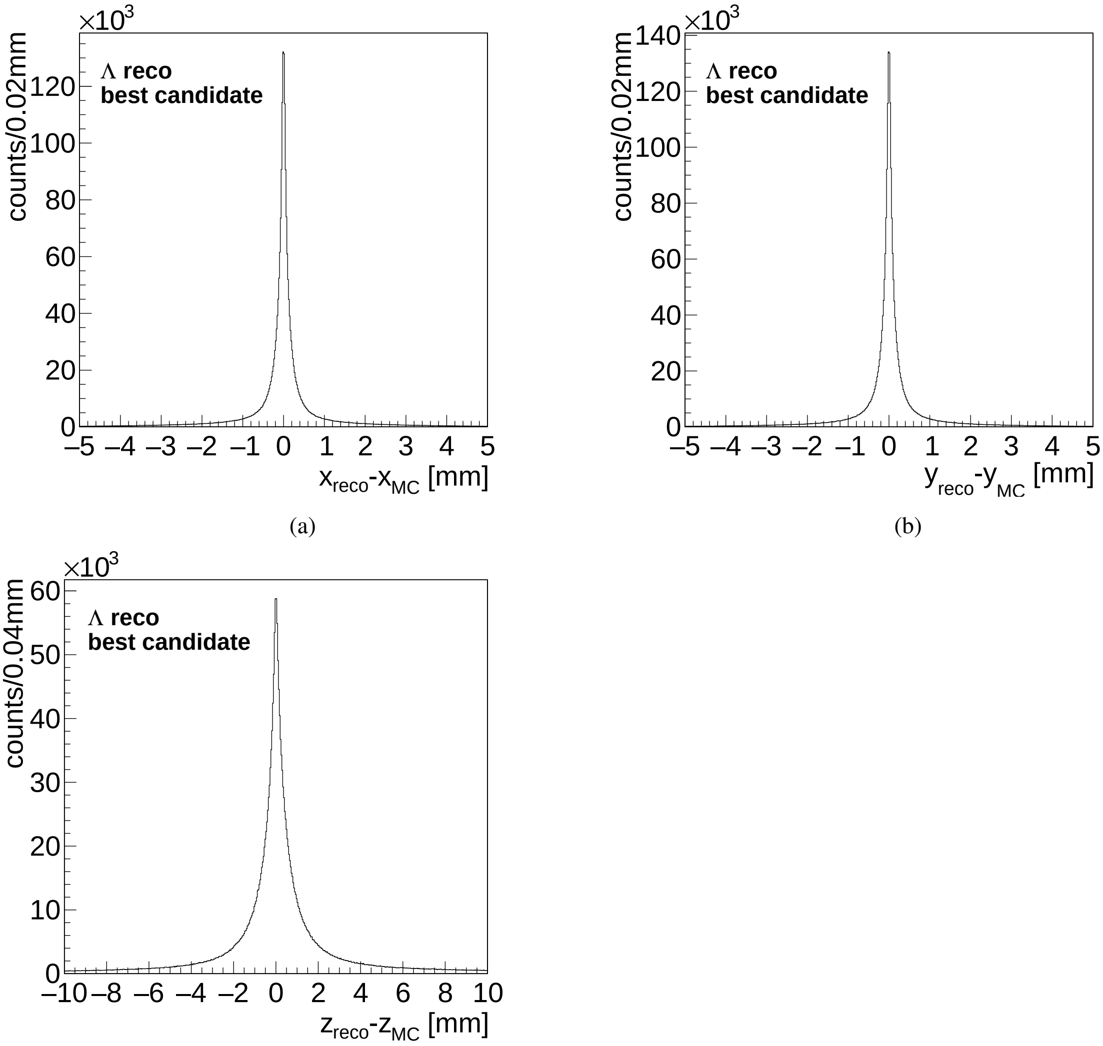

(a)

(b)

(c)

Figure 5.15: Deviation of the reconstructed Λ decay vertex position and the corresponding MC decay vertex position for the x coordinate (a), the y coordinate (b) and the z coordinate (c).

Table 5.8: Vertex resolution for the three spatial coordinates for Λ and $\bar{\Lambda}$, respectively.

position	Λ	$\bar{\Lambda}$
x[mm]	(0.14 ± 0.02)	(0.14 ± 0.02)
y[mm]	(0.14 ± 0.02)	(0.14 ± 0.02)
z[mm]	(0.06 ± 0.03)	(0.52 ± 0.03)

(a) $\bar{p}p \rightarrow \bar{\Xi}^{+}\ \Lambda\ K^{-}$

position	Λ	$\bar{\Lambda}$
x[mm]	(0.14 ± 0.02)	(0.14 ± 0.02)
y[mm]	(0.14 ± 0.02)	(0.14 ± 0.02)
z[mm]	(0.52 ± 0.03)	(0.64 ± 0.03)

(b) $\bar{p}p \rightarrow \Xi^{-}\ \bar{\Lambda}\ K^{+}$

Proper Time Distribution The proper time P denotes the flight path of a particle in the lab frame multiplied with the lab momentum divided by the hyperon mass. The ratio of the lab momentum and the hyperon mass can be expressed by $\beta\gamma$ where $\beta = p/E$, $\gamma = E/m$ and E is the energy of the particle in the lab frame. Therefore, it can be written:

$$P = \frac{\left|\vec{x}_{\mathrm{vtx}} - \vec{x}_{\mathrm{pos}}\right|}{\beta\gamma} \tag{5.2}$$

where $\vec{x}_{\mathrm{vtx}}$ is the decay vertex position and $\vec{x}_{\mathrm{pos}}$ the origin of the particle. One expects the proper time distribution of the generated candidates to be an exponential function, or a linear function on the logarithmic scale. A comparison of the generated proper time distribution with the expectation will validate the correctness of the generation process and can be used as reference for the reconstructed distribution.

The generated distribution for Λ is shown in Figure 5.16(a) and is consistent with a linear function on the logarithmic scale. Due to the selection and the position-dependent reconstruction efficiency of the decay vertex position, an exponential shape is not expected for the reconstructed proper time distribution and the distribution of the MC truth matched partners. By fitting an exponential function to the proper time distribution and inverting the result, the evaluation of $c\tau$ is possible. Since the fit values for $c\tau$ of the reconstructed best candidates will not match the literature value of $c\tau = 7.89\,\mathrm{cm}$[1], the evaluation will be done on the final selected Λ and $\bar{\Lambda}$ candidates at a later stage of this analysis.

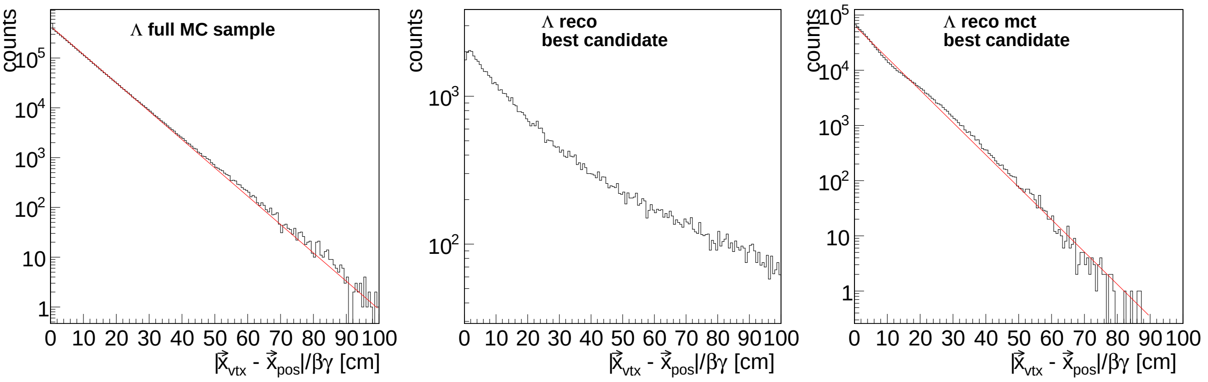

(a) (b) (c)

Figure 5.16: Proper time distribution for a) the generated candidates b) for the reconstructed best candidates and c) for the MC truth matched partners of the reconstructed candidates.

5.3.1.3 Reconstruction of $\overline{\Xi}^+$ and Ξ^-

The next step of the analysis is the reconstruction of $\overline{\Xi}^+$ and Ξ^- which is described in this paragraph. The reconstruction of both particles follows a similar scheme as used for the Λ and $\bar{\Lambda}$ reconstruction. By combining a $\bar{\Lambda}$ and π^+ a $\overline{\Xi}^+$ candidate is defined. The same is done with Λ and π^- for the Ξ^-. In case of a correct selection of the π^+ or π^- candidate as daughter of a $\bar{\Lambda}$ or Λ, respectively, only one π^+ or π^- candidate remains within the primary particles of the reaction chain. This particle must be the daughter particle of the $\overline{\Xi}^+$ or Ξ^-, respectively. A correct selection of the Λ and $\bar{\Lambda}$ daughter pions is assured by choosing the best fitted Λ and $\bar{\Lambda}$ candidate as described in the last paragraph. As said before, the pions associated to the $\bar{\Lambda}$ and Λ decay are removed from the pion candidate lists used for the reconstruction of

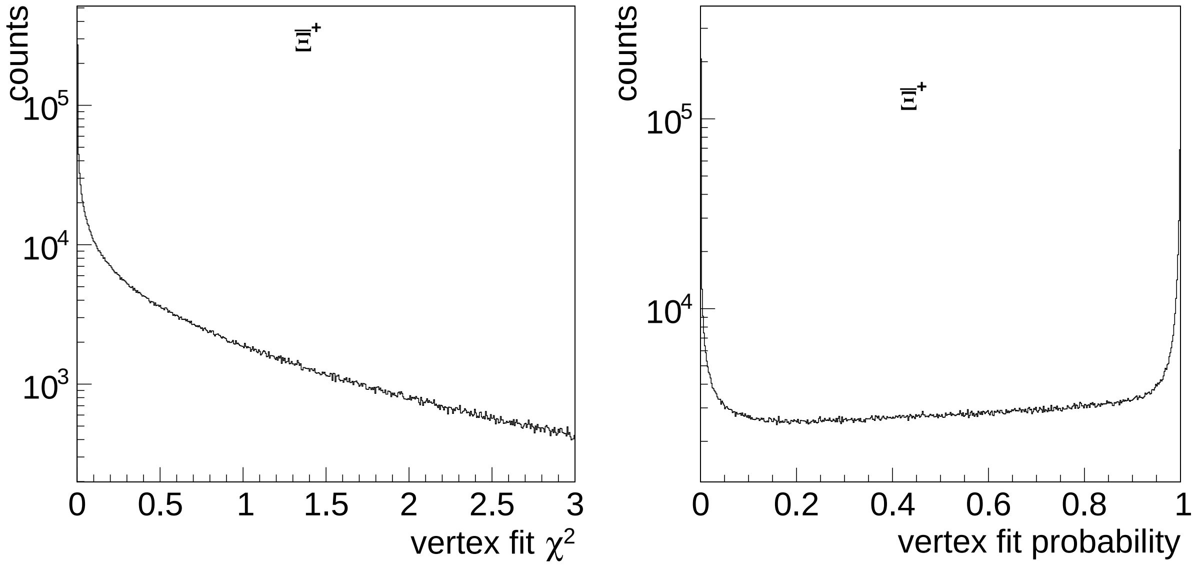

(a)

(b)

Figure 5.17: Vertex fit χ^2 (a) and probability (b) distribution for Ξ^-.

$\overline{\Xi}^+$ and Ξ^-. For the selection of the $\overline{\Xi}^+$ and Ξ^- candidates a mass cut corresponding to a window with a full width of 0.3 GeV/c^2 symmetric around the Ξ^- mass M_Ξ = 1.32171 GeV/c^2 [1] is performed.
As was the case for the Λ and $\bar{\Lambda}$ reconstruction, in this paragraph only the evaluated plots for the $\overline{\Xi}^+$ are shown. The corresponding plots for the Ξ^- are illustrated in Appendix A.2.4.

Candidate Selection The selection of the $\overline{\Xi}^+$ and Ξ^- candidates is similar to the selection of the Λ and $\bar{\Lambda}$ candidates, as already mentioned before.
After the mass window cut the daughter particles are fitted to a common vertex with the PndKinVtxFitter. Figure 5.17 shows the χ^2 and the fit probability distribution for $\overline{\Xi}^+$. The probability distribution (Fig. 5.17(b)) has again a strong increase towards a probability of 1, even stronger than the probability distribution for Λ in Figure 5.7(b). In addition to the vertex fit, a kinematic fit with mass constraint is performed. If a candidate has a fit probability lower than 1% in one of the fits, the candidate is rejected. As for Λ and $\bar{\Lambda}$ a best candidate selection is done. Here again, the candidate with the smallest χ^2 in the kinematic fit with mass constraint is chosen.
After applying all cuts, the reconstruction efficiency for $\overline{\Xi}^+$ is 30.3% and for Ξ^- 34.4%. The purity at that stage of selection is 95.1% for $\overline{\Xi}^+$ and 94.5% for Ξ^-.

Mass Resolution The different applied cuts have a significant impact on the mass distribution of $\overline{\Xi}^+$, shown in Figure 5.19, and on the Ξ^- mass distribution (Fig. A.103(a)). The number of candidates is mostly reduced by the cut on the vertex fit probability. Also the width of the mass distribution is narrowed. The mass distribution of the best $\overline{\Xi}^+$ candidates is shown in Figure 5.20 By fitting a Gaussian function within a fit region close to the peak position the reconstructed $\overline{\Xi}^+$ and Ξ^- mass can be determined. Here again, the FWHM is calculated with the fitted σ value. The achieved fit values for $\overline{\Xi}^+$ and Ξ^- listed in Table 5.10 are consistent with the input value M_Ξ = 1.32171 GeV/c^2 [1]. The mass resolution is determined by performing a double Gaussian fit to the deviation of the reconstructed and generated $\overline{\Xi}^+$

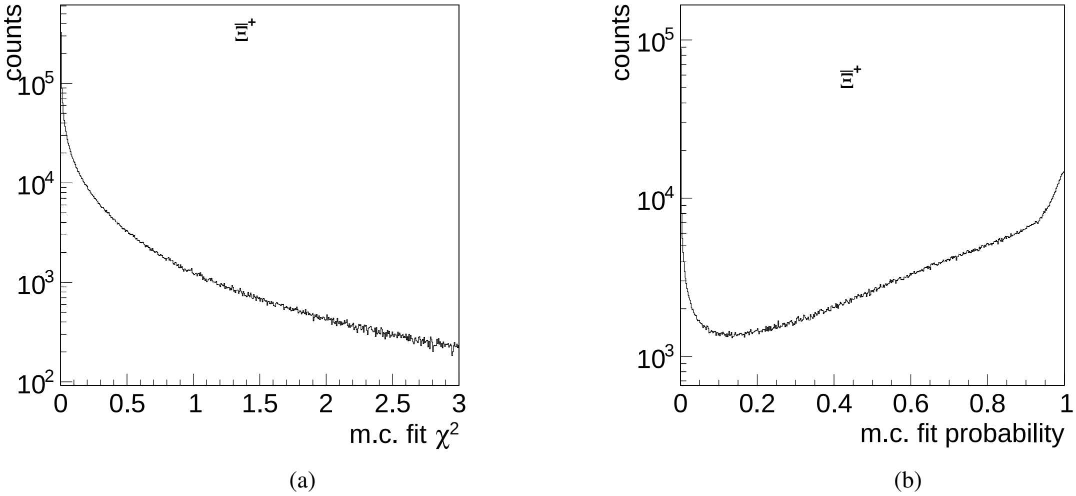

(a)

(b)

Figure 5.18: χ^2 (a) and probability (b) distribution of the kinematic fit with mass constraint for $\bar{\Xi}^+$.

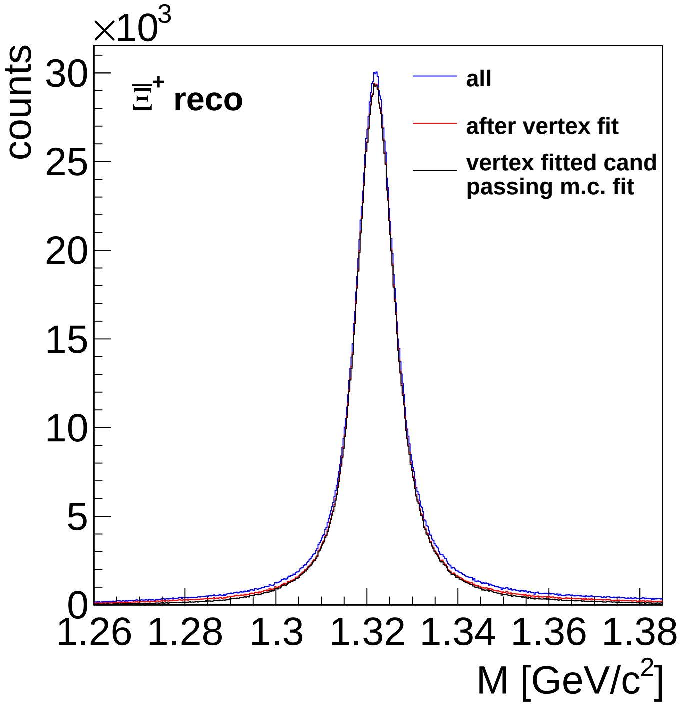

Figure 5.19: Mass distribution of the reconstructed candidates after the mass window cut (blue line), of the vertex fitted candidates (red line) and of the fitted candidates passing the kinematic mass constraint fit (black line).

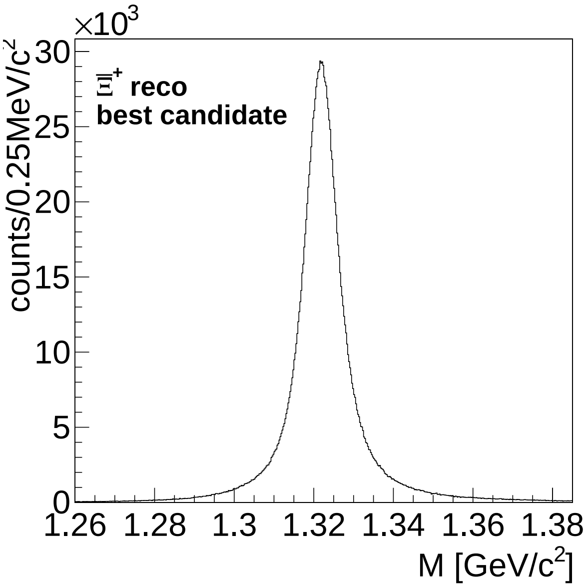

Figure 5.20: Mass distribution of the best $\overline{\Xi}^+$ candidates.

and Ξ^- mass, respectively. Because the error on the fit values is dominated by the systematic error, only the systematic error is indicated. By varying the fit parameters, the systematic error is estimated to be in the order of $\sigma_{\text{sys.}} = 0.1\,\text{MeV/c}^2$ The achieved values for the mass resolution are $\sigma_M = 4.2\,\text{MeV/c}^2$ for $\overline{\Xi}^+$ and $\sigma_M = 4.3\,\text{MeV/c}^2$ for Ξ^-.

Table 5.10: Fit values for the $\overline{\Xi}^+$ and Ξ^- mass distributions.

	Mean [GeV/c²]	FWHM [MeV/c²]
$\overline{\Xi}^+$	$1.3219 \pm^{0.0015(\text{sys.})}_{6\cdot 10^{-6}(\text{stat.})}$	4.2 ± 0.1
Ξ^-	$1.3219 \pm^{0.0021(\text{sys.})}_{7\cdot 10^{-6}(\text{stat.})}$	4.3 ± 0.1

Momentum Distribution and Momentum Resolution Since the $\overline{\Xi}^+$ is produced either together with one of the resonances or together with a Λ K^- pair, the two-dimensional distribution of transverse versus longitudinal momentum is expected to show the superposition of all production channels. This is clearly observed in Figure 5.22 which shows the generated two dimensional distributions of the transverse versus the longitudinal momentum and the total momentum versus the Θ angle. In case of the $\overline{\Xi}^+$ production together with one of the resonances the kinematics is defined by a two-body decay. Therefore, we expect to see sharp ellipses in the p_t vs. p_z distribution with respect to the resonance type, $\Xi\,(1690)^-$ or $\Xi\,(1820)^-$. In case of the continuum production the kinematics is defined by a three-body decay, meaning that the distribution shows a fully populated half-ellipse. The longitudinal momentum is expected to be in the range from 0.9 GeV/c to 3.3 GeV/c while the transverse momentum is up to 0.7 GeV/c. A similar superposition is expected for the two-dimensional distribution of the total momentum versus Θ with

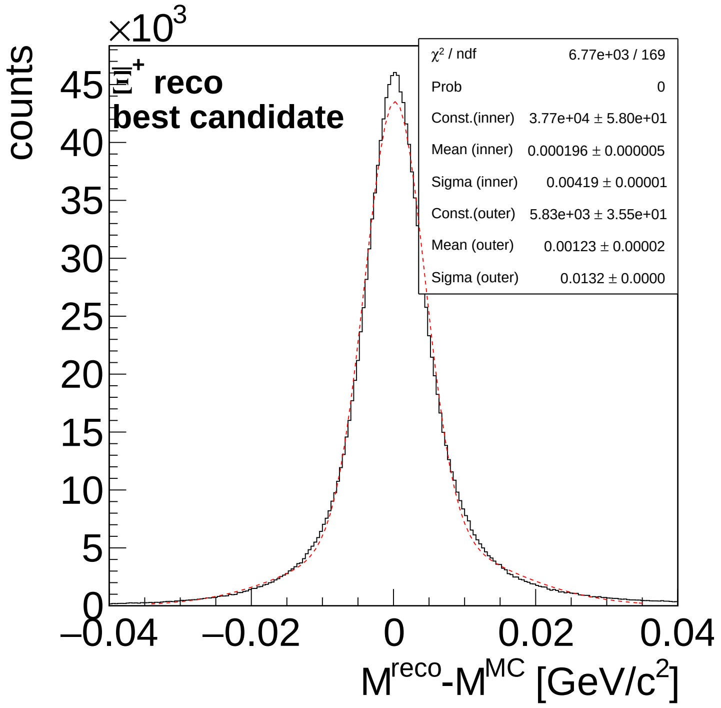

Figure 5.21: Deviation of the reconstructed and the generated $\overline{\Xi}^+$ mass.

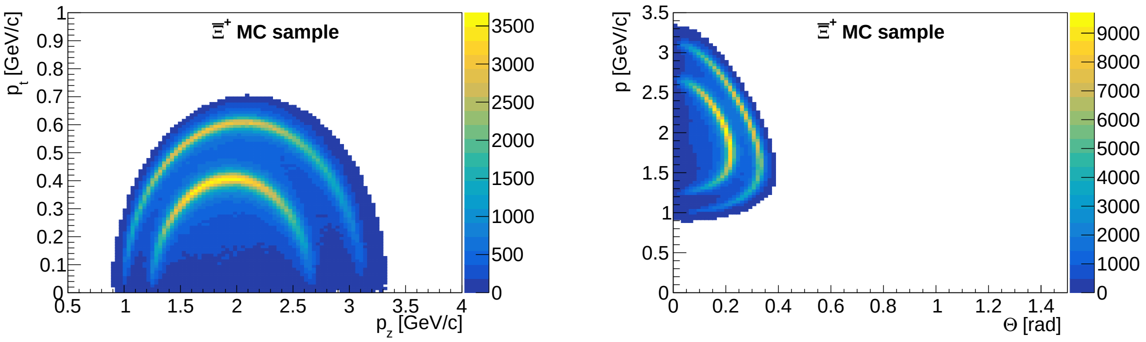

(a)

(b)

Figure 5.22: Generated distributions of transverse vs. longitudinal momentum (a) and total momentum vs. θ angle (b) for the best $\overline{\Xi}^+$ candidates.

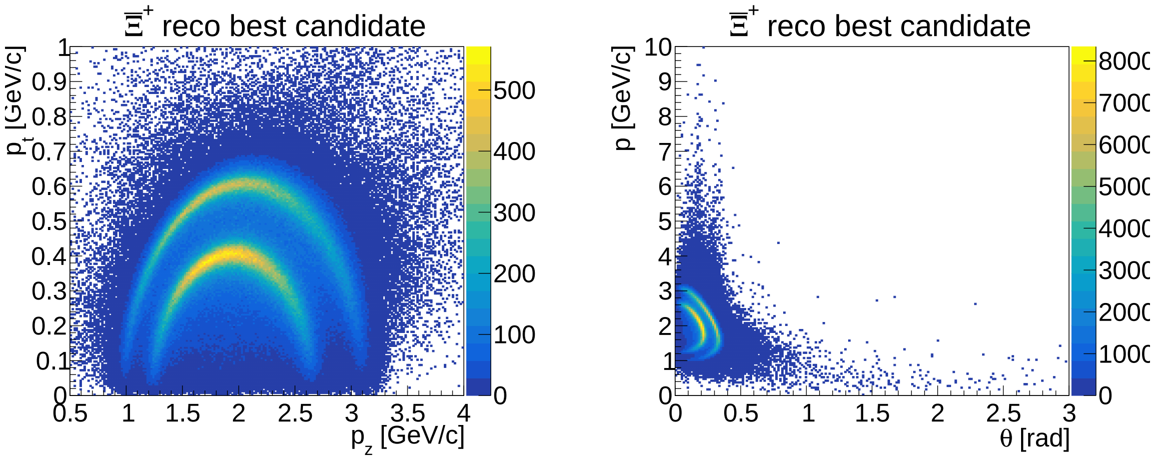

(a) (b)

Figure 5.23: Reconstructed transverse vs. longitudinal momentum (a) and total momentum vs. θ angle (b) for the best $\overline{\Xi}^+$ candidates.

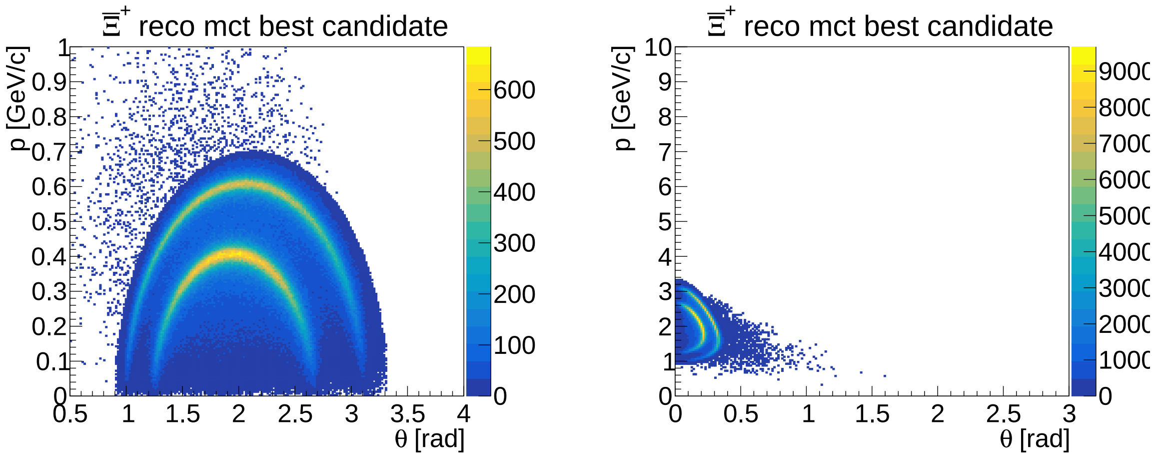

(a) (b)

Figure 5.24: Transverse vs. longitudinal momentum (a) and total momentum vs. θ angle (b) for the MC truth partners of the best $\overline{\Xi}^+$ candidates.

a total momentum between 0.9 GeV/c to 3.3 GeV/c and Θ between 0 rad and 0.4 rad. The relative deviation of the reconstructed and generated total momentum for $\overline{\Xi}^+$ is illustrated in Figure 5.25. By performing a double Gaussian fit, the momentum resolution is determined by taking the inner σ value. For $\overline{\Xi}^+$ a momentum resolution of $dp/p = 1.48\%$ and for Ξ^- a resolution of $dp/p = 1.44\%$ is evaluated. Again, the systematic error dominated and the estimated value is 0.09%. From the profile plot one can see, that for generated momenta up to 1.5 GeV/c the reconstructed total momentum is smaller than the generated total momentum.

Vertex Resolution The deviation of the reconstructed $\overline{\Xi}^+$ decay vertex and its MC truth value is plotted in Figure 5.26 for each spatial coordinate. Since the distributions for $\overline{\Xi}^+$ and Ξ^- are not Gaussian shaped, like for $\bar{\Lambda}$ and Λ, the vertex resolution is evaluated by determine the FWHM for each given distribution.

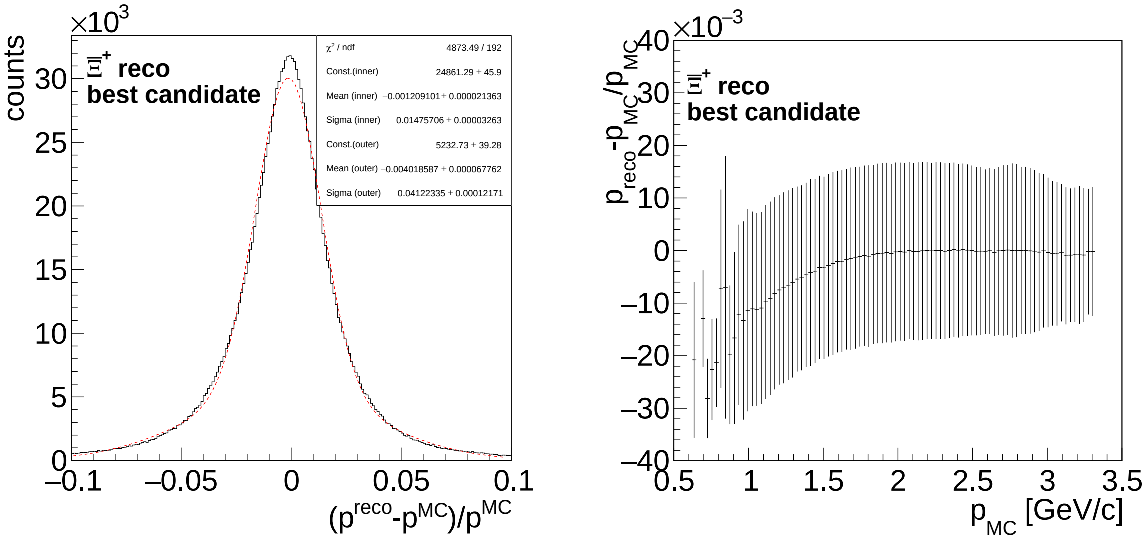

(a) (b)

Figure 5.25: Relative deviation of reconstructed and generated momentum (a) and Relative deviation of reconstructed and generated total momentum versus generated momentum (b) for $\overline{\Xi}^+$.

Table 5.11: Evaluated FWHM values for each spatial coordinate as a measurement for the vertex resolution.

coordinate	$\overline{\Xi}^+$	Ξ^-
x	(0.38 ± 0.02) mm	(0.36 ± 0.02) mm
y	(0.38 ± 0.02) mm	(0.36 ± 0.02) mm
z	(1.38 ± 0.04) mm	(1.32 ± 0.04) mm

The determined values for both the $\overline{\Xi}^+$ and Ξ^- are listed in Table 5.11, respectively. Obviously, the achieved values for $\overline{\Xi}^+$ and Ξ^- are similar.

Proper Time Distribution Analogous to the proper times of $\bar{\Lambda}$ and Λ, the proper times of $\overline{\Xi}^+$ and Ξ^- are determined. The generated distribution for $\overline{\Xi}^+$ is shown in Figure 5.27 and is consistent with a linear function on the logarithmic scale. Again, the fit values for $c\tau$ for the reconstructed best $\overline{\Xi}^+$ and Ξ^- candidates will not match the literature value of $c\tau = 4.91$ cm[1]. Therefore, the evaluation will be done on the final selected candidates later.

5.3.1.4 Reconstruction of the $\overline{\Xi}^+$ Λ K^- and Ξ^- $\bar{\Lambda}$ K^+

In the following part of the analysis, the reconstruction of the full decay chain is described. Since the Ξ^- and $\overline{\Xi}^+$ resonances have a short lifetime and decay at their production vertex, the signal is defined as $\overline{\Xi}^+$ Λ K^- and Ξ^- $\bar{\Lambda}$ K^+. Therefore, the former selected best candidates of $\overline{\Xi}^+$ and Λ are combined with a K^- as well as Ξ^- and $\bar{\Lambda}$ with a K^+ in the charge conjugate channel.

In addition to the results of the final selected candidates of the full tree, the results for the final selected daughter particles are shown here. Again, the illustration of all plots corresponding to the evaluated results in this section would be beyond the scope. For this reason, this analysis part contains only the

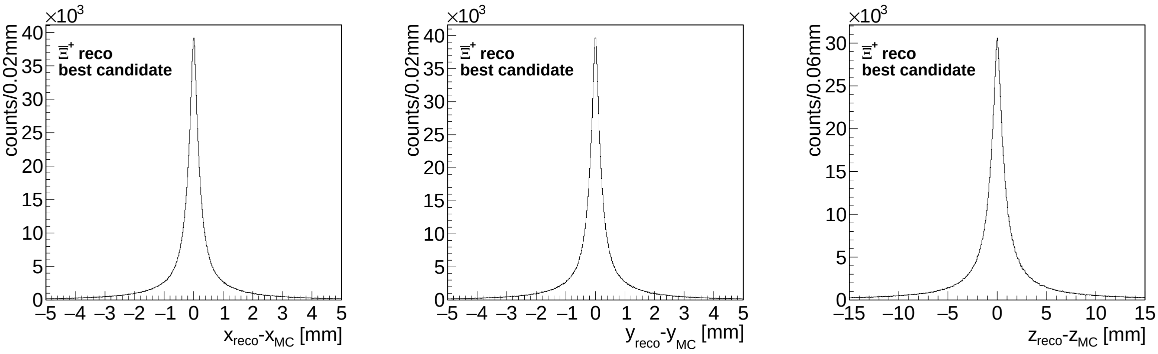

(a) (b) (c)

Figure 5.26: Deviation of the reconstructed $\overline{\Xi}^+$ decay vertex and its MC truth value for the x coordinate (a), y coordinate (b), and z coordinate (c).

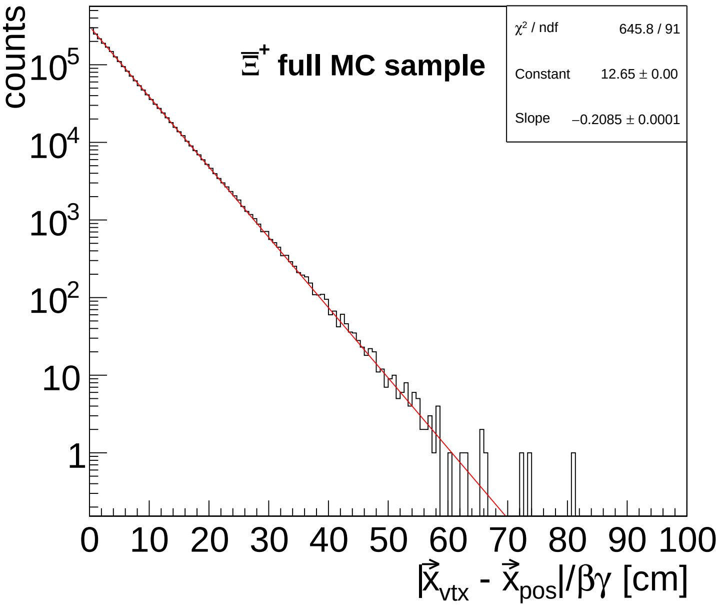

Figure 5.27: Proper time distribution for the generated $\overline{\Xi}^+$.

illustrated results of the $\overline{\Xi}^+$ Λ K^- analysis. However, the plots corresponding to the Ξ^- $\bar{\Lambda}$ K^+ analysis can be found in Appendix A.2.5.

Candidate Selection Since all three particles should come from the interaction point, a vertex fit is performed to assure that this condition is fulfilled. If the vertex fit probability is better than 1% the candidate is passed to the next stage of the selection. The vertex fit probability as well as the corresponding χ^2 distribution is shown in Figure 5.28. Due to momentum and energy conservation one expects the four-momentum vector of a true candidate to match to the initial four-momentum of the p̄p system $\left(p_x, p_y, p_z, E\right) = (0, 0, 4.6, 5.63)$ GeV. Therefore, the four-momentum vector of the fitted candidate is subsequently fitted with the constraint to match this initial four-momentum vector, called 4C-fit in the following. As used before, a cut on the fit probability (Fig. 5.29) of more than 1% is applied

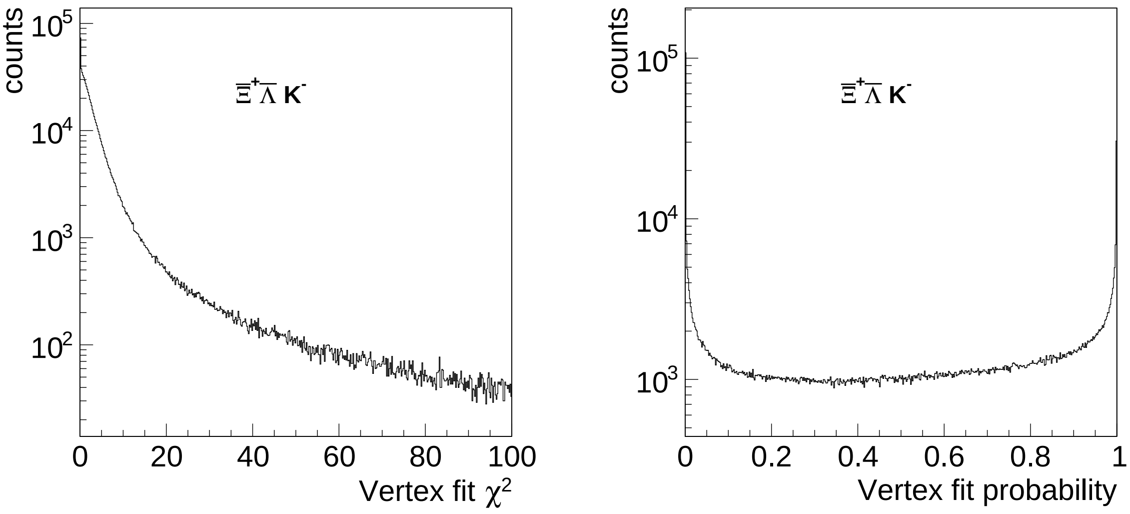

(a) (b)

Figure 5.28: Vertex fit χ^2 (a) and probability (b) distribution for $\overline{\Xi}^+$ Λ K$^-$.

to the candidate selection. Since there are still candidates passing the kinematic fit but not fulfilling the 4-constraint condition, an additional cut on the system mass $M_{4\text{C}} < 3.2512$ is applied. In addition, some candidates cause entries outside the kinematically allowed region in the Dalitz plots (Fig. 5.35(b). One reason for those entries is that the masses of the $\overline{\Xi}^+$ and Λ, same for Ξ^- and $\bar{\Lambda}$ in the charge conjugate channel, are not fixed to a single value but have a Gaussian shaped distribution. To reject those candidates, cuts rejecting the tails of the daughter mass distributions are applied. The chosen cut values are listed in Table 5.12.

After all applied cuts the reconstruction efficiency for $\overline{\Xi}^+$ Λ K$^-$ is 8.2% and for Ξ^- $\bar{\Lambda}$ K$^+$ is 9.2% with a

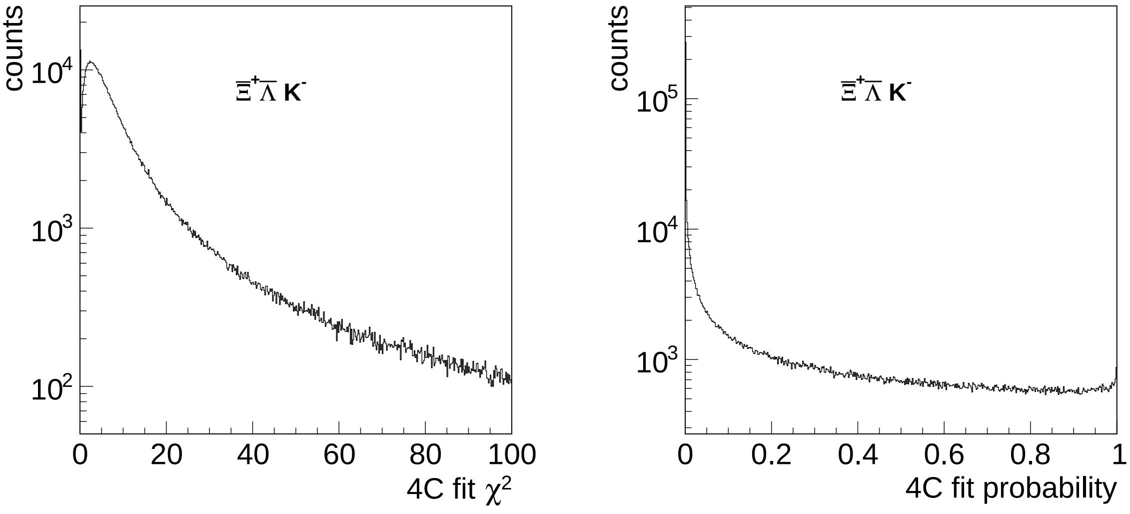

(a) (b)

Figure 5.29: 4C-fit χ^2 (a) and probability (b) distribution for $\overline{\Xi}^+$ Λ K$^-$.

Table 5.12: Cut values for the additional selection on the $\overline{\Xi}^{+}$ and Λ mass.

particle	lower cut	upper cut
Λ	$M > 1.1\,\mathrm{GeV/c^2}$	$M < 1.135\,\mathrm{GeV/c^2}$
$\overline{\Xi}^{+}$	$M > 1.3\,\mathrm{GeV/c^2}$	$M < 1.345\,\mathrm{GeV/c^2}$

sample purity of 98.6% for both $\overline{\Xi}^{+}\,\Lambda\,\mathrm{K}^{-}$ and $\Xi^{-}\,\bar{\Lambda}\,\mathrm{K}^{+}$. This result implies an efficient suppression of combinatorial background.

Table 5.13 shows the ratio between the non-resonant and resonant decay modes for the final selected sample. The reconstructed fraction for the decay modes are consistent with the input. The ratio between the generated resonant and non-resonant decay modes is assumed to be 80% for the resonant modes and 20% for the non-resonant mode, see also Table 5.3 in Section 5.2.

Table 5.13: Decay modes and ratios for the $\bar{p}p \to \overline{\Xi}^{+}\,\Lambda\,\mathrm{K}^{-}$ (a) and $\bar{p}p \to \Xi^{-}\,\bar{\Lambda}\,\mathrm{K}^{+}$ (b) final selected sample.

Channel	Fraction [%]	Error [%]
$\overline{\Xi}^{+}\,\Xi(1690)^{-}$	37.9	0.3
$\overline{\Xi}^{+}\,\Xi(1820)^{-}$	42.0	0.3
$\overline{\Xi}^{+}\,\Lambda\,\mathrm{K}^{-}$	20.1	0.3

(a) $\bar{p}p \to \overline{\Xi}^{+}\,\Lambda\,\mathrm{K}^{-}$

channel	fraction [%]	error [%]
$\Xi^{-}\,\overline{\Xi}(1690)^{+}$	37.9	0.5
$\Xi^{-}\,\overline{\Xi}(1820)^{+}$	42.0	0.5
$\Xi^{-}\,\bar{\Lambda}\,\mathrm{K}^{+}$	20.0	0.4

(b) $\bar{p}p \to \Xi^{-}\,\bar{\Lambda}\,\mathrm{K}^{+}$

Momentum Resolution After the four-momentum constraint fit, all two-dimensional distributions should have sharp borders according to the kinematic boundaries of the decay. As an example, the transverse versus longitudinal momentum and the total momentum versus Θ for the final selected Λ

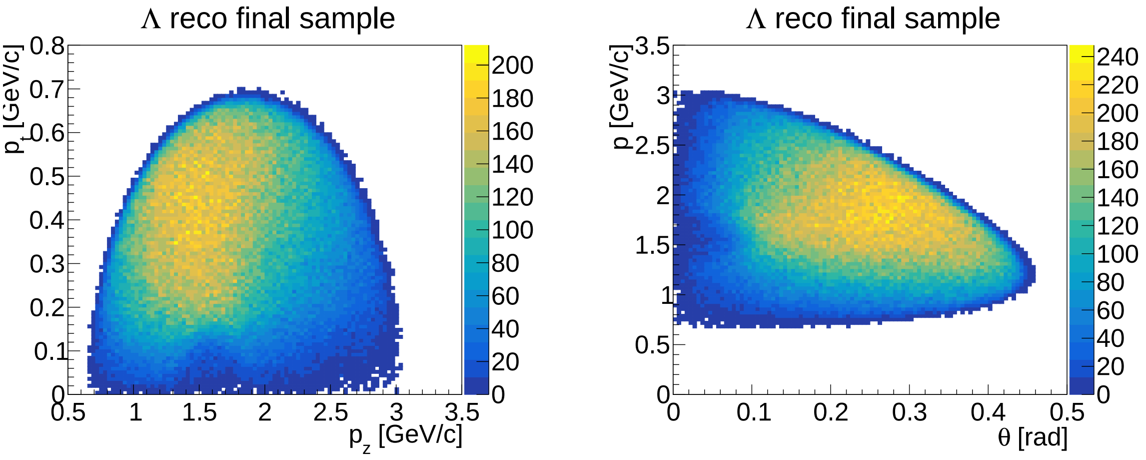

(a) (b)

Figure 5.30: Reconstructed transverse versus longitudinal momentum and reconstructed total momentum versus Θ angle for final selected Λ.

candidates are illustrated in Figure 5.30. Both distributions show the expected sharp border line. The comparison of the reconstructed and the generated distributions (Fig. 5.11) shows not only the consistency of the distributions but also that those candidates not corresponding to the signal are rejected by the final selection. Since the four-momentum constraint fit is correcting the momentum of the particles, the final selection should also have an effect on the momentum resolution. Again, the illustration of the results for Λ (Fig.5.31) is chosen as an example, while the plots for all other particles are listed in the Appendix A.2.5. The momentum resolution is determined from the inner σ of the performed double Gaussian fit on the relative deviation of the reconstructed and the generated total momentum. Table 5.15 lists the achieved results for all composite state particles. For all composite state particles the momentum resolution is improved. This improvement is also visible in the profile plot for the relative deviation of the reconstructed and the generated total momentum against the generated total momentum. Different the case at the stage of the best reconstructed Λ candidates (Fig. 5.14(b)), the profile plot for the final selected Λ (Fig. 5.31(b)) does not show a tendency to smaller reconstructed momenta in the range up to 1.5 GeV/c generated momentum.

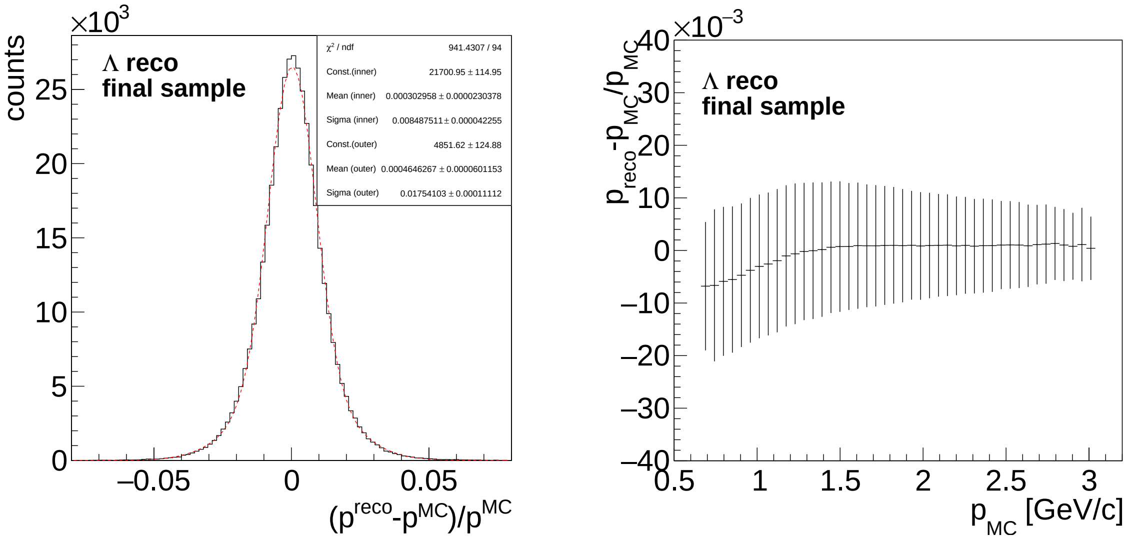

(a)

(b)

Figure 5.31: Relative deviation of the reconstructed and the generated total momentum (a) and the relative deviation of the total momentum versus total generated momentum (b) for the final selected Λ candidates.

Table 5.15: Evaluated momentum resolution for the composite state particles of a) $\overline{\Xi}^{+}$ Λ K^{-} and b) Ξ^{-} $\bar{\Lambda}$ K^{+}

particle	dp/p [%]	$\sigma_{\text{sys.}}$ [%]
Λ	0.85	0.09
$\bar{\Lambda}$	1.38	0.09
$\overline{\Xi}^{+}$	0.86	0.09

(a)

particle	dp/p [%]	$\sigma_{\text{sys.}}$ [%]
Λ	1.36	0.09
$\bar{\Lambda}$	0.85	0.09
Ξ^{-}	0.73	0.09

(b)

Mass resolution The selection of the final sample has an impact on the mass resolution of the daughter particles shown in Figure 5.32. Like before, the mass resolution is obtained by performing a

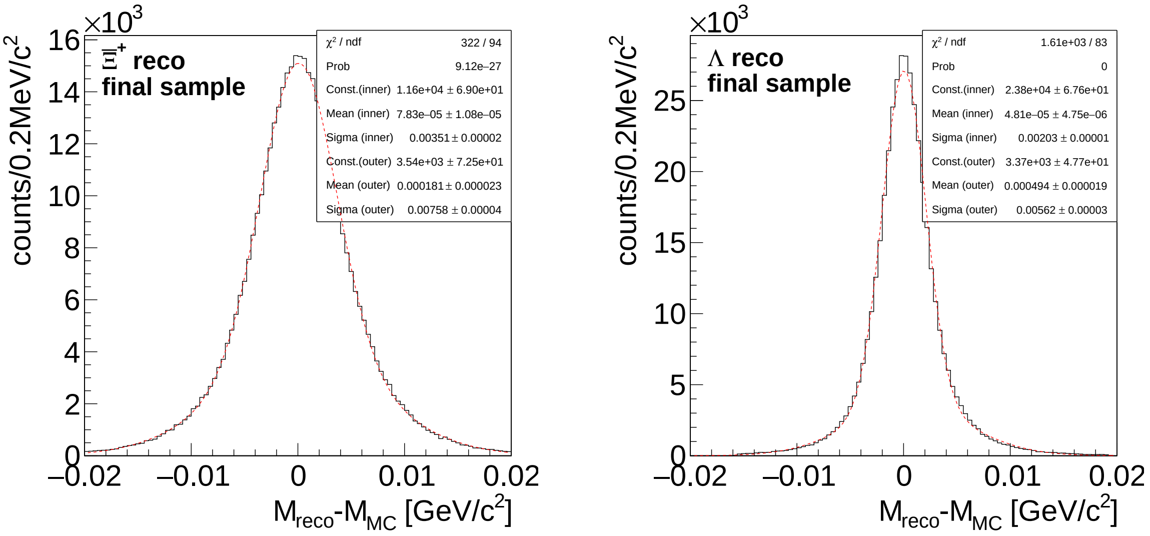

(a) (b)

Figure 5.32: Mass resolution of the final selected composite state particles.

double Gaussian fit to the deviation of the reconstructed and the generated mass of $\bar{\Xi}^{+}$, Ξ^{-}, Λ and $\bar{\Lambda}$, respectively. Table 5.17 shows the determined results for the composite daughter particles. The error on the mass resolution is dominated by the systematic error which is estimated by varying the fit parameters. Comparing the evaluated fit results with the fit results from the best candidate selection shows that the mass resolution is improved for the final selected candidates.

Table 5.17: Mass resolution of the final selected $\bar{\Xi}^{+}$, Ξ^{-}, Λ and $\bar{\Lambda}$. a) shows the table for $\bar{p}p \rightarrow \bar{\Xi}^{+}\ \Xi^{*}$ and b) for $\bar{p}p \rightarrow \bar{\Xi}^{*}\ \Xi^{-}$

particle	σ_M [MeV/c^2]	syst. error [MeV/c^2]
Λ	2.0	0.1
$\bar{\Lambda}$	2.1	0.1
$\bar{\Xi}^{+}$	3.7	0.4

(a)

particle	σ_M [MeV/c^2]	syst. error [MeV/c^2]
Λ	2.0	0.1
$\bar{\Lambda}$	2.1	0.1
Ξ^{-}	3.5	0.4

(b)

Decay Vertex Resolution The decay vertex resolution for the final selected composite state candidates is determined by calculating the FWHM from the deviation of the reconstructed and the generated decay vertex position. Like it was done in the previous sections, the decay vertex resolution is evaluated for all the spatial coordinates. As an example, the plots for $\bar{\Xi}^{+}$ are shown in Figure 5.33. The corresponding plots for Λ, Ξ^{-} and $\bar{\Lambda}$ are presented in the Appendix. Table 5.19 summarizes the achieved decay vertex resolution for the composite state particles. The decay vertex resolution for Λ and $\bar{\Lambda}$ are in the same order. This is also the case in the charge conjugate channel. Since the FWHM depends on the bin size of the histogram, a systematic error for the vertex resolution is estimated by varying the number of bins. For the x and y position the error is estimated to $\sigma_{x,y} = 0.02$ mm and for the z position to $\sigma_z = 0.05$ mm. Comparing the achieved results for the final selected candidates and the best fitted candidates, it is obvious that there is no improvement, but the values are consistent within the estimated errors.

Table 5.19: Decay vertex resolution for all three spatial coordinated of the composite state particles.

particle	x [mm]	y [mm]	z [mm]
Λ	0.15	0.15	0.60
$\bar{\Lambda}$	0.15	0.15	0.50
$\overline{\Xi}^{+}$	0.35	0.35	1.30

(a) $\bar{p}p \rightarrow \overline{\Xi}^{+} \Lambda K^{-}$

particle	x [mm]	y [mm]	z [mm]
Λ	0.15	0.15	0.50
$\bar{\Lambda}$	0.15	0.15	0.60
Ξ^{-}	0.35	0.35	1.30

(b) $\bar{p}p \rightarrow \Xi^{-} \bar{\Lambda} K^{+}$

Proper Time As already described in Section 5.3.1.2, the proper time denotes the flight path of the particle in the lab frame multiplied with the momentum divided by the hyperon mass. Figure 5.34(b) shows the proper time distribution for Λ. The proper time distribution for $\overline{\Xi}^{+}$ is shown in Figure 5.34(a), while the plots for all other composite state particles are listed in Appendix A.1.3. The values on the x-axis are plotted according to Equation (5.2). Both proper time distributions are first linear, but is than flattening at a value around 60 cm, while the proper time distribution for $\overline{\Xi}^{+}$ is already flattening around 30 cm. Therefore, the shape of both shown distributions deviate from any exponential shape. But, as already discussed, the shape of the reconstructed distributions is not expected to follow an exponential function. However, since the distributions deviate so much from an exponential one, it is not possible to determine the corresponding $c\tau$ values from the final selected composite state particles.

Dalitz Plots and Resonance Masses As already mentioned, the Ξ^{-} and $\overline{\Xi}^{+}$ resonances decay promptly into Λ K systems. The underlying force is the strong interaction. Therefore, one can define $\overline{\Xi}^{+}$ Λ K^{-} and Ξ^{-} $\bar{\Lambda}$ K^{+} as three-body final states of the strong interaction. The kinematics of this three-body decay can be described by two variables. This is used in a Dalitz plot [136]. Each axis of the Dalitz plot shows the invariant squared mass of one two-body subsystem. In this analysis these are $M^2(\Lambda\ K^{-})$ and $M^2(\overline{\Xi}^{+}\ K^{-})$ as well as their charge conjugate particles. For decays where the three-body continuum final state is produced, the Dalitz plot shows a flat distribution in the complete kinematically allowed region. Three-body decays can be dominated by a resonant process, where first a resonance is produced which is then decaying into two particles, In that case, the resonance will be visible as a band in the Dalitz plot. The Dalitz plot for the generated $\overline{\Xi}^{+}$ Λ K^{-} sample is shown in Figure 5.35(a) and can be used as a reference plot for the reconstruction. The resonances $\Xi(1690)^{-}$ and $\Xi(1820)^{-}$ are represented as ver-

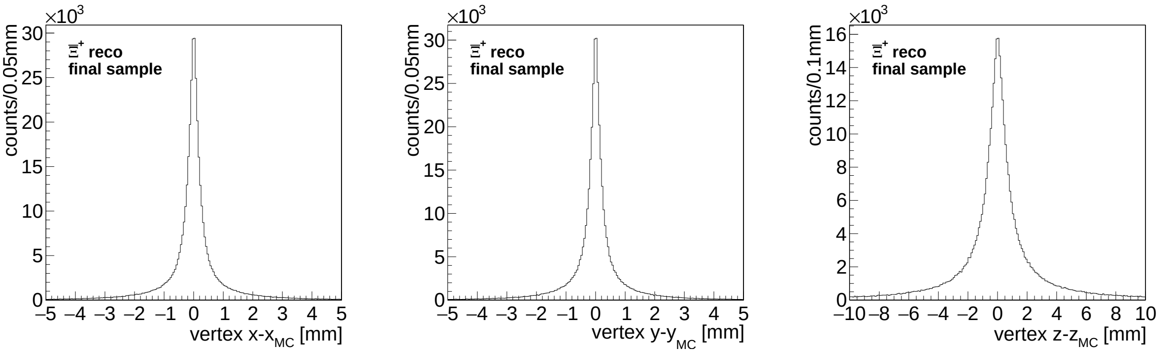

(a) (b) (c)

Figure 5.33: Deviation of the reconstructed and the generated decay vertex position in all three spatial coordinates for $\overline{\Xi}^{+}$.

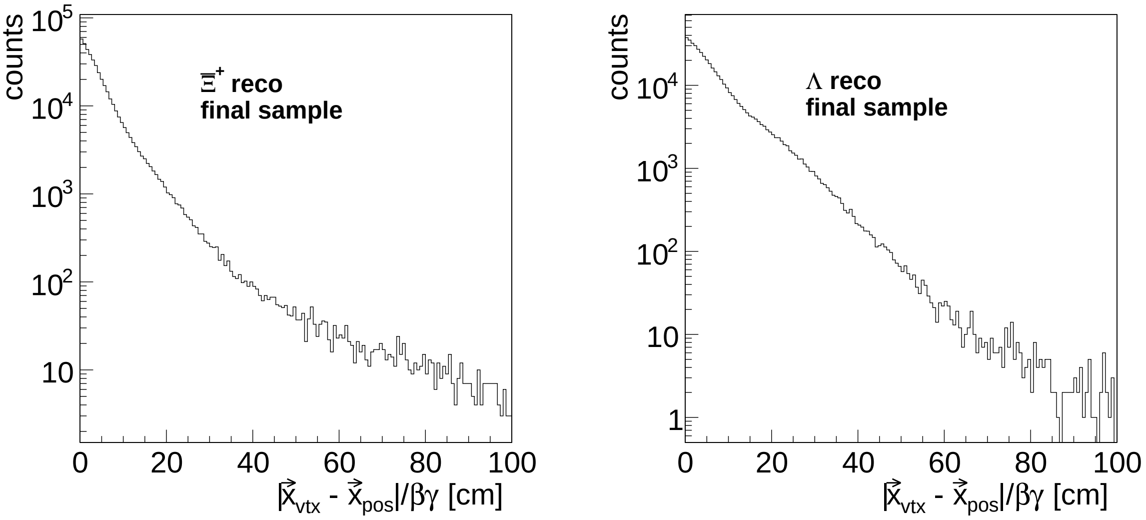

(a) (b)

Figure 5.34: Proper Time distribution a) for reconstructed $\bar{\Xi}^+$ candidates and b) for the reconstructed Λ candidates.

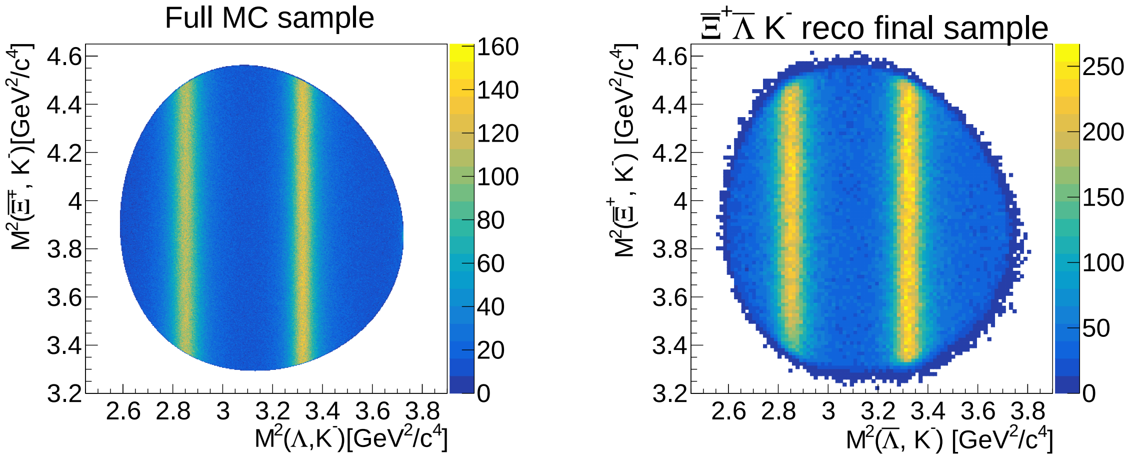

(a) (b)

Figure 5.35: Dalitz plot for the generated sample (a) and the final selected reconstructed candidates (b). The Ξ^- resonances are shown as vertical bands.

tical bands around their expected squared masses. If one compares the Dalitz plot for the generated sample with the Dalitz plot of the final selected reconstructed candidates in Figure 5.35(b), they are in qualitative agreement, apart from the smaller number of entries and the diffuse boundaries in case of the reconstructed sample. The ratio plot (Fig. 5.36) between the Dalitz plot for the MC truth partners of the reconstructed candidates and the generated candidates shows a uniform distribution. This means, that the detector acceptance is uniform for this channel.

To determine the mass and the width of $\Xi(1690)^-$ and $\Xi(1820)^-$, and their charge conjugate particles, a function containing the sum of two Voigt functions [137] and a polynomial is fitted to the mass distributions of Λ K^- (Fig. 5.37) and $\bar{\Lambda}$ K^+ (Fig. A.127). The best fit result is achieved by fixing the σ for both resonances. The value of σ is evaluated by fitting a double Gaussian function to the deviation of

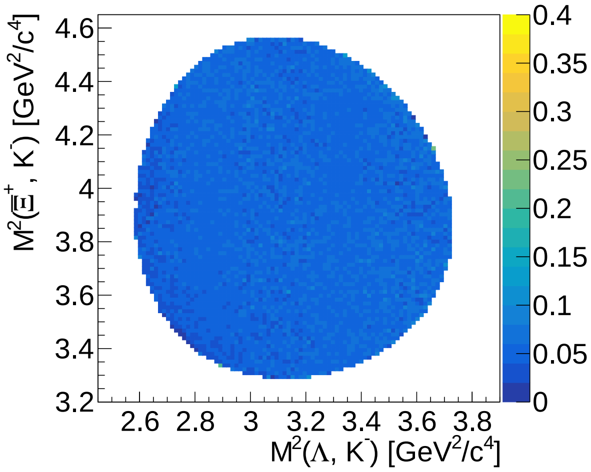

Figure 5.36: Ratio plot between the Dalitz plots of MC truth partners of the final reconstructed candidates and the generated sample.

the resonance mass from its MC truth value. The corresponding distribution is shown in Figure 5.38. The determined value is $\sigma = 3.38\,\mathrm{MeV/c^2}$. Table 5.21 lists the resulting fit values for the resonances. The fitted mass values as well as the width of $\Xi(1690)^-$ are consistent with the input values shown in Table 5.2. But for the fitted width of $\Xi(1820)^-$ the input value is not included within the error and deviates by $7.8\,\sigma$.

To complete the analysis, Figure 5.39 shows the mass distribution of the $\bar{\Xi}^+$ K$^-$ system. As expected, the distribution is structureless.

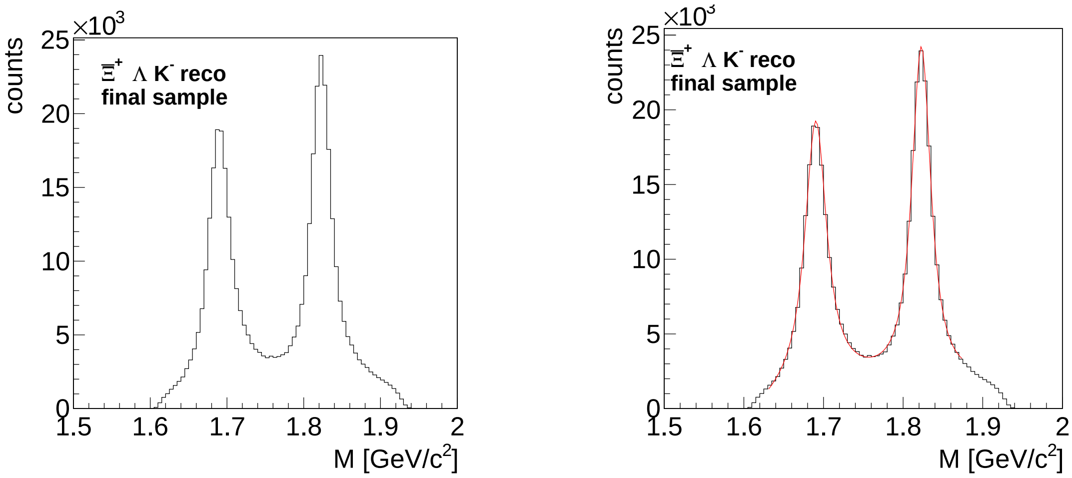

(a)

(b)

Figure 5.37: Mass distribution of the Λ K$^-$ system: a) unfitted and b) fitted with the sum of two Voigt functions and a polynomial.

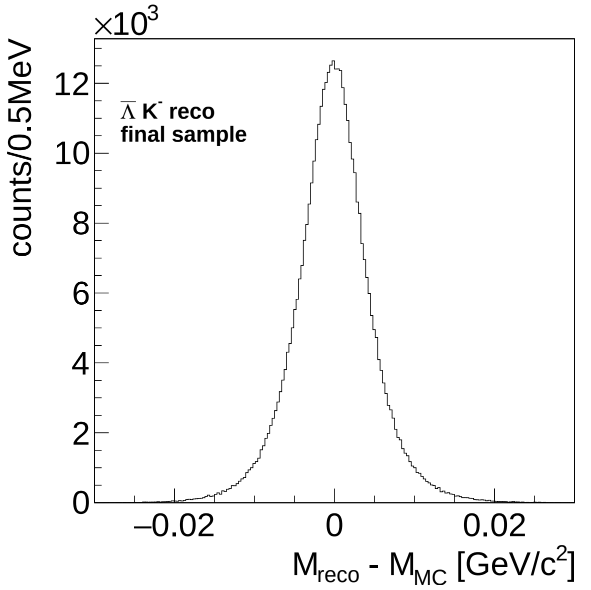

Figure 5.38: Deviation of the reconstructed resonance mass from its MC truth value. To evaluate the width of the distributions, a Gaussian function is fitted to the peak.

Table 5.21: Fit results for the mass and the width of the Ξ^- and $\overline{\Xi}^+$ resonances achieved with the sum of two Voigt functions and a polynomial.

	$\Xi(1690)^-$	$\Xi(1820)^-$	$\overline{\Xi}(1690)^+$	$\overline{\Xi}(1820)^+$
M [GeV/c^2]	$1.6904\pm^{6\cdot10^{-4}(\text{sys.})}_{6\cdot10^{-5}(\text{stat.})}$	$1.8229\pm^{3\cdot10^{-4}(\text{sys.})}_{5\cdot10^{-5}(\text{stat.})}$	$1.6905\pm^{6\cdot10^{-4}(\text{sys.})}_{6\cdot10^{-5}(\text{stat.})}$	$1.8229\pm^{3\cdot10^{-4}(\text{sys.})}_{5\cdot10^{-5}(\text{stat.})}$
$\Gamma\left[\text{MeV/c}^2\right]$	$30.2\pm^{0.3(\text{sys.})}_{0.2(\text{stat.})}$	$26.5\pm^{0.2(\text{sys.})}_{0.2(\text{stat.})}$	$30.2\pm^{0.3(\text{sys.})}_{0.6(\text{stat.})}$	$27.0\pm^{0.2(\text{sys.})}_{0.5(\text{stat.})}$

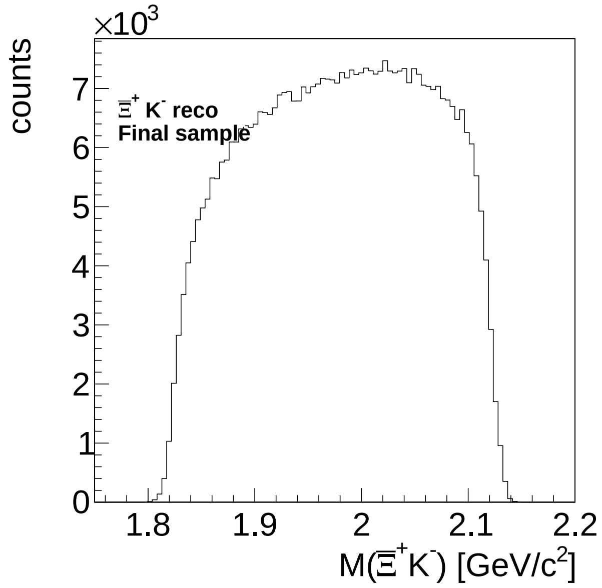

Figure 5.39: Mass distribution of the $\overline{\Xi}^+$ K$^-$ system.

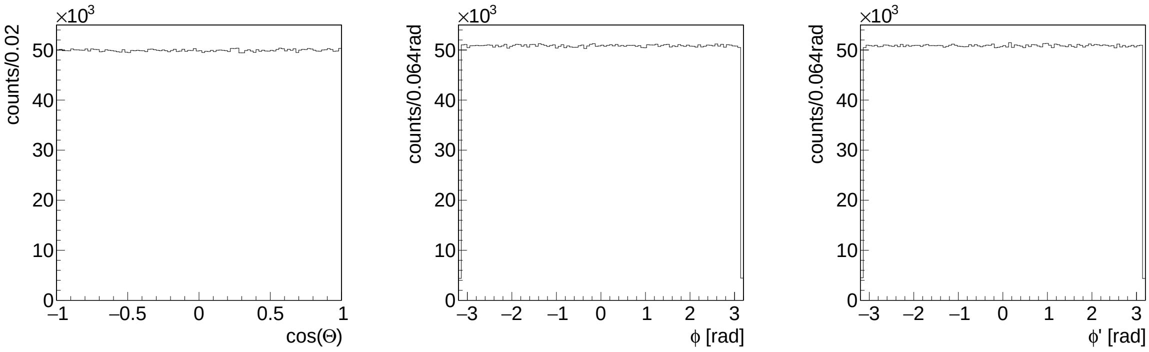

(a) (b) (c)

Figure 5.40: Generated distribution for $\cos\theta$(a), ϕ (b) and ϕ' (c) in the center-of-mass frame.

Angular Distributions A three-body final state has five degrees of freedom, which are two of the three masses of the two-particle systems $\Lambda\ K^-$, $\overline{\Xi}^+\ K^-$ and $\overline{\Xi}^+\ \Lambda$, the alignment of the plane generated by the three momentum vectors in the center-of-reference frame, i.e. $\cos(\theta_{\mathrm{cm}})$ and ϕ_{cm}, and the alignment of the momentum vectors ϕ'_{cm} within that plane. In the following, the plane generated by the three momentum vectors in the center-of-mass frame is called *center-of-mass plane*. The angular distributions for the generated sample, see Figure 5.40, are expected to be flat, since an isotropic angular distribution was assumed. Figure 5.41 shows the ratio of the angular distributions for the final reconstructed sample.

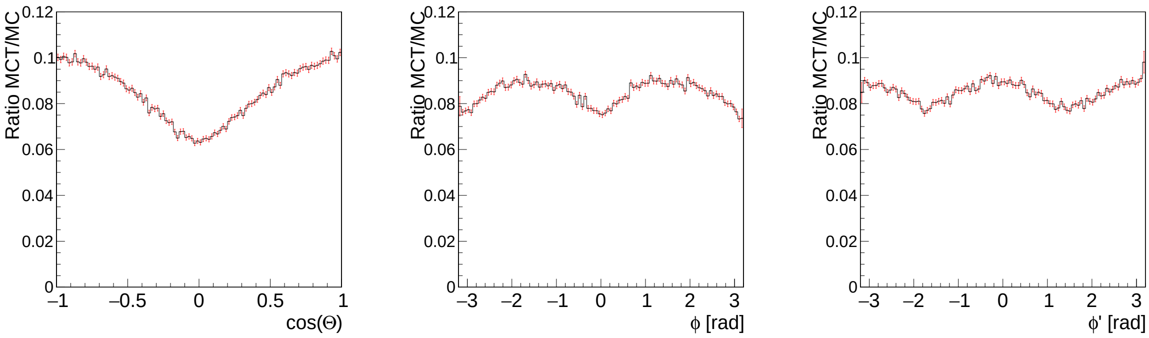

(a) (b) (c)

Figure 5.41: $\cos\theta_{\mathrm{cm}}$ (a), ϕ_{cm} (b) and ϕ'_{cm} (c) ratio between the MC partners of the final reconstructed candidates and the generated sample.

This ratio is determined by dividing the MC partner of the reconstructed candidates by the generated sample. The ratio for $\cos\theta$, shown in Figure 5.41(a), has two maxima at $\cos\theta = \pm 1$ and a minimum at around zero. $\cos\theta = \pm 1$ corresponds to a plane alignment perpendicular to the beam direction, i.e the z-axis in Cartesian coordinates, while $\cos\theta = 0$ indicates, that the beam direction is included in the plane. If a particle is emitted in the direction of the positive or negative z-axis, i.e. inside the beam pipe, it is not possible to detect this particle, meaning that it is missing in the reconstruction. Therefore, the efficiency loss around $\cos\theta = 0$ is caused by the beam pipe. A similar explanation can be found for the efficiency loss observable in the ratio of the ϕ distribution, see Figure 5.41(b). Here, $\phi = 0$ and $\phi = \pm\pi$ indicates, that the plane includes the y-axis of the Cartesian coordinate, i.e. the direction in which the target pipe will be installed. Thus, for ϕ the drop in the efficiency is caused by the target pipe.

As already described, the alignment of the momentum vectors in the center-of-mass frame is ϕ'. In this study, ϕ' is determined for the center-of-mass momentum vector of the $\overline{\Xi}^{+}$. Therefor, the intersection line between the center-of-mass plane and the x-z-plane is determined which is then used as reference axis. Thus, ϕ' is defined as the angle between the momentum vector $P^{\mathrm{cm}}_{\overline{\Xi}^{+}}$ and the intersection line. According to this choice, for $\phi' = \pm\pi/2$ the y-axis of the Cartesian coordinate system is part of center-of-mass plane and hence one expects to see a drop in the ϕ' distribution of the reconstructed events around $\pm\pi/2$. This drop is observable as loss of efficiency in the ratio plot shown in Figure 5.41(c) To deduce the reconstruction efficiency for any center-of-mass angular distribution, the ratio between the MC partners of the final reconstructed and the generated $\cos\Theta$ distribution for $\overline{\Xi}^{+}$ in the center-of-mass frame is determined. For the generated candidates one expects to see a flat distribution, since a uniform angular distribution is assumed. The $\cos\theta$ distributions for the generated, the final reconstructed as well as for the MC partner of the reconstructed $\overline{\Xi}^{+}$ candidates are shown in Figure 5.73. It is observable, that the distribution for the final selected $\overline{\Xi}^{+}$ deviates from the generated one. This deviation is due to the loss of generated particles which are stuck inside the beam pipe. The corresponding ratio plot is shown in Figure 5.43.

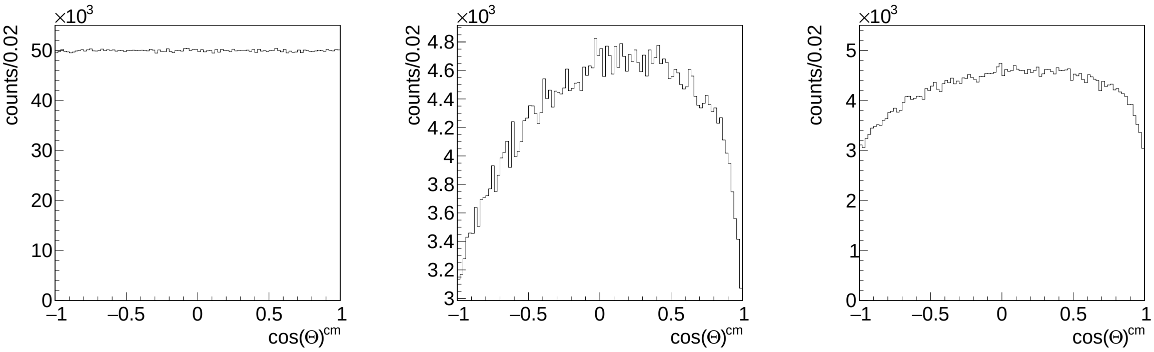

(a) (b) (c)

Figure 5.42: Generated (a) and reconstructed (b) $\cos\theta$ distribution in the center-of-mass frame for final selected $\overline{\Xi}^{+}$ as well as the distribution for the MC partners of the reconstructed $\overline{\Xi}^{+}$ candidates (c).

5.3.2 Full Decay Tree Fit

The previous analysis described in section 5.3.1 has shown that the conventional fitters have issues as e.g. the rising behavior of the fit probability distributions, which are partly not understood. Therefore, a second analysis using a DecayTreeFitter is done. Since the usage of the DecayTreeFitter required a newer version of the PandaRoot framework, a new data sample of 10 million events in total is generated, 5 million events for $\overline{\Xi}^{+}$ Λ K^{-} and an additional 5 million events for Ξ^{-} $\bar{\Lambda}$ K^{+}.
The DecayTreeFitter mainly uses raw reconstructed candidates, this means that no pre-selection is carried out, with the exception of mass window cuts. Therefore the decay vertex resolution and the proper time distributions for the composite candidates are shown only for the final selection.

5.3.2.1 Final State Particle Reconstruction

The reconstruction of the final state candidates follows a similar scheme as the final state reconstruction presented in Section 5.3.1.1. Unlike the previously shown selection, no PID information is used for the candidates selection. This means that for each candidate list all candidates are stored. The stored

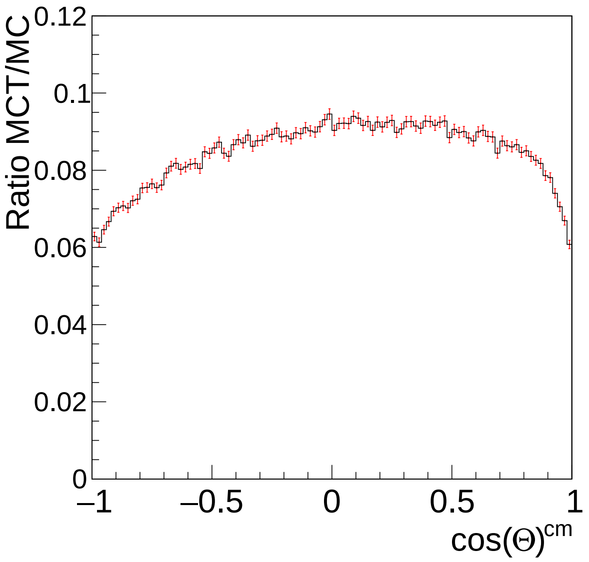

Figure 5.43: Ratio plot of the cos θ distribution in the center-of-mass frame for the final selected $\overline{\Xi}^{+}$ candidates.

Table 5.22: Reconstruction efficiency for the final state particles of a) $\bar{p}p \rightarrow \overline{\Xi}^{+}\ \Lambda\ K^{-}$ and b) $\bar{p}p \rightarrow \Xi^{-}\ \bar{\Lambda}\ K^{+}$.

particle type	reco. eff. [%]
π^{-}	71.2
π^{+} ($\bar{\Lambda}$)	68.6
π^{+} ($\overline{\Xi}^{+}$)	73.7
K^{-} (res.)	84.9
K^{-} (cont.)	85.1
p	88.7
$\bar{p}$	82.3

particle type	reco. eff. [%]
π^{+}	70.6
π^{-} (Λ)	68.3
π^{-} (Ξ^{-})	73.1
K^{+} (res.)	86.7
K^{+} (cont.)	86.9
p	86.2
$\bar{p}$	83.4

candidates differ only in the mass hypothesis, which is set according to the species specified in the lists, respectively.

To avoid the reconstruction of incomplete signal events, only "reconstructable" events are selected. Since no PID information is used, an event is marked as reconstructable if it contains at least one positive and one negative track. Table 5.22 lists the reconstruction efficiencies for the final state particles. The error on the final state reconstruction efficiency is in the order of $\sigma_{\epsilon} \simeq 0.1\%$.

Momentum and Angular Distributions Each channel consists of six final state particles. Showing all plots for the momentum and the angular distribution would extend this paragraph too much. Therefore, Figures 5.44 – 5.47 show exemplarily the transverse momentum versus the longitudinal momentum as well as the total momentum versus the Θ angle for the proton as daughter of Λ. The plots for all other final state particles are shown in Appendix A.3.1 and those for the final states of the charge conjugate channel in Appendix A.4.1. The transverse momentum of the proton is expected to have a maximum between 0.1 GeV/c and 0.5 GeV/c. The longitudinal momentum range is 0.5 GeV/c $\leq p_t \leq$ 2.9 GeV/c with a maximum between 0.6 GeV/c and 1.8 GeV/c. Figure 5.45 illustrates also the expectation for the total proton momentum and the Θ angle. The total momentum ranges from 0.5 GeV/c up to 3.9 GeV/c

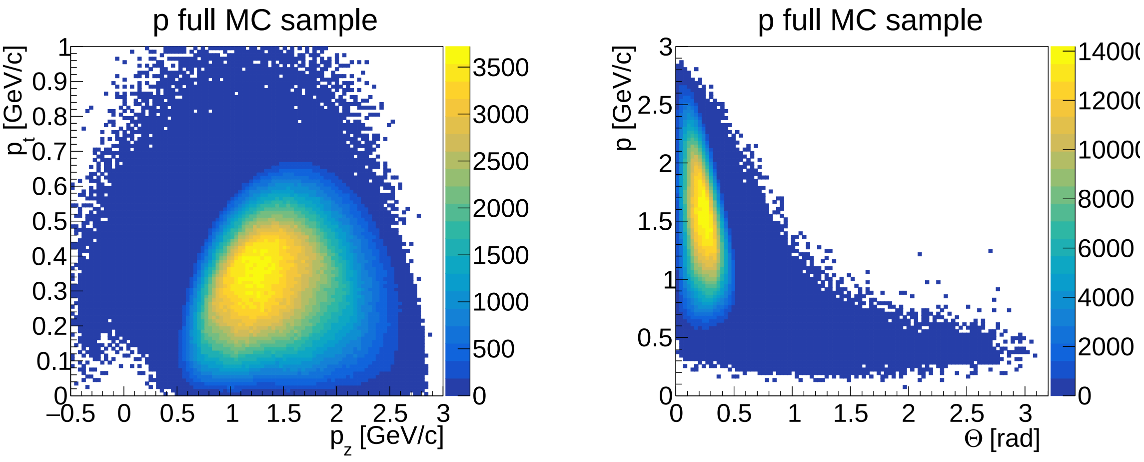

(a)

(b)

Figure 5.44: Generated transverse vs. longitudinal momentum (a) and generated total momentum vs. Θ angle (b) for proton.

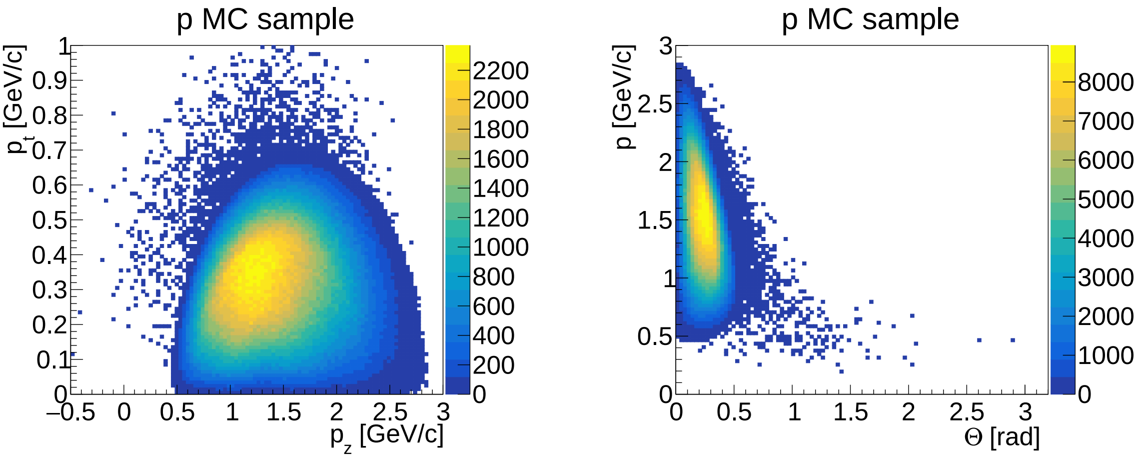

(a)

(b)

Figure 5.45: Transverse vs. longitudinal momentum (a) and total momentum vs. Θ angle (b) for generated proton from the cleaned MC sample.

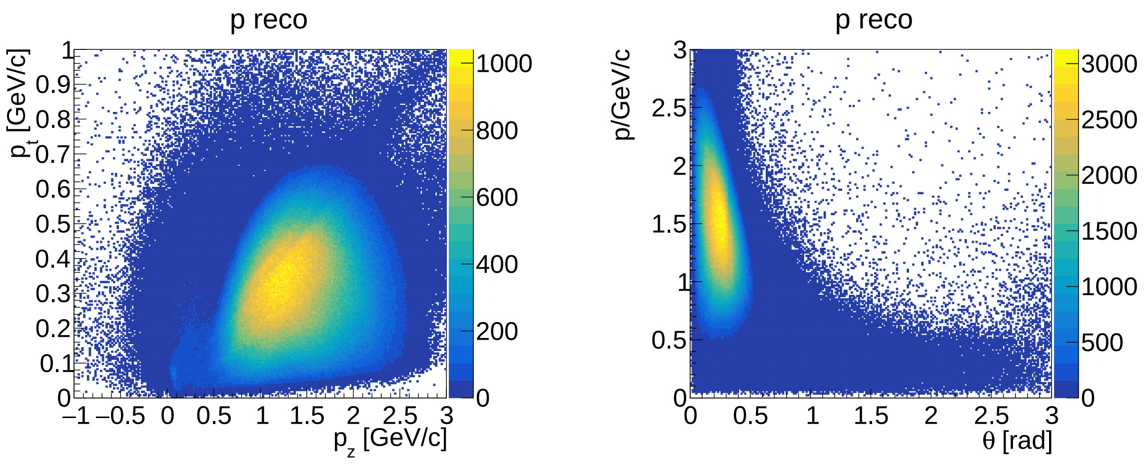

(a) (b)

Figure 5.46: Transverse vs. longitudinal momentum (a) and total momentum vs. Θ angle (b) for reconstructed protons.

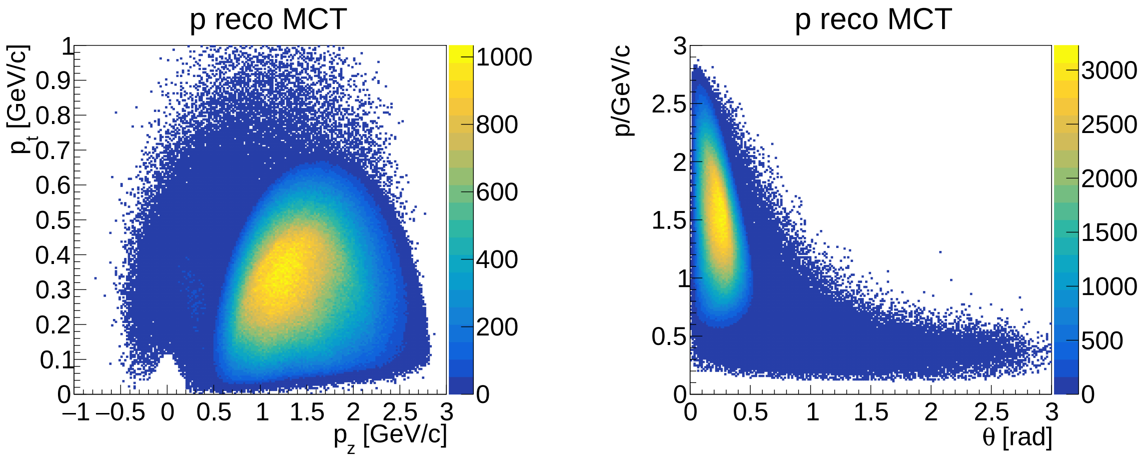

(a) (b)

Figure 5.47: Transverse vs. longitudinal momentum and total momentum vs. Θ angle for the MC truth partner of the reconstructed protons.

while the range for the Θ angle is expected to be up to 0.5 rad which corresponds to a range of 0°–29°. Here again, the distribution for all final state particles contain a significant number of events outside the boundaries given by the kinematics of the decay. The reason for this was previously described in Section 5.3.1.1. Requiring that Λ and $\overline{\Xi}^{+}$ as well as $\bar{\Lambda}$ and Ξ^{-} in the charge conjugate channel have only two daughters, rejects a significant number of entries outside the kinematically allowed region.

Momentum Resolution The momentum resolution is evaluated for all final state particles. As with the previous analysis, the resolution is determined by performing a double Gaussian fit. The width of the inner Gauss fit is taken as resolution. Again, the error on the fit value is dominated by the systematic error which is estimated by varying the fit parameters to be on the second decimal digit. The fit values for the momentum resolution for both channels, $\bar{\mathrm{p}}\mathrm{p} \rightarrow \overline{\Xi}^{+}\ \Lambda\ \mathrm{K}^{-}$ and $\bar{\mathrm{p}}\mathrm{p} \rightarrow \Xi^{-}\ \bar{\Lambda}\ \mathrm{K}^{+}$, are listed in Table 5.23. The best fit value is determined for the π^{+} coming from $\overline{\Xi}^{+}$ with a momentum resolution $dp/p = 1.48\%$. In the charge conjugate channel the best fit value is determined for π^{-} (Ξ^{-}) with $dp/p = 1.48\%$. The

Table 5.23: Momentum resolution for the final state particles of $\bar{\mathrm{p}}\mathrm{p} \rightarrow \overline{\Xi}^{+}\ \Lambda\ \mathrm{K}^{-}$ (a) and $\bar{\mathrm{p}}\mathrm{p} \rightarrow \Xi^{-}\ \bar{\Lambda}\ \mathrm{K}^{+}$ (b). The error on the fit values is dominated by the systematic error which is estimated to be 0.09%.

particle type	$dp/p[\%]$	$\sigma_{\mathrm{stat.}}[\%]$
π^{-}	1.61	0.003
π^{+} ($\bar{\Lambda}$)	1.64	0.003
π^{+} ($\overline{\Xi}^{+}$)	1.48	0.002
K^{-} (res.)	1.65	0.002
K^{-} (cont.)	1.66	0.005
p	1.63	0.003
$\bar{\mathrm{p}}$	1.59	0.003

(a)

particle type	$dp/p[\%]$	$\sigma_{\mathrm{stat.}}[\%]$
π^{+}	1.61	0.003
π^{-} (Λ)	1.64	0.003
π^{-} (Ξ^{-})	1.48	0.002
K^{+} (res.)	1.65	0.002
K^{+} (cont.)	1.65	0.005
p	1.60	0.003
$\bar{\mathrm{p}}$	1.61	0.003

(b)

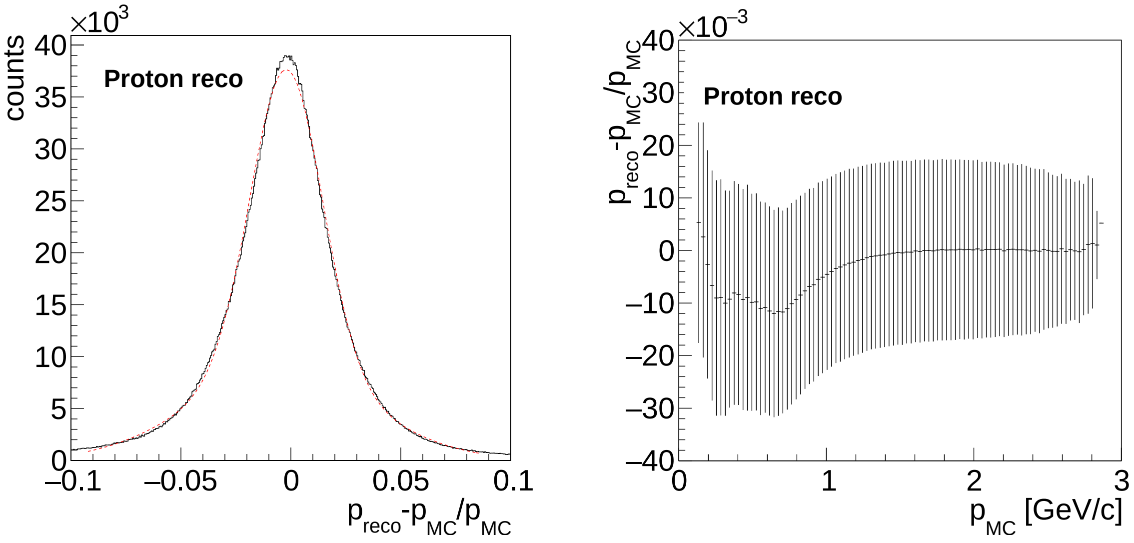

(a)

(b)

Figure 5.48: Relative deviation of the reconstructed and generated total proton momentum (a) and relative deviation versus generated total proton momentum (b).

momentum resolution of the proton is shown in Figure 5.48. As already seen in Section 5.3.1.1, the profile plots of the relative total momentum deviation plotted against the generated total momentum show smaller values for the reconstructed than for the generated total momentum at low generated momenta. Figure 5.48(b) shows exemplarily the profile plot for the proton. For a total momentum between 0.15 GeV/c up to 0.2 GeV/c the reconstructed momentum values are higher than the generated one, from 0.2 GeV/c up to above 1 GeV/c the reconstructed momentum is lower than the generated one. Above 1 GeV/c the relative deviation has a plateau close to 0. The profile plot for the $\bar{\mathrm{p}}$ is in qualitative agreement with the proton profile plot. Nearly the same behavior is observed for π^- from Λ and π^+ from $\bar{\Lambda}$. Both profile plots show a drop to negative values for the relative deviation between 0.05 GeV/c and around 0.3 GeV/c, while for generated momenta above 0.3 GeV/c the relative deviation is nearly stable and close to zero, meaning that the reconstructed and the generated total momentum are consistent. The profile plot for π^+ from the $\overline{\Xi}^+$ shows a drop between 0.1 GeV/c and 0.2 GeV/c. A similar drop can be observed for K^- around 0.4 GeV/c.

5.3.2.2 Reconstruction of Λ and $\bar{\Lambda}$

This paragraph describes the reconstruction of Λ and $\bar{\Lambda}$ candidates used in the DecayTreeFitter. As already mentioned in Section 5.3.1.2, the proper time distribution for the reconstructed Λ and $\bar{\Lambda}$ is not expected to follow an exponential function. Therefore, the fit values of $c\tau$ will not match the literature value of $c\tau = 7.89\,\mathrm{cm}$ [1]. For this reason the investigation of proper time distributions for all composite state particles will be done on the final selected sample in Section 5.3.2.4.
The following figures correspond to the reconstructed Λ. Appendix A.3.2 presents the figures of the reconstructed $\bar{\Lambda}$. The corresponding figures for Λ and $\bar{\Lambda}$ from the charge conjugate channel are listed in Appendix A.4.2.

Candidate Selection To reconstruct the Λ and $\bar{\Lambda}$ baryons, a π^- and a proton for Λ and a π^+ and a $\bar{\mathrm{p}}$ for $\bar{\Lambda}$ are combined. Subsequently a pre-selection is done by applying a loose mass window cut of 0.15 GeV/c^2 symmetrically around the nominal Λ mass $M_\Lambda = 1.116\,\mathrm{GeV/c^2}$. This pre-selection rejects those Λ and $\bar{\Lambda}$ candidates of with a mass much higher than the input Λ mass.
Compared with Section 5.3.1.2 the candidate selection in this analysis has no further steps. The reconstruction efficiency after the pre-selection is 60% (57.5%) for Λ and 55.9% (58.1%) for $\bar{\Lambda}$ with a purity of 21% (13%) for Λ and 13% (21%) for $\bar{\Lambda}$. The value in parenthesis are the reconstruction efficiencies and the purity values for the charge conjugate channel. It is visible that the purities for Λ and $\bar{\Lambda}$ are different. This issue is due to the different numbers of π^- and π^+ in the decay tree. In $\bar{\mathrm{p}}\mathrm{p} \rightarrow \overline{\Xi}^+ \Lambda \mathrm{K}^-$, we expect to have one π^- and two π^+ for the signal events. Therefore, the combinatorial background for $\bar{\Lambda}$ is higher than for Λ. The same is valid for the charge conjugate particles in the $\bar{\mathrm{p}}\mathrm{p} \rightarrow \Xi^- \bar{\Lambda} \mathrm{K}^+$ channel.

Mass Resolution The resulting mass distribution for Λ is shown in Figure 5.49. As expected, the peak of the mass distribution is around 1.116 GeV/c^2 which is in agreement with the input value. The plateau above a mass value of 1.12 GeV/c^2 is caused by wrong combinations of π^- and proton. To determine the mass resolution, a double Gaussian Fit is performed on the deviation of the reconstructed and the generated mass distribution (Fig. 5.49(b)). The evaluated mass resolution is $\sigma_M = \left(3.32 \pm 4 \cdot 10^{-3}(\mathrm{stat.}) \pm 0.04(\mathrm{sys.})\right)\,\mathrm{MeV/c^2}$ for Λ and $\sigma_M = \left(3.38 \pm 4 \cdot 10^{-3}(\mathrm{stat.}) \pm 0.04(\mathrm{sys.})\right)\,\mathrm{MeV/c^2}$ for $\bar{\Lambda}$. The fit error is dominated by the systematic error which is estimated by varying the fit parameters.

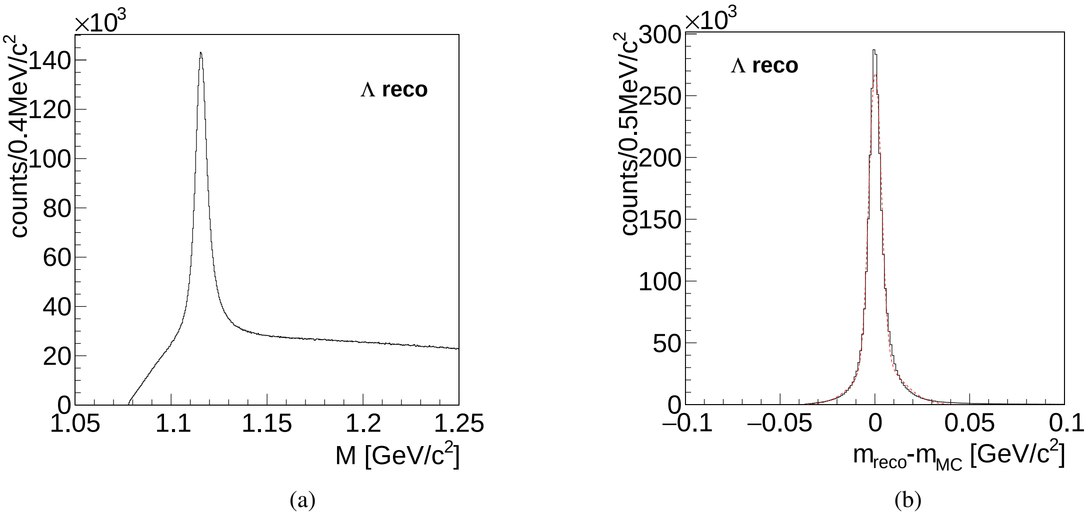

(a) (b)

Figure 5.49: Mass distribution for Λ candidates (a) and deviation of the reconstructed from the generated Λ mass (b) for the same sample. The mass resolution is evaluated by performing a double Gaussian fit. The long tail on the right side of the distribution in (b) is caused by combinatorial background.

Momentum Distribution and Momentum Resolution The transverse momentum versus the longitudinal momentum and the total momentum versus the θ angle for the generated, the MC partner of the reconstructed, and the reconstructed Λ are shown in Figure 5.50 – 5.51. For the signal Λ candidates the p_t versus p_z region is expected to be populated within elliptic boundaries. The longitudinal momentum reaches from 0.6 GeV/c up to 3.1 GeV/c with a maximum between 0.8 GeV/c and 2.5 GeV/c. The transverse momentum distribution is expected to have a maximum between 0.2 GeV/c and 0.7 GeV/c. For the total Λ momentum we expect a contribution in the range between 0.6 GeV/c and 3 GeV/c while the Θ range will be up to 0.5 rad.

Since the selection of the Λ and $\bar{\Lambda}$ candidates are only including a mass window cut, the background contribution to the two-dimensional distributions dominates. As visible in Figure 5.51, the background overlaps the signal. Nevertheless, the signal is still visible in the distribution. Looking at the distributions MC truth partner of the reconstructed Λ candidates one can see that the contribution of the correctly

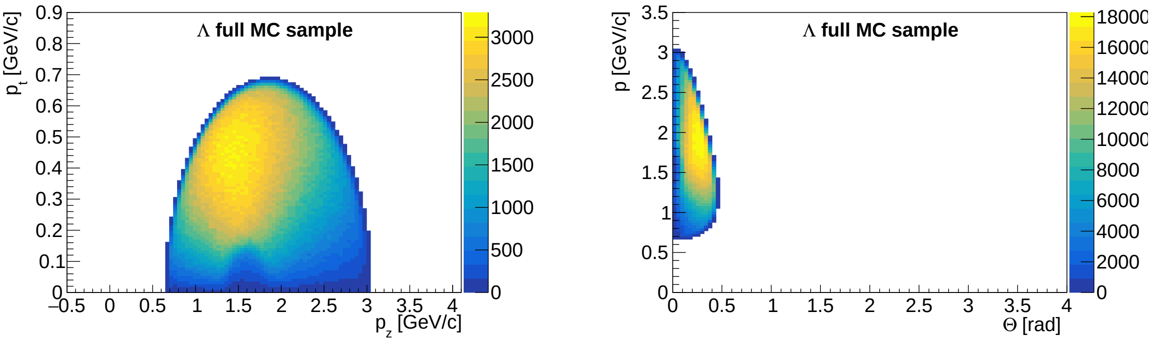

(a) (b)

Figure 5.50: Generated transverse vs. longitudinal momentum (a) and generated total momentum plotted against the Θ angle (b) for Λ.

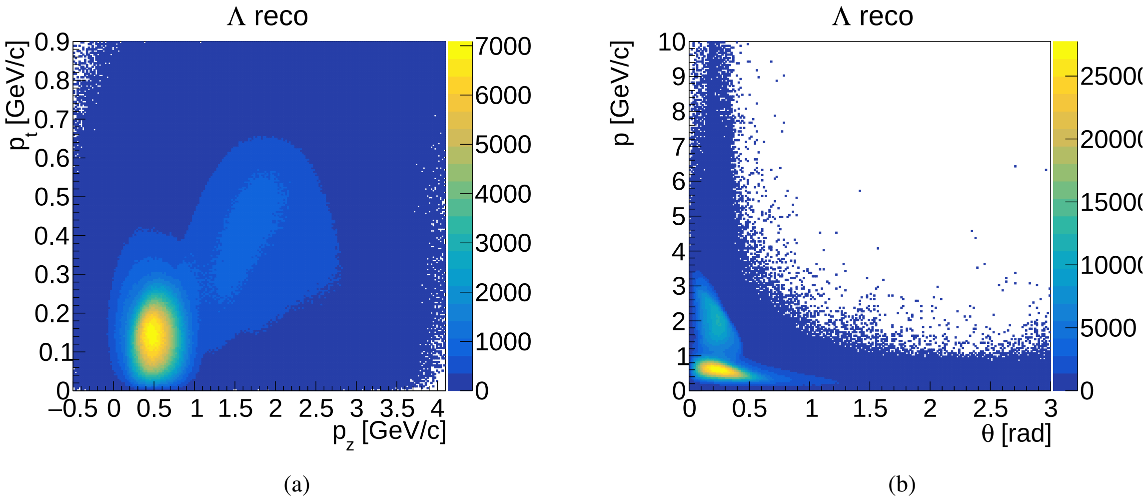

(a)

(b)

Figure 5.51: Reconstructed transverse vs. longitudinal momentum (a) and reconstructed total momentum plotted against the Θ angle (b) for Λ.

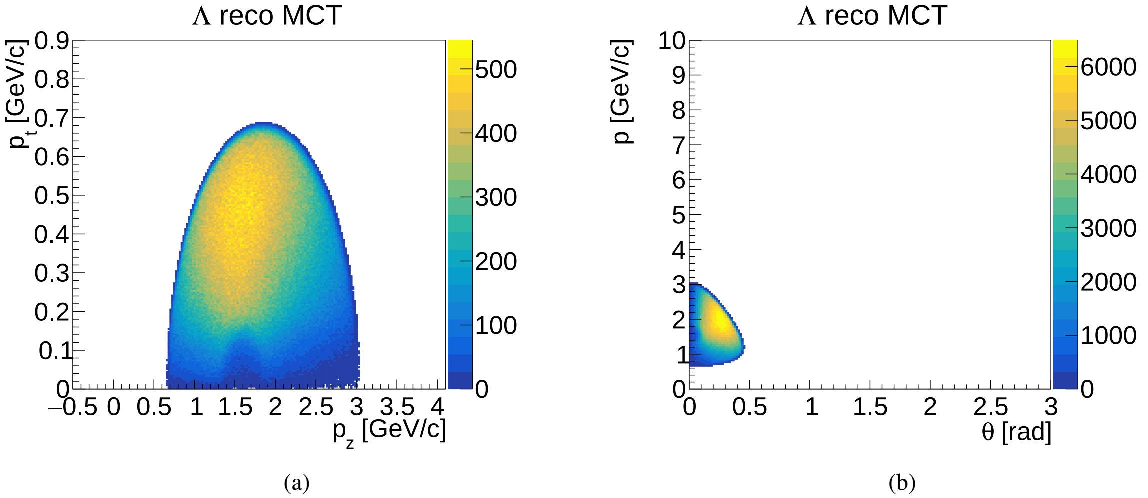

(a)

(b)

Figure 5.52: Transverse vs. longitudinal momentum (a) and total momentum plotted against the Θ angle (b) for the MC truth partners of the reconstructed Λ.

selected candidates are consistent with the input. The relative deviation of the reconstructed and the generated momentum for this stage of the Λ selection is shown in Figure 5.53. Again, the momentum resolution of Λ and $\bar{\Lambda}$ is evaluated by performing a double Gaussian Fit to the distributions, respectively. The determined values for the momentum resolutions as well as their estimated systematic errors are shown in Table 5.25. Figure 5.53(b) shows the dependence between the relative deviation of the momenta and the total generated momentum. For momenta up to 1 GeV/c the reconstructed total momentum is smaller than the generated total momentum. Between 1 GeV/c and 3.1 GeV/c the relative deviation reaches a stable value of $\sim 1 \cdot 10^{-3}$.

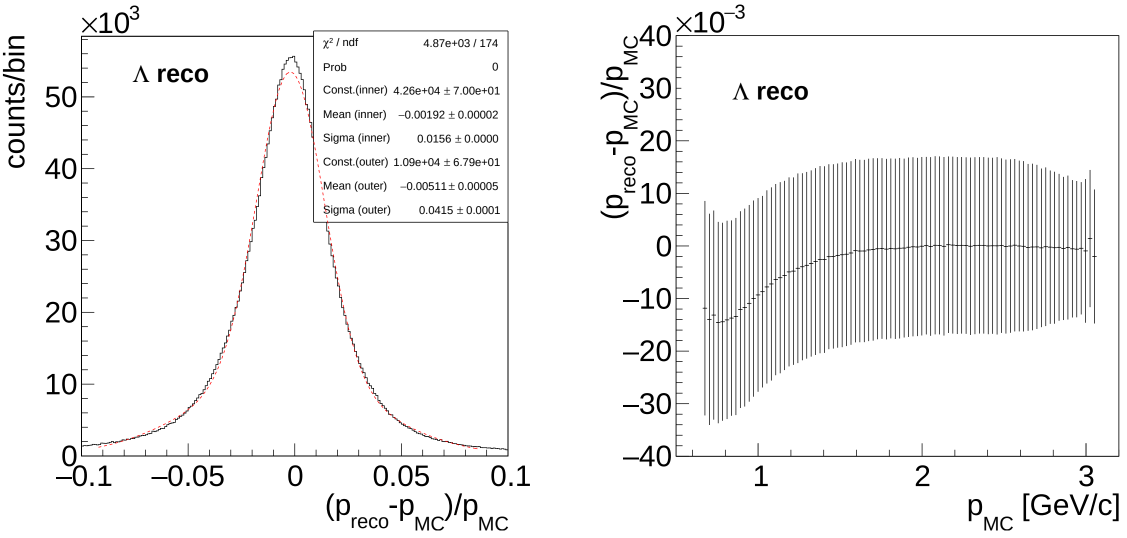

(a)

(b)

Figure 5.53: Relative deviation of the reconstructed and generated total Λ momentum (a) and relative deviation versus generated total Λ momentum (b).

Table 5.25: Evaluated values for the momentum resolution of Λ and $\bar{\Lambda}$

	σ[%]	stat. error [%]	sys. error [%]
Λ	1.606	0.003	0.09
$\bar{\Lambda}$	1.603	0.003	0.09

5.3.2.3 Reconstruction of $\overline{\Xi}^+$ and Ξ^-

In this paragraph the selection of the $\overline{\Xi}^+$ and Ξ^- candidates is described. As done for the other candidate selections, here, only the evaluated plots for $\overline{\Xi}^+$ are shown. The plots for the Ξ^- in the charge conjugate channel can be found in Appendix A.4.3.

Candidate Selection Since the Λ and $\bar{\Lambda}$ candidates have been reconstructed, it is possible to reconstruct $\overline{\Xi}^+$ and Ξ^- by combining $\bar{\Lambda}$ and π^+ for $\overline{\Xi}^+$ as well as Λ and π^- for the Ξ^- in the charge conjugate channel. To reduce the number of combinatorial background, a cut on the mass window with the width of 0.3 GeV/c^2 symmetric around the nominal Ξ^- mass $M_\Xi = 1.321$ GeV/c^2 is applied. The mass window cut reduces the number of events by around 50%. As for the Λ and $\bar{\Lambda}$ selection in the previous section, no additional cut is applied and the candidate is passed to the next stage of the reconstruction. The final selection is completed in the last step of the reconstruction by performing the full decay tree fit. At this stage, the reconstruction efficiency for $\overline{\Xi}^+$ is 40.7% and 41.6% for Ξ^- with. In both cases the purity is around 10%. The purity for the selected $\overline{\Xi}^+$ and Ξ^- sample is lower compared to the purity of the $\bar{\Lambda}$ and Λ sample. This decreasing number for the purity is due to the higher number of combinatorial background in the $\overline{\Xi}^+$ and Ξ^- sample.

Mass Resolution The mass distributions for $\overline{\Xi}^+$ after the mass window cut is shown in Figure 5.54 and for Ξ^- in Figure A.216. Both reconstructed mass distributions show prominent peaks around the 1.32 GeV/c^2 which is in agreement with the input value $M_\Xi = 1.32171\,\mathrm{GeV/c^2}$ [1]. In addition starting from 1.34 GeV/c^2 a plateau is visible in the mass distribtuion which is, as already explained in Section 5.3.2.2, caused by wrongly combined $\bar{\Lambda}$ and π^+ as well as wrongly combined Λ and π^- in the charge conjugate channel. To evaluate the mass resolution of $\overline{\Xi}^+$ and Ξ^- a double Gaussian fit is performed on the deviation of the reconstructed and the generated masses. The width σ of the inner fit is used as a measure for the mass resolution. A mass resolution of $\sigma_M = (5.89 \pm 0.01(\mathrm{stat.}) \pm 0.04(\mathrm{sys.}))\ \mathrm{MeV/c^2}$ $\overline{\Xi}^+$ and $\sigma_M = (5.89 \pm 0.009(\mathrm{stat.}) \pm 0.04(\mathrm{sys.}))\ \mathrm{MeV/c^2}$ for Ξ^- is evaluated.

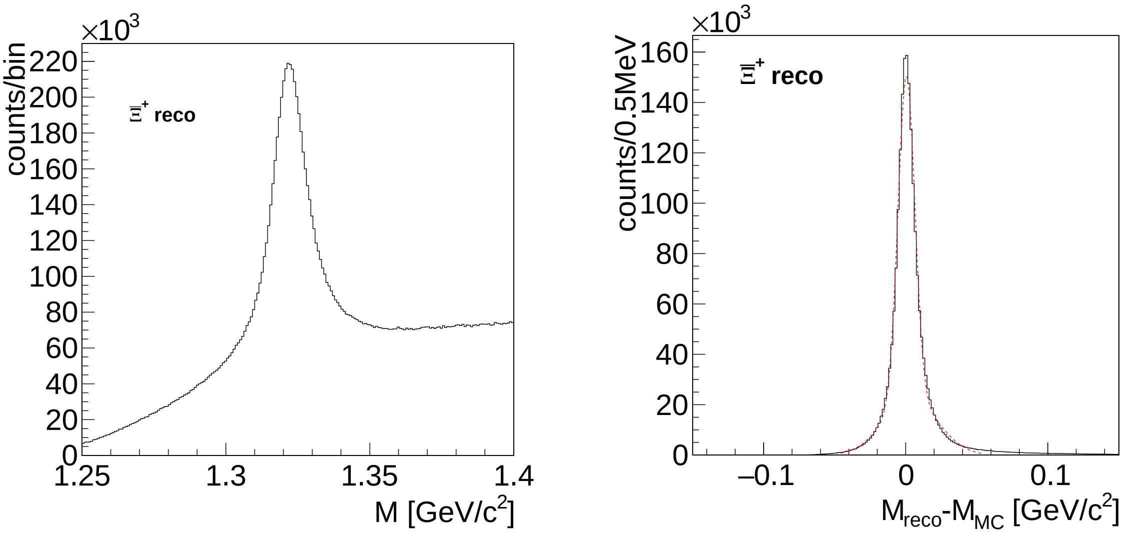

(a) (b)

Figure 5.54: Mass distribution (a) and deviation of the reconstructed and generated mass (b) for $\overline{\Xi}^+$ after the mass window cut. Both illustrations show the same sample.

Momentum Distribution and Momentum Resolution How the two-dimensional distributions for transverse versus longitudinal momentum and total momentum versus polar angle Θ should look like, has been described in Section 5.3.1.3. The distributions for the reconstructed $\overline{\Xi}^+$ after the mass window cut are illustrated in Figure 5.56. Since the mass window cut is only a coarse cut applied to suppress candidates with a too large deviation from the nominal Ξ mass, the distribution which is expected for the signal is partly covered by the combinatorial background. Nevertheless, parts of the signal are observable in the expected region between 1 GeV/c and 3.1 GeV/c longitudinal momentum. Comparing the MC truth partners of the reconstructed $\overline{\Xi}^+$ candidates with the generated sample shows that a significant

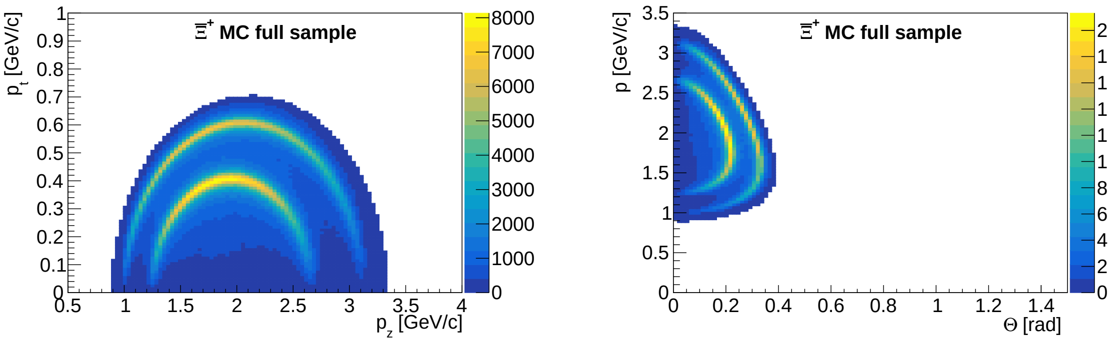

(a) (b)

Figure 5.55: Generated transverse vs. generated longitudinal momentum (a) and generated total momentum vs. Θ angle (b) for $\overline{\Xi}^+$.

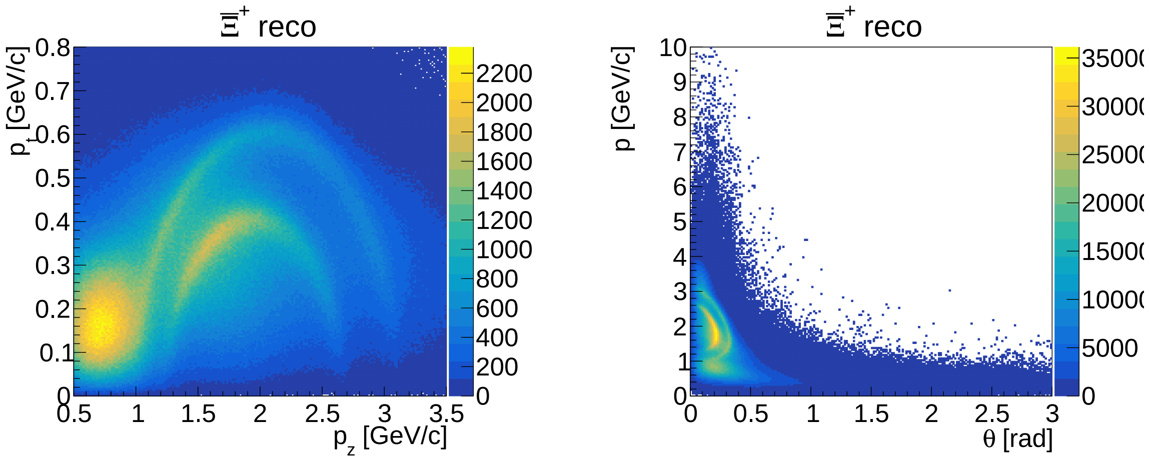

(a) (b)

Figure 5.56: Transverse vs. longitudinal momentum (a) and total momentum vs. Θ angle (b) for the reconstructed $\overline{\Xi}^+$ after the mass window cut.

number of entries are not related to the signal $\overline{\Xi}^+$. Those candidates should be rejected in the final selected sample. From the relative deviation of the reconstructed and the generated total momentum the momentum resolution is determined by performing a double Gaussian fit. Here again, the σ of the inner fit is taken as measure of the momentum resolution. The determined momentum resolution for $\overline{\Xi}^+$ is $\sigma = (2.53 \pm 0.01(\text{stat.}) \pm 0.09(\text{sys.}))$ % and $\sigma = (2.52 \pm 0.01(\text{stat.}) \pm 0.09(\text{sys.}))$ % for Ξ^- in the charge conjugate channel. As an example, the relative deviation for $\overline{\Xi}^+$ as well as the corresponding profile plot are shown in Figure 5.58. Similar to the previous shown profile plots, for lower momenta, here for both $\overline{\Xi}^+$ and Ξ^- up to 1.5 GeV/c the reconstructed total momentum is smaller than the generated one.

5.3.2.4 Reconstruction of the $\overline{\Xi}^+ \Lambda K^-$ and $\Xi^- \bar{\Lambda} K^+$

In this section the reconstruction of the full decay tree with full decay tree fit is described. The full decay tree fit procedure considers the 4-momentum conservation of the initial energy and momentum vector $P_{\text{ini}} = (0, 0, 4.6, 5.633)$, the mass conservation for $\bar{\Lambda}$, Λ, $\overline{\Xi}^+$ and Ξ^- as well as constraints on the hyperon

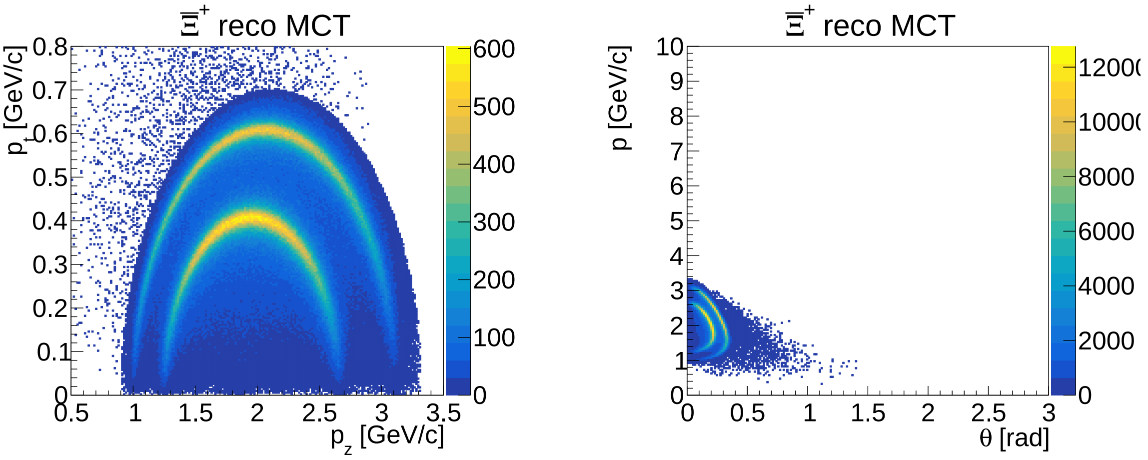

(a) (b)

Figure 5.57: Transverse vs. longitudinal momentum (a) and total momentum vs. Θ angle (b) for the MC truth partner of the reconstructed $\overline{\Xi}^+$.

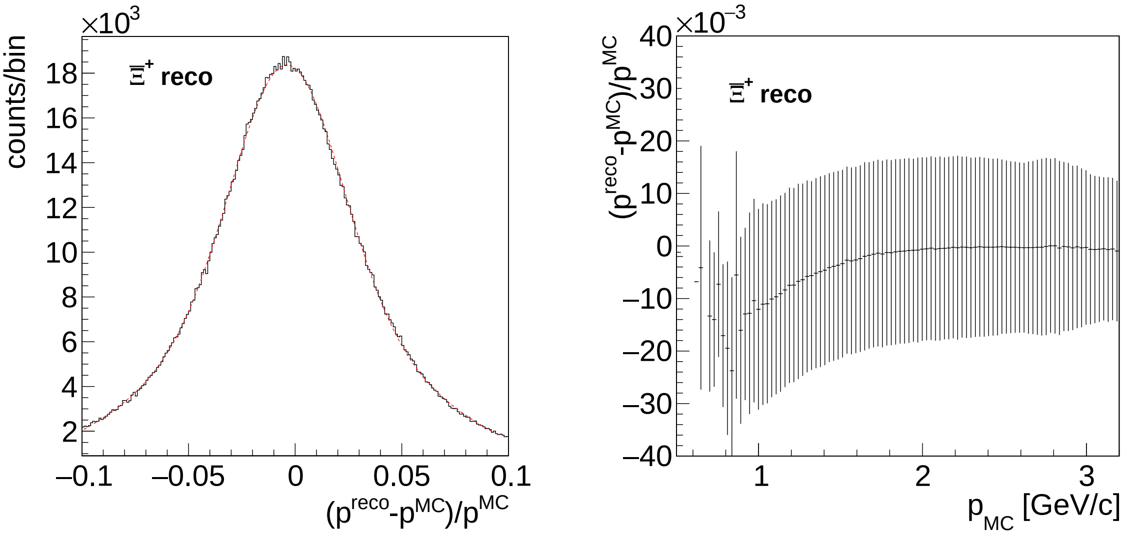

(a) (b)

Figure 5.58: Relative deviation of reconstructed and generated total momentum (a) and the relative deviation versus the generated total momentum (b) for $\overline{\Xi}^+$.

decay vertex. This section contains the illustrated results for $\overline{\Xi}^+$ Λ K^-, while the plots for the Ξ^- $\bar{\Lambda}$ K^+ reconstruction are shown in Appendix A.4.4.

Candidate Selection As mentioned before, the resonances decay instantaneously into Λ K^- and $\bar{\Lambda}$ K^+ in the charge conjugate channel. Therefore, the reconstruction of the full decay tree is done by combining $\overline{\Xi}^+$ Λ K^- and Ξ^- $\bar{\Lambda}$ K^+ in the charge conjugate channel. The resulting candidates are then fitted with the DecayTreeFitter implemented in PandaRoot. The quality of the fit is represented by χ^2 value. In addition, for each fitted candidate a probability is calculated. Both corresponding distributions are shown in Figure 5.59. For the selection of the final sample a cut on the fit probability with $P > 1 \cdot 10^{-4}$ is applied. The chosen cut on the probability corresponds to a cut on χ^2 value with $\chi^2 < 43$. Since the fit is not converging or even failing for a significant number of possible candidates, an additional cut on the fit status (Fig. 5.60) is performed to make sure that the fit for all final selected candidates converges. After all applied cuts, the reconstruction efficiency for $\overline{\Xi}^+$ Λ K^- is 5.4% and the efficiency for Ξ^- $\bar{\Lambda}$ K^+ 5.5%. Both final samples have a purity of 97.7%.

Table 5.26 shows the ratio between the non-resonant and resonant decay modes for the final selected sample. The reconstructed fraction for the decay modes are consistent with the input.

Table 5.26: Decay modes and ratios for the $\bar{p}p \rightarrow \overline{\Xi}^+ \Lambda K^-$ (a) and $\bar{p}p \rightarrow \Xi^- \bar{\Lambda} K^+$ (b) final selected sample.

Channel	Fraction [%]	Error [%]
$\overline{\Xi}^+$ $\Xi(1690)^-$	37.7	0.8
$\overline{\Xi}^+$ $\Xi(1820)^-$	42.4	0.8
$\overline{\Xi}^+$ Λ K^-	19.9	0.5

(a) $\bar{p}p \rightarrow \overline{\Xi}^+ \Lambda K^-$

Channel	Fraction [%]	Error [%]
Ξ^- $\overline{\Xi}(1690)^+$	37.8	0.8
Ξ^- $\overline{\Xi}(1820)^+$	42.2	0.8
Ξ^- $\bar{\Lambda}$ K^+	19.9	0.5

(b) $\bar{p}p \rightarrow \Xi^- \bar{\Lambda} K^+$

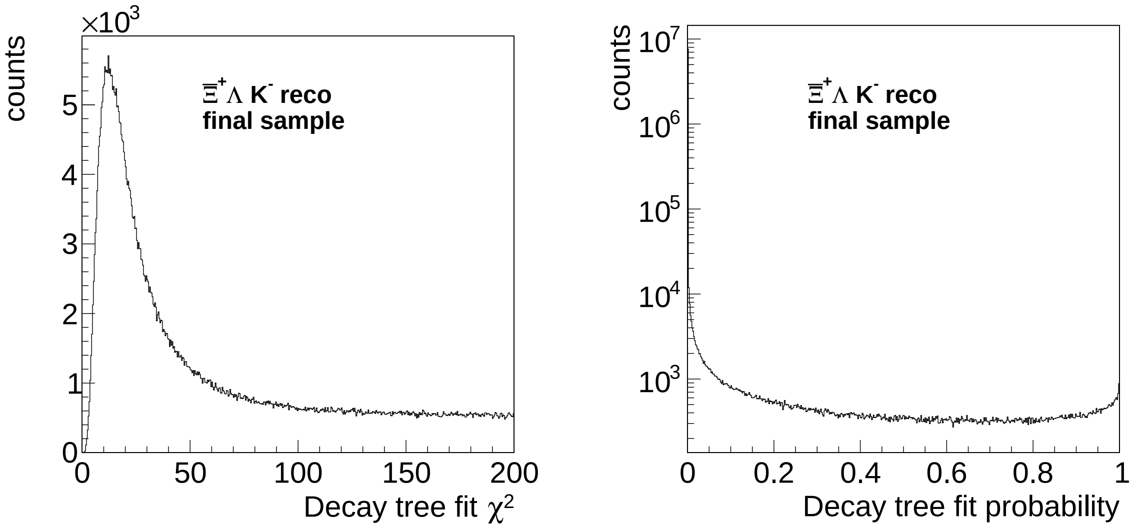

(a)

(b)

Figure 5.59: χ^2 (a) and probability (b) distribution for the DecayTreeFitter used on the $\overline{\Xi}^+$ Λ K^- sample.

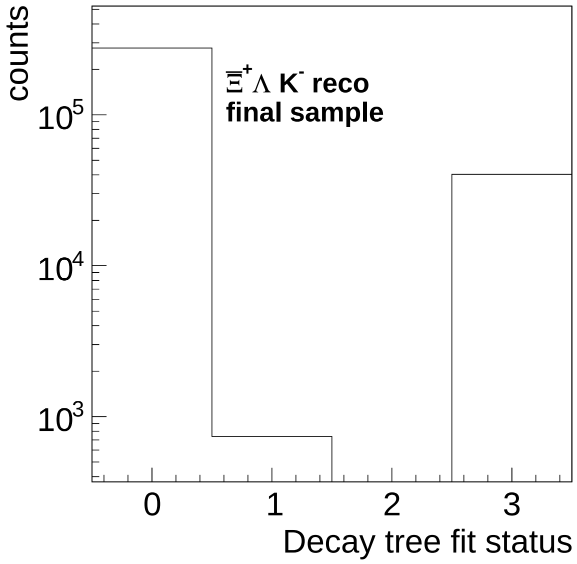

Figure 5.60: Fit status for the fitted candidates after the cut on the fit probability. The status is coded with an integer: 0 means O.K., 1 means failed and 3 means non-converged.

Momentum Resolution In this paragraph the results for the composite state particles, namely $\overline{\Xi}^+$, Λ and $\bar{\Lambda}$ are shown. In the following only the plots for the final selected Λ candidates are shown, because a presentation of all figures would expand this paragraph too much. The plots for $\overline{\Xi}^+$ and $\bar{\Lambda}$ can be found in Appendix A.3.3, while the plots for the charge conjugate channel can be found in Appendix A.4.4. The transverse versus longitudinal momentum and the total momentum versus polar angle Θ distributions for Λ (Fig. 5.61) are consistent with the expectations. From the comparison of the distributions for the final selected candidates and their MC truth partners, one can conclude the high purity of the final selected sample. Since the DecayTreeFitter uses kinematic fits, like the four-momentum

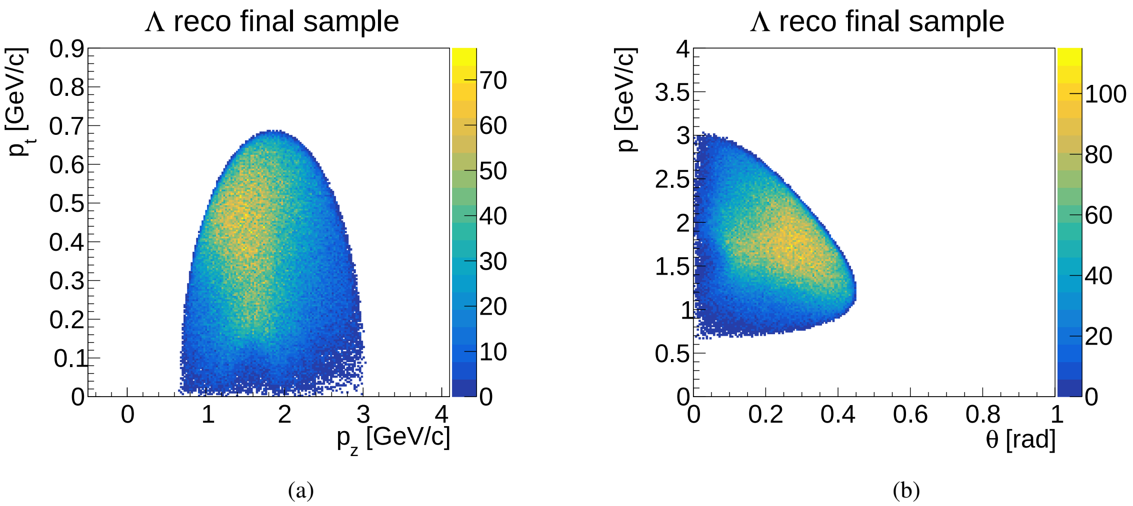

(a) (b)

Figure 5.61: Transverse vs. longitudinal momentum (a) and total momentum vs Θ angle (b) for final selected Λ candidates.

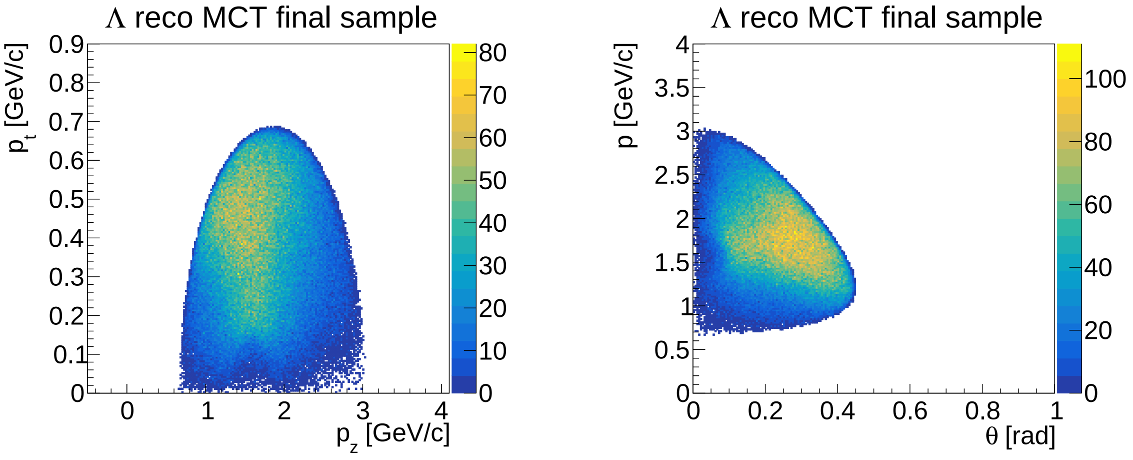

(a)

(b)

Figure 5.62: Transverse vs. longitudinal momentum (a) and total momentum vs Θ angle (b) for the MC partner of the final selected Λ candidates.

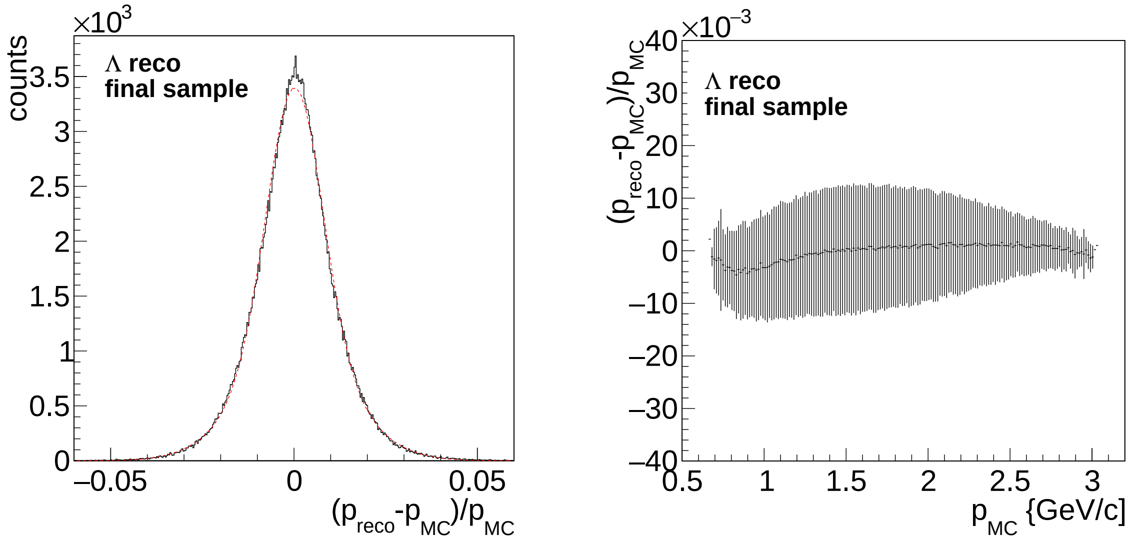

(a)

(b)

Figure 5.63: Relative deviation of the reconstructed and generated total momentum (a) and relative deviation versus generated total momentum (b) for the final selected Λ candidates.

Table 5.28: Momentum resolution for the composite state particles of $\bar{p}p \rightarrow \overline{\Xi}^+ \Lambda K^-$ (a) and $\bar{p}p \rightarrow \Xi^- \bar{\Lambda} K^+$ (b).

particle	σ [%]	syst. error [%]
Λ	0.777	0.007
$\bar{\Lambda}$	0.803	0.007
$\overline{\Xi}^+$	1.30	0.01

(a) $\bar{p}p \rightarrow \overline{\Xi}^+ \Lambda K^-$

particle	σ [%]	syst. error [%]
Λ	0.795	0.006
$\bar{\Lambda}$	0.748	0.006
Ξ^-	1.29	0.01

(b) $\bar{p}p \rightarrow \Xi^- \bar{\Lambda} K^+$

constraint fit, the momentum as well as the energy of the fitted candidates are corrected to match the initial four-momentum vector. This correction has an impact on the momentum resolution of the involved particles. The momentum resolution is evaluated by performing a double Gaussian fit to the relative deviation of the reconstructed and the generated total momentum. As an example, the relative deviation of the reconstructed and the generated total Λ momentum are shown in Figure 5.63. Table 5.28 shows the fit results for all composite state particles and their charge conjugate. Comparing Figure 5.63(b) with Figure 5.53(b) shows an improvement of the momentum resolution for lower generated momenta. This improvement can be observed for all composite state particles after the final selection.

Decay Vertex Resolution By evaluating the FWHM from the deviation of the reconstructed and the generated decay vertex positions in all three spatial coordinates, the decay vertex resolution can be determined. Figure 5.64 shows the three distributions for the final selected $\overline{\Xi}^+$ candidates. The achieved resolutions for all composite state particles are listed in Table 5.30. Since the bin size of the histogram is

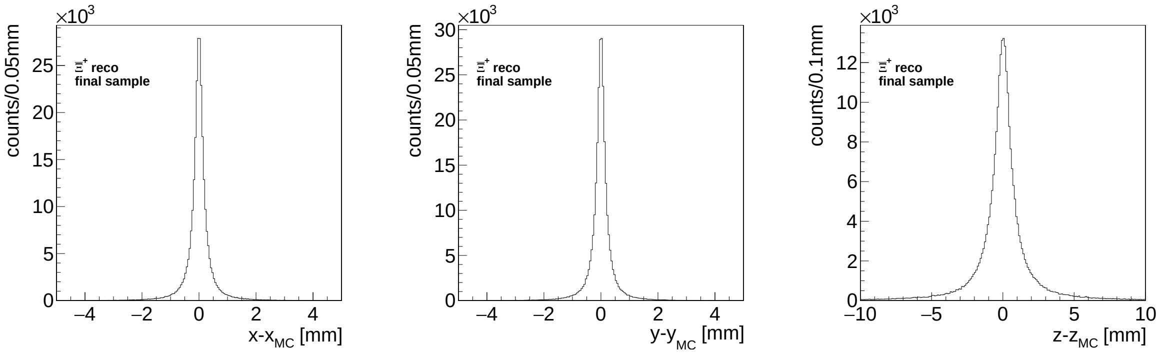

(a) (b) (c)

Figure 5.64: Deviation of the reconstructed and the generated decay vertex position of $\overline{\Xi}^+$ for the x coordinate (a), y coordinate (b), and z coordinate (c).

Table 5.30: Decay vertex resolution of all three spatial coordinates for the final selected composite particle candidates of $\bar{p}p \rightarrow \overline{\Xi}^+ \Lambda K^-$ (a) and $\bar{p}p \rightarrow \Xi^- \bar{\Lambda} K^+$ (b).

particle	x[mm]	y[mm]	z[mm]
Λ	0.26	0.22	1.28
$\bar{\Lambda}$	0.3	0.26	1.40
$\overline{\Xi}^+$	0.28	0.28	1.20

(a) $\bar{p}p \rightarrow \overline{\Xi}^+ \Lambda K^-$

particle	x[mm]	y[mm]	z[mm]
Λ	0.3	0.26	1.36
$\bar{\Lambda}$	0.26	0.26	1.28
Ξ^-	0.28	0.28	1.20

(b) $\bar{p}p \rightarrow \Xi^- \bar{\Lambda} K^+$

effecting the value of the FWHM, the corresponding error is estimated by varying the number of bins for the histograms. Therefore, the error is estimated to be in the order of 0.02 mm.

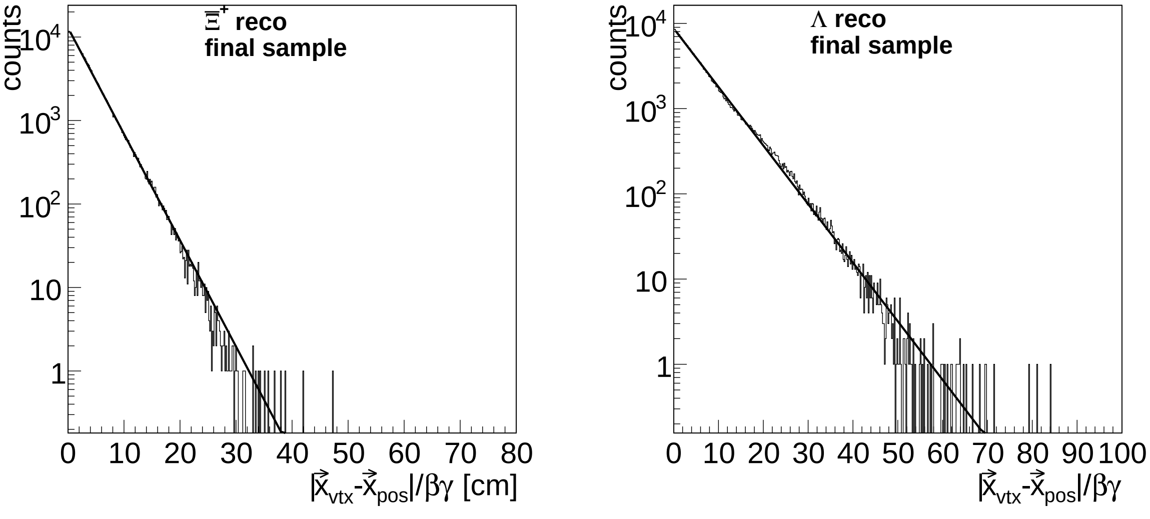

(a) (b)

Figure 5.65: Proper time distributions for a) final selected $\overline{\Xi}^+$ and b) final selected Λ candidates.

Proper Time Distribution Exemplarily, the proper time distributions for the final selected Λ and $\overline{\Xi}^+$ candidates are shown in Figure 5.65. By fitting an exponential function to the proper time distribution and inverting the fit result, the $c\tau$ value for the composite state particles is determined. The error on the $c\tau$ value is purely statistical and was calculated from the error on the fit value by Gaussian error propagation. Table 5.32 lists the determined $c\tau$ values for all composite state particles in the $\overline{\Xi}^+$ Λ K^- and Ξ^- $\bar{\Lambda}$ K^+ state, respectively. The fitted values for Λ and $\bar{\Lambda}$ differ by about 20% from the literature value $c\tau_\Lambda$ = 7.89 cm[1]. A similar difference for $\overline{\Xi}^+$ and Ξ^- is observed. Here, the fitted values differ by about 30% from the literature value of $c\tau_\Xi$ = 4.91 cm. Since the resolution of the decay vertex is depending on the detector part, the observed deviation could be caused by the uncertainty on this position.

Table 5.32: Determined $c\tau$ values for the composite state particles of $\bar{p}p \rightarrow \overline{\Xi}^+ \Lambda K^-$ (a) and $\bar{p}p \rightarrow \Xi^- \bar{\Lambda} K^+$ (b).

particle	$c\tau$ [cm]	$\sigma_{c\tau}$ [cm]
Λ	6.32	0.01
$\bar{\Lambda}$	6.43	0.08
$\overline{\Xi}^+$	3.409	0.005

(a) $\bar{p}p \rightarrow \overline{\Xi}^+ \Lambda K^-$

particle	$c\tau$ [cm]	$\sigma_{c\tau}$ [cm]
Λ	6.45	0.01
$\bar{\Lambda}$	6.34	0.01
Ξ^-	3.389	0.006

(b) $\bar{p}p \rightarrow \Xi^- \bar{\Lambda} K^+$

Different from the proper time distributions shown in the previous analysis, see Figure 5.34(b), in this analysis the proper time distributions have an exponential shape. Why the shape of the proper time distributions differ is difficult to evaluate, since for this analysis a newer version of the software framework was used. One reason could be, that the DecayTreeFitter uses different fitting procedure including also a fit to constrain the decay vertex of the hyperons which is used to calculate the proper time, see Equation (5.2).

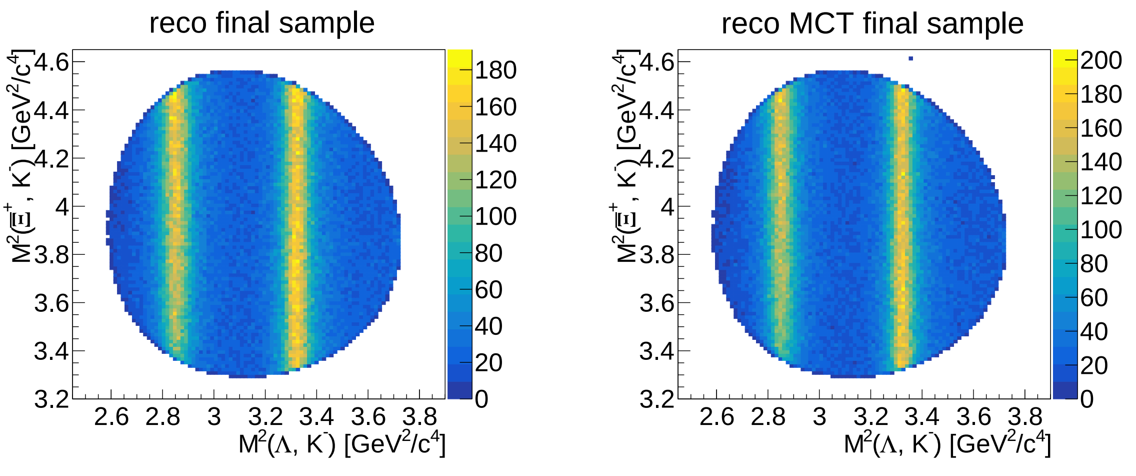

(a) (b)

Figure 5.66: Dalitz plot for the final sample (a) and the MC truth partners (b) of the final selected $\overline{\Xi}^+$ Λ K^- candidates.

Dalitz Plots Figure 5.66(a) shows the Dalitz plot for the $\overline{\Xi}^+$ Λ K^- final state. On the x-axis the squared mass of the Λ K^- system is plotted against the squared mass of the $\overline{\Xi}^+$ K^- system. The Ξ resonances are visible as vertical bands around the expected masses in the Dalitz plot. For comparison, the Dalitz plot of the generated events is shown in Figure 5.67 and the Dalitz plot for the MC truth partners of the reconstructed final sample is shown in Figure 5.66(b). The ratio of both Dalitz plots is illustrated in Figure 5.67 and shows a uniform distribution. To confirm this uniformity also the ratio plots for the masses of the Λ K^- and $\overline{\Xi}^+$ K^- systems, shown in Figure 5.68, are determined. Both distributions are mainly flat, while the ratio for the Λ K^- mass shows a decreasing efficiency for lower masses. This is caused by slow Λ particles since their daughter particles, i.e. the pions, are produced with low momenta and hence leave curled tracks inside the detectors. These curling tracks cannot be properly reconstructed by the tracking algorithms. Nevertheless, this uniformity points to a flat detector acceptance.

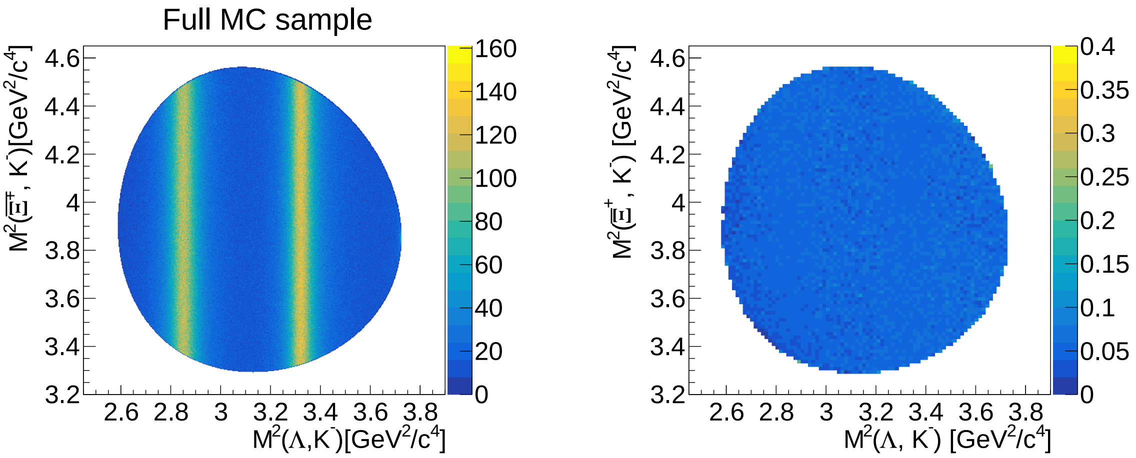

(a) (b)

Figure 5.67: Dalitz plot for the generated sample (a) and ratio of the MC truth partners of the final sample and the generated sample(b).

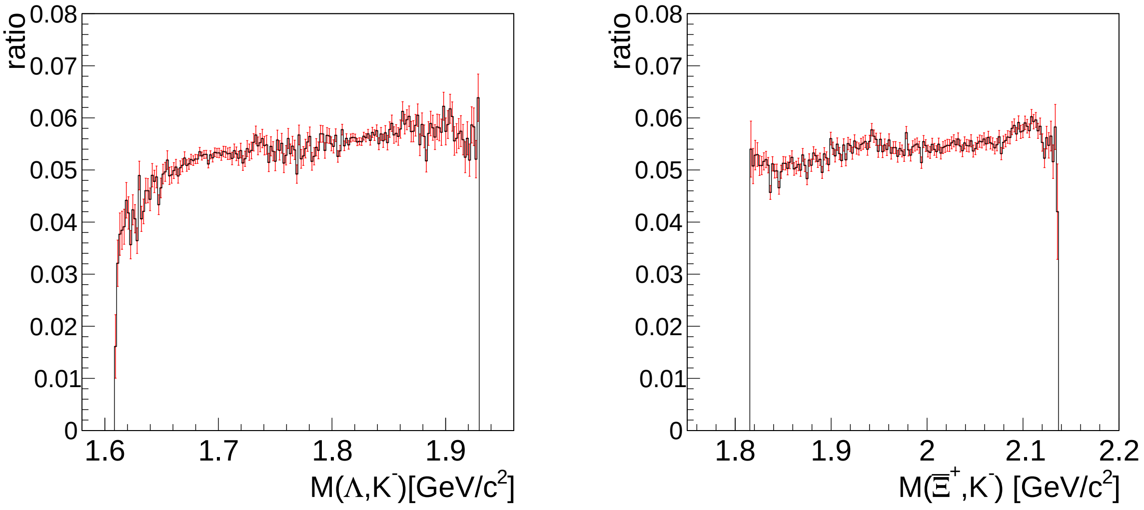

(a)

(b)

Figure 5.68: Ratio of the generated and the MC truth partner of the reconstructed Λ K$^-$ (a) and $\overline{\Xi}^+$ K$^-$ (b) mass distributions.

Resonance Masses and Widths As explained in Section 5.3.1.4 the mass and the width for both resonances is determined by fitting the sum of two Voigt functions and a polynomial to the mass distribution of the Λ K$^-$ (Fig. 5.69) and the $\bar{\Lambda}$ K$^+$ (Fig. A.241) system. Again, the best fit result is

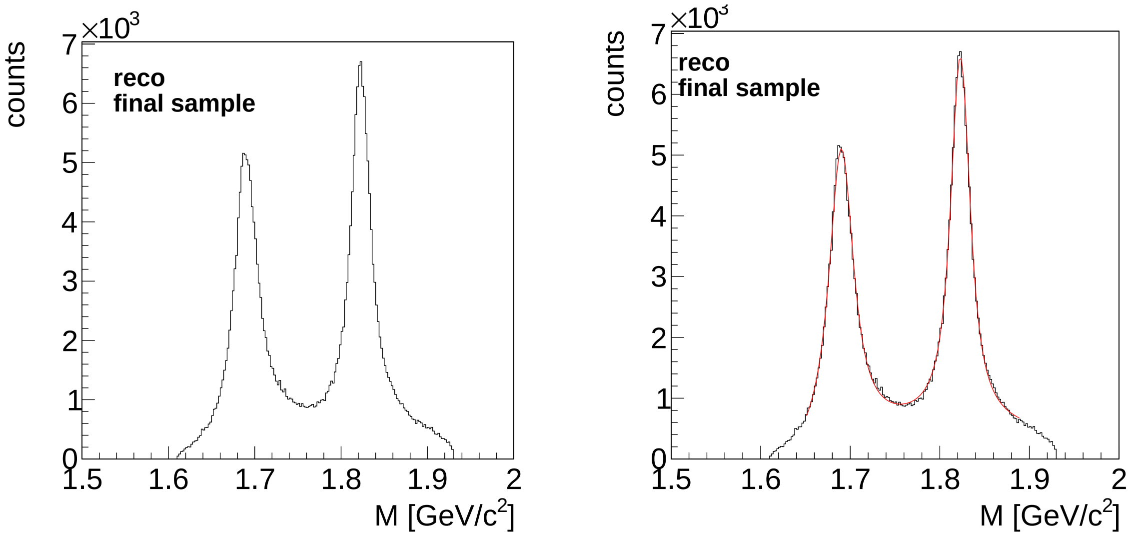

(a)

(b)

Figure 5.69: Mass distribution of Λ K$^-$ without (a) and with (b) fit. The fit function consists of two Voigt functions and a polynomial.

achieved by fixing the σ value for both resonances which is determined by calculating the FWHM for the deviation of the final reconstructed and the generated mass distribution, see also Figure 5.70. The determined value is $\sigma = 0.004\,\mathrm{GeV/c^2}$ for both resonances. Table 5.34 shows the resulting fit values for the Ξ resonances. The values are consistent with the input values shown in Table 5.2. The mass

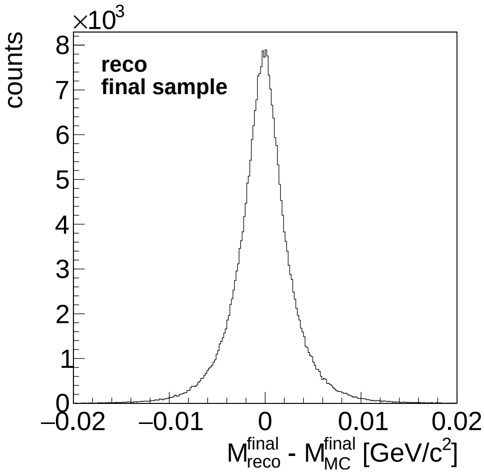

Figure 5.70: Deviation of the final reconstructed and the generated Λ K^- mass distribution.

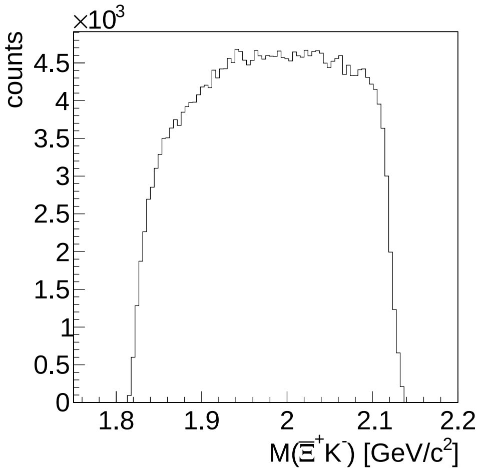

Figure 5.71: Mass distribution for the $\overline{\Xi}^+$ K^- system.

distribution of the $\overline{\Xi}^+$ K^- system (Fig. 5.71) shows as structureless distribution, as expected.

Table 5.34: Fit results for the mass and the width of the Ξ^- and $\overline{\Xi}^+$ resonances determined with a fit function containing two Voigt functions and a polynomial.

	$\Xi(1690)^-$	$\Xi(1820)^-$	$\overline{\Xi}(1690)^+$	$\overline{\Xi}(1820)^+$
M[MeV/c²]	$1689.99\pm^{0.09(stat.)}_{0.1(sys.)}$	$1822.98\pm^{0.06(stat.)}_{0.1(sys.)}$	$1690.16\pm^{0.08(stat.)}_{0.1(sys.)}$	$1823.12\pm^{0.06(stat.)}_{0.1(sys.)}$
Γ[MeV/c²]	$30.1\pm^{0.4(stat.)}_{0.5(sys.)}$	$22.9\pm^{0.2(stat.)}_{0.4(sys.)}$	$30.2\pm^{0.4(stat.)}_{0.5(sys.)}$	$22.7\pm^{0.2(stat.)}_{0.4(sys.)}$

Angular Distributions As already described in Section 5.3.1.4, the angular distributions $\cos(\theta_{\mathrm{cm}})$, ϕ_{cm} and ϕ'_{cm} in the center-of-mass frame are the remaining three degrees of freedom of the three-body final state. Figure 5.72 shows the ratio of the angular distributions for the final reconstructed sample. The shape of all three ratios are in qualitative agreement with the ratio plots shown in the previous analysis, see Section 5.3.1.4. But the maxima are not as prominent as it is the case in case of the sequential fit procedure. This difference is due to the lower efficiency which is achieved in this analysis. Again, the ratio for $\cos\theta$, shown in Figure 5.72(a), has two maxima at $\cos\theta = \pm 1$ and a minimum at around zero which is due to the beam pipe. Figure 5.72(b) shows the ratio of the ϕ distribution. The drop in the efficiency in ϕ in the center-of-mass frame is due to the target pipe.

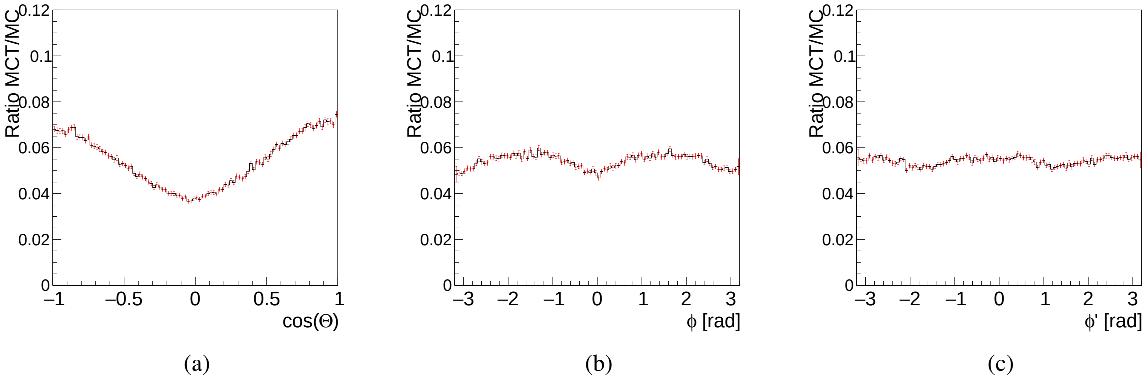

(a) (b) (c)

Figure 5.72: $\cos\theta_{\mathrm{cm}}$ (a), ϕ_{cm} (b) and ϕ'_{cm} ratio between the MC partners of the final reconstructed candidates and the generated sample.

ϕ' is a measure for the alignment of the momentum vectors in the center-of-mass frame. Like it is done in the previous analysis, ϕ' is defined as the angle between the momentum vector $P^{\mathrm{cm}}_{\bar{\Xi}^+}$ and the intersection line of the center-of-mass plane and the x-z-plane. The corresponding ratio plot is shown in Figure 5.72(c). Around $\phi' = \pm\pi/2$ the efficiency decreases due to the target pipe. The $\cos\theta$ distributions for the generated, the final reconstructed as well as for the MC partner of the reconstructed $\overline{\Xi}^+$ candidates are shown in Figure 5.73. It is observable that the distribution of the final selected $\overline{\Xi}^+$ deviates from the generated one. This deviation is due to the loss generated particles inside the beam pipe. From the ratio of the MC partners and the generated sample, shown in Figure 5.74, the reconstruction efficiency for any center-of-mass angular distribution can be determined.

5.4 Background Studies

This section describes the study done on two different data sets with 100 million generated background events each. Since the analysis of the signal based on the step-by-step reconstruction and based on the full decay tree fit is done with two different PandaRoot versions, two background samples using these two software versions are generated. The event generation is done with the Dual Parton Model [138] based generator Dual Parton Model (DPM) including only inelastic processes.

The same analysis strategies as for the signal are used to study the background events. For both analyzes no event out of 100 million generated survived the applied cuts. The non-observation of any background events corresponds to a 90% confidence upper limit of 2.3 events.

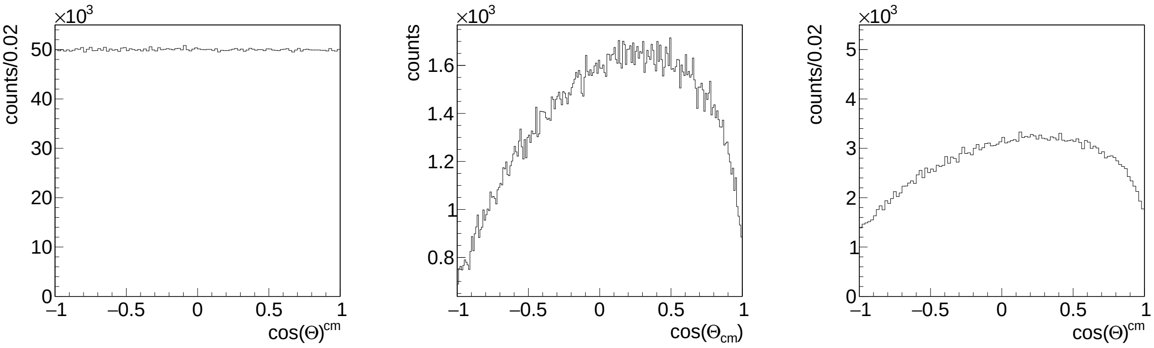

(a) (b) (c)

Figure 5.73: Generated (a) and reconstructed (b) $\cos\theta$ distribution in the center-of-mass frame for final selected $\overline{\Xi}^{+}$ as well as the distribution for the MC partners of the reconstructed $\overline{\Xi}^{+}$ candidates (c).

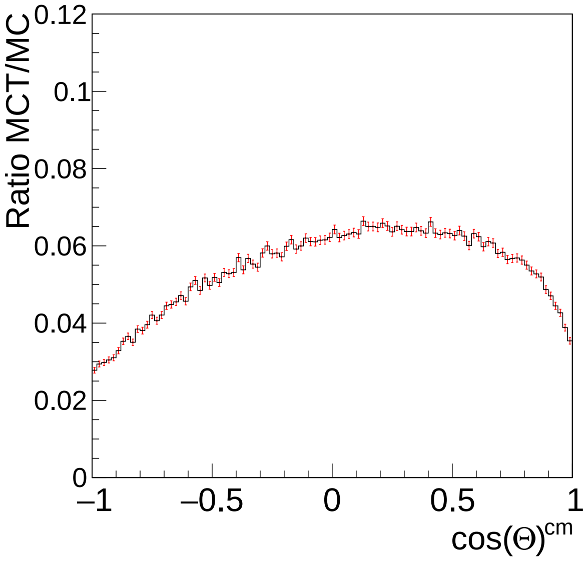

Figure 5.74: Ratio plot of the $\cos\theta$ distribution in the center-of-mass frame for the final selected $\overline{\Xi}^{+}$ candidates.

The signal-to-background ratio is calculated by

$$\frac{S}{B} = \frac{\sigma_{\text{sig}} \cdot \epsilon_{\text{sig}} \cdot b_{\text{sig}}}{\sigma_{\text{bg}} \cdot \epsilon_{\text{bg}}}, \tag{5.3}$$

where σ_{sig} is the signal and σ_{bg} the background cross section, b_{sig} is the total branching fraction of the final selected signal events and ϵ_{sig} and ϵ_{bg} are the reconstruction efficiencies for signal and background events, respectively. As already mention in section 5.2, the signal cross section has not yet been measured. Therefore, I assume $\sigma_{\text{sig}} = 1\,\mu\text{b}$ according to [23]. Furthermore, the inelastic cross section at a beam momentum of 4.6 GeV/c is $\sigma_{\text{bg}} = 50\,\text{mb}$ [1]. During the event generation the branching fraction of Λ and $\bar{\Lambda}$ was set to 100%. To correct this value for the following calculations, the branching ratio of $b_{\text{sig}} = b_{\Lambda}^{2} = 0.4083$ for the two Λ decays in the decay tree is taken into account.

For the sequential fitting procedure the reconstruction efficiency is $\epsilon_{\text{sig}} = 8.2\,\%$ for $\overline{\Xi}^{+}\ \Lambda\ \text{K}^{-}$ and

$\epsilon_{\text{sig}} = 9.2\,\%$ for $\Xi^-\ \bar{\Lambda}\ K^+$, while the reconstruction efficiencies achieved with the full decay tree fit are $\epsilon_{\text{sig}} = 5.4\,\%$ for $\overline{\Xi}^+\ \Lambda\ K^-$ and $\epsilon_{\text{sig}} = 5.5\,\%$ for $\Xi^-\ \bar{\Lambda}\ K^+$.
At the 90% confidence level the reconstruction efficiency background events is $\epsilon_{\text{bg}} = 2.3 \cdot 10^{-8}$. The different signal-to-background ratios are listed in table 5.35. The significance S_{sig} of the signal is given by

Table 5.35: Signal-to-Background ratio and signal significance for the sequential fitting procedure (a) and the full decay tree fit (b).

	$\overline{\Xi}^+\ \Lambda\ K^-$	$\Xi^-\ \bar{\Lambda}\ K^+$
S/B	> 29.11	> 32.7
S_{sig}	> 644	> 685

(a) sequential fitting procedure

	$\overline{\Xi}^+\ \Lambda\ K^-$	$\Xi^-\ \bar{\Lambda}\ K^+$
S/B	> 19.1	> 19.5
S_{sig}	> 513	> 507

(b) full decay tree fit

$$S_{\text{sig}} = \frac{N_{\text{sig}}}{\sqrt{N_{\text{sig}} + N_{\text{bg}} \cdot F_{\text{bg}}}}, \tag{5.4}$$

where F_{bg} is a scaling factor to correct the number of background events according to the number of signal events, because this ratio does not reflect the cross sections. The scaling factor is given by

$$F_{\text{bg}} = \frac{N^{\text{gen}}_{\text{sig}} \cdot \sigma_{\text{bg}}}{N^{\text{gen}}_{\text{bg}} \cdot \sigma_{\text{sig}} \cdot b_{\text{sig}}} \tag{5.5}$$

with $N^{\text{gen}}_{\text{sig}}$ and $N^{\text{gen}}_{\text{sig}}$ the number of generated signal and background events, respectively. At 90% confidence level a significance of 644 for $\overline{\Xi}^+\ \Lambda\ K^-$ and 685 for $\Xi^-\ \bar{\Lambda}\ K^+$ is obtained for the analysis with the sequential fitting procedure. The results of the analysis with the full decay tree lead to a lower limit for the signal significance of 513 for $\overline{\Xi}^+\ \Lambda\ K^-$ and 507 for $\Xi^-\ \bar{\Lambda}\ K^+$.

5.5 Results

The performed analyzes presented in section 5.3.1 and section 5.3.2 show that the study of the chosen reaction channels, namely $\bar{p}p \to \overline{\Xi}^+\ \Lambda\ K^-$ and $\bar{p}p \to \Xi^-\ \bar{\Lambda}\ K^+$, are feasible. In both channels the excited cascade baryons $\Xi\,(1690)^-$ and $\Xi\,(1820)^-$ as well as their charge conjugate particles are included. All resonances can be clearly identified in the performed analyzes. In the following, the achieved results for each kind of analysis are discussed, separately.

The analysis of about 10 million events using the sequential fit procedure achieves a reconstruction efficiency of about 8% for $\overline{\Xi}^+\ \Lambda\ K^-$ and about 9% for $\Xi^-\ \bar{\Lambda}\ K^+$. The final selected samples consist of 429,044 $\overline{\Xi}^+\ \Lambda\ K^-$ events, whereof 409,591 events are true signal events, and of 483,149 $\Xi^-\ \bar{\Lambda}\ K^+$ events with 461,066 true signal events. Therefore, the purity of the sample is 95.4% meaning that the genealogy of the decay tree itself is already suppressing the combinatorial background. Nevertheless, one has to keep in mind, that for this analysis not only an ideal pattern recognition but also an ideal particle identification is used. Thus it is expected that the sample purity is decreasing for a more realistic particle identification. However, the achieved value can be taken as an upper limit. Furthermore, the analysis shows that the expected resonance masses, as well as the width of the associated distributions, can be reconstructed in accordance with the input values. From fits to the mass distribution of $\overline{\Xi}^+\ \Lambda$

K^- and $\Xi^-\ \bar{\Lambda}\ \mathrm{K}^+$ the resonance masses $\mathrm{M}(\Xi\,(1690)^-)=1.6904\,\mathrm{GeV/c^2}$, $\mathrm{M}(\overline{\Xi}\,(1690)^+)=1.6905\,\mathrm{GeV/c^2}$, $\mathrm{M}(\Xi\,(1820)^-)=1.8229\,\mathrm{GeV/c^2}$ and $\mathrm{M}(\overline{\Xi}\,(1820)^+)=1.8229\,\mathrm{GeV/c^2}$ are determined. The evaluated momentum resolutions for all involved particles is between 0.73% and 1.65%, which is consistent with the expectation for the PANDA detector [9]. In this analysis a decay vertex resolution between $150\,\mu\mathrm{m}$ and $350\,\mu\mathrm{m}$ in x and y directions and between 0.5 mm and 1.3 mm in z direction is achieved. The mass resolution is in the range of $2\,\mathrm{MeV/c^2}$ and $3.7\,\mathrm{MeV/c^2}$.
The analysis also shows that there are issues with the kinematic fitters implemented in PandaRoot. The most obvious issue can be observed in the Dalitz plot for the final selected sample. Here, a small number of entries, in the order of 0,1%, are outside the kinimatically allowed region. An additional cut has to be used to reduce this number. A further issue seems to be in the kinematic fit using a mass constraint. The mass distribution of a composite particle is expected to be a delta function after performing a kinematic fit with mass constraint on the candidates. But the mass distributions show entries to lower masses. Those issues are not understood, yet, and are still under investigation.

Since the named issues of the kinematic fitter are affecting the selection of the final sample, a second analysis of about 10 million events using a full decay fit procedure is done. The 10 million events are consisting of 5 million $\overline{\Xi}^+\ \Lambda\ \mathrm{K}^-$ events and another 5 million $\Xi^-\ \bar{\Lambda}\ \mathrm{K}^+$ events. For this analysis a reconstruction efficiency of around 5% for both channels is achieved. The final selected sample for $\overline{\Xi}^+\ \Lambda\ \mathrm{K}^-$ contains 277,133 events, whereof 270,867 are true signal events. For the charge conjugate channel the final sample contains 283,617 events with 277,280 MC true events. Both samples end up with a sample purity of 97.7 %. Different from the analysis with the sequential fitting procedure, in this analysis no PID information is used for the final state candidate selection. This implies again, that the genealogy of the signal events is suppressing the combinatorial background efficiently.
The achieved momentum resolutions are between 0.77% and 1.66%, which is consistent with the expectations [9]. For the decay vertex resolution values between $220\,\mu\mathrm{m}$ and $300\,\mu\mathrm{m}$ in x- and y-direction and 1.2 mm and 1.4 mm in z-direction are achieved with this analysis. Different from the proper time distribution in the first analysis, the reconstructed proper time distributions shown in this analysis have an exponential shape. Even so, the fitted values are not matching the input values $c\tau_\Lambda = 7.89\,\mathrm{cm}$ and $c\tau_\Xi = 4.91\,\mathrm{cm}$, respectively. The fit values for $c\tau$ differs from the literature values by about 20% for $\bar{\Lambda}$ and Λ, and about 30% for $\overline{\Xi}^+$ and Ξ^-. The fitted values for the mass $\mathrm{M}(\Xi\,(1690)^-)=1.6899\,\mathrm{GeV/c^2}$, $\mathrm{M}(\overline{\Xi}\,(1690)^+)=1.6902\,\mathrm{GeV/c^2}$, $\mathrm{M}(\Xi\,(1820)^-)=1.8229\,\mathrm{GeV/c^2}$ and $\mathrm{M}(\overline{\Xi}\,(1820)^+)=1.8231\,\mathrm{GeV/c^2}$, as well as the determined width of the reconstructed resonances are consistent with the input values given in [1].

By comparing the two procedures used in the analyzes, it is shown that the reconstruction efficiency of the final selected sample is higher for the sequential fitting procedure while the corresponding purity is lower than the purity achieved with the full tree fit. Nevertheless, it has to be taken into account, that the first presented analysis is using MC information during the particles selection. Therefore, the achieved numbers are not directly comparable. Looking onto the evaluated resolutions and the quality of the selected events shows that the results for both analysis strategies are comparable. The discussion above leads to the conclusion that for the analysis of the shown reaction channel the full decay tree fitting procedure would be preferable.
The presented physics channel will be part of the so-called "phase one" physics program of $\overline{\mathrm{P}}$ANDA. For this phase the luminosity achieved at the HESR will be $\mathcal{L} = 1 \cdot 10^{31}\,\mathrm{cm^{-2}\,s^{-1}}$. With the assumed cross section of $1\mu\mathrm{b}$ for each of the considered final states $\overline{\Xi}^+\ \Lambda\ \mathrm{K}^-$ and $\Xi^-\ \bar{\Lambda}\ \mathrm{K}^+$ and the reconstruction efficiency of 5.4 % and 5.5 % one expects 38,500 events to be reconstructed per day of running. This

corresponds to about 15 days of data taking to collect data with the size of the reconstructed sample.

5.6 Summary

For the feasibility study of the reactions $\bar{p}p \rightarrow \overline{\Xi}^{+} \Lambda K^{-}$ and $\bar{p}p \rightarrow \Xi^{-} \bar{\Lambda} K^{+}$ two analysis strategies were presented. The first analysis was based on the sequential fit procedures so fare mostly used in $\overline{\text{P}}$ANDA analyzes, while the second analysis was based on a full decay tree fit, newly introduced in the PandaRoot framework. Two different data sets, containing 10 million generated events each, were analyzed. Both data sets are consisting of 50% $\overline{\Xi}^{+} \Lambda K^{-}$ and 50% $\Xi^{-} \bar{\Lambda} K^{+}$ events. A fraction of 80% resonance content and 20% continuum content is chosen. For both samples a beam momentum of $p_{\bar{p}} = 4.6\,\text{GeV/c}$, corresponding to a center-of-mass energy about 320 MeV above the $\overline{\Xi}^{+} \Lambda K^{-}$ and about 100 MeV above the $\overline{\Xi}^{+} \Xi(1820)^{-}$ production threshold has been chosen. Because the production is close to threshold, only lower partial waves contribute to the angular distribution. Since there are no theoretical predictions or experimental data available, an isotropic angular distribution was chosen. But the reconstruction efficiency for the angular distributions in the center-of-mass system can be deduced from, e.g. the reconstructed $\overline{\Xi}^{+}$ polar angle in the center-of-mass system.

For the analysis using the sequential fitting procedure, an ideal PID algorithm was used. This algorithm uses information which are based on the MC information of the final state particles. After the final state particle selection, a reconstruction efficiency between 61% and 87% is achieved depending on the particle species and their production point. The main analysis strategy is to reconstruct the composite state particle, namely Λ, $\bar{\Lambda}$, Ξ^{-} and $\overline{\Xi}^{+}$, by combining the daughter particles starting with the final state particles. Different fits, like a vertex fit and various kinematic fits, are performed on the reconstructed composite state particles to select the candidate with the highest probability for being part of the true signal. At the final stage of the analysis, all reconstructed candidates are combined to the $\overline{\Xi}^{+} \Lambda K^{-}$ state, and to the $\Xi^{-} \bar{\Lambda} K^{+}$ state in the charge conjugate case. A vertex fit is performed on the resulting candidates, to assure that all particles of the system are coming from the same origin. In the next step a kinematic fit with 4-momentum constraint is performed on the vertex fitted candidates to match to the initial four-momentum of the $\bar{p}p$ system. Candidates with a fit probability of less than 1% in both fits are rejected.
Since the results of this fit shows candidates which are passing the cut criteria but have momenta not matching the kinematically allowed region, an additional cut on the daughter masses has to be introduced. With this analysis strategy a reconstruction efficiency of about 8% for the $\overline{\Xi}^{+} \Lambda K^{-}$ and about 9% for the $\Xi^{-} \bar{\Lambda} K^{+}$ sample is achieved with a purity of 95.4%.
However, this analysis has revealed various problems in the fit routines of the PndKinFitter implemented in $\overline{\text{P}}$ANDA. Therefore, another analysis using a different fitting scheme is performed.

The second analysis uses a full decay tree fit procedure. This full decay tree fit is performed with the DecayTreeFitter implemented in PandaRoot. Different from the other analysis, no PID information is used for the selection of the final state particles. The achieved reconstruction efficiencies for those particles are between 68% and 89%. For the reconstruction of the composite state particles, again, the daughter particles are combined. In this analysis, only a cut on the mass window is applied to the selected candidates. This cut rejects those candidates which have a mass far from the nominal particle mass, so that the combinatorial background is reduced. After the coarse selection the composite particles are combined to the $\overline{\Xi}^{+} \Lambda K^{-}$ and $\Xi^{-} \bar{\Lambda} K^{+}$ system. To the resulting candidates the full decay tree fit is

performed. Candidates having a fit probability less than 0.01% are rejected. An additional cut on the fit status is applied to assure that the decay tree fit has converged for the final selected candidates. For the final sample a reconstruction efficiency of 5.4% for $\overline{\Xi}^{+}$ Λ K^{-} and 5.5% for Ξ^{-} $\bar{\Lambda}$ K^{+} is achieved. The purity of both samples is 97.7%.
According to the issues of the PndKinFitter used for the sequential fitting procedure and the promising results achieved with the DecayTreeFitter, the full decay tree fit would be preferred as procedure for the analysis of future $\overline{\text{P}}$ANDA data. Assuming the luminosity $\mathcal{L} = 1 \cdot 10^{31}\,\text{cm}^{-2}\,\text{s}^{-1}$ at phase one of the $\overline{\text{P}}$ANDA experiment and including the evaluated reconstruction efficiencies from the full decay tree fit, one expects about 38,500 reconstructed events per day. Therefore, a sample comparable in size to the reconstructed sample could be collected within 15 days of running.

For the study of the hadronic background the same algorithms were used, as for both analyzes. In both cases, out of 100 million generated background events no event survives the applied cuts. This non-observation of background events corresponds on the 90% confidence level to 2.3 events. Assuming a signal cross section of $\sigma_{\text{sig}} = 1\,\mu\text{b}$ and cross section of $\sigma_{\text{bg}} = 50\,\text{mb}$ for the background, a lower limit for the signal-to-background ratio and the signal significance can be estimated. Focusing on the analysis using the full decay tree fit, the signal-to-background ratio is estimated to be $S/B > 19.1$ for $\overline{\Xi}^{+}$ Λ K^{-} and $S/B > 19.5$ for Ξ^{-} $\bar{\Lambda}$ K^{+}. Taking the correct ratio between the cross sections into account, the lower limit for the signal significance is $S_{\text{sig}} > 513$ for $\overline{\Xi}^{+}$ Λ K^{-} and for Ξ^{-} $\bar{\Lambda}$ K^{+} to $S_{\text{sig}} > 507$.

The presented work demonstrates that the experimental study of the process $\bar{p}p \to \overline{\Xi}^{+}$ Λ K^{-} and $\bar{p}p \to \Xi^{-}$ $\bar{\Lambda}$ K^{+}, including also the production of resonant baryon states, is feasible with the $\overline{\text{P}}$ANDA detector. Since the decay tree includes six final state particles, the limiting factor on the efficiency of the reconstruction is the combined acceptance of those final state particles. However, the topology of the decay provides a significant background suppression. To reduce the model dependency, a second study of events generated with a different background generator, as well as the study of, e.g. the reaction $\bar{p}p \to \bar{p}\, p\, K^{-}\, K^{+}\, \pi^{+}\, \pi^{-}$, could be considered. But both studies are beyond the scope of the present work.

Since the tracking algorithms in $\overline{\text{P}}$ANDA are not suitable for displaced vertices, a future study could also include the effect of a more realistic tracking algorithm. As soon as realistic tracking algorithms, including also displaced vertices, are available this study should be redone. Since there are no experimental data or theoretical predictions to the angular distribution of the signal events available, this study assumed a uniform phase space distribution. But in the presented studies the reconstruction efficiency for the angular distribution of the $\overline{\Xi}^{+}$ in the center-of-mass frame could be determined. First investigations on the angular distributions by focusing only on specific resonances are presented in the following chapter. The analysis using the sequential fit procedure, shows critical issues for the kinematic fit algorithms implemented in PandaRoot. The origin of those issues is still not understood and needs some more investigations.

CHAPTER 6

Partial Wave Analysis

As discussed in Section 2.2.2, the excited states of Ξ baryons are not well investigated. Therefore, not much information is available on the quantum numbers of the resonance states.
The PWA is a toolkit to extract complex amplitudes of a certain process from experimental data to investigate the dynamics of the process. Figure 6.1 shows an example of a such a process. If the process is dominated by resonances, the PWA gives the possibility to determine the mass and width of the resonances as well as their spin and parity. In this thesis, the PArtial Wave Interactive ANalysis Sofware (PAWIAN) package [139] is used.

This chapter introduces the formalism and methods used in the PWA, and presents the first results on the possibility to determine the J^P quantum numbers for Ξ resonances produced in $\bar{\mathrm{p}}\mathrm{p}$ collisions.

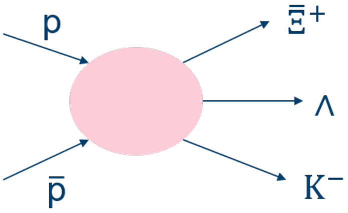

Figure 6.1: Schematic diagram of the process $\bar{\mathrm{p}}\mathrm{p} \rightarrow \bar{\Xi}^+ \Lambda \mathrm{K}^-$. The pink ellipse denotes the dynamics to be investigated.

6.1 Antiproton Proton Collisions

In general, there are two ways to study inelastic reactions in the $\bar{\mathrm{p}}\mathrm{p}$ entrance channel: the case where the $\bar{\mathrm{p}}\mathrm{p}$ system is at rest, meaning that the relative momentum of the $\bar{\mathrm{p}}\mathrm{p}$ system is zero, or the case where the $\bar{\mathrm{p}}\mathrm{p}$ system is "in-flight". Since in this thesis final states including a baryon-antibaryon pair are studied, the focus will be on the $\bar{\mathrm{p}}\mathrm{p}$ system "in-flight". For the process $\bar{\mathrm{p}}\mathrm{p} \rightarrow \bar{\Xi}^+ \Lambda \mathrm{K}^-$, the production of the final states require a center-of-mass energy of $\sqrt{s} \geq 2.93\,\mathrm{GeV}$, which corresponds to an antiproton momentum of $p_{\bar{\mathrm{p}}} \geq 3.5\,\mathrm{GeV/c}$. In the study presented in Chapter 5, an antiproton momentum of 4.6 GeV/c was chosen, which corresponds to a center-of-mass energy of $\sqrt{s} = 3.25\,\mathrm{GeV}$. Since the chosen beam momentum corresponds to a $\sqrt{s}$ that is about 300 MeV above the production threshold of the final state particles, the number of contributing angular momentum states increases. Furthermore, due to the higher

center-of-mass energy, one or more resonances with higher masses compared to their ground state can be produced.
The inelastic reaction of antiproton and proton is a strong process and therefore conserves all quantum numbers of the initial state. Here, the most important quantum numbers are the P, C, and G parity, which are related to the quantum numbers L,S and I as followed:

- $P = (-1) \cdot (-1)^L$
- $C = (-1)^{L+S}$
- $G = (-1)^{L+S+I}$

Here, for the P parity a fermion antifermion system is considered. By convention the parity of a fermion is $P = 1$ while an antifermion has parity $P = (-1)$. Therefore, the quark has positive parity while the antiquark has negative parity [1]. Since the parity is a multiplicative quantum number, the parity of a composite systems is derived from the product of all its constituents. For ground state ($L = 0$) baryons and antibaryons, this leads to $P_{\text{Baryon}} = 1^3 = 1$ and $P_{\text{antibaryon}} = (-1)^3 = -1$. The parity for baryon which are not in the ground state ($L > 0$) depends on the angular momentum and is given as $P = P_0 \cdot (-1)^L$, where P_0 is the parity of baryon or antibaryon in the ground state. The C parity is only defined for a particle or system which is its own antiparticle, meaning that particle and antiparticle are indistinguishable. The G parity is a generalization of the C parity which also includes the isospin partners of neutral unflavored mesons. The inelastic process of p̄p into three final state particles is illustrated in Figure 6.2. The shown scheme is indenpendent of whether the final state is purely mesonic [140] or x_1 and x_2 are baryon and antibaryon(c.c.). An empirical approach, called the isobar model, is used for the mathematical description of the process. It assumes that the final state is reached by a chain of subsequent two-body reaction, but without rescattering with any other particle. The spins of antiproton and proton which have an orbital angular momentum L, couple to a total spin of either $S = 0$ or $S = 1$. The z-component of the spin is $\lambda = \lambda_{\bar{p}} - \lambda_p$, where the flight direction is defined as the quantization axis. Since the isospin for both the proton and antiproton is 1/2, respectively, the isospin of the p̄p system is either 0 or 1.
Like it is shown in Figure 6.2, the antiproton and proton form an intermediate state with the quantum numbers J^{PC}, decaying subsequently into a resonance and a recoil particle. The resulting two-body system can be described by the production angles of the resonances, as well as the quantum numbers l and s. In a second step, the resonance decays again into two-body system with quantum numbers l' and s', and the corresponding production angles. In addition to the conservation of angular momentum,

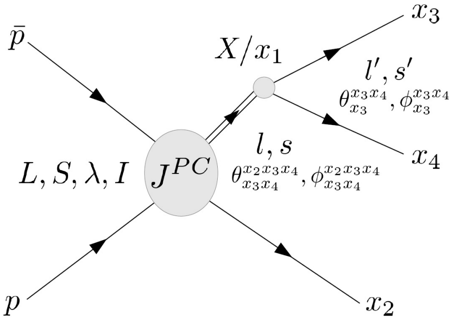

Figure 6.2: Illustration of the resonance production in the p̄p inelastic processes for the specific case that x_1 and x_2 are baryon and antibaryon. Here, the isobar model is used. Image from [140].

electromagnetic charge, and four-momentum, the isospin, as well as P, C, and G parity have to be conserved. Therefore, the initial states of the p̄p system are defining the basis for the description of the total amplitude.

6.1.1 Initial States

The possible quantum number combinations for the J^{PC} system can be calculated from the values of P and C parity, and using the law for the angular momentum coupling

$$J = L + S, L + S - 1, \dots, |L - S| \tag{6.1}$$

For the spin singlet ($S = 0$) Equation (6.1) leads to $J = L$, while for the spin triplet ($S = 1$) two different cases have to be taken into account. As mentioned before, the flight direction of the antiproton is equal to the quantization axis which implies that L is orthogonal to the z-direction, $L_z = 0$. Therefore, it is $J_z = \lambda$. Since the Clebsch-Gordon coefficient $\langle LL_z S\lambda | JJ_z\rangle = \langle J010|J0\rangle$ is vanishing, only two spin directions $\lambda = \pm 1$ are possible for the combination of $S = 1$ and $J = L$. In contrast, for $S = 1$ and $J = L \pm 1$, $\lambda = 0$ is also possible. Table 6.1 summarizes the p̄p initial states up to $J = 6$. P and C are the parity values for the p̄p system and are calculated as explained in the previous paragraph.

Table 6.1: Antiproton-proton initial states up to $J = 6$. The possible quantum numbers for the J^{PC} intermediate states are given in the form ${}^{(2S+1)}L_J$. Adopted from [140].

J	Singlet $\lambda = 0$	J^{PC}	Triplet $\lambda = \pm 1$	J^{PC} $\lambda = 0, \pm 1$	Triplet	J^{PC}
0	${}^1S_0$	0^{-+}			${}^3P_0$	0^{++}
1	${}^1P_1$	1^{+-}	${}^3P_1$	1^{++}	${}^3S_1, {}^3D_1$	1^{--}
2	${}^1D_2$	2^{-+}	${}^3D_2$	2^{--}	${}^3P_2, {}^3F_2$	2^{++}
3	${}^1F_3$	3^{+-}	${}^3F_3$	3^{++}	${}^3D_3, {}^3G_3$	3^{--}
4	${}^1G_4$	4^{-+}	${}^3G_4$	4^{--}	${}^3F_4, {}^3H_4$	4^{++}
5	${}^1H_5$	5^{+-}	${}^3H_5$	5^{++}	${}^3G_5, {}^3I_5$	5^{--}
6	${}^1I_6$	6^{-+}	${}^3I_6$	6^{--}	${}^3H_6, {}^3J_6$	6^{++}

For the description of the partial wave amplitude, the formation of the J^{PC} intermediate state has to be taken into account. Otherwise, the elements of the spin density matrices, described in Section 6.4, would not fulfill the required symmetry. With the helicity formalism (see Sec. 6.2), it is possible to include the J^{PC} states by splitting the possible LS combinations. The momentum of the antiproton defines the maximum value of the angular momentum $L_{\max}$ and therefore the number of contributing amplitudes. A good approximation for the $L_{\max}$ is given by truncating or rounding [141]:

$$L_{\max} \approx \frac{p_{\bar{p}}^{\mathrm{cms}}}{200\,\mathrm{MeV/c}}, \tag{6.2}$$

where $p_{\bar{p}}^{\mathrm{cms}}$ is the antiproton momentum in the center-of-mass frame.
Since endothermic reactions are investigated in this study, the maximum orbital angular momentum is determined by the mass of the final states.

6.1.2 Conservation of J^{PC}

Since the C parity is only defined for a particles which is its own antiparticle, for the production of a Ξ^- and $\overline{\Xi}^+$ pair in a p̄p reaction, all initial states with $C = \pm 1$ are possible. Due to the L dependence of the parity, both values $P = 1$ and $P = -1$ are possible for the baryon and antibaryon system. The conservation of parity and C parity leads to the fact, that the angular distributions for unpolarized antiproton beam and target proton need to show several symmetries.
In the following, the reaction $\bar{p}p \rightarrow 1 + 2 + R$ is considered, where 1 and 2 are two produced particles, and R is any assembly of particles. Due to the conservation of parity, for the intensity it is [142]:

$$W(1, E_1, \Theta_1; 2, E_2, \Theta_2, \phi) = W(1, E_1, \Theta_1; 2, E_2, \Theta_2, -\phi), \tag{6.3}$$

where E_i is the energy of particle i, Θ_i is the angle of particle i relative to the antiproton direction, and ϕ is the azimuth angle of particle 2 relative to the production plane defined by the antiproton and particle 1. The conservation of the C parity introduces an additional symmetry:

$$W(1, E_1, \Theta_1; 2, E_2, \Theta_2, \phi) = \bar{W}\left(\bar{1}, E_1, \pi - \Theta_1; \bar{2}, E_2, \pi - \Theta_2, \pi - \phi\right). \tag{6.4}$$

For the production of a resonance and a recoil particle in reactions like $\bar{p}p \rightarrow \bar{\Xi}^+\Xi^{*-}$ and $\bar{p}p \rightarrow \bar{\Xi}^{*+}\Xi^-$ (R means "‘zero particles"’ in the reaction type mentioned above) Equation (6.4) implies only a mirror symmetry. Applying CP to the final states results in

$$W(1, E_1, \Theta_1; 2, E_2, \Theta_2, \phi) = \bar{W}\left(\bar{1}, E_1, \pi - \Theta_1; \bar{2}, E_2, \pi - \Theta_2, \pi + \phi\right). \tag{6.5}$$

In case of a decaying particle in its rest frame, the conservation of parity leads to the relation [143]:

$$W(\Theta, \phi) = W(\pi - \Theta, \pi + \phi), \tag{6.6}$$

where Θ and ϕ are related to any quantization axis.

6.2 Helicity Formalism

Due to the transformation properties of the angular momentum states, the decay of particles with certain spin shows characteristic angular distributions. In order to describe the amplitudes of a reaction, which are depending on the production angle, various spin formalism are available [141]. There are three basic spin formalism types having different advantages and disadvantages. Since the helicity formalism is often used for spectroscopy experiments, the helicity formalism is used in this thesis. This formalism describes the particle according to its helicity and the particle spin is quantized parallel to the particle's direction of motion. The helicity of a particle is defined as $\lambda = \vec{S} \cdot \vec{p} / \left|\vec{p}\right|$.
In this section, an overview of the helicity formalism will be given. Therefore, only the most important equations are shown here. For further information, the reader can consult for example [143].

A particle at rest can be described by $\mid jm \rangle$ where j is the particle spin and m the spin projection to a given axis. A rotation around the Euler angles α, β and γ using the operator $\hat{R}$ leads to [144]:

$$\begin{aligned} \hat{R}\,(\alpha,\beta,\gamma) &= \sum_{m'} |\; jm' \;\rangle\, D^{j}_{m'm}\,(\alpha,\beta,\gamma) && (6.7) \\ &= \sum_{m'} |\; jm' \;\rangle\, e^{-in'\alpha} d^{j}_{m'm}\,(\beta)\, e^{-im\gamma} && (6.8) \end{aligned}$$

For the definition of $d^{j}_{m'm}$ the reader can consult [1]. The particle state with momentum $\vec{p}$ is obtained by applying a Lorentz transformation L_z to the particle at rest. This transformation includes two rotations. In the first step, the rest frame is rotated so that the z-axis is equal to the direction of the momentum $\vec{p}$. Subsequently, a Lorentz boost along the z-axis is applied. In the last step, the system is rotated to match the original orientation of the coordinate axes [143]:

$$|\; \vec{p}, jm \;\rangle = \hat{R}^{-1}\,(\phi,\Theta,0)\,\hat{L}_z\hat{R}\,(\phi,\Theta,0)\,|\; jm \;\rangle \tag{6.9}$$

In the helicity frame, the second rotation is not applied. Therefore, the quantization axis of the spin is parallel to the direction of the momentum.

$$|\; \vec{p}, \lambda m \;\rangle = \hat{L}_z\hat{R}\,(\phi,\Theta,0)\,|\; j\lambda \;\rangle \tag{6.10}$$

Since the quantization axis is parallel to the flight direction of the particle and the new obtained y-axis is directed perpendicular to the production plane $\vec{n} = \vec{z} \times \vec{p}$, λ is equal to the given definition of the helicity. In a two body decay of a particle, X → a + b, the state of the decay products a and b can be described by the direction of the decay axis and the corresponding helicities λ_a, λ_b ($|\; \phi\,\Theta\,\lambda_a\,\lambda_b\;\rangle$) or the quantum numbers l and s ($|\; \phi\,\Theta\, l\; s\;\rangle$). Since the decaying particle has spin J, the coupling of the decay products to the state with quantum numbers JM can be written as

$$\left\langle \phi\,\Theta\,\lambda'_a\lambda'_b | JM\lambda_a\lambda_b \right\rangle = \sqrt{\frac{2J+1}{4\pi}}\, D^{J*}_{M\lambda_{ab}}\,\delta_{\lambda'_a\lambda_a}\delta_{\lambda'_b\lambda_b}, \tag{6.11}$$

where $\lambda_{ab} = \lambda_a - \lambda_b$ [144]. According to [143], Equation (6.11) can be written in terms of the quantum numbers l and s as

$$\langle J'M'ls | JM\lambda_a\lambda_b \rangle = \sqrt{\frac{2l+1}{2J+1}}\,\langle l0s\lambda_{ab} | J\lambda_{ab} \rangle\,\langle s_a\lambda_a s_b - \lambda_b | s\lambda_{ab} \rangle\,\delta_{JJ'}\delta_{MM'}. \tag{6.12}$$

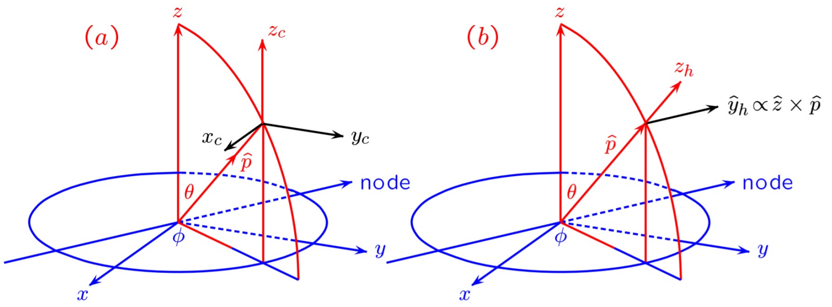

Figure 6.3: Definition of angles in the (a) canonical and (b) helicity formalism. Image from [143].

Here, s_a and s_b denote the spin of the particles a and b, respectively. The normalization of the relations is given by:

$$\begin{aligned}\sum_{JM\lambda_a\lambda_b} \mid JM\lambda_a\lambda_b \,\rangle\langle\, JM\lambda_a\lambda_b \mid &= I &\quad (6.13)\\ \sum_{JMls} \mid JMls \,\rangle\langle\, JMls \mid &= I &\quad (6.14)\end{aligned}$$

In the next step, the helicity amplitude will be deduced. Therefore, the reaction $a + b \rightarrow c + d$ is considered. If particle a is moving along the z-axis of the center-of-mass system, the invariant transition amplitude can be written as

$$\mathcal{M} = (4\pi)^2 \sqrt{\frac{s}{p_c p_a}} \left\langle \phi\,\Theta\,\lambda_c\lambda_d \left| \hat{T} \right| 00\lambda_a\lambda_b \right\rangle \tag{6.15}$$

where $\hat{T}$ is the transition operator, $\sqrt{s}$ the center-of-mass energy, and p the particle momentum [143]. Since the quantum numbers J^{PC} have to be conserved, the amplitude has to be expanded according to $JMLSls$. Therefore, $\mid JM\lambda_a\lambda_b\,\rangle$ and $\mid JM\lambda_c\lambda_d\,\rangle$ are fully included and Equation (6.11) is applied to $\left\langle \phi\,\Theta\,\lambda_c\lambda_d \left| \hat{T} \right| 00\lambda_a\lambda_b \right\rangle$ which leads to:

$$\begin{aligned}\left\langle \phi\,\Theta\,\lambda_c\lambda_d \left| \hat{T} \right| 00\lambda_a\lambda_b \right\rangle &= \langle \phi\,\Theta\,\lambda_c\lambda_d | JM\lambda_c\lambda_d \rangle \left\langle JM\lambda_c\lambda_d \left| \hat{T}^J \right| JM\lambda_a\lambda_b \right\rangle \langle JM\lambda_a\lambda_b | 00\lambda_a\lambda_b \rangle\\ &= \frac{1}{4\pi} \sum_J (2J+1) \left\langle \lambda_c\lambda_d \left| \hat{T}^J \right| \lambda_a\lambda_b \right\rangle D^{J*}_{\lambda_{ab}\lambda_{cd}}(\phi, \Theta, 0)\,. \end{aligned}\tag{6.16}$$

For the second line of Equation (6.16) the relation $D^{J*}_{\lambda\lambda'} = \sum_M D^{J*}_{M\lambda}(R')\, D^{J*}_{M\lambda'}(R'')$ [140] is used. In the next step, $\mid JMls\,\rangle$ and $\mid JMLS\,\rangle$ are included and Equation (6.12) is applied, which leads to:

$$\begin{aligned}\left\langle \lambda_c\lambda_d \left| \hat{T}^J \right| \lambda_a\lambda_b \right\rangle = &\sum_{ls} \sqrt{\frac{2l+1}{2J+1}} \langle l0\lambda_{cd} | J\lambda_{cd} \rangle \langle s_c\lambda_c s_d - \lambda_d | s\lambda_{cd} \rangle\\ &\times \sum_{LS} \sqrt{\frac{2L+1}{2J+1}} \langle L0S\,\lambda_{ab} | J\lambda_{ab} \rangle \langle s_a\lambda_a s_b - \lambda_b | S\,\lambda_{ab} \rangle\\ &\times \left\langle JMls \left| \hat{T}^J \right| JMLS \right\rangle. \end{aligned}\tag{6.17}$$

$\left\langle JMls \left| \hat{T}^J \right| JMLS \right\rangle$ is the partial wave amplitude and contains free parameters, which have to be fitted. The amplitude of a resonance which decays according to $X_J \rightarrow$ a + b is given in analogy to Equations (6.15) and (6.16) [143]:

$$\begin{aligned}\mathcal{A} &= 4\pi \sqrt{\frac{s}{p}} \langle \phi\,\Theta\,\lambda_a\lambda_b \,|\mathcal{M}|\, JM \rangle &\quad (6.18)\\ &= 4\pi \sqrt{\frac{s}{p}} \langle \phi\,\Theta\,\lambda_a\lambda_b | JM\lambda_a\lambda_b \rangle \langle JM\lambda_a\lambda_b \,|\mathcal{M}|\, JM \rangle &\quad (6.19)\\ &= \sqrt{\frac{2J+1}{4\pi}} F^J_{\lambda_a\lambda_b} D^{J*}_{M\lambda_{ab}}(\phi, \Theta, 0) &\quad (6.20)\end{aligned}$$

where $F^J_{\lambda_a\lambda_b}$ is the helicity amplitude given as

$$F^J_{\lambda_a\lambda_b} = 4\pi\sqrt{\frac{s}{p}}\,\langle JM\lambda_a\lambda_b\,|\mathcal{M}|\,JM\rangle\,. \tag{6.21}$$

Rewriting Equation (6.21) in the ls basis leads to

$$F^J_{\lambda_a\lambda_b} = \sum_{ls}\sqrt{\frac{2l+1}{2J+1}}\alpha^J_{ls}\,\langle l0s\lambda_{ab}|J\lambda_{ab}\rangle\,\langle s_a\lambda_a s_b-\lambda_b|s\lambda_{ab}\rangle\,. \tag{6.22}$$

where

$$\alpha^J_{ls} = 4\pi\sqrt{\frac{s}{p}}\,\langle JM\lambda_a\lambda_b\,|\mathcal{M}|\,JM\rangle \tag{6.23}$$

is the partial wave amplitude.

For the fit of the amplitudes a weighting function w is needed. This weighting function can be developed in the same way as the helicity amplitude. The weighting function w is proportional to the cross section with the difference that w has no description of the phase space.
The helicities of the antiproton and proton are included into the weighting function as incoherent sum. Here, an alternative description of w according to [145] is chosen, including also λ and S in the incoherent sum.

$$w = \left|\sum A^{S=0}_{\lambda=0}\right|^2 + \left|\sum A^{S=1}_{\lambda=0}\right|^2 + \left|\sum A^{S=1}_{\lambda=-1}\right|^2 + \left|\sum A^{S=1}_{\lambda=1}\right|^2 \tag{6.24}$$

For a consistent notation, the previous used nomenclature is chosen for the description of w. Equation (6.24) includes already the results of the Clebsch-Gordan coupling for the p̄p system. Beside the production p̄p → X^J $(= a)$ + b and the decay of the resonance X^J → c + d, described by Equations (6.15) to (6.22), for the weighting function additional factors are needed which are [140]:

- sum over all resonances and p̄p isospins
- sum over all helicities
- Clebsch-Gordon couplings for all isospins
- a factorization of $\left\langle JMls\left|\hat{T}^J\right|JMLS\right\rangle$ in a resonance independet part $\alpha^{J^{PC}}_{LS}$ and a production part α^X_{ls}
- the barrier factor B_l for the production and a dynamic function F_l, e.g. a Breit-Wiegner parameterization, which is depending l'

This leads to the expression [140]:

$$
\begin{aligned}
w = \sum_{S\lambda} \Bigg| & 4\pi \sum_{J^{PC}} (2J+1) \sum_{L} \sqrt{\frac{2L+1}{2J+1}} \alpha_{LS}^{J^{PC}} \langle L0S\lambda | J\lambda \rangle \sum_{X} \sum_{I} i_{0/1}(I) \\
& \times \langle I_a I_{az} I_b I_{bz} | I0 \rangle \sum_{\lambda_a} \sum_{\lambda_b} D^{J*}_{\lambda,\lambda_a b}(\phi,\Theta,0) \left(\sum_{ls} \sqrt{\frac{2l+1}{2J+1}} \alpha^{X}_{ls} B_l\left(\sqrt{s}, m_a, m_b\right) \right. \\
& \times \langle l0s\lambda_{ab} | J\lambda_{ab} \rangle \langle s_a \lambda_a s_b - \lambda_b | s\lambda_{ab} \rangle) \\
& \times \langle I_c I_{cz} I_d I_{dz} | I_a I_a z \rangle \sqrt{4\pi(2s_a+1)} \sum_{\lambda_c} \sum_{\lambda_d} D^{s_a *}_{\lambda_a,\lambda_{cd}}(\phi',\Theta',0) \\
& \times \left(\sum_{l's'} \sqrt{\frac{2l'+1}{2s_a+1}} \alpha^{s_a}_{l's'} F_{l'}(m_a, m_c, m_d) \langle l'0s'\lambda_{cd} | s_a, \lambda_{cd} \rangle \langle s_c \lambda_c s_4 - \lambda_4 | s' \lambda_{cd} \rangle \right) \Bigg|^2 .
\end{aligned}
\tag{6.25}
$$

6.3 Barrier Factors

In the following, the decay of a resonance with mass M into particles with mass m_1 and m_1, respectively, is considered. In a two body decay the transferred momentum is given by [1]

$$
q = \frac{\sqrt{\left[M^2 - (m_1 + m_2)^2\right]\left[m^2 - (m_1 - m_2)^2\right]}}{2M}. \tag{6.26}
$$

In analogy to L_{max} in Section 6.1, the maximum value for the orbital angular momentum in the decay is defined by the transferred momentum. If the sum mass of the decay products $m_1 + m_2$ is only little smaller than the resonance mass M, high orbital angular momenta are not contributing in the decay of the resonance. The phase space dependence is accounted by the *barrier factors* [141]

$$
F_l(q) = F_l\left(x = \frac{q}{q_{\text{scale}}}\right) = \sqrt{\frac{\left|h_l^{(1)}(1)\right|^2}{x^2 \left|h_l^{(1)}(x)\right|^2}}, \tag{6.27}
$$

where q is the momentum of the daughter particles in the center-of-mass frame at any mass of the parent resonance. $h_l^{(1)}$ is the spherical Hankel function of the first order. The dimension of the variable q_{scale} is that of a momentum. q_{scale} is depending on a certain interaction radius R. For decays of light mesons, for example, commonly a value of $q_{\text{scale}} \approx 200\,\text{MeV/c}$ or $R \approx 1\,\text{fm}$ is used [140]. Further, Equation (6.27) is normalized by

$$
F_l(q) \underset{q \to q_{\text{scale}}}{\longrightarrow} 1. \tag{6.28}
$$

For $l = 0, 1$ the barrier factor is written as

$$
F_0(z) = 1 \tag{6.29}
$$

$$
F_1(z) = \sqrt{\frac{2z}{z+1}}, \tag{6.30}
$$

where the substitution $z = x^2$ is used. An additional normalization is applied to the nominal mass of the resonance by

$$B_l(q, q_R) = \frac{F_l(q)}{F_l(q_R)} \tag{6.31}$$

where q_R is the momentum of each of the daughter particles in the rest frame of the resonance. The barrier factors have two effects on the cross section: for low invariant masses they cause a distortion in the line shape of the decay amplitude of the resonance and for high invariant masses a distortion of the decay amplitude of the parent p̄p state depending on its J^{PC} quantum numbers.

6.4 Spin Density Matrix

6.4.1 Density Matrices

In general, a quantum mechanical state $|\,\Psi\,\rangle$ is described in terms of the eigenvectors $|\,\phi_i\,\rangle$ as

$$|\,\Psi\,\rangle = \sum_i c_i\,|\,\phi_i\,\rangle \tag{6.32}$$

where $c_i = \langle\phi_i|\Psi\rangle$ are the expansion coefficients for which applies $\sum_i |c_i|^2 = 1$. The eigenstates are required to be orthogonal and complete, implying the relations

$$\left\langle\phi_i|\phi_j\right\rangle = \delta_{ij} \text{ and } \quad \sum_i |\,\phi_i\,\rangle\langle\,\phi_i\,| = I. \tag{6.33}$$

For an ensemble of these *pure* states, it is possible to find a common basis, so that a measurement of this ensemble always results in the same eigenstate. Nevertheless, there are quantum mechanical systems which cannot be described by the pure states. The states describing such systems are called *mixed* quantum states. These mixed states cannot be represented by Equation (6.32), but by an incoherent superposition of pure states [146]. A mixed state can be described by the density operator ρ [146, 147]:

$$\rho = \sum_n W_n\,|\,\Psi_n\,\rangle\langle\,\Psi_n\,| = \sum_{nm'm} W_n a_{m'}^{(n)} a_m^{(n)*}\,|\,\phi_{m'}\,\rangle\langle\,\phi_m\,| \tag{6.34}$$

where W_n are the statistical weights. The spin density matrix can be then defined as

$$\rho_{ij} = \left\langle\phi_i\,|\rho|\,\phi_j\right\rangle = \sum_n W_n a_i^{(n)} a_j^{(n)*} \tag{6.35}$$

with the following properties:

- ρ is hermitian: $\rho_{ij} = \rho_{ij}^*$,
- positive semidefinite: $\rho_{ij} \geq 0$ and
- the trace of ρ is equal to one: $tr(\rho) = 1$.

The expectation value of an operator Q is given by

$$\langle Q\rangle = tr(\rho Q)\,. \tag{6.36}$$

This implies, that a certain diagonal element of the spin density matrix corresponds to the probability to measure a specific eigenstate.

6.4.2 Properties of the Spin Density Matrix

In p̄p annihilations where the beam and target particles are unpolarized, it is not possible to describe the spin distribution for the ensemble of produced resonances by a pure state. For this reason, a Spin Density Matrix (SDM) ρ is used for each kind of particle with a certain spin. The SDM is a complex $n \times n$ matrix with $n = 2J + 1$ for a given particle spin J. Which values and symmetries the matrix values have depends on the chosen quantization axis. Since this thesis focuses in the helicity frame, the SDM is given in helicity frame of the resonances.
Due to parity conservation in the production process of the resonance, the matrix elements fulfill the symmetry condition [148]:

$$\rho_{\lambda_1\lambda_1'} = (-1)^{\lambda_1\lambda_1'}\rho_{-\lambda_1\lambda_1'} \tag{6.37}$$

Therefore, the matrix elements for $S = 0, \frac{1}{2}, 1$ and $\frac{3}{2}$ have the form

$$S = 0: \quad \rho = 1 \tag{6.38}$$

$$S = \frac{1}{2}: \quad \rho = \begin{pmatrix} \Re\rho_{1/21/2} & \Im\rho_{1/2-1/2} \\ -\Im\rho_{1/2-1/2} & \Re\rho_{1/21/2} \end{pmatrix} \tag{6.39}$$

$$S = 1: \quad \rho = \begin{pmatrix} \Re\rho_{11} & \rho_{10} & \rho_{1-1} \\ \rho^*_{10} & \Re\rho_{00} & -\rho^*_{10} \\ \Re\rho_{1-1} & -\rho_{10} & \Re\rho_{11} \end{pmatrix} \tag{6.40}$$

$$S = \frac{3}{2}: \quad \rho = \begin{pmatrix} \Re\rho_{3/23/2} & \rho_{3/21/2} & \rho_{3/2-1/2} & \Im\rho_{3/2-3/2} \\ \rho^*_{3/21/2} & \Re\rho_{1/21/2} & \Im\rho_{1/2-1/2} & \rho^*_{3/2-1/2} \\ \rho^*_{3/2-1/2} & -\Im\rho_{1/2-1/2} & \Re\rho_{1/21/2} & -\rho^*_{3/21/2} \\ \Im\rho_{3/2-3/2} & \rho_{3/2-1/2} & -\rho_{3/21/2} & \Re\rho_{3/23/2} \end{pmatrix} \tag{6.41}$$

Since the trace of the SDM has to be one, it is

$$S = \frac{1}{2}: \quad 2\Re\rho_{1/21/2} = 1$$

$$S = 1: \quad 2\Re\rho_{11} + \Re\rho_{00} = 1 \Rightarrow \Re\rho_{11} = \frac{1}{2}\cdot(1 - \Re\rho_{00})$$

$$S = \frac{3}{2}: \quad 2\Re\rho_{3/23/2} + 2\Re\rho_{1/21/2} = 1 \Rightarrow \Re\rho_{1/21/2} = \frac{1}{2} - \Re\rho_{3/23/2}$$

Therefore, the number of independent parameters is 1 for $S = \frac{1}{2}$, 4 for $S = 1$, and 8 for $S = \frac{3}{2}$. Often, only the diagonal elements of the SDM are needed to determine J^P from the measured angular distribution. This reduces the number of independent parameters to 1 for $S = 1$ and $S = \frac{3}{2}$. Parity conservation leads to an additional restriction due to the symmetry relation of the helicity amplitude of $J^P \to \mathrm{a} + \mathrm{b}$ [143]:

$$F^J_{\lambda_a\lambda_b} = PP_aP_b\,(-1)^{J-s_a-s_b}\,F^J_{-\lambda_a-\lambda_b}. \tag{6.42}$$

The differential cross section of a reaction a+b → c + X with X → e + f can be expressed in terms of the SDM. According to [143] and [149], the intensity distribution $W^J(\theta,\phi)$ is obtained by integrating over all variables, except the decay angles of the resonance in its center-of-mass system. The intensity distribution is written as

$$W^J(\theta,\phi) = \left(\frac{2J+1}{4\pi}\right)\sum_{\lambda\lambda'\lambda_e\lambda_f}\mathcal{D}^J_{\lambda\lambda_{ef}}(\phi,\theta,-\phi)^*\,\rho_{\lambda\lambda'}\mathcal{D}^J_{\lambda\lambda_{ef}}(\phi,\theta,-\phi)\,g^J_{\lambda_e\lambda_f}, \tag{6.43}$$

with SDM ρ of the resonance X. $g^J_{\lambda_e\lambda_f}$ is defined as [143]:

$$g^J_{\lambda_e\lambda_f} \approx \int dmK\left(m\right)\left|F^J_{\lambda_e\lambda_f}\right|^2 \tag{6.44}$$

where $K\left(m\right)$ is the mass-dependent part of the cross section. Since this thesis focuses on the $\Xi\left(1690\right)^-$ and $\Xi\left(1820\right)^-$, both resonances decaying into Λ K^-, the intensity distributions for spin $S = 1/2$ and $S = 3/2$ particles are shown in the following. Starting with the intensity distribution for a resonance with $S = 1/2$ decaying into an $S = 1/2$ and an $S = 0$ particle [150]:

$$W^{J=1/2}\left(\theta,\phi\right) \propto \frac{1}{2\pi}\left\{\rho_{1/2\,1/2} - \Im\rho_{1/2\,-1/2}\sin\theta\sin\phi\right\} \tag{6.45}$$

where C is a constant value. With the trace condition $2\rho_{1/2\,1/2} = 1$, Equation (6.45) can be written as

$$W^{J=1/2}\left(\theta,\phi\right) \propto \frac{1}{4\pi}\left\{1 - 2\Im\rho_{1/2\,-1/2}\sin\theta\sin\phi\right\}. \tag{6.46}$$

For a resonance with $S = 3/2$ decaying into a $S = 1/2$ and a $S = 0$ particle, the intensity distribution is [149]:

$$\begin{aligned} W^{J=3/2}\left(\theta,\phi\right) \propto \frac{1}{\pi}\Bigg\{&\rho_{3/2\,3/2}\sin^2\theta + \left(\frac{1}{2} - \rho_{3/2\,3/2}\right)\left(\frac{1}{3} + \cos^2\theta\right) - \frac{2}{\sqrt{3}}\Re\rho_{3/2\,-1/2}\sin^2\theta\cos 2\phi \\ &- \frac{2}{\sqrt{3}}\Re\rho_{3/2\,1/2}\sin 2\theta\cos\phi\Bigg\}. \end{aligned} \tag{6.47}$$

Integration over ϕ gives then:

$$W^{J=1/2}\left(\cos\theta\right) = \frac{1}{2}\rho_{1/2\,1/2} \tag{6.48}$$

$$W^{J=3/2}\left(\cos\theta\right) = \rho_{3/2\,3/2}\sin^2\theta + \left(\frac{1}{2} - \rho_{3/2\,3/2}\right)\left(\frac{1}{3} + \cos^2\theta\right) \tag{6.49}$$

In case of a resonance with $S = 3/2$ the fit will give access to only three of the eight free parameters.

6.5 Methods

Beside the formulation of the cross section and the amplitudes, the partial wave analysis also includes several mathematical approaches, like the minimization of a likelihood function. In addition, statistical approaches like error calculations as well as the visualization of the results are needed. In this subsection, an overview on those methods is given.

Likelihood Function

A typical optimization procedure is a fit to measured data by the variation of free parameters. The most common method is the *least square method*. In the least square method, the sum of the squared residuals – the difference between the measured data and the fit – is minimized, taking into account their errors. Since the description of frequency distributions requires that events are binned, meaning that the entries have to be filled in discrete cells, the least square method is not applicable in partial waves analyzes. Therefore, a method called maximum-likelihood method, is used in which the fit function is a normalized probability distribution assigning a probability p_i to each event. Subsequently, the product of all probabilities

$$\mathcal{L} = \prod_i p_i \tag{6.50}$$

is maximized. Since neither the phase space factor nor the reconstruction efficiency are included in the weighting function w, they must be taken into account in the likelihood function. The function used in the PAWIAN is [140]:

$$\mathcal{L} \propto N! \cdot \exp\left[-\frac{(N-\theta)^2}{2N}\right] \cdot \prod_{i=1}^{N} \frac{w\left(\vec{r}_i, \vec{\alpha}\right)}{\int w\left(\vec{r}, \vec{\alpha}\right) \rho\left(\vec{r}\right) \epsilon\left(\vec{r}\right) d\vec{r}}, \tag{6.51}$$

where N is the number of events, θ the normalization, $\vec{r}$ the phase space coordinates, i.e. invariant masses and decay angles, $\vec{\alpha}$ the fit parameters, $w\left(\vec{r}, \vec{\alpha}\right)$ the weighting function which has to be fitted, $\epsilon\left(\vec{r}\right)$ the reconstruction efficiency including detector acceptance, and $\rho\left(\vec{r}\right)$ the phase space factor. The normalization is given by

$$\theta = N \cdot \frac{\int w\left(\vec{r}, \vec{\alpha}\right) \rho\left(\vec{r}\right) \epsilon\left(\vec{r}\right) d\vec{r}}{\int \rho\left(\vec{r}\right) \epsilon\left(\vec{r}\right) d\vec{r}} = N \cdot \bar{w} \tag{6.52}$$

and leads in combination with the exponential function in Equation (6.51) to an average weight of $\bar{w} = 1$ after the maximization. Often, the parameterization of ρ and ϵ is not trivial. Therefore, Equation (6.52) is obtained by the number of generated and reconstructed events which are phase space distributed, also called Monte-Carlo-Integration [140]. This leads to:

$$\theta \approx \frac{N}{M_{\text{reco}}} \sum_{j=1}^{M_{\text{reco}}} w_j. \tag{6.53}$$

A similar approximation can be done for the likelihood function in Equation (6.51). Here, the substitutions

$$w\left(\vec{r}_i, \vec{\alpha}\right) \rightarrow Q_i \cdot w\left(\vec{r}_i, \vec{\alpha}\right) \tag{6.54}$$

$$N \rightarrow \sum_{i=1}^{N} Q_i \tag{6.55}$$

can be used, which keeps the weighting of the events.

In the following the logarithm is applied to Equation (6.51) to avoid problems in the calculation of the product for large numbers. In order to use the standard minimization algorithms, in addition, a negative sign is introduced. This leads to the Negative Log-Likelihood function (NLL) used in PAWIAN:

$$\begin{aligned} NLL = l \ln \mathcal{L} = &- \sum_{i=1}^{N} \ln\left(w\left(\vec{r}_i, \vec{\alpha}\right) \cdot Q_i\right) \\ &+ \left(\sum_{i=1}^{N} Q_i\right) \cdot \ln\left(\frac{\sum_{j=1}^{M_{\text{reco}}} w\left(\vec{r}_j, \vec{\alpha}\right)}{M_{\text{reco}}}\right) \\ &\frac{1}{2} \cdot \left(\sum_{i=1}^{N} Q_i\right) \cdot \left(\frac{\sum_{j=1}^{M_{\text{reco}}} w\left(\vec{r}_j, \vec{\alpha}\right)}{M_{\text{reco}}} - 1\right)^2 . \end{aligned} \tag{6.56}$$

Here, additive constants are neglected, since they do not affect the minimization.

Minimization

PAWIAN makes use of the minimization software package MINUIT2, which is a newer version of MINUIT [151]. The MIGRAD algorithm used in MINUIT2 is based on the method developed by Fletcher and Powell [152]. This method is based on the Newton method and is intended to determine iteratively the local minimum of a function $f(x_1, x_2, \ldots, x_n)$ of various variables $\vec{x} = (x_1, \ldots, x_n)$. In each step of iteration the gradient $g_i(x_i) = \delta f / \delta x_i$ has to be fully determined. This is not the case for the Hesse-Matrix $G_{ij} = \delta^2 f / \delta x_i \delta x_j$ nor the covariance matrix $H = G^{-1}$. In a first step an approximation or even the identity matrix is is chosen as matrix H which is modified after each iteration. In each iteration, a line search along the direction

$$| s^i \rangle = -H^i \, | g^i \rangle \tag{6.57}$$

is performed to obtain a α^i that minimizes the function $F\left(| x^i \rangle + \alpha^i \, | s^i \rangle\right)$. At the end of each iteration a case differentiation is done and H is corrected according to [153]:

$$H^{i+1} = H^i + \frac{| \delta^i \rangle \langle \delta^i |}{\langle \delta^i | \gamma^i \rangle} - \frac{H^i \, | \gamma^i \rangle \langle \gamma^i | \, H^i}{\left\langle \gamma^i \left| H^i \right| \gamma^i \right\rangle} \qquad \text{or} \tag{6.58}$$

$$H^{i+1} = \left(1 - \frac{| \delta^i \rangle \langle \gamma^i |}{\langle \delta^i | \gamma^i \rangle}\right) H^i \left(1 - \frac{| \gamma^i \rangle \langle \delta^i |}{\langle \gamma^i | \delta^i \rangle}\right) + \frac{| \delta^i \rangle \langle \delta^i |}{\langle \delta^i | \gamma^i \rangle}, \tag{6.59}$$

where $| \delta^i \rangle = \alpha \, | s \rangle$ and $| \gamma^i \rangle = g^i\left(| x^i \rangle + | \delta^i \rangle\right) - g^i\left(| x^i \rangle\right)$. The Hesse-Matrix H should then converge to the correct error matrix [151]. If the Estimated Distance to Minimum (EDM) is smaller than a certain threshold value $\text{EDM} = || \, s^i \rangle|$, the minimization is stopped. In that case, the full Hesse-Matrix is calculated and the algorithm checks the break condition again to decide if the fit has converged or not.

Selection Criteria

To determine the cross section, the contributing resonances, production and decay amplitudes must be specified. Beside these physically relevant contributions, also an unphysical extension of a model will lead to a better fit result. Therefore, it is necessary to compare the consistency of the data and the fit with the complexity of the used model. Several techniques which can be used to determine the contributions to the cross section. Since the information criteria Akaike information criterion (AIC) and Bayesian information criterion (BIC) are used in this thesis, this paragraph focuses on these two criteria, while only a short overview on the other criteria is given.

The AIC [154] is based on the Kullback-Leibler (KL) divergence

$$I(f, g) = \int f(x) \ln\left(\frac{f(x)}{g\left(x|\vec{\theta}\right)}\right) dx. \tag{6.60}$$

It describes the information lost, if model g is used as an approximation of model f. In general, f is unknown so that $I(f, g)$ cannot be used directly. But it is possible to determine a relative KL divergence for different g which lead to

$$\text{AIC} = -2 \ln\left(\mathcal{L}\left(\vec{\theta}|\vec{y}\right)\right) + 2K \tag{6.61}$$

where $\mathcal{L}$ is the maximized likelihood and K the number of free parameters. This definition implies, that the model with the smallest AIC value is preferred. The AIC is meant for a high number of data points n with respect to K. If n is small compared to K, a corrected criterion

$$\mathrm{AIC}_c = \mathrm{AIC} + \frac{2K\,(K+1)}{n-K-1} \tag{6.62}$$

should be used. Since individual AIC are not interpretable, because they contain arbitrary constants, it is better to rescale the AIC to [154]

$$\Delta_i = \mathrm{AIC}_i - \mathrm{AIC}_{\mathrm{min}} \tag{6.63}$$

to compare or rank the candidate hypotheses or models. According to this rescaling, the preferred model has $\Delta = 0$, while all other models will have positive values. In order to assess the relative merit the following rules are often used [154]:

- $\Delta_i \leq 2$: model is supported
- $4 \leq \Delta_i \leq 7$: model has less support
- $\Delta_i > 10$: model is not supported

Another model selection criterion is the BIC, developed by Schwarz *et al.* [155]. It is based on the likelihood function and closely related to the AIC:

$$\mathrm{BIC} = -2\ln(\mathcal{L}) + K\log(n)\,. \tag{6.64}$$

After the BIC for each model is calculated, the model with the smallest BIC value is chosen as the most preferable. Analogue to Equation (6.63), the difference between the smallest BIC value to all other values is defined as

$$\Delta_i^{\mathrm{BIC}} = \mathrm{BIC}_i - \mathrm{BIC}_{\mathrm{min}}. \tag{6.65}$$

With this difference, it is possible to define a posterior model probability

$$p_i = \frac{\exp\left(\frac{1}{2}\Delta_i^{\mathrm{BIC}}\right)}{\sum_{r=1}^{R}\exp\left(-\frac{1}{2}\Delta_r^{\mathrm{BIC}}\right)} \tag{6.66}$$

assuming the prior model probabilities to be all $1/R$ [156]. A high probability does not necessarily mean, that the corresponding model is the true model. The Bayesian posterior model probability is rather a inferred probability for the quasi-true model in the set of models [154]. Since the BIC is asymptotically consistent, for an infinite number of data points, the true model will be selected by the criterion, if the true model is included in the set of models.

The sole use of the BIC leads to underfitting, while the sole application of the AIC leads to overfitting. This means, that the addition of free parameters has more impact on the BIC value than on the AIC value. Therefore, for the model selection, there are two scenarios. If AIC and BIC have the same trend for the compared models, the better hypothesis can be selected directly. In some cases, the trends for AIC and BIC are different. For example, assuming two models A and B, it may happen that model A will be preferred by the BIC, whereas the AIC would prefer model B. In this case, good experiences has been made with a model selection based on the sum of AIC and BIC [157]. Here, the model with the smallest value for $S_i = \mathrm{AIC}_i + \mathrm{BIC}_i$ is preferred.

One of the most commonly used hypothesis tests in particle physics is the Likelihood Ratio Test (LRT). It compares the goodness of fit of two statistical models: the null hypothesis against an alternative hypothesis. For this purpose, the ratio of the likelihood of both models is calculated, which provides a measure of how many times a model is more likely than the other. Since the LRT requires a model to be nested this hypothesis test is not used in this thesis. Assuming two models 1 and 2, then model 1 is nested in model 2 if the parameters of model 1 are a subset of the parameters of model 2.
Other methods to compare and select models are the *Minimum Description Length*, the *cross-validation*, and the bayesian model selection as well as various techniques based on the AIC, like the QAIC. Most of these methods need a high amount of computing power.

6.6 Determination of J^P for $\Xi\,(1690)^-$ and $\Xi\,(1820)^-$

According to the analyzes presented in Section 5.3, first steps toward the PWA of $\overline{\Xi}^+\ \Lambda\ K^-$ as final state of the strong interaction are presented in this section. Beside the investigation on $\bar{p}p \to \overline{\Xi}^+\ \Lambda\ K^-$ including one of the Ξ resonances, $\Xi\,(1690)^-$ or $\Xi\,(1820)^-$, data samples containing also a so-called crossed channel are investigated. Crossed channel means, that an additional reaction channel is included which contains a $\bar{\Lambda}$ resonance decaying into $\overline{\Xi}^+\ K^-$ meaning that the reaction path is $\bar{p}p \to \bar{\Lambda}\ \Lambda$.

6.6.1 Event Generation

PAWIAN gives the possibility to generate events based on a user-defined decay model or on fit results obtained with real data. The former method is used to generate events for the reaction $\bar{p}p \to \overline{\Xi}^+\ \Lambda\ K^-$. As for the generated samples in Section 5.2, a beam momentum of $p_{\bar{p}} = 4.6\,\text{GeV/c}$ is chosen. As already mentioned in Section 6.1.1, the number of contributing amplitudes depends on the number of contributing orbital angular momentum states L_{max} which depends on the beam momentum in the center-of-mass frame. According to Equation (6.2), a beam momentum of $p_{\bar{p}} = 4.6\,\text{GeV/c}$ corresponds to $L_{\text{max}} = 6$. But as already discussed, in the case of an endothermic reaction with a baryon antibaryon pair in the final state L_{max} is determined by the final state. The chosen beam momentum corresponds to a center-of-mass energy of $\sqrt{s} = 3.25\,\text{GeV}$. This leads to a momentum in the center-of-mass frame of $p_{\text{cm}} \approx 600\,\text{MeV/c}$ for $\Xi\,(1690)^-$ and of $p_{\text{cm}} \approx 410\,\text{MeV/c}$ for $\Xi\,(1820)^-$. Therefore, the maximum orbital angular momentum is $L_{\text{max}} = 3$ for $\Xi\,(1690)^-$ and $L_{\text{max}} = 2$ for $\Xi\,(1690)^-$. Higher L_{max} values as well as the generation and fit of high statistic samples need a high amount of computing time and resources. Due to time limitations, only $L_{\text{max}} = 0$ and $L_{\text{max}} = 1$ as well as sample containing 3,000 events are chosen in this study. Beside L_{max} the event generator also need certain parameters for the event generation. These parameters are mainly the mass and the width of the resonances as well as the magnitude and phase of all possible initial LS combinations for the $\bar{p}p$ system. For this, PAWIAN provides the possibility to generate a parameter file with so-called default parameters, which is used in this study. Another option is to generate a set of random parameters.
In general, three kinds of data sets are generated. As described in Section 6.5, the normalization of the fit is done by a Monte-Carlo-Integration. Therefore, the first kind of data sets consist of phase space distributed events. The second kind of data sets includes a $\overline{\Xi}^+$ and a Ξ resonance, i.e. $\bar{p}p \to \overline{\Xi}^+\ \Xi\,(1690)^-$ and $\bar{p}p \to \overline{\Xi}^+\ \Xi\,(1820)^-$. In addition to the single Ξ resonance, in the third kind of data sets, the reaction $\bar{p}p \to \bar{\Lambda}\,(1890)\Lambda$ is included. Since there are neither experimental data nor theoretical predictions, the yields of the Ξ resonance and $\bar{\Lambda}\,(1890)$ are assumed to be equal. Table 6.2 summarizes the properties of the generated data sets used in this analysis.

Table 6.2: Properties of the generated data sets for this analysis.

Data set	Reaction	Number of Events	L_{max}
1	$\bar{\mathrm{p}}\mathrm{p} \rightarrow \overline{\Xi}^{+}\,\Lambda\,\mathrm{K}^{-}$	10,000	0
2		10,000	1
3		100,000	0
4		100,000	1
5	$\bar{\mathrm{p}}\mathrm{p} \rightarrow \overline{\Xi}^{+}\,\Xi\,(1690)^{-}$	3,000	0
6	$\bar{\mathrm{p}}\mathrm{p} \rightarrow \overline{\Xi}^{+}\,\Xi\,(1690)^{-}$	3,000	1
7	$\bar{\mathrm{p}}\mathrm{p} \rightarrow \overline{\Xi}^{+}\,\Xi\,(1820)^{-}$	3,000	0
8	$\bar{\mathrm{p}}\mathrm{p} \rightarrow \overline{\Xi}^{+}\,\Xi\,(1820)^{-}$	3,000	1
9	$\bar{\mathrm{p}}\mathrm{p} \rightarrow \overline{\Xi}^{+}\,\Xi\,(1690)^{-}$ $\bar{\mathrm{p}}\mathrm{p} \rightarrow \bar{\Lambda}\,(1890)\,\Lambda$	30,000	1
10	$\bar{\mathrm{p}}\mathrm{p} \rightarrow \overline{\Xi}^{+}\,\Xi\,(1820)^{-}$ $\bar{\mathrm{p}}\mathrm{p} \rightarrow \bar{\Lambda}\,(1890)\,\Lambda$	30,000	0

6.6.2 Determination of Quantum Numbers

One of the questions to be answered in this study is whether it is possible to determine the quantum numbers of the Ξ resonances with PAWIAN. Therefore, for each kind of data set (data set 5–10), samples with different hypotheses for the quantum numbers ($1/2^{+}$, $1/2^{-}$, $3/2^{+}$, $3/2^{-}$) for $\Xi\,(1690)^{-}$ and $\Xi\,(1820)^{-}$, respectively, have been generated. The choice of quantum numbers is motivated by the estimation from [1]. Here, for $\Xi\,(1690)^{-}$ $J^{P} = 1/2^{+}$ is chosen. For $\Xi\,(1820)^{-}$ there is an indication for $J^{P} = 3/2^{-}$ from experimental data.

The individual generated data sample is then fitted, successively, with all mentioned hypotheses. For example, in the reaction $\bar{\mathrm{p}}\mathrm{p} \rightarrow \overline{\Xi}^{+}\,\Xi\,(1690)^{-}$ the $\Xi\,(1690)^{-}$ is generated with hypothesis $1/2^{+}$ and fitted subsequently with the hypotheses $1/2^{+}$, $1/2^{-}$, $3/2^{+}$, and $3/2^{-}$. Afterward, the results are compared by determining ΔAIC (Eq. 6.63), ΔBIC (Eq. 6.65) and AIC + BIC. Since there is no relation between the selection criteria, AIC and BIC, and the conventional significance, here, ΔAIC is as taken as a measure for the significance. This selection method is already described in Section 6.5.

To fit the model to the data, start values for the parameters are necessary. As already mentioned in Section 6.6.1, within the software package, it is possible to create a parameter file with random parameter values. To avoid a bias in the fit, this method is used to generate random start parameters for each fit. Beforehand, the influence of different start parameters on the fit result was studied. The obtained results showed that the choice of the start parameters does not affect the fit results, significantly, as long as the global minimum of the NLL is found.

For the performed fit only the relative phases are important. For this reason, one phase of the $\bar{\mathrm{p}}\mathrm{p}$ spin singlet, e.g. $J^{PC} = 0^{-+}$, $L = S = 0$, and one phase of the $\bar{\mathrm{p}}\mathrm{p}$ spin triplet, e.g. $J^{PC} = 0^{++}$, $L = 1$, $S = 1$, have to be fixed [140].

Since the magnitudes of the $\bar{\mathrm{p}}\mathrm{p}$ amplitudes are open to the fit, it is necessary to fix one production amplitude for the resonance production [157]. Furthermore, the amplitude for the resonance decay, i.e. Ξ^{*} into $\Lambda\,\mathrm{K}^{-}$ and $\bar{\Lambda}$ (1890) into $\overline{\Xi}^{+}\,\mathrm{K}^{-}$, has to be fixed.

Table 6.3: Results of the different generated and fitted hypotheses for $\Xi(1690)^-$. The maximal orbital angular momentum is set to $L_{\max} = 0$.

generated hypothesis	fit hypothesis	NLL	BIC	AIC	ΔBIC	ΔAIC	AIC + BIC	N_{par}
$1/2^+$	$1/2^+$	-3,989.3	-7,930.5	-7,966.5	0	0	-15,897.0	6
	$1/2^-$	-3,970.3	-7,893.7	-7,929.8	36.8	36.7	-15,823.5	6
	$3/2^+$	-3,963.3	-7,862.6	-7,910.6	67.9	55.9	-15,773.2	8
	$3/2^-$	-3,928.9	-7,793.8	-7,841.9	136.7	124.6	-15,645.7	8
$1/2^-$	$1/2^+$	-4,010.9	-7,973.7	-8,009.7	76.9	77.2	-15,983.4	6
	$1/2^-$	-4,049.4	-8,050.6	-8,086.9	0	0	-16,137.5	6
	$3/2^+$	-4,011.9	-7,958.0	-8,006.1	92.6	80.8	-15,964.1	8
	$3/2^-$	-3,865.9	-7,667.8	-7,715.9	382.8	371.0	-15,383.7	8
$3/2^+$	$1/2^+$	-4,115.2	-8,182.4	-8,218.5	147.8	159.8	-16,400.9	6
	$1/2^-$	-4,105.3	-8,162.5	-8,198.6	167.7	179.7	-16,361.1	6
	$3/2^+$	-4,197.1	-8,330.2	-8,378.3	0	0	-16,708.5	8
	$3/2^-$	-4,132.8	-8,201.6	-8,249.6	128.6	128.7	-16,451.2	8
$3/2^-$	$1/2^+$	-3,740.0	-7,431.9	-7,467.9	101.0	113.6	-14,899.8	6
	$1/2^-$	-3,658.3	-7,268.6	-7,304.6	264.8	276.9	-14,573.2	6
	$3/2^+$	-3,762.9	-7,461.8	-7,509.9	71.6	71.6	-14,971.7	8
	$3/2^-$	-3,798.7	-7,533.4	-7,581.5	0	0	-15,114.9	8

Single Resonances

In case of the single resonances, the investigation on the quantum numbers is done for two different maximum orbital angular momenta: $L_{\max} = 0$ and $L_{\max} = 1$. Therefore, data sets 5 to 8, containing 3,000 events each, have been generated for the different J^P hypotheses. Subsequently, all hypotheses were fitted to the generated samples. Here, based on the generated phase space distributed events, the triple amount of generated data points are fitted. Therefore, Equation (6.25) is used to determine the weight with which the phase space distributed events are weighted in order to match the selected hypothesis.
The fit results are shown in Tables 6.3 to 6.6. Beside the generated and fitted hypothesis, the tables show the values for the NLL, AIC, BIC, ΔBIC, ΔAIC, AIC + BIC, and the number of free parameters N_{par}. The number of free parameters are used to calculate BIC and AIC and are therefore added for completeness.
For $\Xi(1690)^-$ and a maximum orbital angular momentum of $L_{\max} = 0$, the fit results (see Table 6.3) show that the determination of the quantum numbers is possible, if the data sample includes only a single resonance. In each case, the fitted hypothesis is in good agreement with the input. In addition, the values of $\Delta\mathrm{AIC} >> 10$ show, that the fit excludes all other hypotheses significantly. The number of free parameters is different for $J = 1/2$ and $J = 3/2$. This difference is caused by the higher number of possible LS combinations for $J = 3/2$ with respect to $J = 1/2$. In the Dalitz plot for the events fitted with the $1/2^+$ hypothesis, shown in Figure 6.4, the $\Xi(1690)^-$ can be clearly identified as vertical band in the region between 2.75 GeV^2/c^4 and 2.95 GeV^2/c^4 of the Λ K$^-$ mass squared. The comparison of the Dalitz plots for the fitted and generated events, shows that the fitted events are in agreement with the generated sample. Due to the low statistics of the generated data sample, a data sample with 60,000 generated events was used for the illustration of the Dalitz plot shown in Figure 6.4(a). Since the Dalitz plots for the generated events with different hypotheses do not differ from each other, only the Dalitz plot for the generated sample with $J^P = 1/2^+$ is shown. All other Dalitz plots for both generated and fitted events, are shown in Appendix B.1 and Appendix B.2. The above mentioned agreement is confirmed by

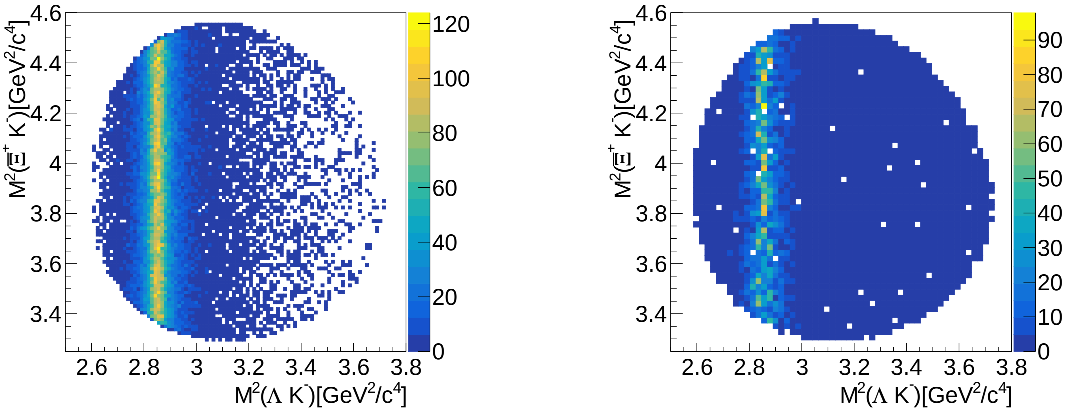

(a) (b)

Figure 6.4: Dalitz plot for the generated (a) and fitted (b) events of the reaction $\bar{p}p \rightarrow \bar{\Xi}^{+}\ \Xi(1690)^{-}$ with generated and fitted $J^P_{\Xi^*} = 1/2^+$. Here, a sample of 60,000 events was used for the Dalitz plot of the generated events.

comparing also the mass distributions shown in Figure 6.5.

In case that the fitted hypothesis differs from the generated quantum numbers, it is expected to see a difference mainly the angular distributions of the K^- and Λ in the rest frame of the resonance. In the rest frame of the mother particle the daughter particles are back-to-back, and their angular distributions are not independent of each other. The dependency of the angular distribution is given by $\theta_{K^-} = \theta_\Lambda + \pi$. Therefore, only the angular distributions for K^- are shown in the following. Angular distribution of K^- from $\Xi(1820)^-$ with generated $J^P = 3/2^-$ ($L_{\text{max}} = 0$) hypothesis and fitted $1/2^+$ and $1/2^-$ hypothesis. The corresponding distributions for the $\Xi(1690)^-$ with generated $J^P = 1/2^+$ are shown in Figure 6.6. It illustrates the angular distribution of the K^- as daughter of $\Xi(1690)^-$ for the fitted $J^P = 1/2^-$ hypothesis (Figure 6.6(a)), as well as the for the fitted $3/2^+$ hypothesis (Figure 6.6(b)). Both illustrations do not show a visible difference between the generated distributions for the two different spin and parity input values, as well as for the respective input and fitted distributions, although in both cases the input and the fitted hypothesis differ both in spin and parity. Further investigations are done to determine, if the similarity

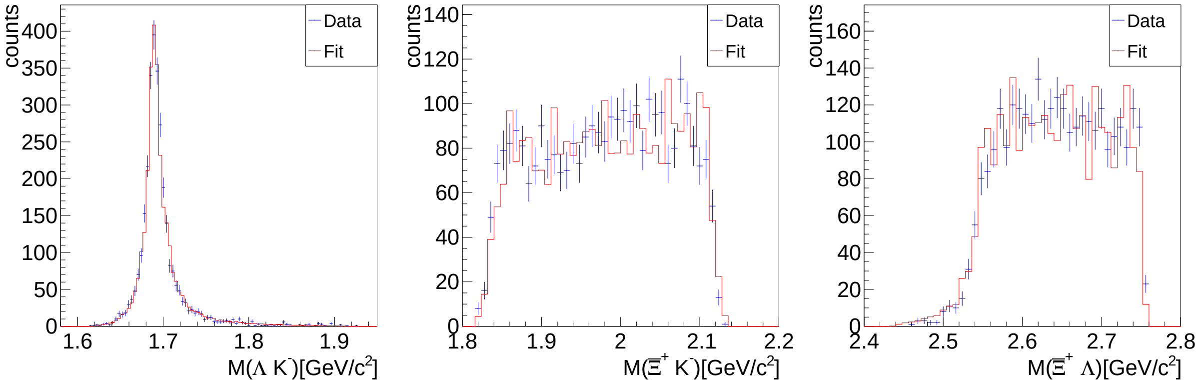

(a) (b) (c)

Figure 6.5: Comparison of generated and fitted mass distributions for $\Lambda\ K^-$ (a), $\bar{\Xi}^{+}\ K^-$ (b) and $\bar{\Xi}^{+}\ \Lambda$ (c) for $\bar{p}p \rightarrow \bar{\Xi}^{+}\ \Xi(1690)^{-}$ with generated $1/2^+$ and fitted $1/2^+$ hypothesis.

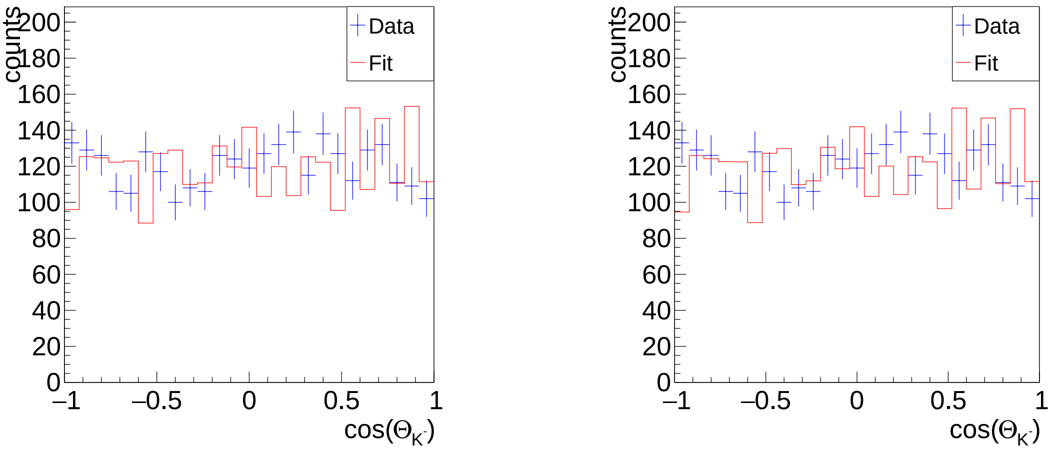

(a) Generated $J^P = 1/2^+$ and fitted $J^P = 1/2^-$ (b) Generated $J^P = 1/2^+$ and fitted $J^P = 3/2^+$

Figure 6.6: Angular distribution for K^- from $\Xi(1690)^-$ with generated $1/2^+(L_{\max} = 0)$ hypothesis and fitted (a) $J^P = 1/2^-$ and (b) $J^P = 3/2^+$.

in the angular distribution is caused by statistical effects. Therefore, data sets with 60,000 events each are generated. The generated angular distributions are shown in Figure 6.7. In both cases, $J = 1/2$ and $J = 3/2$, the distributions have similar shapes for different parity. Nevertheless, in case of generated spin $J = 3/2$ and fitted $J = 1/2$, a clear discrepancy between the generated and fitted angular distribution is visible (see Figure 6.8). One explanation for the good agreement of a fitted $3/2^+$ hypothesis to a $1/2^+$ input could be, that the fit procedure is forced to match the fitted distribution in this kinematic quantity at the expense of some deviations in other quantities, whereas in the complementary case, $1/2^+$ is fitted to $3/2^+$, see Figure 6.8, the overall likelihood is better if the deviations are in the angular distribution. Further illustrations for the comparison of the angular distributions can be found in Appendix B.3.
The fit results for $\Xi(1690)^-$ and $L_{\max} = 1$, summarized in Table 6.4, are consistent with the result for $L_{\max} = 0$. Here again, in all cases the generated hypothesis is preferred by the fit and all other hypotheses can be excluded with ΔAIC > 20. The main difference to $L_{\max} = 0$ is the higher number of free parameters which leads to smaller values for BIC and AIC. The values for NLL are in the same order as for $L_{\max} = 0$. Figure 6.9 shows the Dalitz plots for the generated events for $\bar{p}p \to \overline{\Xi}^+ \, \Xi(1690)^-$ with $J^P = 1/2^-$ and for the fitted events with $3/2^-$ hypothesis. Within the statistical fluctuations the two Dalitz plots do not show a visible difference between each other. Figure 6.10 shows the comparison between the mass distributions for the generated $1/2^-$ and fitted $3/2^-$hypotheses. In the $\Lambda\, K^-$ mass distribution a clear difference between the generated and the fitted distribution is visible. Although in the peak region the fitted distribution is consistent with the generated one, the fitted distribution does not describe the tails of the generated distribution. Figure 6.11 shows the angular distributions of K^- for the generated $1/2^+$ hypothesis and all fitted hypotheses, respectively. The input and all fit hypothesis distributions look flat within the statistical fluctuations.
In analogy to the determination of the quantum numbers for $\Xi(1690)^-$, the quantum numbers for $\Xi(1820)^-$ are determined. Table 6.5 summarizes the fit results for $L_{\max} = 0$. Although the fit prefers the true hypothesis for each generated data sample, the results are not as significant as for $\Xi(1690)^-$. For the generated $1/2^+$ hypothesis, for example, ΔAIC = 2.3 for the fitted $3/2^+$ hypothesis. According to the selection criteria described in Section 6.5, this hypothesis cannot be excluded.
Figure 6.12 shows the generated and fitted Dalitz plots for the generated and fitted $J^P = 3/2^-$ hypothesis.

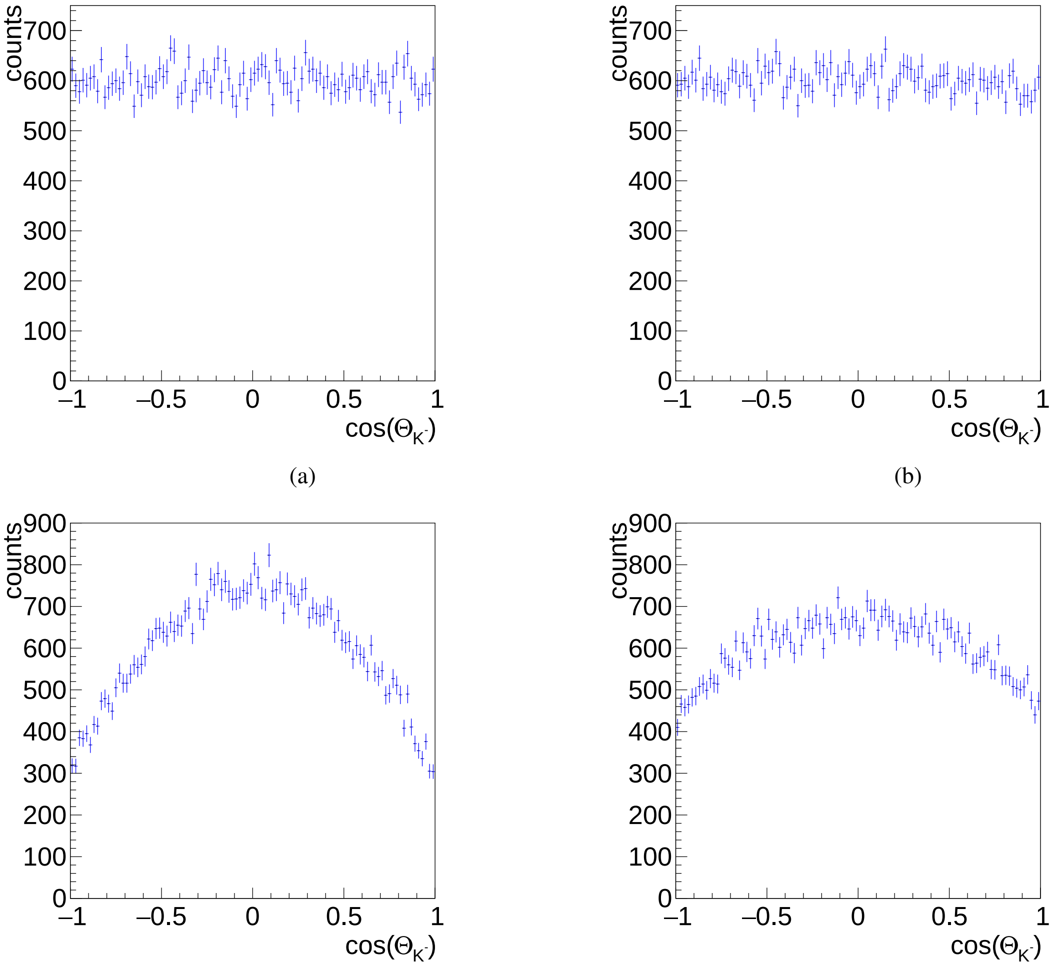

(a)

(b)

(c)

(d)

Figure 6.7: Generated angular distributions for $J^P = 1/2^+$ (a), $J^P = 1/2^-$ (b), $J^P = 3/2^+$ (c) and $J^P = 3/2^-$ (d), consisting of 60,000 events each.

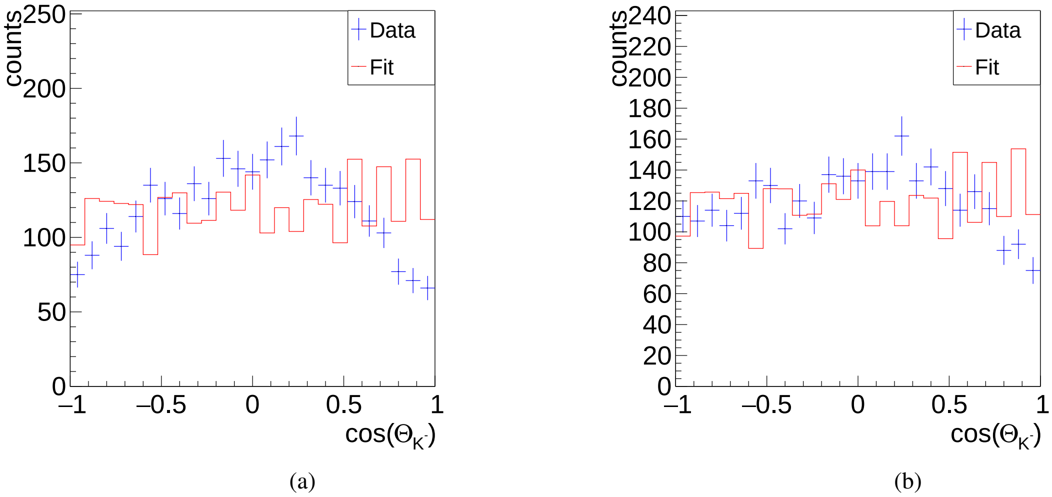

(a) (b)

Figure 6.8: Angular distributions for K$^-$ from $\Xi(1690)^-$ ($L_{\max} = 0$) with (a) generated $3/2^+$ and fitted $1/2^+$, and (b) generated $3/2^-$ and fitted $1/2^-$.

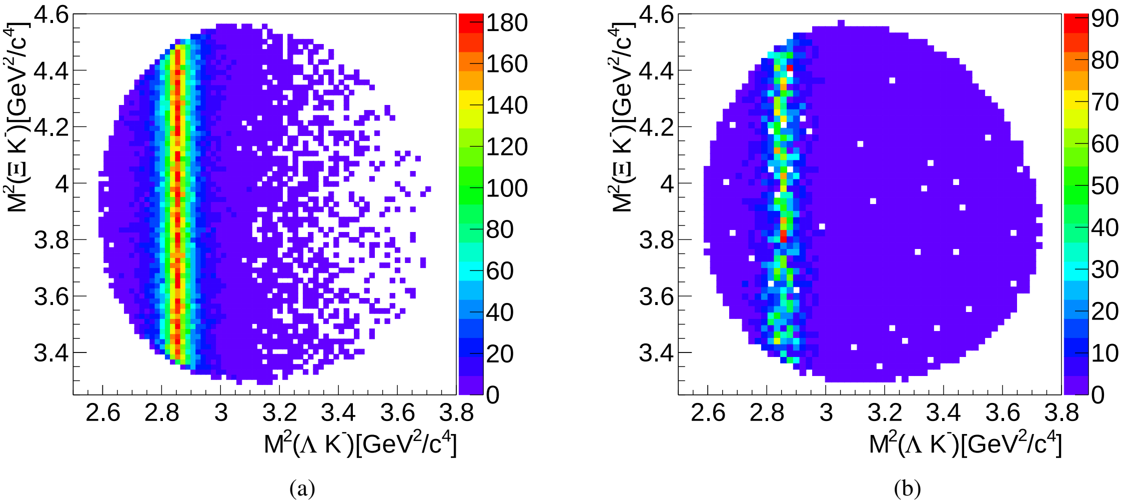

(a) (b)

Figure 6.9: Dalitz plots for generated (a) and fitted (b) events for the reaction $\bar{p}p \rightarrow \overline{\Xi}^+ \, \Xi(1690)^-$ with generated $1/2^-$ and fitted $3/2^-$ hypothesis, and $L_{\max} = 1$. For the illustration of the generated Dalitz plot a data sample with 60,000 events is used.

The $\Xi(1820)^-$ can be clearly identified. A comparison of the mass distributions for generated data and fitted events are shown in Figure 6.13. For all three two-body systems the mass distributions show that the fitted mass distributions are in good agreement with the generated distributions.

As it is the case for $\Xi(1690)^-$, the K$^-$ angular distributions only differ for $J = 1/2$ and $J = 3/2$. In both cases, it is not possible to distinguish between positive and negative parity. The corresponding plots, here for the generated $J = 3/2^-$ hypothesis, are shown in Figure 6.14. The illustrations of $\cos\Theta$ for all other generated hypotheses can be found in Appendix B.3.

In the case of $L_{\max} = 1$, the identification of $J^P = 1/2^+$ is more ambiguous than for $L_{\max} = 0$. As the results in Table 6.6 show, in this case still the true hypothesis is preferred, but also $1/2^-$ (ΔAIC = 0.8) and $3/2^+$ (ΔAIC = 2.0) are probable. In addition, the angular distributions for the above mentioned

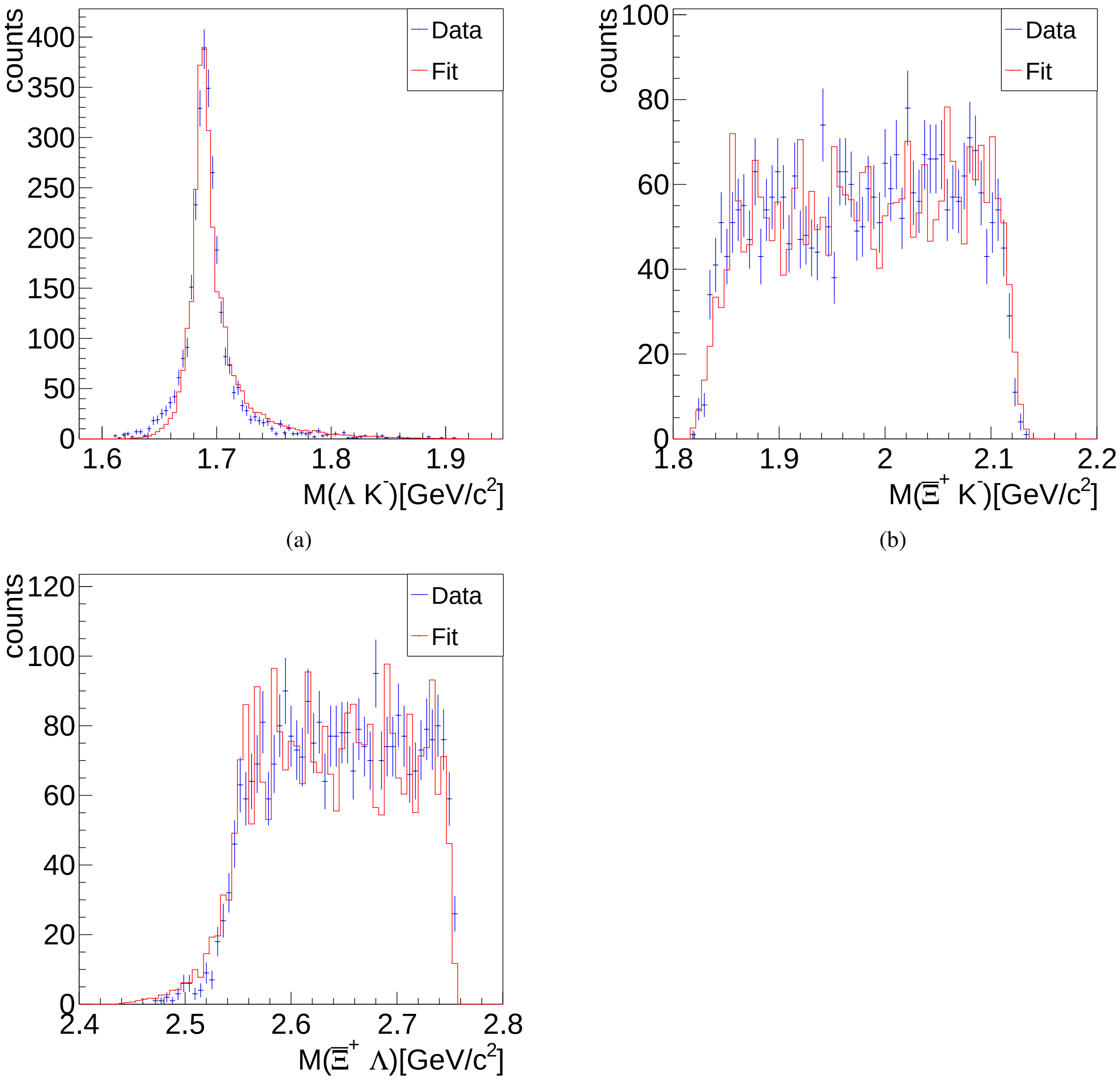

(a)

(b)

(c)

Figure 6.10: Mass distributions for Λ K^- (a), $\overline{\Xi}^+$ K^- (b), and $\overline{\Xi}^+$ Λ (c) for the generated $J^P = 1/2^-$ and fitted $J^P = 3/2^-$ hypothesis and $L_{\max} = 1$.

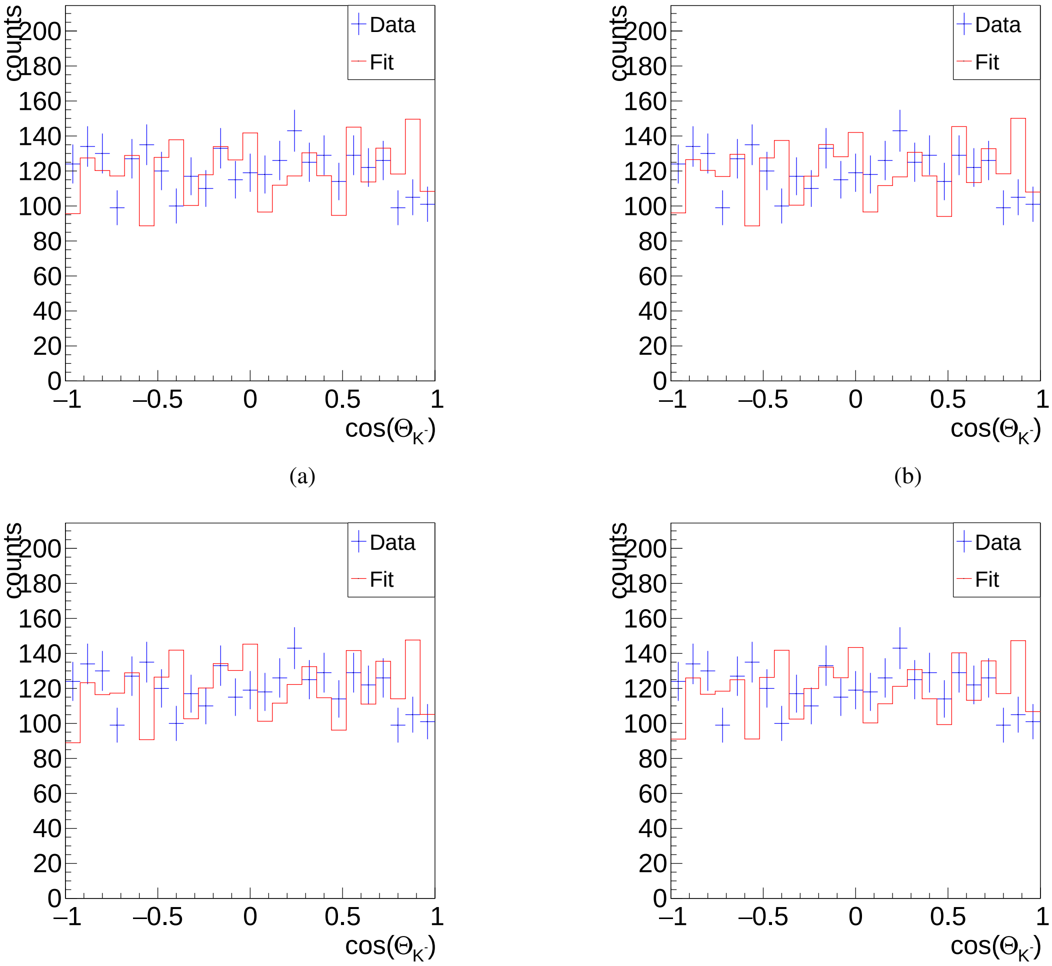

(a)

(b)

(c)

(d)

Figure 6.11: Angular distribution for K^- from $\Xi\,(1690)^-$ with generated $1/2^+(L_{\text{max}} = 1)$ and fitted $1/2^+$ (a), $1/2^-$ (b), $3/2^+$ (c), and $3/2^-$ (d).

Table 6.4: Results of the different generated and fitted hypotheses for $\Xi(1690)^-$. The maximal orbital angular momentum is set to $L_{\text{max}} = 1$.

generated hypothesis	fit hypothesis	NLL	BIC	AIC	ΔBIC	ΔAIC	AIC + BIC	N_{par}
$1/2^+$	$1/2^+$	-4,259.2	-8,359.7	-8,479.9	0	0	-16,839.6	20
	$1/2^-$	-4,249.4	-8,338.6	-8,458.7	21.1	21.2	-16,797.3	20
	$3/2^+$	-4,282.5	-7,862.6	-7,910.6	497,1	569,3	-15,773.2	30
	$3/2^-$	-4,186.7	-8,324.8	-8,505.0	34.9	25.1	-16,829.8	30
$1/2^-$	$1/2^+$	-4,233.7	-8,307.2	-8,427.3	37.3	37.5	-16,734.5	20
	$1/2^-$	-4,252.3	-8,344.5	-8,464.8	0	0	-16,809.3	20
	$3/2^+$	-4,254.0	-8,267.8	-8,447.9	76.7	16.9	-16,715.7	30
	$3/2^-$	-4,124.4	-8,008.6	-8,188.8	335.9	276.0	-16,197.4	30
$3/2^+$	$1/2^+$	-4,158.2	-8,156.2	-8,276.3	189.3	243.3	-16,432.5	20
	$1/2^-$	-4,146.0	-8,131.8	-8,252.0	213,7	267.6	-16,383.8	20
	$3/2^+$	-4,288.8	-8,345.5	-8,519.6	0	0	-16,865.1	30
	$3/2^-$	-4,230.1	-8,219.9	-8,400.1	125.6	119.5	-16,620.0	30
$3/2^-$	$1/2^+$	-3,870.5	-7,580.8	-7,700.9	309.8	369.8	-15,281.7	20
	$1/2^-$	-3,802.6	-7,445.0	-7,565.1	445.6	505.6	-15,010.1	20
	$3/2^+$	-4,013.9	-7,795.6	-7,969.8	95	100.9	-15,765.4	30
	$3/2^-$	-4,065.4	-7,890.6	-8,070.7	0	0	-15,961.3	30

fitted quantum numbers (Figure 6.15) show agreement with the input. The distributions seem to be indistinguishable from each other. For all other generated hypotheses the fit prefers the true hypothesis with ΔAIC > 24.2. Figure 6.16 shows the angular distributions for the generated $1/2^-$ hypothesis. Here again, all fits have a similar distribution and are in good agreement with the generated data sample.

Table 6.5: Results of the different generated and fitted hypotheses for $\Xi\,(1820)^-$. The maximum orbital momentum is set to $L_{\max} = 0$.

generated hypothesis	fit hypothesis	NLL	BIC	AIC	ΔBIC	ΔAIC	AIC + BIC	N_{par}
$1/2^+$	$1/2^+$	-3,010.5	-6,092.9	-6,128.9	0	0	-12,221.8	6
	$1/2^-$	-3,059.8	-6,071.5	-6,107.5	21.4	12.4	-12,179.0	6
	$3/2^+$	-3,071.1	-6,078.1	-6,126.6	14.8	2.3	-12,204.7	8
	$3/2^-$	-3,055.1	-6,046.2	-6,094.3	46.7	34.6	-12,140.5	8
$1/2^-$	$1/2^+$	-2,985.1	-5,922.1	-5,958.1	23.1	23	-11,880.2	6
	$1/2^-$	-2,996.6	-5,945.2	-5,981.2	0	0	-11,926.4	6
	$3/2^+$	-2,985.6	-5,907.1	-5,955.2	38.1	26	-11,862.3	8
	$3/2^-$	-2,951.0	-5.837.9	-5,886.0	107.3	95.2	-11,723.9	8
$3/2^+$	$1/2^+$	-3,033.9	-6,019.8	-6,055.8	243.6	255.6	-12,075.6	6
	$1/2^-$	-3,034.0	-6,019.7	-6,056.0	243.7	255.6	-12,075.7	6
	$3/2^+$	-3,163.7	-6,263.4	-6,311.4	0	0	-12,574.8	8
	$3/2^-$	-3,139.9	-6,215.8	-6,263.8	47.6	47.6	-12,479.6	8
$3/2^-$	$1/2^+$	-3,271.4	-6,536.5	-6,541.5	54.9	56.5	-13,078.0	6
	$1/2^-$	-3,254.9	-6,503.5	-6,508.5	87.9	89.5	-13,012.0	6
	$3/2^+$	-3,292.2	-6,576.1	-6,582.7	15.3	15.3	-13,158.8	8
	$3/2^-$	-3,299.8	-6,591.4	-6,598.0	0	0	-13,189.4	8

Table 6.6: Results of the different generated and fitted hypotheses for $\Xi\,(1820)^-$. The maximum orbital momentum is set to $L_{\max} = 1$.

generated hypothesis	fit hypothesis	NLL	BIC	AIC	ΔBIC	ΔAIC	AIC + BIC	N_{par}
$1/2^+$	$1/2^+$	-3,170.1	-6,180.0	-6,300.1	0	0	-12,480.1	20
	$1/2^-$	-3,169.6	-6,179.1	-6,299.4	0.9	0.8	-12,478.4	20
	$3/2^+$	-3,179.0	-6,117.9	-6,298.1	62.1	2.0	-12,416.0	30
	$3/2^-$	-3,166.1	-6,092.9	-6,272.3	87.1	27.8	-12,365.2	30
$1/2^-$	$1/2^+$	-3,082.4	-6,004.6	-6,124.7	24.2	24.2	-12,129.3	20
	$1/2^-$	-3,094.5	-6,028.8	-6,148.9	0	0	-12,177.7	20
	$3/2^+$	-3,089.6	-5,939.0	-6,119.2	89.8	29.7	-12,058.2	30
	$3/2^-$	-3,054.3	-5.868.5	-6,048.7	160.3	100.2	-11,917.2	30
$3/2^+$	$1/2^+$	-3,092.4	-6,024.7	-6,144.8	306.3	366.4	-12,169.5	20
	$1/2^-$	-3,089.7	-6,019.3	-6,139.4	311.7	371.8	-12,158.7	20
	$3/2^+$	-3,285.6	-6,331.0	-6,511.2	0	0	-12,842.2	30
	$3/2^-$	-3,265.8	-6,291.4	-6,471.6	39.6	39.6	-12,763.0	30
$3/2^-$	$1/2^+$	-3,404.4	-6,648.7	-6,768.8	256.8	316.8	-13,417.5	20
	$1/2^-$	-3,392.7	-6,625.1	-6,745.3	280.4	340.3	-13,370.4	20
	$3/2^+$	-3,556.7	-6,873.3	-7,053.5	32.2	32.1	-13,926.8	30
	$3/2^-$	-3,572.8	-6,905.5	-7,085.6	0	0	-13,991.1	30

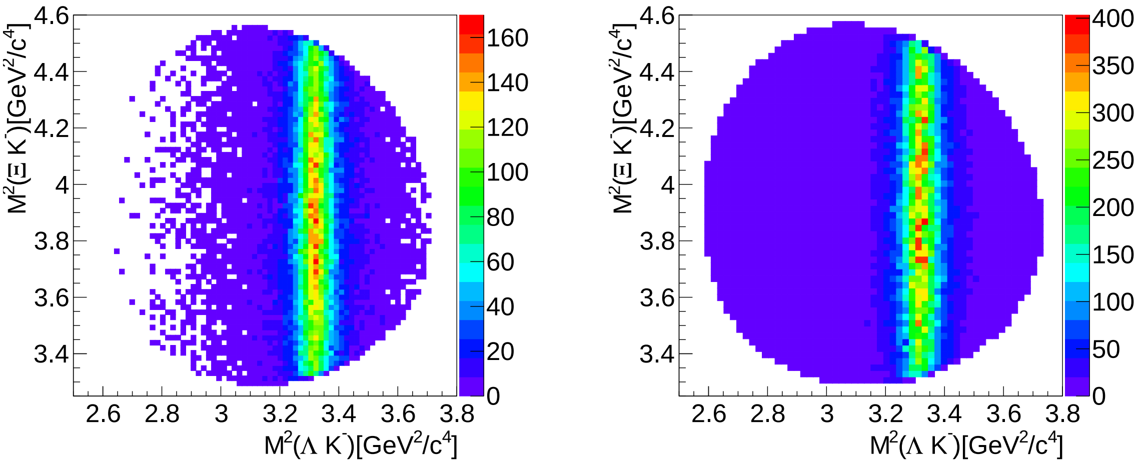

(a)

(b)

Figure 6.12: Dalitz plot for the generated data sample (a) and the fitted events (b) for $L_{\text{max}} = 0$. In both cases $J^P = 3/2^-$ is used. For the illustration of the generated Dalitz plot a data sample with 60,000 events is used.

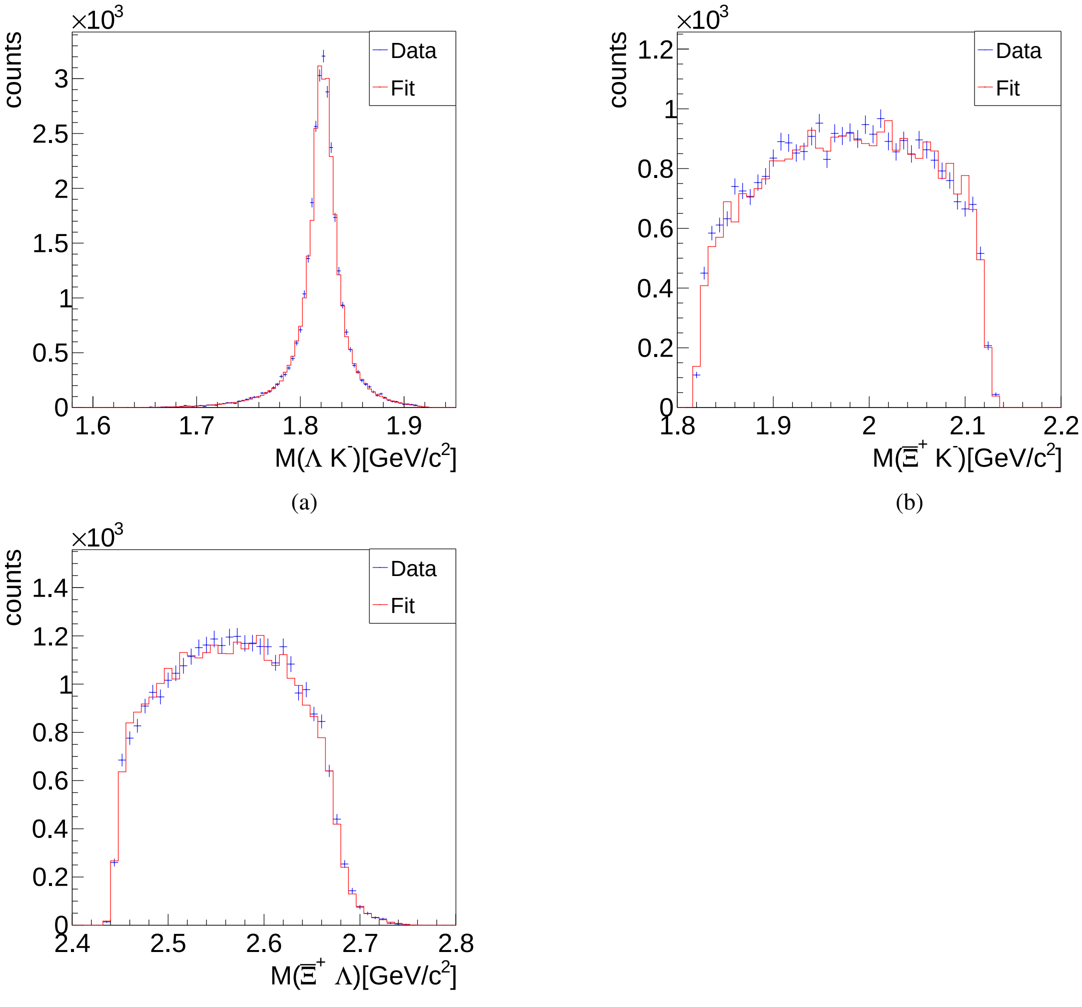

(a)

(b)

(c)

Figure 6.13: Mass distributions for $\Lambda\ K^-$ (a), $\overline{\Xi}^+\ K^-$ (b) and $\overline{\Xi}^+\ \Lambda$ (c). The $\Xi\,(1820)^-$ is generated and fitted with $J^P = 3/2^-$.

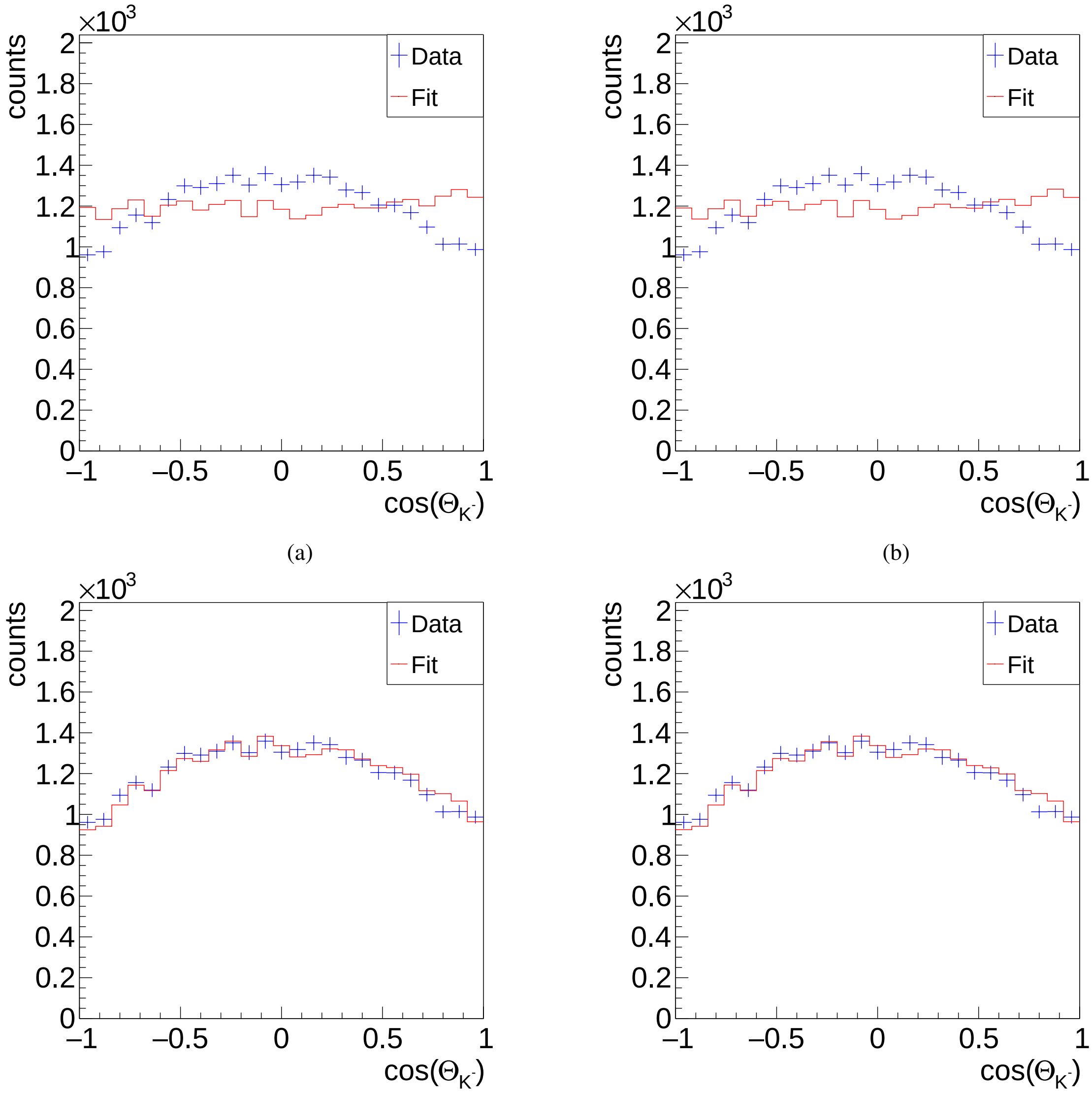

(a)

(b)

(c)

(d)

Figure 6.14: Angular distribution for K$^-$ from Ξ (1820)$^-$ with generated $J^P = 3/2^-$ ($L_{\max} = 0$) and fitted $1/2^+$ (a), $1/2^-$ (b), $3/2^+$ (c) and $3/2^-$ (d) hypothesis.

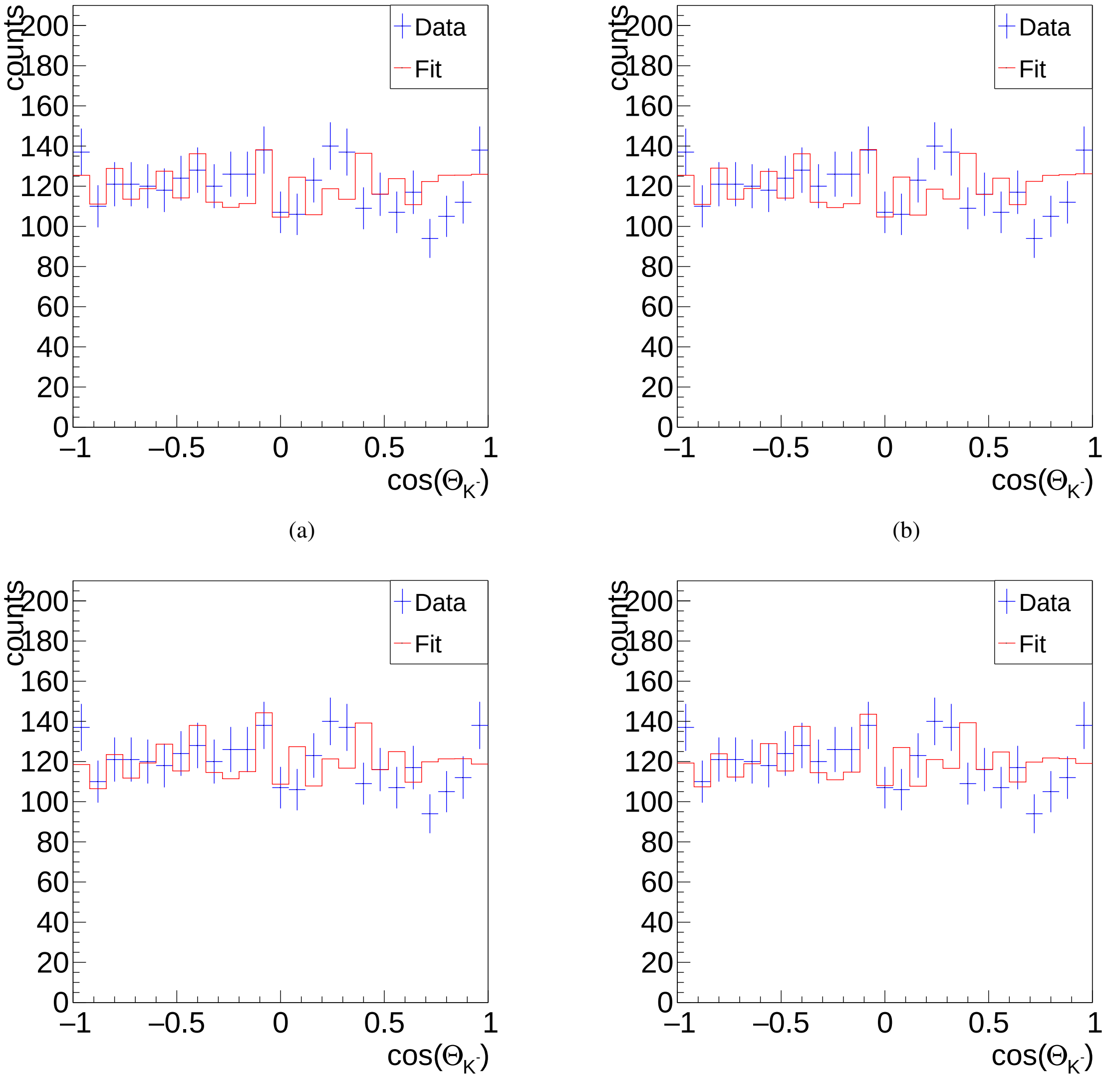

(a)

(b)

(c)

(d)

Figure 6.15: Angular distribution for K^- from $\Xi\,(1820)^-$ with generated $1/2^+$ ($L_{\text{max}} = 1$) compared with the fitted $1/2^+$ (a), $1/2^-$ (b), $3/2^+$ (c) and $3/2^-$ (d) hypotheses.

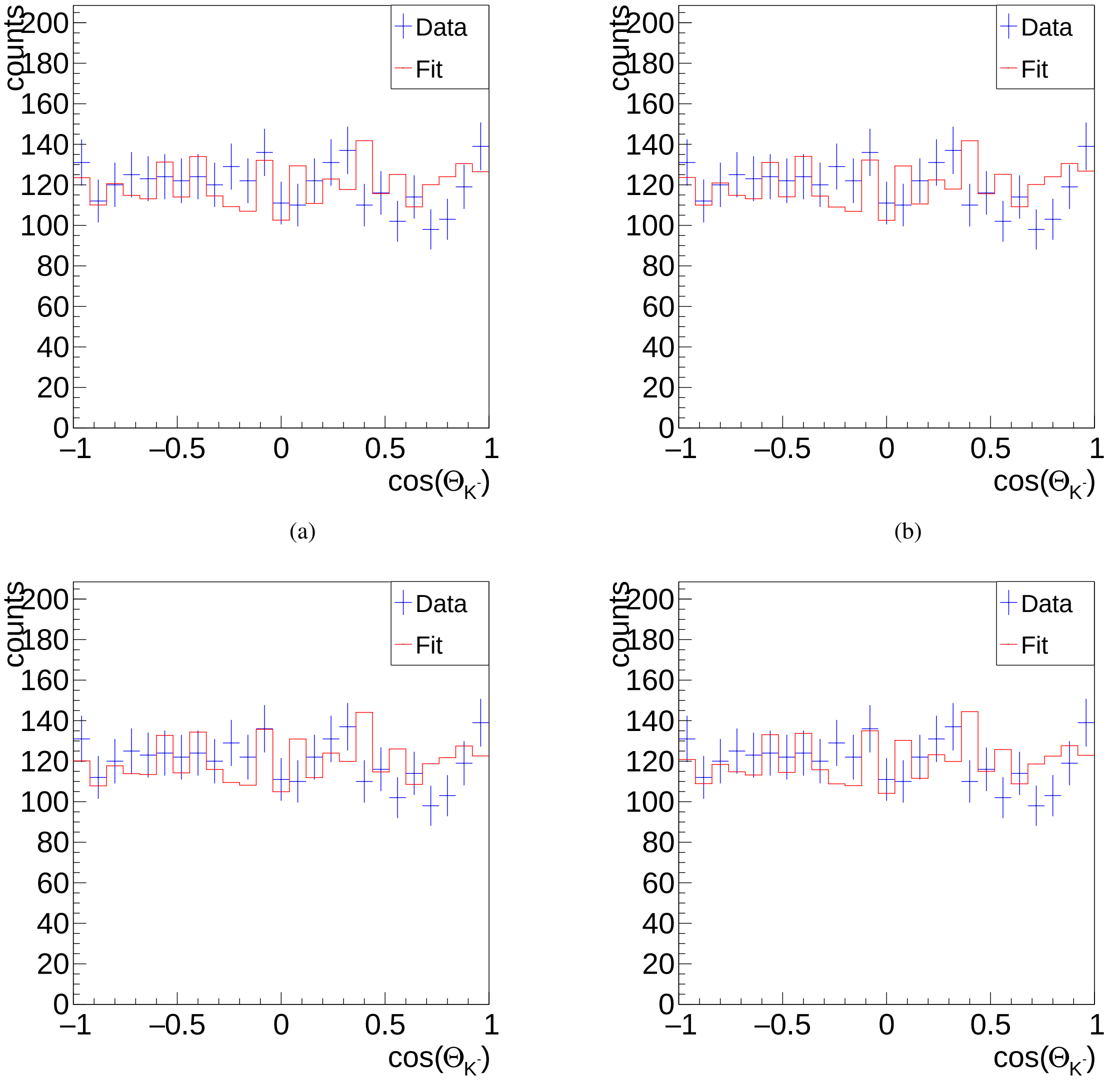

(a)

(b)

(c)

(d)

Figure 6.16: Angular distribution for K^- from $\Xi(1820)^-$ with generated $1/2^-$ ($L_{\max} = 1$) compared with the fitted $1/2^+$ (a), $1/2^-$ (b), $3/2^+$ (c) and $3/2^-$ (d) hypotheses.

Including a Crossed Channel Resonance

In experimental data, one expects to observe resonances not only in the Λ K^- system, but also in the $\overline{\Xi}^+$ K^- system due to excited Λ and Σ states. There are many excited Λ and Σ states listed in [1]. In the mass region between 1.8 GeV/c^2 and 2.2 GeV/c^2 the resonances are rather wide, $\Gamma > 50\,\mathrm{MeV}$. Since the spectrum in the relevant mass region is not well known, the existence of some of the resonances is uncertain. In analogy to the reaction $N^* \rightarrow K\Lambda, K\Sigma$, here, the considered decay branch is "‘upwards"’ in strangeness and thus implies the creation of an $s\bar{s}$ pair. Therefore, this decay mode is not expected to be strong as compared to other decay modes. Furthermore, nothing is known on the production cross section in $\bar{p}p$ collisions and on this specific decay branch. To include all of these resonances is beyond the scope of this thesis. But to see the effect caused by a "‘crossed channel"’ resonance in principle, an exploratory study with one single resonance is presented in this work. Here, $\bar{\Lambda}$ (1890)Λ with $\bar{\Lambda}$ (1890)$\rightarrow\overline{\Xi}^+$ K^- is chosen. $\bar{\Lambda}$ (1890) has a mass of $M \approx 1.890\,\mathrm{GeV/c^2}$ and a width of $\Gamma \approx 100\,\mathrm{MeV}$ [1].

Due to time constraints, only a single value for L_{max} was investigated for each Ξ resonance. As a starting point, $L_{\mathrm{max}} = 1$ is chosen for $\Xi\,(1690)^-$ and $L_{\mathrm{max}} = 0$ for $\Xi\,(1820)^-$. The lower L_{max} value for the $\Xi\,(1820)^-$ is justified by the smaller available phase space if this state is populated as compared to $\Xi\,(1690)^-$.

As shown in Table 6.2, 30,000 events are generated for each hypothesis since the generation of 60,000 events including the $\bar{\Lambda}$ (1890) take more time. Since the fit procedure with higher statistics is too time consuming as in the previously described cases, only 3,000 generated events are used as reference for the fit. The Dalitz plots of the generated full sample for $\Xi\,(1690)^-$ and $\Xi\,(1820)^-$ are illustrated in Figure 6.17. The mass distributions for Λ K^-, $\overline{\Xi}^+$ K^- and $\overline{\Xi}^+$ Λ are shown in Figure 6.19. The fit results for both $\Xi\,(1690)^-$ and $\Xi\,(1820)^-$ are summarized in Tables 6.7 and 6.8. For both investigated resonances, the results show different tendencies for the ΔBIC and ΔAIC in 50% of the cases. Since the BIC takes the number of fitted events into account, the low statistics could cause the different tendencies of BIC and AIC. Therefore, the sum of AIC and BIC is used as selection criterion in the following. By doing so, in all tested cases the true hypothesis is preferred by the fit. In case of $\Xi\,(1690)^-$ with generated $J^P = 3/2^+$ and $\Xi\,(1820)^-$ with generated $J^P = 3/2^-$, ΔBIC and ΔAIC have the same tendency, but the $\Delta\mathrm{AIC} < 4$ indicates, that other hypotheses than the true cannot be excluded.

Nevertheless, both resonances are clearly identifiable in the Dalitz plots for the fitted data (Figure 6.20).

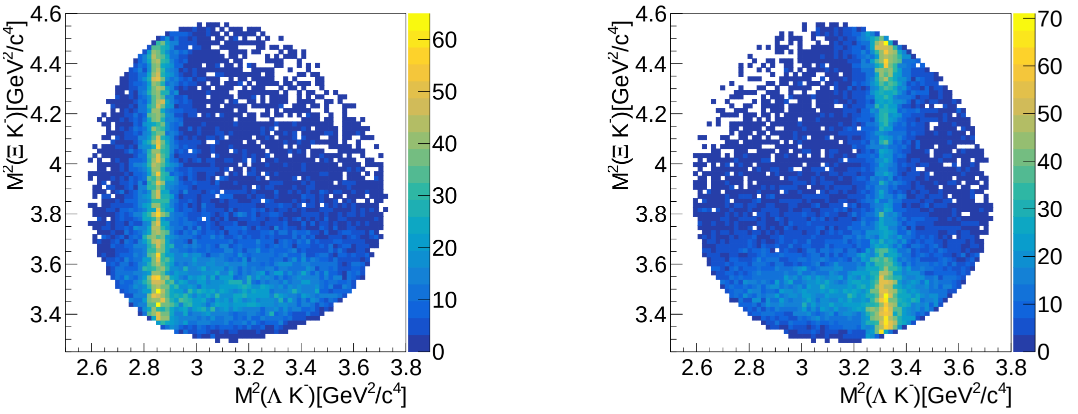

(a) (b)

Figure 6.17: Dalitz plots of generated data sample for (a) $\Xi\,(1690)^-$ ($J^P = 1/2^+$, $L_{\mathrm{max}} = 1$) and (b) $\Xi\,(1820)^-$ ($J^P = 3/2^-$, $L_{\mathrm{max=0}}$) including the crossed channel $\bar{p}p \rightarrow \bar{\Lambda}$ (1890)Λ.

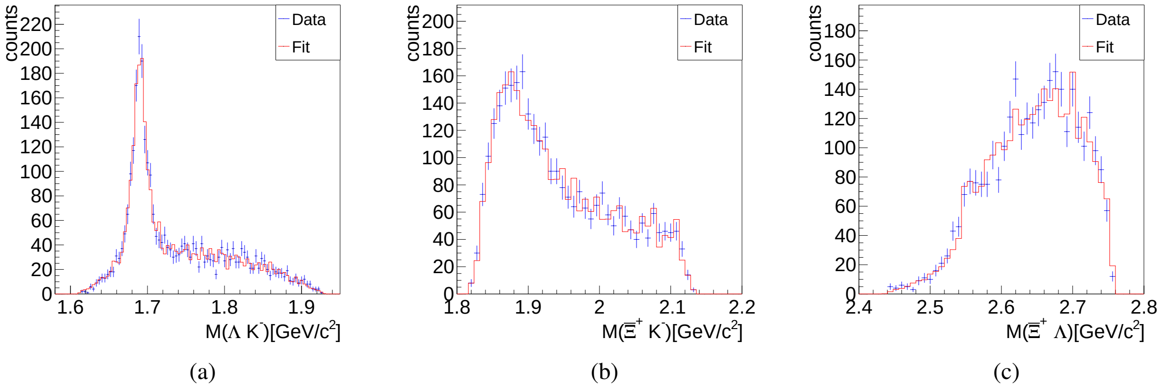

(a) (b) (c)

Figure 6.18: Mass distributions for Λ K$^-$ (a), $\overline{\Xi}^+$ K$^-$ (b) and $\overline{\Xi}^+$ Λ (c) for the generated (blue) and fitted (red) sample including the Ξ(1690)$^-$ with $J^P = 1/2^+$ and $L_{\max} = 1$.

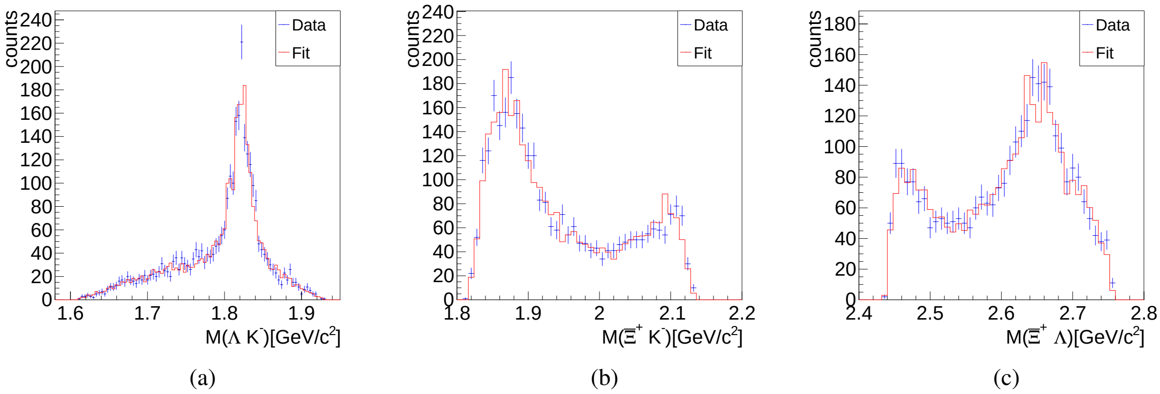

(a) (b) (c)

Figure 6.19: Mass distributions for Λ K$^-$ (a), $\overline{\Xi}^+$ K$^-$ (b) and $\overline{\Xi}^+$ Λ (c) for the generated (blue) and fitted (red) sample including the Ξ(1820)$^-$.

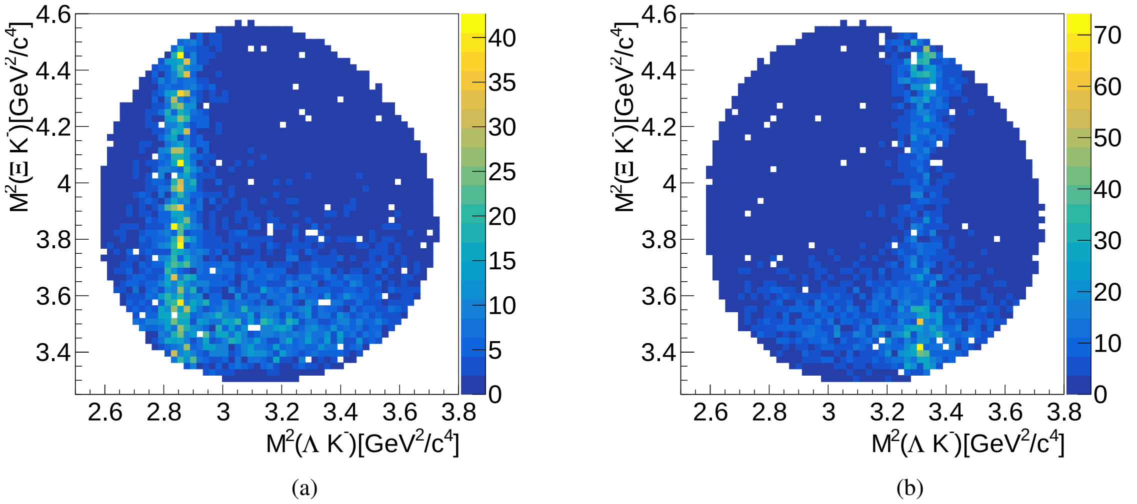

(a) (b)

Figure 6.20: Dalitz plot for the fitted data for the reactions (a) p̄p →$\overline{\Xi}^+$ Ξ(1690)$^-$ ($J^P = 1/2^-$, $L_{\max} = 1$) and (b) p̄p →$\overline{\Xi}^+$ Ξ(1820)$^-$ ($J^P = 3/2^-$, $L_{\max} = 0$) including also the crossed channel.

Table 6.7: Results of the different generated and fitted hypotheses for $\Xi(1690)^-$ including the reaction $\bar{p}p \to \bar{\Lambda}(1890)\Lambda$. The chosen maximum orbital momentum is $L_{\max} = 1$.

generated hypothesis	fit hypothesis	NLL	BIC	AIC	ΔBIC	ΔAIC	AIC + BIC	N_{par}
$1/2^+$	$1/2^+$	-1,627.6	-2,838.9	-3,151.2	0	4.8	-5,990.1	52
	$1/2^-$	-1,622.5	-2,828.7	-3,141.1	10.2	14.9	-5,969.8	52
	$3/2^+$	-1,640.0	-2,783.5	-3,156.0	55.3	0	-5,939.8	62
	$3/2^-$	-1,636.8	-2,777.1	-3,149.5	61.7	6.5	-5,926.6	62
$1/2^-$	$1/2^+$	-1,673.1	-2,929.9	-3,242.3	5.6	7.2	-6,172.2	52
	$1/2^-$	-1,675.9	-2,935.5	-3,247.8	0	1.7	-6,183.3	52
	$3/2^+$	-1,686.7	-2,877.1	-3,249.5	58.4	0	-6,126.6	62
	$3/2^-$	-1,675.5	-2,854.7	3,227.1	80.8	22.4	-6,081.8	62
$3/2^+$	$1/2^+$	-1,811.8	-3,207.3	-3,519.6	106.5	166.6	-6,726.9	52
	$1/2^-$	-1,812.8	-3,209.2	-3,521.5	104.6	164.7	-6,730.7	52
	$3/2^+$	-1,905.1	-3,313.8	-3,686.2	0	0	-7,000.0	62
	$3/2^-$	-1,903.4	-3,310.4	-3,682.8	3.4	3.4	-6,993.2	62
$3/2^-$	$1/2^+$	-1,626.0	-2,835.5	-3,147.9	132.4	192.5	5,983.4	52
	$1/2^-$	-1,620.4	-2,824.5	-3,136.8	143.4	203.5	-5,961.3	52
	$3/2^+$	-1,716.6	-2,936.9	-3,309.3	31	31	-6,246.2	62
	$3/2^-$	-1,732.1	-2,967.8	-3,340.3	0	0	-6,308.1	62

Table 6.8: Results of the different generated and fitted hypothesis for $\Xi(1820)^-$ including the reaction $\bar{p}p \to \bar{\Lambda}(1890)\Lambda$. The chosen maximum orbital momentum is $L_{\max} = 0$.

generated hypothesis	fit hypothesis	NLL	BIC	AIC	ΔBIC	ΔAIC	AIC + BIC	N_{par}
$1/2^+$	$1/2^+$	-1,320.8	-2,513.6	-2,609.7	0	0	-5,123.3	16
	$1/2^-$	-1,318.3	-2,508.6	-2,604.7	5.0	5.0	5,113.3	16
	$3/2^+$	-1,318.5	-2492.8	-2600.9	20.8	8.8	-5,093.7	18
	$3/2^-$	-1,316.5	-2,488.8	-2,596.9	24.8	12.8	-5,085.7	18
$1/2^-$	$1/2^+$	-1,531.5	-2,935.0	-3,031.1	12.1	12.8	-5,966.1	16
	$1/2^-$	-1,537.6	-2,947.1	-3,043.2	0	0.7	-5,990.3	16
	$3/2^+$	-1,533.9	-2,923.7	-3,301.9	23.4	12	-5,955.6	18
	$3/2^-$	-1,539.9	-2,935.8	-3,043.9	11.3	0	-5,979.7	18
$3/2^+$	$1/2^+$	-1,448.8	-2,769.6	-2,865.7	67.1	79.1	-5,635.3	16
	$1/2^-$	-1,453.9	-2,779.7	-2,875.8	57.0	69.0	-5,655.5	16
	$3/2^+$	-1,490.4	-2,836.7	-2,944.8	0	0	-5,781.5	18
	$3/2^-$	-1,489.4	-2,834.8	-2,942.9	1.9	1.9	-5,777.7	18
$3/2^-$	$1/2^+$	-1,492.3	-2,856.4	-2,952.5	200.6	213.5	-5,808.9	16
	$1/2^-$	-1,510.5	-2,892.9	-2,889.0	164.1	176.1	-5,781.9	16
	$3/2^+$	-1,594.7	-3,045.2	-3,153.3	11.8	11.8	-6,198.5	18
	$3/2^-$	-1,600.5	-3,057.0	-3,165.1	0	0	-6,222.1	18

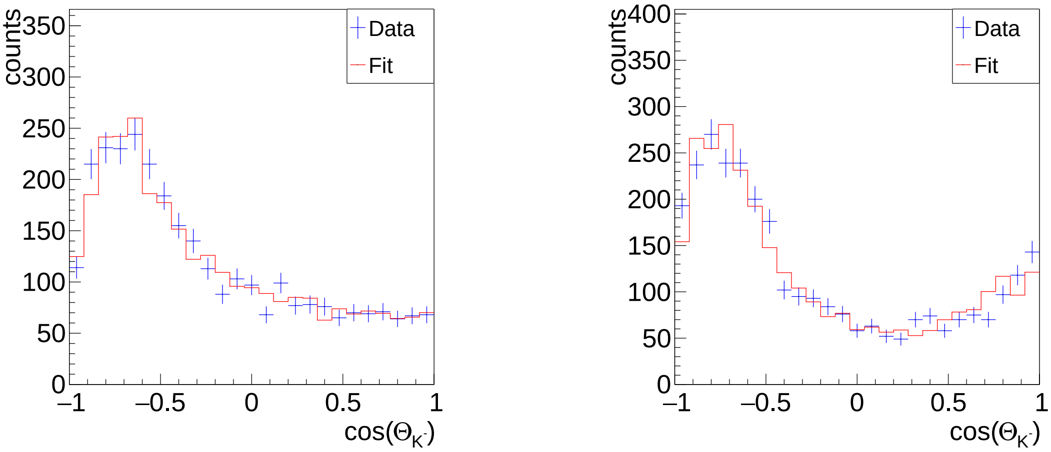

(a)

(b)

Figure 6.21: Comparison of generated and fitted angular distributions for K^- from $\Xi(1690)^-$ (a), with generated and fitted $J^P = 1/2^+$, and $\Xi(1820)^-$ (b) with generated and fitted $J^P = 3/2^-$.

The corresponding mass distributions are shown in Figures 6.18 and 6.19. In both cases, the fitted distributions are in good agreement with the generated distributions.
For the event generation the ratio of the Ξ^* and $\bar{\Lambda}$ (1890) contribution to the studied final state was chosen to be equal, meaning that the relative contribution of the Ξ resonances is 50% to the total number of events in the respective data set. The reconstructed relative contribution of the Ξ^* is in average $(48.9 \pm 2.5)\,\%$ for $\Xi(1690)^-$ and $(50.8 \pm 2.3)\,\%$ for $\Xi(1820)^-$ which is in good agreement with the input.
The angular distribution for the generated and fitted data, illustrated in Figure 6.21, show that the fitted distributions are in good agreement with the generated, $J^P = 1/2^+$ for $\Xi(1690)^-$ and $J^P = 3/2^-$ for $\Xi(1820)^-$. But the single contribution of each resonance is not visible. With PAWIAN it is possible to determine the contribution of each resonance to the mass distributions of the two-body systems and to the angular distributions from the fit. This will give the possibility to compare the fit results for this study with the results obtained in the single resonance case. Therefore, in the following, the data is compared with the different contributions of the resonances determined from the fit instead of a simple data-fit-compare as used for the single resonance case. The angular distributions for K^- from $\Xi(1690)^-$ with generated $1/2^+$ and the two fitted hypotheses $1/2^-$ and $3/2^+$ are shown in Figure 6.22. Here the angular distribution for the fitted $1/2^-$ hypothesis has the expected flat shape. The angular distribution for the fitted $3/2^+$ is also a flat, which is consistent with the results for a single Ξ resonance with generated $J = 1/2$. For $\Xi(1820)^-$, as an example, the angular distributions for K^- for generated $3/2^-$ and fitted $1/2^+$ and $3/2^+$ hypotheses are shown in Figure 6.23. The distribution for $1/2^+$ differs from the generated $3/2^-$ distribution, while the angular distribution of the fitted $3/2^+$ hypothesis has the expected shape. Furthermore, the distribution for $3/2^+$ has the opposite sign with respect to the single resonance case. This difference is caused by the relative phase between the Ξ^* and the Λ (1980).

6.6.3 Results

In the previous subsection the feasibility studies to determine the quantum numbers of the Ξ resonances $\Xi(1690)^-$ and $\Xi(1820)^-$ with PAWIAN have been described. The results of this investigation are summarized in the following.

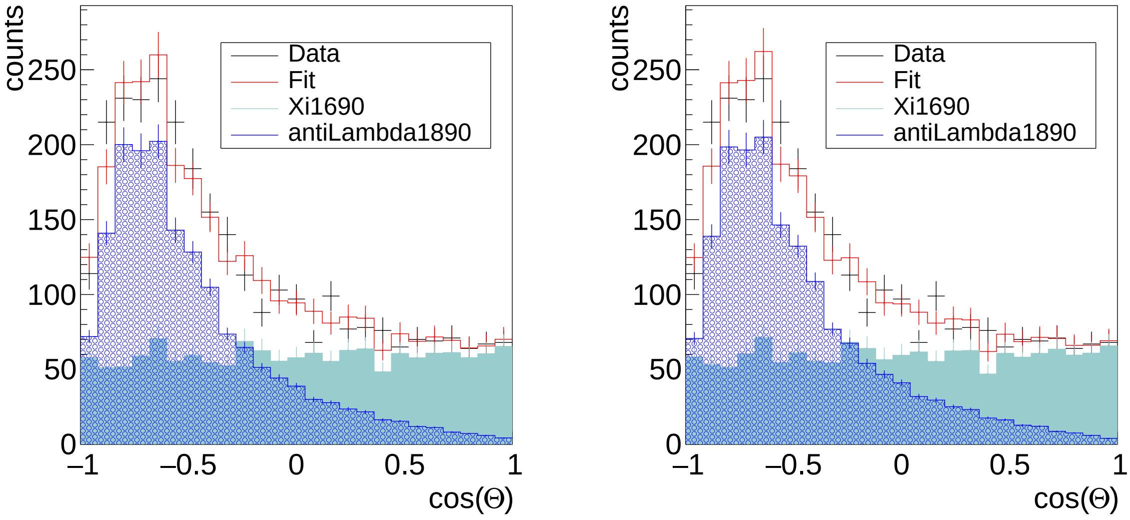

(a)

(b)

Figure 6.22: Angular distributions for K^- from $\Xi(1690)^-$ ($L_{\max} = 1$) with generated $1/2^+$ and fitted $1/2^+$ (a) and $3/2^+$ (b) hypothesis.

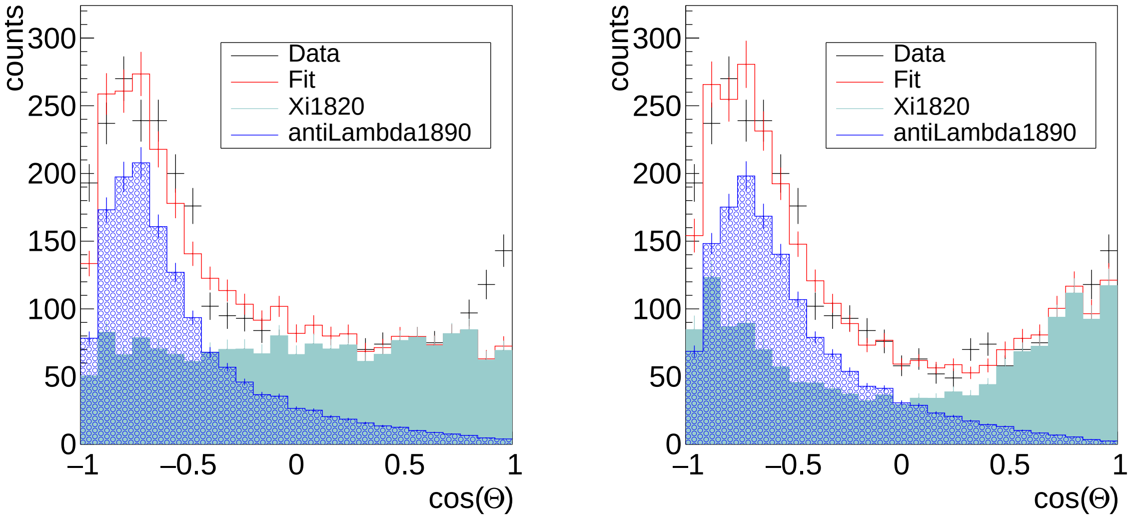

(a)

(b)

Figure 6.23: Angular distributions for K^- from $\Xi(1820)^-$ with generated $3/2^-$ and fitted $1/2^+$ (a) and $3/2^+$ (b) hypothesis.

As first step only the single resonances were investigated. For this purpose, data sets with 3,000 events, each, and different J^P-hypotheses, $1/2^+$, $1/2^-$, $3/2^+$ and $3/2^-$, were generated. Subsequently, the four different hypotheses were fitted to each generated data set.

In case of $\Xi\,(1690)^-$, the comparison of the BIC and AIC values shows that the preferred fit hypothesis is in good agreement with the generated hypothesis for all tested cases. As a measure for the significance, ΔAIC is calculated. For both chosen maximum orbital angular momenta, $L_{\text{max}} = 0$ and $L_{\text{max}} = 1$, $\Delta\text{AIC} > 16.9$. Since in all cases the true hypothesis achieved the smallest AIC value, the wrong hypotheses can be excluded. Although the fit results prefer the generated hypothesis, in case of the $\Xi\,(1690)^-$ with generated $1/2^+$ and $1/2^-$, the angular distributions of K^- as daughter of the Ξ^* in the rest frame of the resonance do not show significant differences for the four fitted hypotheses. Therefore, data sets with 60,000 events for the process $\bar{\mathrm{p}}\mathrm{p} \rightarrow \overline{\Xi}^+\ \Xi\,(1690)^-$ were generated to investigate statistical effects on the angular distribution. But also with higher statistic, the shape of the distributions are similar, implying that the parity cannot be determined from the angular distribution alone.

For $\Xi\,(1820)^-$ the results are not as clear as for $\Xi\,(1690)^-$. Although ΔBIC prefers the true hypothesis for all generated hypotheses and chosen L_{max}, the comparison of the AIC values shows in three cases that at least one of the other hypotheses cannot be excluded. As in the case of the $\Xi\,(1820)^-$ state, it will not be possible to determine the parity of the resonance from the angular distributions of its daughter particles in the rest frame of the resonance.

Since in the experiment one expects not only contributions from Ξ^* resonances in the $\Lambda\ \mathrm{K}^-$ system, but also Λ^* and Σ^{*0} resonances in the $\overline{\Xi}^+\ \mathrm{K}^-$ system, data sets including also the reaction $\bar{\mathrm{p}}\mathrm{p} \rightarrow \bar{\Lambda}\ (1890)\Lambda$ with $\bar{\Lambda}\ (1890) \rightarrow \overline{\Xi}^+\ \mathrm{K}^-$ were generated. Due to time constraints, here only one value for the maximum orbital angular momentum was chosen for each resonance: $L_{\text{max}} = 1$ for $\Xi\,(1690)^-$ and $L_{\text{max}} = 0$ for $\Xi\,(1820)^-$. Different from the case of single resonances, the results for the data sets including the $\bar{\Lambda}$ resonance show in some cases a different tendency for BIC and AIC. Therefore, BIC + AIC are compared in the following.

The obtained results for $\Xi\,(1690)^-$ show that in all tested cases the true hypothesis achieved the best fit result. However, it is difficult to make a statement if all other hypotheses can be safely excluded.

The determination of the quantum number for $\Xi\,(1820)^-$ with included crossed channel is even more difficult, since for the generated $1/2^+$ and $3/2^+$ hypothesis, it is not possible to exclude wrong hypotheses. In addition, no clear statement can be made for the generated $1/2^-$, although the BIC + AIC criterion indicates that the true hypothesis is preferred. As shown before for the case of a single Ξ^* resonance, here again, the angular distribution for $1/2^+$ and $1/2^-$ show similar shapes. The same is true for $3/2^+$ and $3/2^-$. For both Ξ resonances the fitted mass distributions are in good agreement with the input.

As already mentioned in Section 6.6.1, the generated ratio between Ξ^* and $\bar{\Lambda}\ (1890)$ was chosen to be equal. PAWIAN gives the possibility to determine the relative contribution of each resonance to the fit. Here the average ratio, with respect to the total number of events in each data set, is $(48.9 \pm 2.5)\,\%$ for $\Xi\,(1690)^-$ and $(50.9 \pm 2.3)\,\%$ for $\Xi\,(1820)^-$.

6.7 Discussion

The study presented in this chapter shows that the determination of the quantum numbers J^P with PAWIAN is, in general, possible but limited by different issues.

The investigation of data samples with a single narrow Ξ resonance shows that the input values of the quantum numbers can be reproduced. The fit results were obtained from 3,000 generated events. But it was indicated that for sufficient statistics considerably larger data samples of 60,000 events and more are needed. The generation and the fit of data sets with high statistics requires a high computing time and is thus beyond the scope of this work. This also holds for a systematic investigation of the uncertainties of the fit results as a function of the size of data sample.

The comparison of the angular distributions for different spin and party combinations showed, that the different parity values are indistinguishable in the angular distributions of K^- and Λ in the resonance rest frame. A study of data samples with higher statistics confirmed that the generated angular distributions for $1/2^+$ and $1/2^-$, as well as for $3/2^+$ and $3/2^-$, have the same shape, implying that this phenomenon is not caused by statistical effects. The fit is performed in a multi-dimensional space. Since all parameters are fitted at the same time, it is possible to determine the parity from the fit results. But because of this multi-dimensionality, a determination of the parity from a single angular distribution is difficult, since the projection to one parameter implies an integration over all other parameters.

Including a second resonance in a crossed channel, here $\bar{\Lambda}$ (1890)$\rightarrow\overline{\Xi}^+$ K^-, leads to an increase in the number of fit parameters and to results which are not as significant as for the case of a single resonance. The low statistics used for the fit could have an effect on the fit results. Therefore, the fit with PAWIAN should be repeated with higher statistics. Like it is the case for the single resonances, also here a detailed study with different values for $L_{\max}$ is needed, since this work focuses only on one value for each resonance. Beside this, also the influence of the chosen ratio between Ξ^* and $\bar{\Lambda}$ (1890) has to be further investigated. This investigation could also probe the sensitivity of the fit. In the preparation phase of this study, it turned out, that, e.g., for a 10% contribution of the Ξ resonance (this was set by default), the true hypothesis is not preferred anymore by the fit.

6.8 Outlook

The results of this study showed that the determination of the quantum numbers in the future needs a more systematic study based on large statistics generated samples which show the impact of the choice of input parameters on the different angular or mass distributions. In addition, a systematic study of how the input parameters affect the results should be done.

Another point which has to be investigated in the future is the dependence of the fit results on the chosen value for the maximum orbital angular momentum. Here only two values $L_{\max} = 0$ and $L_{\max} = 1$ were investigated, but the chosen beam momentum of 4.6 GeV/c corresponds to a maximum value of $L_{\max} \simeq 6$. The maximum contributing L is however also constrained by the final state. This constraint leads to a maximum orbital angular momentum of $L_{\max} \simeq 3$ for $\Xi\,(1690)^-$ and $L_{\max} \simeq 2$ for $\Xi\,(1820)^-$. Therefore, a study of values up to $L_{\max} = 3$ has to be done which was beyond the scope of this thesis. This also holds for the exploration of the possibility to extract the parity not only from the fit results. Therefore, the angular distributions should be studied depending on the orbital angular momentum of the entrance channel.

One aspect, which was not taken into account for this study, is the weak decay of $\overline{\Xi}^+$ and Λ. It is however expected that the decay asymmetry of the hyperon weak decay sets additional constraints. To keep the study simple in a first step, both hyperons were assumed to be stable. First tests have shown that it is possible to include these decays into PAWIAN [157]. In the next step it needs to be investigated which impact the inclusion of the weak $\overline{\Xi}^+$ and Λ decay has on the determination of the spin and parity quantum numbers of the intermediate resonances.

Since it is expected to have more than one resonance in both the channel of interest and the crossed channel additional resonances should be added as soon as all above mentioned issues have been fully investigated. In addition, the same studies have to be done for the charge conjugate channel $\bar{p}p \rightarrow \Xi^- \ \bar{\Lambda} \ K^+$ which will be an independent cross check.

Furthermore, it is planned in the future to use the generated data samples as alternative set of MC generated events as input to the PandaRoot simulation. This will give the possibility to redo the analyzes presented in Section 5.3 with more realistic angular distributions. Subsequently, the PAWIAN partial wave analysis should be imposed to the reconstructed event sample which includes detection inefficiencies and finite resolution.

CHAPTER 7

Conclusion

Two topics have been investigated in this thesis: the study of excited Ξ baryons in $\bar{p}p$ collisions and the first steps towards a PWA of the $\overline{\Xi}^{+}$ Λ K^{-} (Ξ^{-} $\bar{\Lambda}$ K^{+}) final state with the PArtial Wave Interactive ANalysis Sofware (PAWIAN).

Study of Excited Ξ Baryons

The reactions $\bar{p}p \rightarrow \overline{\Xi}^{+}$ Λ K^{-} and $\bar{p}p \rightarrow \Xi^{-}$ $\bar{\Lambda}$ K^{+} have been studied using two different analysis strategies. For this purpose, two different data sets were generated, containing 5 million $\overline{\Xi}^{+}$ Λ K^{-} events and 5 million Ξ^{-} $\bar{\Lambda}$ K^{+} events each. Beside the non-resonant decay branch, the so-called signal samples include also two Ξ resonances, $\Xi(1690)^{-}$ and $\Xi(1820)^{-}$, as well as their charge conjugate particles. In addition, a background sample of 100 million events has been analyzed with the same analysis strategies applied to the signal samples. In both strategies, the reconstruction of the decay channel starts from the final state particles and proceed backwards up to the $\bar{p}p$ system. At each stage of the analyses, the reconstruction efficiency and the momentum, spatial, and mass resolution have been evaluated. Furthermore, the signal-to-background ratio as well as the significance of the signal have been calculated.

In the first analysis, a sequential fit procedure is used. Here, the candidate selection is based on probability cuts which are applied to the results of several kinematic fits with the following constraints: the point of origin of the daughter particles, the mass of the Λ, $\bar{\Lambda}$, Ξ^{-} and $\overline{\Xi}^{+}$ candidates and the initial four-momentum of the $\bar{p}p$ system. The achieved efficiency for the reconstruction of the full decay tree for $\bar{p}p \rightarrow \overline{\Xi}^{+}$ Λ K^{-} is about 8 % and for $\bar{p}p \rightarrow \Xi^{-}$ $\bar{\Lambda}$ K^{+} about 9 %. For both channels, it was possible to clearly reconstruct the two resonant states. But various issues became apparent in the usage of the kinematic fitters. For this reason, a second analysis with a different selection strategy was performed.

In the second analysis, a full decay tree fit is used. While for the sequential fit procedure a MC based PID selection for the final state particles was used, this analysis is performed with open PID. For the composite state particles only a pre-selection, based on a mass cut, is used to reduce the number of wrong candidates. This mass cut rejects candidates which are not within a certain mass window symmetrical around the nominal composite state mass. After the pre-selection, a fit to the full decay tree with the DecayTreeFitter, implemented in PandaRoot, is applied. The DecayTreeFitter uses similar fits, which are also used for the sequential fit procedure. But the fits used in the DecayTreeFitter are applied recursively to all candidates within the decay tree. In the last step, the candidates are selected by applying a cut on the fit probability. With the DecayTreeFitter a total reconstruction efficiency of about

5 % is measured for both channels. Although the reconstruction efficiency is relatively low, here, it is also possible to reconstruct the resonant states.

A sample of 100 million hadronic background events was subject to the same algorithms used for the signal reconstruction. Neither with the sequential fit procedure nor with the full decay tree fit a single background event was reconstructed. This leads in case of the sequential fit procedure to a lower limit for the signal-to-background ratio of $S/B > 29.11\,(32.7)$ for $\overline{\Xi}^{+}\ \Lambda\ \mathrm{K}^{-}$ ($\Xi^{-}\ \bar{\Lambda}\ \mathrm{K}^{+}$) and a lower limit for the signal significance of $S_{\mathrm{sig}} > 644\,(685)$. For the full decay tree fit a signal-to-background ratio of $S/B > 19.1\,(19.5)$ for $\overline{\Xi}^{+}\ \Lambda\ \mathrm{K}^{-}$ ($\Xi^{-}\ \bar{\Lambda}\ \mathrm{K}^{+}$) and a signal significance of $S_{\mathrm{sig}} > 513\,(507)$ is achieved.

Due to the many different issues, i.e. the ideal tracking, not only an optimization of the selection is necessary, but also a repetition of the analyses are needed as soon as a more realistic algorithm for the tracking of secondary particles is available. In addition, the analysis using the sequential fit procedure should be redone with open PID and the identical PandaRoot version in order to allow a direct quantitative comparison between the two analysis methods.

The study demonstrates that even with reduced luminosity during the start phase of $\overline{\mathrm{P}}$ANDA a competitive experimental investigation of Xi^{*} resonances can be done.

Determination of J^{P} for Ξ resonances

A study to determine the quantum number of the Ξ resonances $\Xi\,(1690)^{-}$ and $\Xi\,(1820)^{-}$ with the PAWIAN software package is done. For this study different data sets with four J^{P}-hypotheses for the Ξ resonances were generated. A subsequent fit of all hypotheses to each generated data set should show, if the true hypothesis can be obtained from the fit results.

The determination of the quantum numbers was tested for each Ξ resonance first. The results for $\Xi\,(1690)^{-}$ shows that the best fitted hypotheses are in agreement with the input, respectively. But the results for $\Xi\,(1820)^{-}$ show the first limitations. For some generated J^{P}-hypotheses the fit results are ambiguous, since more than one hypothesis fulfills the selection criteria. In addition, the angular distributions for $1/2^{+}$ and $1/2^{-}$, as well as for $3/2^{+}$ and $3/2^{-}$, cannot be distinguished according to their shape. Nevertheless, in most cases it is possible to distinguish the parity on the basis of the fit results. Due to the fact that only 3,000 events can be used for the fit with PAWIAN, statistical effects cannot be excluded as reason for the ambiguity of the results. Further investigations on the impact of statistics should be done in the future.

For the results discussed in the first step, a very simplified assumption was used to investigate the possibility to determine the quantum numbers in general. To study the effect of a second resonance in a so-called crossed channel, here $\bar{\mathrm{p}}\mathrm{p} \rightarrow \bar{\Lambda}\,(1890)\Lambda$ with $\bar{\Lambda}\,(1890) \rightarrow \overline{\Xi}^{+}\ \mathrm{K}^{-}$ is included in the generated data sets using the same hypotheses for the Ξ resonances as used before. Each data set consists of 30,000 generated events. Since the fit of 30,000 events was by far too time consuming, the statistics for the fit was reduced again to 3,000 generated events. This low statistics seems to make the investigation more challenging. The results show that it is difficult to make a statement, since either ΔBIC and ΔAIC have a different tendency or $\Delta\mathrm{AIC} < 4$ for one of the other fit hypotheses, implying that this hypothesis cannot not be excluded. Nevertheless, using the BIC + AIC criterion for the selection leads to an agreement of best fit and input hypothesis. In addition, the generated contribution ratios for the Ξ resonances and $\bar{\Lambda}$

(1890) can be reproduced and are in good agreement with the input.

In future, samples with higher statistics should be used for the fit procedure. Furthermore, it is planned to use the data generated with PAWIAN as input for the simulation and analysis with PandaRoot. One goal is to study the possibility to determine the Ξ resonance quantum numbers with PAWIAN for data delivered by the $\overline{\text{P}}$ANDA detector.

Bibliography

[1] M. Tanabashi *et al.*
Review of Particle Physics, Phys. Rev. D **98** (3 Aug. 2018) 030001,
URL: `https://link.aps.org/doi/10.1103/PhysRevD.98.030001`
(cit. on pp. 3–12, 24, 43–46, 52, 57, 58, 63, 79, 83, 90, 95, 97, 102, 105, 108, 116, 131).

[2] *The Nobel Prize in Physics 2004*, Nobel Media AB 2019, 2004,
URL: `https://www.nobelprize.org/prizes/physics/2004/advanced-information/`
(cit. on p. 4).

[3] S. L. Glashow
Partial-symmetries of weak interactions, Nuclear Physics **22**.4 (1961) 579 (cit. on p. 4).

[4] P. W. Higgs
Broken symmetries and the masses of gauge bosons, Physical Review Letters **13**.16 (1964) 508
(cit. on p. 4).

[5] *The Nobel Prize in Physics 1969*, Nobel Media AB 2019, 1969,
URL: `https://www.nobelprize.org/prizes/physics/1969/summary/` (cit. on p. 4).

[6] F. Halzen and A. D. Martin
Quarks And Leptons: An Introductory Course in Modern Particle Physics, 1984,
ISBN: 9780471887416 (cit. on pp. 4–6).

[7] K. G. Wilson
Confinement of quarks, Physical review D **10**.8 (1974) 2445 (cit. on p. 6).

[8] S. Weinberg
Nuclear forces from chiral lagrangians, Physics Letters B **251**.2 (1990) 288, ISSN: 0370-2693,
URL: `http://www.sciencedirect.com/science/article/pii/037026939090938З`
(cit. on p. 6).

[9] M. F. M. Lutz *et al.*
Physics Performance Report for PANDA: Strong Interaction Studies with Antiprotons, (2009),
arXiv: `0903.3905 [hep-ex]` (cit. on pp. 6, 17, 97).

[10] E. D. Bloom *et al.*
High-Energy Inelastic e- p Scattering at 6 and 10, Physical Review Letters **23**.16 (1969) 930
(cit. on p. 6).

[11] D. Griffiths
Introduction to elementary particles, John Wiley & Sons, 2008 (cit. on pp. 6–8).

[12] M. Gell-Mann
The Eightfold Way: A Theory of strong interaction symmetry, (1961),
URL: `https://authors.library.caltech.edu/89508/1/eightfold.pdf` (cit. on p. 6).

[13] V. Ziegler
Hyperon And Hyperon Resonance Properties From Charm Baryon Decays At BaBar, (2007),
URL: `http://www.slac.stanford.edu/cgi-wrap/getdoc/slac-r-868.pdf`
(cit. on p. 7).

[14] A. Herten
GPU-based online track reconstruction for $\bar{P}$ANDA and application to the analysis of $D \rightarrow K\pi\pi$,
Me (2015),
URL: `https://hss-opus.ub.rub.de/opus4/frontdoor/index/index/docId/4384`
(cit. on pp. 8, 9, 22, 25).

[15] USER E2m
The spin-0 nonet of mesons, Wikimedia Commons, Apr. 2008,
URL: `https://commons.wikimedia.org/wiki/File:Meson_nonet_-_spin_0.svg`
(cit. on p. 8).

[16] USER E2m
The spin-1 nonet of mesons, Wikimedia Commons, Apr. 2008,
URL: `https://commons.wikimedia.org/wiki/File:Meson_nonet_-_spin_1.svg`
(cit. on p. 8).

[17] USER E2m
Baryon octet, Wikimedia Commons, Apr. 2008,
URL: `Melhttps://commons.wikimedia.org/wiki/File:Baryon_octet.svg`
(cit. on p. 9).

[18] USER Wierdw12
Baryon decuplet, Wikimedia Commons, Feb. 2008,
URL: `https://commons.wikimedia.org/wiki/File:Baryon_decuplet.svg`
(cit. on p. 9).

[19] S. Capstick and W. Roberts
Quasi-two-body decays of nonstrange baryons, Physical Review D **49**.9 (1994) 4570
(cit. on p. 10).

[20] N. Isgur and G. Karl
Positive-parity excited baryons in a quark model with hyperfine interactions,
Physical Review D **19**.9 (1979) 2653 (cit. on p. 9).

[21] T. Melde, W. Plessas and B. Sengl
Quark-Model Identification of Baryon Ground and Resonant States,
arXiv preprint arXiv:0806.1454 (2008), URL: `https://arxiv.org/abs/0806.1454`
(cit. on p. 11).

[22] K. Schönning, E. Thomé, Panda Collaboration *et al.*
“Spin observables in antihyperon-hyperon production with PANDA”,
Journal of Physics: Conference Series, vol. 556, 1, IOP Publishing, 2014 012007 (cit. on p. 11).

[23] B. Musgrave *et al.*
Study of YY production in two, three and four body final states by 3.0, 3.6 and 4.0 GeV/c antiprotons in hydrogen, Il Nuovo Cimento (1955-1965) **35**.3 (1965) 735
(cit. on pp. 11, 25, 45, 95).

[24] H. Genz, M. Nowakowski and D. Woitschitzky
Proton-antiproton reactions via double annihilation of quarks,
Physics Letters B **260**.1-2 (1991) 179, URL: `https://cds.cern.ch/record/101631?ln=de`
(cit. on pp. 11, 12).

[25] P. Kroll, B. Quadder and W. Schweiger
Exclusive production of heavy flavours in proton-antiproton annihilation,
Nuclear Physics B **316**.2 (1989) 373 (cit. on p. 11).

[26] V. Flaminio *et al.*
Compilation of Cross-sections, (1984), URL: `http://inspirehep.net/record/206657`
(cit. on pp. 12, 44, 45).

[27] A. Zambanini
Development of a free-running readout ASIC for the PANDA micro vertex detector and investigation of the performance to reconstruct anti pp$\rightarrow \bar{\Xi}^{+}\Xi^{-}$*(1690)*, (2015),
URL: `http://hss-opus.ub.ruhr-uni-bochum.de/opus4/files/4667/diss.pdf`
(cit. on pp. 12, 49, 50).

[28] J. Haidenbauer, K. Holinde and J. Speth
$\bar{p}p \rightarrow \bar{\Xi}\Xi$ *reaction in the meson exchange picture*, Phys. Rev. C **47** (6 June 1993) 2982,
URL: `https://link.aps.org/doi/10.1103/PhysRevC.47.2982` (cit. on p. 12).

[29] M. Gell-Mann
A schematic model of baryons and mesons, Physics Letters **8**.3 (1964) 214 (cit. on p. 13).

[30] H. J. Lipkin
New possibilities for exotic hadron – anticharmed strange baryons,
Physics Letters B **195**.3 (1987) 484 (cit. on p. 13).

[31] R. Aaij *et al.*
Observation of $J/\psi\, p$ *Resonances Consistent with Pentaquark States in* $\Lambda_b^0 \rightarrow J/\psi K^- p$ *Decays*,
Physical review letters **115**.7 (2015) 072001,
URL: `https://arxiv.org/pdf/1507.03414.pdf` (cit. on p. 13).

[32] T. Skwarnicki
Hadron spectroscopy and exotic states at LHCb, Talk at the 54th Rencontres de Moriond,
Mar. 2019,
URL: `http://moriond.in2p3.fr/QCD/2019/TuesdayMorning/Skwarnicki.pptx`
(cit. on p. 13).

[33] H. Högaasen and P. Sorba
The systematics of possibly narrow quark states with baryon number one,
Nuclear Physics B **145**.1 (1978) 119 (cit. on p. 13).

[34] R. Jaffe and F. Wilczek
Diquarks and exotic spectroscopy, Physical Review Letters **91**.23 (2003) 232003 (cit. on p. 13).

[35] M. Karliner and H. J. Lipkin
A diquark–triquark model for the KN pentaquark, Physics Letters B **575**.3-4 (2003) 249
(cit. on p. 13).

[36] J.-J. Wu *et al.*
Prediction of narrow $N*$ and $\Lambda*$ resonances with hidden charm above 4 GeV,
Physical review letters **105**.23 (2010) 232001, URL: `https://arxiv.org/pdf/1007.0573`
(cit. on p. 13).

[37] Y. Zhong-Cheng *et al.*
Possible hidden-charm molecular baryons composed of an anti-charmed meson and a charmed baryon, Chinese Physics C **36**.1 (2012) 6 (cit. on p. 13).

[38] F.-K. Guo *et al.*
How to reveal the exotic nature of the P_c (4450), arXiv preprint arXiv:1507.04950 (2015),
URL: `https://arxiv.org/pdf/1507.04950.pdf` (cit. on p. 13).

[39] I. Schmidt and M. Siddikov
Production of pentaquarks in p A-collisions, Physical Review D **93**.9 (2016) 094005
(cit. on p. 13).

[40] Z.-E. Meziani *et al.*
A Search for the LHCb Charmed 'Pentaquark' using Photo-Production of J/ψ at Threshold in Hall C at Jefferson Lab, arXiv preprint arXiv:1609.00676 (2016),
URL: `https://arxiv.org/abs/1609.00676` (cit. on p. 13).

[41] *FAIR – Facility for Antiproton and Ion Research*, Online, URL: `https://fair-center.eu/`
(cit. on p. 15).

[42] H. H. Gutbrod *et al.*
FAIR-Baseline technical report. Executive summary, (2006),
URL: `https://repository.gsi.de/record/54062` (cit. on pp. 15–17).

[43] BIOMAT Collaboration
High-Energy Irradiation Facility for Biophysics and Materials Research,
Online (December 2017), URL: `http://www.fair-center.eu/en/public/experiment-program/appa-physics/biomat.html` (cit. on p. 15).

[44] FLAIR Collaboration
FLAIR: A Facility for Low-energy Antiproton and Ion Research, Online (November 2017), 2004,
URL: `http://www.flairatfair.eu` (cit. on p. 15).

[45] EFAIR GmbH and GSI
Green Paper, The Modularized Start Version : FAIR - Facility for Antiproton and Ion Research,
tech. rep., FAIR, 2009, URL: `https://repository.gsi.de/record/54094/` (cit. on p. 15).

[46] E. Widmann
Low-energy antiprotons physics and the FLAIR facility,
Physica Scripta **2015**.T166 (2015) 014074 (cit. on p. 16).

[47] T. Stöhlker *et al.*
SPARC collaboration: new strategy for storage ring physics at FAIR,
Hyperfine interactions **227**.1-3 (2014) 45 (cit. on p. 16).

[48] V. Friese
The CBM experiment at GSI/FAIR, Nuclear Physics A **774** (2006) 377 (cit. on p. 16).

[49] CBM Collaboration
Letter of Intent for the Compressed Baryonic Matter Experiment, (2004),
URL: `https://www.researchgate.net/profile/Adam_Kiss2/publication/277290854_The_CBM_Collaboration/links/56e93b1308ae7cb977838953.pdf`
(cit. on p. 16).

[50] *NuSTAR – Experiments*, Online, URL:
`https://fair-center.eu/en/for-users/experiments/nustar/experiments.html`
(cit. on p. 16).

[51] R. Krücken, N. Collaboration *et al.*
The NuSTAR facilty at FAIR,
Journal of Physics G: Nuclear and Particle Physics **31**.10 (2005) S1807 (cit. on p. 16).

[52] H. H. Gutbrod *et al.*
FAIR-Baseline technical report, Volume 2 Accelerator and Scientific Infrastructure, (2006),
URL: `https://repository.gsi.de/record/54068` (cit. on pp. 17–19).

[53] P. Schütt, O. Geithner and P. Forck
FAIR Operation Modes – Reference Modes for the Modularized Start Version (MSV), Apr. 2016,
URL: `https://indico.gsi.de/event/7647/contribution/23/material/0/0.pdf`
(cit. on pp. 18, 20).

[54] R. Maier *et al.*
The high energy storage ring (HESR), Proceedings of PAC2011, New York, USA (2011) 2104,
URL: `https://accelconf.web.cern.ch/AccelConf/PAC2011/papers/thocn2.pdf`
(cit. on p. 19).

[55] G. I. Budker
An effective method of damping particle oscillations in proton and antiproton storage rings,
Soviet Atomic Energy **22**.5 (May 1967) 438, ISSN: 1573-8205,
URL: `https://doi.org/10.1007/BF01175204` (cit. on p. 19).

[56] S. Van der Meer
Stochastic damping of betatron oscillations, The Development of Colliders (1995) 261,
URL: `https://cds.cern.ch/record/312939/files/197200067.pdf` (cit. on p. 20).

[57] A. Lehrach *et al.*
Beam performance and luminosity limitations in the high-energy storage ring (HESR),
Nuclear Instruments and Methods in Physics Research Section A: Accelerators, Spectrometers, Detectors and Associated Equipment **561**.2 (2006) 289 (cit. on p. 20).

[58] W. Erni *et al.*
Physics performance report for PANDA: Strong interaction studies with antiprotons,
arXiv preprint arXiv:0903.3905 (2009), URL: `https://arxiv.org/pdf/0903.3905`
(cit. on pp. 21, 24, 27).

[59] P. Gianotti
Results and perspectives in hadron spectroscopy, Physica Scripta **T150** (Sept. 2012) 014014,
URL: `https://doi.org/10.1088%2F0031-8949%2F2012%2Ft150%2F014014`
(cit. on pp. 22, 25).

[60] S. Godfrey and S. L. Olsen
The exotic XYZ charmonium-like mesons,
Annual Review of Nuclear and Particle Science **58** (2008) 51 (cit. on p. 22).

[61] T. Armstrong *et al.*
Measurement of the $J\,\psi$ *and* $\psi\prime$ *resonance parameters in* $\overline{p}p$ *annihilation*,
Physical Review D **47**.3 (1993) 772 (cit. on p. 22).

[62] G. Garzoglio *et al.*
Experiment E835 at Fermilab, Nuclear Instruments and Methods in Physics Research Section A: Accelerators, Spectrometers, Detectors and Associated Equipment **519**.3 (2004) 558 (cit. on p. 22).

[63] PANDA Collaboration
Technical progress report for: PANDA, (2005),
URL: `https://panda.gsi.de/oldwww/archive/public/panda_tpr.pdf` (cit. on p. 23).

[64] PANDA Collaboration and others
Precision resonance energy scans with the PANDA experiment at FAIR,
The European Physical Journal A **55**.3 (Mar. 2019) 42, ISSN: 1434-601X,
URL: `https://doi.org/10.1140/epja/i2019-12718-2` (cit. on p. 23).

[65] S.-K. Choi *et al.*
Observation of a narrow charmoniumlike state in exclusive $B\pm\longrightarrow K\pm\pi+\ \pi-\ J/\psi$ *decays*,
Physical review letters **91**.26 (2003) 262001 (cit. on p. 23).

[66] C. Patrignani
Exotic hadrons at LHCb, tech. rep., 2017,
URL: `http://cds.cern.ch/record/2292497/files/patrignani-LHCb-EMMI.pdf` (cit. on p. 23).

[67] M. Alford and R. Jaffe
Insight into the scalar mesons from a lattice calculation, Nuclear Physics B **578**.1-2 (2000) 367 (cit. on p. 23).

[68] L. Maiani *et al.*
Diquark-antidiquark states with hidden or open charm and the nature of X (3872),
Physical Review D **71**.1 (2005) 014028 (cit. on p. 23).

[69] Z. Liu *et al.*
Study of $e+\ e-\longrightarrow\pi+\ \pi-\ J/\psi$ *and Observation of a Charged Charmoniumlike State at Belle*,
Physical review letters **110**.25 (2013) 252002 (cit. on p. 23).

[70] M. Ablikim *et al.*
Observation of a Charged Charmoniumlike Structure in $e+\ e-\longrightarrow\pi+\ \pi-\ J/\psi$ *at* $s=4.26$ *GeV*,
Physical review letters **110**.25 (2013) 252001 (cit. on p. 23).

[71] P. Adlarson *et al.*
Evidence for a new resonance from polarized neutron-proton scattering,
Physical review letters **112**.20 (2014) 202301 (cit. on p. 23).

[72] A. Chodos *et al.*
Baryon structure in the bag theory, Phys. Rev. D **10** (8 Oct. 1974) 2599,
URL: `https://link.aps.org/doi/10.1103/PhysRevD.10.2599` (cit. on p. 23).

[73] J. Paton
The flux tube model, Nuclear Physics. A **446**.1/2 (1985) 419 (cit. on p. 23).

[74] D. Horn and J. Mandula
Model of mesons with constituent gluons, Physical Review D **17**.3 (1978) 898 (cit. on p. 23).

[75] P. Chen, X. Liao and T. Manke
Relativistic quarkonia from anisotropic lattices,
Nuclear Physics B-Proceedings Supplements **94**.1-3 (2001) 342 (cit. on p. 23).

[76] C. Michael
Quarkonia and hybrids from the lattice, arXiv preprint hep-ph/9911219 (1999) (cit. on p. 23).

[77] C. J. Morningstar and M. Peardon
Glueball spectrum from an anisotropic lattice study, Physical Review D **60**.3 (1999) 034509 (cit. on p. 24).

[78] P. R. Page
"Multi - GeV gluonic mesons", *Low-energy anti-p storage ring. Proceedings, Workshop, anti-p 2000, Chicago, USA, August 3-5, 2000*, 2001 55, arXiv: `hep-ph/0107016 [hep-ph]`,
URL: `https://arxiv.org/pdf/hep-ph/0107016.pdf` (cit. on p. 24).

[79] R. T. Jones
Partial wave analysis results from JETSET, Talk at Gluonic Excitations Workshop,
JLab, May 2003, URL: `https://www.jlab.org/gluonic2003/talks/RJones.pdf`
(cit. on p. 24).

[80] F. Nichitiu *et al.*
Study of the K^+ K^- π^+ π^- π^0 final state in antiproton annihilation at rest in gaseous hydrogen at NTP with the OBELIX spectrometer, Physics Letters B **545**.3-4 (2002) 261 (cit. on p. 24).

[81] A. Bertin et al.
A search for axial vectors in $pp \to K^{\pm}K^{0}_{miss}\pi^{\mp}\pi^{+}\pi^{-}$ annihilations at rest in gaseous hydrogen at NTP, Physics Letters B **400**.1 (1997) 226, ISSN: 0370-2693,
URL: `http://www.sciencedirect.com/science/article/pii/S0370269397003006`
(cit. on p. 24).

[82] A. De Rujula, H. Georgi and S. Glashow
Charm spectroscopy via electron-positron annihilation,
Physical Review Letters **37**.12 (1976) 785 (cit. on p. 24).

[83] B. Aubert *et al.*
Observation of a Narrow Meson State Decaying to $D_s^+\pi^0$ at a Mass of 2.32 GeV/c^2,
Physical Review Letters **90**.24 (2003) 242001 (cit. on p. 24).

[84] S.-K. Choi *et al.*
*Measurements of $B \to \bar{D}^- D*^{+}_{s0}$(2317) decay rates and a search for isospin partners of the $D *^{+}_{s0}$ *(2317)*, Physical Review D **91**.9 (2015) 092011 (cit. on p. 24).

[85] S. Godfrey and N. Isgur
Mesons in a relativized quark model with chromodynamics, Physical Review D **32**.1 (1985) 189 (cit. on p. 25).

[86] M. Di Pierro and E. Eichten
Excited heavy-light systems and hadronic transitions, Physical Review D **64**.11 (2001) 114004,
URL: `https://arxiv.org/pdf/hep-ph/0104208` (cit. on p. 25).

[87] M. C. Mertens, P. collaboration *et al.*
Determination of the D_s0^*(2317) width with the PANDA detector,
Hyperfine Interactions **209**.1-3 (2012) 111 (cit. on p. 24).

[88] F.-K. Guo *et al.*
Subleading contributions to the width of the D^*_{s0}(2317), Physics Letters B **666**.3 (2008) 251 (cit. on p. 24).

[89] E. Klempt
Mass formula for baryon resonances, Physical Review C **66**.5 (2002) 058201 (cit. on p. 24).

[90] I. Zychor *et al.*
Evidence for an Excited Hyperon State in $pp \to pK^+Y^{0*}$,
Physical review letters **96**.1 (2006) 012002,
URL: `https://link.aps.org/pdf/10.1103/PhysRevLett.96.012002` (cit. on p. 25).

[91] M. Adamovich *et al.*
Observation of a resonance in the K_S p decay channel at a mass of 1765 MeV/c^2,
The European Physical Journal C **50**.3 (2007) 535 (cit. on p. 25).

[92] U. Löring, B. C. Metsch and H. R. Petry
The light-baryon spectrum in a relativistic quark model with instanton-induced quark forces,
The European Physical Journal A-Hadrons and Nuclei **10**.4 (2001) 395 (cit. on p. 25).

[93] V. Guzey and M. Polyakov
SU (3) systematization of baryons, arXiv preprint hep-ph/0512355 (2005),
URL: `https://arxiv.org/pdf/hep-ph/0512355` (cit. on p. 25).

[94] M. Diehl
Generalized parton distributions, Physics Reports **388**.2-4 (2003) 41 (cit. on p. 26).

[95] B. Singh *et al.*
Feasibility study for the measurement of π N transition distribution amplitudes at $\overline{\text{P}}$ANDA in $\bar{p}p\to J/\psi\ \pi$ 0, Physical Review D **95**.3 (2017) 032003 (cit. on p. 26).

[96] J. Lees *et al.*
Measurement of the e+ e-→ p $\bar{p}$ cross section in the energy range from 3.0 to 6.5 GeV,
Physical Review D **88**.7 (2013) 072009,
URL: `https://link.aps.org/pdf/10.1103/PhysRevD.88.072009` (cit. on p. 26).

[97] G. Bardin *et al.*
Determination of the electric and magnetic form factors of the proton in the time-like region,
Nuclear Physics B **411**.1 (1994) 3 (cit. on p. 26).

[98] M. Ablikim *et al.*
Measurement of the proton form factor by studying e+ e-→ p $\bar{p}$,
Physical Review D **91**.11 (2015) 112004,
URL: `https://link.aps.org/pdf/10.1103/PhysRevD.91.112004` (cit. on p. 26).

[99] PANDA Collaboration
Feasibility studies of time-like proton electromagnetic form factors at $\overline{\text{P}}$ANDA at FAIR,
The European Physical Journal A **52**.10 (Nov. 2016) 325, ISSN: 1434-601X,
URL: `https://doi.org/10.1140/epja/i2016-16325-5` (cit. on p. 26).

[100] M. Danysz *et al.*
Observation of a double hyperfragment, Physical Review Letters **11**.1 (1963) 29 (cit. on p. 26).

[101] N. Kaiser and W. Weise
Chiral SU (3) dynamics and Λ hyperons in the nuclear medium 1,
Physical Review C **71**.1 (2005) 015203 (cit. on p. 26).

[102] J. Pochodzalla
Future hypernuclear physics at MAMI-C and PANDA-GSI, Nuclear Physics A **754** (2005) 430 (cit. on p. 27).

[103] PANDA Collaboration
RN-DET-2017-001: General PANDA material, Release Note (cit. on p. 28).

[104] PANDA Collaboration and others
Technical Design Report for the PANDA Internal Targets: The Cluster-Jet Target and Developments for the Pellet Target, 2012, URL: `https://panda.gsi.de/system/files/user_uploads/u.kurilla/RE-TDR-2012-002.pdf` (cit. on pp. 28, 29).

[105] A. Boukharov *et al.*
Dynamics of cryogenic jets: Non-rayleigh breakup and onset of nonaxisymmetric motions, Physical review letters **100**.17 (2008) 174505 (cit. on p. 29).

[106] W. Erni *et al.*
Technical design report for the panda solenoid and dipole spectrometer magnets, arXiv preprint arXiv:0907.0169 (2009), URL: `https://arxiv.org/abs/0907.0169` (cit. on p. 29).

[107] PANDA Collaboration
Technical design report for the: PANDA Micro Vertex Detector, 2011, URL: `https://panda.gsi.de/system/files/user_uploads/u.kurilla/RE-TDR-2011-001.pdf` (cit. on pp. 30, 31).

[108] PANDA Collaboration
Technical Design Report for the: PANDA Straw Tube Tracker, arXiv preprint arXiv:1205.5441 (2012) (cit. on pp. 30, 33).

[109] PANDA Collaboration and others
Technical Design Report for the PANDA Forward Tracker, 2018, URL: `https://panda.gsi.de/system/files/user_uploads/admin/RE-TDR-2017-001.pdf` (cit. on pp. 30, 33, 34).

[110] F. Hugging
"Development of a Micro Vertex Detector for the PANDA-Experiment at the FAIR Facility", *2006 IEEE Nuclear Science Symposium Conference Record*, vol. 2, IEEE, 2006 1239 (cit. on p. 31).

[111] D. Grunwald, Private Communication (cit. on p. 31).

[112] T. Quagli
Hardware developments for the strip detector of the PANDA MVD, (2015), URL: `http://geb.uni-giessen.de/geb/volltexte/2015/11820/` (cit. on p. 31).

[113] F. Sauli
The gas electron multiplier (GEM): Operating principles and applications, Nuclear Instruments and Methods in Physics Research Section A: Accelerators, Spectrometers, Detectors and Associated Equipment **805** (2016) 2 (cit. on p. 33).

[114] D. Melnychuk, B. Voss and B. Zwieglinski
Study of resolution of the PANDA GEM detector with Garfield, Hyperfine Interactions **229**.1-3 (2014) 165 (cit. on p. 33).

[115] J. Schwiening
Technical Design Report for the PANDA Barrel DIRC Detector,
Journal of Physics G: Nuclear and Particle Physics (2018) (cit. on p. 35).

[116] K. Föhl *et al.*
The Endcap Disc DIRC detector of PANDA, Nuclear Instruments and Methods in Physics Research Section A: Accelerators, Spectrometers, Detectors and Associated Equipment (2018) (cit. on p. 35).

[117] M. Düren *et al.*
The Endcap Disc DIRC of PANDA, Nuclear Instruments and Methods in Physics Research Section A: Accelerators, Spectrometers, Detectors and Associated Equipment **876** (2017) 198, The 9th international workshop on Ring Imaging Cherenkov Detectors (RICH2016),
ISSN: 0168-9002,
URL: `http://www.sciencedirect.com/science/article/pii/S0168900217302772`
(cit. on p. 35).

[118] PANDA Collaboration
Technical design report for the: PANDA Barrel Time of Flight, 2018,
URL: `https://panda.gsi.de/system/files/user_uploads/ken.suzuki/RE-TDR-2016-003_0.pdf` (cit. on pp. 35, 36).

[119] PANDA Collaboration
Technical design report for the: PANDA Forward Time of Flight (FToF wall), 2018, URL:
`https://panda.gsi.de/system/files/user_uploads/admin/RE-TDR-2016-004.pdf`
(cit. on p. 36).

[120] PANDA collaboration and others
Technical Design Report for the PANDA Muon System, 2012, URL: `https://panda.gsi.de/system/files/user_uploads/u.kurilla/RE-TDR-2012-003.pdf`
(cit. on p. 37).

[121] W. Erni *et al.*
Technical Design Report for PANDA Electromagnetic Calorimeter (EMC),
arXiv preprint arXiv:0810.1216 (2008), URL: `https://arxiv.org/pdf/0810.1216.pdf`
(cit. on pp. 37, 38).

[122] PANDA collaboration and others
Technical Design Report for the Panda Forward Spectrometer Calorimeter,
arXiv preprint arXiv:1704.02713 (2017), URL: `https://arxiv.org/pdf/1704.02713.pdf`
(cit. on pp. 38, 39).

[123] PANDA Collaboration
Technical Design Report for the PANDA Luminosity Detector, tech. rep., 2017 (cit. on p. 39).

[124] R. Brun and F. Rademakers
ROOT—an object oriented data analysis framework,
Nuclear Instruments and Methods in Physics Research Section A: Accelerators, Spectrometers, Detectors and Associated Equipment **389**.1-2 (1997) 81 (cit. on p. 40).

[125] I. Hrivnacova *et al.*
The virtual monte carlo, arXiv preprint cs/0306005 (2003),
URL: `https://arxiv.org/abs/cs/0306005` (cit. on p. 40).

[126] M. Al-Turany *et al.*
"The FAIRROOT framework", *Journal of Physics: Conference Series*, vol. 396, 2, IOP Publishing, 2012 022001 (cit. on p. 40).

[127] S. Spataro
"The PandaRoot framework for simulation, reconstruction and analysis", *Journal of Physics: Conference Series*, vol. 331, 3, IOP Publishing, 2011 032031 (cit. on pp. 40, 44).

[128] C. Höppner *et al.*
A novel generic framework for track fitting in complex detector systems, Nuclear Instruments and Methods in Physics Research Section A: Accelerators, Spectrometers, Detectors and Associated Equipment **620**.2-3 (2010) 518 (cit. on p. 40).

[129] A. Fontana *et al.*
"Use of GEANE for tracking in virtual Monte Carlo", *Journal of Physics: Conference Series*, vol. 119, 3, IOP Publishing, 2008 032018 (cit. on p. 40).

[130] M. Kunze
Rho analysis framework, online, Jan. 2014, URL: `https://github.com/marcelkunze/rhoframework` (cit. on p. 41).

[131] M. Sumihama *et al.*
Observation of $\Xi\,(1620)^0$ *and evidence for* $\Xi\,(1690)^0$ *in* $\Xi_c^+ \to \Xi^-\pi^+\pi^+$ *decays*, arXiv preprint arXiv:1810.06181 (2018), URL: `https://arxiv.org/abs/1810.06181` (cit. on p. 44).

[132] D. J. Lange
The EvtGen particle decay simulation package, Nuclear Instruments and Methods in Physics Research Section A: Accelerators, Spectrometers, Detectors and Associated Equipment **462**.1 (2001) 152 (cit. on pp. 44, 285).

[133] W. D. Hulsbergen
Decay chain fitting with a Kalman filter, Nuclear Instruments and Methods in Physics Research Section A: Accelerators, Spectrometers, Detectors and Associated Equipment **552**.3 (2005) 566, ISSN: 0168-9002 (cit. on p. 45).

[134] J. Rauch and T. Schlüter
"GENFIT–a Generic Track-Fitting Toolkit", vol. 608, 1, IOP Publishing, 2015 012042 (cit. on pp. 49, 285).

[135] A. Lai
Development of a Data Acquisition System for the Custom Front-End Prototypes of the PANDA Micro Vertex Detector and Study of the Reaction pp -> $\Xi^-\bar{\Xi}^+\pi^+\pi^-$, (2018) (cit. on pp. 49, 50).

[136] R. H. Dalitz
CXII. On the analysis of τ*-meson data and the nature of the* τ*-meson*, The London, Edinburgh, and Dublin Philosophical Magazine and Journal of Science **44**.357 (1953) 1068, ISSN: 1941-5982 (cit. on p. 69).

[137] N. Temme
Voigt function, NIST Handbook of Mathematical Functions; Olver Frank, WJ, Lozier, DM, Boisvert, RF, Eds (2010) (cit. on p. 70).

[138] A. Capella
"Introduction to the Dual Parton Model", *Perspectives in the Structure of Hadronic Systems*, ed. by M. N. Harakeh, J. H. Koch and O. Scholten, Boston, MA: Springer US, 1994 287, ISBN: 978-1-4615-2558-5, URL: `https://doi.org/10.1007/978-1-4615-2558-5_12` (cit. on p. 94).

[139] B. Kopf and M. Albrecht
PAWIAN (PArtial Wave Interactive ANalysis), Online, website, June 2019, URL: `https://www.ep1.ruhr-uni-bochum.de/en/research/partial-wave-analysis/` (cit. on p. 101).

[140] Julian Pychy
Gekoppelte Partialwellenanalyse von $\bar{p}p$ -Annihilationen im Fluge in die Endzustände $K^+K^-\pi^0$, $\pi^0\pi^0\eta$ und $\pi^0\eta\eta$, PhD thesis: Ruhr-Universität Bochum, Apr. 2016, URL: `https://www.ep1.rub.de/wp-content/uploads/DissJulianPychy.pdf` (cit. on pp. 102, 103, 106–108, 112, 116).

[141] K. Peters
A Primer on partial wave analysis, International Journal of Modern Physics A **21**.27 (2006) 5618, ISSN: 0217-751X, URL: `https://arxiv.org/abs/hep-ph/0412069` (cit. on pp. 103, 104, 108).

[142] A. Pais
Notes on antibaryon interactions, Physical Review Letters **3**.5 (1959) 242 (cit. on p. 104).

[143] S. U. Chung
Spin formalisms, tech. rep., 2014, URL: `http://suchung.web.cern.ch/suchung/spinfm1.pdf` (cit. on pp. 104–106, 110, 111).

[144] J. D. Richman
An experimenter's guide to the helicity formalism, tech. rep., 1984, URL: `http://cds.cern.ch/record/153636/files/cer-000064884.pdf` (cit. on p. 105).

[145] H. Koch
Helicity Amplitude for pp -> $\omega\pi^0$, ω -> $\pi^0\gamma$, (2011), URL: `https://panda-wiki.gsi.de/foswiki/pub/PWA/HelicityFormalism/helAmpPbarPKochv3.pdf` (cit. on p. 107).

[146] U. Fano
Description of states in quantum mechanics by density matrix and operator techniques, Reviews of Modern Physics **29**.1 (1957) 74 (cit. on p. 109).

[147] K. Blum
Density Matrix Theory and Applications, Springer, 2012 (cit. on p. 109).

[148] H. Koch
J^P-determination from decay chains, v1, (2011), URL: `https://panda-wiki.gsi.de/foswiki/pub/PWA/HelicityFormalism/JPdeterminationKoch.pdf` (cit. on p. 110).

[149] K. Gottfried and J. D. Jackson
On the connection between production mechanism and decay of resonances at high energies, Il Nuovo Cimento (1955-1965) **33**.2 (1964) 309 (cit. on pp. 110, 111).

[150] S. Deen
Generalised partial wave analysis, RPP/H/86, (unpublished), RHEL (cit. on p. 111).

[151] F. James and M. Roos
MINUIT: a system for function minimization and analysis of the parameter errors and corrections, Comput. Phys. Commun. **10**.CERN-DD-75-20 (1975) 343 (cit. on pp. 113, 286).

[152] R. Fletcher and M. J. Powell
A rapidly convergent descent method for minimization, The computer journal **6**.2 (1963) 163 (cit. on p. 113).

[153] R. Fletcher
A new approach to variable metric algorithms, The computer journal **13**.3 (1970) 317 (cit. on p. 113).

[154] K. P. Burnham and D. R. Anderson
Multimodel inference: understanding AIC and BIC in model selection, Sociological methods & research **33**.2 (2004) 261 (cit. on pp. 113, 114).

[155] G. Schwarz *et al.*
Estimating the dimension of a model, The annals of statistics **6**.2 (1978) 461, URL: `https://projecteuclid.org/euclid.aos/1176344136` (cit. on p. 114).

[156] A. Raftery
Bayesian Model Selection in Social Research (With Discussion by Andre B. Xelman, and Donald B. Rubin, and Robert M. Hauser, and a Rejoinder), (1995), URL: `https://www.stat.washington.edu/sites/default/files/Other%20Online/bic.pdf` (cit. on p. 114).

[157] Bertram Kopf, private Communication (cit. on pp. 114, 116, 137).

[158] S. Agostinelli *et al.*
GEANT4–a simulation toolkit, Nuclear instruments and methods in physics research section A: Accelerators, Spectrometers, Detectors and Associated Equipment **506**.3 (2003) 250, ISSN: 0168-9002 (cit. on p. 285).

APPENDIX A

Additional Figures for the Study of the Ξ Resonances

A.1 Analysis of $\bar{p}p \rightarrow \overline{\Xi}^+ \Lambda K^-$ with the Sequential Fit Procedure

A.1.1 Final State Particles

π^+ from $\bar{\Lambda}$

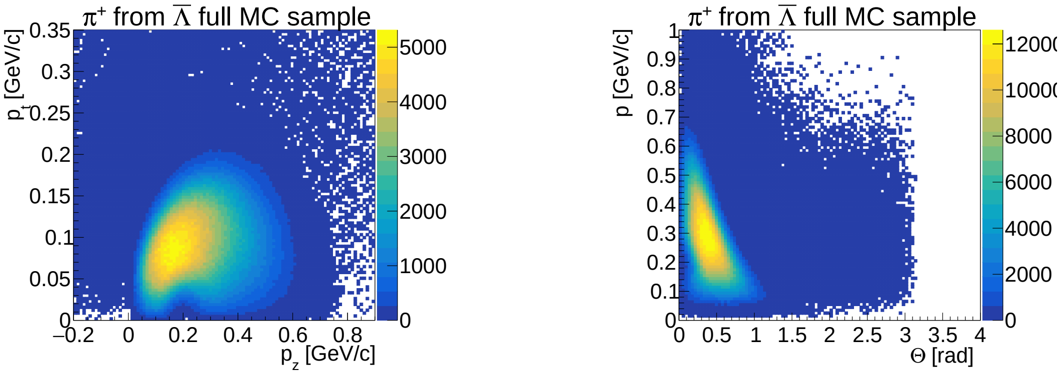

(a) (b)

Figure A.1: Transverse versus longitudinal momentum (a) and total momentum vs. Θ angle (b) for generated π^+ from $\bar{\Lambda}$.

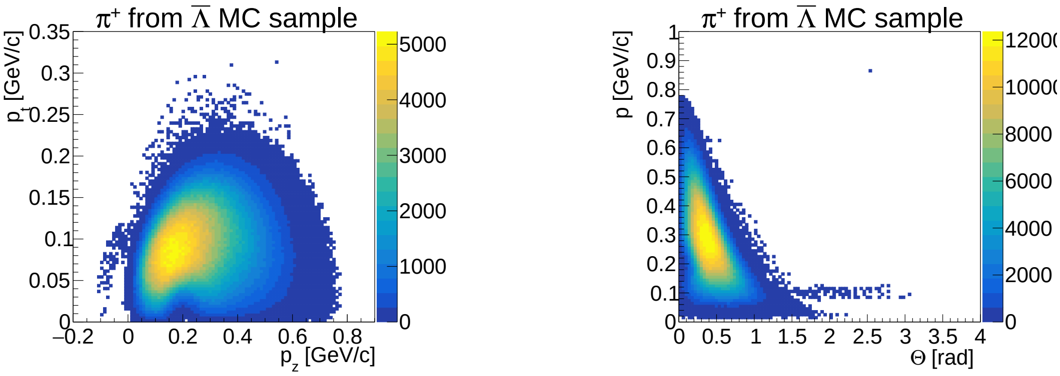

(a) (b)

Figure A.2: Transverse versus longitudinal momentum (a) and total momentum vs. Θ angle (b) for generated π^+ from $\bar{\Lambda}$ requesting that $\bar{\Lambda}$ and $\overline{\Xi}^+$ have only two daughters.

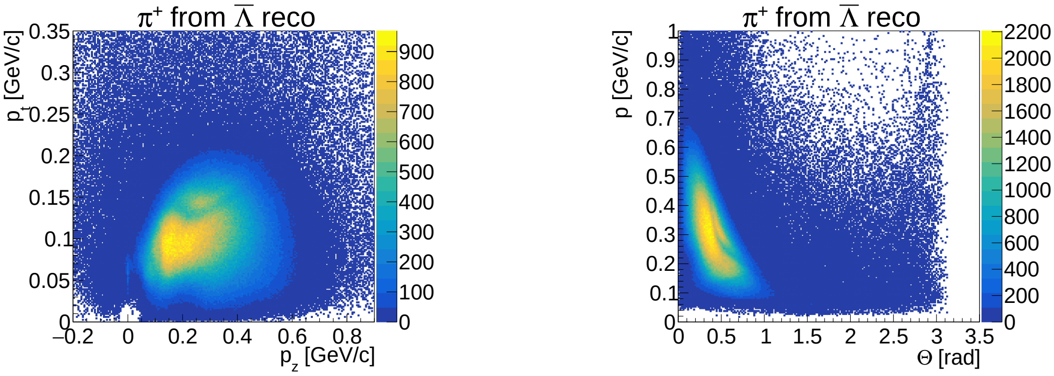

(a) (b)

Figure A.3: Transverse versus longitudinal momentum (a) and total momentum vs. Θ angle (b) for reconstructed π^+ from $\bar{\Lambda}$.

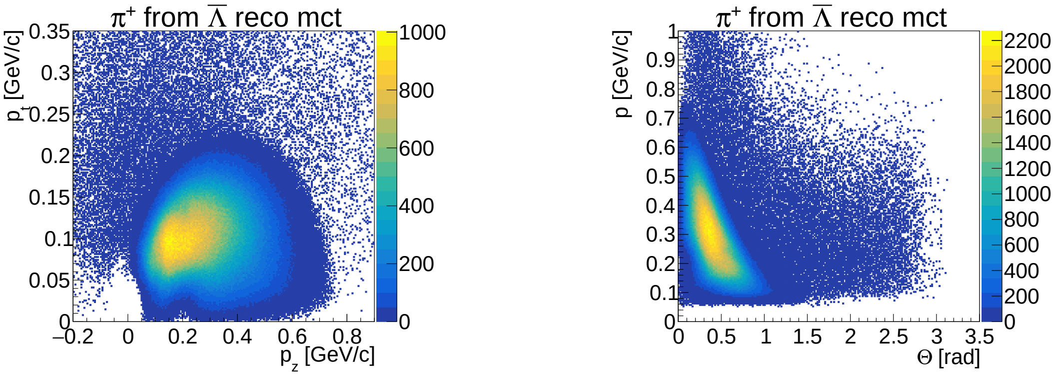

(a) (b)

Figure A.4: Transverse versus longitudinal momentum (a) and total momentum vs. Θ angle (b) for MC partner of reconstructed π^+ from $\bar{\Lambda}$.

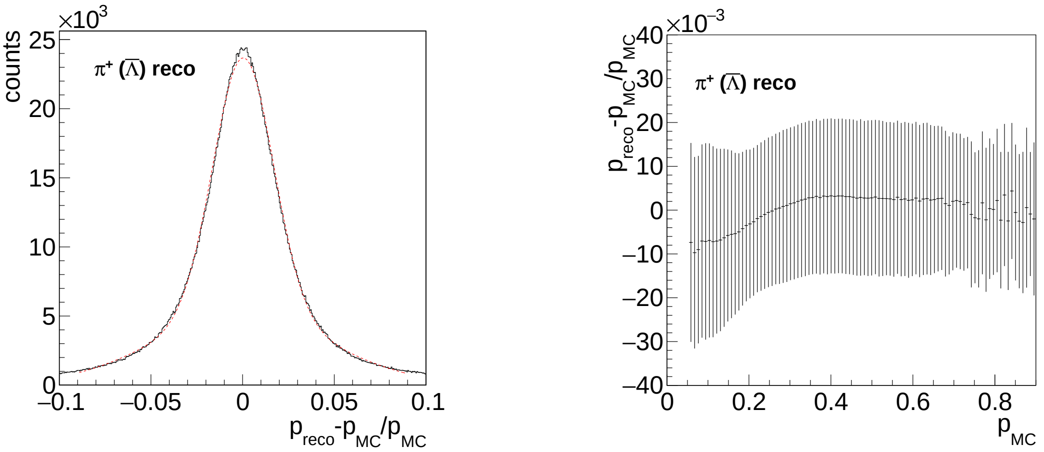

(a)

(b)

Figure A.5: Momentum resolution (a) and relative deviation of the reconstructed and generated total momentum (b) for π^+ from $\bar{\Lambda}$.

π^+ from $\overline{\Xi}^+$

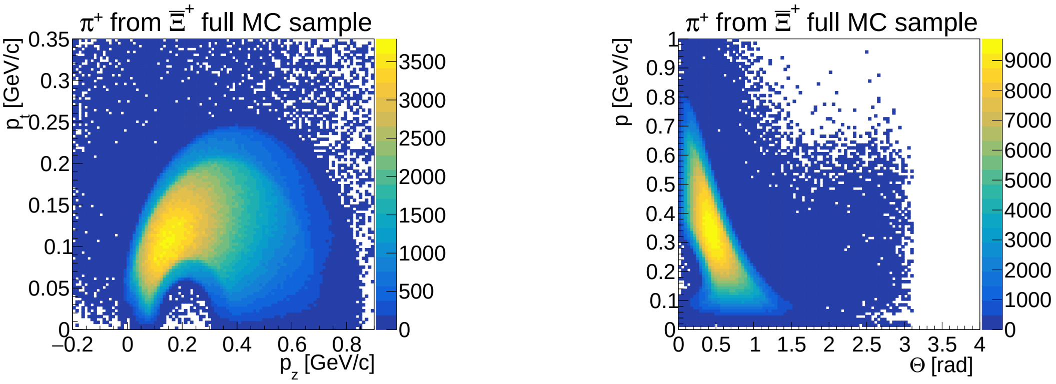

(a)

(b)

Figure A.6: Transverse versus longitudinal momentum (a) and total momentum vs. Θ angle (b) for generated π^+ from $\overline{\Xi}^+$.

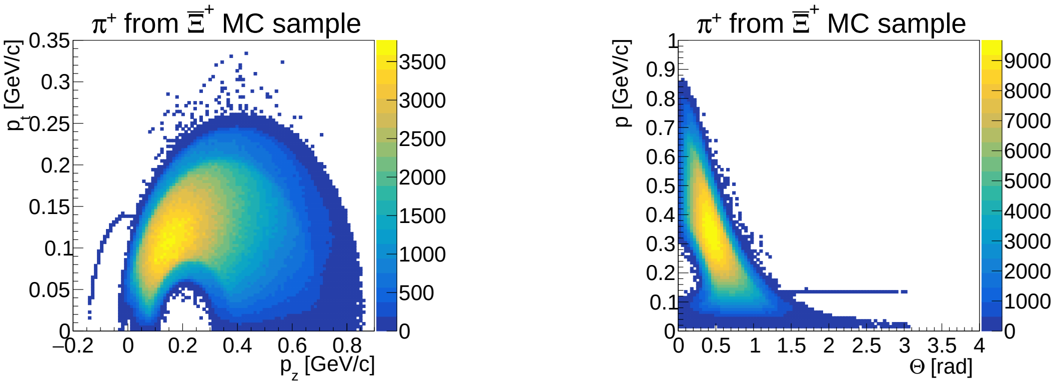

(a) (b)

Figure A.7: Transverse versus longitudinal momentum (a) and total momentum vs. Θ angle (b) for generated π^+ from $\overline{\Xi}^+$ requesting that $\overline{\Xi}^+$ and $\overline{\Xi}^+$ have only two daughters.

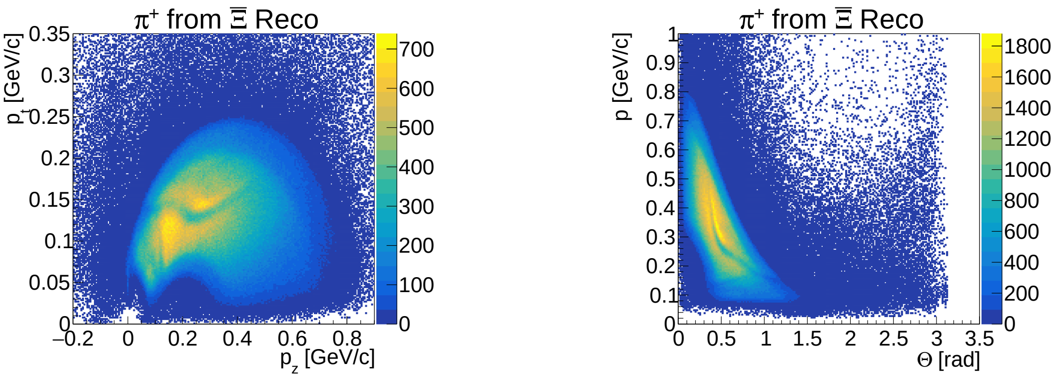

(a) (b)

Figure A.8: Transverse versus longitudinal momentum (a) and total momentum vs. Θ angle (b) for reconstructed π^+ from $\overline{\Xi}^+$.

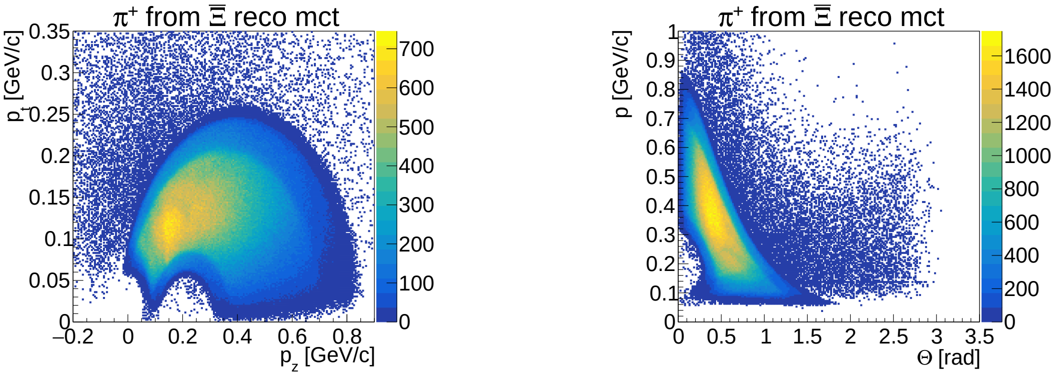

(a) (b)

Figure A.9: Transverse versus longitudinal momentum (a) and total momentum vs. Θ angle (b) for MC partner of reconstructed π^+ from $\overline{\Xi}^+$.

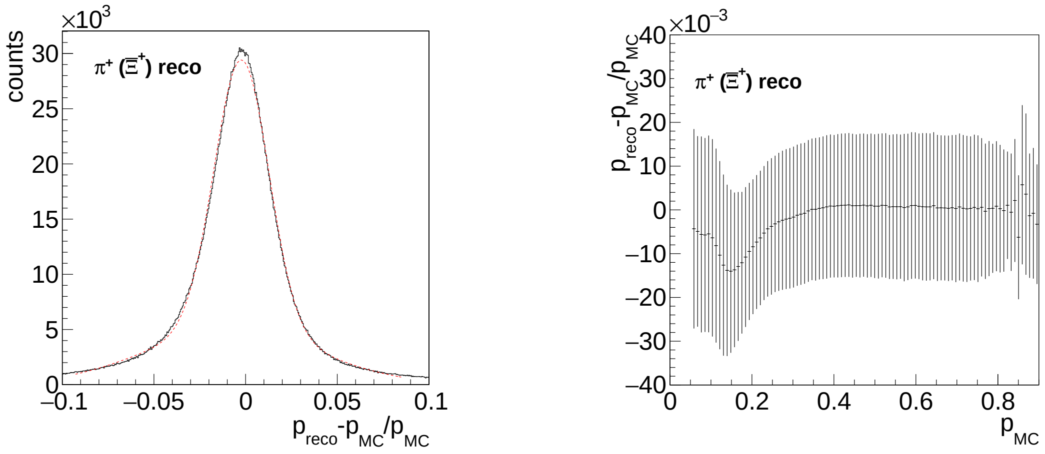

(a)

(b)

Figure A.10: Momentum resolution (a) and relative deviation of the reconstructed and generated total momentum (b) for π^{+} from $\bar{\Xi}^{+}$.

K⁻ from Ξ*

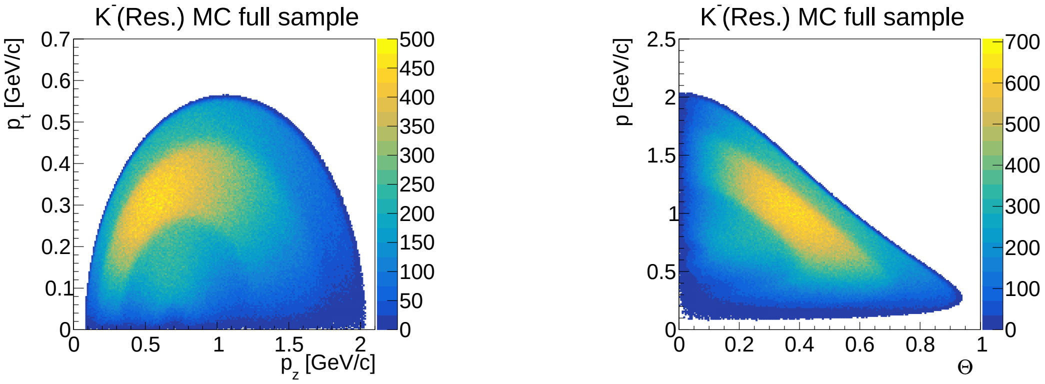

(a)

(b)

Figure A.11: Transverse versus longitudinal momentum (a) and total momentum vs. Θ angle (b) for generated K^{-} from Ξ^{*}.

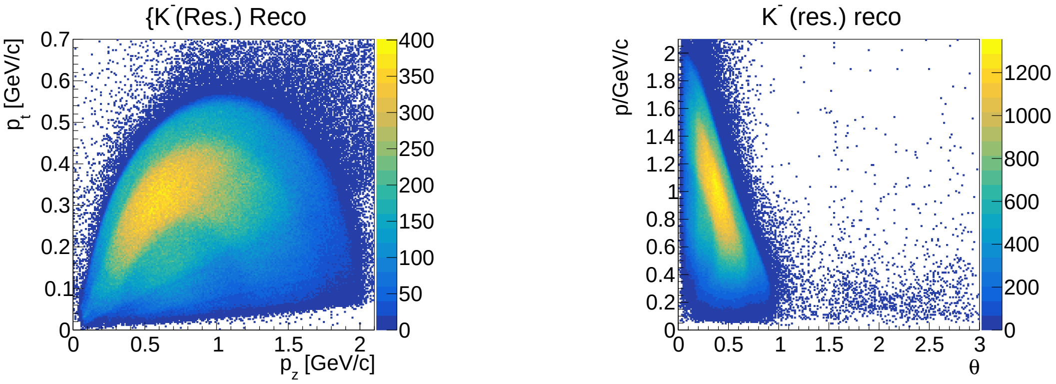

(a) (b)

Figure A.12: Transverse versus longitudinal momentum (a) and total momentum vs. Θ angle (b) for reconstructed K⁻ from Ξ*.

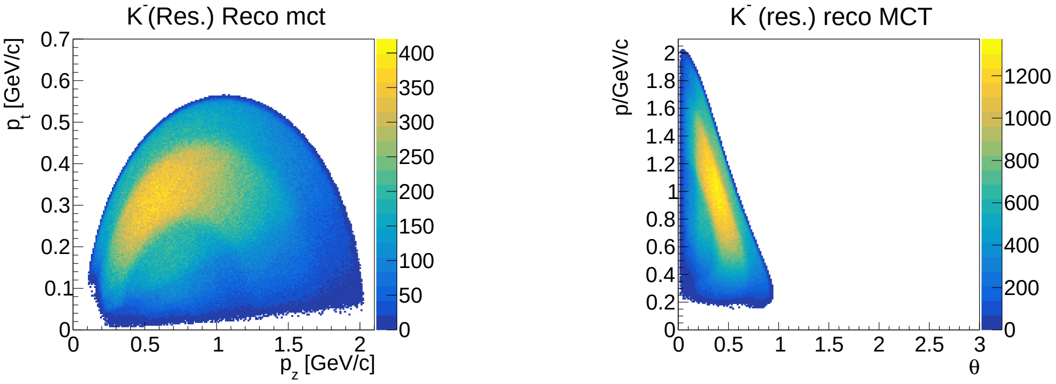

(a) (b)

Figure A.13: Transverse versus longitudinal momentum (a) and total momentum vs. Θ angle (b) for MC partner of reconstructed K⁻ from Ξ*.

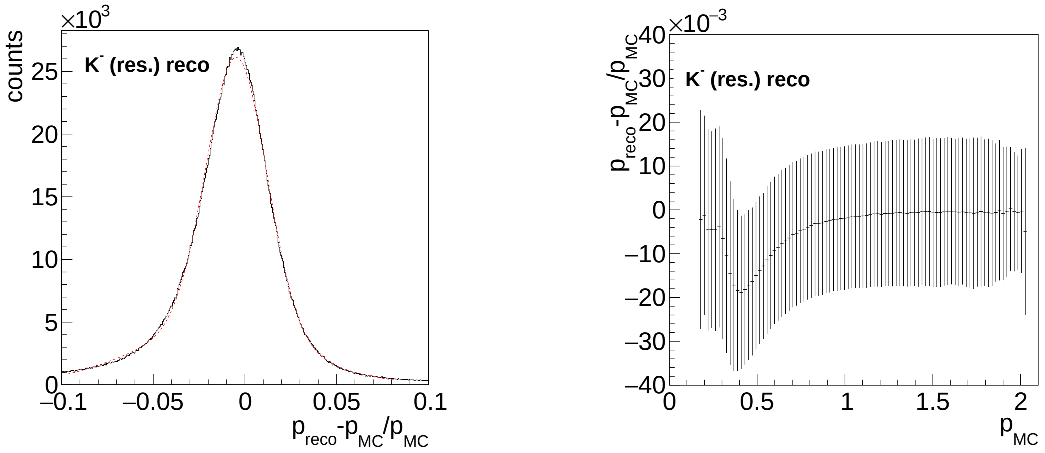

(a) (b)

Figure A.14: Momentum resolution (a) and relative deviation of the reconstructed and generated total momentum (b) for K⁻ from Ξ*.

K^- from Continuum

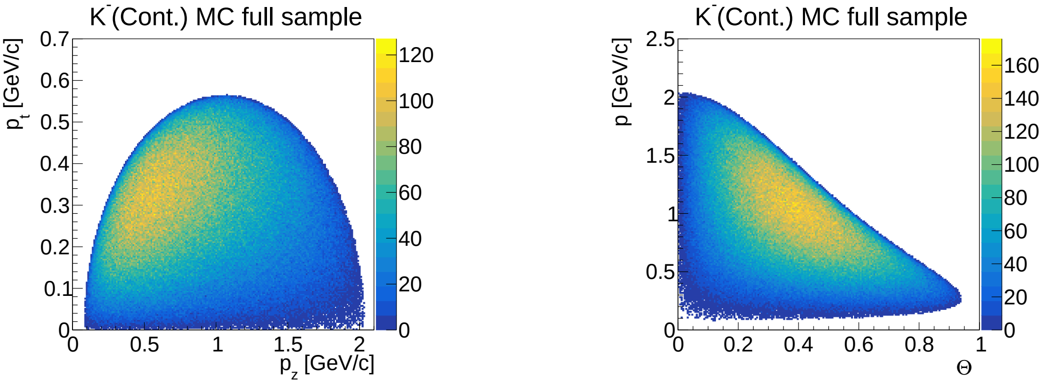

(a)

(b)

Figure A.15: Transverse versus longitudinal momentum (a) and total momentum vs. Θ angle (b) for generated K^- from continuum.

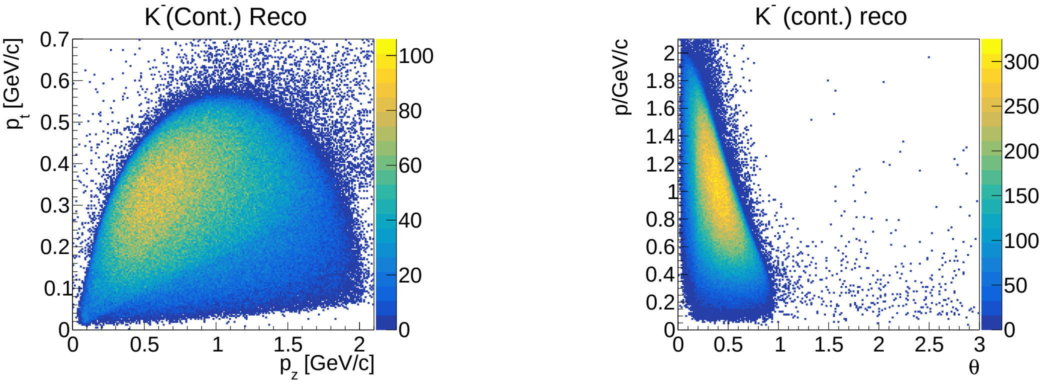

(a)

(b)

Figure A.16: Transverse versus longitudinal momentum (a) and total momentum vs. Θ angle (b) for reconstructed K^- from continuum.

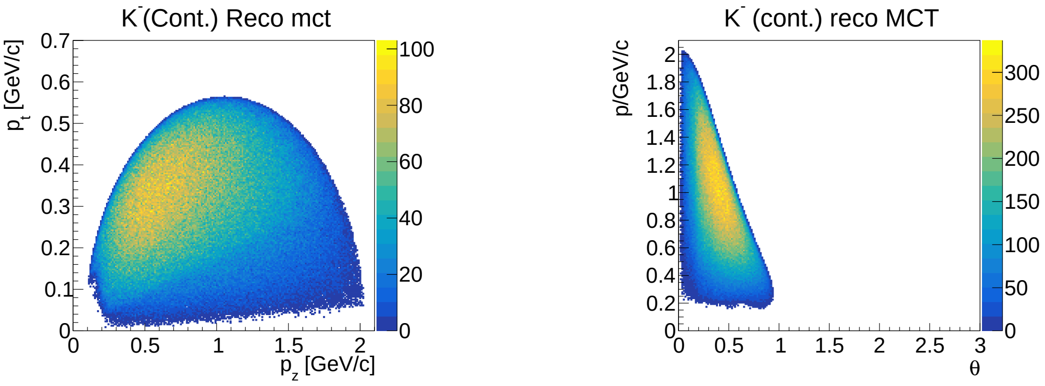

(a)

(b)

Figure A.17: Transverse versus longitudinal momentum (a) and total momentum vs. Θ angle (b) for MC partner of reconstructed K^- from continuum.

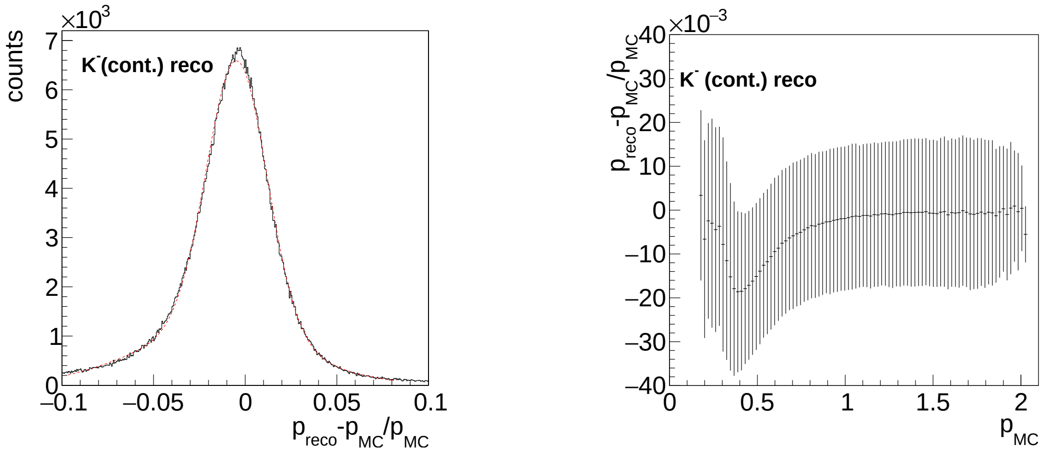

(a)

(b)

Figure A.18: Momentum resolution (a) and relative deviation of the reconstructed and generated total momentum (b) for K^- from continuum.

p and $\overline{\text{p}}$

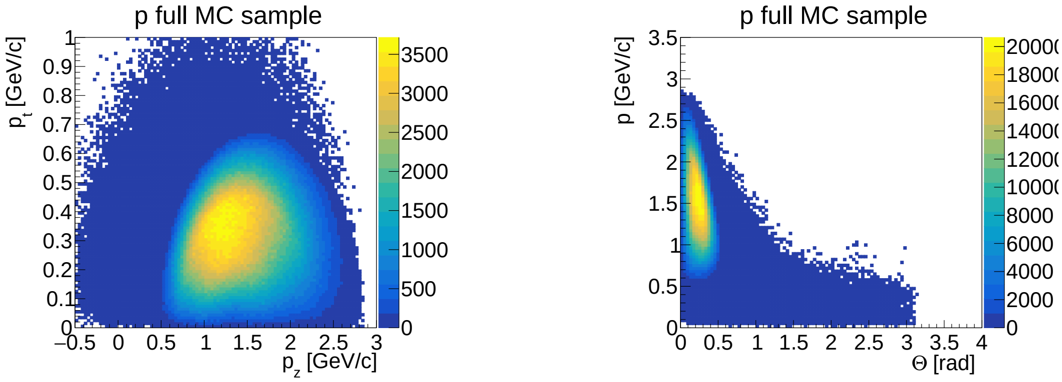

(a)

(b)

Figure A.19: Transverse versus longitudinal momentum (a) and total momentum vs. Θ angle (b) for generated p from Λ.

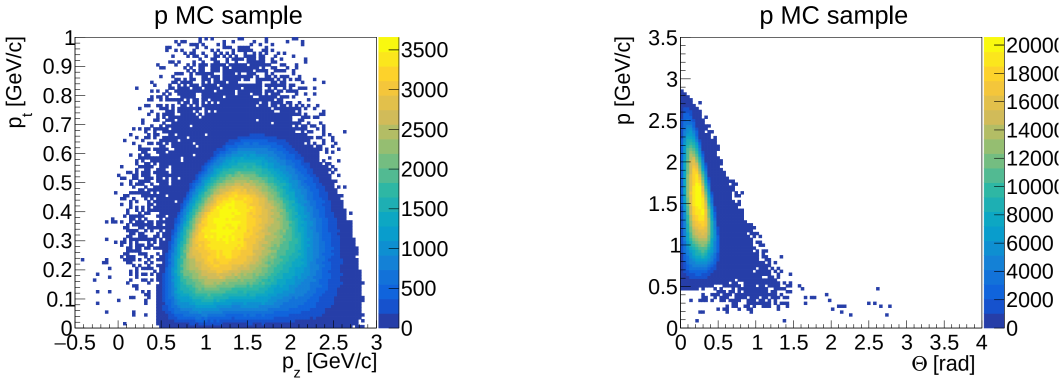

(a)

(b)

Figure A.20: Transverse versus longitudinal momentum (a) and total momentum vs. Θ angle (b) for generated p from Λ requesting that Λ and $\overline{\Xi}^{+}$ have only two daughters.

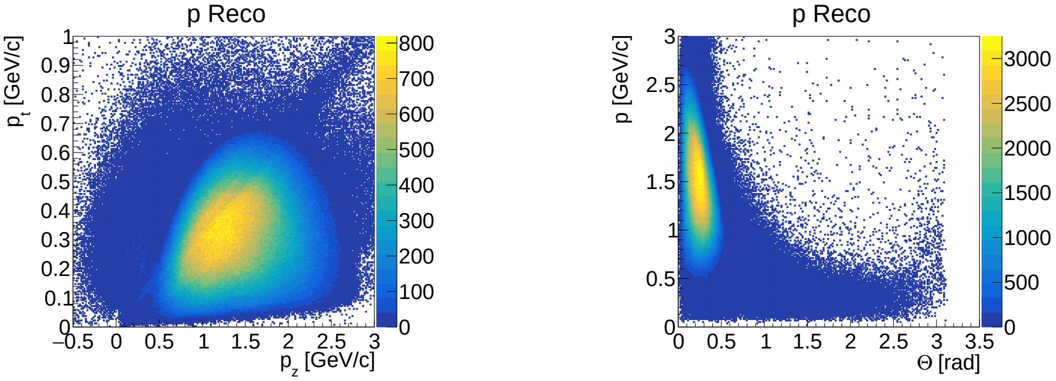

(a) (b)

Figure A.21: Transverse versus longitudinal momentum (a) and total momentum vs. Θ angle (b) for reconstructed p as daughter of Λ.

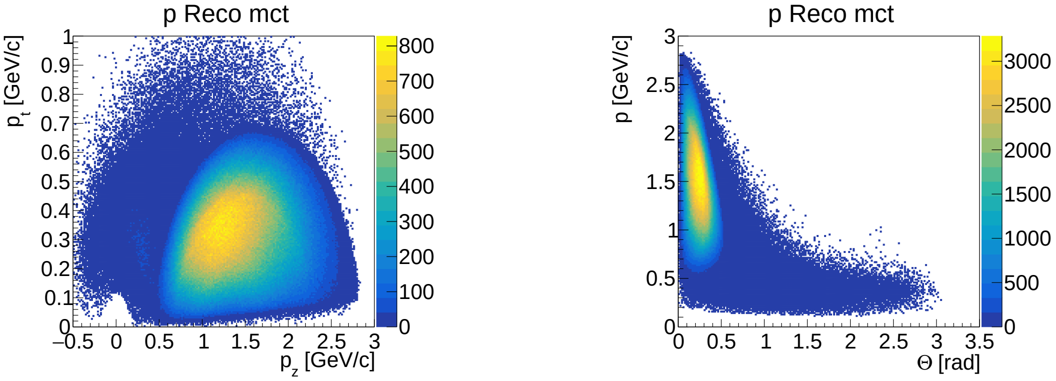

(a) (b)

Figure A.22: Transverse versus longitudinal momentum (a) and total momentum vs. Θ angle (b) for MC partner of reconstructed p from Λ.

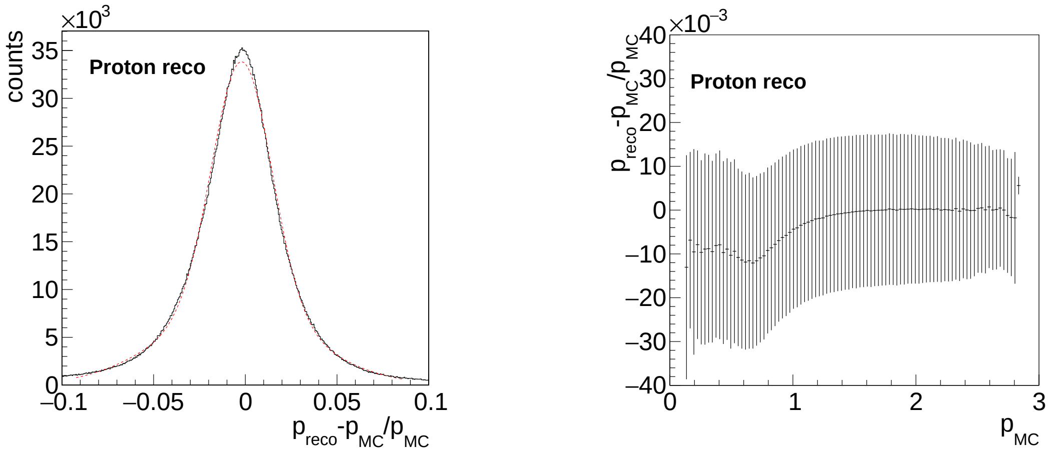

(a) (b)

Figure A.23: Momentum resolution (a) and relative deviation of the reconstructed and generated total momentum (b) for p from Λ.

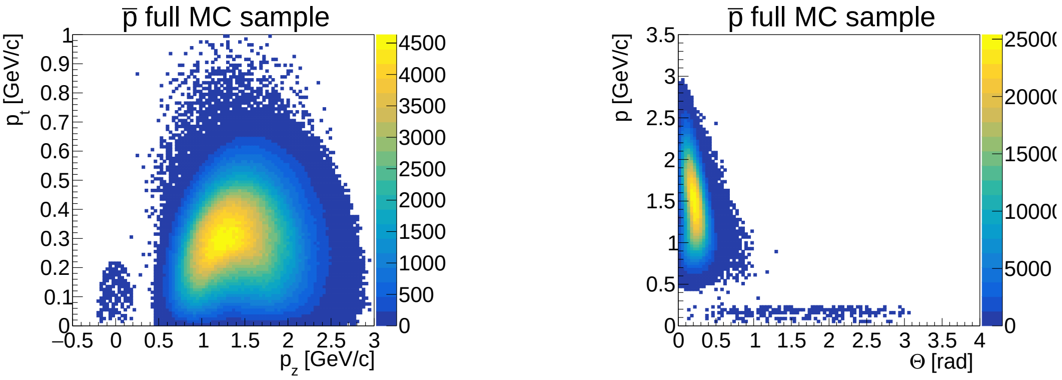

(a)

(b)

Figure A.24: Transverse versus longitudinal momentum (a) and total momentum vs. Θ angle (b) for generated $\bar{p}$ from $\bar{\Lambda}$.

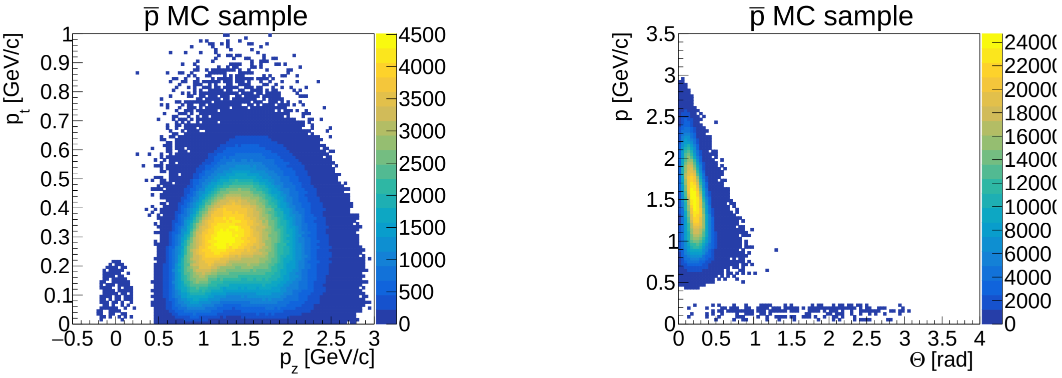

(a)

(b)

Figure A.25: Transverse versus longitudinal momentum (a) and total momentum vs. Θ angle (b) for generated $\bar{p}$ from $\bar{\Lambda}$ requesting that $\bar{\Lambda}$ and $\overline{\Xi}^{+}$ have only two daughters.

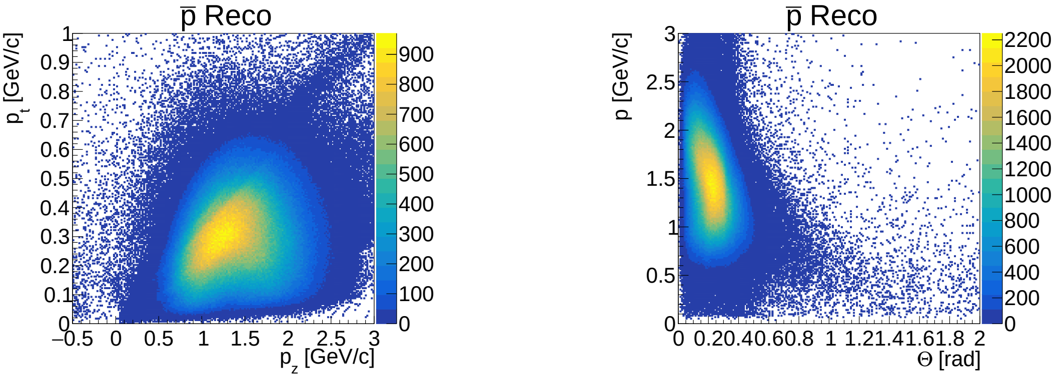

(a)

(b)

Figure A.26: Transverse versus longitudinal momentum (a) and total momentum vs. Θ angle (b) for reconstructed $\bar{p}$ as daughter of $\bar{\Lambda}$.

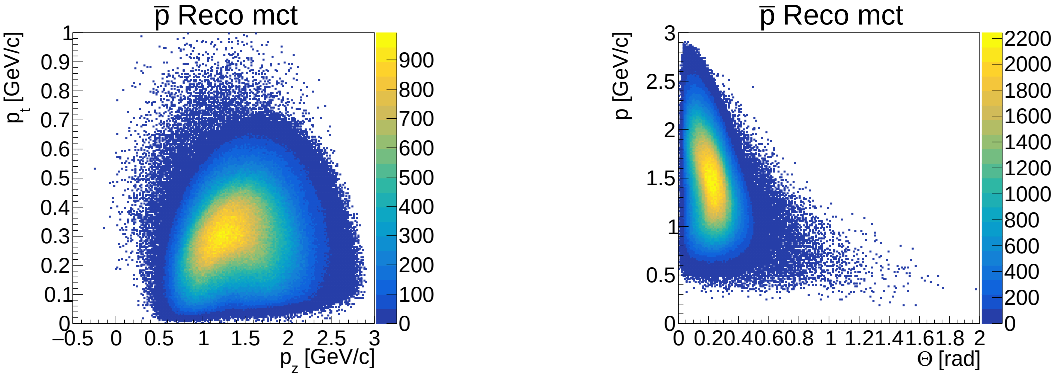

(a)

(b)

Figure A.27: Transverse versus longitudinal momentum (a) and total momentum vs. Θ angle (b) for MC partner of reconstructed $\bar{p}$ from $\bar{\Lambda}$.

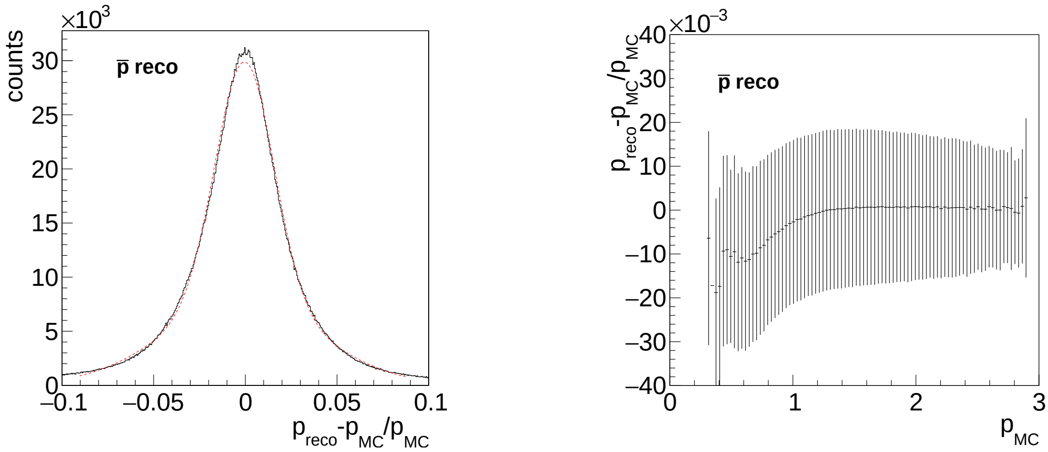

(a)

(b)

Figure A.28: Momentum resolution (a) and relative deviation of the reconstructed and generated total momentum (b) for $\bar{p}$ from $\bar{\Lambda}$.

A.1.2 $\bar{\Lambda}$ Candidates

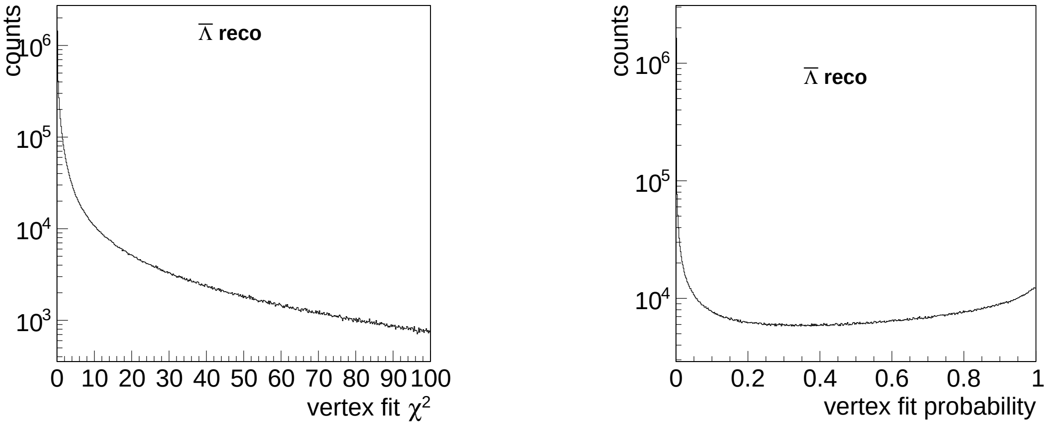

(a)

(b)

Figure A.29: χ^2 and probability distributions for the vertex fit.

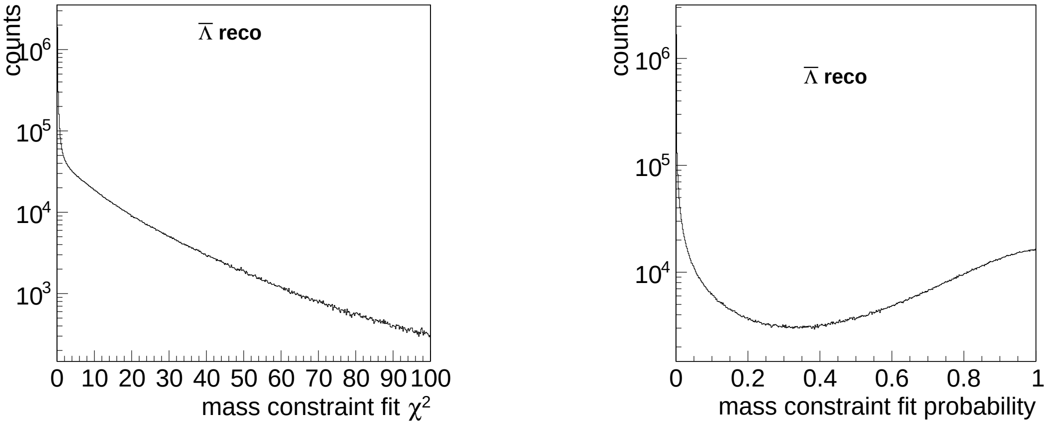

(a)

(b)

Figure A.30: χ^2 and probability distributions for the kinematic fit with mass constraint condition.

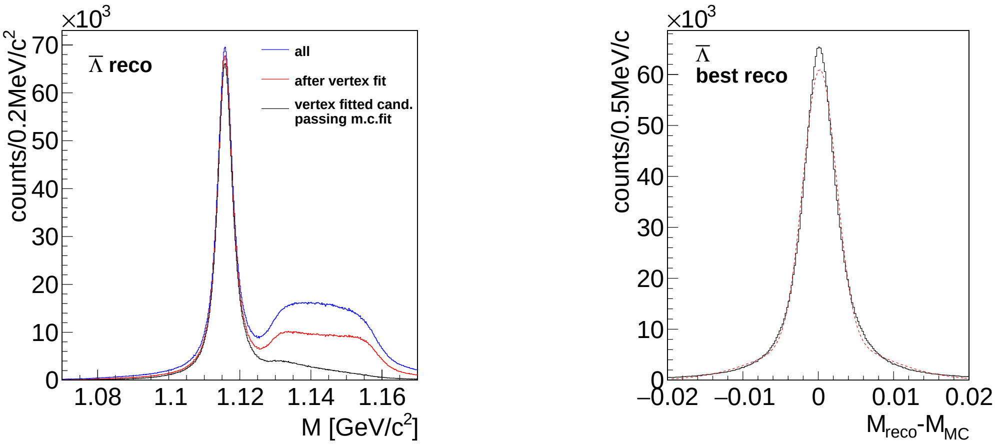

(a) (b)

Figure A.31: a) Mass distribution for $\bar{\Lambda}$ after the different steps of reconstruction. b) Deviation of reconstructed and generated $\bar{\Lambda}$ mass.

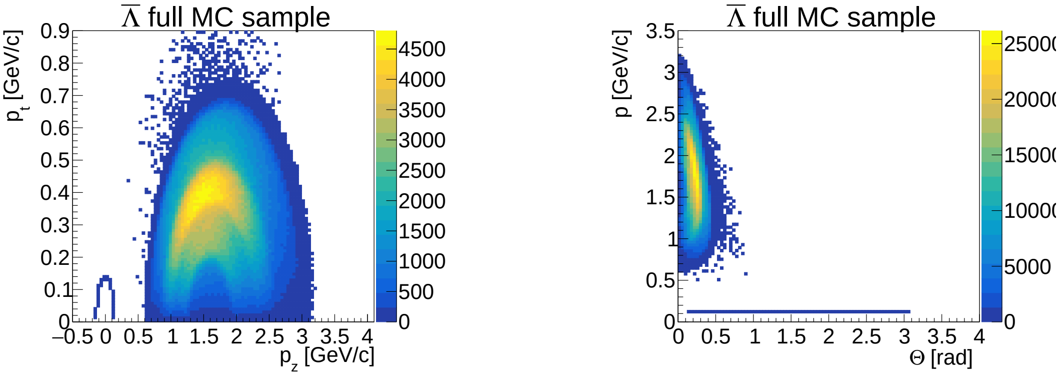

(a) (b)

Figure A.32: Generated $\bar{\Lambda}$.

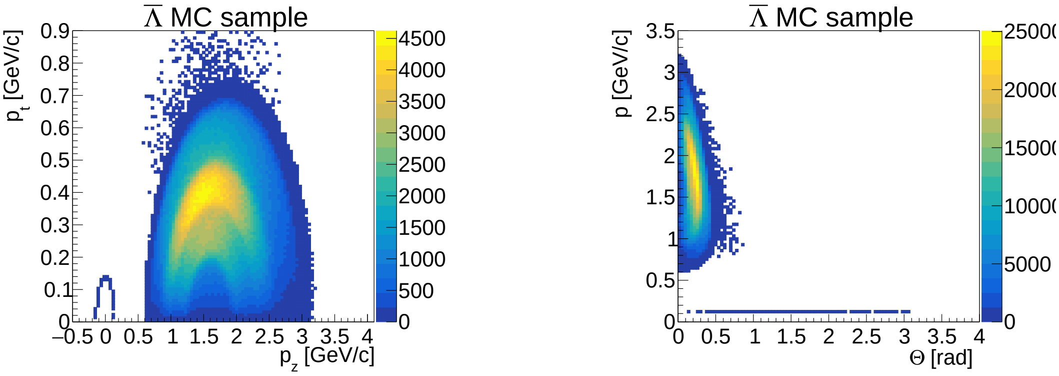

(a) (b)

Figure A.33: Generated $\bar{\Lambda}$ requesting that $\bar{\Lambda}$ and $\bar{\Xi}^+$ have only two daughters.

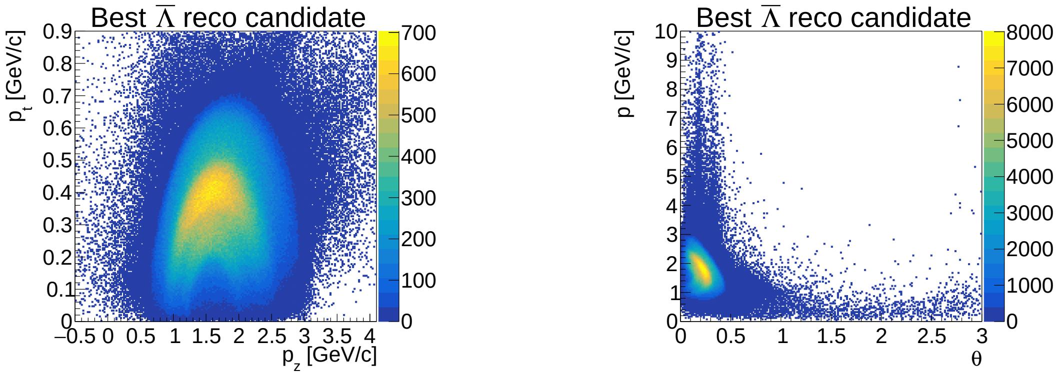

(a)

(b)

Figure A.34: Reconstructed $\bar{p}$ as daughter of $\bar{\Lambda}$.

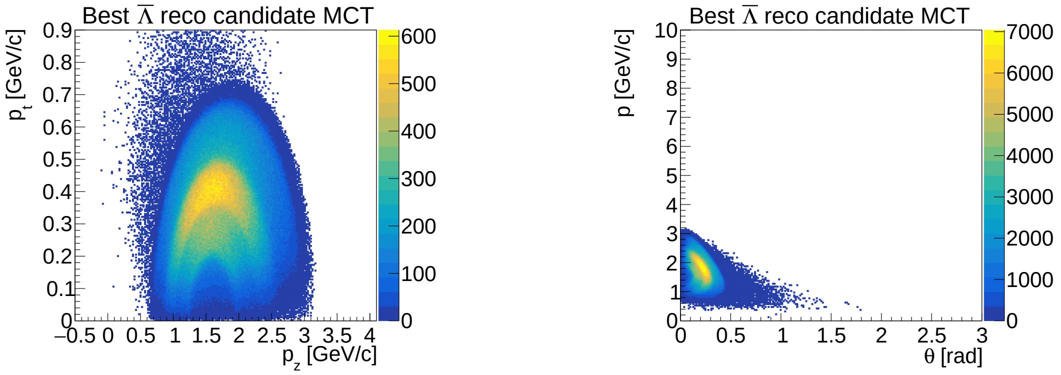

(a)

(b)

Figure A.35: MC partner of reconstructed $\bar{\Lambda}$.

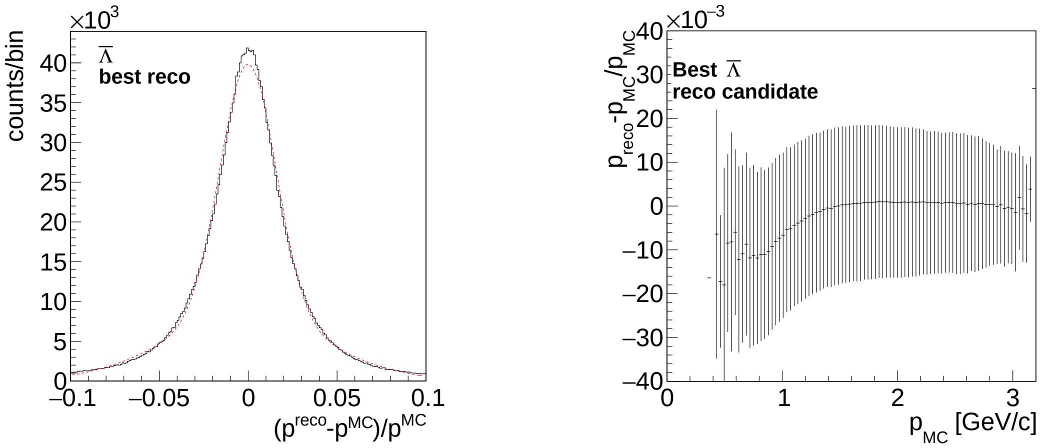

(a)

(b)

Figure A.36: Momentum resolution of $\bar{\Lambda}$.

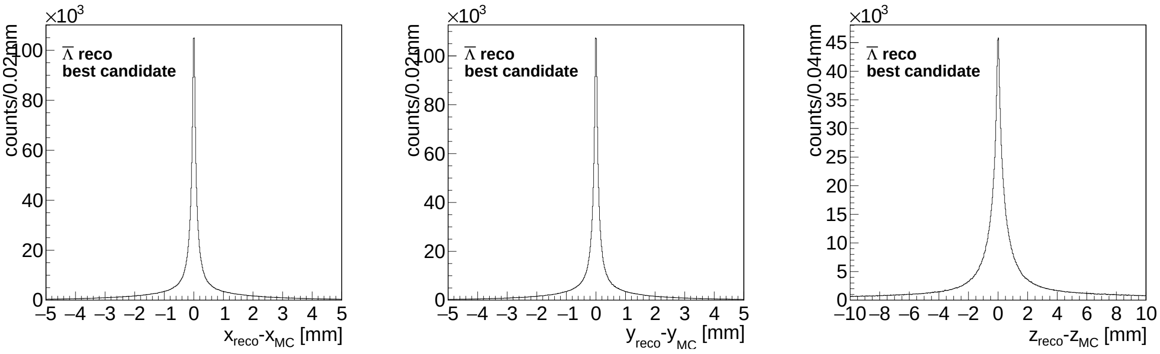

(a) (b) (c)

Figure A.37: Vertex resolution of all three spatial coordinates for best $\bar{\Lambda}$ candidates.

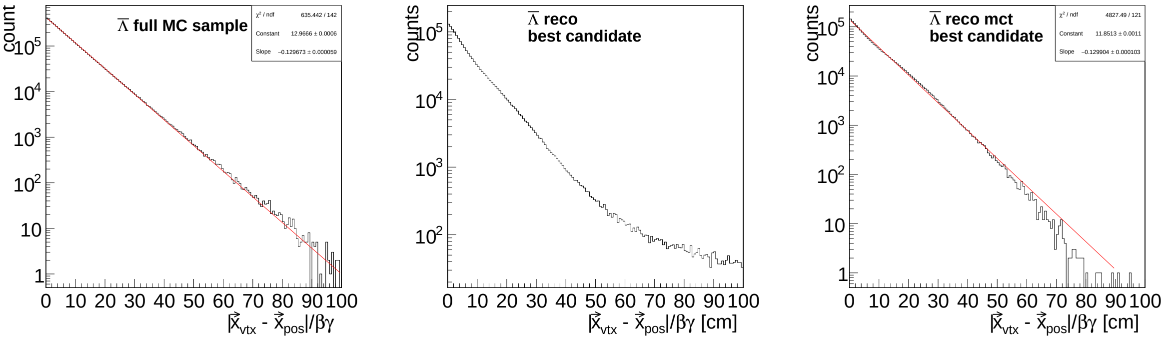

(a) (b) (c)

Figure A.38: Proper time distributions for a) generated, b) reconstructed best $\bar{\Lambda}$ candidates and c) MC partner of best $\bar{\Lambda}$ candidates.

A.1.3 $\overline{\Xi}^{+}\,\Lambda\,K^{-}$

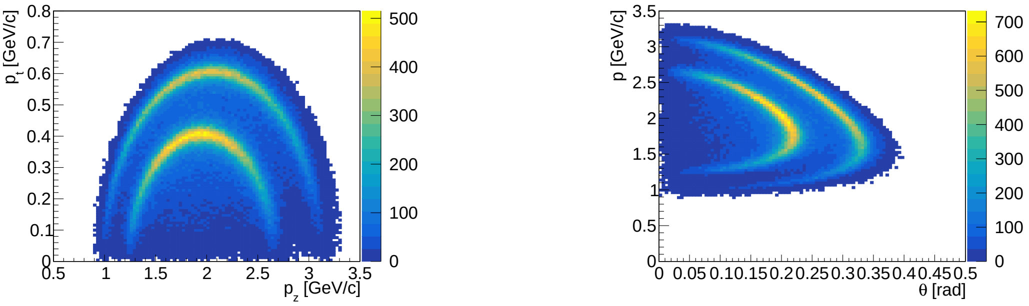

(a) (b)

Figure A.39: Transverse vs. longitudinal momentum and total momentum vs. Θ angle for final selected $\overline{\Xi}^{+}$.

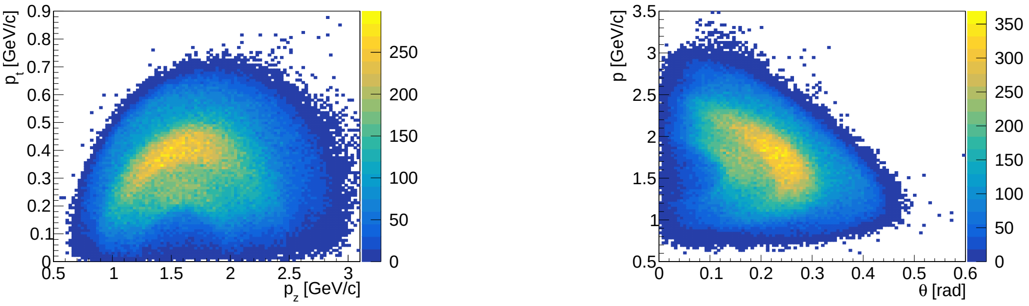

(a) (b)

Figure A.40: Transverse vs. longitudinal momentum and total momentum vs. Θ angle for final selected $\bar{\Lambda}$.

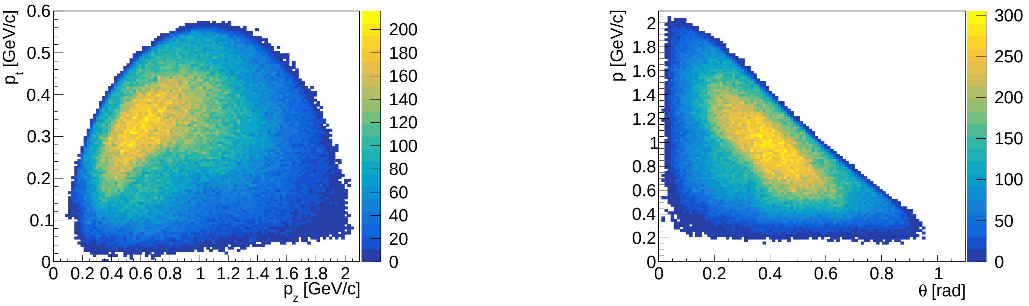

(a) (b)

Figure A.41: Transverse vs. longitudinal momentum and total momentum vs. Θ angle for final selected K^{-}.

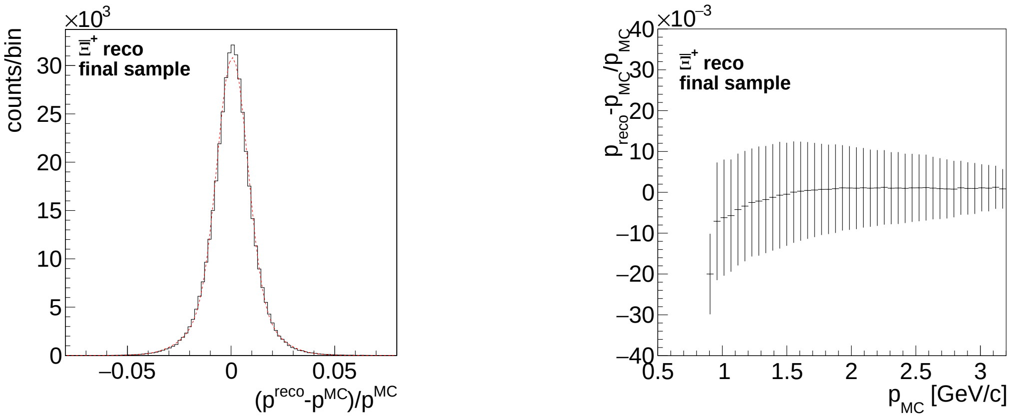

(a) (b)

Figure A.42: Momentum resolution (a) and relative deviation of the reconstructed and generated total momentum (b) for the final selected $\overline{\Xi}^{+}$ candidates.

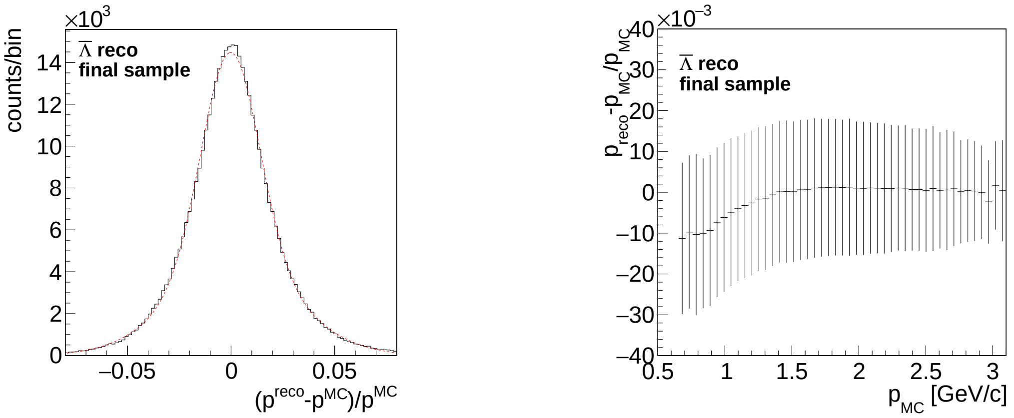

(a) (b)

Figure A.43: Relative deviation of the reconstructed and the generated total momentum for the final selected $\bar{\Lambda}$ candidates.

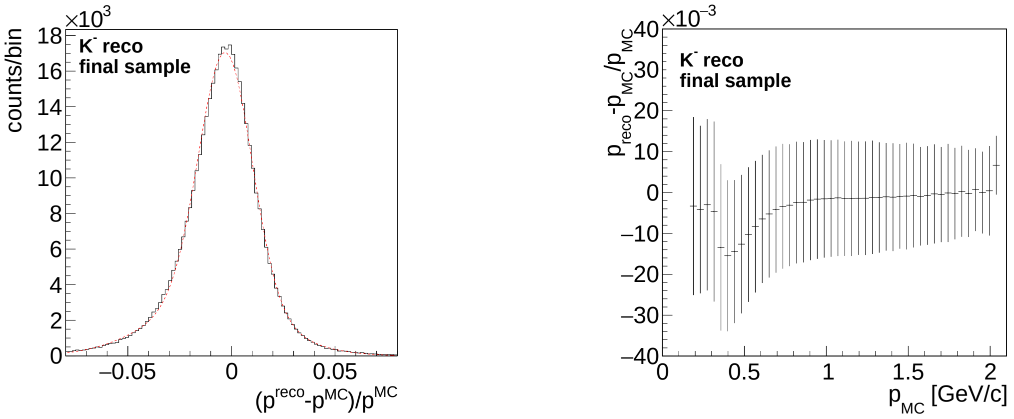

(a)

(b)

Figure A.44: Relative deviation of the reconstructed and the generated total momentum for the final selected K^{-} candidates.

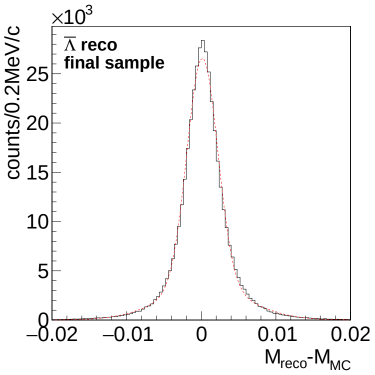

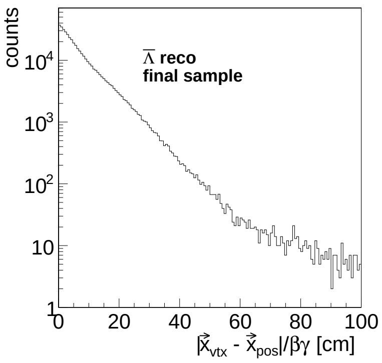

Figure A.45: Mass resolution of the final selected $\bar{\Lambda}$.

Figure A.46: Proper Time distribution for $\bar{\Lambda}$.

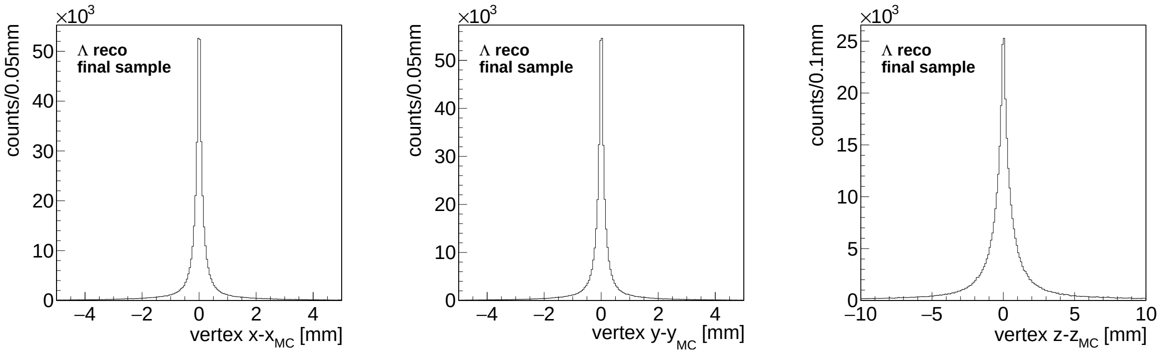

(a)

(b)

(c)

Figure A.47: Deviation of the reconstructed and the generated decay vertex position in all three spatial coordinates for Λ.

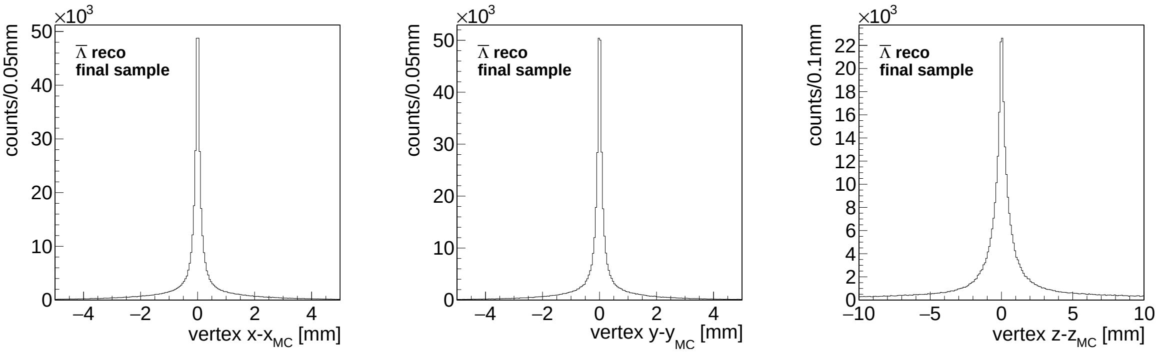

(a) (b) (c)

Figure A.48: Deviation of the reconstructed and the generated decay vertex position in all three spatial coordinates for $\bar{\Lambda}$.

A.2 Analysis of $\bar{p}p \rightarrow \Xi^- \bar{\Lambda} K^+$ with the Sequential Fit Procedure

A.2.1 Final State Particles

π^+ from $\bar{\Lambda}$

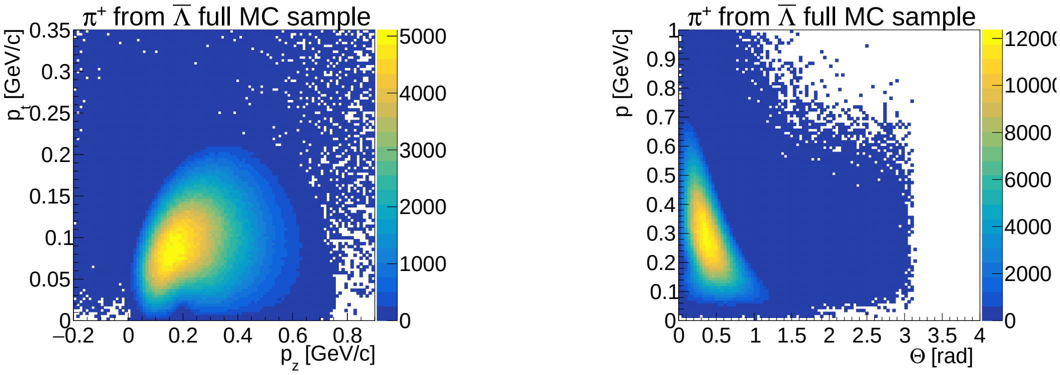

(a) (b)

Figure A.49: Transverse versus longitudinal momentum (a) and total momentum vs. Θ angle (b) for generated π^+ from $\bar{\Lambda}$.

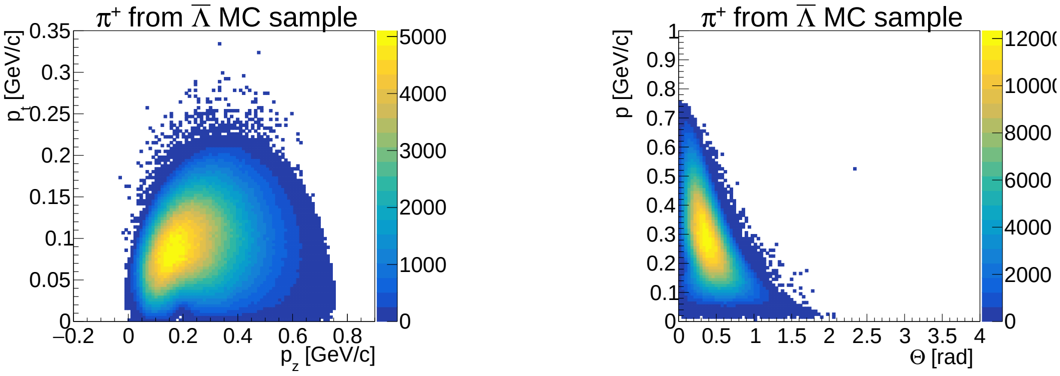

(a) (b)

Figure A.50: Transverse versus longitudinal momentum (a) and total momentum vs. Θ angle (b) for generated π^+ from $\bar{\Lambda}$ requesting that $\bar{\Lambda}$ and $\bar{\Xi}^+$ have only two daughters.

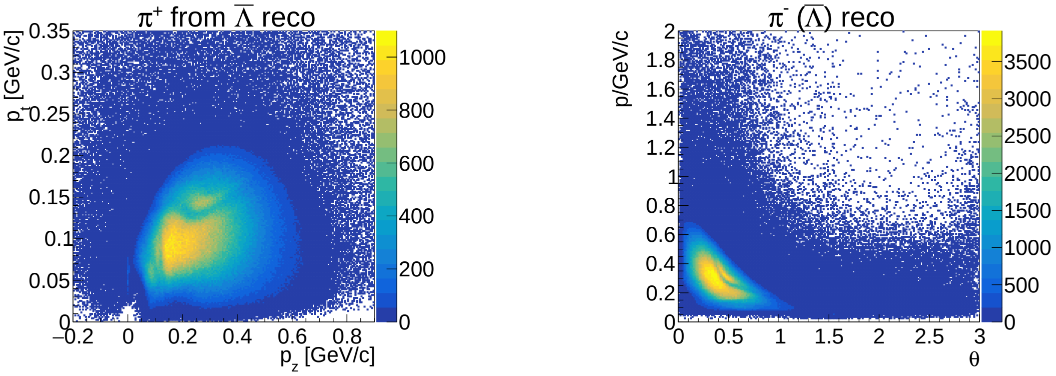

(a)

(b)

Figure A.51: Transverse versus longitudinal momentum (a) and total momentum vs. Θ angle (b) for reconstructed π^+ as daughter of $\bar{\Lambda}$.

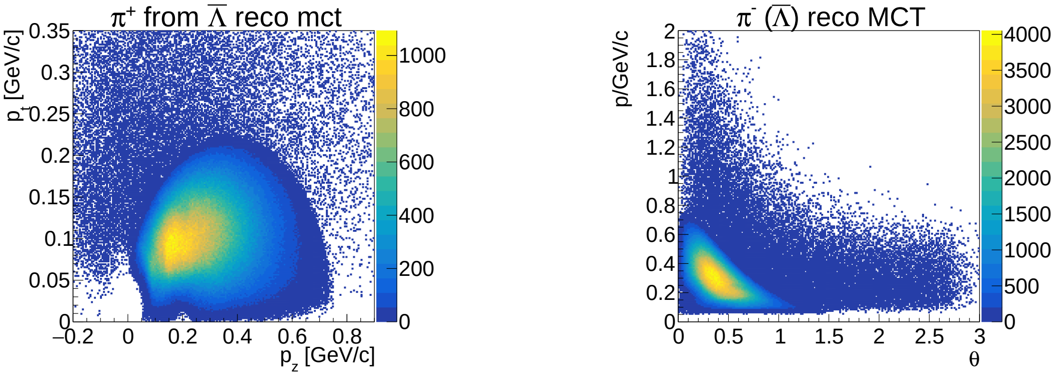

(a)

(b)

Figure A.52: Transverse versus longitudinal momentum (a) and total momentum vs. Θ angle (b) for MC partner of reconstructed π^+ from $\bar{\Lambda}$.

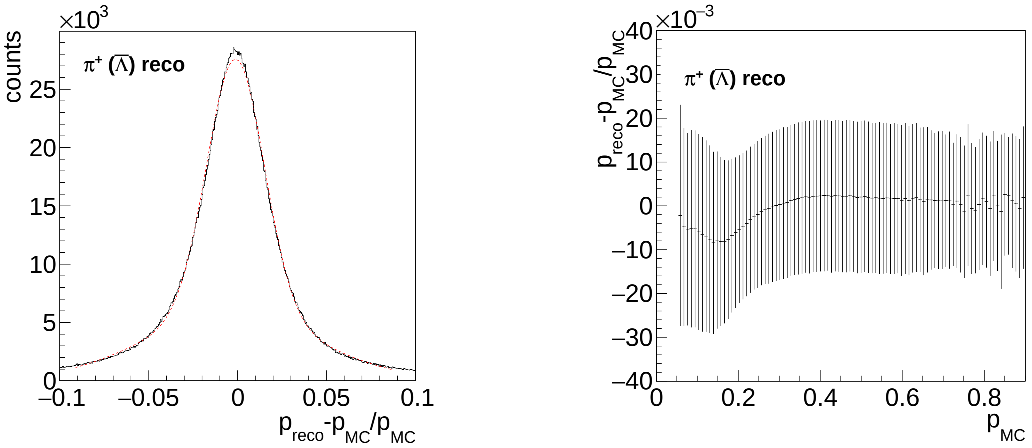

(a)

(b)

Figure A.53: Momentum resolution (a) and relative deviation of the reconstructed and generated total momentum (b) for π^+ from $\bar{\Lambda}$.

π^- from Λ

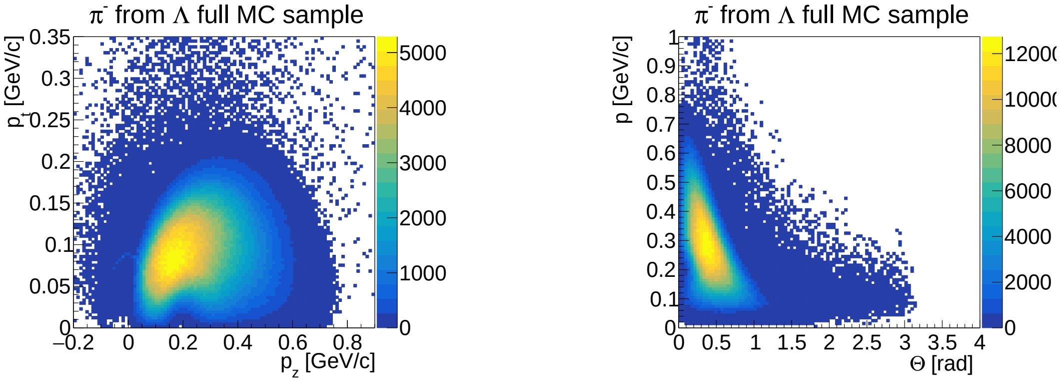

(a) (b)

Figure A.54: Transverse versus longitudinal momentum (a) and total momentum vs. Θ angle (b) for generated π^- from Λ.

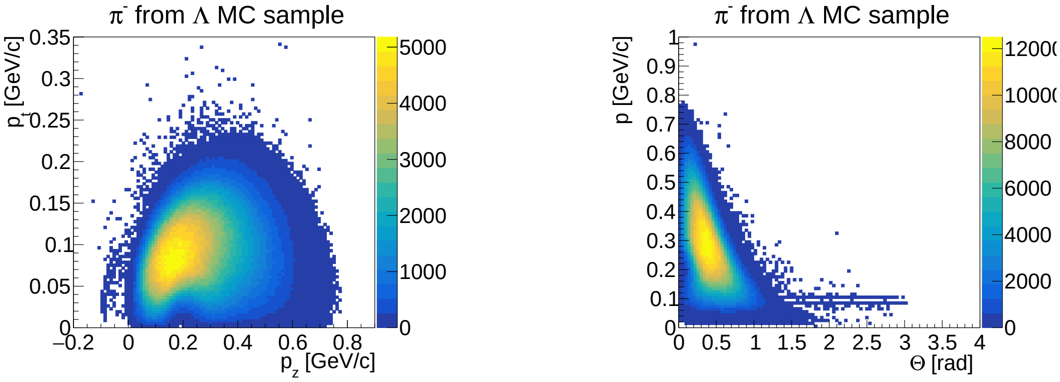

(a) (b)

Figure A.55: Transverse versus longitudinal momentum (a) and total momentum vs. Θ angle (b) for generated π^- from Λ requesting that Λ and Ξ^- have only two daughters.

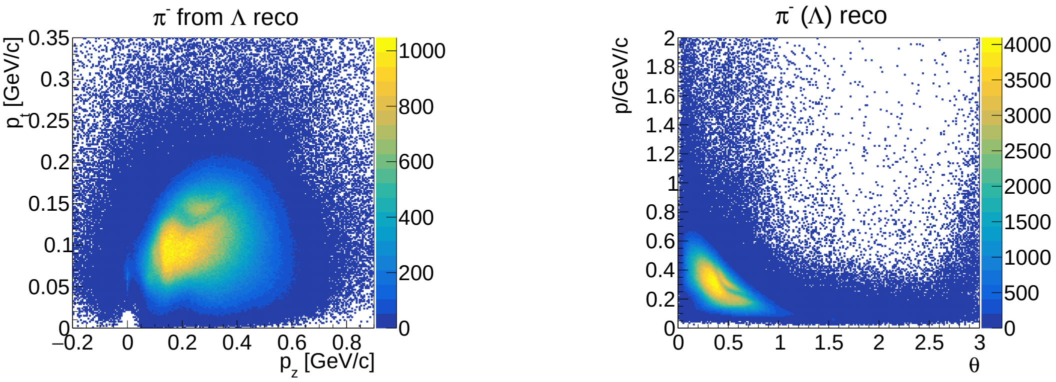

(a) (b)

Figure A.56: Transverse versus longitudinal momentum (a) and total momentum vs. Θ angle (b) for reconstructed π^- as daughter of Λ.

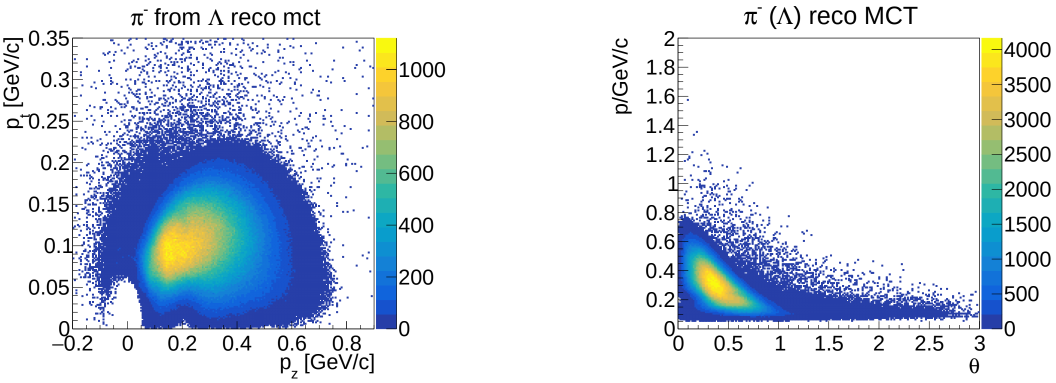

(a) (b)

Figure A.57: Transverse versus longitudinal momentum (a) and total momentum vs. Θ angle (b) for MC partner of reconstructed π^- from Λ.

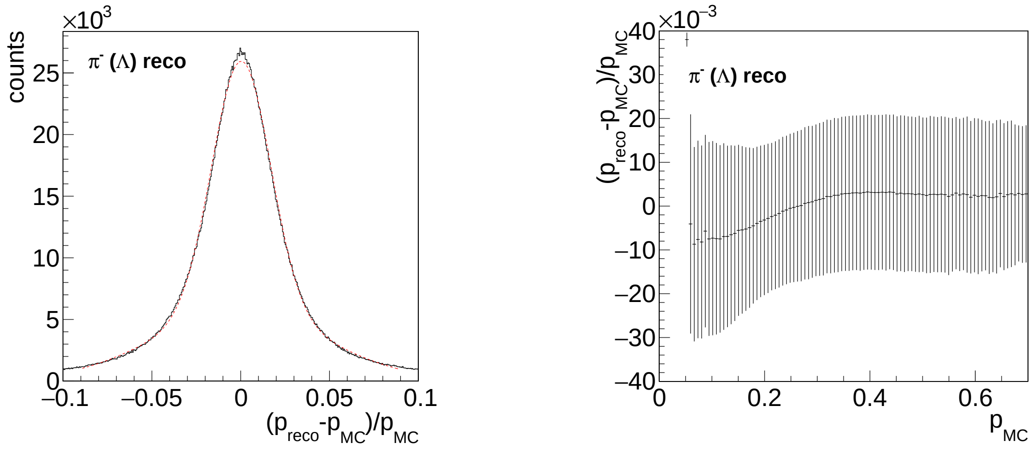

(a) (b)

Figure A.58: Momentum resolution (a) and relative deviation of the reconstructed and generated total momentum (b) for π^- from Λ.

π^- from Ξ^-

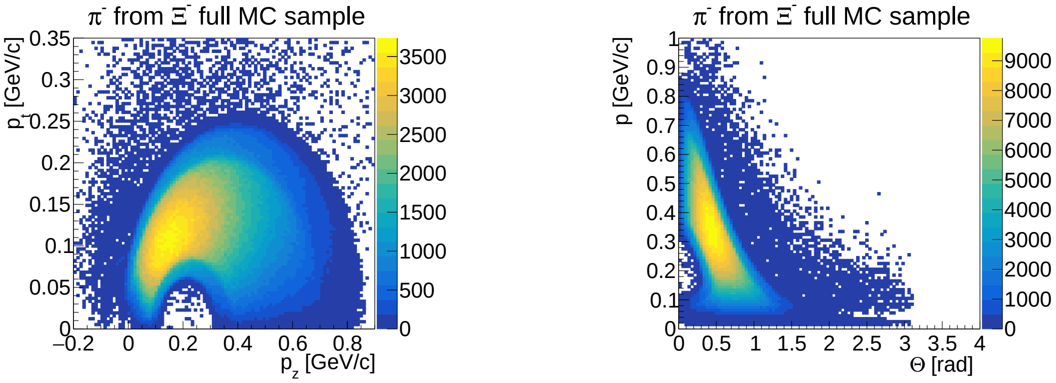

(a) (b)

Figure A.59: Generated π^- from Ξ^-.

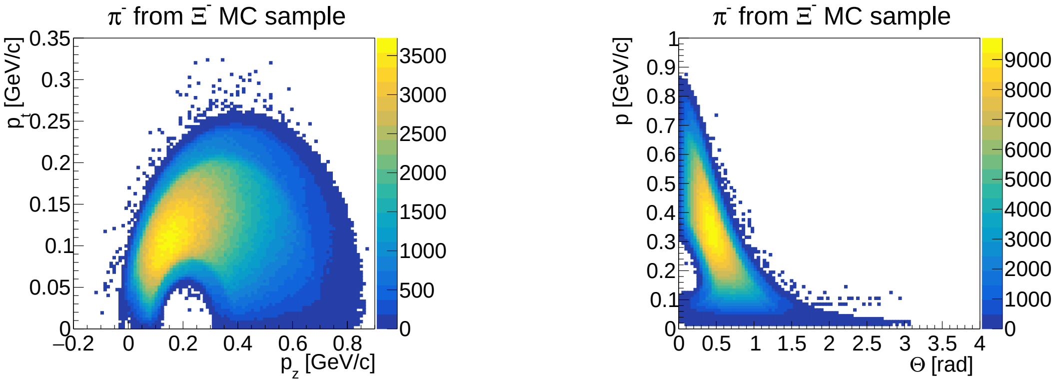

(a) (b)

Figure A.60: Transverse versus longitudinal momentum (a) and total momentum vs. Θ angle (b) for generated π^- from Ξ^- requesting that the Ξ^- has only two daughters.

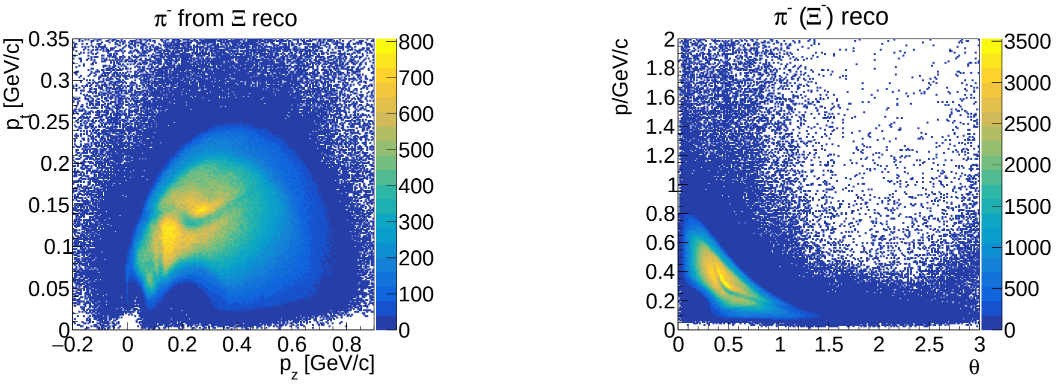

(a)

(b)

Figure A.61: Transverse versus longitudinal momentum (a) and total momentum vs. Θ angle (b) for reconstructed π^- as daughter of Ξ^-.

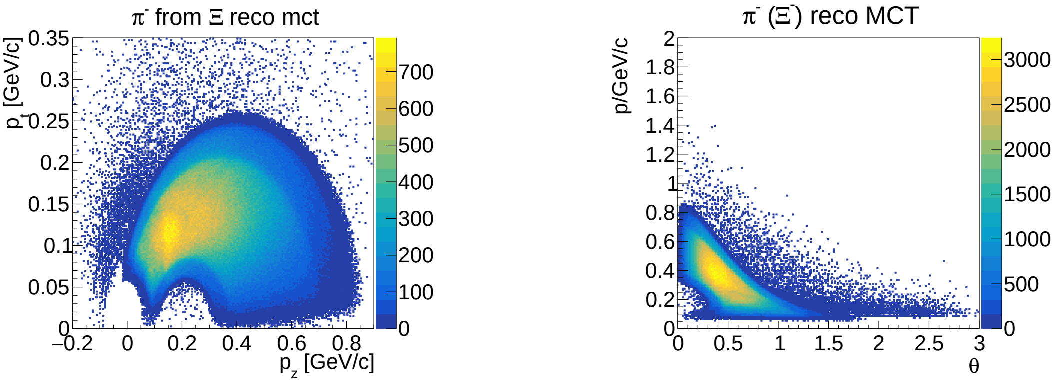

(a)

(b)

Figure A.62: Transverse versus longitudinal momentum (a) and total momentum vs. Θ angle (b) for MC partner of reconstructed π^- from Ξ^-.

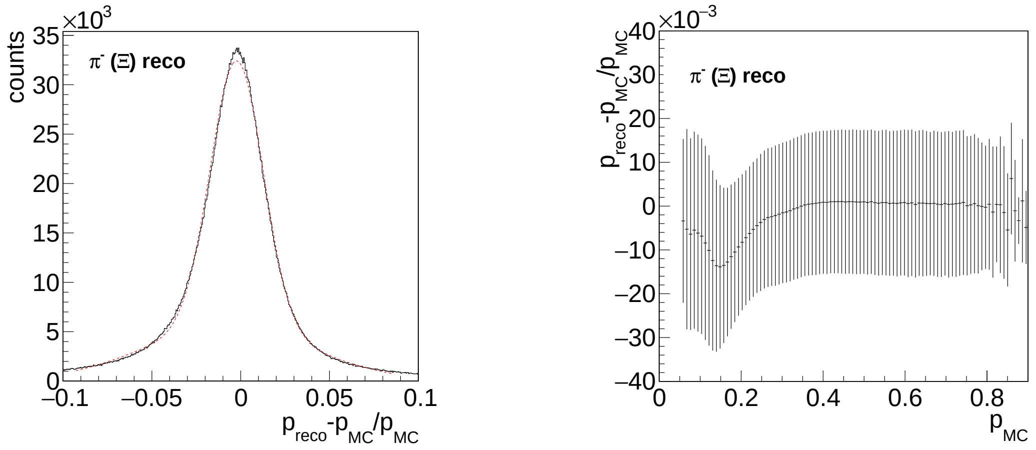

(a)

(b)

Figure A.63: Momentum resolution (a) and relative deviation of the reconstructed and generated total momentum (b) for π^- from Ξ^-.

K^+ from $\bar{\Xi}^*$

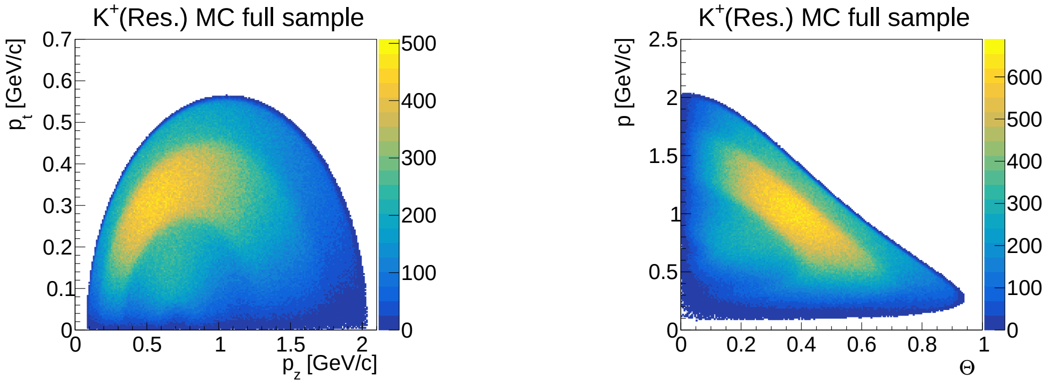

(a)

(b)

Figure A.64: Transverse versus longitudinal momentum (a) and total momentum vs. Θ angle (b) for generated K^+ from $\bar{\Xi}^*$.

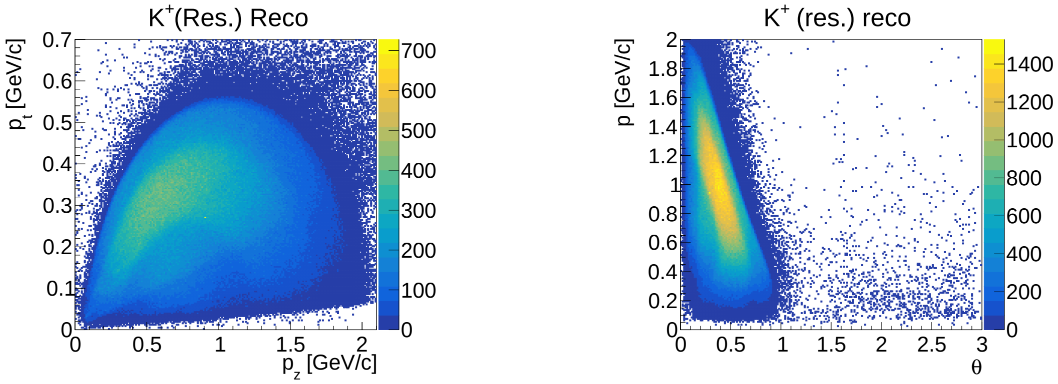

(a)

(b)

Figure A.65: Transverse versus longitudinal momentum (a) and total momentum vs. Θ angle (b) for reconstructed K^+ as daughter of $\bar{\Xi}^*$.

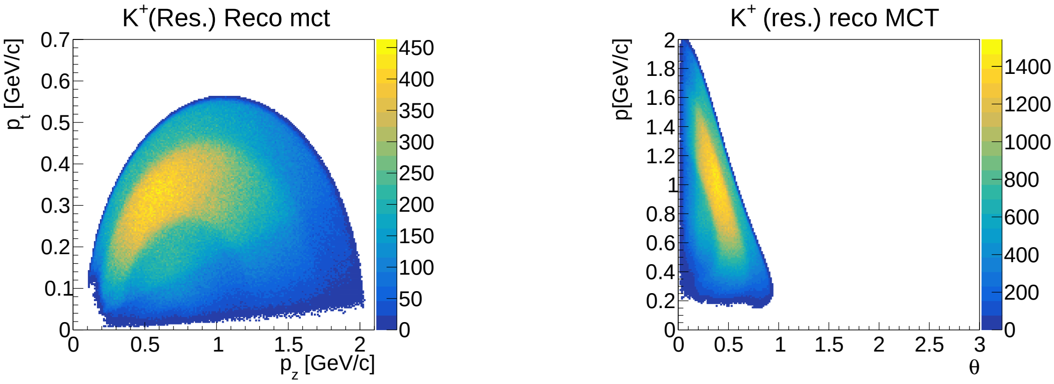

(a) (b)

Figure A.66: Transverse versus longitudinal momentum (a) and total momentum vs. Θ angle (b) for MC partner of reconstructed K$^+$ from $\overline{\Xi}^*$.

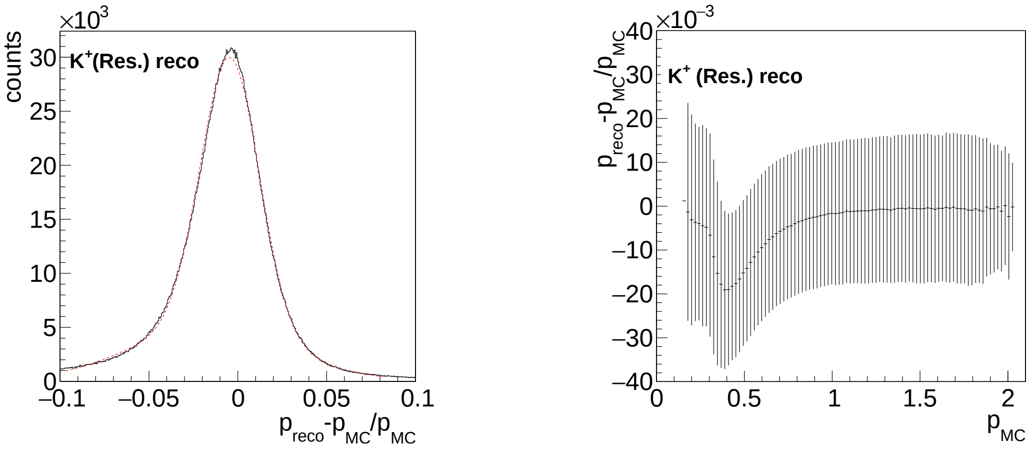

(a) (b)

Figure A.67: Momentum resolution (a) and relative deviation of the reconstructed and generated total momentum (b) for K$^+$ from $\overline{\Xi}^*$.

K^+ from Continuum

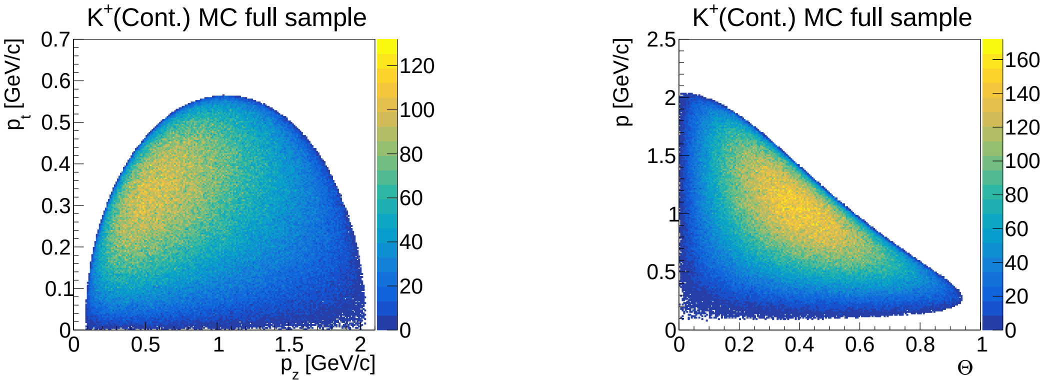

(a) (b)

Figure A.68: Transverse versus longitudinal momentum (a) and total momentum vs. Θ angle (b) for generated K^+ from continumm.

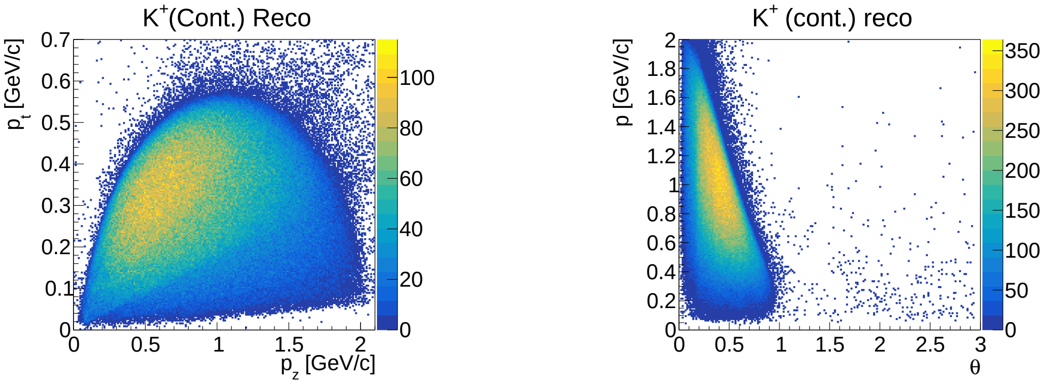

(a) (b)

Figure A.69: Transverse versus longitudinal momentum (a) and total momentum vs. Θ angle (b) for reconstructed K^+ as daughter of continumm.

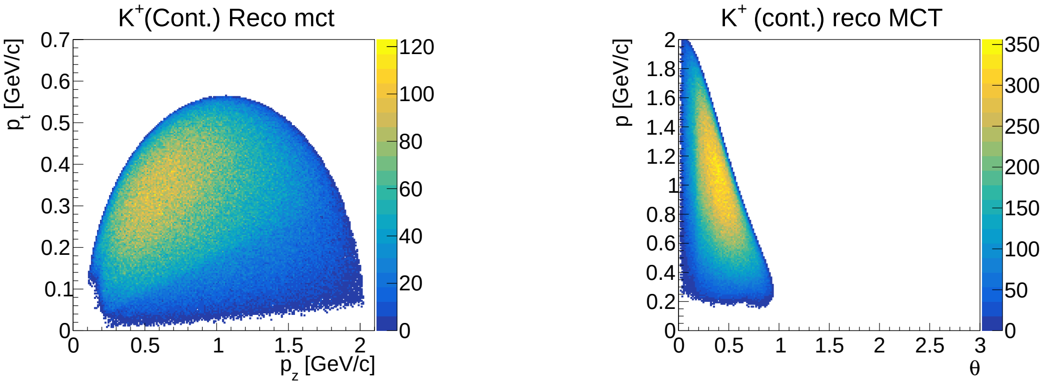

(a)

(b)

Figure A.70: Transverse versus longitudinal momentum (a) and total momentum vs. Θ angle (b) for MC partner of reconstructed K^+ from continumm.

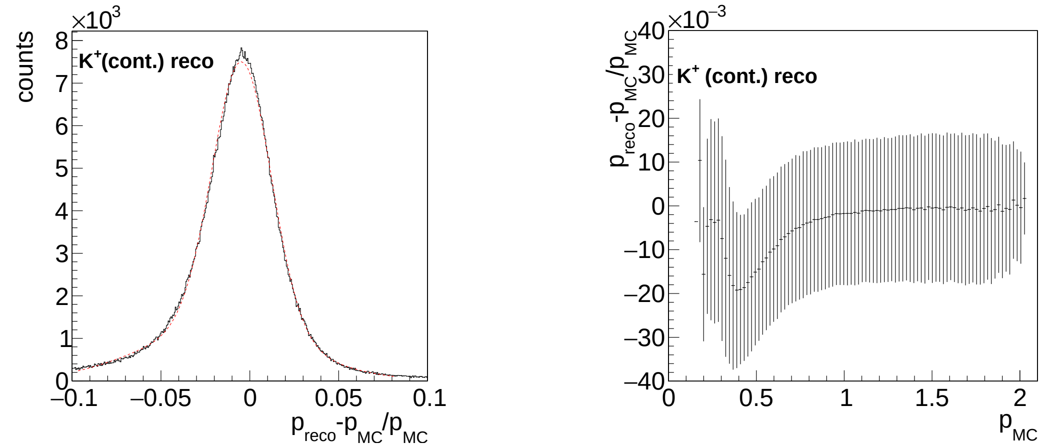

(a)

(b)

Figure A.71: Momentum resolution (a) and relative deviation of the reconstructed and generated total momentum (b) for K^+ from continumm.

p and $\bar{p}$

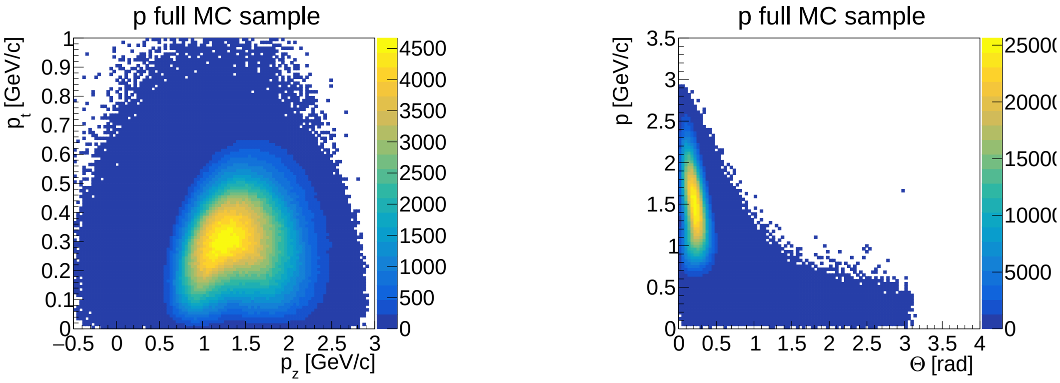

(a)

(b)

Figure A.72: Transverse versus longitudinal momentum (a) and total momentum vs. Θ angle (b) for generated p from Λ.

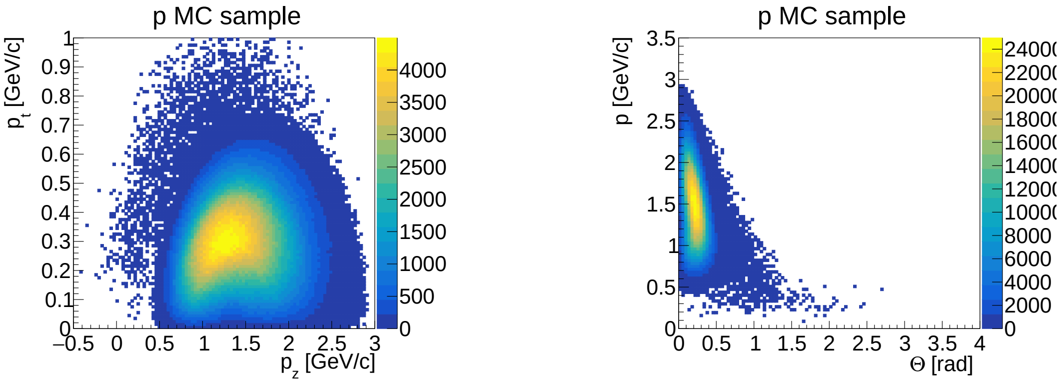

(a)

(b)

Figure A.73: Transverse versus longitudinal momentum (a) and total momentum vs. Θ angle (b) for generated p from Λ requesting that Λ and $\overline{\Xi}^+$ have only two daughters.

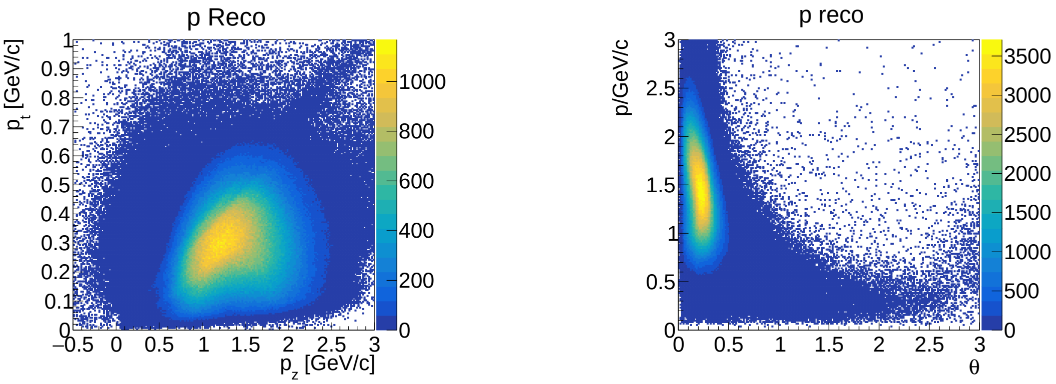

(a)

(b)

Figure A.74: Transverse versus longitudinal momentum (a) and total momentum vs. Θ angle (b) for reconstructed p as daughter of Λ.

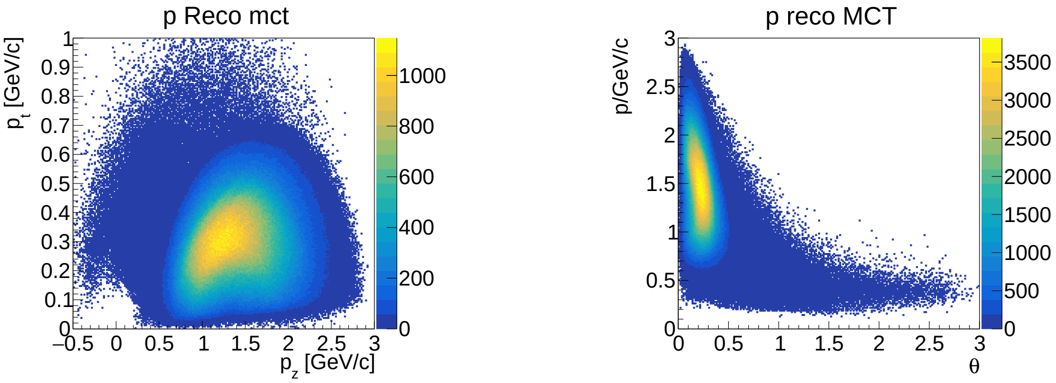

(a)

(b)

Figure A.75: Transverse versus longitudinal momentum (a) and total momentum vs. Θ angle (b) for MC partner of reconstructed p from Λ.

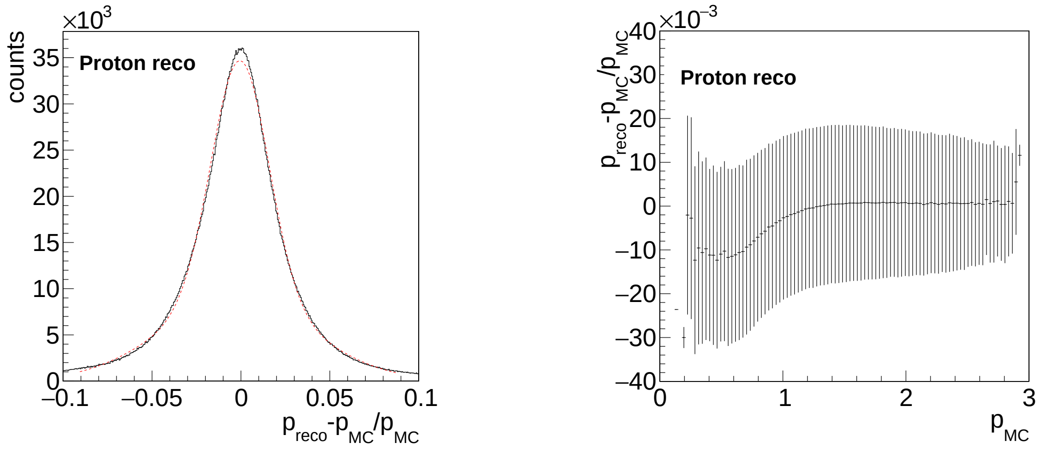

(a)

(b)

Figure A.76: Momentum resolution (a) and relative deviation of the reconstructed and generated total momentum (b) for p from Λ.

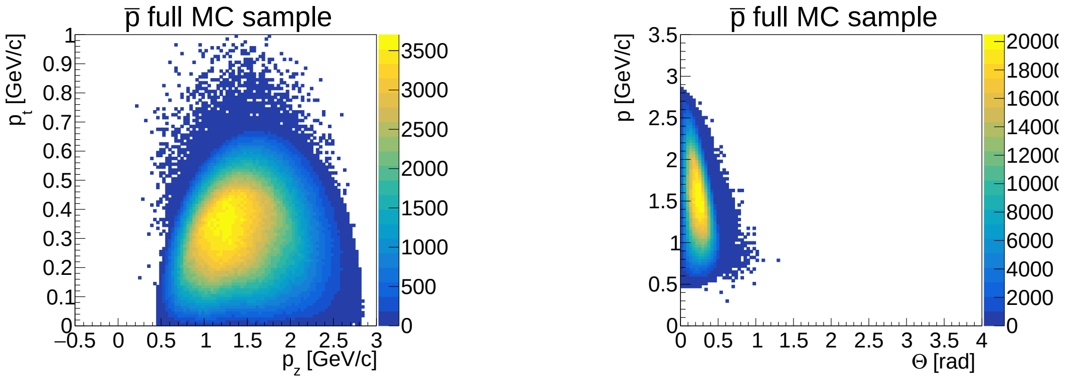

(a) (b)

Figure A.77: Transverse versus longitudinal momentum (a) and total momentum vs. Θ angle (b) for generated $\bar{p}$ from $\bar{\Lambda}$.

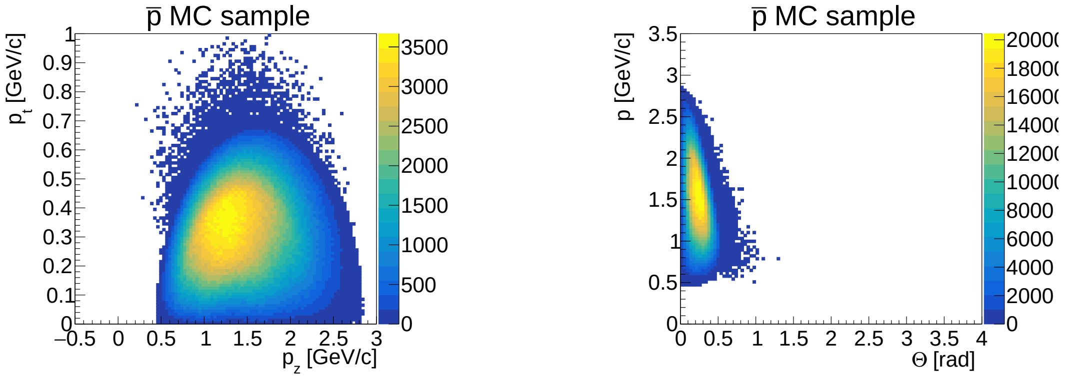

(a) (b)

Figure A.78: Transverse versus longitudinal momentum (a) and total momentum vs. Θ angle (b) for generated $\bar{p}$ from $\bar{\Lambda}$ requesting that $\bar{\Lambda}$ and $\overline{\Xi}^+$ have only two daughters.

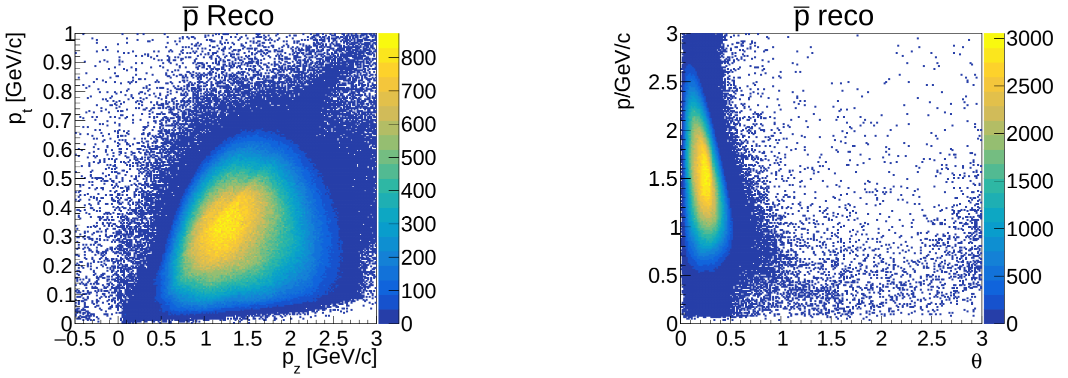

(a) (b)

Figure A.79: Transverse versus longitudinal momentum (a) and total momentum vs. Θ angle (b) for reconstructed $\bar{p}$ as daughter of $\bar{\Lambda}$.

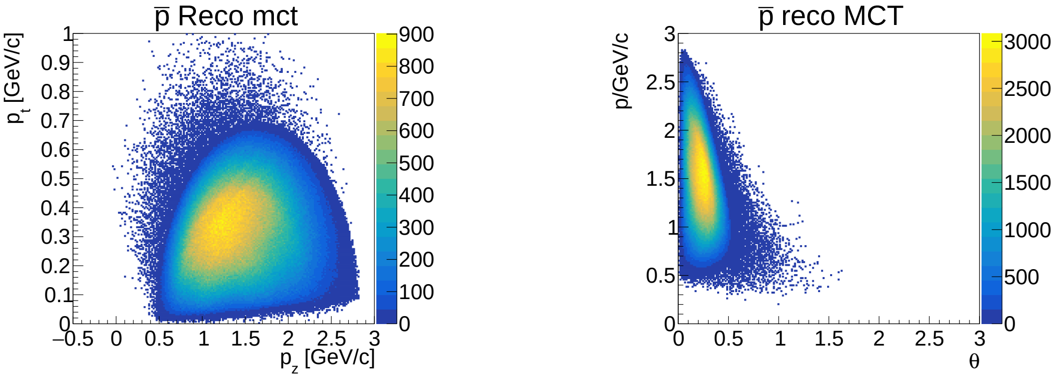

(a) (b)

Figure A.80: Transverse versus longitudinal momentum (a) and total momentum vs. Θ angle (b) for MC partner of reconstructed $\bar{\mathrm{p}}$ from $\bar{\Lambda}$.

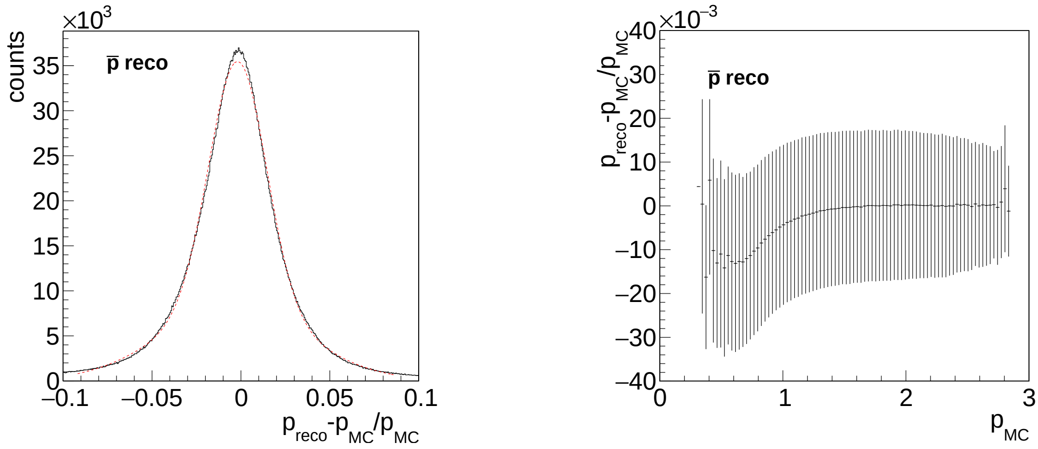

(a) (b)

Figure A.81: Momentum resolution (a) and relative deviation of the reconstructed and generated total momentum (b) for $\bar{\mathrm{p}}$ from $\bar{\Lambda}$.

A.2.2 Λ Candidates

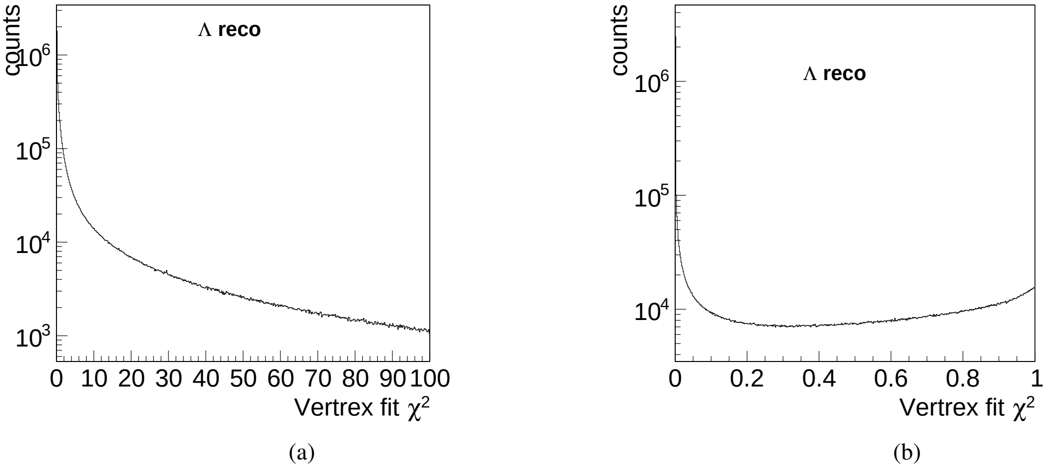

(a) (b)

Figure A.82: χ^2 and probability distributions for the vertex fit.

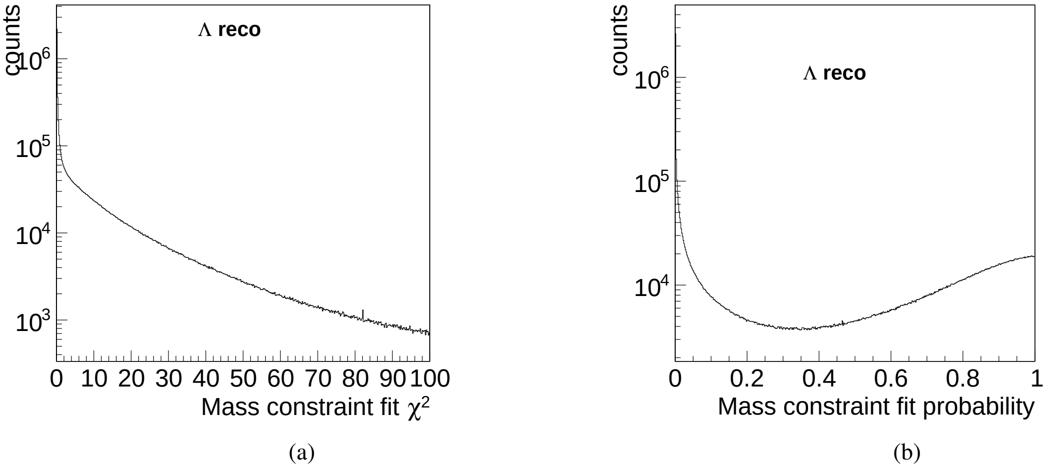

(a) (b)

Figure A.83: χ^2 and probability distributions for the kinematic fit with mass constraint condition.

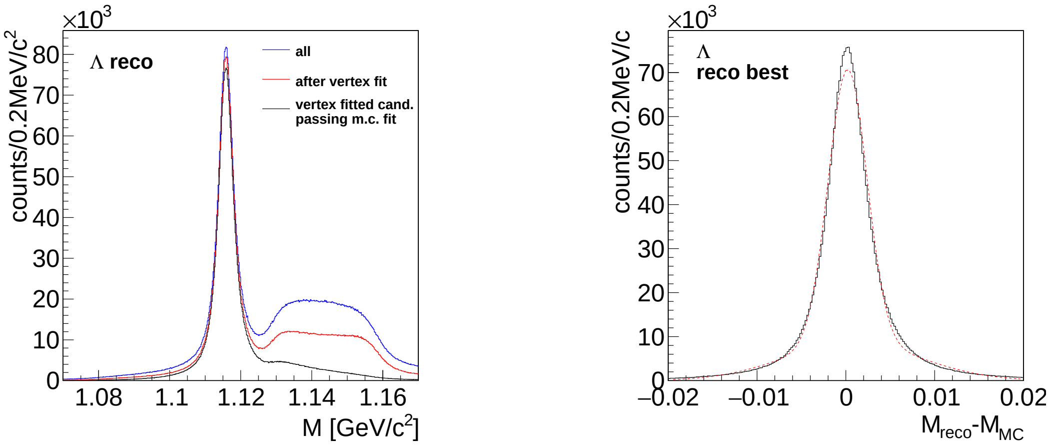

(a) (b)

Figure A.84: a) Mass distribution for Λ after the different steps of reconstruction. b) Deviation of reconstructed and generated Λ mass.

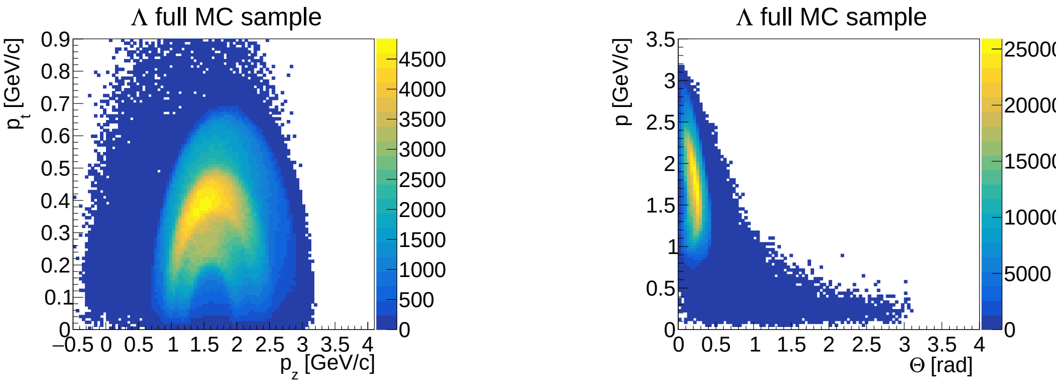

(a) (b)

Figure A.85: Transverse versus longitudinal momentum (a) and total momentum vs. Θ angle (b) for generated Λ.

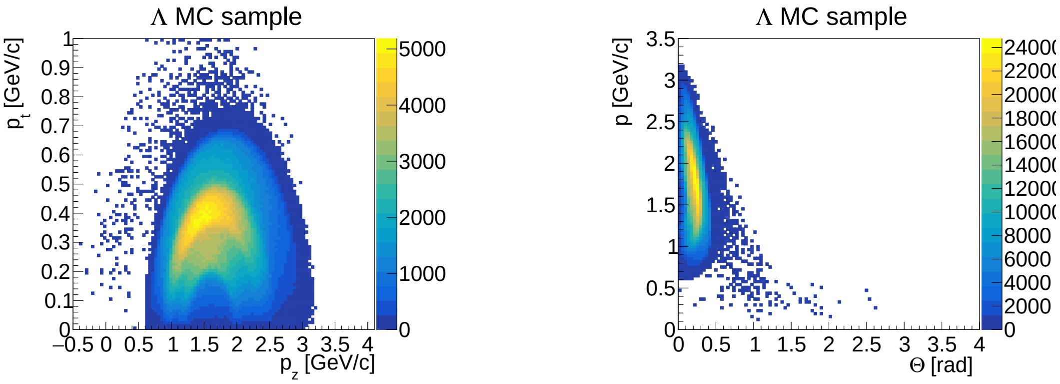

(a) (b)

Figure A.86: Transverse versus longitudinal momentum (a) and total momentum vs. Θ angle (b) for generated Λ requesting that Λ and Ξ^- have only two daughters.

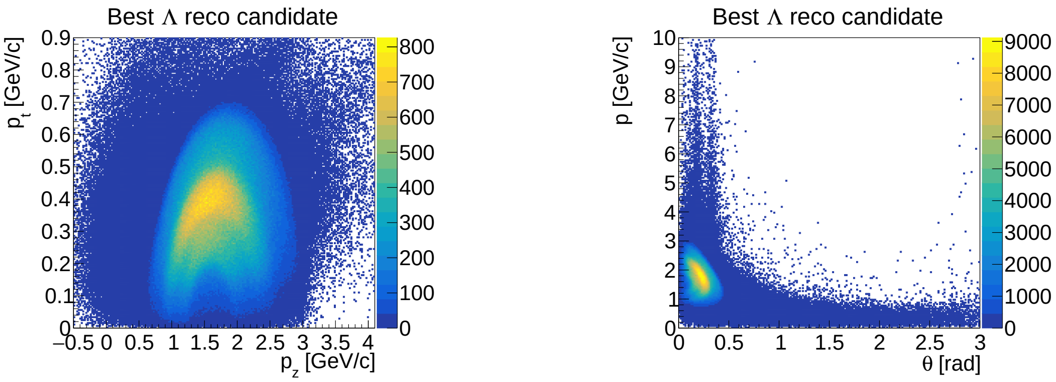

(a)

(b)

Figure A.87: Transverse versus longitudinal momentum (a) and total momentum vs. Θ angle (b) for reconstructed $\bar{p}$ as daughter of Λ.

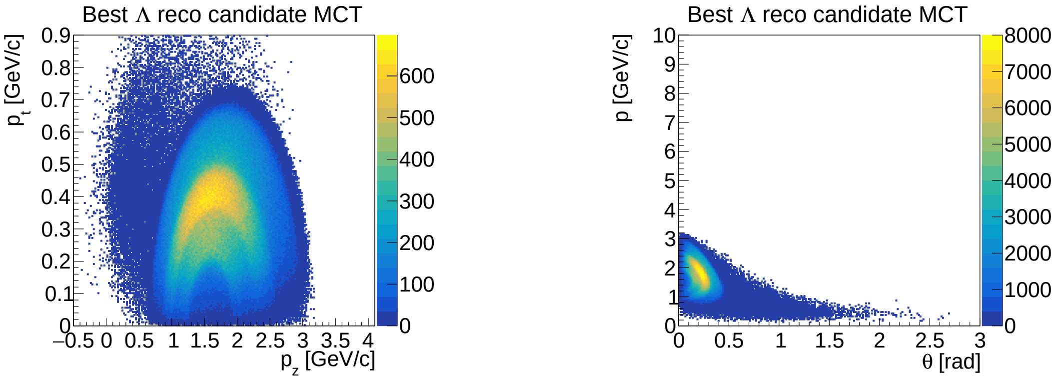

(a)

(b)

Figure A.88: Transverse versus longitudinal momentum (a) and total momentum vs. Θ angle (b) for MC partner of reconstructed Λ.

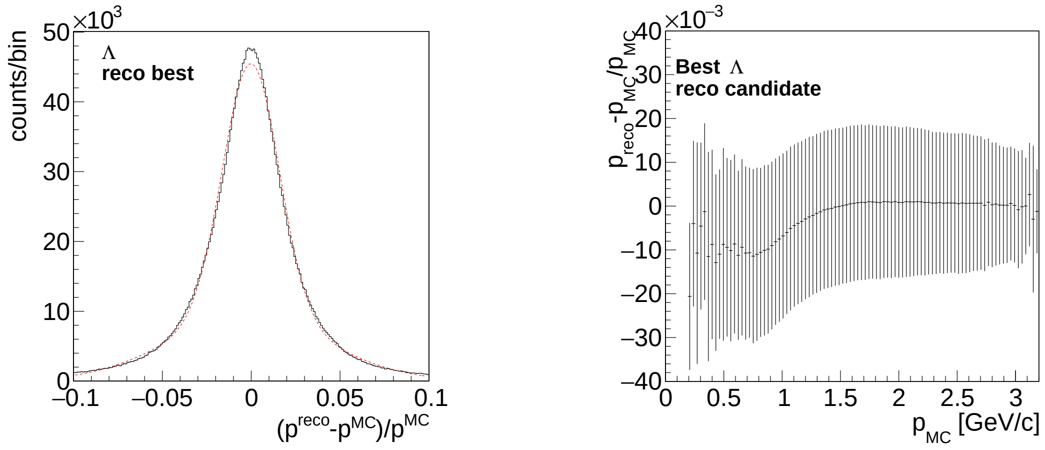

(a)

(b)

Figure A.89: Momentum resolution (a) and relative deviation of the reconstructed and generated total momentum (b) for Λ.

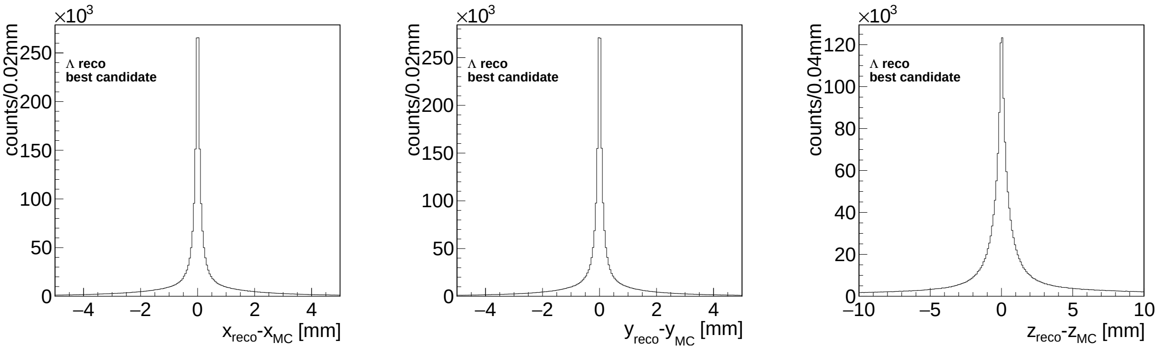

(a) (b) (c)

Figure A.90: Deviation of generated and reconstructed decay vertex position for the x coordinate (a), y coordinate (b) and z coordinate (c) for best Λ candidates.

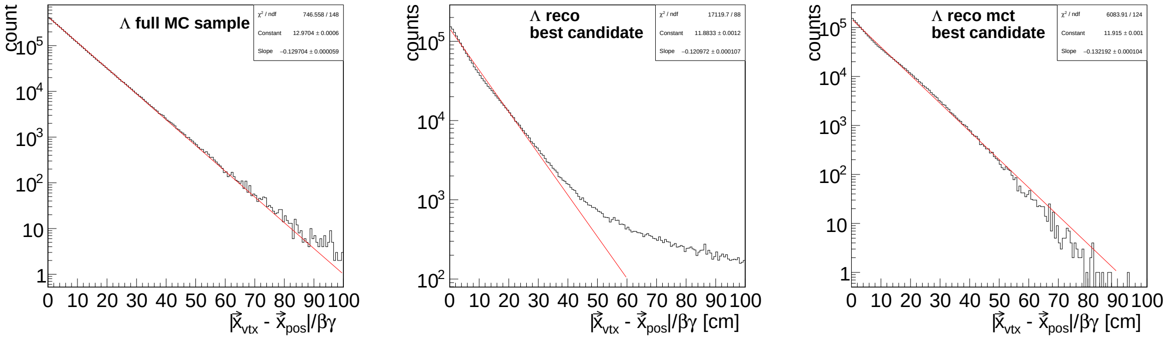

(a) (b) (c)

Figure A.91: Proper time distributions for a) generated, b) reconstructed best Λ candidates and c) MC partner of best Λ candidates.

A.2.3 $\bar{\Lambda}$ Candidates

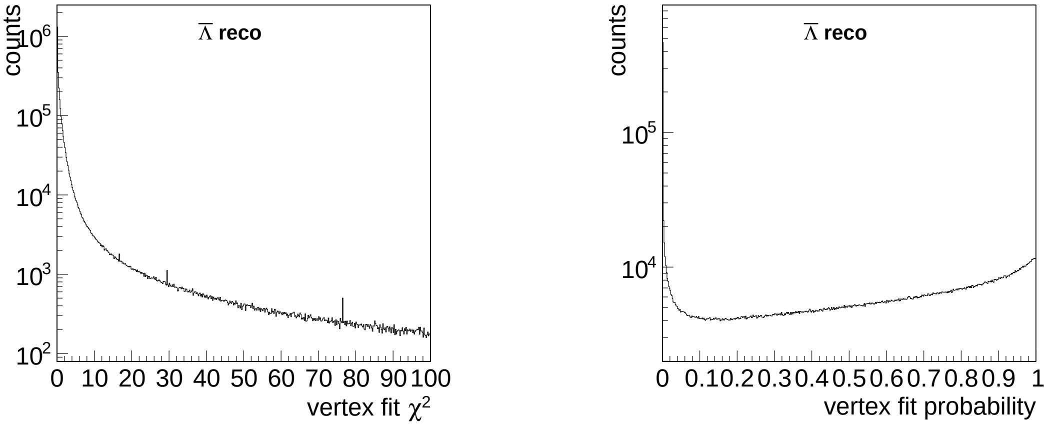

(a) (b)

Figure A.92: χ^2 and probability distributions for the vertex fit.

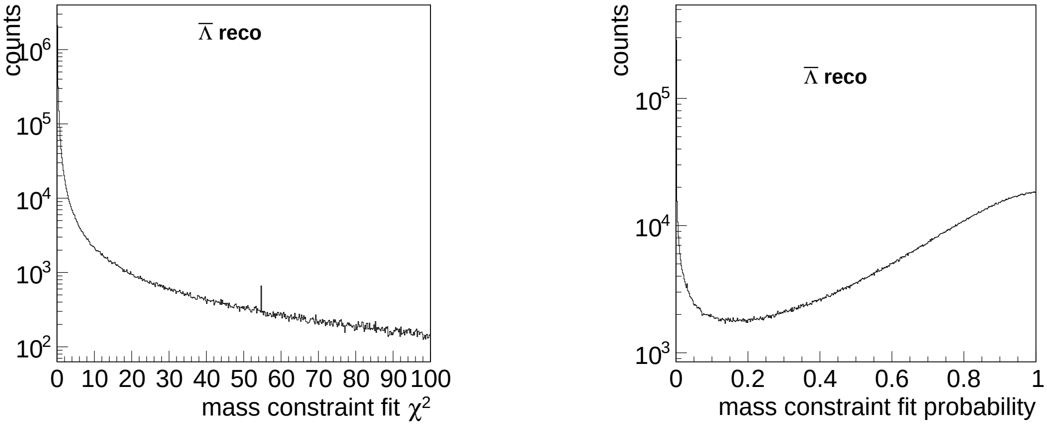

(a) (b)

Figure A.93: χ^2 and probability distributions for the kinematic fit with mass constraint condition.

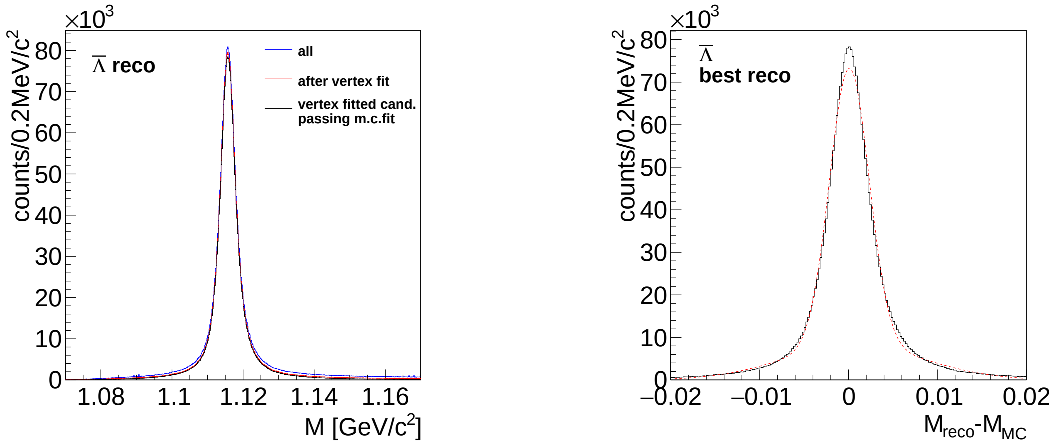

(a)

(b)

Figure A.94: a) Mass distribution for $\bar{\Lambda}$ after the different steps of reconstruction. b) Deviation of reconstructed and generated $\bar{\Lambda}$ mass.

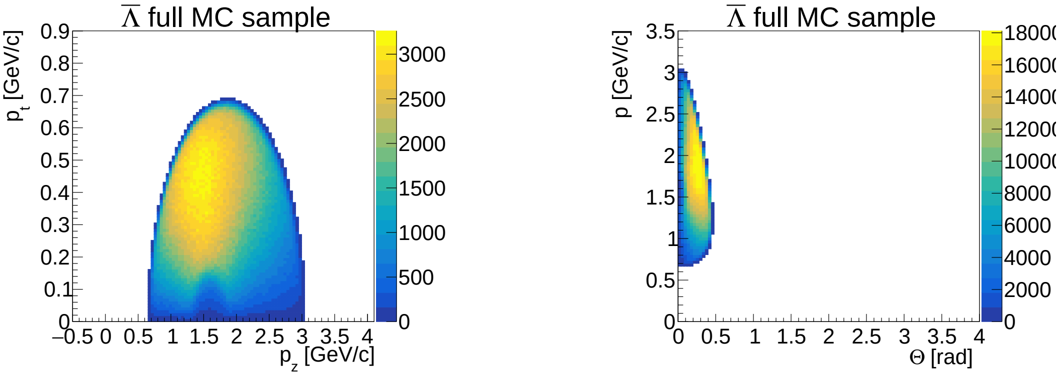

(a)

(b)

Figure A.95: Transverse versus longitudinal momentum (a) and total momentum vs. Θ angle (b) for generated $\bar{\Lambda}$.

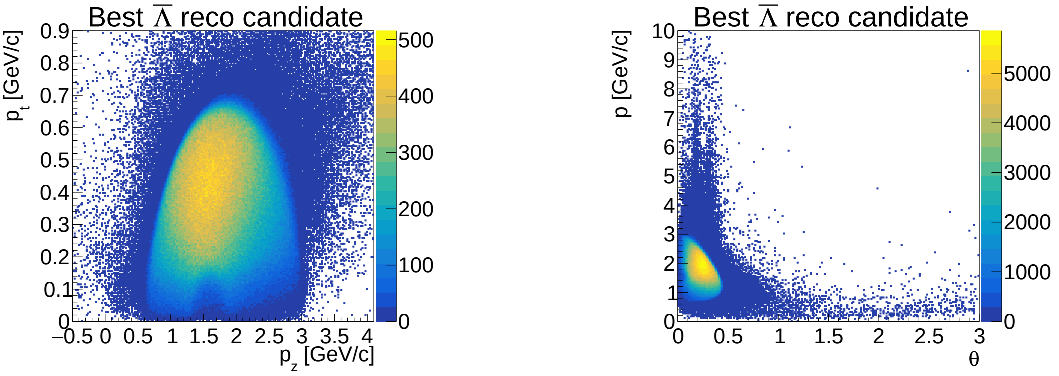

(a)

(b)

Figure A.96: Transverse versus longitudinal momentum (a) and total momentum vs. Θ angle (b) for reconstructed $\bar{p}$ as daughter of $\bar{\Lambda}$.

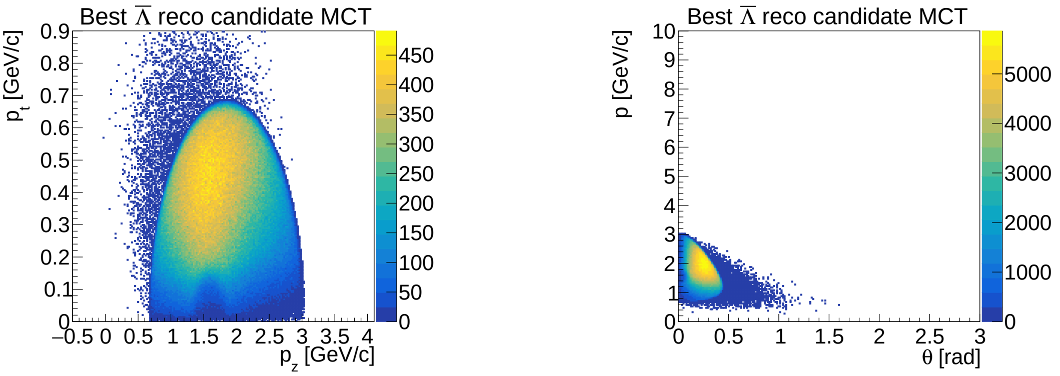

(a) (b)

Figure A.97: Transverse versus longitudinal momentum (a) and total momentum vs. Θ angle (b) for MC partner of reconstructed $\bar{\Lambda}$.

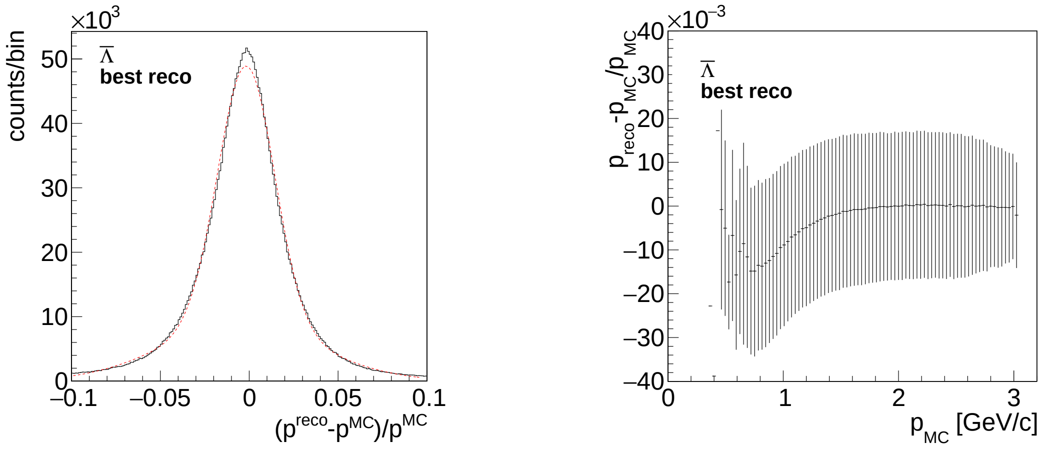

(a) (b)

Figure A.98: Momentum resolution (a) and relative deviation of the reconstructed and generated total momentum (b) for $\bar{\Lambda}$.

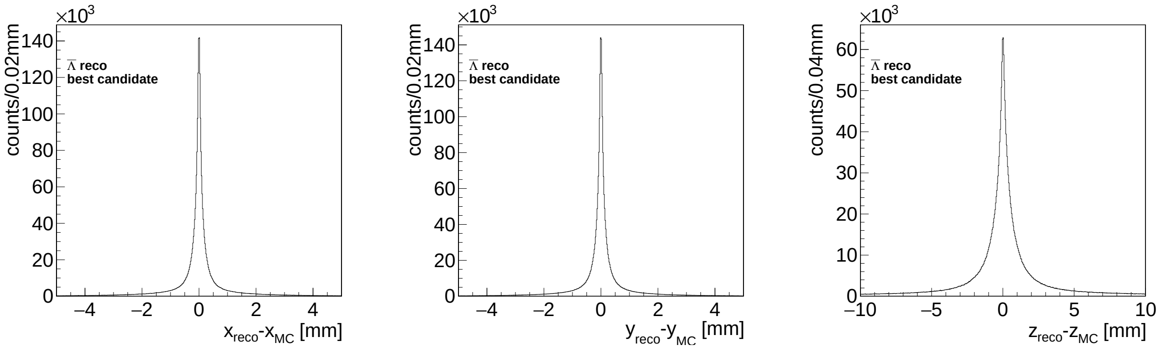

(a) (b) (c)

Figure A.99: Deviation of generated and reconstructed decay vertex position for the x coordinate (a), y coordinate (b) and z coordinate (c) for best $\bar{\Lambda}$ candidates.

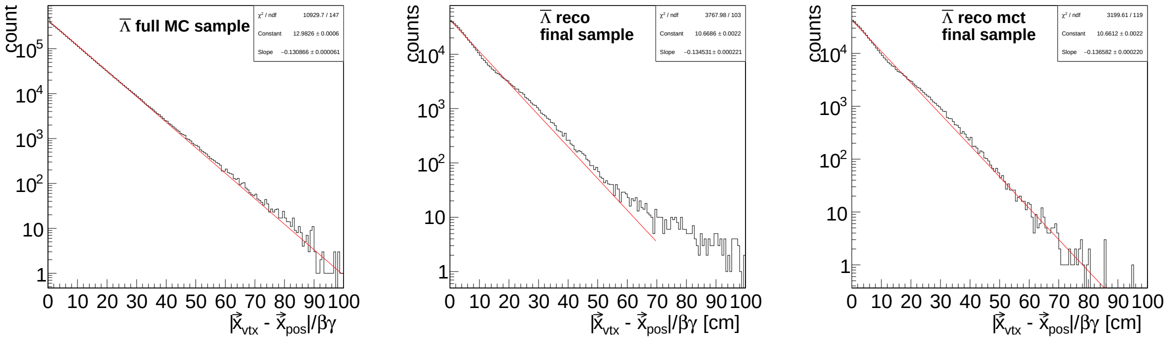

(a) (b) (c)

Figure A.100: Proper time distributions for a) generated, b) reconstructed best $\bar{\Lambda}$ candidates and c) MC partner of best $\bar{\Lambda}$ candidates.

A.2.4 Ξ^- Candidates

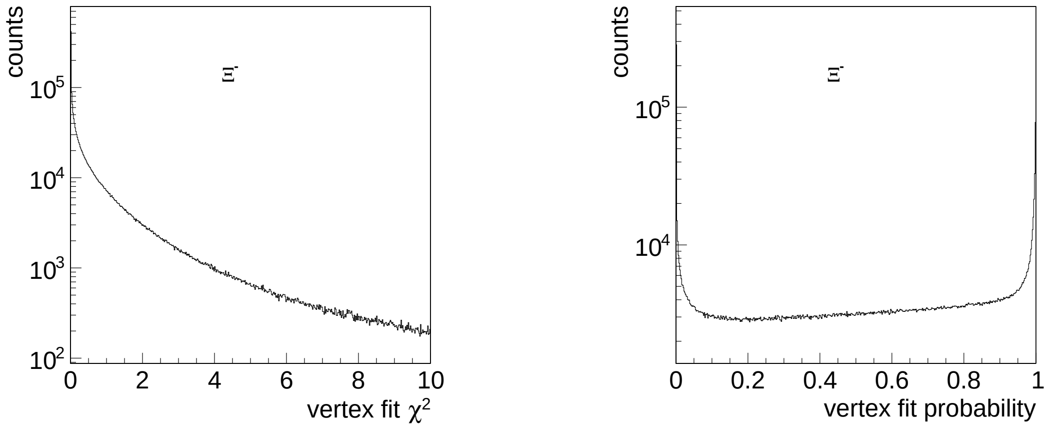

(a)

(b)

Figure A.101: χ^2 and probability distributions for the vertex fit.

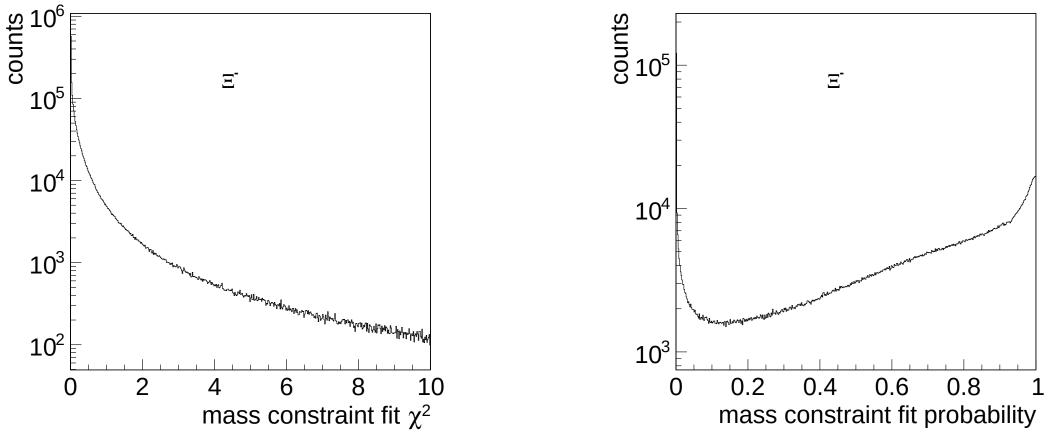

(a)

(b)

Figure A.102: χ^2 and probability distributions for the kinematic fit with mass constraint condition.

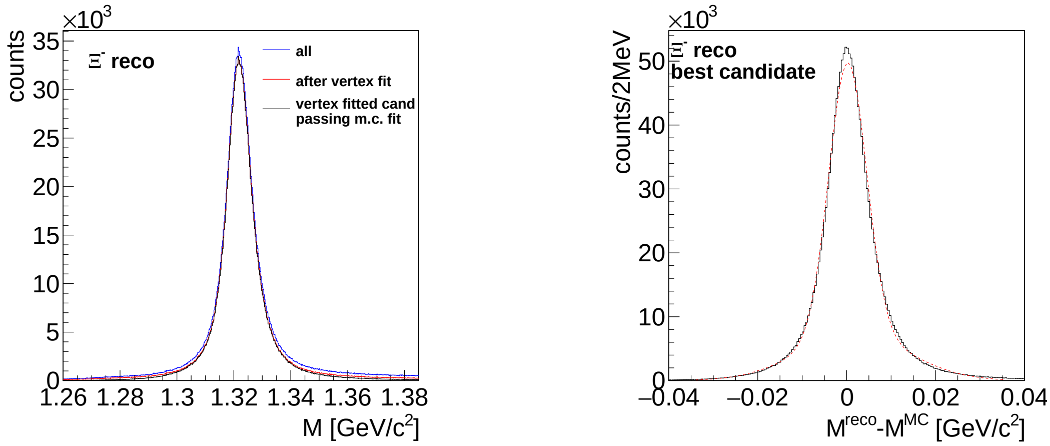

(a)

(b)

Figure A.103: a) Mass distribution for Ξ^- after the different steps of reconstruction. b) Deviation of reconstructed and generated Ξ^- mass.

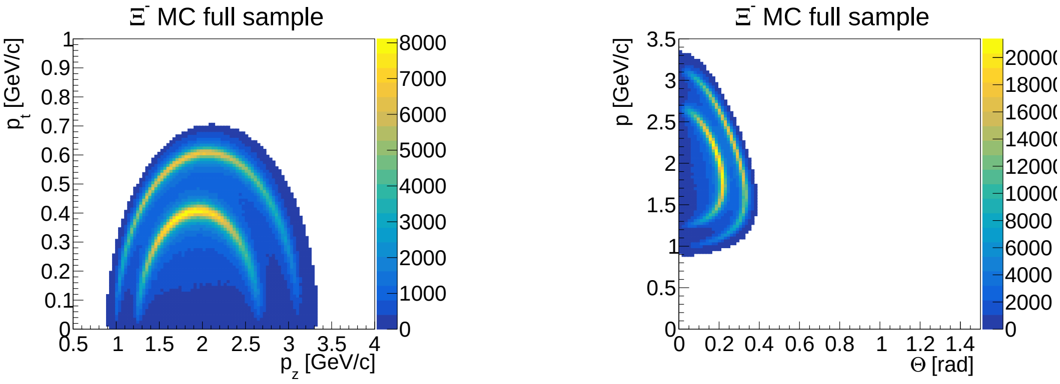

(a)

(b)

Figure A.104: Transverse versus longitudinal momentum (a) and total momentum vs. Θ angle (b) for generated Ξ^-.

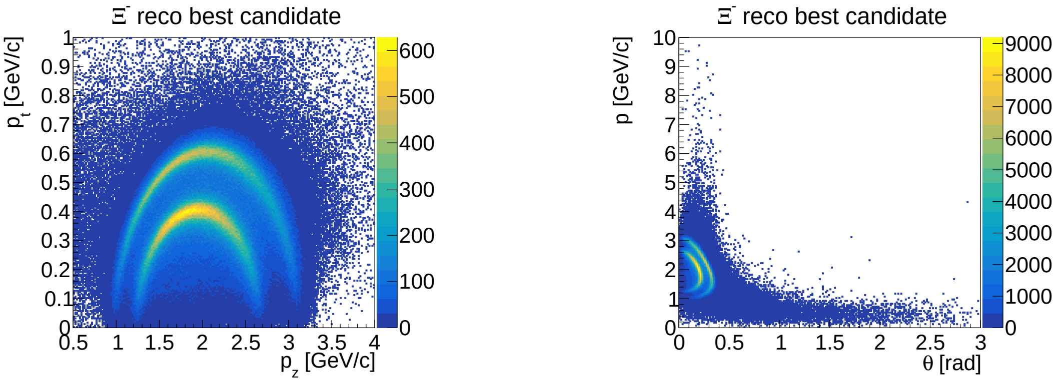

(a)

(b)

Figure A.105: Transverse versus longitudinal momentum (a) and total momentum vs. Θ angle (b) for reconstructed Ξ^-.

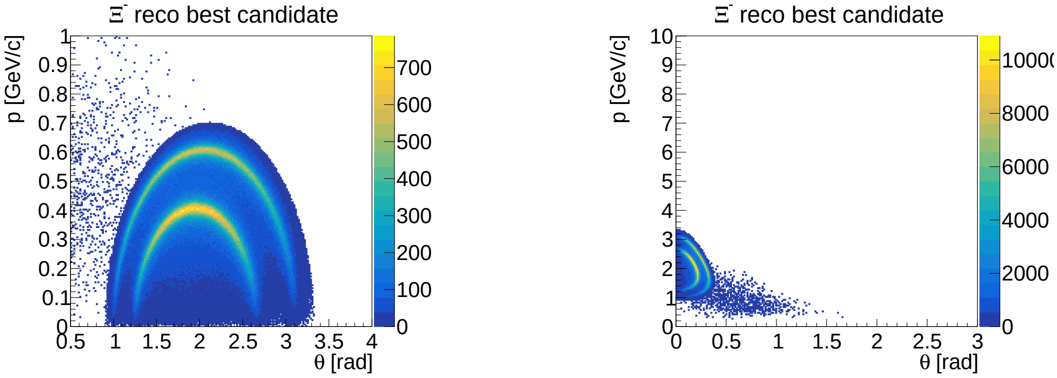

(a) (b)

Figure A.106: Transverse versus longitudinal momentum (a) and total momentum vs. Θ angle (b) for MC partner of reconstructed Ξ^-.

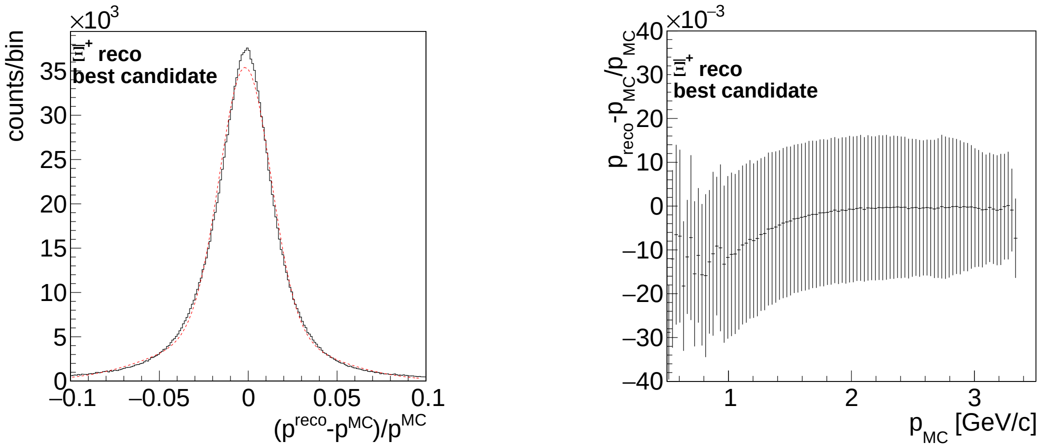

(a) (b)

Figure A.107: Momentum resolution (a) and relative deviation of the reconstructed and generated total momentum (b) for Ξ^-.

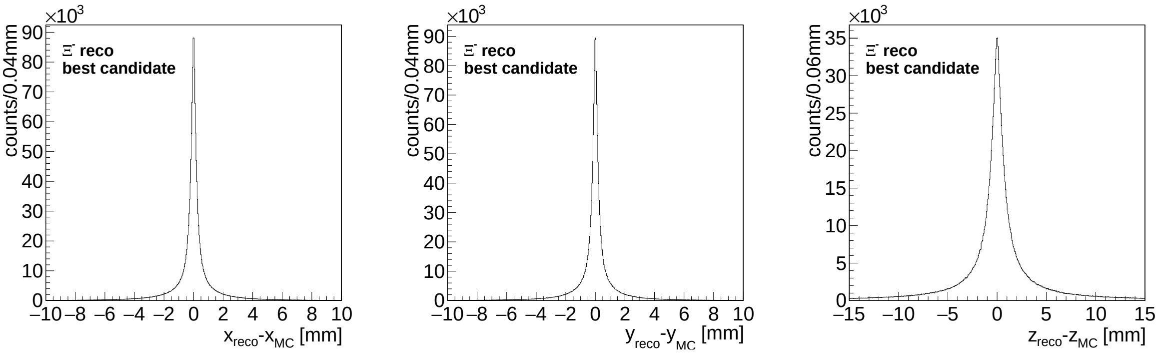

(a) (b) (c)

Figure A.108: Deviation of generated and reconstructed decay vertex position for the x coordinate (a), y coordinate (b) and z coordinate (c) for best Ξ^- candidates.

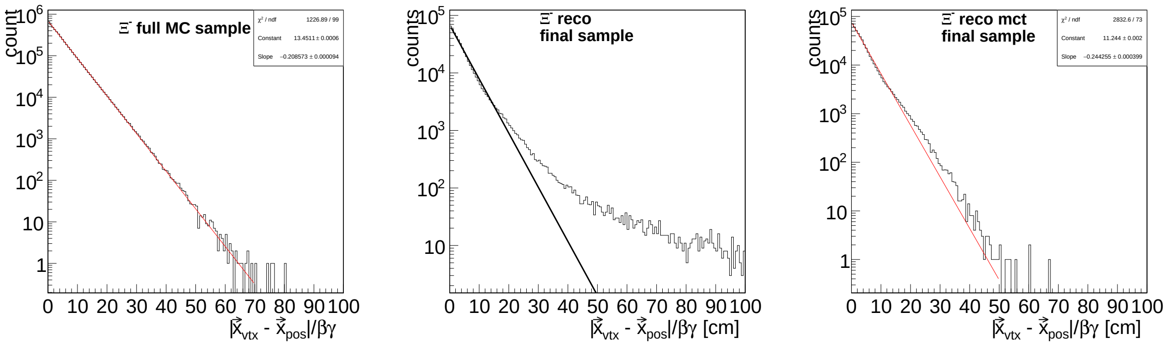

(a) (b) (c)

Figure A.109: Proper time distributions for a) generated, b) reconstructed best Ξ^- candidates and c) MC partner of best Ξ^- candidates.

A.2.5 $\Xi^- \bar{\Lambda}\, \text{K}^+$

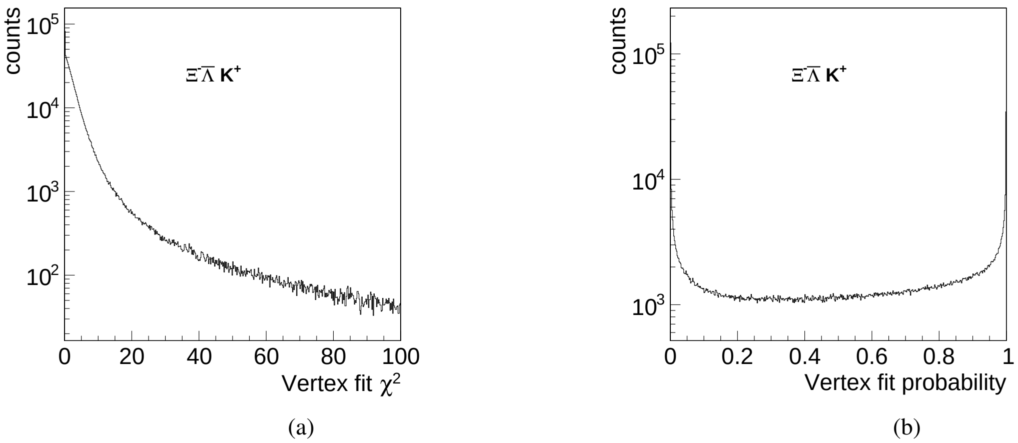

(a) (b)

Figure A.110: Vertex fit χ^2 (a) and probability (b) distribution for $\bar{\text{p}}\text{p} \rightarrow \Xi^- \bar{\Lambda}\, \text{K}^+$

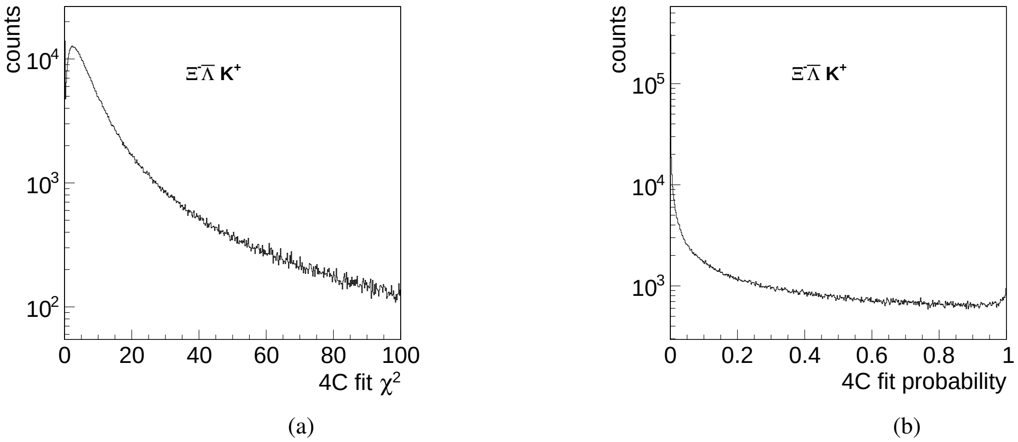

(a) (b)

Figure A.111: 4C-fit χ^2 (a) and probability (b) distribution.

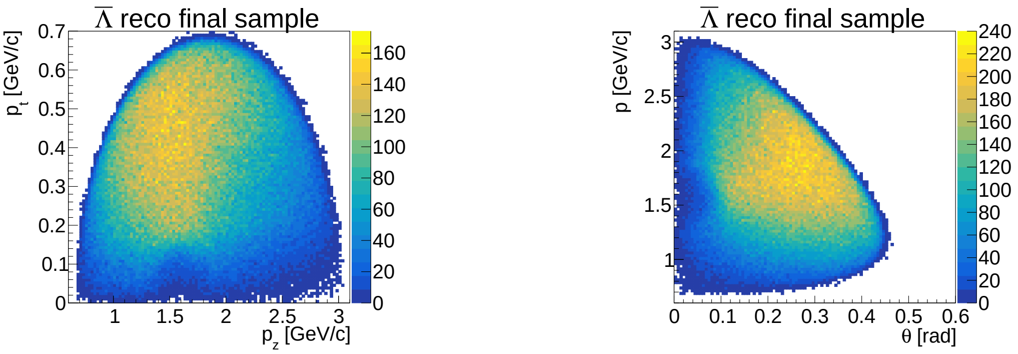

(a) (b)

Figure A.112: Transverse versus longitudinal momentum (a) and total momentum vs. Θ angle (b) for final selected $\bar{\Lambda}$.

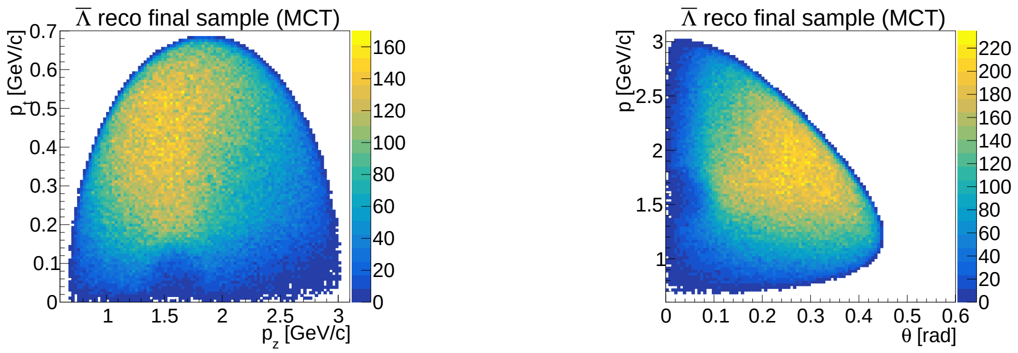

(a) (b)

Figure A.113: Transverse vs. longitudinal momentum and total momentum vs. Θ angle for the MC-truth partner of the final selected $\bar{\Lambda}$.

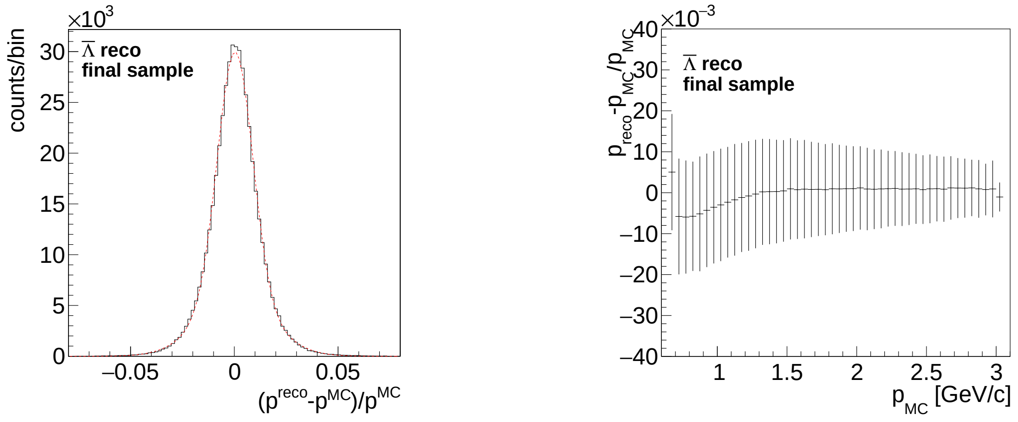

(a) (b)

Figure A.114: Momentum resolution (a) and relative deviation of the reconstructed and generated total momentum (b) for the final selected $\bar{\Lambda}$ candidates.

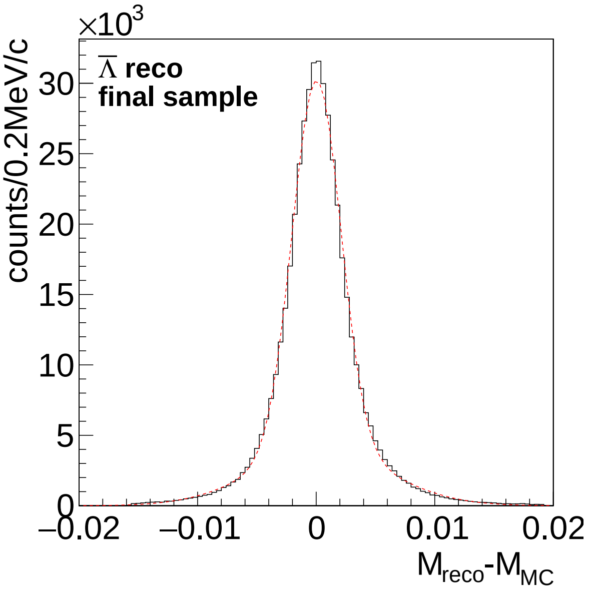

Figure A.115: Deviation of final reconstructed and generate $\bar{\Lambda}$ mass.

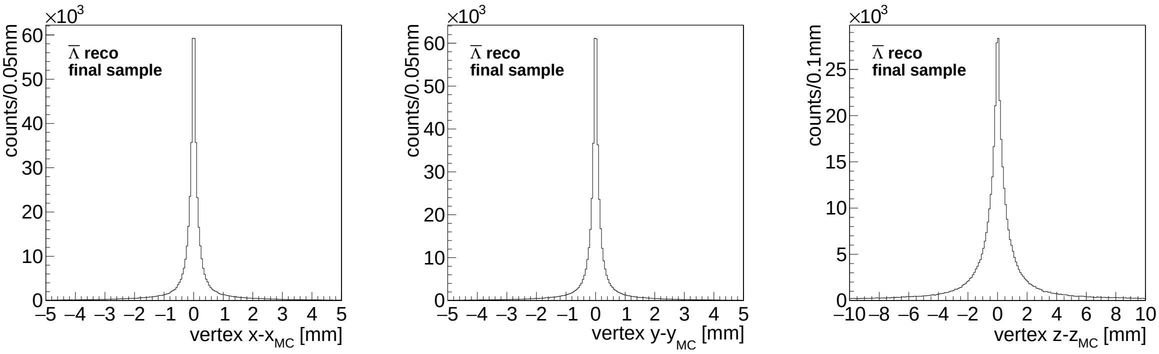

(a) (b) (c)

Figure A.116: Deviation of the final reconstructed $\bar{\Lambda}$ decay vertex position and the corresponding MC decay vertex position for the x coordinate (a), the y coordinate (b) and the z coordinate (c).

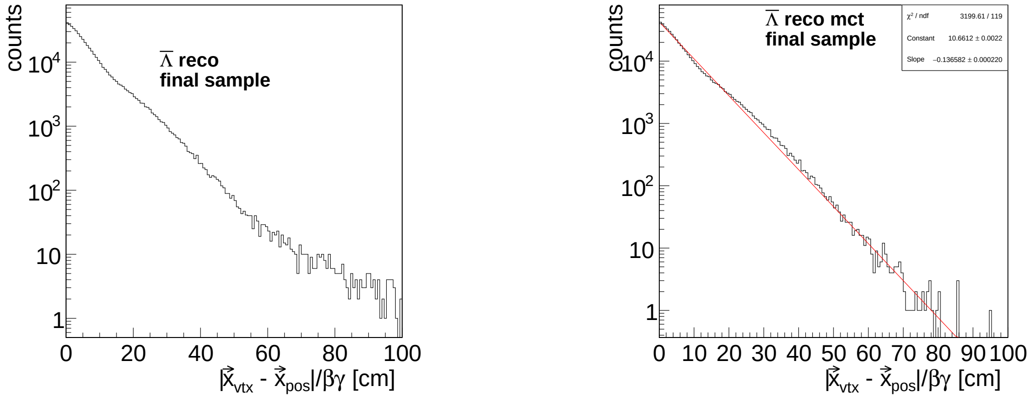

(a) (b)

Figure A.117: Propertime distribution for the reconstructed (a) and the MC partners (b) of the final selected $\bar{\Lambda}$.

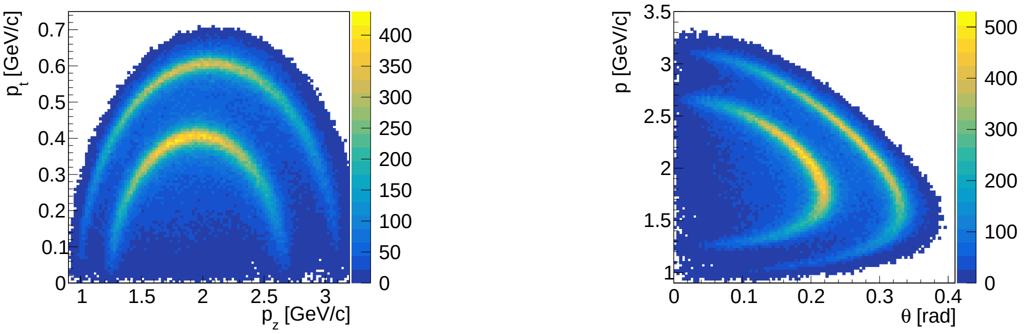

(a)

(b)

Figure A.118: Transverse versus longitudinal momentum (a) and total momentum vs. Θ angle (b) for final selected Ξ^-.

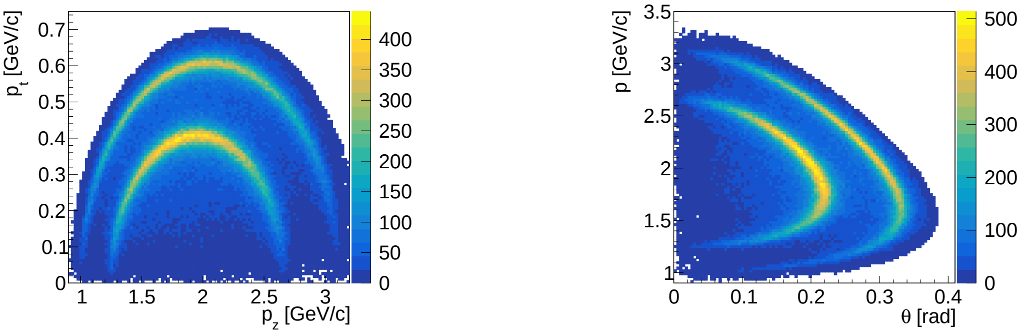

(a)

(b)

Figure A.119: Transverse versus longitudinal momentum (a) and total momentum vs. Θ angle (b) for the MC partner of the final selected Ξ^-.

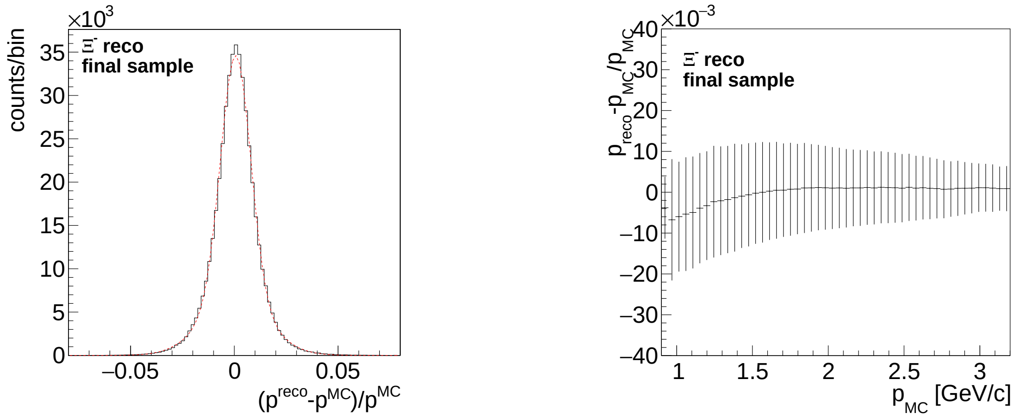

(a)

(b)

Figure A.120: Momentum resolution (a) and relative deviation of the reconstructed and generated total momentum (b) for the final selected Ξ^-.

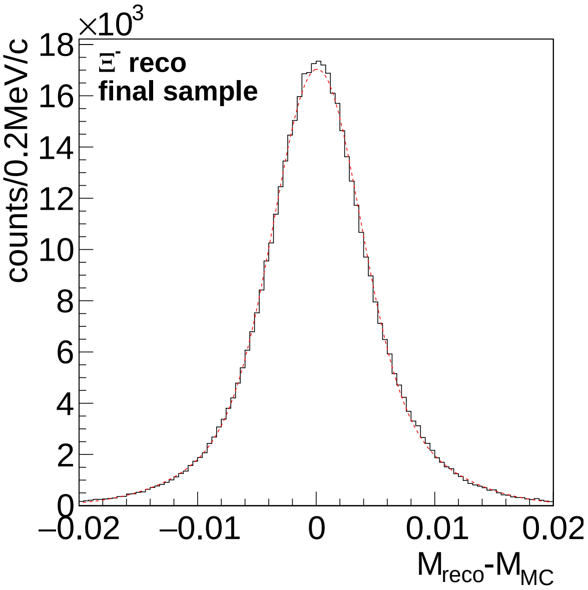

Figure A.121: Deviation of final reconstructed and generate Ξ^- mass.

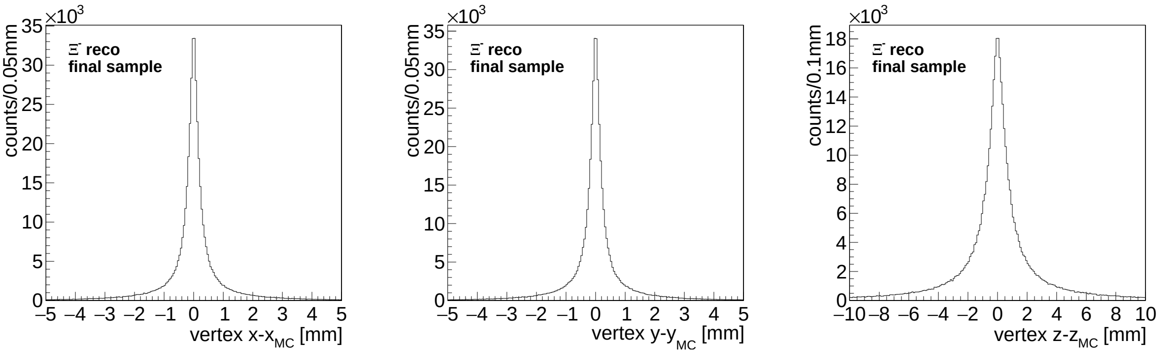

(a)

(b)

(c)

Figure A.122: Deviation of the final reconstructed Ξ^- decay vertex position and the corresponding MC decay vertex position for the x coordinate (a), the y coordinate (b) and the z coordinate (c).

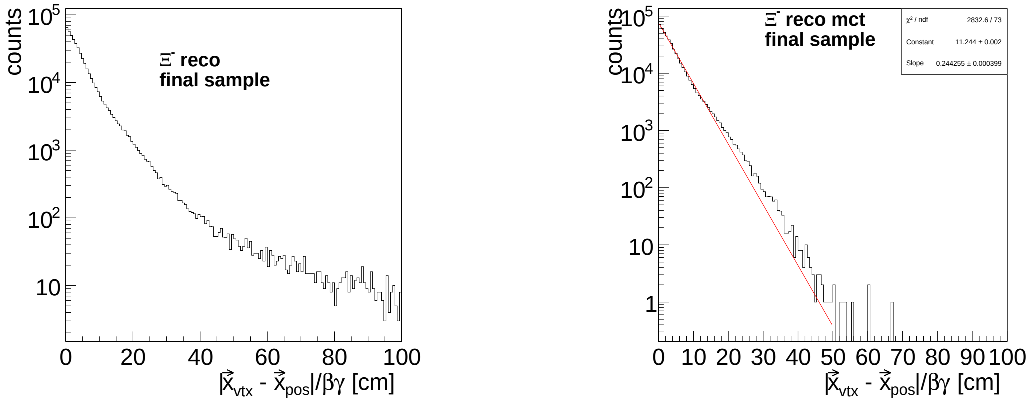

(a)

(b)

Figure A.123: Propertime distribution for the reconstructed (a) and the MC partners (b) of the final selected Ξ^-.

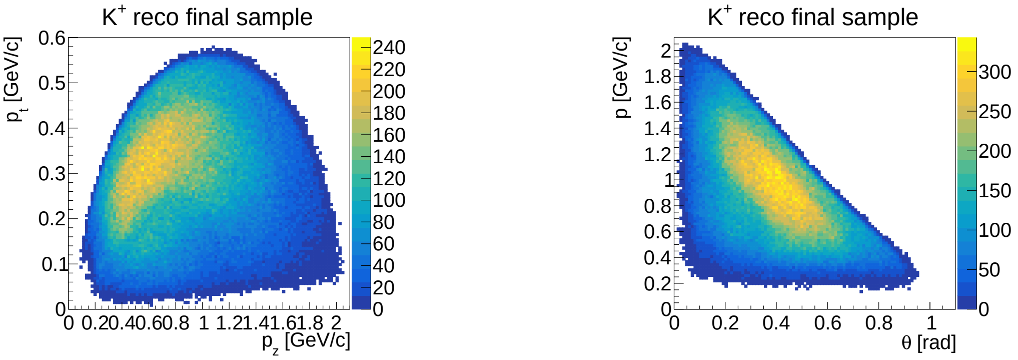

(a) (b)

Figure A.124: Transverse versus longitudinal momentum (a) and total momentum vs. Θ angle (b) for final selected K^+

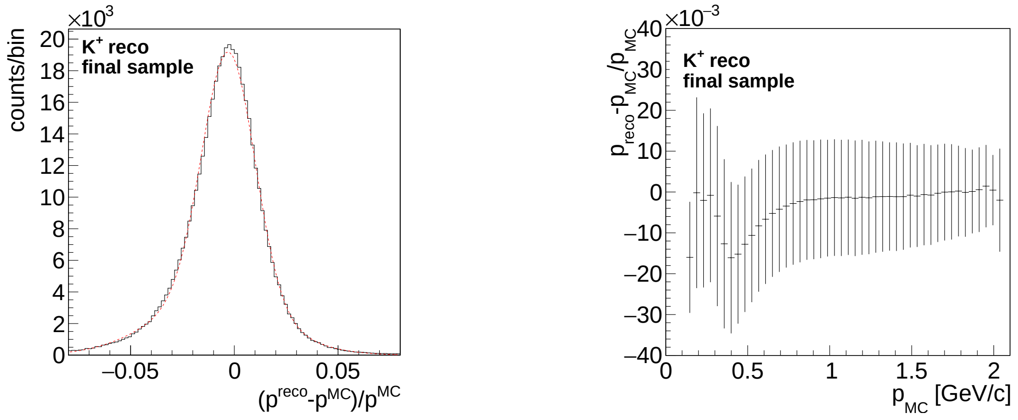

(a) (b)

Figure A.125: Momentum resolution (a) and relative deviation of the reconstructed and generated total momentum (b) for the final selected K^+ candidates.

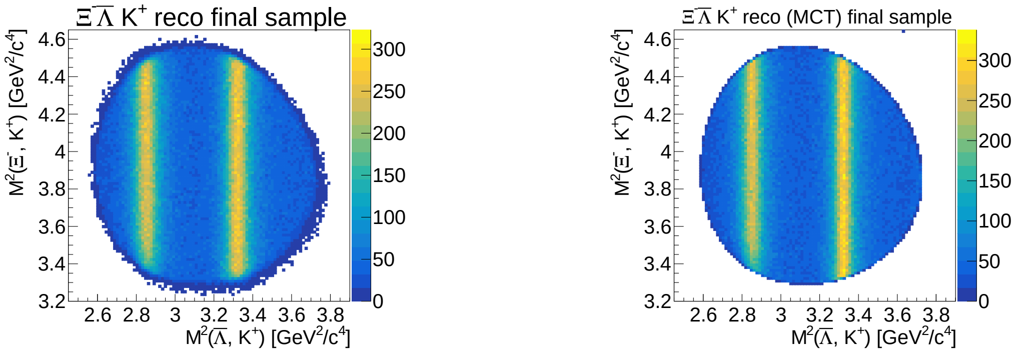

(a) (b)

Figure A.126: Dalitz plot for the final selected candidate (a) and their MC partners (b).

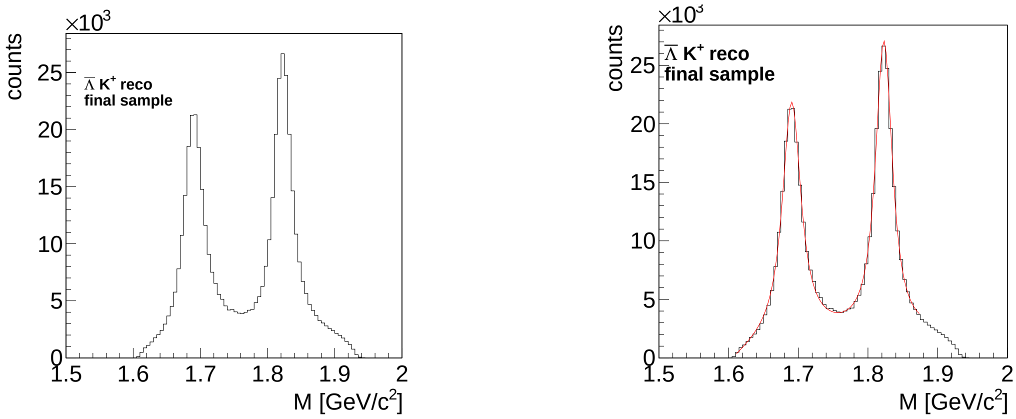

(a)

(b)

Figure A.127: Mass distribution of the $\bar{\Lambda}$ K^+ system: a) unfitted and b) fitted with the sum of two Voigt functions and a polynomial.

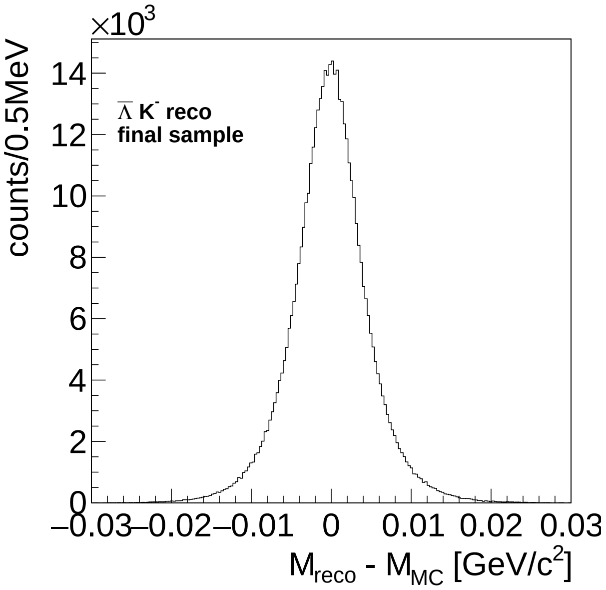

Figure A.128: Deviation of final reconstructed and generate $\bar{\Lambda}$ K^+ mass

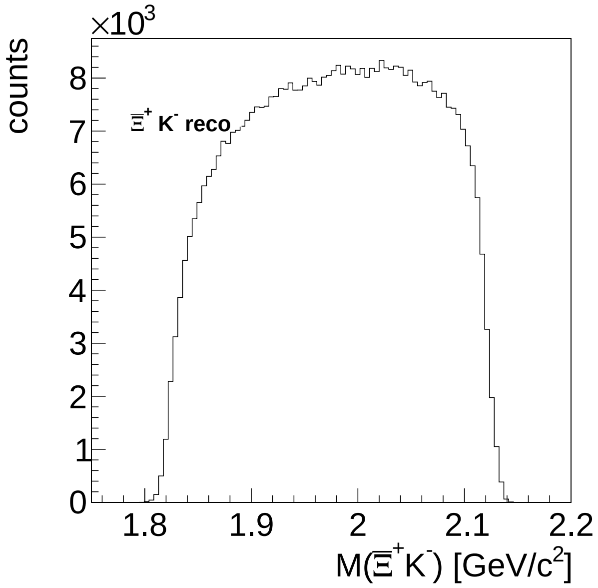

Figure A.129: Mass distribution for the final selected Ξ^- K^+.

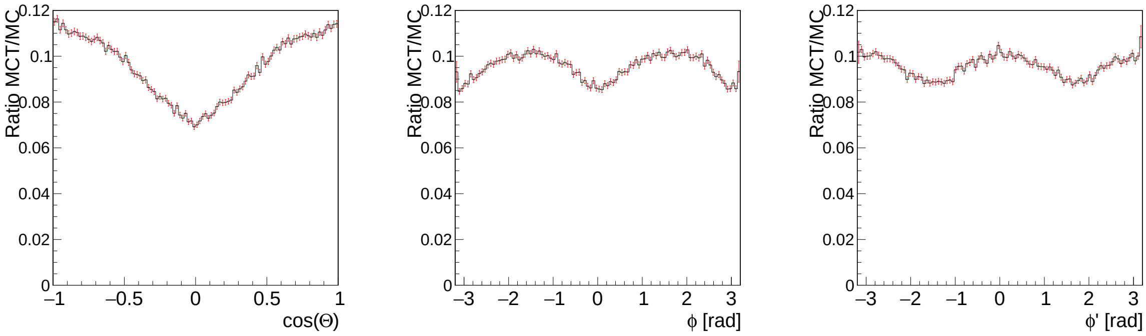

(a) (b) (c)

Figure A.130: $\cos\theta_{\text{cm}}$ (a), ϕ_{cm} (b) and $\phi\prime_{\text{cm}}$ ratio between the MC partners of the final reconstructed candidates and the generated sample.

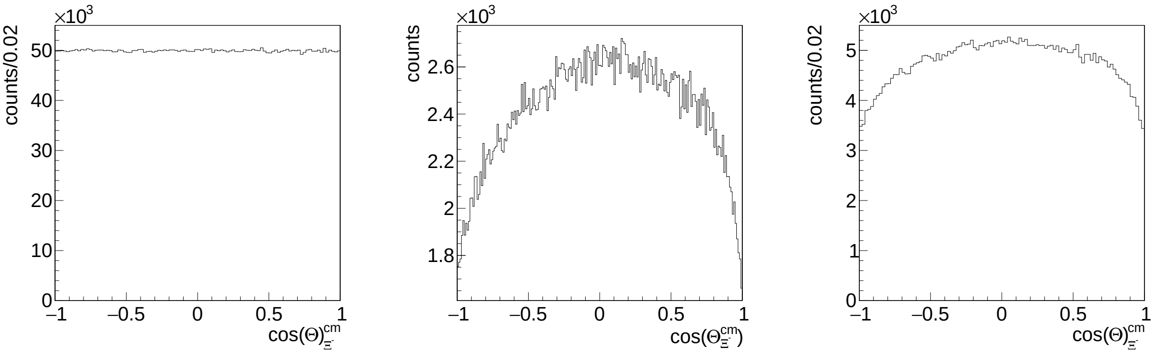

(a) (b) (c)

Figure A.131: Generated (a) and reconstructed (b) $\cos\theta$ distribution in the center-of-mass frame for final selected Ξ^- as well as the distribution for the MC partners of the reconstructed Ξ^- candidates (c).

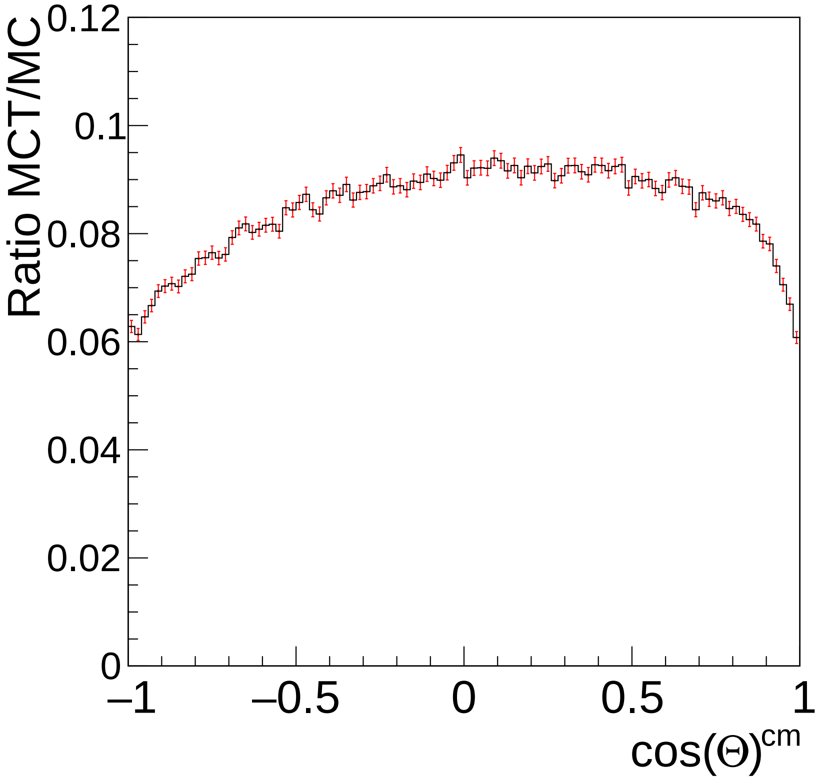

Figure A.132: Ratio plot of the $\cos\theta$ distribution in the center-of-mass frame for the final selected Ξ^- candidates.

A.3 Analysis of $\bar{\mathrm{p}}\mathrm{p} \to \overline{\Xi}^{+}\,\Lambda\,\mathrm{K}^{-}$ with the Full Decay Tree Fit

A.3.1 Final State Particles

π^{-} from Λ

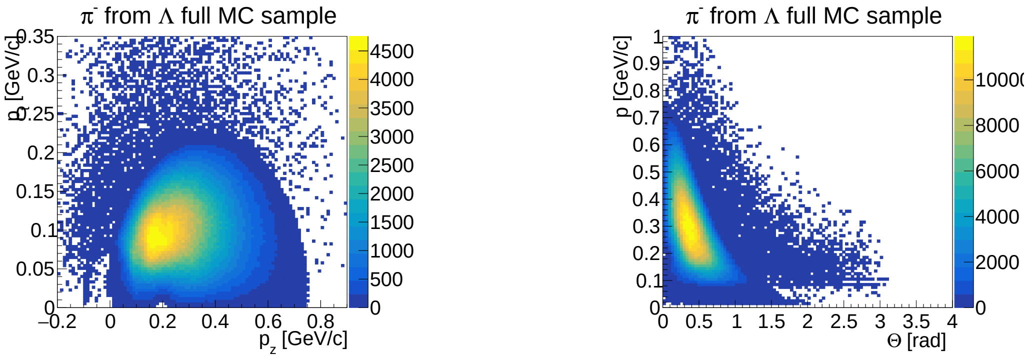

(a) (b)

Figure A.133: Transverse versus longitudinal momentum (a) and total momentum vs. Θ angle (b) for generated π^{-} from Λ.

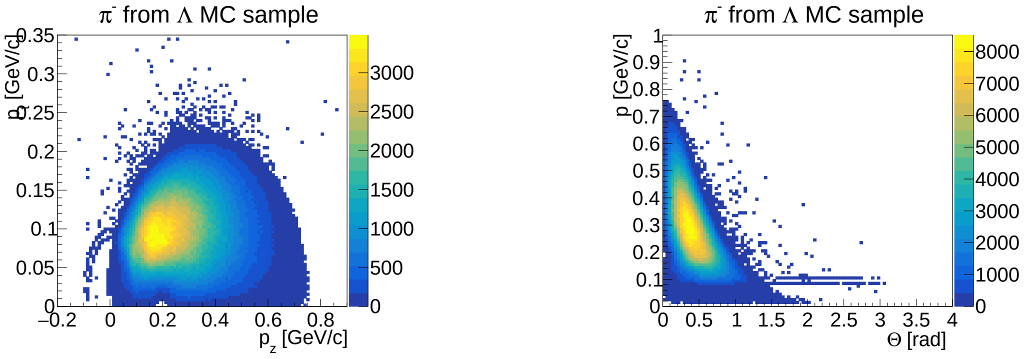

(a) (b)

Figure A.134: Transverse versus longitudinal momentum (a) and total momentum vs. Θ angle (b) for generated π^{-} from Λ requesting that Λ and Ξ^{*} have only two daughters.

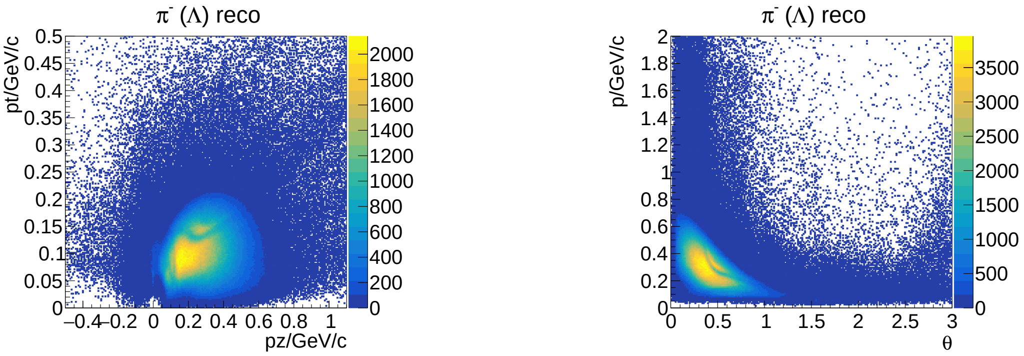

(a) (b)

Figure A.135: Transverse versus longitudinal momentum (a) and total momentum vs. Θ angle (b) for the reconstructed π^- from Λ.

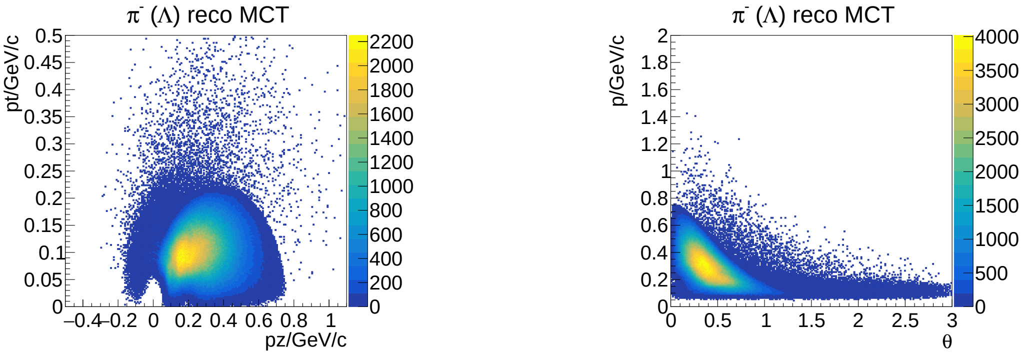

(a) (b)

Figure A.136: Transverse versus longitudinal momentum (a) and total momentum vs. Θ angle (b) for the MC partner of the reconstructed π^- from Λ.

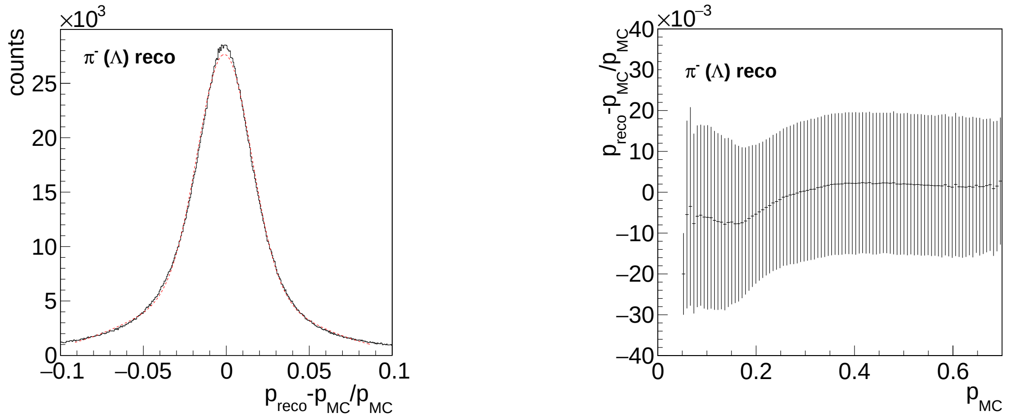

(a) (b)

Figure A.137: Momentum resolution (a) and relative deviation of the reconstructed and generated total momentum (b) for π^- from Λ.

π^{+} from $\bar{\Lambda}$

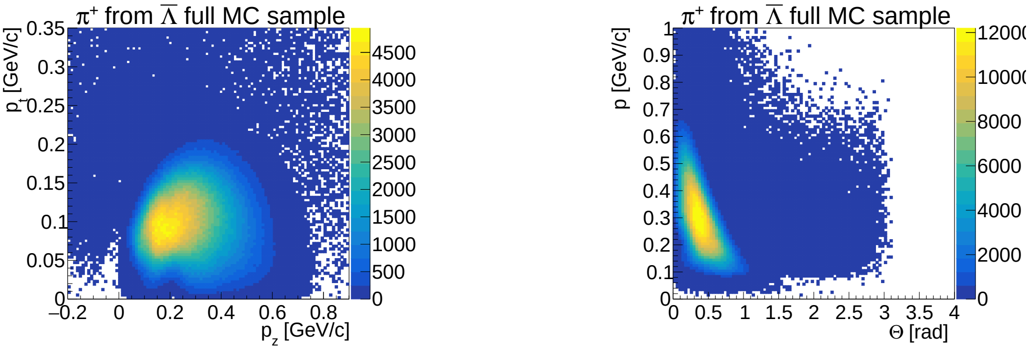

(a) (b)

Figure A.138: Transverse versus longitudinal momentum (a) and total momentum vs. Θ angle (b) for generated π^{+} from $\bar{\Lambda}$.

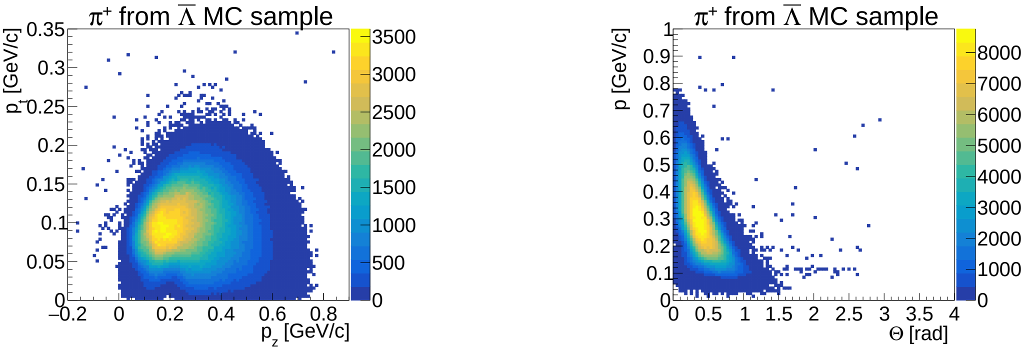

(a) (b)

Figure A.139: Transverse versus longitudinal momentum (a) and total momentum vs. Θ angle (b) for generated π^{+} from $\bar{\Lambda}$ requesting that $\bar{\Lambda}$ and $\overline{\Xi}^{+}$ have only two daughter particles.

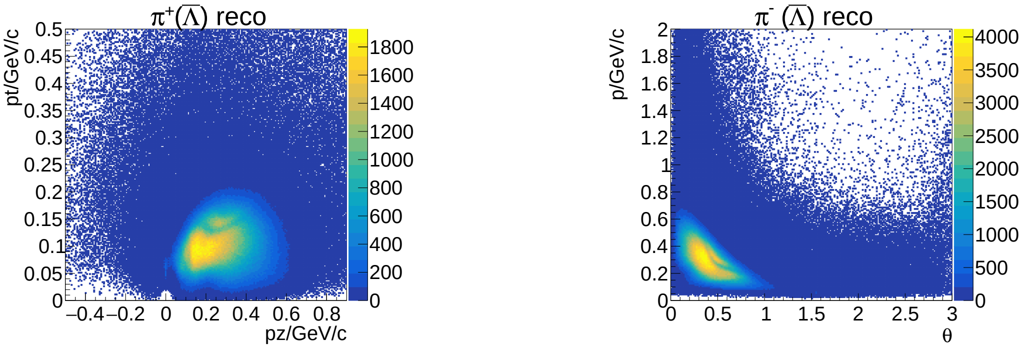

(a)

(b)

Figure A.140: Transverse versus longitudinal momentum (a) and total momentum vs. Θ angle (b) for reconstructed π^+ from $\bar{\Lambda}$.

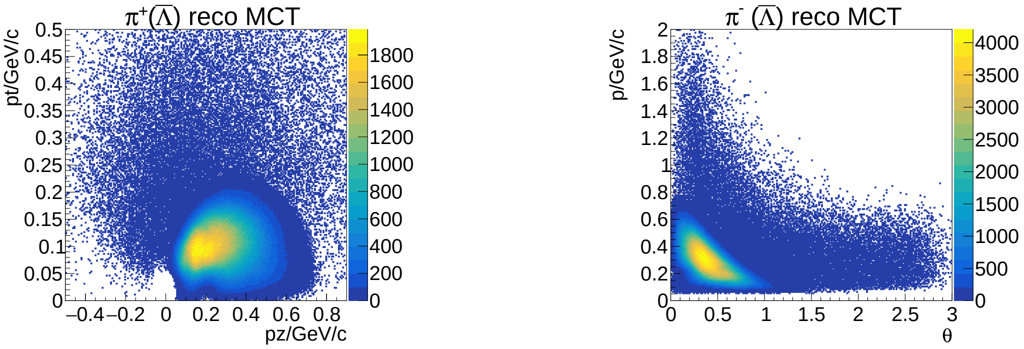

(a)

(b)

Figure A.141: Transverse versus longitudinal momentum (a) and total momentum vs. Θ angle (b) for the MC partner of the reconstructed π^+ from $\bar{\Lambda}$.

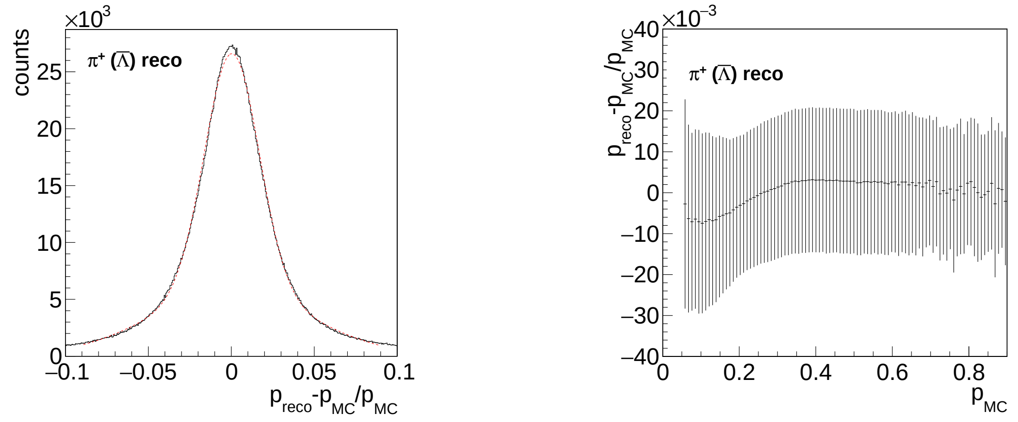

(a)

(b)

Figure A.142: Momentum resolution (a) and relative deviation of the reconstructed and generated total momentum (b) for π^+ from $\bar{\Lambda}$.

π^+ from $\overline{\Xi}^+$

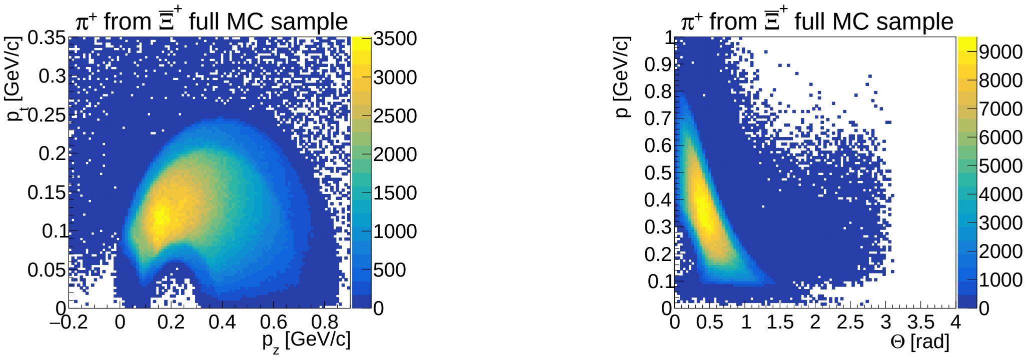

(a) (b)

Figure A.143: Transverse versus longitudinal momentum (a) and total momentum vs. Θ angle (b) for generated π^+ from $\overline{\Xi}^+$.

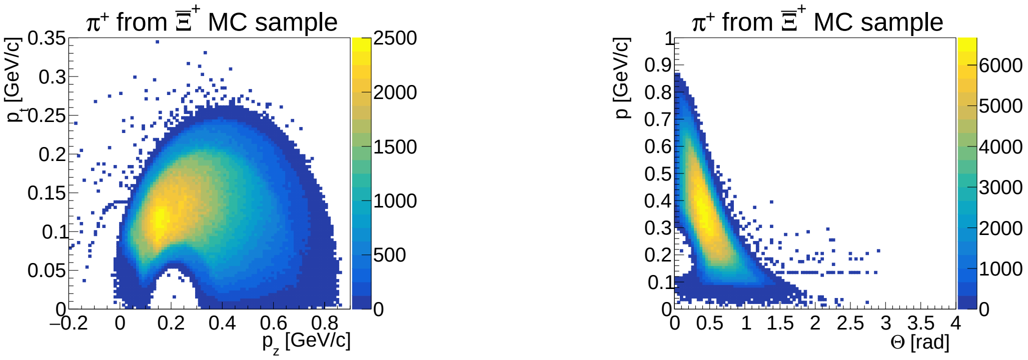

(a) (b)

Figure A.144: Transverse versus longitudinal momentum (a) and total momentum vs. Θ angle (b) for generated π^+ from $\overline{\Xi}^+$ requesting that $\overline{\Xi}^+$ has only two daughter particles.

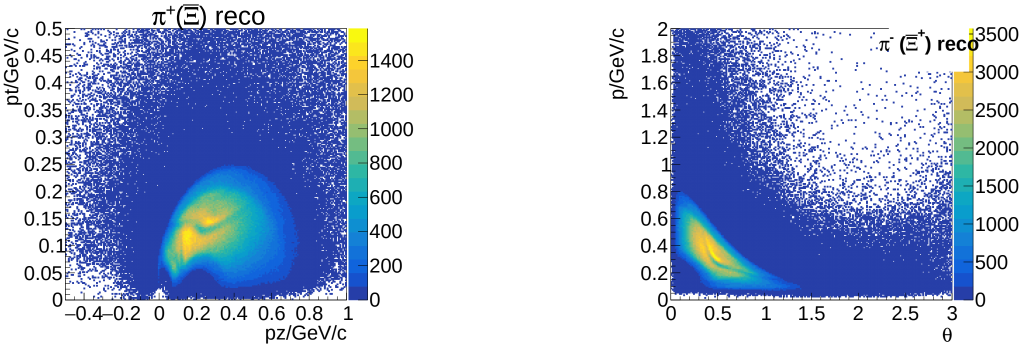

(a) (b)

Figure A.145: Transverse versus longitudinal momentum (a) and total momentum vs. Θ angle (b) for reconstructed π^+ from $\overline{\Xi}^+$.

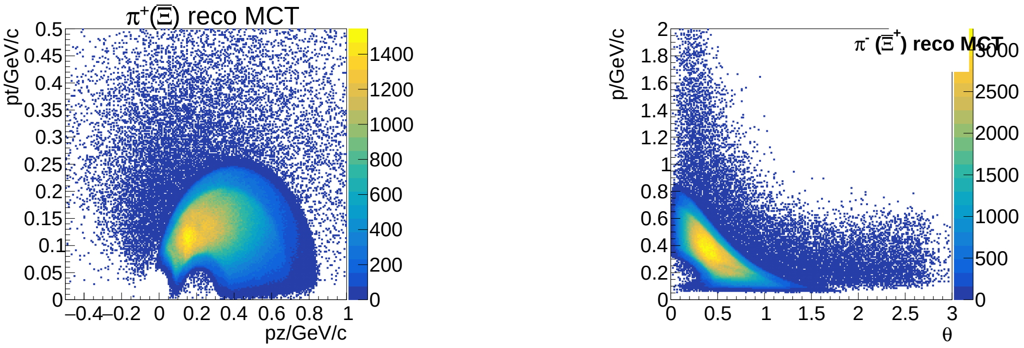

(a) (b)

Figure A.146: Transverse versus longitudinal momentum (a) and total momentum vs. Θ angle (b) for MC partner of the reconstructed π^+ from $\overline{\Xi}^+$.

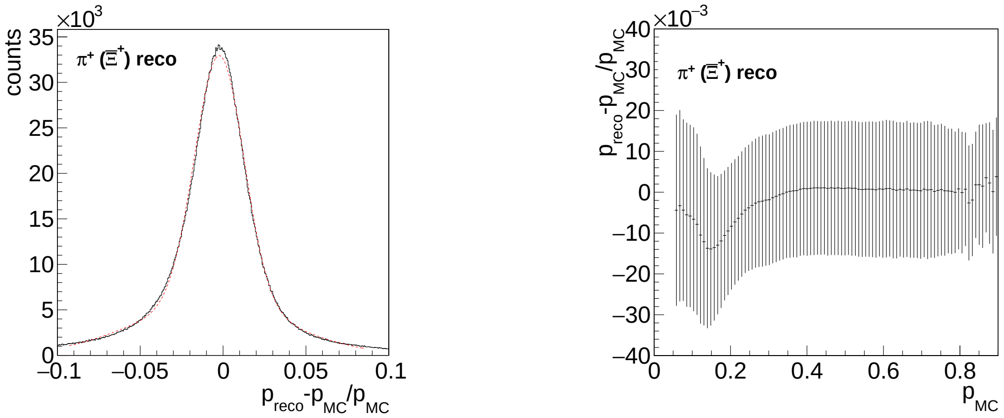

(a) (b)

Figure A.147: Momentum resolution (a) and relative deviation of the reconstructed and generated total momentum (b) for π^+ from $\overline{\Xi}^+$.

K^{-} from Ξ^{*}

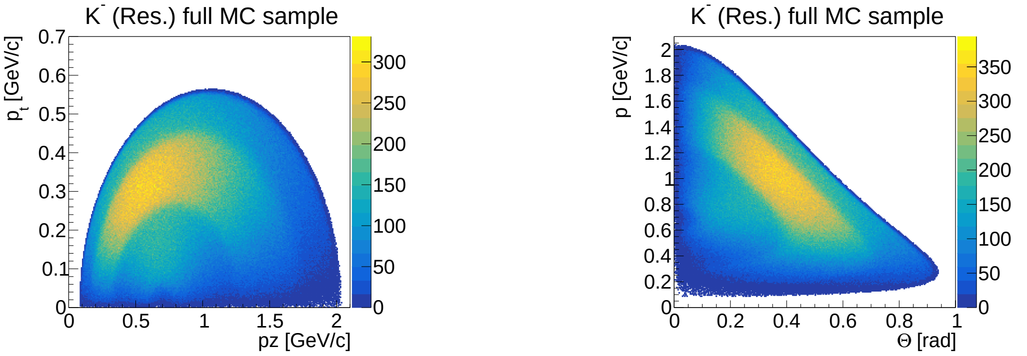

(a) (b)

Figure A.148: Transverse versus longitudinal momentum (a) and total momentum vs. Θ angle (b) for generated K^{-} from Ξ^{*}.

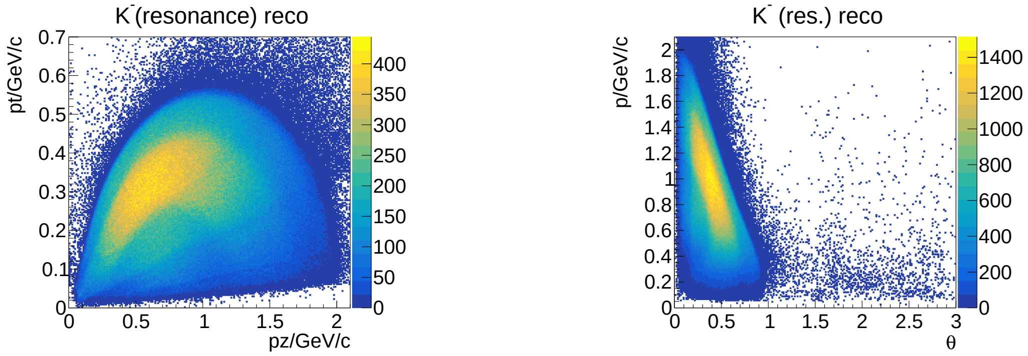

(a) (b)

Figure A.149: Transverse versus longitudinal momentum (a) and total momentum vs. Θ angle (b) for reconstructed K^{-} from Ξ^{*}.

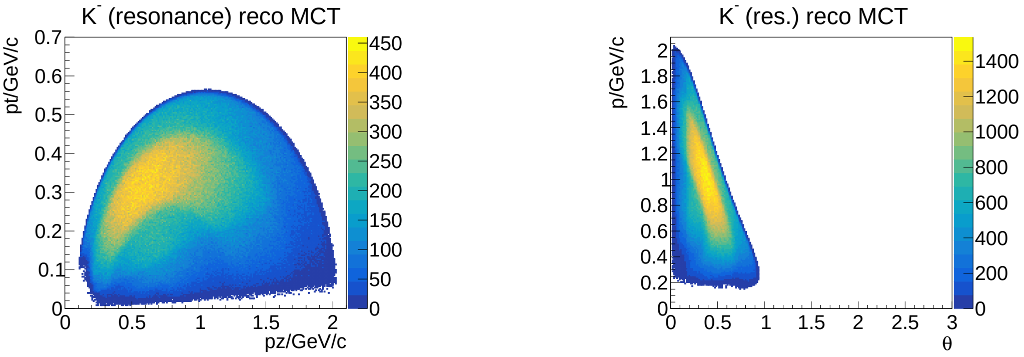

(a) (b)

Figure A.150: Transverse versus longitudinal momentum (a) and total momentum vs. Θ angle (b) for MC partner of the reconstructed K⁻ from Ξ*.

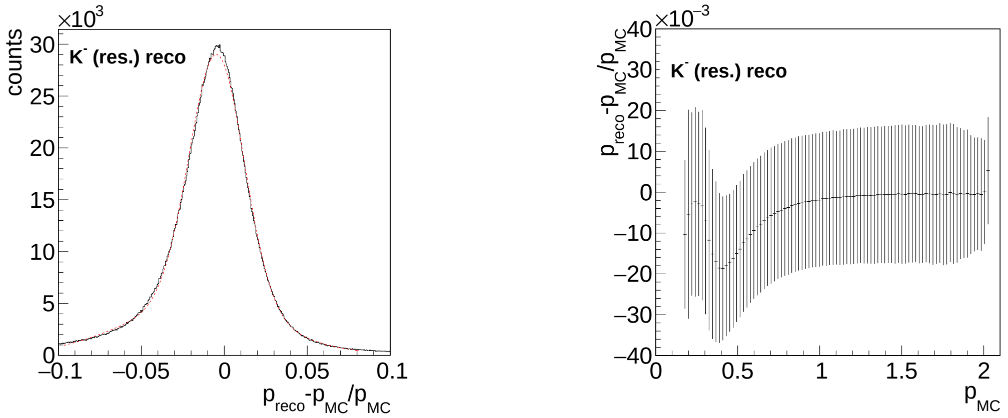

(a) (b)

Figure A.151: Momentum resolution (a) and relative deviation of the reconstructed and generated total momentum (b) for K⁻ from Ξ*.

K^{-} from Continuum

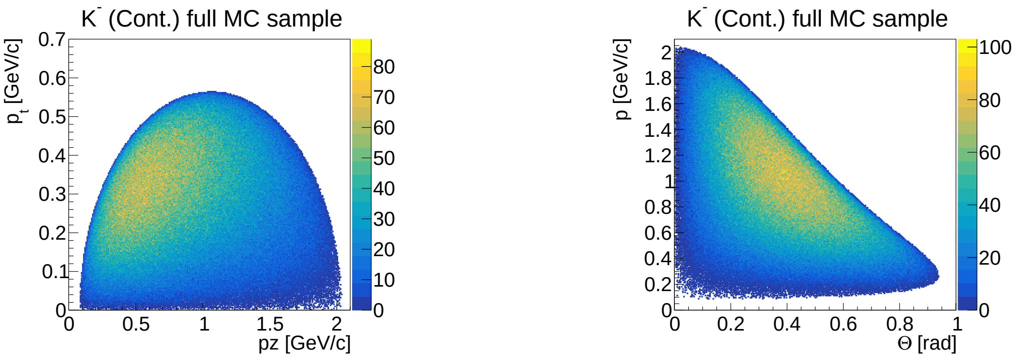

(a)

(b)

Figure A.152: Transverse versus longitudinal momentum (a) and total momentum vs. Θ angle (b) for generated K^{-} from continuum.

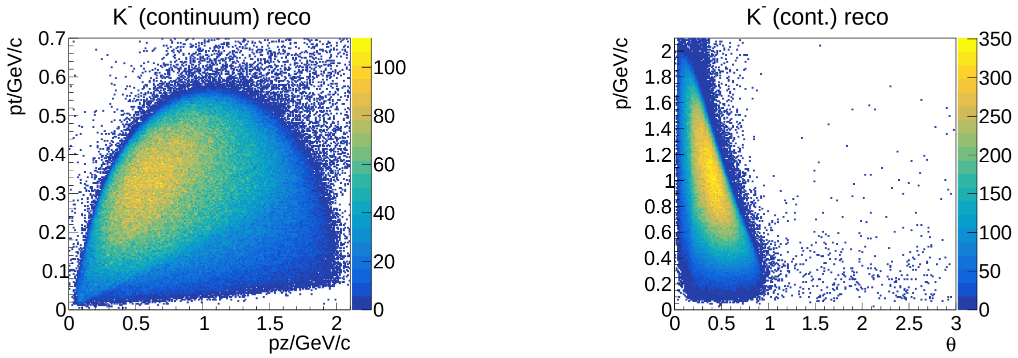

(a)

(b)

Figure A.153: Transverse versus longitudinal momentum (a) and total momentum vs. Θ angle (b) for reconstructed K^{-} from continuum.

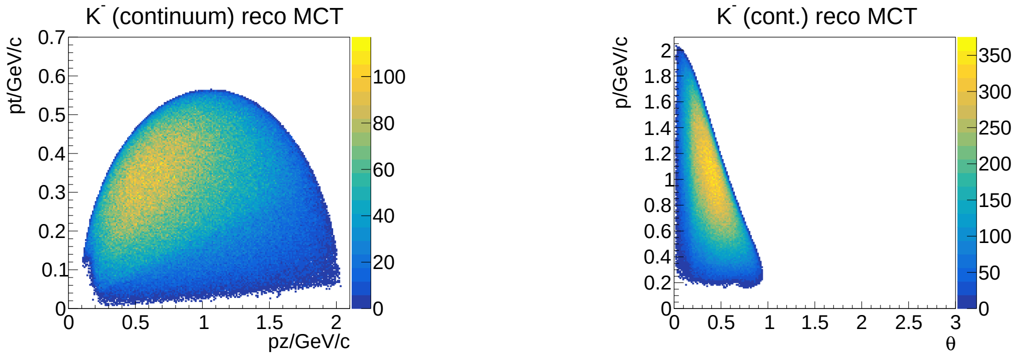

(a) (b)

Figure A.154: Transverse versus longitudinal momentum (a) and total momentum vs. Θ angle (b) for MC partner of reconstruced K$^-$ from continuum.

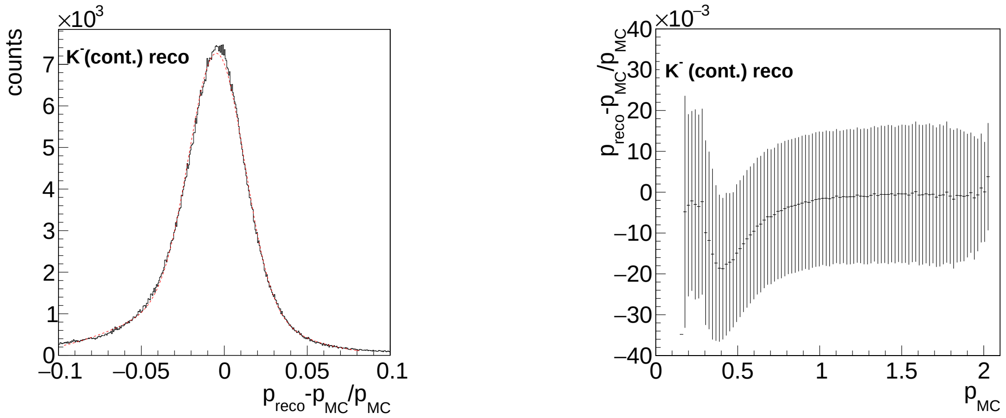

(a) (b)

Figure A.155: Momentum resolution (a) and relative deviation of the reconstructed and generated total momentum (b) for K$^-$ from continuum.

$\bar{\mathbf{p}}$

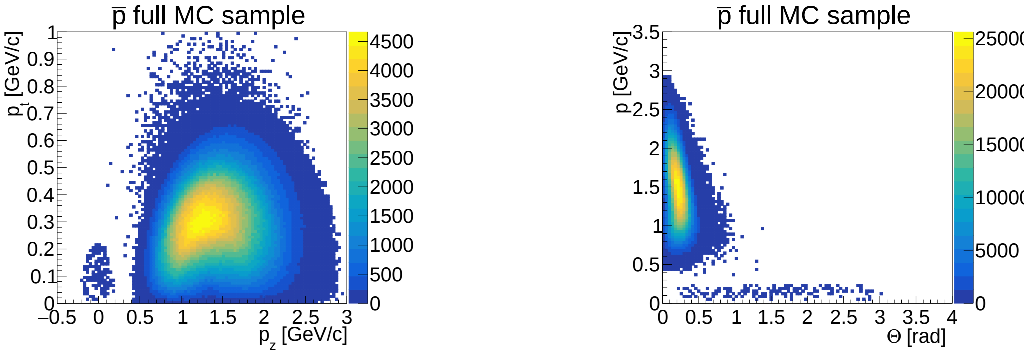

(a)

(b)

Figure A.156: Transverse versus longitudinal momentum (a) and total momentum vs. Θ angle (b) for generated $\bar{p}$.

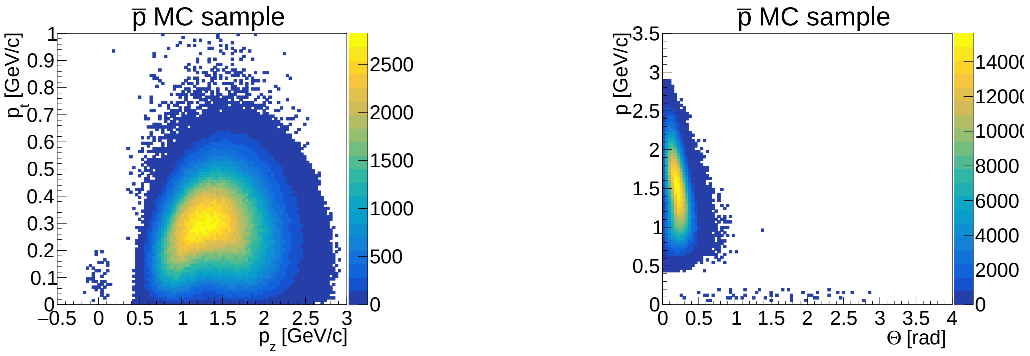

(a)

(b)

Figure A.157: Transverse versus longitudinal momentum (a) and total momentum vs. Θ angle (b) for generated $\bar{p}$ form $\bar{\Lambda}$ requesting that $\bar{\Lambda}$ and $\bar{\Xi}^{+}$ have only two daugher particles.

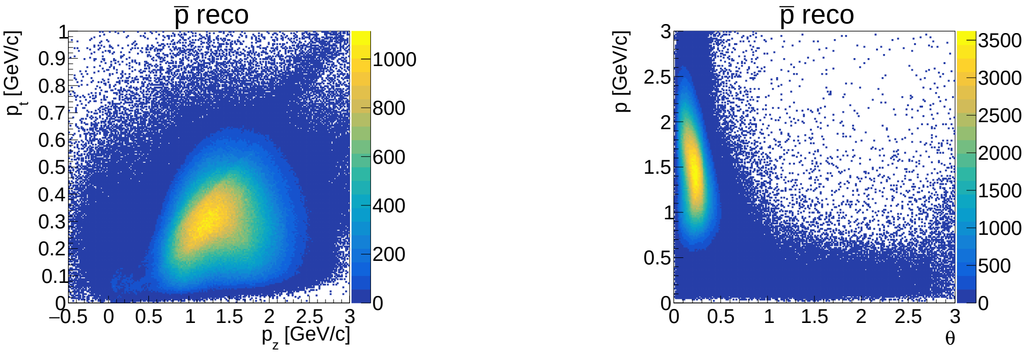

(a)

(b)

Figure A.158: Transverse versus longitudinal momentum (a) and total momentum vs. Θ angle (b) for reconstructed p̄.

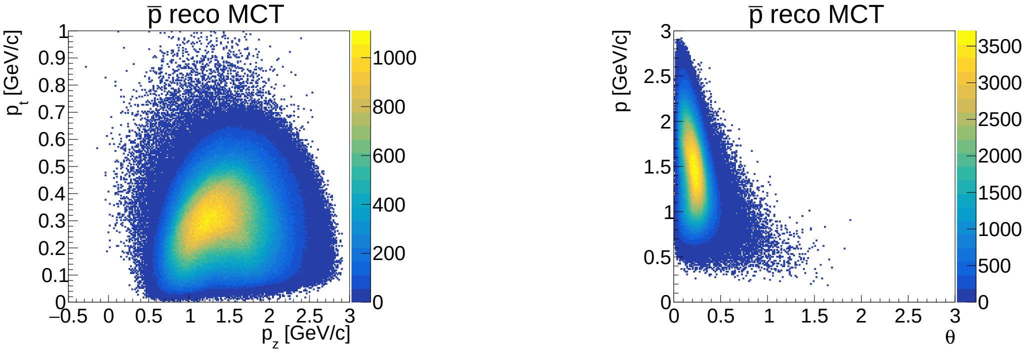

(a)

(b)

Figure A.159: Transverse versus longitudinal momentum (a) and total momentum vs. Θ angle (b) for MC partner of the reconstructed p̄.

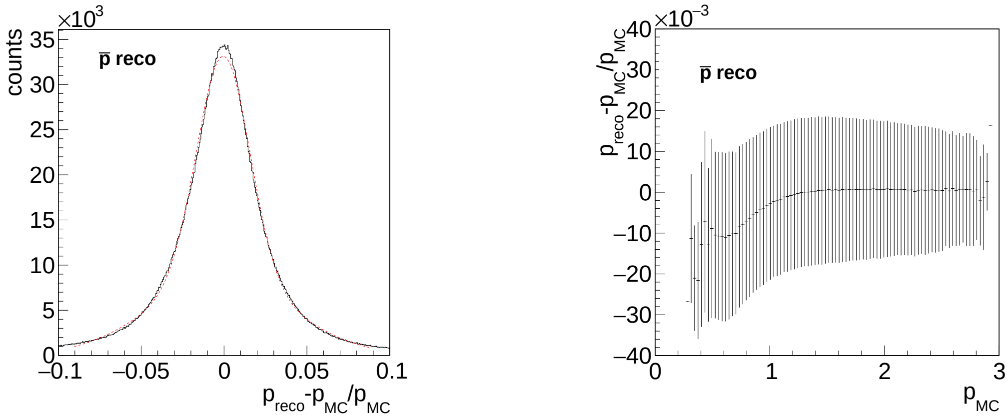

(a)

(b)

Figure A.160: Momentum resolution (a) and relative deviation of the reconstructed and generated total momentum (b) for p̄ from $\bar{\Lambda}$.

A.3.2 $\bar{\Lambda}$

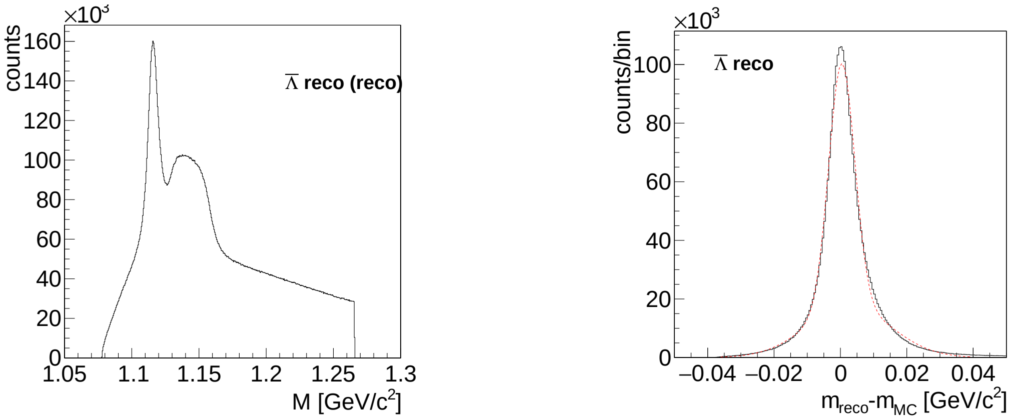

(a) (b)

Figure A.161: Mass distribution (a) for reconstructed $\bar{\Lambda}$ candidates and deviation of reconstructed and generated $\bar{\Lambda}$ mass.

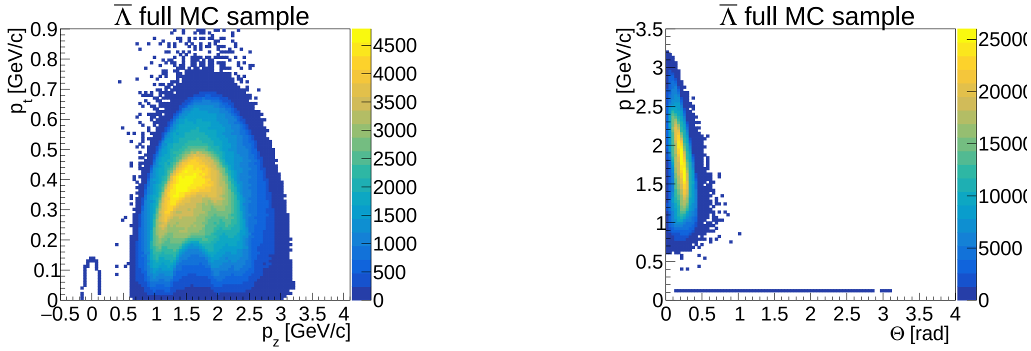

(a) (b)

Figure A.162: Transverse versus longitudinal momentum (a) and total momentum vs. Θ angle (b) for generated $\bar{\Lambda}$.

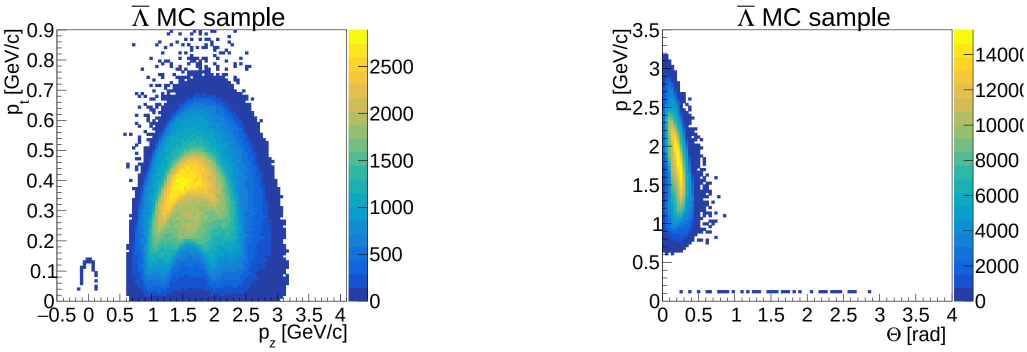

(a) (b)

Figure A.163: Transverse versus longitudinal momentum (a) and total momentum vs. Θ angle (b) for generated $\bar{\Lambda}$ requesting that the $\overline{\Xi}^+$ has only two daughter particles.

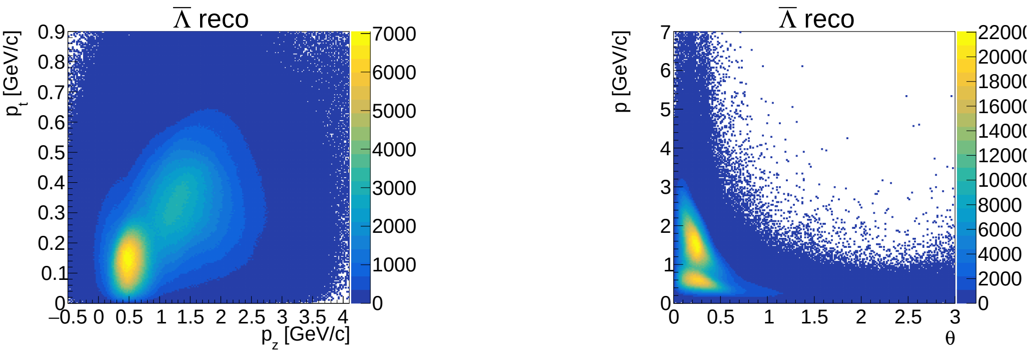

(a) (b)

Figure A.164: Transverse versus longitudinal momentum (a) and total momentum vs. Θ angle (b) for reconstructed $\bar{\Lambda}$ candidates.

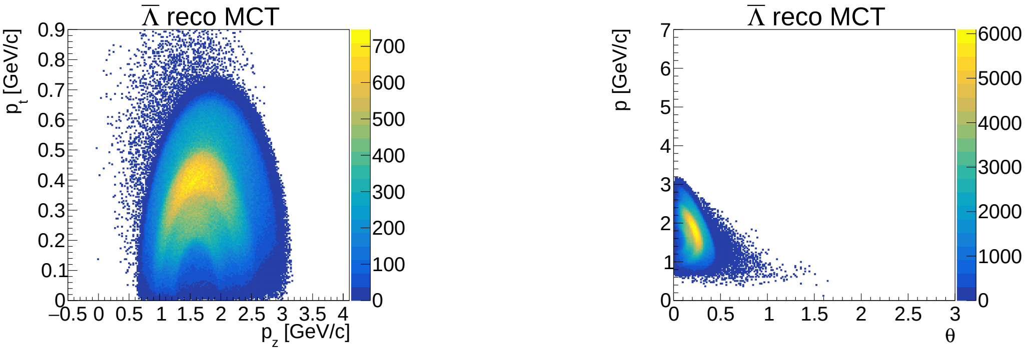

(a) (b)

Figure A.165: Transverse versus longitudinal momentum (a) and total momentum vs. Θ angle (b) for the MC partners of the reconstructed $\bar{\Lambda}$ candidates.

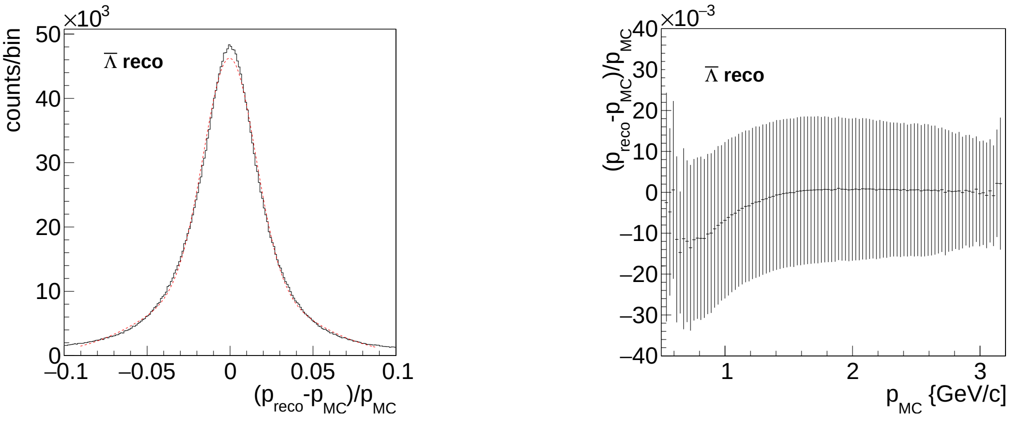

(a) (b)

Figure A.166: Momentum resolution (a) and relative deviation of the reconstructed and generated total momentum (b) for $\bar{\Lambda}$.

A.3.3 $\overline{\Xi}^{+}$ Λ K⁻

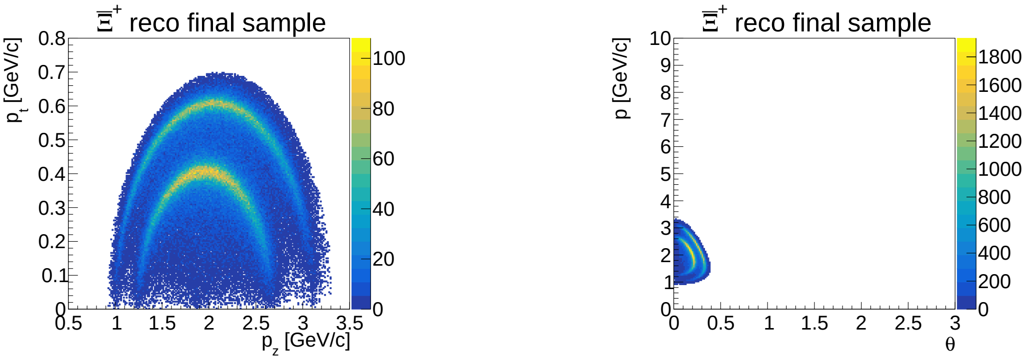

(a) (b)

Figure A.167: Transverse versus longitudinal momentum (a) and total momentum vs. Θ angle (b) for final reconstructed $\overline{\Xi}^{+}$.

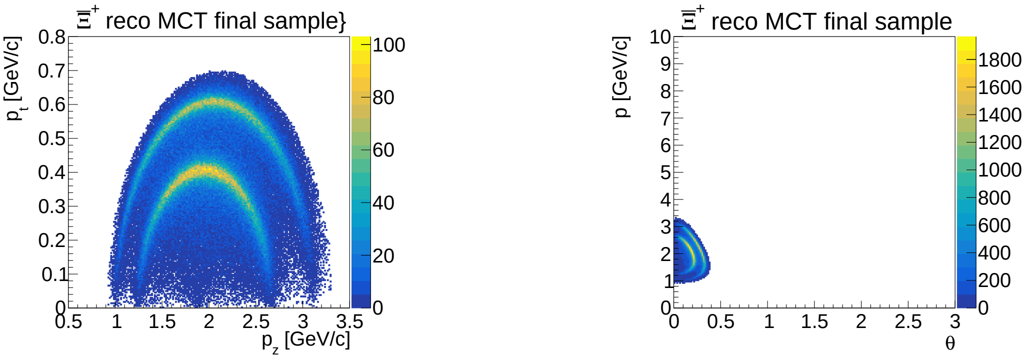

(a) (b)

Figure A.168: Transverse versus longitudinal momentum (a) and total momentum vs. Θ angle (b) for MC partner of final reconstructed $\overline{\Xi}^{+}$.

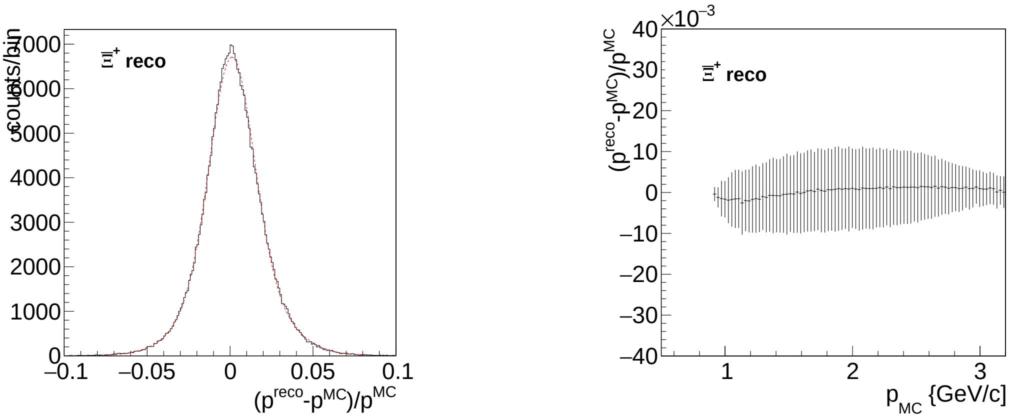

(a) (b)

Figure A.169: Momentum resolution (a) and relative deviation of the reconstructed and generated total momentum (b) for final reconstructed $\overline{\Xi}^{+}$.

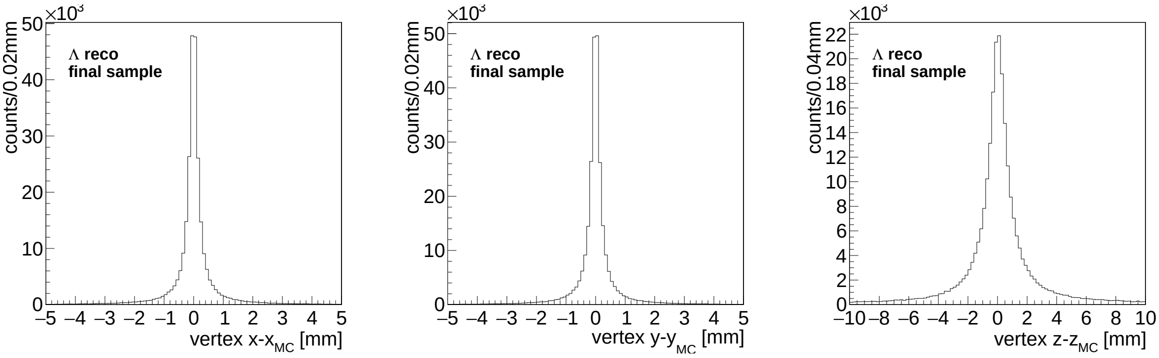

(a) (b) (c)

Figure A.170: Deviation of the final reconstructed Λ decay vertex position and the corresponding MC decay vertex position for the x coordinate (a), the y coordinate (b) and the z coordinate (c).

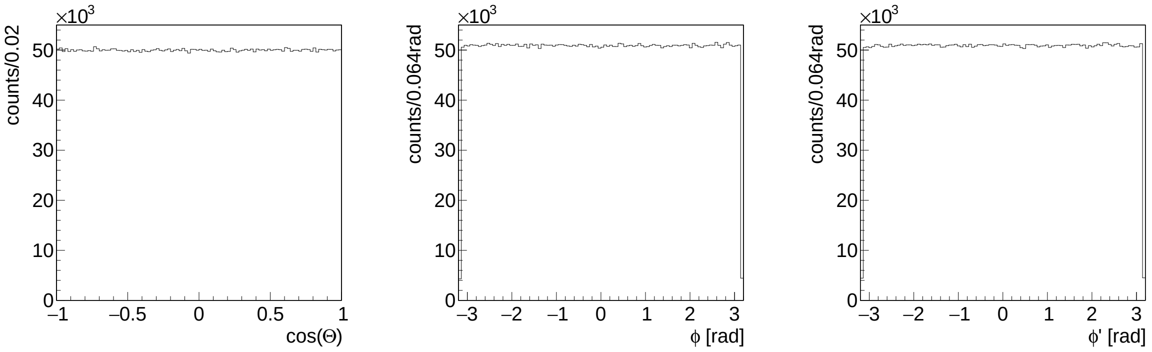

(a) (b) (c)

Figure A.171: Generated distribution for $\cos\theta$(a), ϕ (b) and $\phi\prime$ in the center-of-mass frame.

A.4 Analysis of $\bar{p}p \rightarrow \Xi^- \bar{\Lambda} K^+$ with the Full Decay Tree Fit

A.4.1 Final State Particles

π^- from Λ

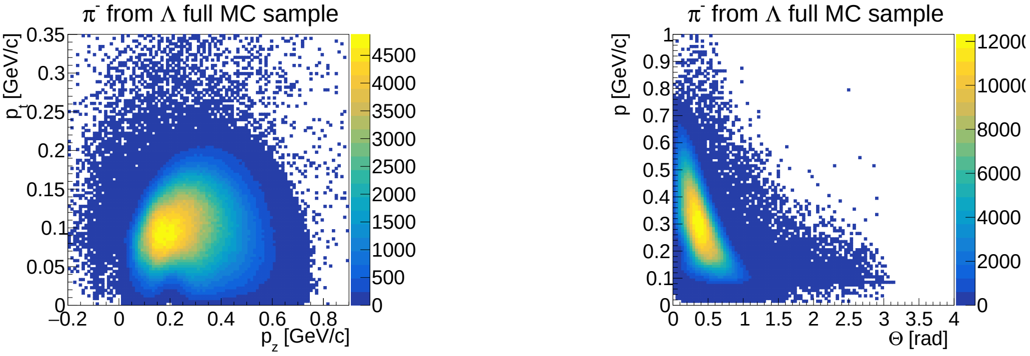

(a) (b)

Figure A.172: Transverse versus longitudinal momentum (a) and total momentum vs. Θ angle (b) for generated π^- from Λ.

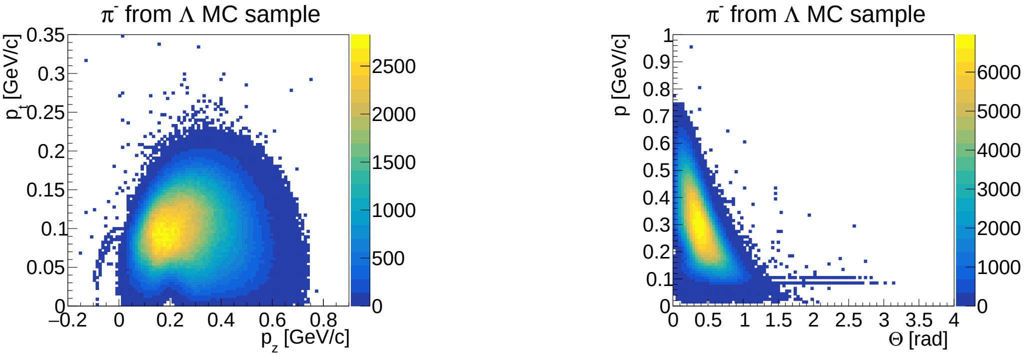

(a) (b)

Figure A.173: Transverse versus longitudinal momentum (a) and total momentum vs. Θ angle (b) for generated π^- from Λ requesting that Λ and Ξ^- have only two daughter particles.

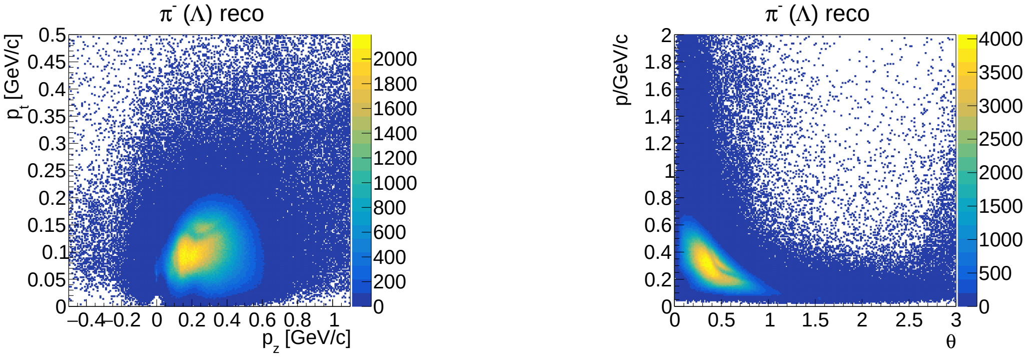

(a) (b)

Figure A.174: Transverse versus longitudinal momentum (a) and total momentum vs. Θ angle (b) for reconstructed π^- from Λ.

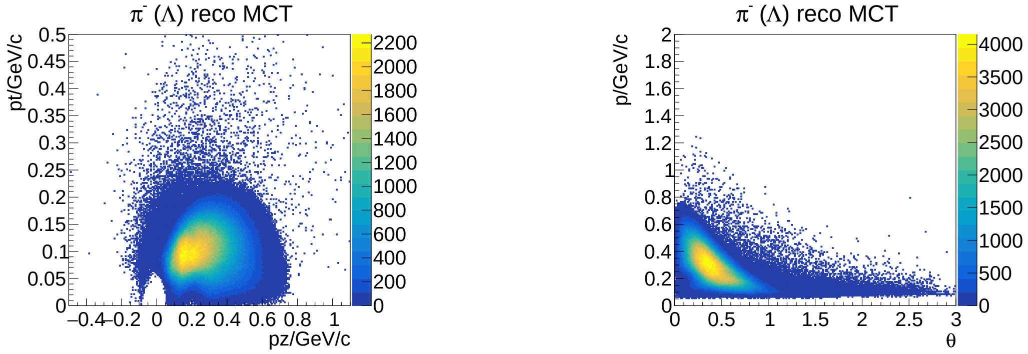

(a) (b)

Figure A.175: Transverse versus longitudinal momentum (a) and total momentum vs. Θ angle (b) for MC partner of reconstructed π^- from Λ.

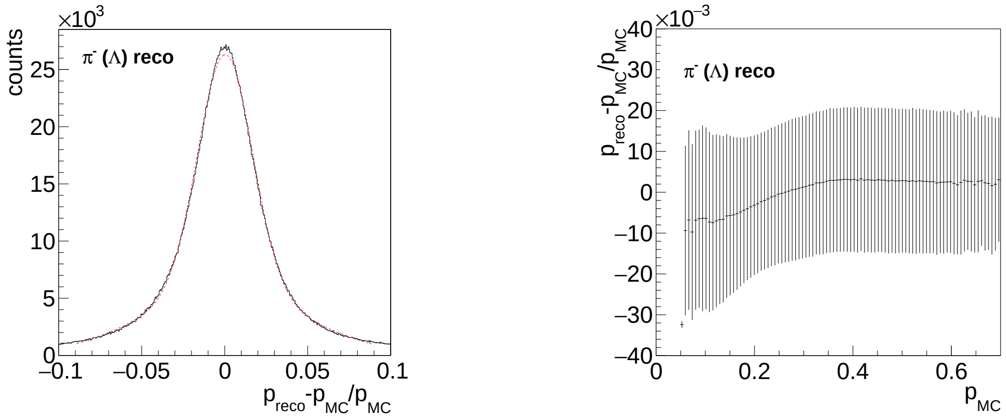

(a) (b)

Figure A.176: Momentum resolution (a) and relative deviation of the reconstructed and generated total momentum (b) for π^- from Λ.

π^- from Ξ^-

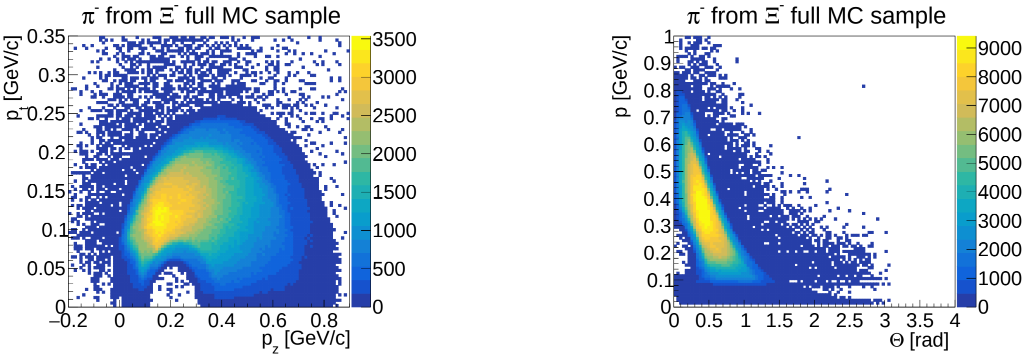

(a) (b)

Figure A.177: Transverse versus longitudinal momentum (a) and total momentum vs. Θ angle (b) for generated π^- from Ξ^-.

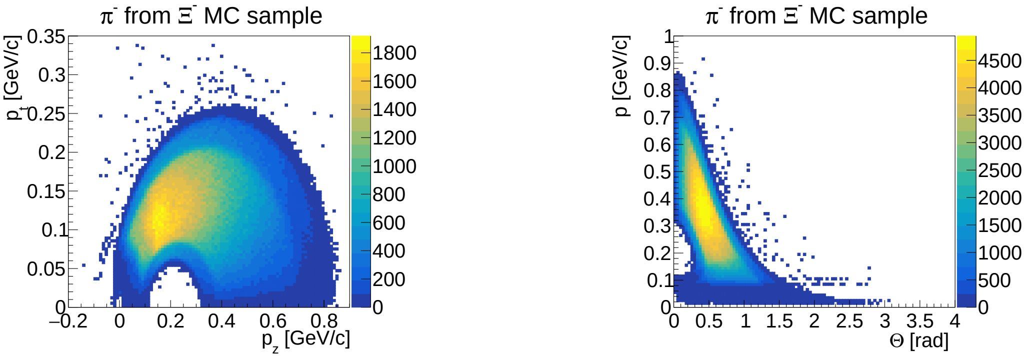

(a) (b)

Figure A.178: Transverse versus longitudinal momentum (a) and total momentum vs. Θ angle (b) for generated π^- from Ξ^- requesting that Ξ^- has only two daughter particles.

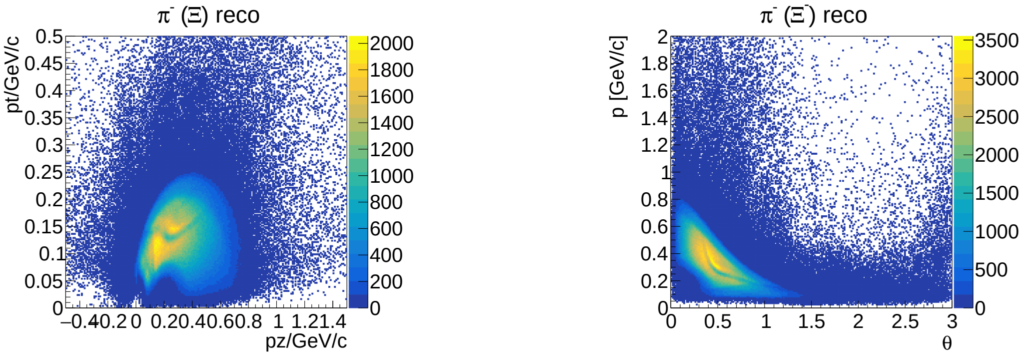

(a) (b)

Figure A.179: Transverse versus longitudinal momentum (a) and total momentum vs. Θ angle (b) for reconstructed π^- from Ξ^-.

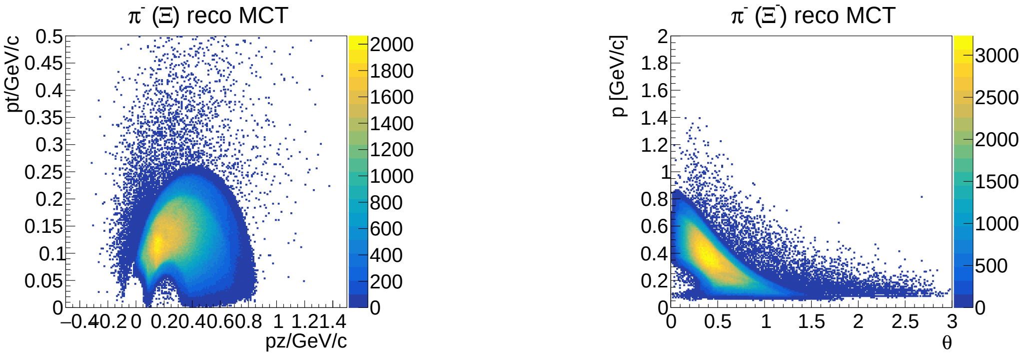

(a) (b)

Figure A.180: Transverse versus longitudinal momentum (a) and total momentum vs. Θ angle (b) for MC partner of reconstructed π^- from Ξ^-.

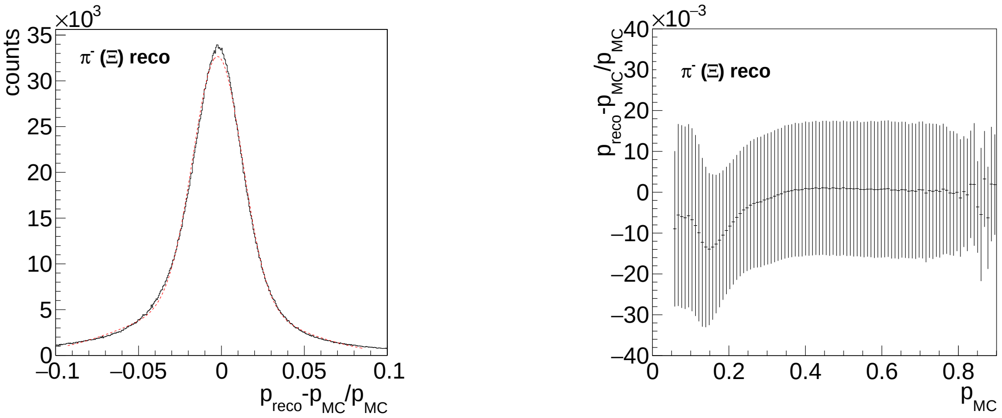

(a) (b)

Figure A.181: Momentum resolution (a) and relative deviation of the reconstructed and generated total momentum (b) for π^- from Ξ^-.

π^+ from $\bar{\Lambda}$

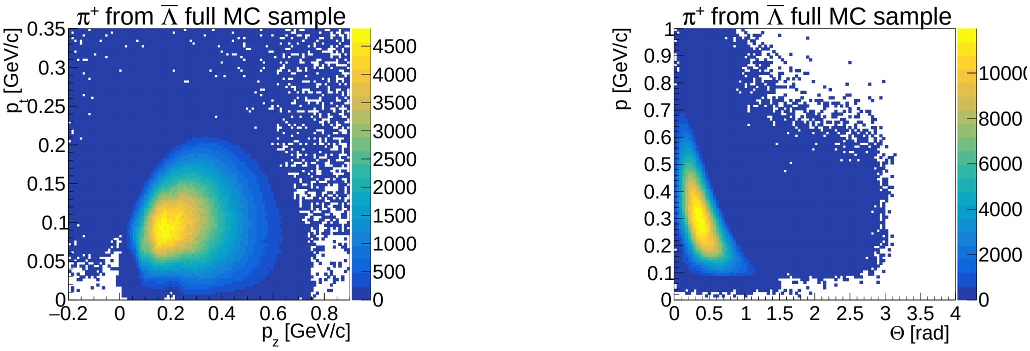

(a) (b)

Figure A.182: Transverse versus longitudinal momentum (a) and total momentum vs. Θ angle (b) for generated π^+ from $\bar{\Lambda}$.

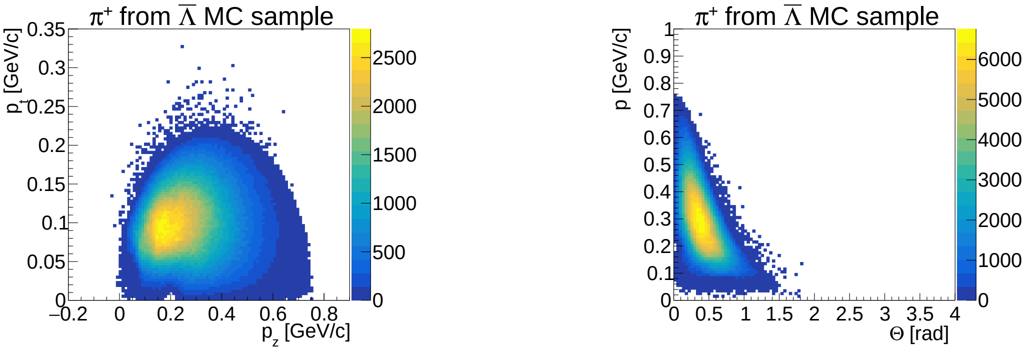

(a) (b)

Figure A.183: Transverse versus longitudinal momentum (a) and total momentum vs. Θ angle (b) for generated π^+ from $\bar{\Lambda}$ requesting that $\bar{\Lambda}$ has only two daughters.

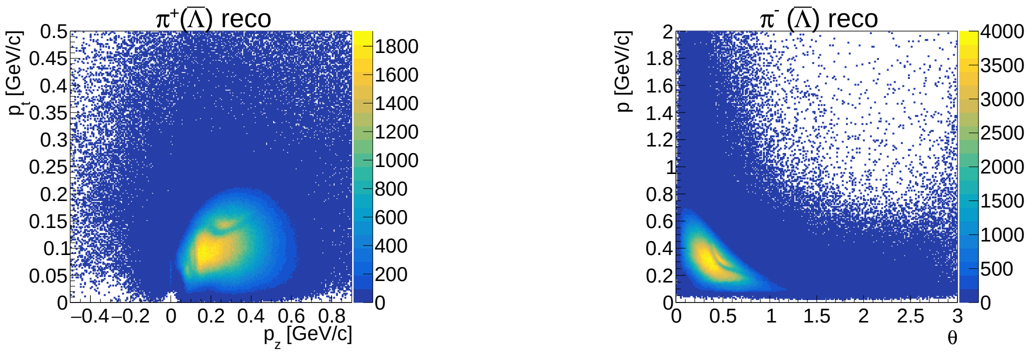

(a)

(b)

Figure A.184: Transverse versus longitudinal momentum (a) and total momentum vs. Θ angle (b) for reconstructed π^+ from $\bar{\Lambda}$.

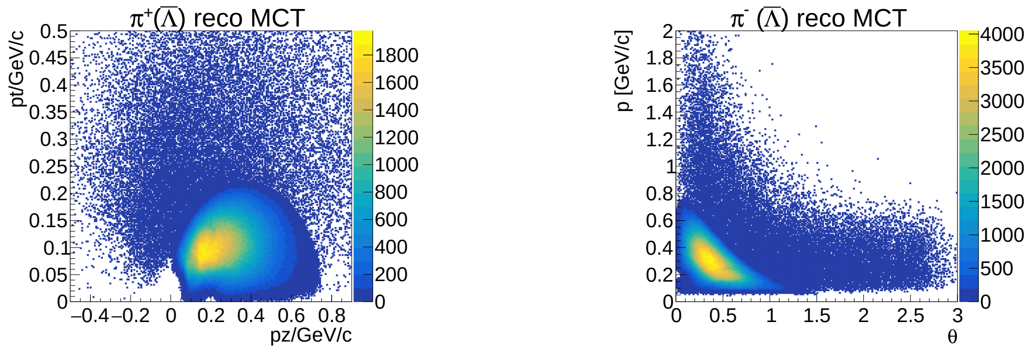

(a)

(b)

Figure A.185: Transverse versus longitudinal momentum (a) and total momentum vs. Θ angle (b) for MC partner of reconsturcted π^+ from $\bar{\Lambda}$.

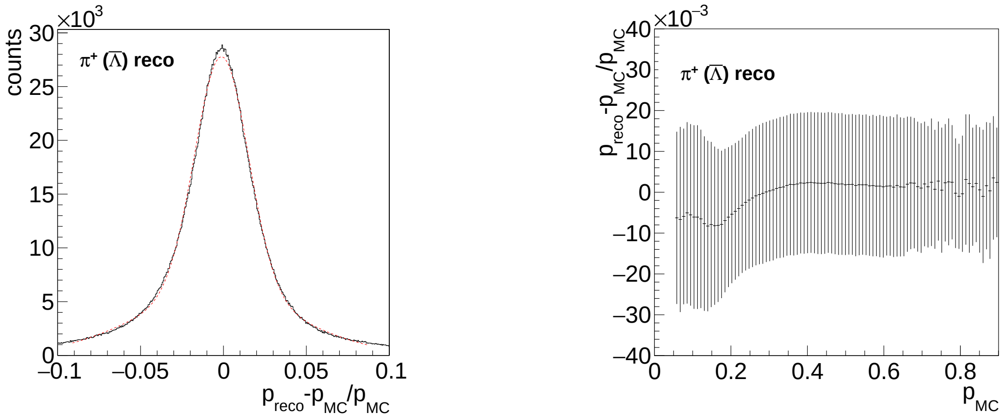

(a)

(b)

Figure A.186: Momentum resolution (a) and relative deviation of the reconstructed and generated total momentum (b) for π^+ from $\bar{\Lambda}$.

K^+ from $\overline{\Xi}^*$

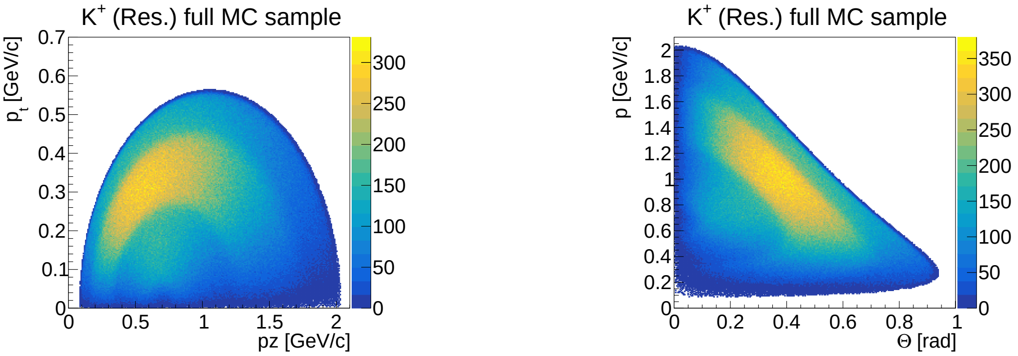

(a) (b)

Figure A.187: Transverse versus longitudinal momentum (a) and total momentum vs. Θ angle (b) for generated K^+ from $\overline{\Xi}^*$.

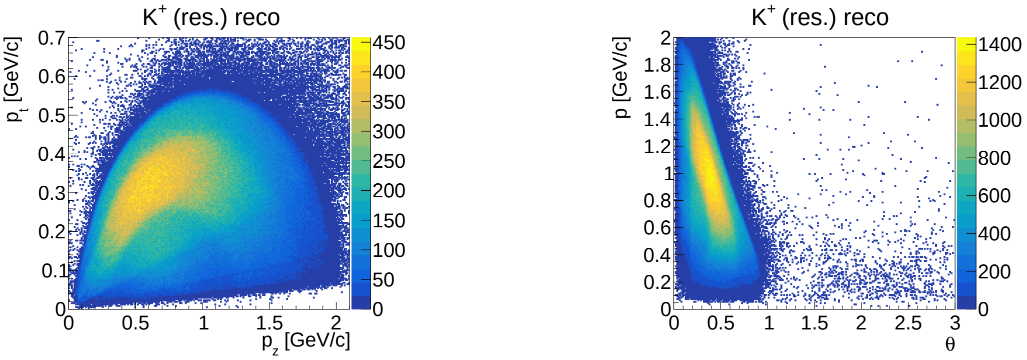

(a) (b)

Figure A.188: Transverse versus longitudinal momentum (a) and total momentum vs. Θ angle (b) for reconstructed K^+ from $\overline{\Xi}^*$.

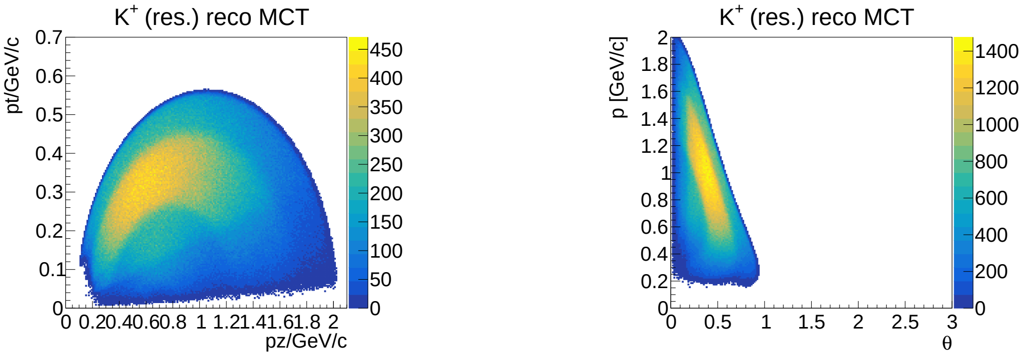

(a)

(b)

Figure A.189: Transverse versus longitudinal momentum (a) and total momentum vs. Θ angle (b) for MC partner of reconstructed K^+ from $\overline{\Xi}^*$.

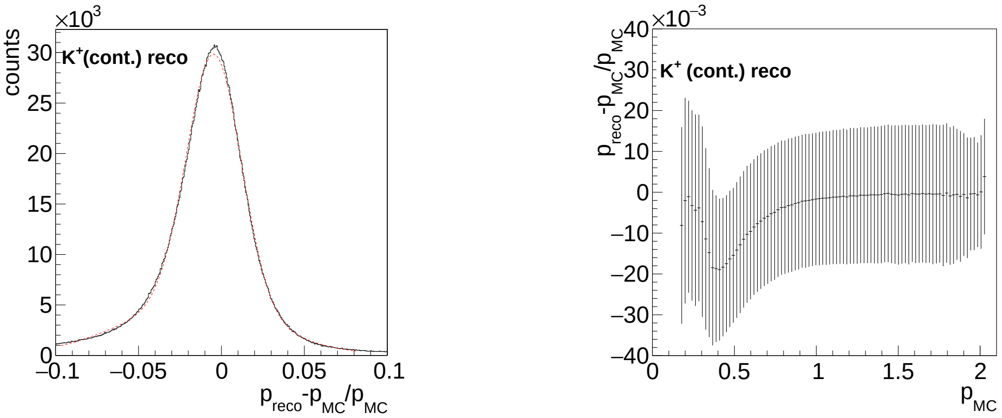

(a)

(b)

Figure A.190: Momentum resolution (a) and relative deviation of the reconstructed and generated total momentum (b) for K^+ from $\overline{\Xi}^*$.

K^+ from Continuum

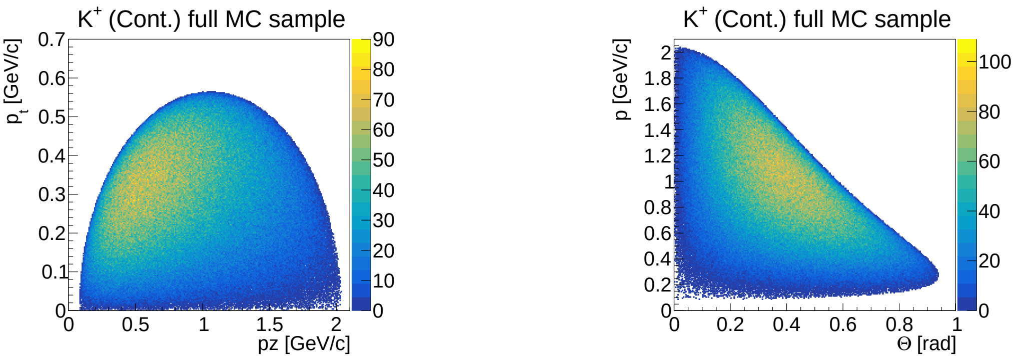

(a)

(b)

Figure A.191: Transverse versus longitudinal momentum (a) and total momentum vs. Θ angle (b) for generated K^+ from continuum.

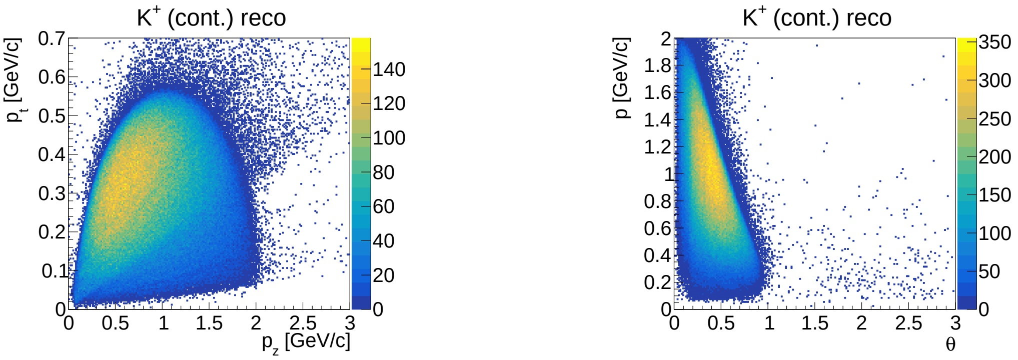

(a)

(b)

Figure A.192: Transverse versus longitudinal momentum (a) and total momentum vs. Θ angle (b) for reconstructed K^+ from continuum.

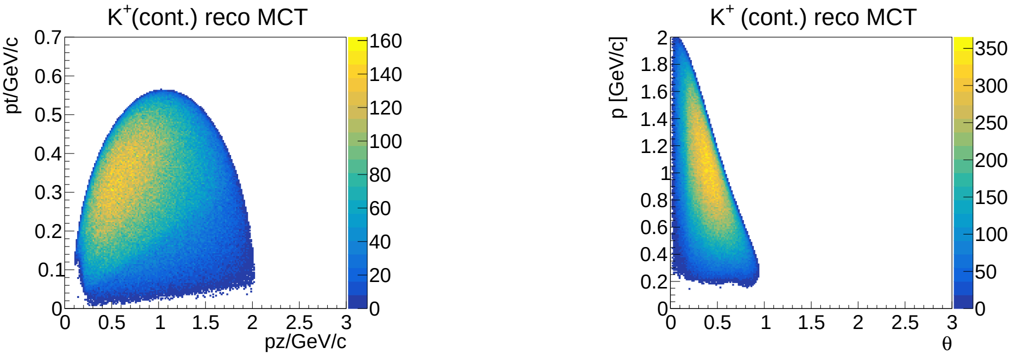

(a)

(b)

Figure A.193: Transverse versus longitudinal momentum (a) and total momentum vs. Θ angle (b) for MC partner of reconstructed K^+ from continuum.

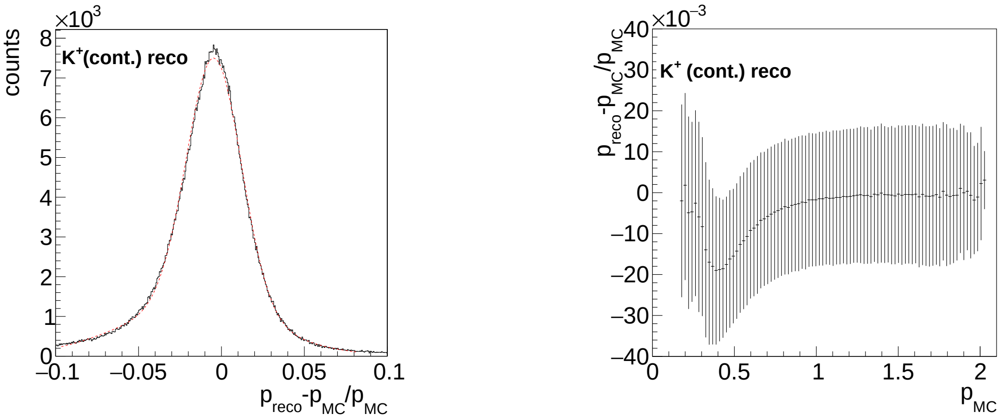

(a)

(b)

Figure A.194: Momentum resolution (a) and relative deviation of the reconstructed and generated total momentum (b) for K^+ from continuum.

p and $\overline{\mathrm{p}}$

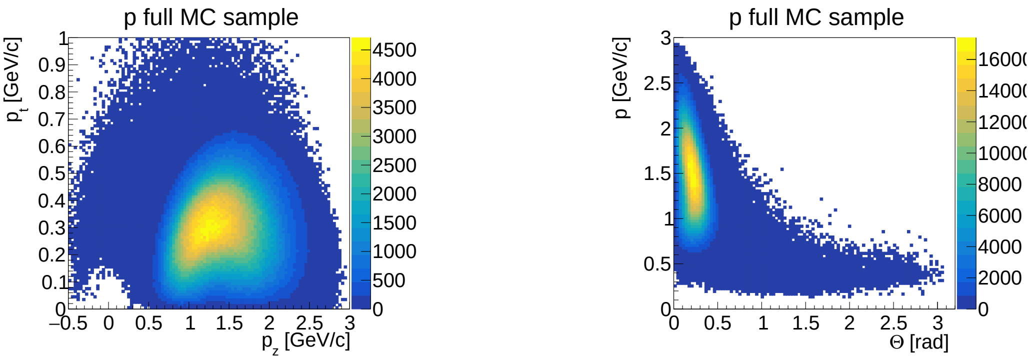

(a) (b)

Figure A.195: Transverse versus longitudinal momentum (a) and total momentum vs. Θ angle (b) for generated p from Λ.

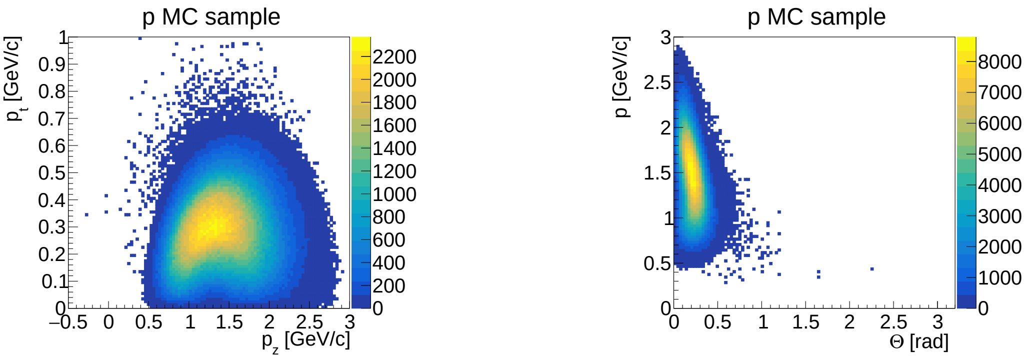

(a) (b)

Figure A.196: Transverse versus longitudinal momentum (a) and total momentum vs. Θ angle (b) for generated p from Λ requesting that Λ and Ξ^- have only two daughter particles.

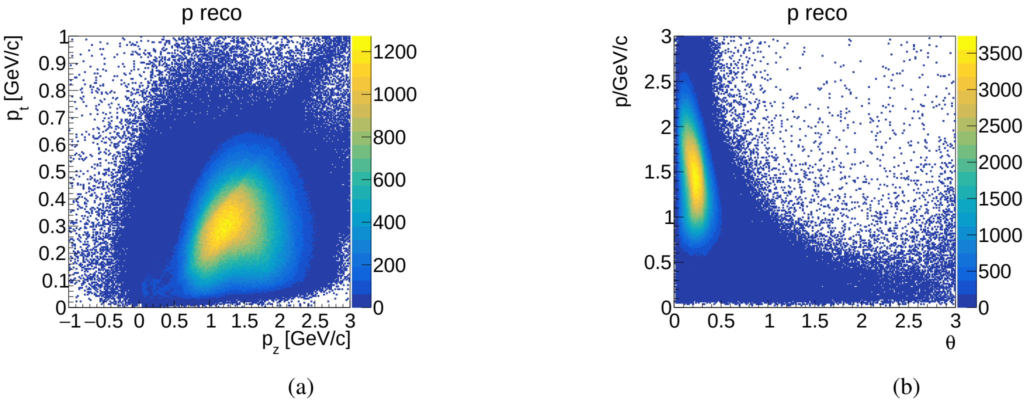

Figure A.197: Transverse versus longitudinal momentum (a) and total momentum vs. Θ angle (b) for recontructed p from Λ.

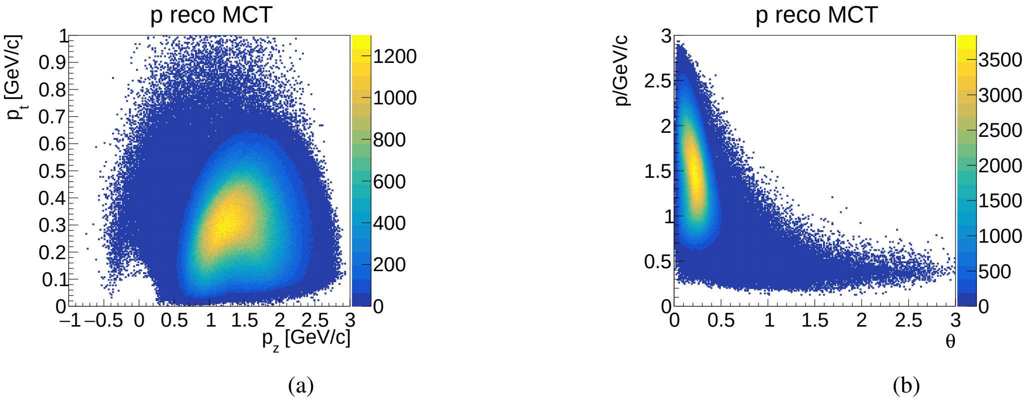

Figure A.198: Transverse versus longitudinal momentum (a) and total momentum vs. Θ angle (b) for MC partner of reconstructed p from Λ.

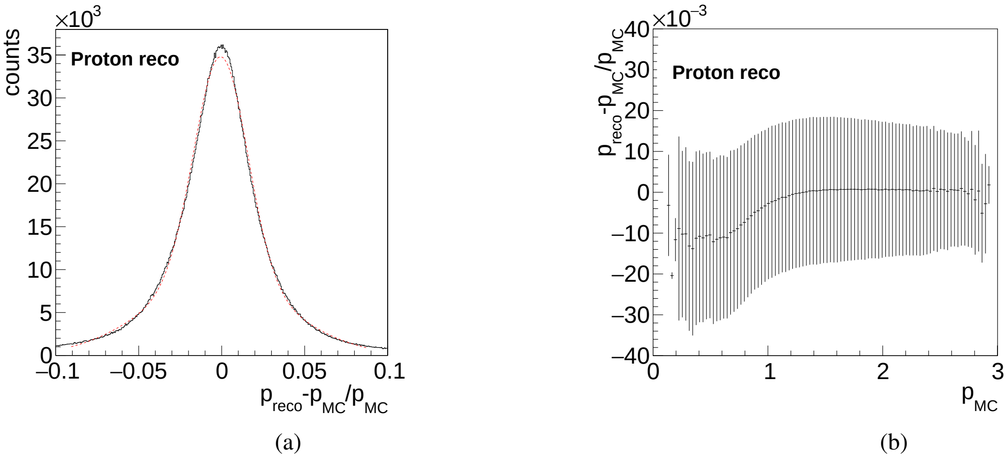

Figure A.199: Momentum resolution (a) and relative deviation of the reconstructed and generated total momentum (b) for p from Λ.

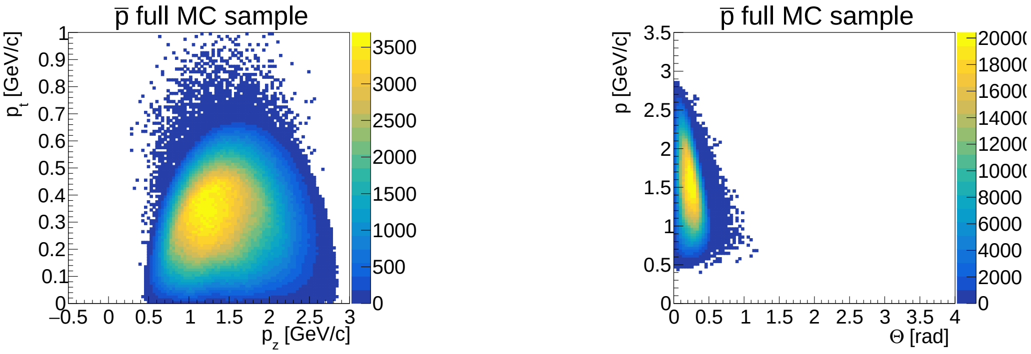

(a)

(b)

Figure A.200: Transverse versus longitudinal momentum (a) and total momentum vs. Θ angle (b) for generated $\bar{p}$ from $\bar{\Lambda}$.

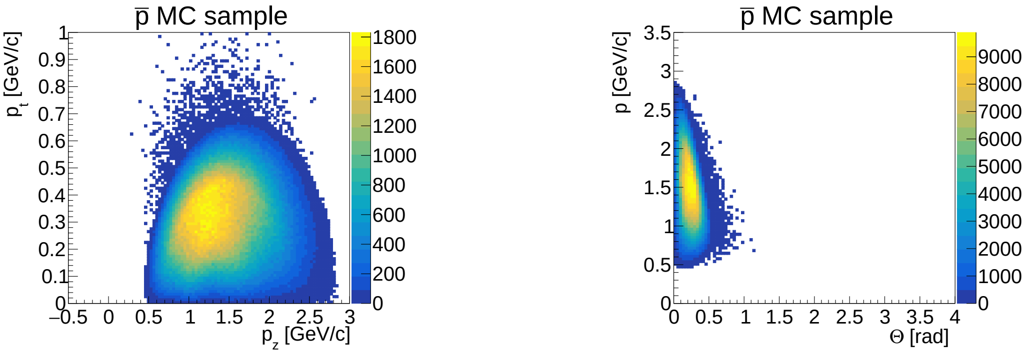

(a)

(b)

Figure A.201: Transverse versus longitudinal momentum (a) and total momentum vs. Θ angle (b) for generated $\bar{p}$ from $\bar{\Lambda}$ requesting that $\bar{\Lambda}$ has only two daughter particles.

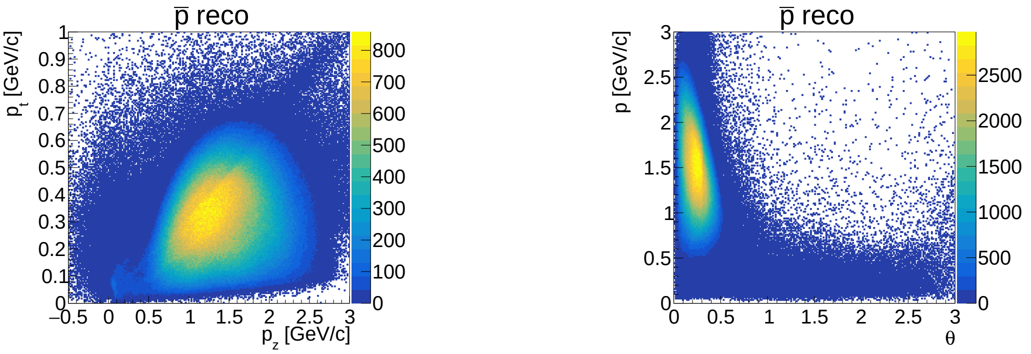

(a)

(b)

Figure A.202: Transverse versus longitudinal momentum (a) and total momentum vs. Θ angle (b) for recontructed $\bar{p}$ from $\bar{\Lambda}$.

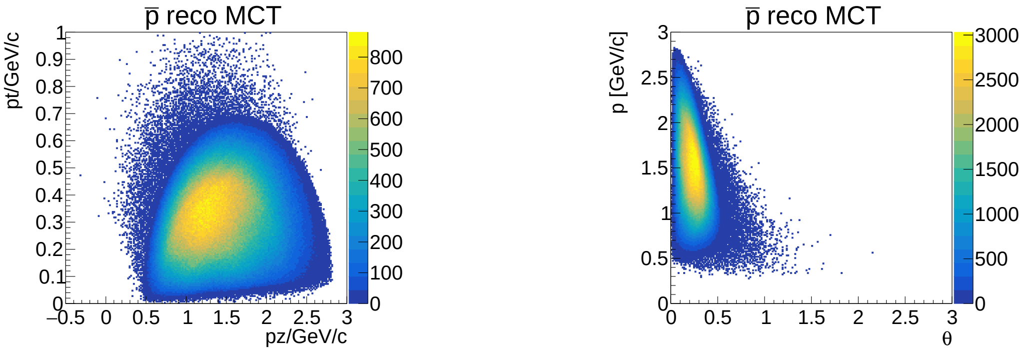

(a)

(b)

Figure A.203: Transverse versus longitudinal momentum (a) and total momentum vs. Θ angle (b) for MC partner of reconstructed $\bar{p}$ from $\bar{\Lambda}$.

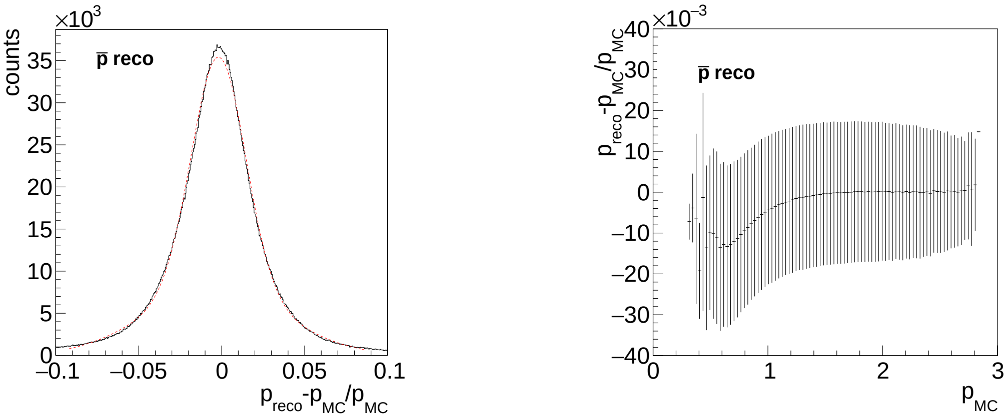

(a)

(b)

Figure A.204: Momentum resolution (a) and relative deviation of the reconstructed and generated total momentum (b) for $\bar{p}$ from $\bar{\Lambda}$.

A.4.2 Λ and $\bar{\Lambda}$

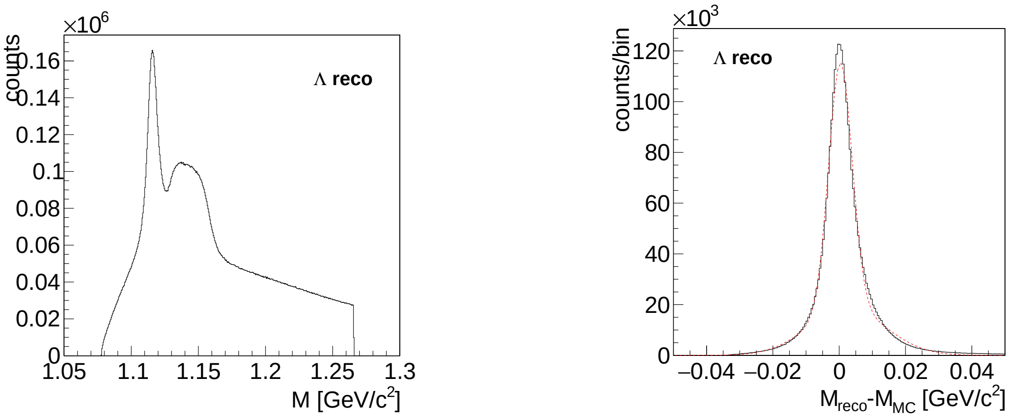

(a) (b)

Figure A.205: Mass distribution (a) and deviation of reconstructed and generates mass (b) for Λ candidates.

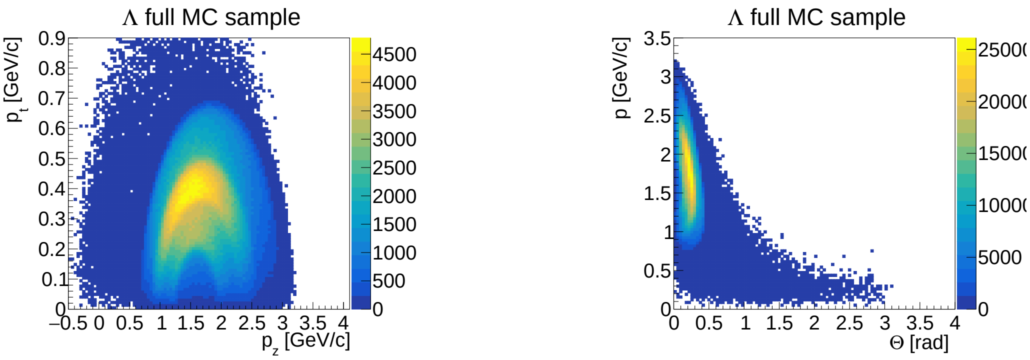

(a) (b)

Figure A.206: Transverse versus longitudinal momentum (a) and total momentum vs. Θ angle (b) for generated Λ from Ξ^-.

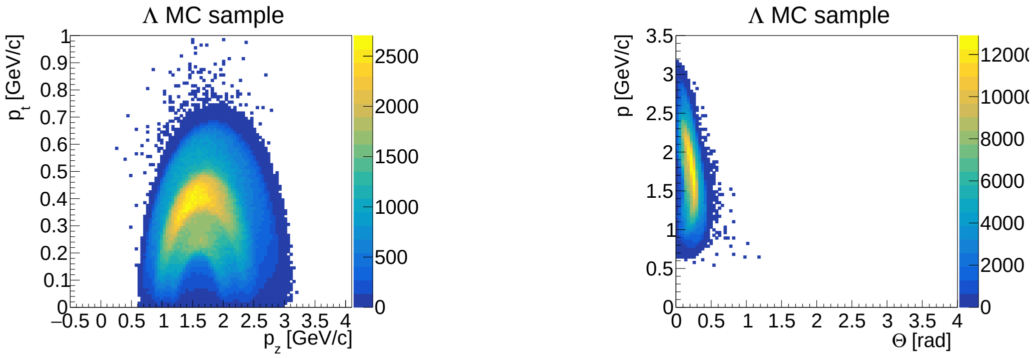

(a) (b)

Figure A.207: Transverse versus longitudinal momentum (a) and total momentum vs. Θ angle (b) for generated Λ from Ξ^- requesting that Ξ^- has only two daughter particles.

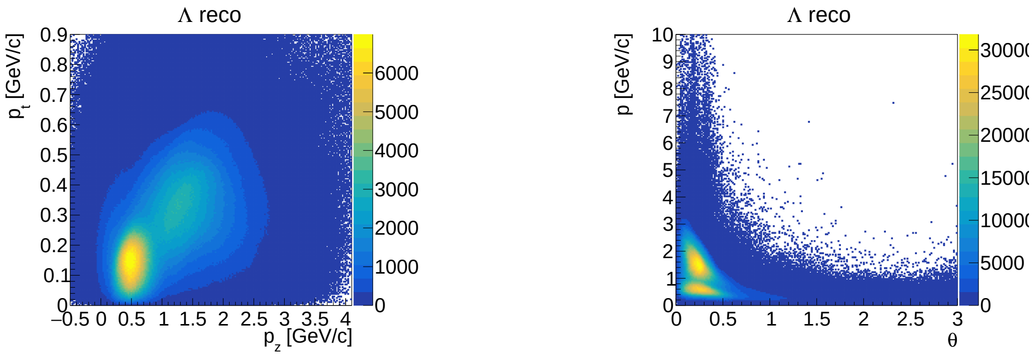

(a) (b)

Figure A.208: Transverse versus longitudinal momentum (a) and total momentum vs. Θ angle (b) for reconstructed Λ from Ξ^-.

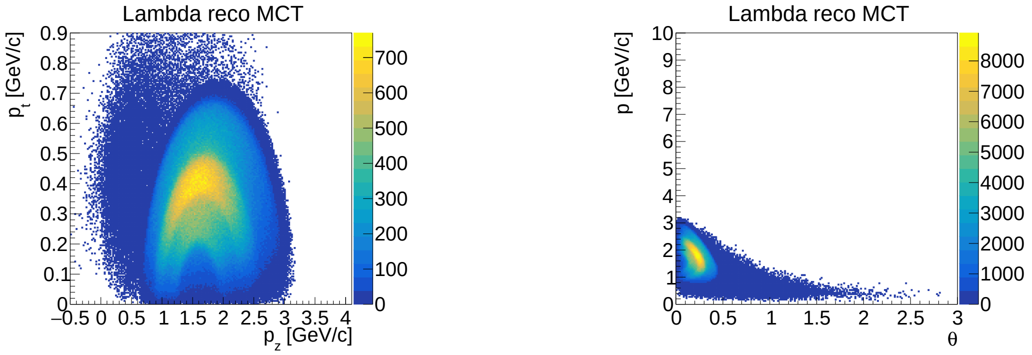

(a) (b)

Figure A.209: Transverse versus longitudinal momentum (a) and total momentum vs. Θ angle (b) for MC partner of reconstructed Λ from Ξ^-.

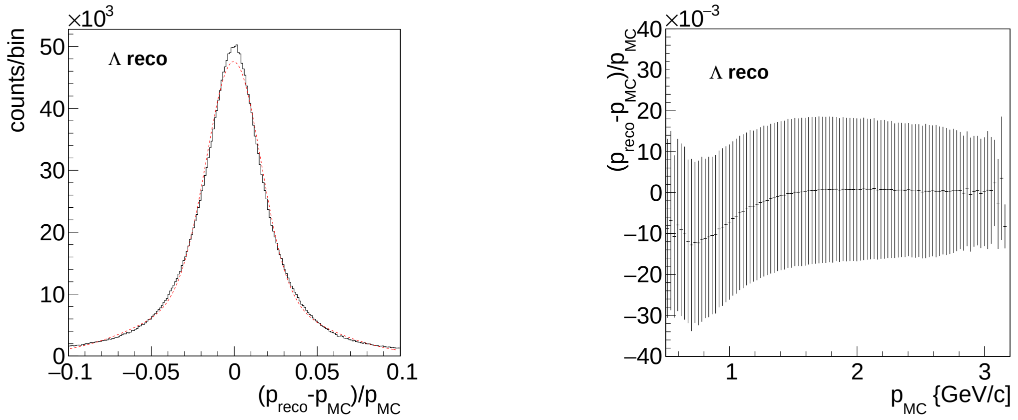

(a)

(b)

Figure A.210: Momentum resolution (a) and relative deviation of the reconstructed and generated total momentum (b) for generated Λ from Ξ^-.

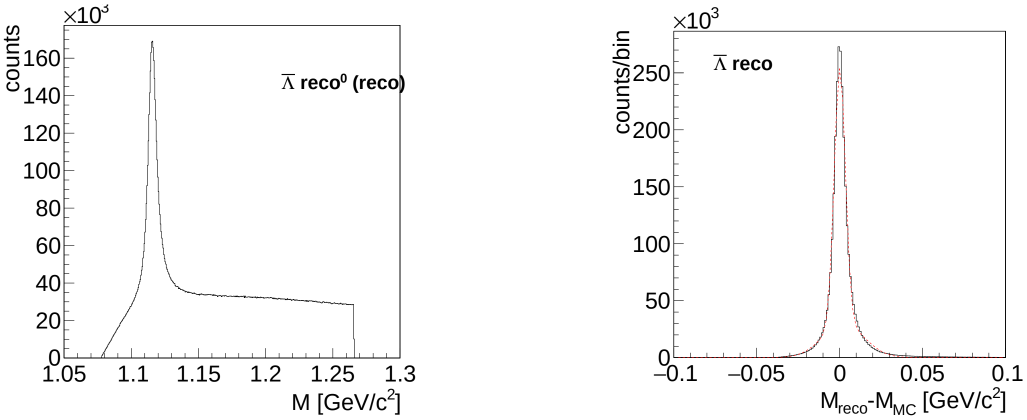

(a)

(b)

Figure A.211: Mass distribution (a) and deviation of reconstructed and generates mass (b) for $\bar{\Lambda}$ candidates.

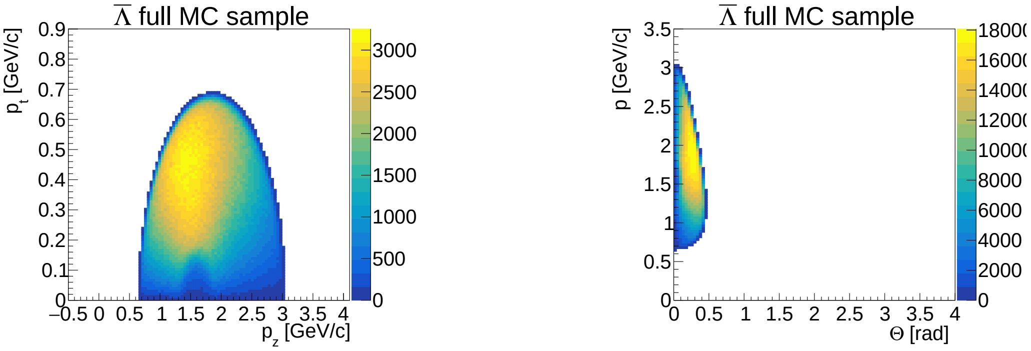

(a)

(b)

Figure A.212: Transverse versus longitudinal momentum (a) and total momentum vs. Θ angle (b) for generated $\bar{\Lambda}$.

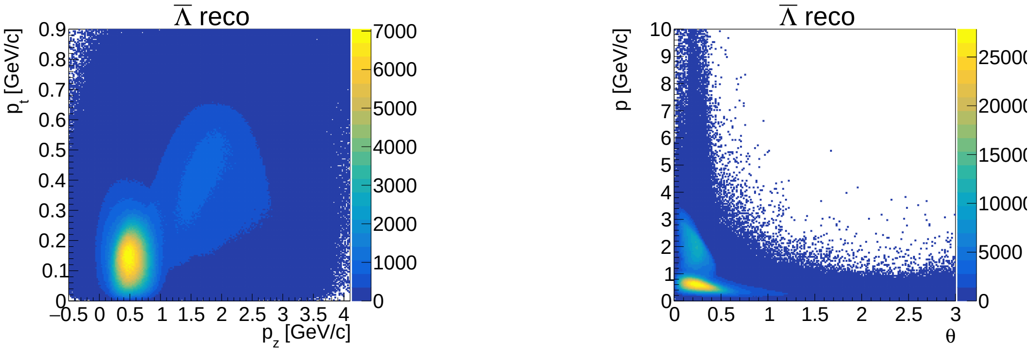

(a) (b)

Figure A.213: Transverse versus longitudinal momentum (a) and total momentum vs. Θ angle (b) for reconstructed $\bar{\Lambda}$.

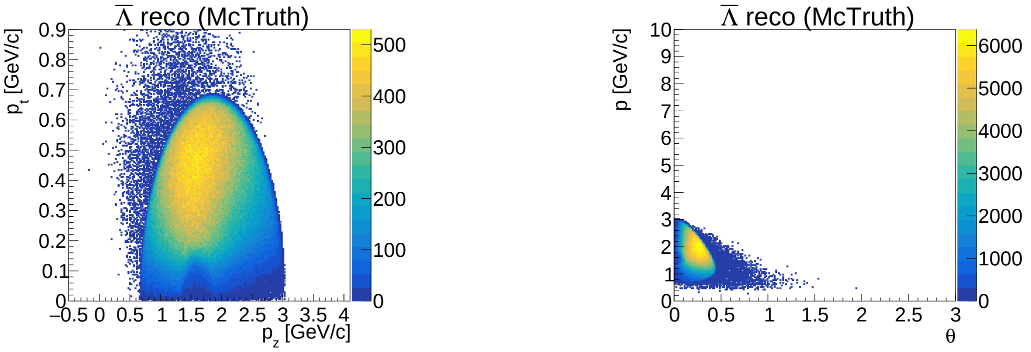

(a) (b)

Figure A.214: Transverse versus longitudinal momentum (a) and total momentum vs. Θ angle (b) for MC partner of reconstructed $\bar{\Lambda}$.

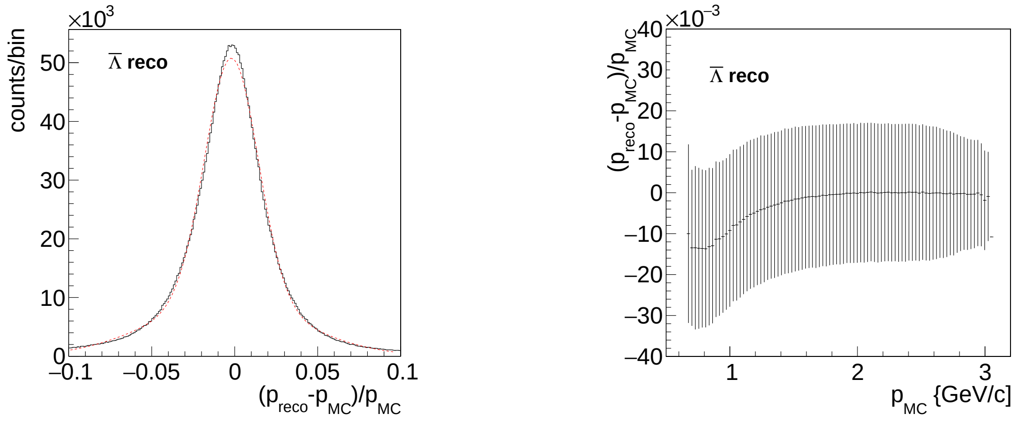

(a) (b)

Figure A.215: Momentum resolution (a) and relative deviation of the reconstructed and generated total momentum (b) for generated $\bar{\Lambda}$.

A.4.3 Ξ^-

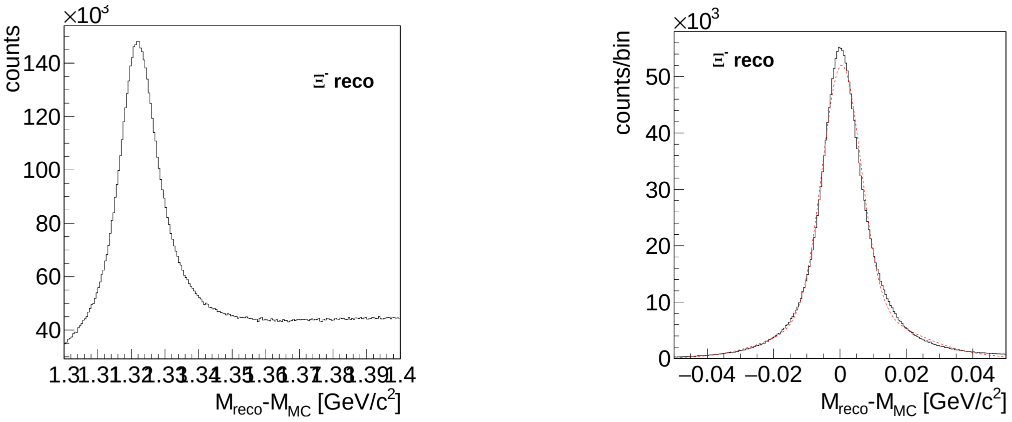

(a) (b)

Figure A.216: Mass distribution (a) and deviation of reconstructed and generates mass (b) for Ξ^- candidates.

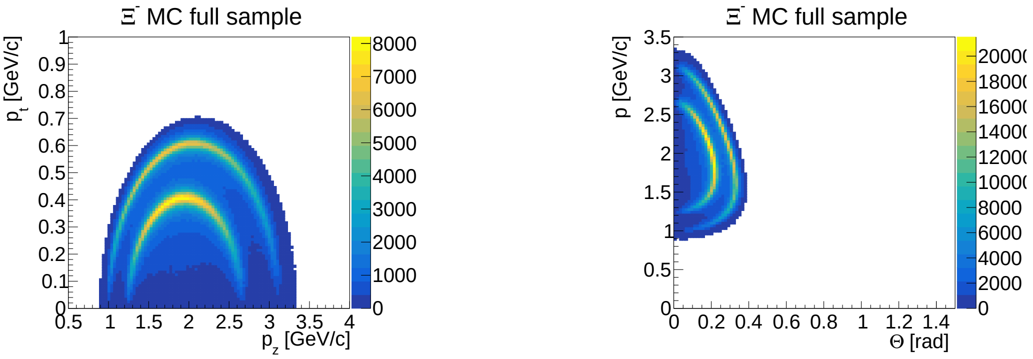

(a) (b)

Figure A.217: Transverse versus longitudinal momentum (a) and total momentum vs. Θ angle (b) for generated Ξ^-.

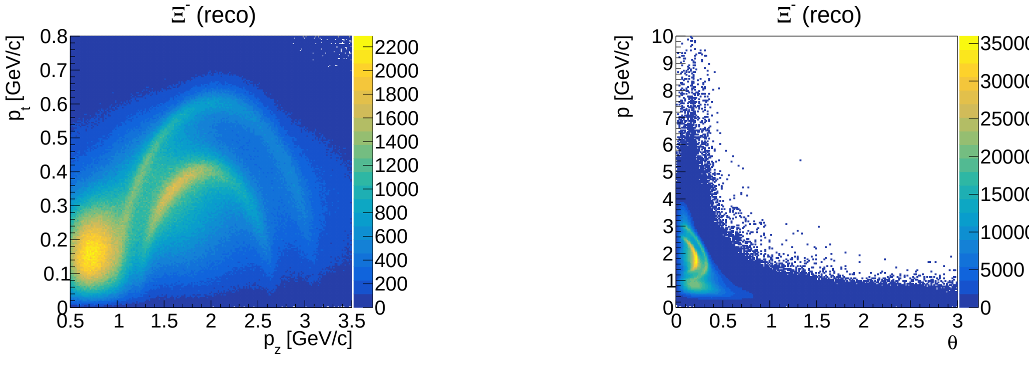

(a) (b)

Figure A.218: Transverse versus longitudinal momentum (a) and total momentum vs. Θ angle (b) for reconstructed Ξ^-.

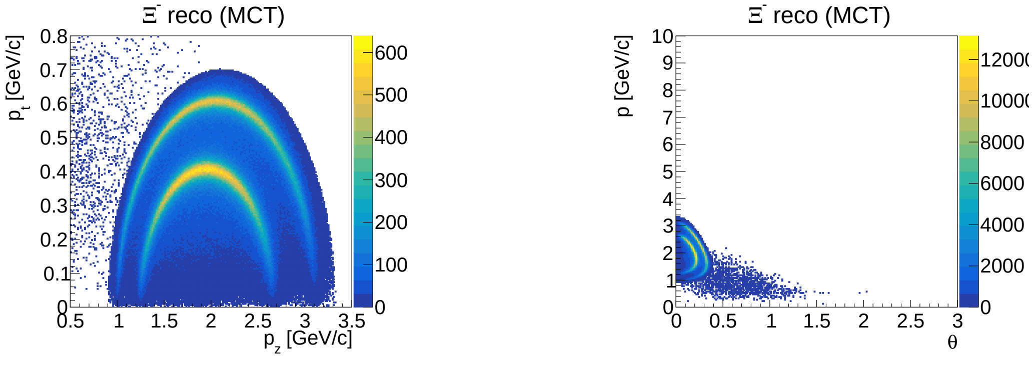

(a) (b)

Figure A.219: Transverse versus longitudinal momentum (a) and total momentum vs. Θ angle (b) for MC partner of reconstructed Ξ^-.

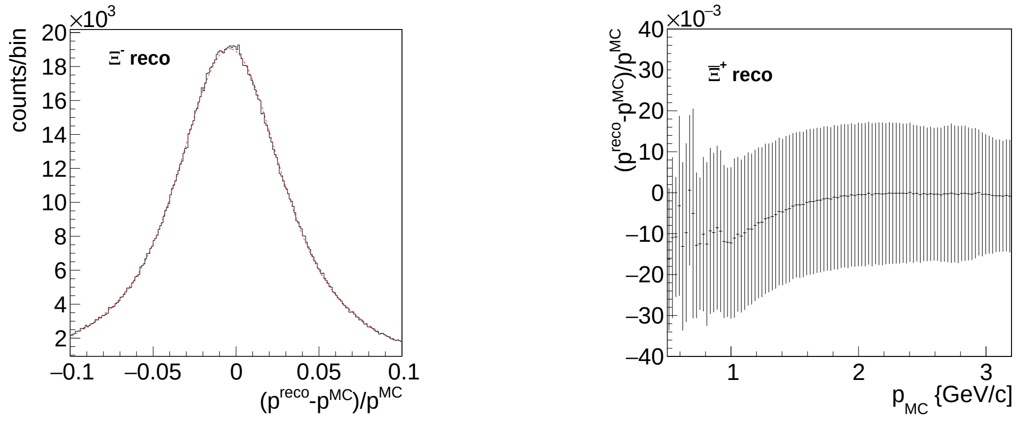

(a) (b)

Figure A.220: Momentum resolution (a) and relative deviation of the reconstructed and generated total momentum (b) for generated Ξ^-.

A.4.4 $\Xi^- \bar{\Lambda} K^+$

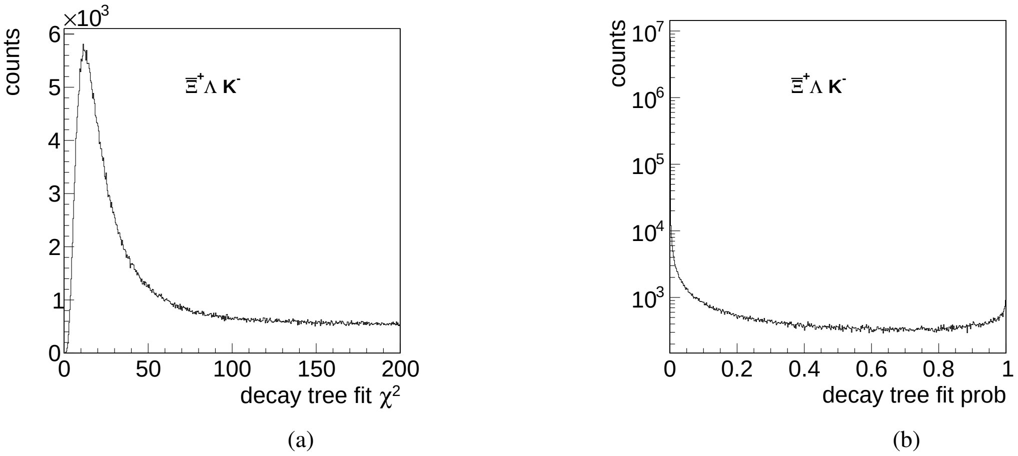

(a) (b)

Figure A.221: Full decay tree fit χ^2 (a) and probability (b) distribution for $\Xi^- \bar{\Lambda} K^+$

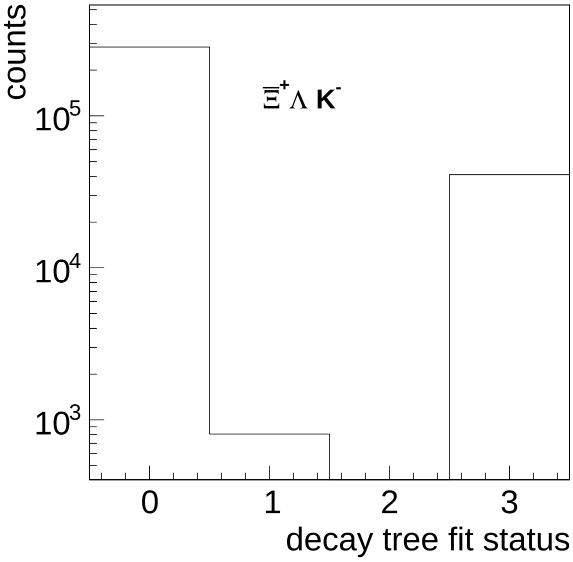

Figure A.222: Status of the decay tree fitter for $\Xi^- \bar{\Lambda} K^+$

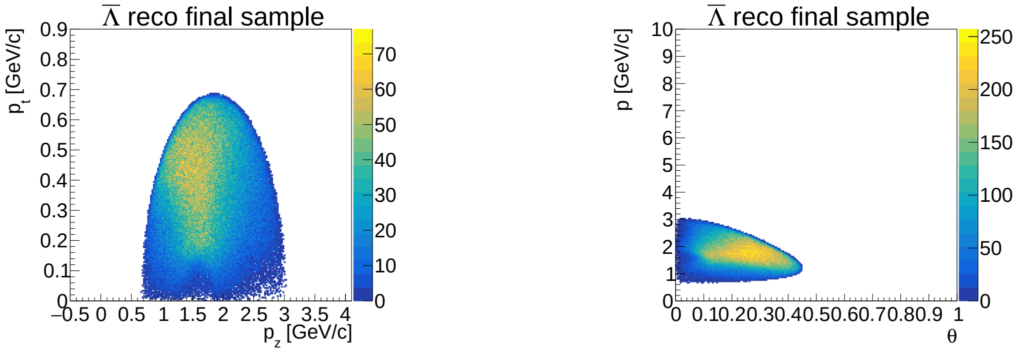

(a) (b)

Figure A.223: Transverse versus longitudinal momentum (a) and total momentum vs. Θ angle (b) for final selected $\bar{\Lambda}$.

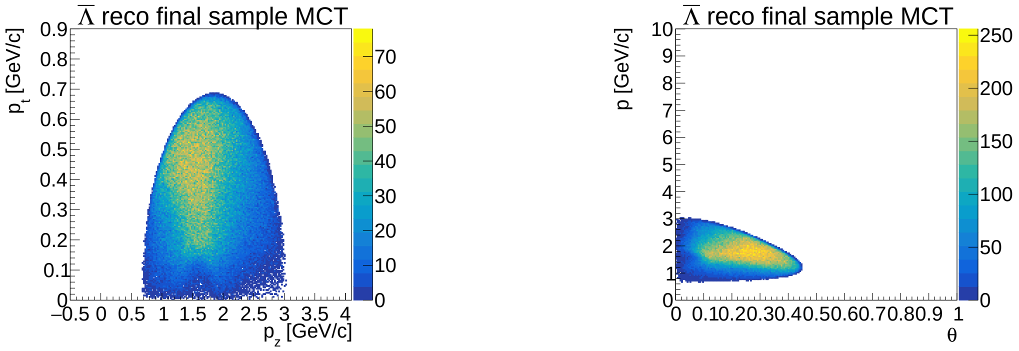

(a) (b)

Figure A.224: Transverse vs. longitudinal momentum and total momentum vs. Θ angle for the MC-truth partner of the final selected $\bar{\Lambda}$.

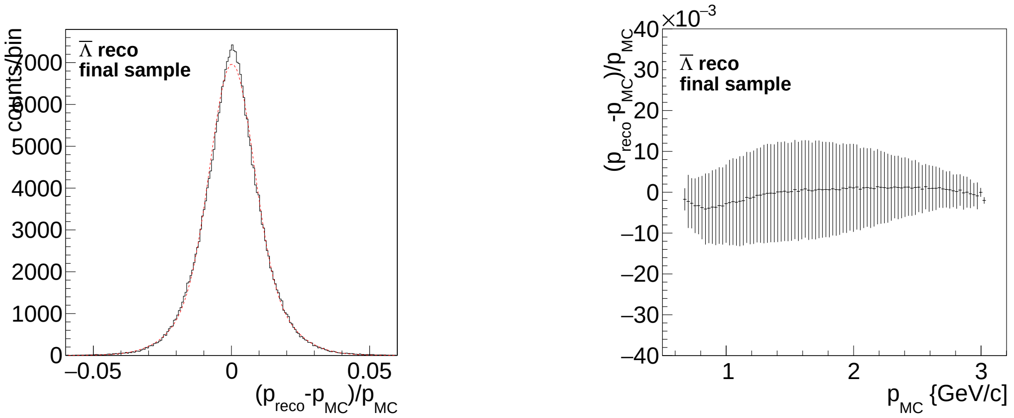

(a) (b)

Figure A.225: Momentum resolution (a) and relative deviation of the reconstructed and generated total momentum (b) for the final selected $\bar{\Lambda}$ candidates.

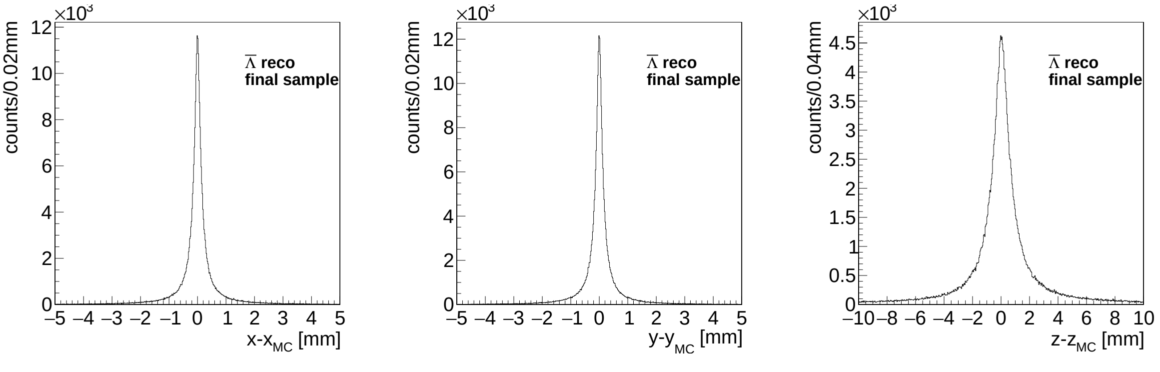

(a) (b) (c)

Figure A.226: Deviation of the final reconstructed $\bar{\Lambda}$ decay vertex position and the corresponding MC decay vertex position for the x coordinate (a), the y coordinate (b) and the z coordinate (c).

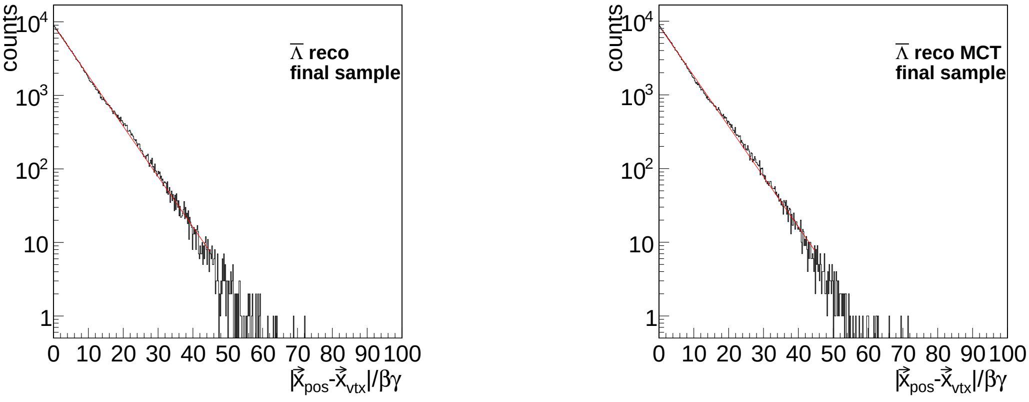

(a) (b)

Figure A.227: Propertime distribution for the reconstructed (a) and the MC partners (b) of the final selected $\bar{\Lambda}$.

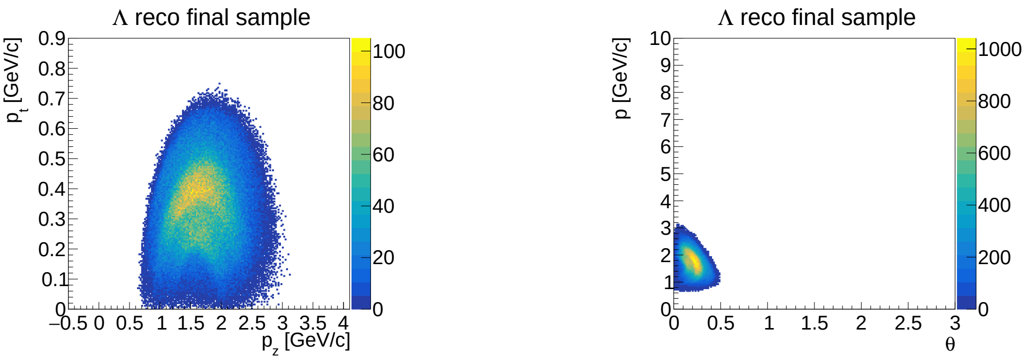

(a) (b)

Figure A.228: Transverse versus longitudinal momentum (a) and total momentum vs. Θ angle (b) for final selected Λ from Ξ^-.

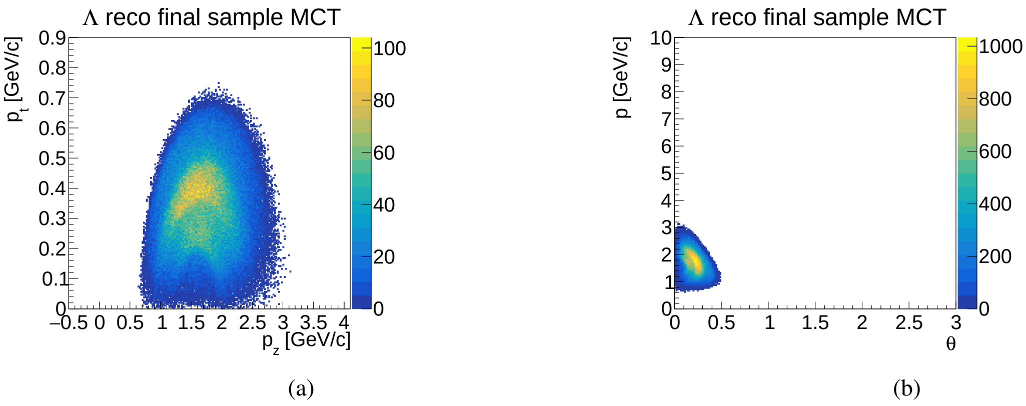

Figure A.229: Transverse vs. longitudinal momentum and total momentum vs. Θ angle for the MC-truth partner of the final selected Λ from Ξ^-.

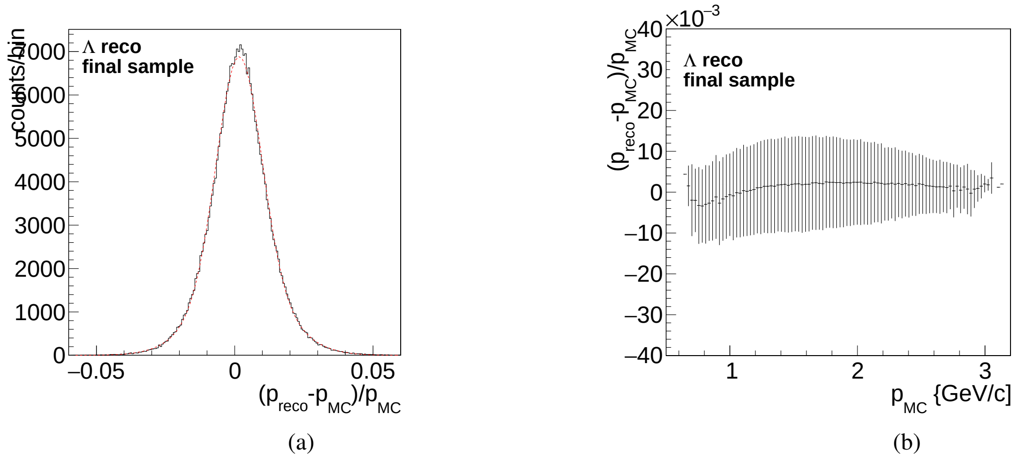

Figure A.230: Momentum resolution (a) and relative deviation of the reconstructed and generated total momentum (b) for the final selected Λ from Ξ^- candidates.

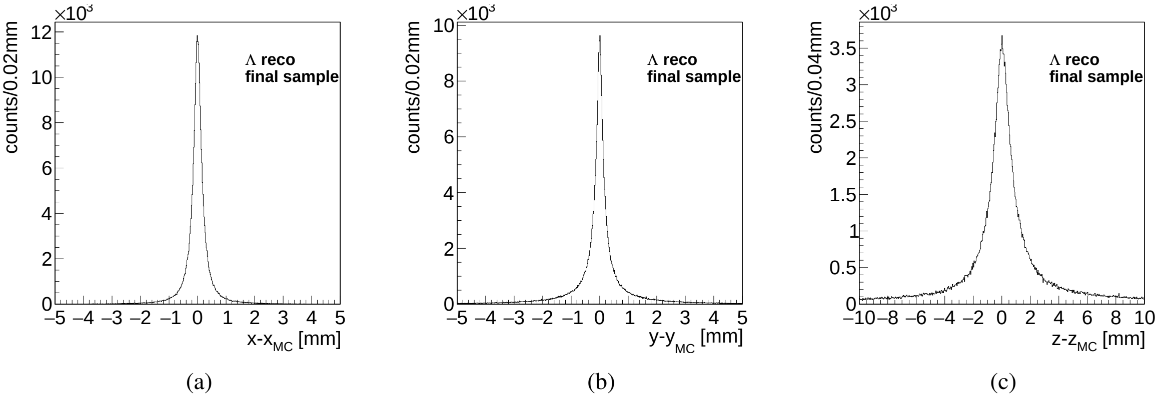

Figure A.231: Deviation of the final reconstructed Λ decay vertex position and the corresponding MC decay vertex position for the x coordinate (a), the y coordinate (b) and the z coordinate (c).

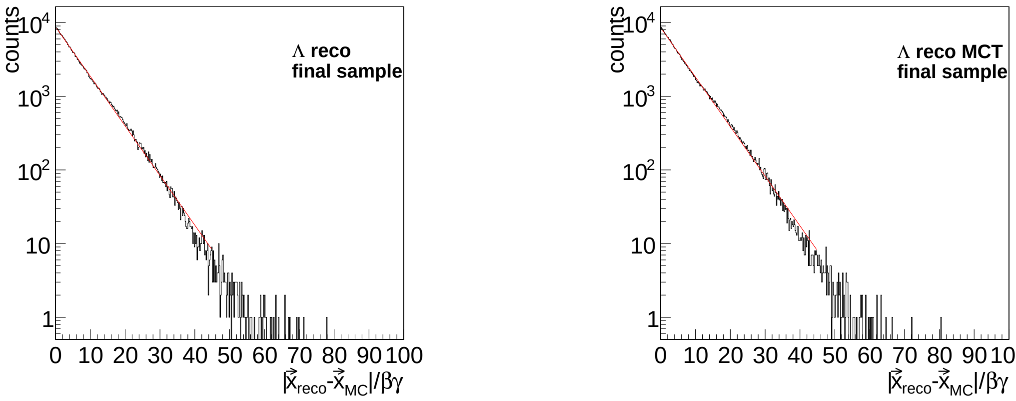

(a) (b)

Figure A.232: Propertime distribution for the reconstructed (a) and the MC partners (b) of the final selected Λ from Ξ^-.

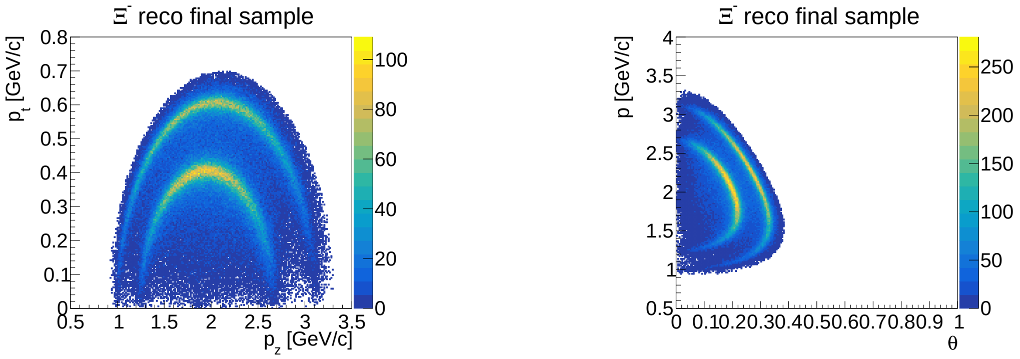

(a) (b)

Figure A.233: Transverse versus longitudinal momentum (a) and total momentum vs. Θ angle (b) for final selected Ξ^-.

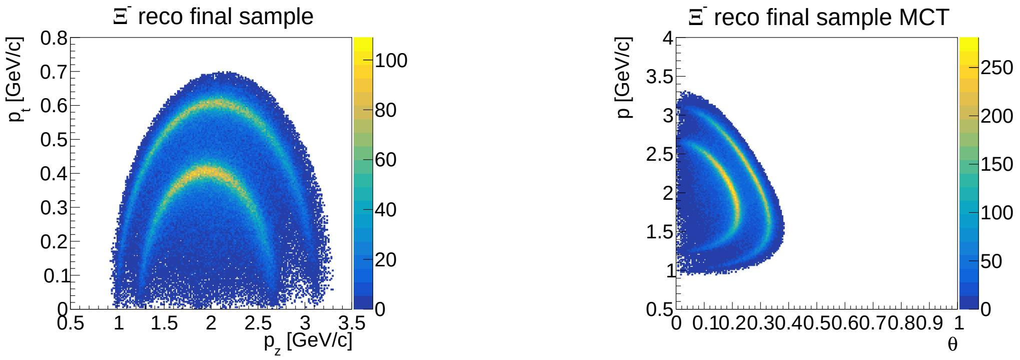

(a) (b)

Figure A.234: Transverse versus longitudinal momentum (a) and total momentum vs. Θ angle (b) for the MC partner of the final selected Ξ^-.

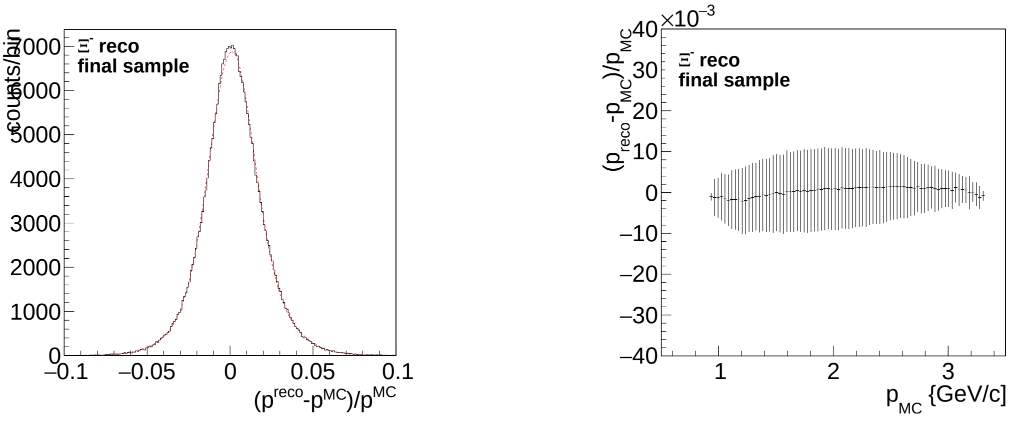

(a) (b)

Figure A.235: Momentum resolution (a) and relative deviation of the reconstructed and generated total momentum (b) for the final selected Ξ^-.

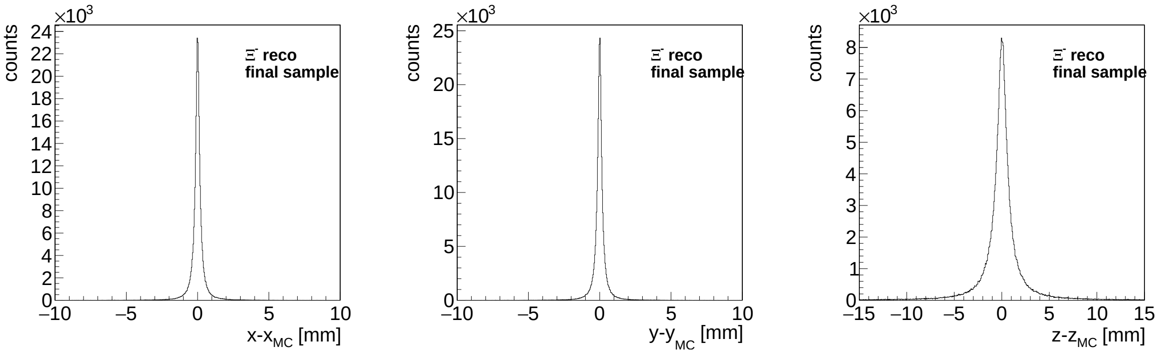

(a) (b) (c)

Figure A.236: Deviation of the final reconstructed Ξ^- decay vertex position and the corresponding MC decay vertex position for the x coordinate (a), the y coordinate (b) and the z coordinate (c).

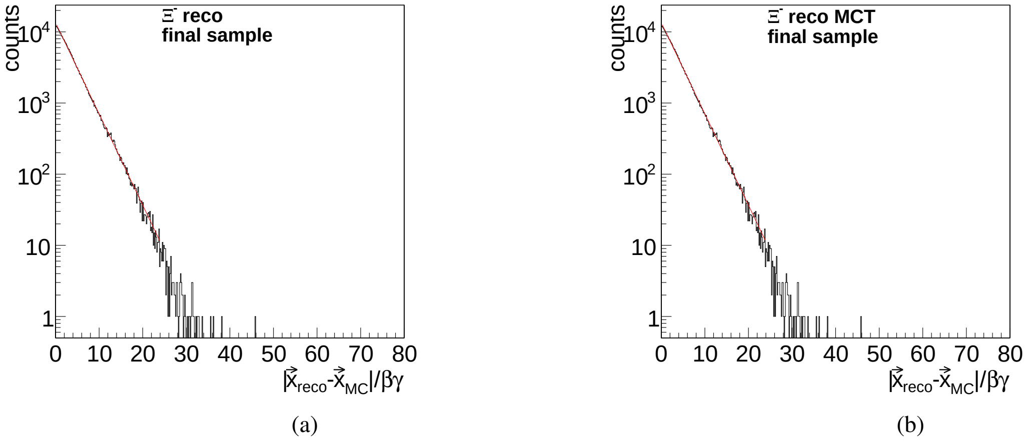

Figure A.237: Propertime distribution for the reconstructed (a) and the MC partners (b) of the final selected Ξ^-.

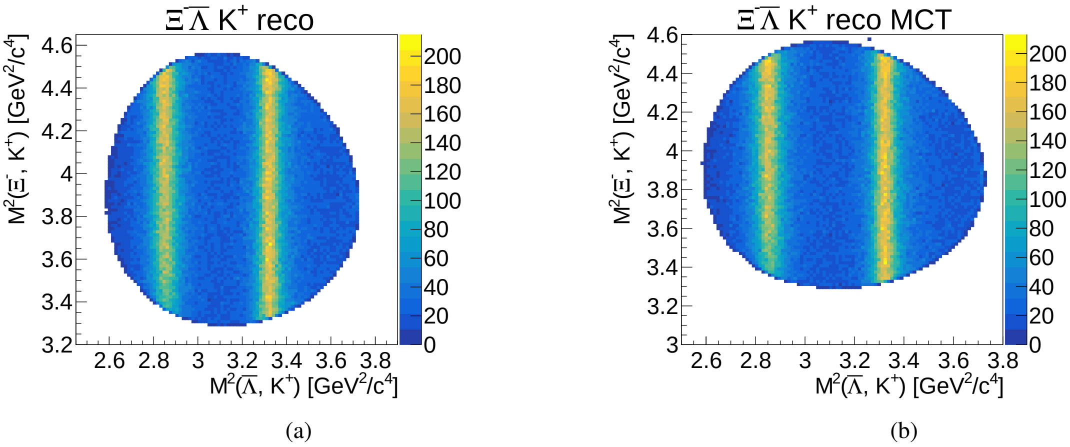

Figure A.238: Dalitz plot for the final selected candidate (a) and their MC partners (b).

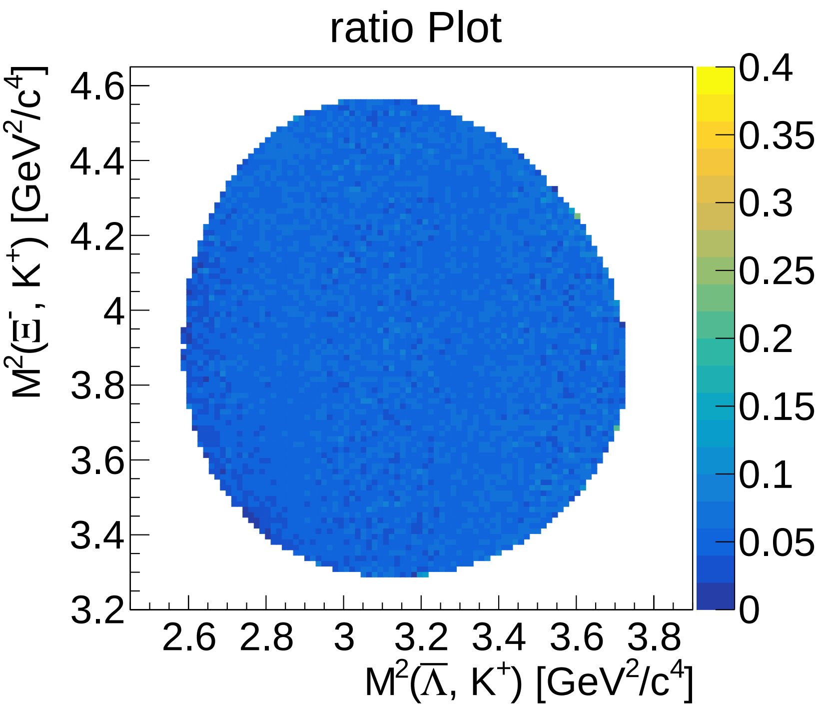

Figure A.239: Ratio of generated Dalitz plot and Dalitz plot for the MC truth partner of the final selected $\bar{p}p \to \Xi^-$ $\bar{\Lambda}$ K^+ candidates.

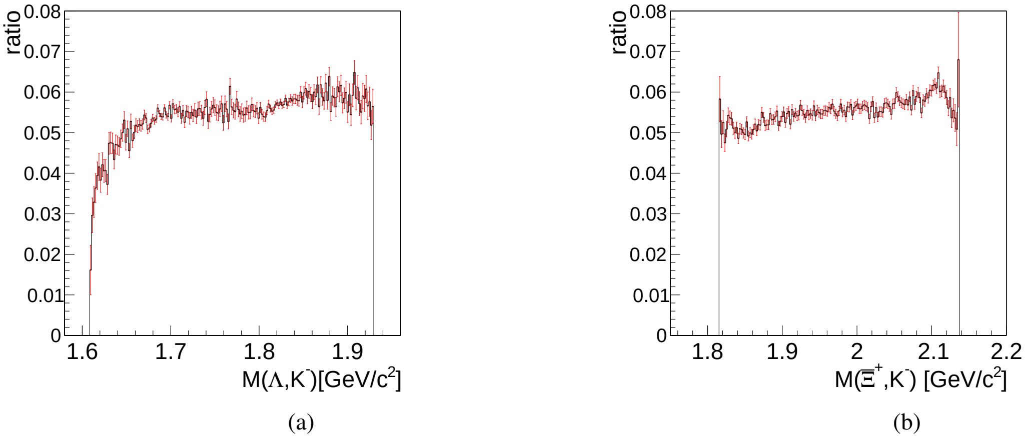

(a)

(b)

Figure A.240: Ratio of generated mass and mass of MC partner of the final selected $\bar{\Lambda}$ K^+ (a) and Ξ^- K^+ (b).

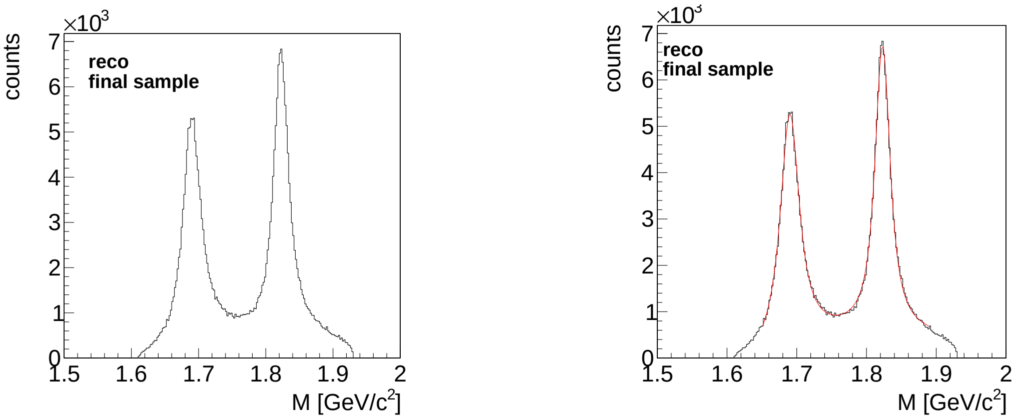

(a)

(b)

Figure A.241: Mass distribution of the $\bar{\Lambda}$ K^+ system: a) unfitted and b) fitted with the sum of two Voigt functions and a polynomial.

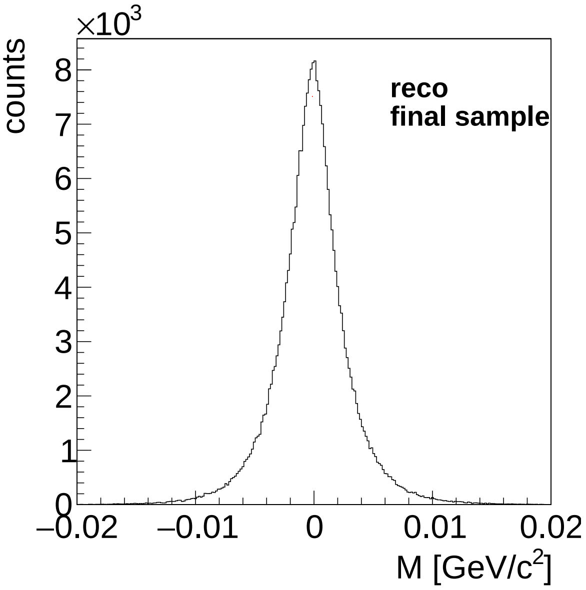

Figure A.242: Deviation of final reconstructed and generate $\bar{\Lambda}$ K^+ mass

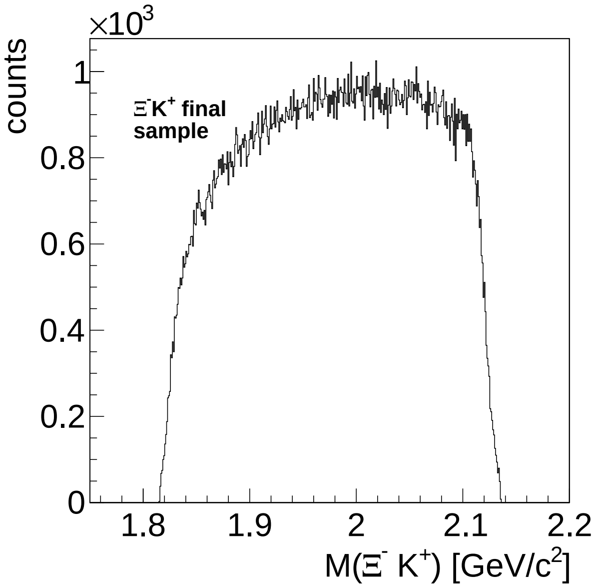

Figure A.243: Mass distribution for the final selected Ξ^- K^+.

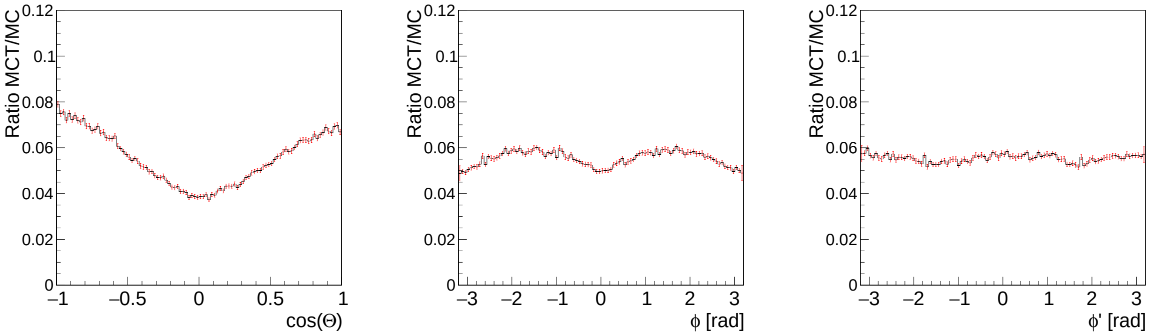

(a) (b) (c)

Figure A.244: $\cos\theta_{\rm cm}$ (a), $\phi_{\rm cm}$ (b) and $\phi\prime_{\rm cm}$ ratio between the MC partners of the final reconstructed candidates and the generated sample.

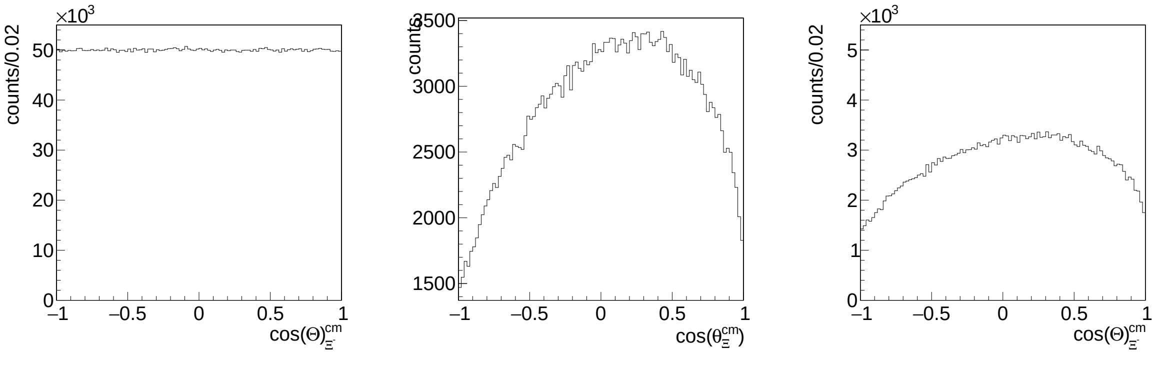

(a) (b) (c)

Figure A.245: Generated (a) and reconstructed (b) $\cos\theta$ distribution in the center-of-mass frame for final selected Ξ^- as well as the distribution for the MC partners of the reconstructed Ξ^- candidates (c).

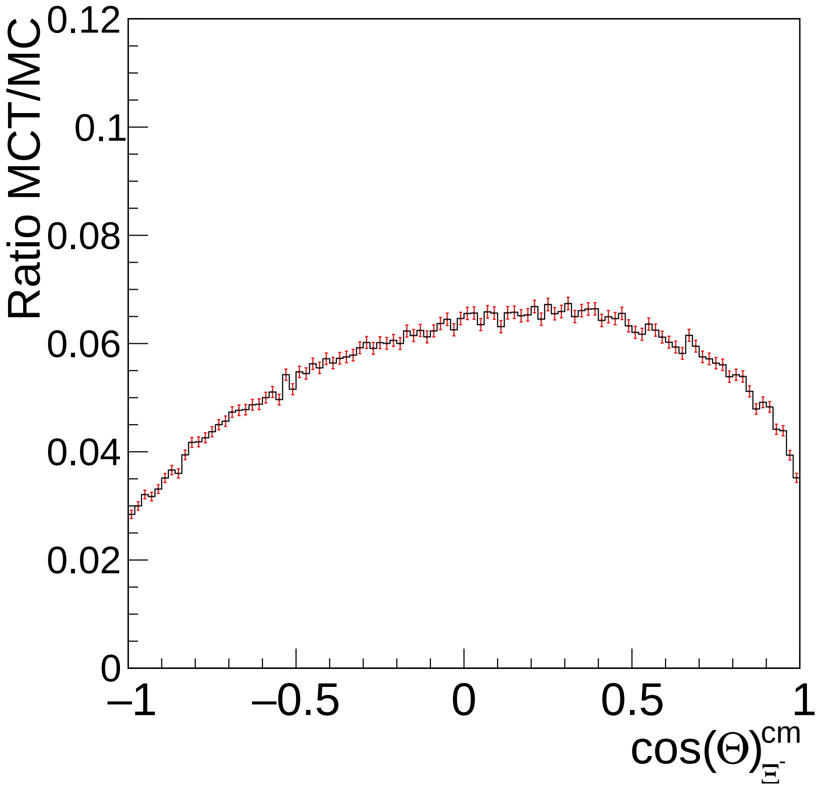

Figure A.246: Ratio plot of the cos θ distribution in the center-of-mass frame for the final selected $\overline{\Xi}^+$ candidates.

APPENDIX **B**

Additional Plots for the Determination of J^P

B.1 Dalitz Plots for Generated Events

Single Resonances

Ξ (1690)$^-$

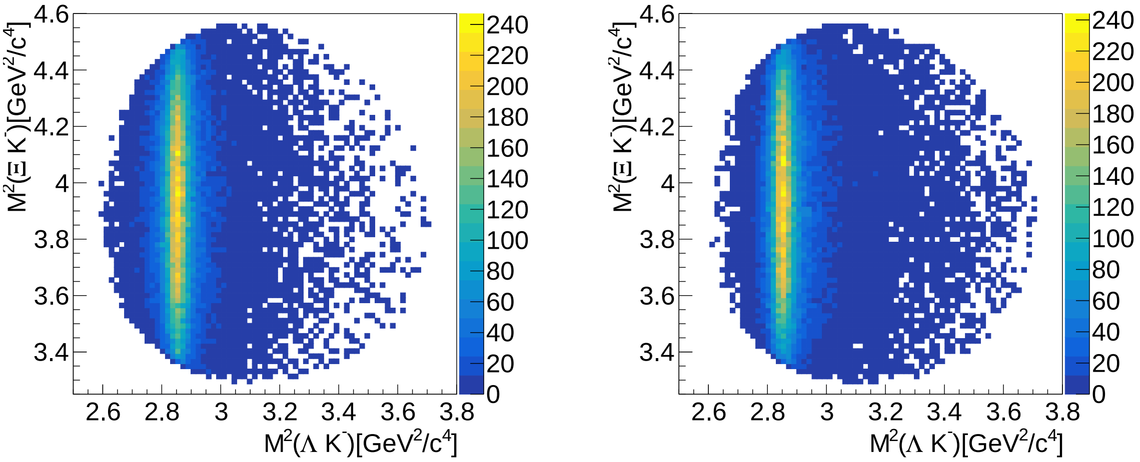

(a) (b)

Figure B.1: Dalitz plot for generated $\Xi\,(1690)^-$ with $3/2^+$ (a) and $3/2^-$ (b) hypothesis.

Ξ (1820)$^-$

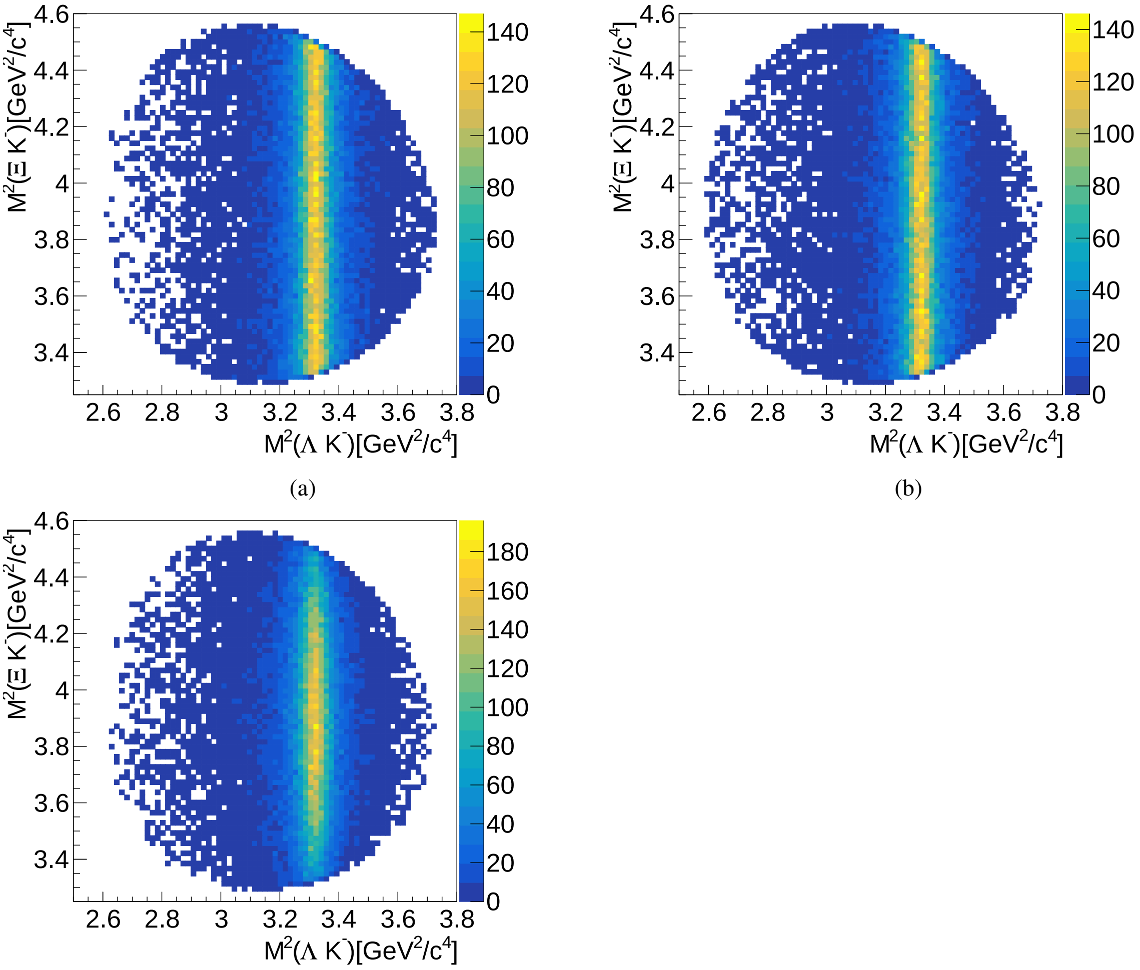

(a)

(b)

(c)

Figure B.2: Dalitz plot for generated Ξ (1820)$^-$ with 1/2$^+$ (a), 1/2$^-$ (b) and 3/2$^+$ (c) hypothesis.

Included Cross Channel

Ξ (1690)⁻

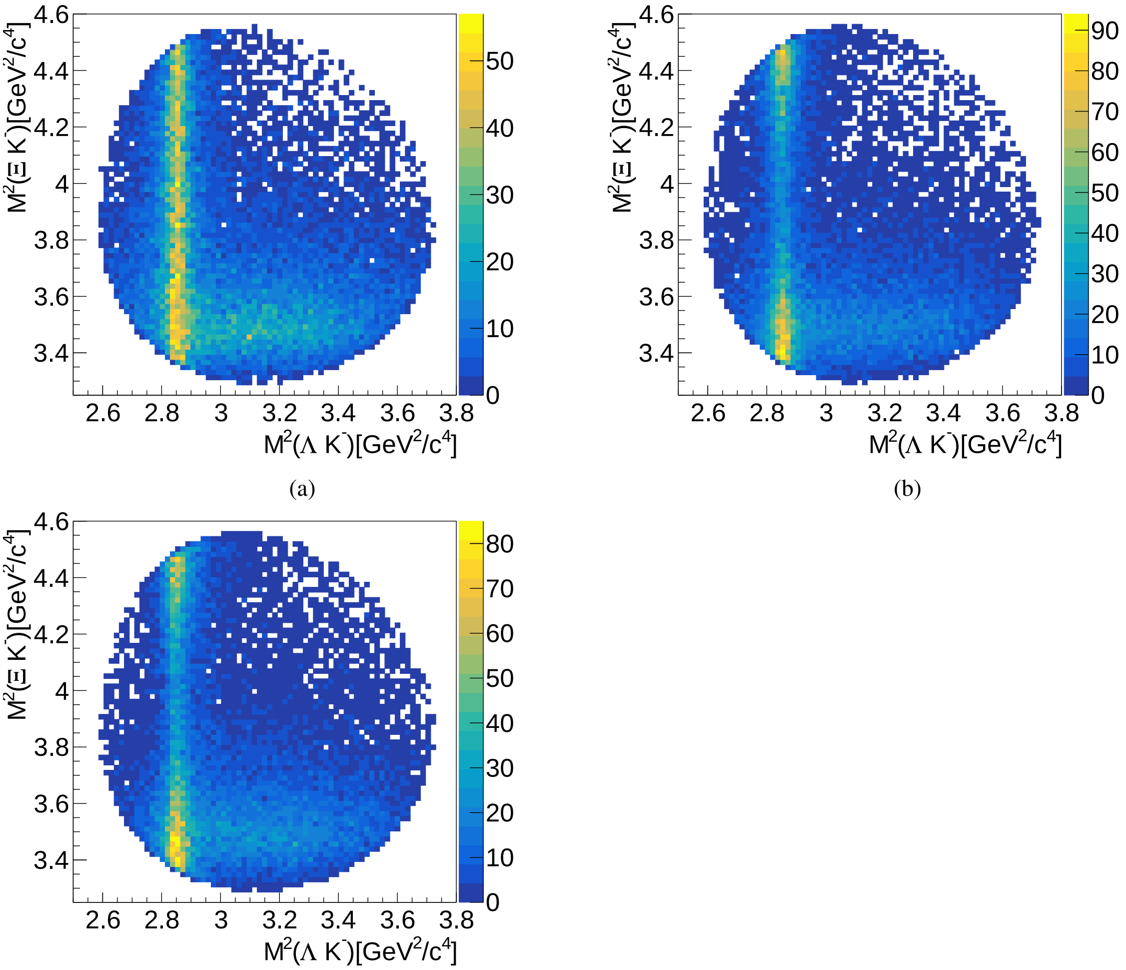

(a)

(b)

(c)

Figure B.3: Dalitz plot for generated Ξ (1690)⁻ with $1/2^-$ (a), $3/2^+$ (b) and $3/2^-$ (c) hypothesis including also the crossed channel.

Ξ (1820)$^-$

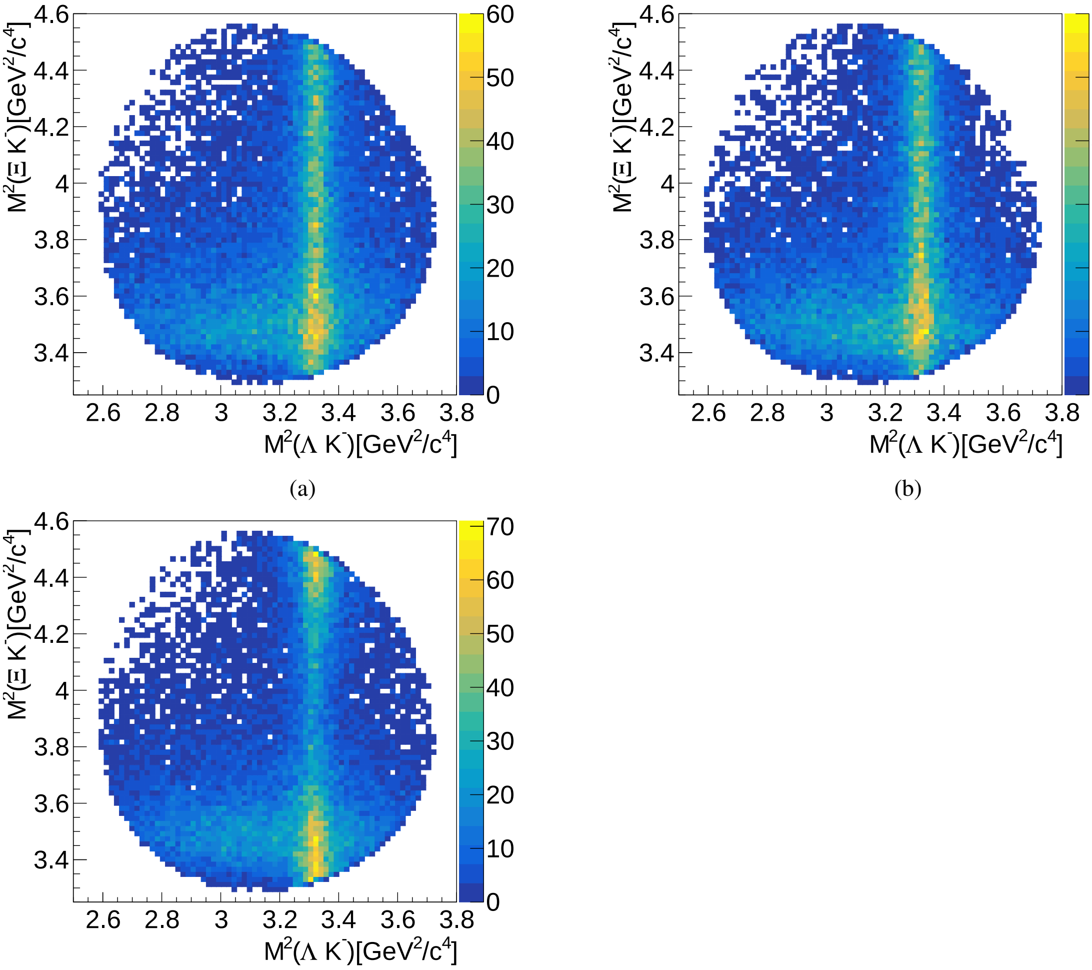

(a)

(b)

(c)

Figure B.4: Dalitz plot for generated Ξ (1820)$^-$ with $1/2^+$ (a), $1/2^-$ (b) and $3/2^+$ hypothesis including also the crossed channel.

B.2 Dalitz Plots for Fitted Events

Single Resonances

Ξ (1690)$^-$

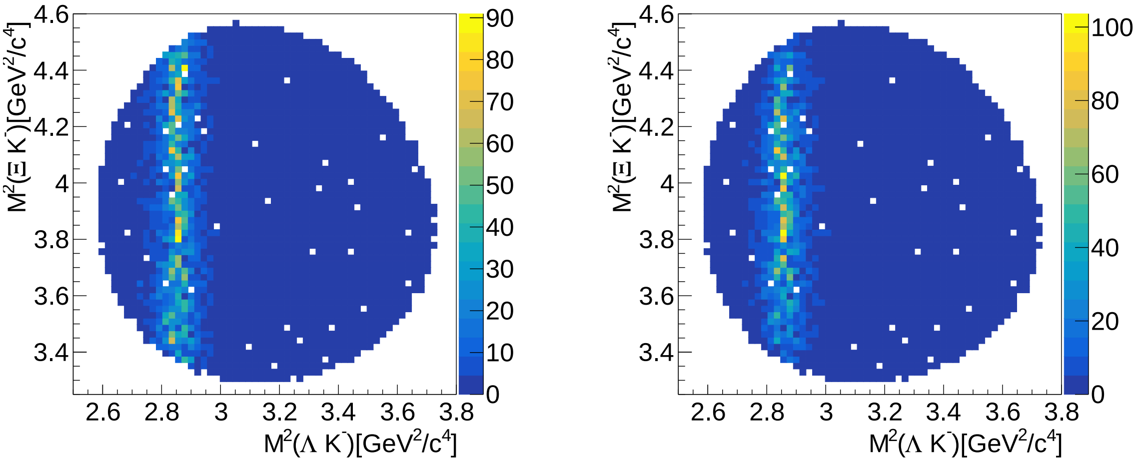

(a)

(b)

Figure B.5: Dalitz plot for Ξ (1690)$^-$ with fitted $3/2^+$ (a) and $3/2^-$ (b) hypothesis.

Ξ (1820)⁻

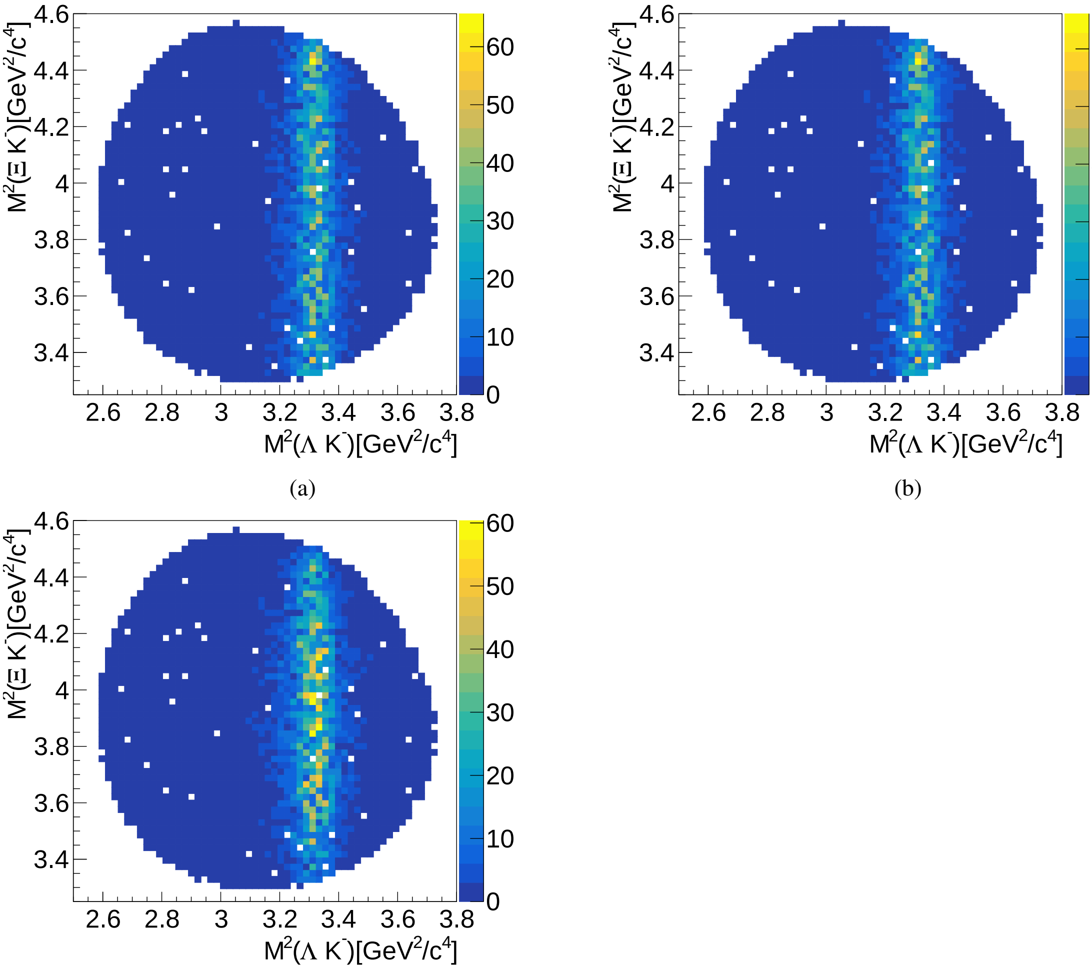

(a)

(b)

(c)

Figure B.6: Dalitz plot for Ξ (1820)⁻ with fitted $1/2^+$ (a), $1/2^-$ (b) and $3/2^+$ hypothesis.

Included Cross Channel

Ξ (1690)⁻

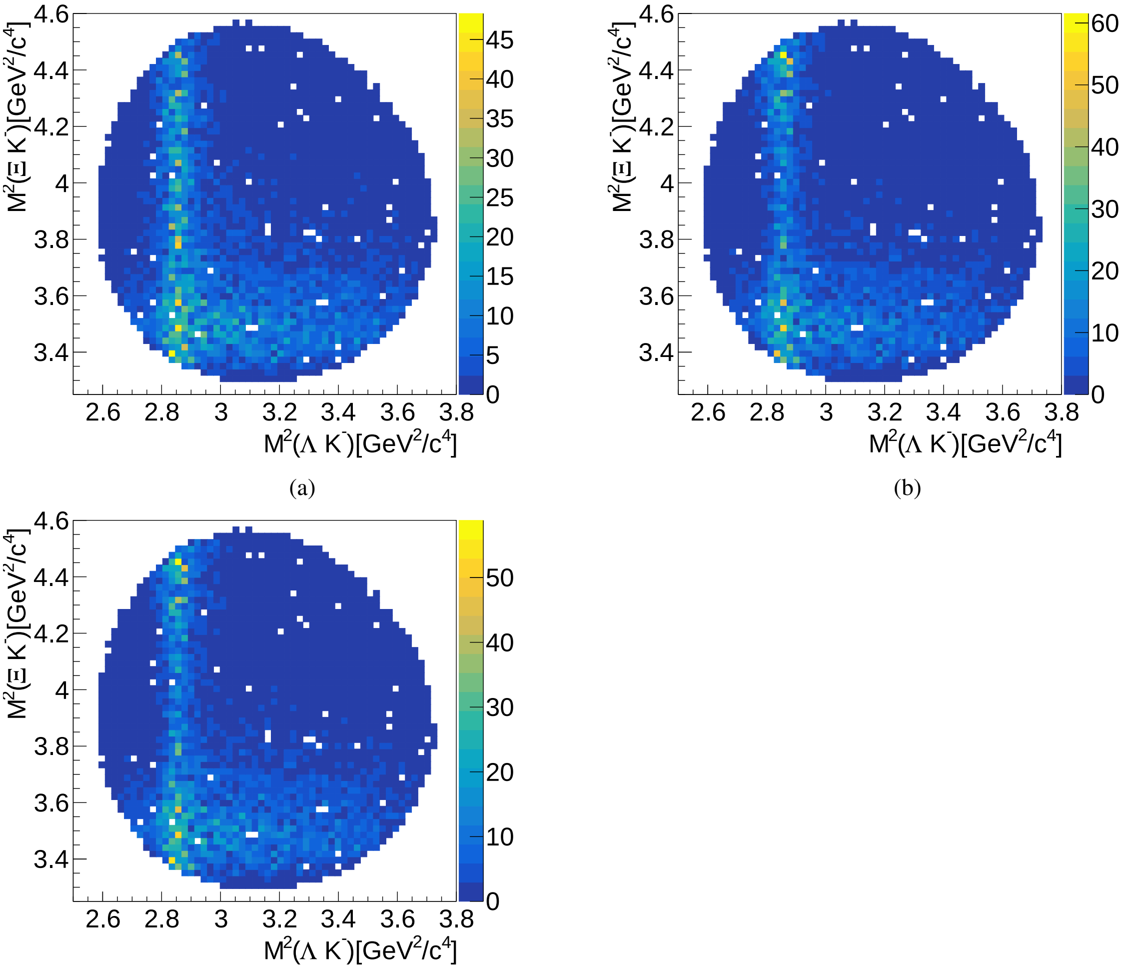

(a)

(b)

(c)

Figure B.7: Dalitz plot for $\Xi(1690)^-$ with fitted $1/2^-$ (a), $3/2^+$ (b) and $3/2^-$ hypothesis including also the crossed channel.

Ξ (1820)$^-$

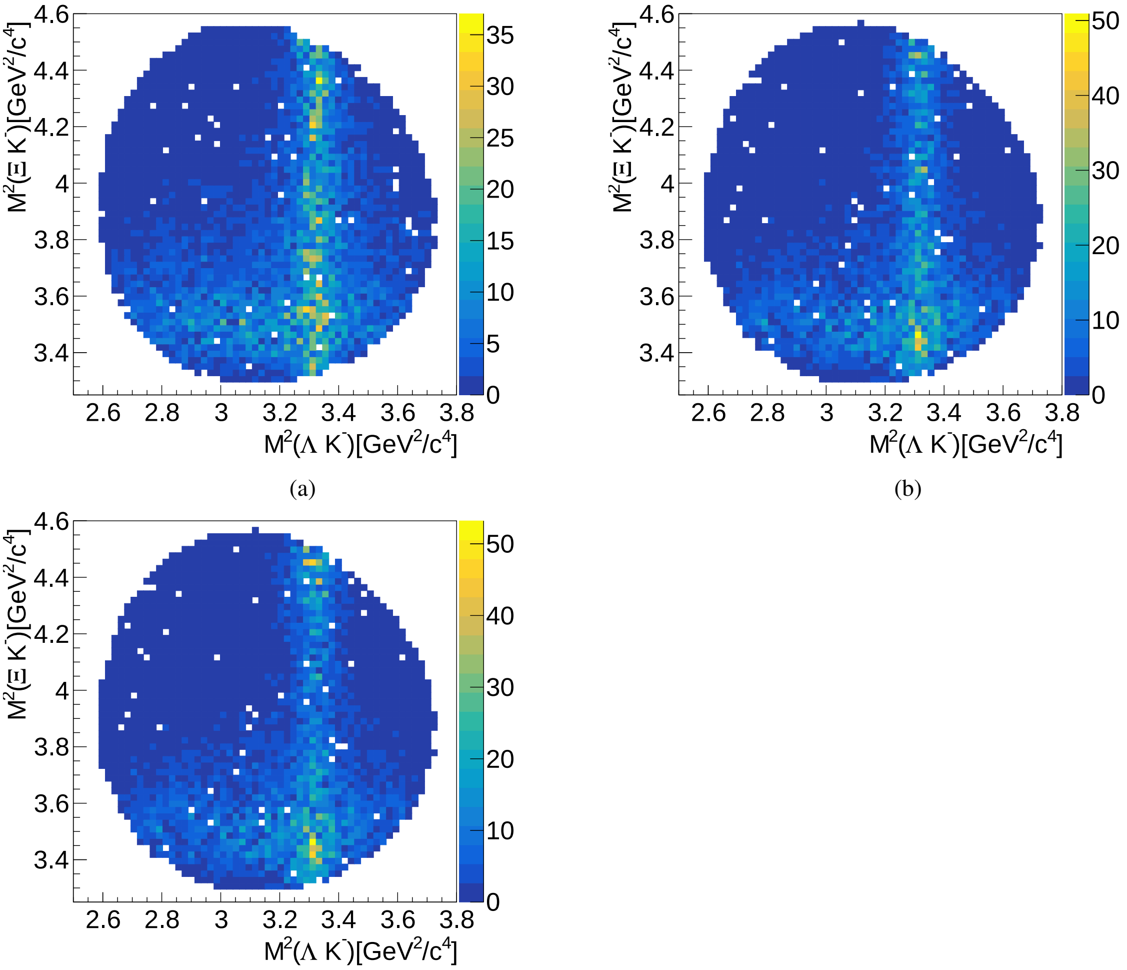

(a)

(b)

(c)

Figure B.8: Dalitz plot for Ξ (1820)$^-$ with fitted $1/2^+$ (a), $1/2^-$ (b) and $3/2^+$ hypothesis including also the crossed channel.

B.3 Comparison of cos Θ Distributions

Single Resonances

Ξ (1690)⁻

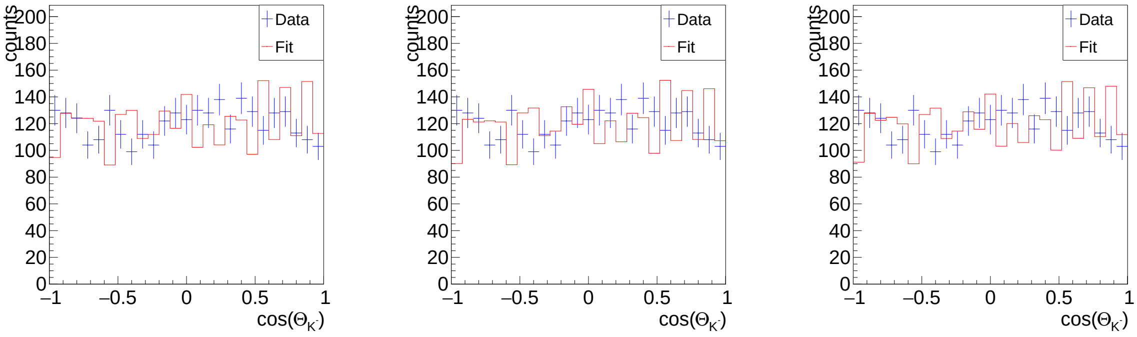

(a) (b) (c)

Figure B.9: Angular distribution of K⁻ from Ξ (1690)⁻ with generated $J^P = 1/2^-$ and fitted $1/2^+$ (a), $3/2^+$ (b) and $3/2^-$ (c).

Ξ (1820)⁻

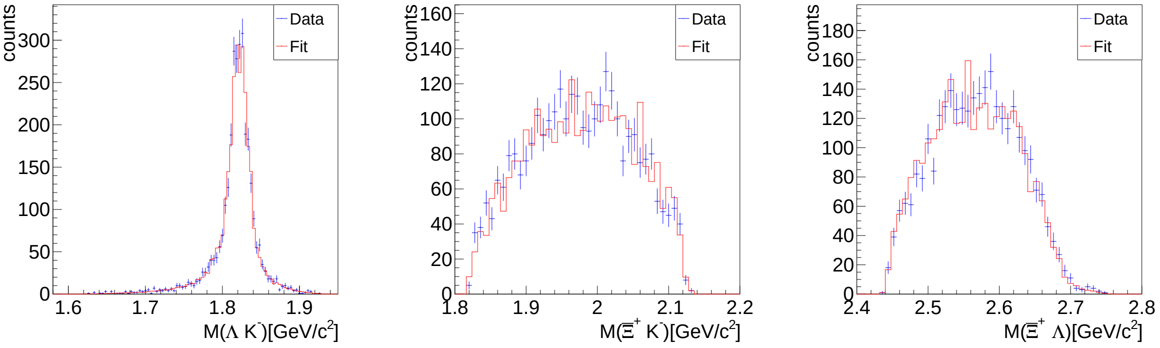

(a) (b) (c)

Figure B.10: Mass distributions for Λ K⁻ (a), $\overline{\Xi}^+$ K⁻ (b) and $\overline{\Xi}^+$ Λ (c). The Ξ (1820)⁻ is generated and fitted with $J^P = 3/2^+$.

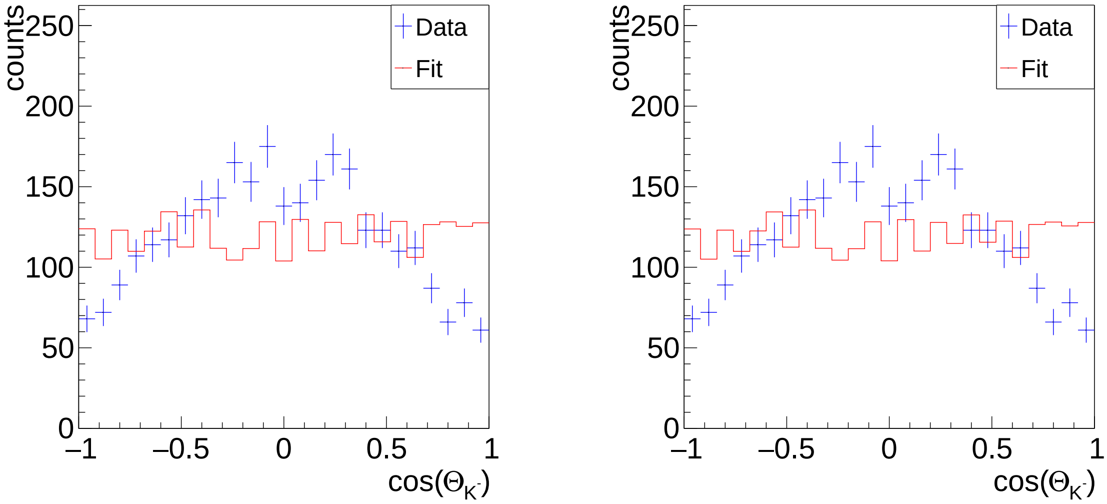

(a) (b)

Figure B.11: Angular distribution of K^- for $\Xi(1820)^-$ with fitted $1/2^+$ (a) and $1/2^-$ (b) hypothesis, and generated $J^P = 3/2^+$ and $L_{\max} = 0$.

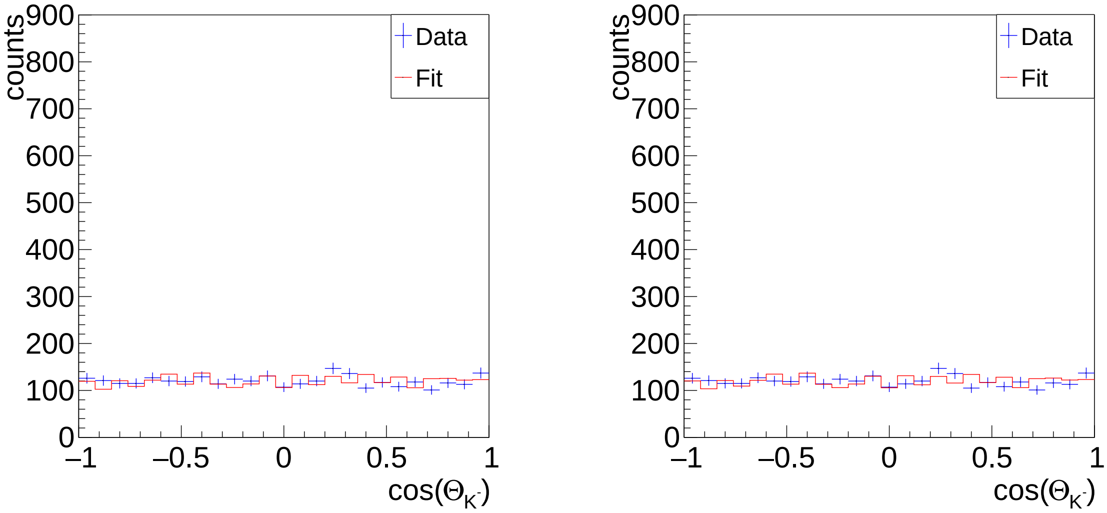

(a) (b)

Figure B.12: Angular distribution of K^- for $\Xi(1820)^-$ with fitted $3/2^+$ (a) and $3/2^-$ (b) hypothesis, and generated $J^P = 1/2^-$ and $L_{\max} = 0$.

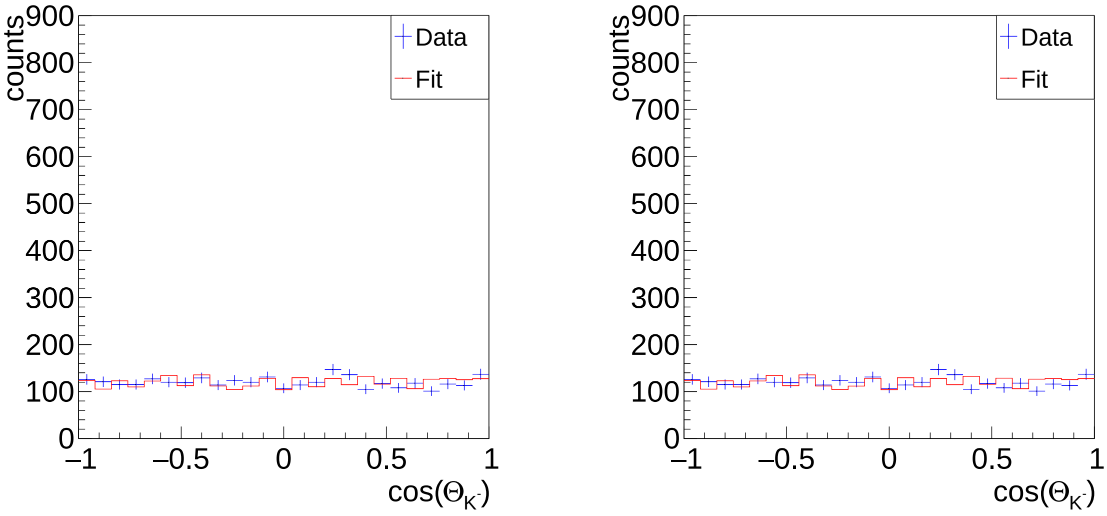

(a) (b)

Figure B.13: Angular distribution of K$^-$ for Ξ (1820)$^-$ with fitted $1/2^+$ (a) and $1/2^-$ (b) hypothesis, and generated $J^P = 1/2^-$ and $L_{\max} = 0$.

Included Cross Channel

Ξ (1690)⁻

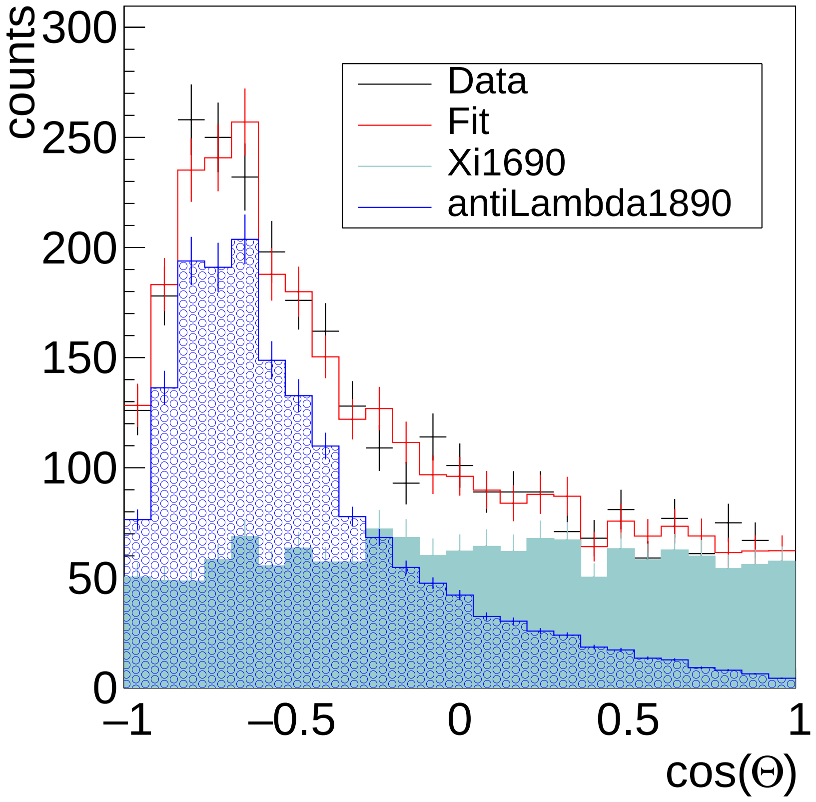

Figure B.14: Angular distribution of K⁻ from Ξ (1690)⁻ with generated $J^P = 1/2^+$ and fitted $3/2^-$.

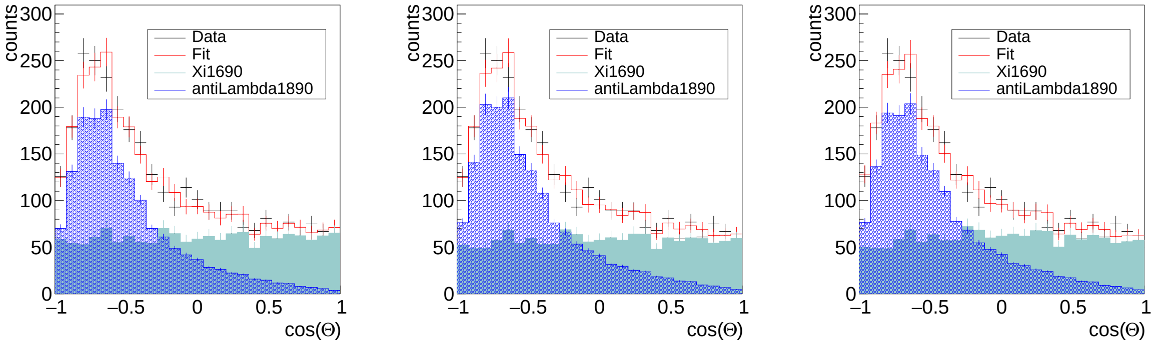

(a) (b) (c)

Figure B.15: Angular distribution of K$^-$ from Ξ (1690)$^-$ with generated $J^P = 1/2^-$ and fitted $1/2^+$ (a), $3/2^+$ (b) and $3/2^-$ (c).

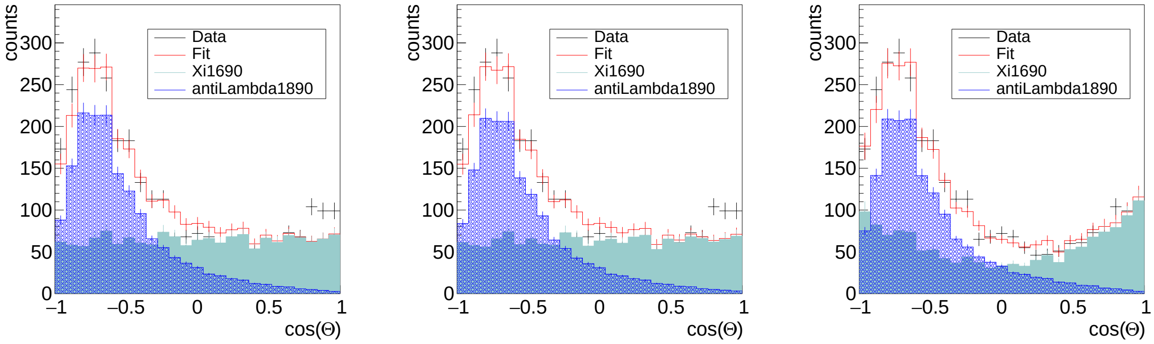

(a) (b) (c)

Figure B.16: Angular distribution of K$^-$ from Ξ (1690)$^-$ with generated $J^P = 3/2^+$ and fitted $1/2^+$ (a), $1/2^-$ (b) and $3/2^-$ (c).

Ξ (1820)$^-$

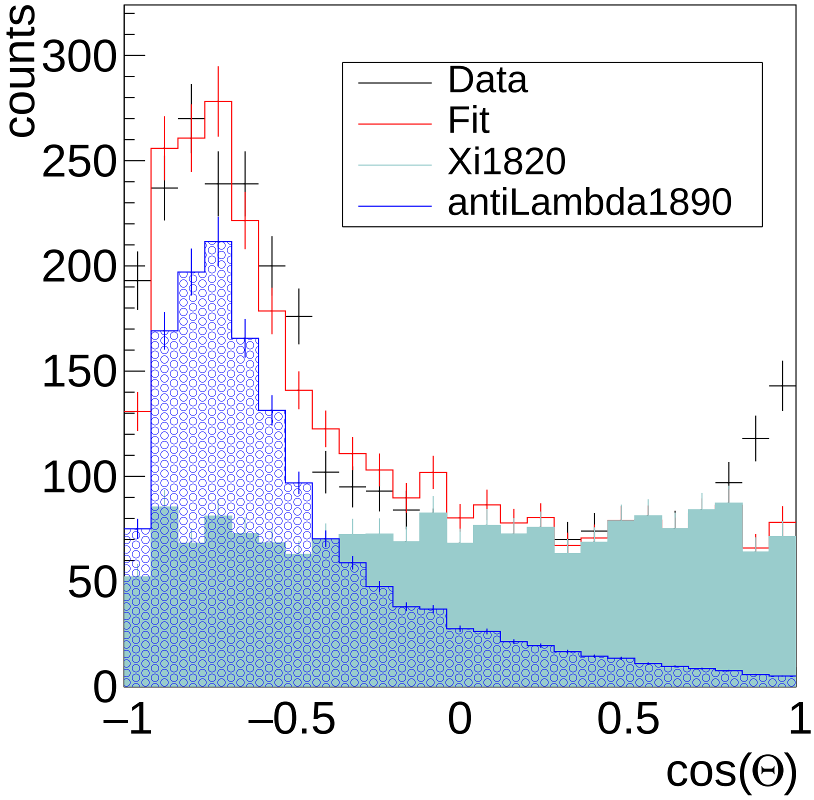

Figure B.17: Angular distribution of K$^-$ from $\Xi(1820)^-$ with generated $J^P = 3/2^-$ and fitted $1/2^-$.

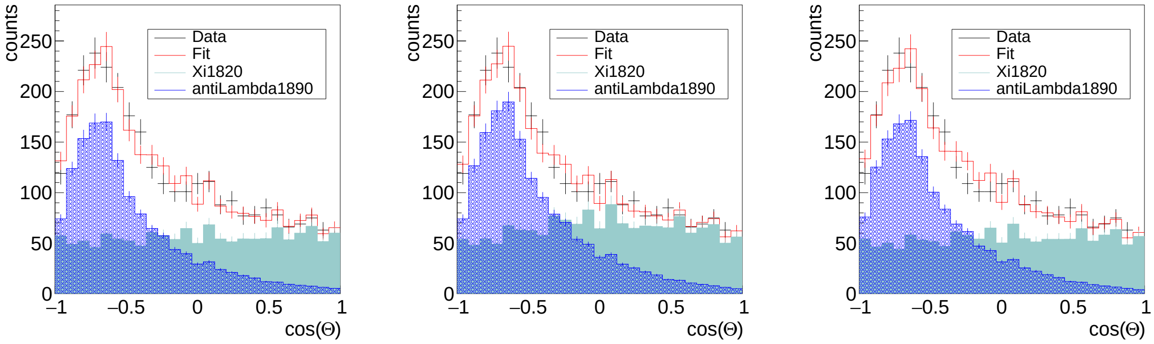

(a)

(b)

(c)

Figure B.18: Angular distribution of K$^-$ from $\Xi(1820)^-$ with generated $J^P = 1/2^+$ and fitted $1/2^-$ (a), $3/2^+$ (b) and $3/2^-$ (c).

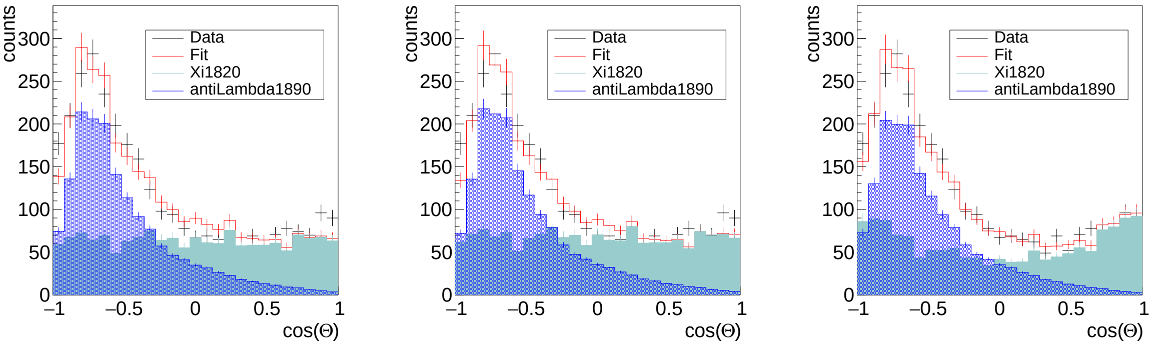

(a) (b) (c)

Figure B.19: Angular distribution of K^- from $\Xi(1820)^-$ with generated $J^P = 3/2^+$ and fitted $1/2^+$ (a), $1/2^-$ (b) and $3/2^-$ (c).

List of Figures

List of Tables

Glossary

4C-fit Kinematic fit with the constraint to match to a given four-momentum vector.. 64, 65, 201, 276

AIC Akaike information criterion estimates the relative quality of statistical models given for a dataset.. 113

BIC Bayesian information criterion is a criterion to select a model among a finite set of models.. 113

CRYRING A heavy ion storage ring which was located at MSL and transferred to GSI.. 15

DecayTreeFitter Fitting procedure to fit the whole decay tree, recursively.. 86, 139

DPM Event generator using the Dual Parton Model.. 94

ESR Storage ring at GSI.. 16, 17

EvtGen EvtGen is a particle decay simulation package. [132]. 40, 44

FairRoot Common software framework used for all FAIR experiments.. 40

Fluka Fully integrated Monte Carlo simulation package for particle physics.. 40

GEANE Software tool to extrapolate the track parameters and their associated errors due to magnetic field, straggling in energy loss and Coulomb multiple scattering inside dense materials.. 40

Geant3 Simulation software for the description of the passage of particles through matter. GEANT is an acronym for GEometry ANd Tracking.. 40

GEANT4 Simulation tool kit for propagation and decay of particles.[158]. 40, 45

GENFIT Generic track fitting toolkit [134].. 40, 49

HESR The High Energy Storage Ring is part of the future FAIR facility.. 18–21, 24, 30, 97, 275

LEAR The Low Energy Antiproton Ring decelerated and stored antimatter between 1982 and 1996 at CERN.. 24

LHCb One of the detectors at the LHC at CERN.. 13

LSR The Low Energy Storage Ring decelerates antiprotons to 300 keV.. 15

MIGRAD Minimization algorithm used in MINUIT2.. 113

MINUIT Minimization package developed at CERN [151].. 113

MINUIT2 Minimization package developed at CERN. It is a new version of MINUIT.. 113

MSV The modularized start version will be the first phase of FAIR. 15, 18, 20

p-LINAC A planned linear accelerator for the FAIR complex.. 17

PandaRoot Software frame work used for the $\overline{\text{P}}$ANDA experiment.. 40, 41, 141

PHSP The Phase Space model generates an isotropic angular distribution for a reaction.. 45

Pyhtia Simulation software for particle collisions at very high energies.. 40

ROOT Software package for data analysis in particle physics developed at CERN.. 40

SIS100 A planned synchrotron of theFAIR complex with a rigidity of 100 Tm.. 17–19

SIS18 Existing synchrotron of the GSI facility.. 17

SIS300 A planned synchrotron of theFAIR complex with a rigidity of 300 Tm.. 15, 17, 18

UNILAC Linear accelerator at GSI.. 17

USR The Ultra-low Energy Storage Ring decelerates antiprotons to 20 keV.. 15

Acronyms

$\overline{\mathrm{P}}$ANDA Antiproton Annihilation at Darmstadt. iii, v, 2, 15–19, 21–40, 97–99, 140, 141, 275

AIC Akaike information criterion . 113–115, 117, 131, 136

APPA Atomic, Plasma Physics and Applications. 15, 16

ASCII American Standard Code for Information Interchange. 40

BIC Bayesian information criterion . 113, 114, 117, 131, 136

BIOMAT Biology and Material Science. 15

c.c. charge conjugate. 44, 45, 102

CAD Computer Aided Design. 31, 33–36, 38–40, 275

CBM Compressed Baryonic Matter. 16

CERN European Organization for Nuclear Research. 9, 20

CR Collector Ring. 17–20

DIRC Detection of Internal Cherenkov Light. 34, 35, 275

DPM Dual Parton Model. 40, 94

EDM Estimated Distance to Minimum. 113

EMC Electromagnetic Calorimeter. 37, 38, 275, 281

ESR Experimental Storage Ring. 16, 17

FAIR Facility for Antiproton and Ion Research. 2, 15, 17–21, 24, 40, 275

FLAIR Facility for Low-Energy Antiproton and Heavy Ion Research. 15

FSC Forward Spectrometer electromagnetic Calorimeter. 38, 39, 275

FT Forward Tracker. 30, 33, 34, 275

FToF Forward Time of Flight. 34, 36, 38, 275

FWHM Full Width at Half Maximum. 51, 52, 55, 58, 60, 62, 68, 89, 90, 92

FZJ Forschungszentrum Jülich. 29

GEM Gaseous Electron Multipliers. 32, 33, 46

GPD Generalized Parton Distribution. 26

GSI Helmholtzzentrum für Schwerionenforschung. 16, 17, 40, 275

HED@FAIR High Energy Density Science at FAIR. 16

HESR High Energy Storage Ring. 18–21, 24, 30, 97, 275

HV-MAPS High Voltage Monolythic Active Pixel Sensors. 39

INP Institut of Nuclear Physics. 19

ITEP Institut für Technische Physik. 29

KL Kullback-Leibler. 113

LEAR Low Energy Antiproton Ring. 24

LHC Large Hadron Collider. 6

LHCb Large Hadron Collider beauty. 13

LMD Luminosity Detector. 39, 275

LQCD Lattice Quantum Chromodynamics. 6, 23, 24

LRT Likelihood Ratio Test. 115

LSR Low Energy Storage Ring. 15

MC Monte Carlo. 23, 46–48, 55–57, 62, 64, 70–74, 76, 77, 80, 81, 83, 85, 87, 88, 91, 94, 95, 97, 98, 138, 139, 156, 158, 160, 162, 164, 166, 169, 170, 192, 202–206, 209, 212, 214, 216, 218, 220, 222, 224, 226, 227, 229, 231, 233, 235, 237, 239, 241, 243, 245, 247, 249–255, 257, 276–278

MCP-PMT Microchannel Plate PhotoMultiplier Tube. 35

MDS Muon Detector System. 34, 37, 38, 275

MDT Mini-Drift Tube. 37

MPEI Moscow Power Engineering Institute. 29

MSL Manne Siegbahn Laboratory. 15

MSV Modularized Start Version. 15, 18, 20

MVD Micro Vertex Detector. 30–32, 46, 275

NESR New Experimental Storage Ring. 15, 17, 18

NLL Negative Log-Likelihood function. 112, 116, 117, 119

NuSTAR Nuclear Structure, Astrophysics and Reactions. 16

p-LINAC Proton Linear Accelerator. 17

PAWIAN PArtial Wave Interactive ANalysis Sofware. 101, 112, 113, 115, 116, 134, 136–141

$PbWO_4$ Lead tungstate. 38

PCB Printed Circuit Board. 36

PDG Particle Data Group. 43

PHSP Phase Space. 45

PID particle identification. 34, 36, 40, 41, 45, 46, 74, 75, 97, 98, 139

PMT Photo Multiplier Tube. 35, 37

PWA Partial Wave Analysis. 2, 101, 115, 139

QAIC Quasi-AIC . 115

QCD Quantum Chromodynamics. 1, 4–7, 16, 23, 24, 26

QED Quantum Electrodynamics. 4, 22

QFT Quantum Field Theory. 4

RESR Recuperated Experimental Storage Ring. 15, 17–20, 24

RICH Ring Imaging Cherenkov. 34–36

RMS Root Mean Square. 49

SDM Spin Density Matrix. 110, 111

SiPM Silicon Photo Multiplier. 35

SLAC Stanford Linear Accelerator Center. 6

SM Standard Model of Particle Physics. 1–4, 281

SPARC Stored Particles Atomic Research Collaboration. 15, 16

STT Straw Tube Tracker. 30, 32–34, 46, 275

TDA Transition Distribution Amplitude. 26

ToF Time of Flight. 34–36, 275

TSL The Svedberg Laboratory. 29

UNILAC Universal Linear Accelerator. 17

UrQMD Ultra relativistic Quantum Molecular Dynamics. 40

USR Ultra-low Energy Storage Ring. 15

VMC Virtual Monte Carlo. 40

Acknowledgements

First of all, I would like to say that this thesis would not have been possible without the enormous support of many people.

I want to thank my supervisor Albrecht Gillitzer. I am very grateful for your supervision and your guidance over the past four years. Our discussions have always been very constructive and fruitful. I would especially like to thank you for your commitment to me and my work.

Another special thanks goes to James Ritman. Thank you for giving me the chance to write this thesis and for being part of your institute.

I would like to express my thanks to Tobias Stockmanns. Without your help with all software related questions, this thesis would have never been finished.

Then I would like to thank my colleagues and former colleagues from IKP. Alessandra, Andi, André, Anna, Dariusch, Elisabetta, Frank, Gabi, Huagen, Jakapat, Lu, Ludovico, Peter, Waleed and Yong: Thanks for the great time in the institute and for the common activities during the meetings. Artur, Günter, Jürgen and René, I really enjoyed our coffee breaks, thank you very much. Also thank you to Dominika, Daniel and Florian.

During the last phase of my thesis, I had the chance to work closely together with my colleagues from the Bochum university. Thank you Bertram and Malte for the chance to visit you and that you took the time to discuss all my questions about PAWIAN.

I would like to express another thanks to Christopher Wiebusch. Thank you for believing in me and encouraging me to proceed with the PhD after I had finished my master studies.

Vielen Dank an meine Eltern, die mir, trotz vieler Hürden, immer wieder den Rücken gestärkt und an mich geglaubt haben. Danke auch an meine Schwiegereltern für ihre tatkräftige Unterstützung bei der Kinderbetreuung.
And finally, my biggest ‘Thank you’ deserves my little family, Andreas and Jakob. Especially in the last phase of this work, you were my strongest moral support.